NASA - HBCU

Space Science and Engineering Research Forum Proceedings

March 22 - 23, 1989
Alabama A&M University
Huntsville, Alabama

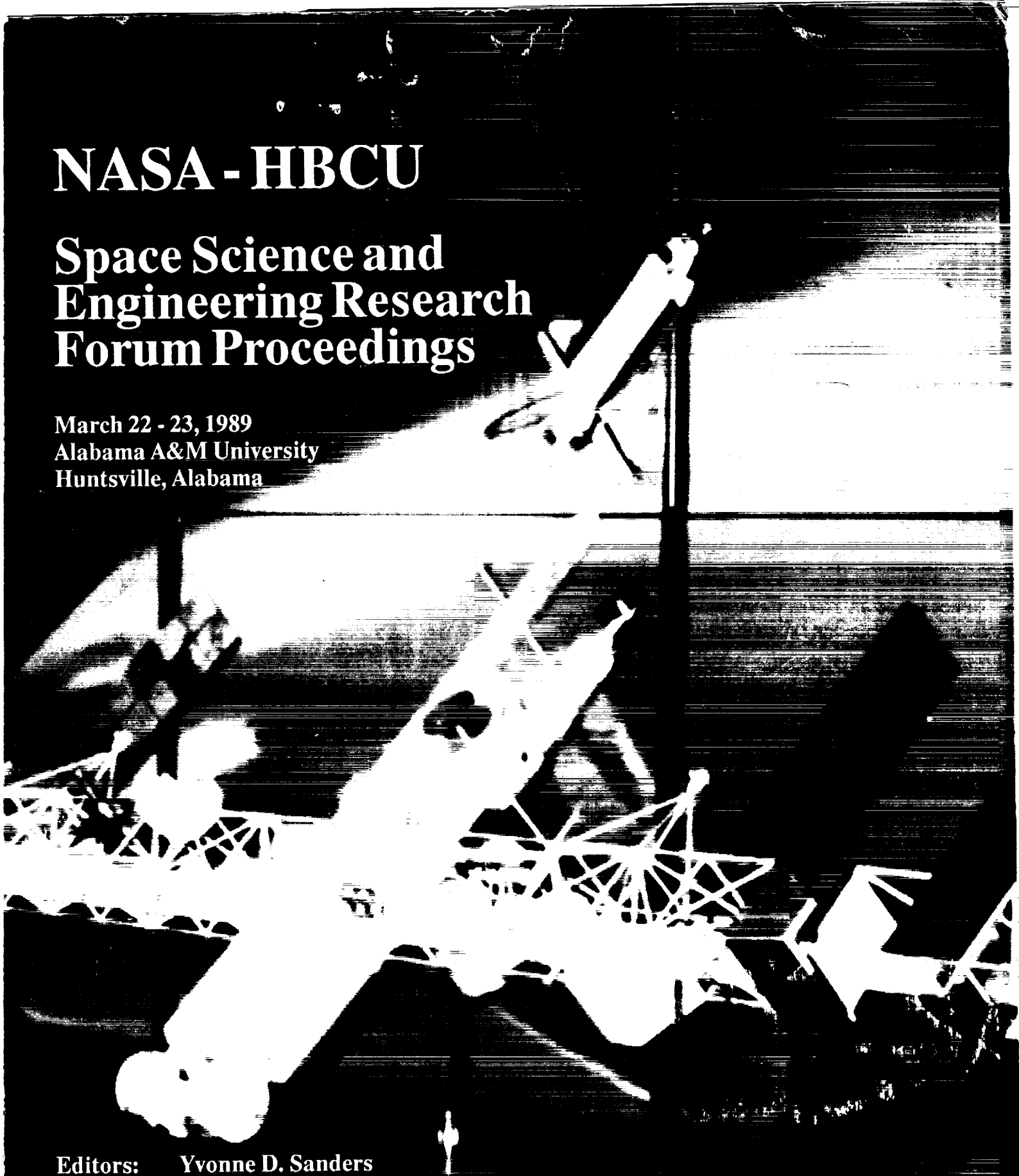

Editors: Yvonne D. Sanders
Yvonne B. Freeman
M.C. George

P536

NASA-HBCU

Space Science and Engineering Research Forum Proceedings

March 22 - 23, 1989
Alabama A&M University
Huntsville, Alabama

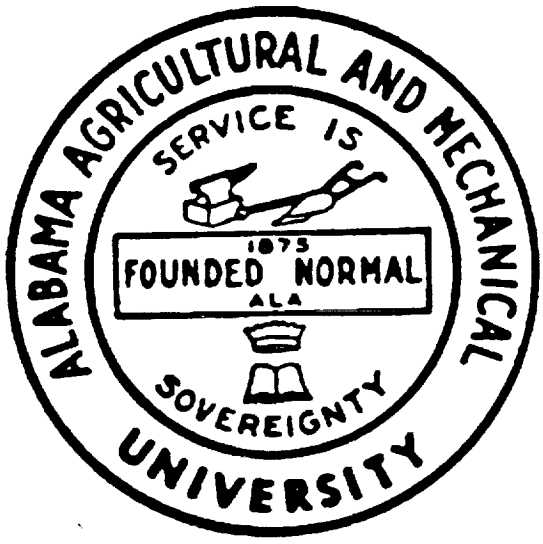

Editors: Yvonne D. Sanders
Yvonne B. Freeman
M.C. George

Typesetting and printing of this publication was performed by the University of Alabama in Huntsville Reproduction Services. Body text typeface is 11 point Dutch.

PREFACE

The role of science and scientific research in universities is well recognized by the public, university administrators, faculty and students. The National Aeronautics and Space Administration (NASA) has been and continues to be a leading supporter of research at universities. To enhance research at Historically Black Colleges and Universities (HBCUs) NASA has embarked upon a special program through its Office of Equal Opportunity that is designed to build greater research and training linkages among HBCUs and NASA centers. The program brings together active scientists and students who are pursuing research in broad areas and subjects of interest to NASA. It encourages collaboration by providing an opportunity for researchers to develop personal contacts with NASA and other universities and discuss the details in a structured, yet informal and relaxed atmosphere. It is hoped that these interactions will lead to long term collaborative research and a strengthening of research programs at HBCUs.

The success of the effort is being evidenced by increased participation of HBCU faculty in NASA-HBCU Space Science and Engineering Research Forums. The first and second NASA HBCU Research Forums held at Atlanta University have amply justified the validity of continuing such efforts. The 1989 forum, third in the series, was hosted by Alabama A&M University in Huntsville, Alabama March 22-23. The excellent participation exceeded previous forums with 338 registered participants representing 38 colleges and universities plus 207 high school students representing 27 regional high schools.

The organizing committee is pleased to publish the proceedings of the 1989 forum. There were many outstanding and significant contributions, keynote addresses, plenary papers, invited papers and contributed papers (both oral and poster) that formed the framework of this forum. The papers presented in this document cover a wide range of research topics from plant science to space science and related academic areas. Outreach activities being supported by NASA with the intention of replication in other educational institutions are also included.

These proceedings are not intended to replace publication of new and complete research results in those technical journals that cover the field. Rather, the brief accounts of research summarized here are intended to provide sufficient description (aided by a listing of key references) to enable the reader to understand the basis of what has been accomplished and where to find more detailed information. In some instances historical perspectives and thoughts on future directives are also presented.

The organizing committee expresses its appreciation to all the participants, the various NASA field centers and other academic and NASA administrators for their continued support. Special thanks goes out to Anesia Holland, Administrative Assistant, and the many Alabama A&M University, Marshall Space Flight Center, and NASA Code "U" coordinators; their efforts were essential for the success of the forum.

The Editors:

Yvonne Sanders, Project Coordinator
Alabama A&M University

Yvonne B. Freeman, Project Manager
NASA Headquarters

M. C. George, Project Director
Alabama A&M University

NASA-HBCU SPACE SCIENCE AND ENGINEERING RESEARCH FORUM

Program Agenda

Tuesday / March 21, 1989

6:00 PM— RECEPTION

Hillcrest
The President's Home
Alabama A&M University

8:00 PM— STUDENT RESEARCHER PRE-CONFERENCE PRESENTATION CLINIC
Elmore Health Science Complex
Room 5

Dr. Mildred Wyatt
Goddard Space Flight Center

Wednesday, March 22, 1989

8:00 AM— 3:00 PM REGISTRATION
Elmore Health Science Complex Lobby

8:00 AM— 8:30 AM CONTINENTAL BREAKFAST
Elmore Health Science Complex Lobby

GENERAL SESSION
Elmore Health Science Complex Gymnasium

8:30 AM OPENING REMARKS AND INTRODUCTION OF GUESTS

Dr. Carl Harris Marbury
President, Alabama A&M University, Presiding

8:40 AM WELCOME

The Honorable Steve Hettinger
Mayor of Huntsville, Alabama

8:45 AM— INTRODUCTION OF NASA ASSOCIATE DEPUTY ADMINISTRATOR

Mr. James R. Thompson
Director, Marshall Space Flight Center

8:50 AM KEYNOTE ADDRESS

Dr. Noel W. Hinners
Associate Deputy Administrator, NASA

9:20 AM INTRODUCTION OF GUEST LECTURER

Dr. M. C. George

Forum Coordinator, Alabama A&M University

9:25 AM GUEST LECTURER
AT&T Bell Laboratories
"Free Electron Laser Program"

Dr. Earl Shaw
AT&T Bell Laboratories

9:45 AM "SCIENTIST OF TOMORROW"
Program Component

Dr. Rather Brown
Director, Minority Access to Research Careers (MARC), Alabama A&M University

9:50 AM BREAK

10:00 AM— CONCURRENT SESSIONS I, II, III

12:00 AM— LUNCH
Elmore Health Science Complex Gymnasium

Mr. J. Albert Diggs
Director, Equal Opportunity Program Office
Kennedy Space Center, Presiding

INTRODUCTION OF LUNCHEON SPEAKER

Dr. Yvonne B. Freeman
Manager, Minority University Program, NASA Headquarters

SPEAKER

Dr. Ivan Van Sertima
Author-Professor, Rutgers University

2:00 PM— **NEW FRONTIER OPPORTUNITIES**
Elmore Health Science Complex, Room 5, Alabama A&M University

Mr. James R. Thompson
Director, Marshall Space Flight Center, Presiding

Dr. Lew Allen
Director, Jet Propulsion Laboratory
The JPL Historically Black College and University Initiative

Dr. C. Richard Chappell
Chief Scientist, Marshall Space Flight Center
NASA/University JOint VEnture to Enhance Space Science and Expand University Space Activities

Dr. Edward Fort,
Chancellor, North Carolina A&T State University

Dr. Samuel Massenberg
Langley Research Center, University Affairs Officer

Mr. Sal Majied, BDM Corporation
Space Technology Development and Utilization Program

Mr. Kyle O. Fairchild
Technology and Commercial Programs Division
New Initiatives Office, Johnson Space Center
Technology Challenges of the Future

1:45 PM— 4:00 PM CONCURRENT SESSIONS IV, V, VI, VII

4:00 PM— 6:00 PM SCIENTIST OF TOMORROW PROGRAM
Space and Rocket Center, 1 Tranquility Base, Huntsville, AL

Dr. Rather Brown
Director, Minority Access to Research Careers (MARC), Alabama A&M University, Presiding

"YOUTH CHALLENGE"

Mr. Homer McCall, Jr.
Senior Class President, Huntsville High School, Huntsville, Alabama

KEYNOTE ADDRESS

Dr. Mae C. Jemison
NASA Astronaut

TOUR
Space and Rocket Center

6:00 PM HOSPITALITY HOUR
The Space and Rocket Center Lobby

7:00 PM BANQUET
Space and Rocket Center

Mr. James Rice
Equal Opportunity Officer, Marshall Space Flight Center, Presiding

RECOGNITION OF SPECIAL GUESTS

Dr. Oscar Montgomery
Director, Office of Government Relations, Alabama A&M University

PRAYER

Dr. Phillip Redrick
Director, Institutional Advancement, Alabama A&M University

DINNER

INTRODUCTION OF SPEAKER

Mr. Lewin Warren
Deputy Assistant Administrator for Equal Opportunity Programs, NASA Headquarters

SPEAKER

Mr. Isaac Gillam
Senior Vice President, OAO Corporation

APPRECIATION

Dr. Bessie Jones
Dean, School of Arts and Sciences, Alabama A&M University

ADJOURNMENT

Thursday, March 23, 1989

8:00 AM— CONTINENTAL BREAKFAST
8:30 AM *Elmore Health Science Complex Lobby*

GENERAL SESSION
Elmore Health Science Complex Gymnasium

8:30 AM— **NASA FELLOWSHIP/TRAINING PROGRAMS**
9:45 AM

THE NATIONAL SPACE GRANT COLLEGE AND FELLOWSHIP PROGRAM

Ms. Sherri McGee
Education Specialist, Educational Affairs, NASA Headquarters

GRADUATE STUDENT RESEARCHER PROGRAM

Dr. Samuel Massenberg
University Affairs Officer, Langley Research Center

MINORITY GRADUATE PROGRAM

NASA/USRA UNIVERSITY ADVANCED SPACE DESIGN PROGRAM —
"MARS SURFACED-BASED FACTORY"

Dr. John Fuller
Professor, Prairie View A&M University

SPACE LIFE SCIENCES TRAINING PROGRAM

Dr. Kenneth Redda
Program Coordinator, Florida A&M University

9:45 AM— BREAK

10:00 AM— CONCURRENT SESSIONS VIII, IX, X
12:00 AM

12:00 AM— LUNCH
1:30 PM *Prentice Hall Banquet Room*

Dr. Joseph D. Atkinson, Jr.
Equal Opportunity Officer, Johnson Space Center, presiding

SPEAKER

Dr. Julian Earls
Chief, Health Safety and Security Division, Lewis Research Center

1:45 PM— CONCURRENT SESSIONS XI, XII, XIII
3:45 PM

POSTER PRESENTATIONS

4:00 PM— TOUR OF RESEARCH LABORATORIES
5:00 PM ALABAMA A&M UNIVERSITY

CONCURRENT SESSIONS

SESSION I

Wednesday / March 22

10:00 AM— *Elmore Health Science Complex, Lecture Room*
12:00 noon

PRESIDING:

Dr. Yvonne B. Freeman
NASA Headquarters

RESEARCH AND TRAINING PROGRAMS

10:00 AM— **"Women in Science and Engineering Scholars Program."** *Institution:* Spelman College, *Project Director:* Dr. Etta Falconer, *Technical Monitor:* Ms. Betty White (HQ-UI)

10:20 AM **"UDC Saturday Academy - Engineering, Mathematics and Computer Sciences for Academically Talented Students."** *Institution:* University of the District of Columbia, *Project Director:* Dr. Winson R. Coleman, *Technical Monitor:* Dr. Yvonne Freeman (HQ-U).

10:40 AM **"Project LEAP Engineering Bridge Program,"** and **"Project PRESERVE Institutional Engineering Program."** *Institution:* Xavier University of New Orleans, *Project Director:* Mr. G. Baker and Dr. Carole Morning, *Technical Monitor:* Dr. Yvonne Freeman (HQ-U).

11:00 AM **"Lincoln University Aerospace and Engineering (LASER) Program."** *Institution:* Lincoln University, *Project Director:* Dr. Willie Williams, *Technical Monitor:* Dillard Menchan (GSFC).

11:20 AM **"Summer Intern Program for Disabled Students in Technical Fields."** *Institution:* Gallaudet University, *Project Director:* Anne Nissen, *Technical Monitor:* Ms. Lynda Sampson (HQ-UI).

11:40 AM **"Massachusetts Pre-Engineering Mass PEP Program for Minority Students."** *Institution:* Wentworth Institute of Technology, *Project Director:* Dr. Anthony Maddox, *Technical Monitor:* Ms. Betty White (HQ-UI).

SESSION II

Wednesday / March 22

10:00 AM— *Elmore Health Science Complex, Room 6*
12:00 NOON

PRESIDING:

Dr. John Hall
Milligan Science Research Institute, Atlanta University Center, Inc.

SPACE PROCESSING AND UTILIZATION

10:00 AM **"Optically Controlled Millimeter Wave Devices"**, Institution: Howard University, *Principal Investigator:* Dr. Raj Chowdhary, *Technical Monitor:* Dr. A. S. Burgess (GSFC).

10:20 AM **"A Study on Growth and Characterization of Ternary ZnxCd1-xTe Single Crystals."** *Institution:* Fisk University, *Principal Investigator:* Dr. Enrique Silberman, *Co-Investigators:* Dr. A. Burger, Dr. D. Henderson, Dr. S. Morgan and Dr. T. Springer, *Technical Monitor:* Dr. S. L. Lehoczky (MSFC).

10:40 AM **"Solution Growth of TGS Crystals on International Microgravity Laboratory (IML-1)."** *Institution:* Alabama A&M University, *Principal Investigator:* Dr. R. B. Lal, *Co-Investigators:* Dr. James Trolinger, Dr. William Wilcox, Dr. A. K. Batra, *Student Researcher:* Li Yang, *Technical Monitor:* Mr. Rudolph Ruff (MSFC).

11:00 AM **"Electrode Erosion in Low Power Constricted Arcjet Thrusters."** *Institution:* Tuskegee University, *Principal Investigator:* Dr. Pradosh K. Ray, *Student Researcher:* A. Ghosh, *Technical Monitor:* Francis M. Curran (LeRC)

11:20 AM **"A Study of Spatial Data Management and Analysis System."** *Institution:* Jackson State University, *Principal Investigator:* Dr. Robert Leflore, *Technical Monitor:* R. A. Galle (SSC).

11:40 AM **"Progress on a Proton Transport Program."** *Institution:* Hampton University, *Principal Investigator:* Dr. Warren Buck, *Student Researcher:* Duc Ngo, *Technical Monitor:* Larry Townsend (LaRC).

SESSION III

Wednesday / March 22

10:00 AM— 12:00 NOON *Elmore Health Science Complex, Room 7*

PRESIDING:

Dr. Walter Watson
Alabama A&M University

PHYSICAL SCIENCES

10:00 AM **"Structures of Cyano-Biphenyl Liquid Crystals."** *Institution:* Howard University, *Principal Investigator:* Dr. Tung Tsang, *Student Researcher:* Y.C. Chu, *Technical Monitor:* Dr. L. Yin (GSFC).

10:20 AM **"Polarographic Study of Cadmium 5-Hydroxy-2-(Hydroxy Methyl)-4H-Pyran-4-one Complex."** *Institution:* Texas Southern University, *Principal Investigator:* Dr. Ray F. Wilson, *Student Researcher:* Robert C. Daniels, *Technical Monitor:* Dr. Donald L. Henninger (JSC)

10:40 AM **"Densitometric Analysis of Commercial 35mm Films."** *Institution:* Morgan State University, *Principal Investigator:* Dr. Ernest C. Hammond, Jr., *Student Researcher:* Christopher M. Ruffin, III, *Technical Monitor:* Mr. Gerald R. Baker (GSFC)

11:00 AM **"Studies of Superconducting Materials with Muon Spin Rotation."** *Institution:* Virginia State University, *Principal Investigator:* Dr. Carey E. Stronach, *Student Researcher:* Michael R. Davis, *Technical Monitor:* Dr. John W. Wilson (LaRC)

11:20 AM **"Non-Linear Polarizabilities of Substituted PI-Conjugated Systems."** *Institution:* Milligan Science Research Institute of Atlanta University Center, Inc., *Principal Investigators:* Dr. R. E. Stickel, Sr., and Dr. B.H. Cardelino, *Technical Monitor:* T. L. Randall (MSFC)

11:40 AM **"Ellipsometric Measurement of Liquid Film Thickness."** *Institution:* Alabama A&M University, *Principal Investigator:* Dr. Ki Joon Chang, *Technical Monitor:* Dr. Donald O. Frazier (MSFC)

SESSION IV

Wednesday / March 22

1:45 PM— 3:45 PM *Elmore Health Science Complex, Lecture Room*

PRESIDING:

Ms. Amanda Harris
Marshall Space Flight Center

SPACE SCIENCE

1:45 PM **"Optically Controlled Solid State Devices"**, *Institution:* Howard University, *Principal Investigator:* Dr. Raj Chowdhary, *Student Researcher:* Mr. Trevor Correia, *Technical Monitor:* Dr. A. S. Burgess (GSFC)

2:05 PM **"Evaluation of On-Board Hydrogen Storage Methods for Hypersonic Vehicles."** *Institution:* Hampton University, *Principal Investigator:* Dr. A. Akyurtlu, *Co-Investigators:* J. F. Akyurtlu, A. A. Adeyiga, *Student Researcher:* Samara Perdue (LaRC).

2:25 PM **"Mossbauer Spectroscopy and Scanning Electron Microscopy of the Murchison Meteorite."** *Institution:* Morgan State University *Principal Investigator:* Dr. Ernest C. Hammond, Jr. and Dr. Frederick Oliver, *Student Researcher: Mr.* Christopher L. Brown, *Technical Monitor:* Mr. Gerald R. Baker (GSFC).

2:45 PM **"The Effect of the Orbital Environment in IIaO Spectroscopy Film."** *Institution:* Morgan State University, *Principal Investigator:* Dr. Ernest C. Hammond, Jr., *Technical Monitor:* Mr. Gerald R. Baker (GSFC).

3:05 PM **"Characterization of Non-Linear Quantum Well Transmission Line Structures using a Photo Cathode Electron Microscope."** *Institution:* Howard University, *Principal Investigator:* Dr. Michael Spencer, *Graduate Student Researcher:* Craig Scott, *Technical Monitor:* Andre Burgess (GSFC).

3:25 PM **"Relativistic Nucleus-Nucleus Collisions and Dense Nuclear Matter Formation."** *Institution:* Alabama A&M University, *Principal Investigator:* Dr. Stephen McGuire, *Technical Monitor:* Thomas A. Parnell (MSFC).

SESSION V

Wednesday / March 22

1:45 AM— 3:45 PM *Elmore Health Science Complex, Room 6*

PRESIDING:

Mr. Leonard Fisher
Lawrence Livermore National Laboratory

SPACE TECHNOLOGY: MEASUREMENTS, TECHNIQUES, MATERIALS

1:45 PM **"Low Energy Sputtering of Cobalt by Cesium Ions."** *Institution:* Tuskegee University, *Principal Investigator:* Dr. Pradosh K. Ray, *Student Researcher:* A. Handoo, *Technical Monitor:* Robert T. Bechtel (MSFC).

2:05 PM **"Parameters of Tensile Strength, Elongation, and Tenacity of 70mm IIaO Spectroscopic Film."** *Institution:* Morgan State University, *Principal Investigators:* Dr. Ernest C. Hammond, Jr. and Kevin Peters, *Technical Monitor:* Mr. Gerald Baker (GSFC).

2:25 PM **"Influence of Temperature on the Permeation Properties of Protective Clothing."** *Institution:* Tuskegee University, *Principal Investigator:* Dr. Nadar Vadat, *Student Researcher:* Michael Bush (KSC).

2:45 PM **"The Preparation and Study of Titanium, Zirconium, and Hafnium Complexes."** *Institution:* Texas Southern University, *Principal Investigator:* Dr. Bobby Wilson, *Technical Monitor:* Dr. David S. McKay (JSC).

3:05 PM **"The Effect of Grinding on the Fatigue Life of Ti-5Ai-2.55n Under Wet and Dry Conditions."** *Institution:* Tuskegee University, *Principal Investigator:* Dr. Shaik Jeelani, *Student Researcher:* Pardha Rangaswamy, *Technical Monitor:* Mr. Paul Munafo (MSFC).

3:25 PM **"A Scanning Elecron Microscopic Study of Crystals of (2,4-Dintrobenzyl) Pyridine."** *Institution:* Morgan State University, *Principal Investigator:* Dr. Ernest C. Hammond, Jr. *Student Researcher:* Jacqueline Ware, *Technical Monitor:* Mr. Gerald Baker (GSFC).

SESSION VI

Wednesday / March 22

1:45 AM— 4:05 PM *Elmore Health Science Complex, Room 7*

PRESIDING:

Mr. Carrington H. Stewart, P.E.
Johnson Space Center

TECHNOLOGY: LASERS, SYSTEMS ENGINEERING, DIFFUSION

1:45 PM **"Atmospheric Effects on Coherent Laser Systems."** *Institution:* Alabama A&M University, *Principal Investigator:* Dr. S. R. Murty, *Technical Monitor:* Mr. James W. Bilbro (MSFC)

2:05 PM **"Analysis of Thermal Lansing in Pumping Laser Rods."** *Institution:* Hampton University, *Principal Investigator:* Dr. Usamah Farrukh, *Student Researcher:* Mr. Vincent Brackett, *Technical Monitor:* Dr. Phillip Brockman (LaRC).

2:25 PM **"A Dynamic Systems Engineering Methodology Research Study."** *Institution:* Howard University, *Principal Investigators:* Dr. Tepper Gill and Dr. Arthur Paul, *Technical Monitor:* A. Goodson (GSFC)

2:45 PM **"Engineering Management for Large Scale Systems."** *Institution:* Howard University, *Principal Investigators:* Dr. Tepper Gill and Dr. Arthur Paul, *Technical Monitor:* A. Goodson (GSFC).

3:05 PM **"Systems Engineering in A Dynamic Environment."** *Intitution:* Howard University, *Principal Investigator:* Dr. Arthur Paul, *Technical Monitor:* A. Goodson (GSFC).

3:25 PM **"Development of Flashlamp-pumped Q-switched Ho:Tm:Cr:YAG Lasers for Mid-Infrared Lidar Application."** *Institution:* Hampton University, *Principal Investigator:* Dr. Donald A. Whitney and Dr. Kyong H. Kim, *Technical Monitor:* Robert V. Hess (LaRC).

3:45 PM **"XeC1 Laser Pumped Iodine Laser Using t-C4F91."** *Institution:* Hampton University, *Principal Investigators:* Dr. Kwang S. Han and Dr. I.H. Hwang, *Technical Monitor:* Mr. Robert Coston (LaRC).

SESSION VII

Wednesday / March 22

1:45 PM— 4:05 PM *Elmore Health Science Complex, Room 8*

PRESIDING:

Mr. Arthur Henderson
Marshall Space Flight Center

SPACE SCIENCE

1:45 PM **"Center for Spatial Data Research Applications: New Facilities and New Paradigms."** *Institution:* Jackson State University, *Principal Investigator:* Dr. Bruce E. Davis, *Technical Monitor:* Rick Galle (SSC).

2:05 PM **"An Analysis of the Moon's Surface Using Reflected Illumination from the Earth During a Waning Crescent Lunar Phase."** *Institution: Morgan State University, Principal Investigator:* Dr. Ernest C. Hammond, Jr., *Student Researcher:* Ms. Brenda J. Queen, *Technical Monitor:* Mr. Gerald R. Baker (GSFC).

2:25 PM **"Laboratory Studies of Acetylene Photochemistry Related to Titan's Atmosphere."** *Institution:* Howard University, *Principal Investigators:* Dr. Hideo Okabe and Dr. Joshua B. Halpern, *Technical Monitor:* J. T. Bergstralh (HQ-EL)

2:45 PM **"A 10-Watt CW Photodissociation Laser with IODO Perfluoro-Tert-Butane."** *Institution:* Hampton University, *Principal Investigators:* Dr. Demetrius D. Venable and Bagher M. Tabibi, *Technical Monitor:* Willard Meador, Jr. (LaRC).

3:05 PM **"Vibrational Excitation of N_2 by Electrons: Application and Development of the PDE Method."** *Institution:* Florida A&M University, *Principal Investigator:* Dr. Charles A. Weatherford, *Co-Investigators:* Dr. Roy Tucker and Gregory Odom, *Technical Monitor:* Aaron Temkin (GSFC).

3:25 PM **"Rapid Characterization of High Tc Superconductors - D.C. Magnetic Susceptibility."** *Institution:* Howard University, *Principal Investigator:* Dr. Arthur N. Thorpe, *Student Researcher:* Mr. Quoc A. Nguyen, *Technical Monitor:* Dr. Sidney Alterescu (GSFC).

4:45 PM **"Photometric and Spectroscopic Study of Chromospherically Active Stars."** *Institution:* Tennessee State University, *Principal Investigator:* Dr. Michael R. Busby, *Student Researcher:* Mathias Teke, *Technical Monitor:* John M. Davis (MSFC).

SESSION VIII

Thursday / March 23

10:00 AM— 12:00 NOON *Elmore Health Science Complex, Room 6*

PRESIDING:

Dr. Daryush Ila
Alabama A&M University

SPACE TECHNOLOGY: MATHEMATICAL MODELING

10:00 AM **Mathematical Models for Film Sensitivity Measurement."** *Institution:* Morgan State University, *Principal Investigator:* Dr. Ernest C. Hammond, Jr., *Co-Investigators:* Dr. Stephen Gerwirtz and Osborne Parchment, *Technical Monitor:* Mr. Gerald R. Baker (GSFC).

10:20 AM **"Finite Difference Models of Differential Equations and Related Topics."** *Institution:* Atlanta University, *Principal Investigator:* Dr. Ronald E. Mickens, *Technical Monitor:* Dr. John Shoosmith (LaRC).

10:40 AM **"Kaon-Nucleus Scattering Calculations."** *Institution:* Hampton University, *Principal Investigator:* Dr. Warren Buck, *Graduate Student Researcher:* B. Hong, *Technical Monitor:* F. C. Owens (HQ-XE).

11:00 AM **"Implementation of an Algorithm for Cylindrical Object Identification Using Range Data."** *Institution:* Spelman College, *Principal Investigators:* Dr. Sylvia Bozeman and Dr. Benjamin Martin, *Technical Monitor:* Michael Goode (LaRC).

11:20 AM **"Image Databases: Problems and Perspectives."** *Institution:* Jackson State University, *Principal Investigator:* Dr. Naidu Gudivada, *Technical Monitor:* Dr. Richard Galle (SSC).

11:40 AM **"Design of Parallel Graphic Application Algorithms."** *Institution:* Hampton University, *Principal Investigator:* Dr. Reginald L. Walker, *Technical Monitor:* Donald Lansing (LaRC).

SESSION IX

Thursday / March 23

10:00 AM— 12:00 NOON *Elmore Health Science Complex, Room 7*

PRESIDING:

Ms. Hazelyn Patterson
Marshall Space Flight Center

SPACE LIFE SCIENCES

10:00 AM **"Nitrogen Transformation and Gaseous N. Emissions in a Pasture Ecosystems."** *Institution:* Prairie View A&M University, *Principal Investigator:* Dr. E. Brams, *Technical Monitors:* Dr. G. Hutchinson (ARS/USDA) and Dr. G. Livingston (ARC).

10:20 AM **"Sweet Potato Production in Soilless Culture for Controlled Ecological Life Support."** *Institution:* Tuskegee University, *Principal Investigator:* Dr. E. R. Martinez, *Co-Investigators:* Dr. C. K. Bonsi, D. G. Mortley, P. A. Loretan, C. R. Ogbuehi, C. Morris, and W. A. Hill, *Technical Monitors:* William M. Knott, III and Ralph Prince (KSC).

10:40 AM **"Influence of the Nutrient Solution Application Protocol on Growth and Yield of Hydroponically Grown 'Georgia Jet' Sweet Potatoes."** *Institution:* Tuskegee University, *Principal Investigators:* Dr. C. R. Ogbuehi, W. A. Hill, P. A. Loretan, C. K. Bosi, C. E. Morris, P. K. Biswas, D. G. Mortley, *Technical Monitors:* William M. Knott, III and Ralph Prince (KSC).

11:00 AM **"Manipulating Cyanobacteria for Potential CELSS Diet."** *Institution:* Alabama A&M University, *Principal Investigator:* Dr. Mahasin Tadros, Student Researchers: B. Joseph, P. Mbuthia and W. Smith, *Technical Monitor:* Dr. Robert MacElroy (ARC)

11:20 AM **"International Food Patterns for Space Station Foods."** *Institution:* Texas Southern University, *Principal Investigator:* Dr. Selina Ahmed, *Student Researchers:* Ms. Amanda Cox and Ms. Pauline V. Cornish, *Technical Monitor:* Dr. Charles T. Bourland (JSC)

11:40 AM **"X-Ray Sensitivity of Diploid Skin Fibroblasts from Patients with Fanconi Anemia."** *Institution:* Alabama A&M University, *Principal Investigator:* Dr. Ranjini Kale, *Technical Monitor:* Mr. Bob Schneider (MSFC).

SESSION X

Thursday / March 23

10:00 AM— 12:00 NOON *Elmore Health Science Complex Lecture Room*

PRESIDING:

Ms. Audrey Robinson
Marshall Space Flight Center

SPACE SCIENCE

10:00 AM **"Dynamic Analysis of Large Space Structures."** *Institution:* Howard University, *Principal Investigator:* Dr. Taft Broome, *Technical Monitors:* Mr. S. Woodard (LaRC).

10:20 AM **"Evaluation and Characterization of Superconducting Materials for Space Applications - D.C. Magnetization."** *Institution:* Howard University, *Principal Investigator:* Dr. Arthur N. Thorpe, *Student Researcher:* Mr. David Davis, *Technical Monitor:* Dr. Sidney Alterescu (GSFC).

10:40 AM **"Coefficient of Linear Expansion of Laser Materials."** *Institution:* Virginia State University, *Principal Investigator:* Dr. George Henderson, *Student Researchers:* Anthony Helm, D'Anthony Woods, and Francine Davis, *Technical Monitors:* Dr. Marty Buoncristinani and Dr. Philip Brockman (LaRC).

11:00 AM **"Computer Simulation of Radiation Damage in Gallium Arsenide."** *Institution:* Virginia State University, *Principal Investigators:* Mr. John J. Stith and Dr. James C. Davenport, *Technical Monitor:* Dr. John Wilson (LaRC).

11:20 AM **"Surface Roughness of Flat and Curved Optical Surfaces"**, *Institution:* Alabama A&M University, *Principal Investigators:* Dr. P. Venkateswarlu, Dr. B. R. Reddi, *Technical Monitor:* Dr. J. L. Randall (MSFC)

SESSION XI

Thursday / March 23

1:45 PM— 3:05 PM *Elmore Health Science Complex, Room 6*

PRESIDING:

Mr. Johnnie Clark
Marshall Space Flight Center

SPACE TECHNOLOGY I

1:45 PM **"Effects of Ionizing Radiation on VLSI Electronic Devices."** *Institution:* Hampton University, *Principal Investigator:* Dr. Demetrius Venable, *Technical Monitor:* E. G. Stassinopoulos (GSFC).

2:05 PM **"Relativistic Nucleon-Nucleus and Antinucleon-Nucleus Interactions."** *Institution:* Hampton University, *Principal Investigator:* Dr. Warren Buck, *Student Researcher:* Khin Maung, *Technical Monitor:* J. W. Wilson (LaRC).

2:25 PM **"Optimal Planar Slewing of the Flexible Orbiting SCOLE."** *Institution:* Howard University, *Principal Investigator:* Dr. P. M. Bainum, *Co-Investigator:* Feiyue Li, *Technical Monitors:* John W. Young and Larry W. Taylor (LaRC).

2:45 PM **"Forced Convection and Flow Boiling With and Without Enhancement Devices for Top-Sided-Heated Horizontal Channels."** *Institution:* Prairie View A&M University, *Principal Investigators:* Mr. Jerry C. Turknett and Dr. Ronald D. Boyd, *Technical Monitor:* Mr. Richard Parish (JSC).

SESSION XII

Thursday / March 23

1:45 PM— 3:05 PM *Elmore Health Science Complex, Room 7*

PRESIDING:

Dr. Shaik Jeelani
Tuskegee University

SPACE TECHNOLOGY II

1:45 PM **"Application of the Schwinger Variational Principle to Electron-Hydrogen Atom Scattering: Investigation of Pseudo-Resonances."** *Institution:* Florida A&M University, *Principal Investigator:* Charles Weatherford, *Co-Investigators:* Roy Tucker and Gregory Odom, *Technical Monitor:* W. M. Huo (GSFC).

2:05 PM **"Study of Non Linear Properties of Organic Materials: Phase Conjugation by Degenerate Four Wave Mixing in Disodium Fluoresein Solution in Methanol."** *Institution:* Alabama A&M University, *Principal Investigators:* P. Venkateswarlu, P. Chandra Sekhar and M.C. George, *Student Researcher:* H. Abdeldayem, *Technical Monitor:* Dr. Joseph Randall (MSFC).

2:25 PM **"An Evaluation of the Interfacial Bond Properties Between Carbon Phenolic and Glass Phenolic Composites."** *Institution:* Tuskegee University, *Principal Investigator:* Dr. Shaik Jeelani, *Technical Monitor:* Mr. Raymond Clinton (MSFC).

2:45 PM **"A Study of Microstructural Characteristics and Differential Themal Analysis of Ni-based Superalloys."** *Institution:* Alabama A&M University, *Principal Investigators:* Dr. R. B. Lal and Dr. M. D. Aggarwal, *Student Researcher:* Mr. Samuel Oyekenu, *Technical Monitor:* Richard Parr (MSFC).

3:05 PM **"Nozzle Materials Investigation."** *Institution:* Alabama A&M University, *Principal Investigator:* Dr. James Thompson, *Student Researcher:* Janet Daniel, *Technical Monitor:* Mr. John Austin (MSFC).

SESSION XIII

Thursday / March 23

1:45 PM— 3:45 PM *Elmore Health Science Complex Lecture Room*

PRESIDING:

Dr. Mildred Wyatt
Goddard Space Flight Center

SPACE TECHNOLOGY III

1:45 PM **"Servo Motor-Linked Articulated Versatile End Effector (SLAVE^2) - Large Robotic Hand."** *Institution:* Central State University, *Principal Investigator:* Dr. William A. Grissom, *Technical Monitors:* Dr. Edwin P. Kan (JPL). Mr. James Aliberti (KSC).

2:05 PM **"Joint Conjugates for Robotic Assembly of Large Truss Structures in Space: A Second Generation."** *Institution:* Jackson State University, *Principal Investigator:* Mr. William Brewer, *Technical Monitors:* Mr. Marvin Rhodes and Ralph Will (LaRC).

2:25 PM **"Subcooled Freon-11 Flow Boiling in Top-Heated Finned Coolant Channels With and Without a Twisted Tape."** *Institution:* Prairie View A&M University, *Principal Investigator:* Mr. Alvin Smith and Dr. Ronald D. Boyd, *Technical Monitor:* Mr. Richard C. Parish (JSC).

2:45 PM **"Growth and Characterization of Crystals for IR Detectors and Second Harmonic Generation Devices."** *Institution:* Alabama A&M University, *Principal Investigators:* Dr. A. K. Batra, Dr. R. B. Lal, and Dr. M. S. Rao, *Student Researchers:* Sandeep Bhatia and Kunar P. Chunduru, *Technical Monitor:* Dr. William Wilcox (Center for Commercialization of Space).

3:05 PM **"Automated Assembly in Space."** *Institution:* Bowie State University, *Principal Investigator:* Dr. Sandanand Srivastava, *Technical Monitor:* Mr. Gary Jones (GSFC).

3:25 PM **"Excimer Laser Interaction with Dentin of the Human Tooth."** *Institution:* Morgan State University, *Principal Investigator:* Dr. Ernest C. Hammond, Jr., *Student Researcher:* Ruth Gilliam, *Technical Monitor:* Mr. Gerald baker (GSFC).

SCIENTISTS OF TOMORROW PROGRAM

Wednesday / March 22, 1989

Elmore Health Science Complex
Alabama A&M University

SCHEDULE OF EVENTS

PRESIDING
Dr. Rather Brown, Director

8:00 AM	REGISTRATION AND CONTINENTAL BREAKFAST *Elmore Health Science Lobby*
8:30 AM	GENERAL SESSION OF THE NASA-HBCU SPACE SCIENCE AND ENGINEERING RESEARCH FORUM *Elmore Health Science Gymnasium*
10:30 AM	BREAK
10:40 AM	VISIT BOOTH DISPLAYS *Elmore Health Science Lobby*
11:15 AM	TOUR OF ALABAMA A&M UNIVERSITY'S SCIENCE DEPARTMENTS 1. Biology 2. Chemistry 3. Mathematics 4. Physics 5. Civil and Mechanical Engineering 6. Computer Science 7. Natural Resources 8. Food and Animal Science 9. Soil Science 10. Military Science
12:00 NOON	LUNCH *AAMU Students Cafeteria*
1:00 PM	*ADMISSIONS AND FINANCIAL AID WORKSHOP* *Carter Hall Auditorium* **Mr. James Heyward**, Director Office of Admissions, AAMU **Mr. P. N. Lanier**, Director Office of Financial Aid, AAMU
1:45 PM	DEPART FOR SPACE AND ROCKET CENTER
2:10 PM	FILM "THE DREAM IS ALIVE" *Museum Theater*
2:30 PM	TOUR SPACE AND ROCKET MUSEUM
3:40 PM	REFRESHMENTS
4:00 PM	"YOUTH CHALLENGE" *Museum Auditorium* **Mr. Homer McCall, Jr.** Sr. Class President, Huntsville High School
4:15 PM	INTRODUCTION OF SPEAKER **Ms. Yvonne Sanders** Program Coordinator, AAMU
4:20 PM	SPEAKER **Astronaut Mae C. Jemison, MD**
5:00 PM	STUDENTS DEPART FOR HOME.

POSTER PRESENTATIONS

1. **"Genetic Effects of Heavy Ions,"** *Institution:* Alabama A&M University, *Principal Investigator:* Dr. Purushottam Kale, *Technical Monitor:* Dr. Stuart Nachtwey (JSC).
2. **"Teacher Training and Improvement in Science: The Alabama A&M Science Improvement Project,"** *Institution:* Alabama A&M University, *Principal Investigator:* Dr. Saundra Y. McGuire, *Technical Monitor:* Mr. James Rice (MSFC).
3. **"Synthesis of 3-(Bromoacetamido)-propylamine Hydrochloride as Sulphydryl Reagent for Myosin Subfragment,"** *Institution:* Miles College, *Principal Investigator:* Dr. Prasanta Sharma.
4. **"Effects of Radiation and Space Flight on Testicular Morphology in Rats and Mice,"** *Institution:* Tuskegee University, *Principal Investigator:* Carol S. Williams and Walter J. Sapp, *Technical Monitor:* Dr. Delbert E. Philpott (ARC).

CONTENTS

I. Life Science

II. Mathematical Modeling, Image Processing, Pattern Recognition, and Algorithms

III. Microgravity Processing, Space Utilization and Application

IV. Physical Science and Chemistry

V. Research and Training Programs

VI. Space Science: Astronomy, Planetary Science, Asteroids, Moon, etc.

VII. Space Technology: Engineering, Structures and Systems for Application in Space

VIII. Space Technology: Physics of Materials and Systems for Space Applications

IX. Technology: Materials, Techniques, Measurements

A COMPARATIVE STUDY OF SEMINIFEROUS TUBULAR EPITHELIUM FROM RATS FLOWN ON COSMOS 1887 AND SL3

Walter J. Sapp, Carol S. Williams, and K. Kato,
Department of Biology
Tuskegee University
Tuskegee, AL

and

Delbert E. Philpott and J. Stevenson
NASA - Ames Research Center
Moffet Field, CA

and

L.V. Serova
Institute for Biomedical Problems
Moscow, USSR

ABSTRACT

Space flight, with its unique environmental constraints such as immobilization, decreased and increased pressures, and radiation, is known to affect testicular morphology and spermatogenesis. Among the several biological experiments and animals on board COSMOS 1887 Biosputnik flight were 10 rats, from which we have collected testicular tissue. Average weights of flight testes were 6.4% below that of the vivarium control when normalized for weight loss / 100 grams body weight. Counts of surviving spermatogonia per tubule cross section indicated an average of 39 spermatogonia for flight animals, 40 for synchronous controls and 44 for the vivarium controls. Serum testosterone was significantly decreased when compared to basal controls but the decrease was not significant when compared in vivarium and synchronous control groups. The significant decrease in spermatogonia and the decrease in serum testosterone are similar to that in animals flown on Space Lab 3 (Challenger Shuttle).

A COMPARATIVE STUDY OF SEMINIFEROUS TUBULAR EPITHELIUM FROM RATS FLOWN ON COSMOS 1887 AND SL3

Introduction

The testes have been shown to be affected by space flight, immobilization, irradiation and increased gravity. Fedorova (1) reported an increase of 30 to 70% atypical spermatozoa consisting of tail curling and absence of a tail. These abnormalities decreased to the high normal range of 30% by 75 days postflight. Rat testes from SL-3 showed a 7.5% decrease in Stage 6 spermatogonia and a weight loss of 7.1% when compared to controls (2). In earlier studies of rats flown aboard COSMOS 690 (3) and COSMOS 605 (4) no specific changes in the testes, directly attributed to flight, were reported. Immobilization, applied for a short or long period, is considered a form of physiological stress, and induces a decrease in plasma testosterone levels (5-7). While most reports indicate no change in the morphology of differentiating germ cells as a result of immobilization (8), a "striking" arrest of spermatogenesis in a primate has been reported (9). The sensitivity of the testes to radiation is well known and well studied. The details of spermatogonial effects of irradiation in mice, rats and primates have been the subject of studies utilizing X-irradiation and gamma irradiation (10-13). Alpen and Powers-Risius (14) have quantitated HZE irradiation effects using testes weight loss. Philpott et al.(15-19) have reported the results of cosmic (HZE) type irradiation on spermatogonial cell counts using an assay method that concentrates on cell numbers in spermatogonial Stage 6 (12) and which provides a means of detecting cell population changes at doses of less than 0.5 rads (17). This sensitive response makes the testes a possible candidate as a biological dosimeter.

Summary of Flight and Recovery

The following is from the "Summary of the COSMOS 1887 flight and specimen collection" as compiled by Dr. R.E. Grindeland, NASA:

The COSMOS 1887 Biosputnik flight was launched September 29, 1987 and landed October 12, 1987 after a flight of 12.5 days. Inflight, 10 male SPF rats of Czechoslovakian origin (Institute of Endocrinology, Brattislava, Czechoslovakia) were housed in a single cage which had 10 nozzles for delivery of a paste diet and 10 lixits for water. Fourteen-gram boluses of food (total 55g/day/rat) were provided ad libitum. The air pressure in the cage was 760 mm Hg, the humidity averaged 58%, and the ambient temperature was 22°C- 23°C. Lights were on from 0800-2400 and off from 2400-0800 hours. Light intensity was 4-8 lumens at the cage floor. The Biosputnik had an orbital inclination of 62.8 degrees; the apogee and perigee were 406 and 224 kilometers, respectively.

Due to difficulties during reentry, the Biosputnik landed in Siberia rather than the designated site where the recovery/ dissection team was located. The calculated landing force was less than 4 g. At the landing site there were about 15 cm of snow and the outside temperature varied from -5°C to -20°C. The Biosputnik was located in 3 hours and a rescue team placed a heated tent (23°C) around the vehicle. The following morning, 20 hours after landing, the animals were placed in transport cages and carried by bus (3 hours), airplane (6.5 hours), and van (0.5 hour) to the designated recovery/dissection site. Rats were sacrificed the next morning. Due to the recovery delays, rats had been without food for 42 hours. While the biosatellite was on the ground, the ventilation system continued to work so the animals

received an adequate air supply. The temperature of the rat cage was not recorded after landing, but calculations indicate that the temperature fell slowly and did not go below +12°C. When examined upon removal from the flight cage, the rats were somewhat dirty but apparently healthy and free from injury. During the airplane trip back from the landing site the animals "appeared exhausted" - much like the rats after the Space Lab 3 flight.

Methods

For each of the five animals in each group (flight, synchronous control and vivarium control) testes were removed, weighed, immediately slit open and immersed in cold Triple Fix (20). The specimens were kept at 4°C, shipped to Ames Research Center and refrigerated until time for processing. Samples were treated with 1% osmium tetroxide for 1 hour, dehydrated in ascending concentrations of acetone, infiltrated with Epon-Araldite and polymerized at 60°C for 48 hours. Six blocks were produced from each testis. Two-micron cross sections were cut on a Porter-Blum ultramicrotome and mounted on glass slides. The sections were stained with 1% toluidine blue in 1% borax. Alternate sections containing maturation Stage 6 (12) were scored for surviving spermatogonia.

Results

The average weight difference of the COSMOS flown rat testes is 6.4% as compared to vivarium controls when normalized for weight/100 grams. There is no difference in testis weight when flight animals and synchronous control animals are compared.

Counts of surviving spermatogonia (Table 1) per tubule cross section indicate an average of 38.79 spermatogonia for flight animals, 40.20 for synchronous controls and 43.75 for vivarium controls. The decreases of spermatogonia in flight tissues are significant when compared to synchronous control ($P<0.02$, 1 tail; $P<0.05$, 2 tail) and vivarium control ($P<0.0002$, 1 tail; $P<0.005$, 2 tail). Rats flown on SL-3 experienced a similar decrease in number of spermatogonia (2). Preliminary counts of Sertoli cells per tube cross section indicate no significant difference ($P>0.05$) when vivarium control animals are compared to either synchronous controls or to flight animals. This consistency in Sertoli cell numbers per tubule cross section demonstrates their stability under the adverse conditions of space flight and indicates that the minor volumetric changes in tubular epithelium due to spermatogonial cell loss do not affect the relative numbers per tubule of cross section. Spermatogonial cell loss can be quantitated per number of Sertoli cells or per tubule cross section. Changes in spermatogonial cell populations are indicative of actual cell loss and are not significantly influenced by volumetric changes in the tubules (Figure 1a, 1b, 1c).

Discussion

While it is general knowledge that the testes are very sensitive to certain environmental factors including stress and irradiation, not all reports agree on the extent and nature of morphologic changes in the seminiferous epithelia (8). Most reports indicate that stress decreases testosterone levels (5-7) but does not cause any morphological changes in seminiferous tubules (8). Interestingly, in human

beings, stress may cause either an increase or decrease in serum testosterone depending upon whether the stress is perceived as a threat to dominance/control (increased testosterone) or a loss of control (decreased testosterone) (7). On the other hand, irradiation, depending on the dosage, can result in the depletion of all spermatogonial cells except a few of the stem cells (17,13), but testosterone levels do not seem to be affected in the serum or intratesticular tissue by irradiation (21). Grindeland et al. (22) measured the serum testosterone in the COSMOS 1887 animals and reported lower hormone levels when flight animals were compared to vivarium and synchronous controls.

Previous space flight investigations prior to SL-3 have not reported changes in seminiferous epithelium while simulated conditions, at least in some investigators' labs, result in changes (4). Data obtained from rats flown on COSMOS 1887 indicated significantly reduced numbers of spermatogonia when compared to both synchronous control animals (4% decrease) and vivarium control animals (11% decrease) and were generally similar to results obtained from rats flown on SL-3 (2,23). Our assay procedure provided excellent quality specimens, sections thin enough to provide morphological differentiation of each spermatogonial cell class, and precise quantitation.

Data indicte a significant difference in spermatogonial population when the two control groups are compared. This difference may be caused by stresses encountered under simulated space flight conditions, or to as yet unexplained responses. A similar decrease in spermatogonia was seen in rats subjected to suspension in a simulated SL-3 flight (Table 1). We postulate that the decrease (4%) in spermatogonia observed in rats actually flown on COSMOS 1887 when compared to the synchronous controls is due to space flight conditions not adequately duplicated on the ground based synchronous experiment. One possible factor is radiation. Dosimetry reports from COSMOS 1887 indicate a dose factor of 0.313 rad at the dosimeter location within the space craft. Dosimeters were not located near the animals; therefore, the exact dosage received in that area is not known. Low radiation levels do not produce gross changes in morphology; however, spermatogonia near the first meiotic division are reduced in number. This is not unexpected and many investigations, including our own, substantiate these results (17). We have shown with X-rays and with HZE particles the extreme sensitivity and predictable response of the testicular epithelium to irradiation. The loss of cells not accounted for except by space travel could have resulted from radiation, especially since any particles penetrating the space craft would have been galactic and of similar energy to Iron. Our previous experiments indicate that irradiation with HZE particles of Iron at 0.5 rad level caused significant decreases in spermatogonia in mice (19) and these changes could be detected down to the 0.1 rad level (Unpublished).

Previous work in our laboratory led us to conclude that the testicular seminiferous epithelium is a good model for radiation sensitivity studies since it is composed of cellular populations which vary in individual radiosensitivities, indicated by the multiple slopes seen in spermatogonial survival curves (17). These characteristics of testicular epithelium provide an accurate means for biological dosimetric assessment of radiation exposure. Data collected from this flight (COSMOS 1887) as well as from the earlier SL-3 flight indicate that the biological effects of space flight are multifaceted. Impact on the morphophysiology of the testes through a number of different pathways, i.e., decreases in serum testosterone and testes weight loss, is observed in the animals described in this report. Stress related gonadal dysfunction and possible galactic radiation exposure, possibly along with other factors, apparently contribute to the significant decrease in spermatogonial cell numbers observed in rats flown in space. Various changes in the environment can alter testicular integrity. The site of action of these various environmental impacts and the mechanisms by which they interfere with both spermatogenesis and steroidogenesis need further investigation. These important investigations should be repeated with longer flights and a shorter time span between recovery and specimen preparation. When it becomes possible, fixation in flight will remove any doubt about the effect recovery may have.

Acknowledgments

This work was supported in part by the NASA/Ames Research Center Cooperative Agreement #NCC2-12 and #NC2-455 (to W.J.S.). Ultrastructural Facility support was provided by NIH/DRR/RCMI grant #G12RR03059-01A1.

Note: The work presented here also appears as a publication in the FASEB Journal.

References

1. Fedorova, N.L., Kosmichesda Biol Med., **1967**, 1, 28. Space Biol. Med. 1, 28.

2. Philpott, D.E.; Sapp, W.; Williams, C.; Fast, T.; Stevenson, J.; Black, S., Proc. EMSA., **1986**, 44, 248.

3. Plakhuta-Plakutina, G.I., Aviat. Space Environ. Med., **1977**, 48, 12.

4. Portugalov, V.V.; Savina, E.A.; Kaplansky, A.S.; Yakovleva, V.I.; Plakhuta-Plakutina, G.I.; Pankova, A.S.; Katunyan, P.I.; Shubich, M.G.; Buvalio, S.A., Aviat Space Environ. Med., **1976**, 47, 813.

5. Carpenet, G.; Tache, Y.; Forest, M.G.; Haour, G.; Saez, J.M.; Bernier, M.; Ducharme, J.R.; Collu, R., Endocrinology, **1981**, 109, 1254.

6. Armario, A.; Castellanos, J.M., Physiol. Behav., **1984**, 32, 517.

7. Collu, R.; Gibb, W.; Ducharme, J.R., J. Endocrinol. Invest., **1984**, 7, 529.

8. McGrady, A.V.; Chakraborty, J., Arch. Androl., **1983**, 10, 95.

9. Zemjanis, R.; Gondos, B.; Adey, W.R.; Crockett, A.T.K., Fertil. Steril., **1970**, 21, 335.

10. Oakberg, E.F.; Clark, E., J. Cell. Comp. Physiol., **1961**, 58 (Suppl 1), 173.

11. Hugon, J.; Borgers, V.M., Anat. Rec., **1966**, 155, 15.

12. Huckins, C., Anat. Rec., **1978**, 190, 905.

13. VanAlphen, M.M.A.; VanDeKant, H.J.G.; DeRooij, D.G., Radiat. Res., **1988**, 113,473.

14. Alpen, E.L.; Powers-Risius, P., Radiat. Res., **1981**, 88, 132.

15. Philpott, D.E.; Sapp, W.; Williams, C.; Stevenson, J.; Black, S., Proc. EMSA., **1981**, 39, 542.

16. Philpott, D.E.; Sapp, W.; Williams, C.; Stevenson, J.; Corbett, R.; Black, S., Proc. EMSA., **1983**, 41, 674.

17. Philpott, D.E.; Sapp, W.; Williams, C.; Stevenson, J.; Corbett, R.; Black, S., Scanning Electron Microsc., **1983**, III, 1345.

18. Philpott, D.E.; Sapp, W.; Williams, C.; Stevenson, J.; Black, S.; Corbett, R., The Physiologist., **1985**, 28(6)suppl, s211.

19. Philpott, D.E.; Sapp, W.; Williams, C.; Stevenson, J.; Black, S.; Corbett, R., Proc. EMSA., **1985**, 43, 652.

20. Philpott, D.E., Corbett, R.; Turnbill, C.; Black, S.; Dayhoff, D.; McGourty, J.; Lee, R.; Harrison, G.; Sovick, L.. Aviat. Space Environ. Med., **1980**, 51, 556.

21. Cunningham, G.R.; Huckins, C., Radiat. Res., **1978**, 76, 331.

22. Grindeland, R.; Popova, I.; Vasquez, M., FASEB J., **1989**, Submitted for publication.

23. Sapp, W.J.; Philpott, D.E.; Williams, C.S.; Kato, K.; Stevenson, J.; Serova, L.V., Proc. EMSA., **1988**, 46, 276.

TABLE 1. TOTAL SURVIVING SPERMATOGONIA PER STAGE 6 SEMINIFEROUS TUBULE PROFILE[a]

Treatment Group Data	Individual Animals[b]	Mean + S.E.M.[c]	SL-3[d]	SL-3[e] Simulation
Flight	37.90 ± 0.15 38.77 ± 0.12 39.36 ± 0.15 39.08 ± 0.12 38.83 ± 0.13	38.79 ± 0.06**	39.75 ± 0.14	26.82 ± 0.27
Synchronous	40.44 ± 0.10 41.13 ± 0.15 39.08 ± 0.19 40.00 ± 0.12 40.35 ± 0.12	40.20 ± 0.06*	N/A	N/A
Vivarium	43.15 ± 0.17 44.36 ± 0.13 43.58 ± 0.16 43.55 ± 0.20 44.12 ± 0.17	43.75 ± 0.07	42.71 ± 0.17	44.24 ± 0.27

---

a Tubules identified according to Huckins (Anat. Rec. 190:905, 1978). Cross section only.

b 200 tubules scored per animal; mean ± standard error.

c 5 animals per treatment; total = 1000 tubules scored.

d SL-3 data shown here for comparison (See Philpott et al., EMSA 44:248, 1986). Mean ± standard error, 200 tubules scored.

e Rat tail suspension; 50 tubules scored; mean ± standard error

* Significantly different from vivarium control, $P<0.001$

** Significantly different from vivarium control, $P<0.0005$

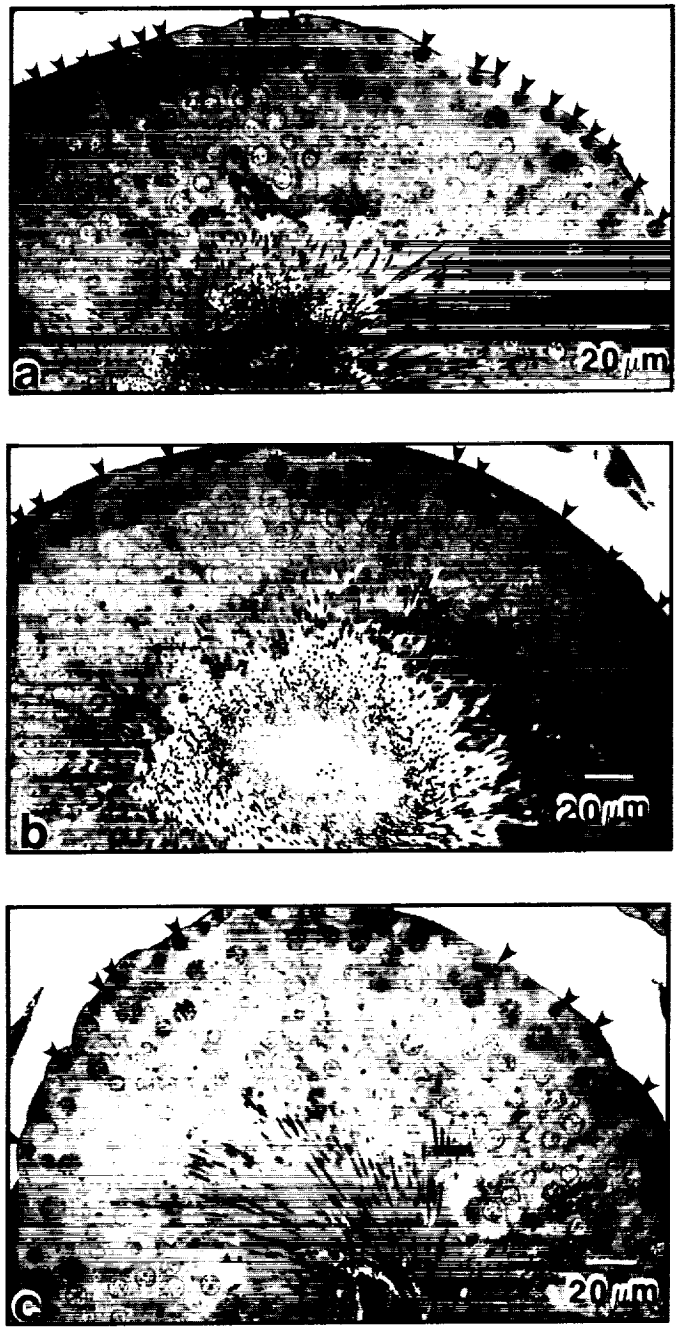

Figure legend

Figure 1. Representative sections of seminiferous tubules: (a) Vivarium control; (b) Synchronous control; (c) Flight animals. Arrows indicate spermatogonia.

Magnification = 300x.

EFFECT OF BIWEEKLY SHOOT TIP HARVESTS ON THE GROWTH AND YIELD OF "GEORGIA JET" SWEET POTATO GROWN HYDROPONICALLY

C.R. Ogbuehi*, P.A. Loretan, C.K. Bonsi, W.A. Hill
C.E. Morris, P.K. Biswas and D.G. Mortley
G.W. Carver Agricultural Experiment Station
Tuskegee University
Tuskegee, AL

ABSTRACT

Sweet potato shoot tips have been shown to be a nutritious green vegetable. This study was conducted to determine the effect of biweekly shoot tip harvests on the growth and yield of "Georgia Jet" sweet potato grown in the greenhouse using the nutrient film technique (NFT). The nutrient solution consisted of a modified half Hoagland solution. Biweekly shoot tip harvests, beginning 42 days after planting, provided substantial amounts of vegetable greens and did not affect the fresh and dry foliage weights or the storage root number and fresh and dry storage root weights at final harvest. The rates of anion and cation uptake were not affected by tip harvests.

*Author presenting paper. Contribution No. PS014 of the George Washington Carver Agricultural Experimental Station, School of Agriculture and Home Economics, Tuskegee University. This research was supported by funds from the National Aeronautics and Space Administration (Grant No. NAG10-0024) and USDA/CSRS (Grant No. ALX-SP-1). We wish to thank Mr. Ralph Prince and Dr. William M. Knott III of the NASA/John F. Kennedy Space Center for technical assistance.

EFFECT OF BIWEEKLY SHOOT TIP HARVESTS ON THE GROWTH AND YIELD OF "GEORGIA JET" SWEET POTATO GROWN HYDROPONICALLY

Introduction

In a number of countries where sweet potato is a staple, the shoot tips (top 10 cm) are eaten as vegetable greens. Villareal et al. (1979) reported that in Southeast Asian countries yields of sweet potato shoot tips consumed as vegetables varied from 10 to 16 t/ha while marketable roots for those cultivars studied as possible dual vegetable crops varied from 1 to 16 t/ha. In West Africa, Liberians consume sweet potato tips on a daily basis (As-Saqui, 1982). Pace et al. (1985a,b) reported that sweet potato green tips are as nutritious in Ca and Fe as are other leafy vegetables such as spinach, mustard, turnip and collard greens and can be similarly prepared. They suggested that sweet potato tips have potential as a new food in the U.S.

Because of its value as a dual vegetable in that both shoot tips and storage roots can be eaten, sweet potatoes have been selected by the National Aeronautics and Space Administration as a potential food source for space missions. Investigations are underway to determine the optimum conditions for production of sweet potatoes in Controlled Ecological Life Support Systems (CELSS). One aspect of this research is to study the effect of periodic harvesting of sweet potato shoot tips on the growth of the plant and its storage root yield.

Dahniya (1980) investigated the effect of leaf harvests and topping on the foliage and root yields of sweet potato. He showed that topping shoot tips resulted in 34 to 42% less shoot yield than did cutting plants at the base of each shoot. Storage root yield was less severely reduced when shoot tips were topped than when vines were cut at the base. Total shoot yield was unaffected when tips were harvested at 2-, 3-, or 4-week intervals.

Bartolini (1981) reported that shoot topping increased storage root yield of sweet potatoes significantly when done between one and two months after planting. Shoot topping beyond two months or continuous topping was detrimental to storage root production. Gonzales et al. (1977) studied the effect of topping and fertilization on yield of sweet potatoes and found that topping reduced storage root yields. The highest storage root yield was obtained from the no topping treatment; successively lower yields were obtained by topping at 3-week intervals and topping at biweekly intervals. In a related study, Hopkinson (1986) investigated the effect of shoot tip harvests of sweet potato at 45, 60 and 75 days after planting. He found that removal of 15 cm from the terminal ends of sweet potato vines at these dates did not significantly reduce storage root yields.

In an open hydroponic system study employing sand as the aggregate, Pace et al. (1988) showed that the dry matter and nutrient content of sweet potato green tips and roots harvested on different dates differed according to cultivar. Loretan et al. (1988) and Hill et al. (1988) also reported that the nutritive quality of storage roots and foliage of hydroponically grown sweet potatoes were similar to field grown sweet potatoes and suggested the crop has high potential for CELSS. However, Hill et al. (1988) reported that there was a higher shoot/storage root ratio, as measured by the harvest index, for sweet potato plants grown using the nutrient film technique (NFT) as compared to those grown using an aggregate. Depending on the cultivar, foliage growth in NFT can be prolific; this can be an advantage for CELSS in that the shoot tips can be cut and used as vegetable greens and the total biomass produced

can be increased. However, too much foliage growth could be a disadvantage because of limited space in the biomass production chamber (BPC) (Prince et al., 1986).

The objective of this study was to evaluate the effect of biweekly cutting of shoot tips on sweet potato plants grown in an NFT system.

Materials and Methods

Experiments on the effect of harvesting foliage shoot tips were carried out with plants grown in the Tuskegee University NFT system. Three channels, each with its own reservoir, were used with the first and third channels holding four plants each. Shoot tips (10 cm) from plants in the first channel were harvested starting at 42 days after planting and thereafter on a biweekly basis until the end of the experiment (Treatment A). The plants in the third channel were the control and were left intact until harvested at 120 days (Treatment C). The middle channel with no plants was used to monitor water loss due to evaporation for the other treatments.

A modified half Hoagland solution (30.4 liters) was used as the nutrient solution in each tank. The solution pH values were maintained at 6.0 by addition of either NaOH or H_2SO_4 (Bakker, 1986) while the temperature, salinity and electrical conductivity were recorded at regular intervals. Nutrient solution was pumped to all the channels by a small submersible pump (Teel Model IP680A, 1/200 HP) in the reservoir and the flow rate was maintained at 16 ml s^{-1}. Solutions were changed at 2-week intervals and were topped with deionized water if the volume was reduced to 8 liters prior to the 2-week interval. Samples of nutrient solutions from treatments A and C were taken at the time of solution preparation and prior to the solution change and analyzed for Cl, NO_3, H_2PO_4 and SO_4 with a Dionex Ion Chromatograph model 4000I. NH_4, K, Mg, and Ca cations were also analyzed in addition to the anions.

Abaxil stomatal conductance (cm s^{-1}) was also measured for five days between 1200 and 1400 h CST. The measurement was made on the third uppermost, fully expanded and unshaded leaf of each plant using a LI-1600 Steady State Porometer (LI-Cor, Inc., Lincoln, NE). If the third leaf was found damaged, measurement was made on the fourth or fifth leaf. The transpiration rate of each plant (ug $cm^{-2}s^{-1}$) was also recorded for five days. All five measurements were done during the last quarter of the plant's growth (90-100 days after planting).

Each shoot tip harvest of a plant was weighed fresh and again following drying at 70°C for 48 h. At the end of the experiment, all foliage was cut at the base, weighed fresh and dried for 48 h at 70°C and reweighed. The fibrous root mat thickness was measured before it was dried and weighed. Storage roots were counted and weighed fresh. A 25 gram sample of the roots from each plant was taken and dried at 70°C for 48 h in order to find percentage dry matter and storage dry root weight. The amount of solution taken up by the plants in each treatment was calculated by subtracting the volume of water that evaporated out of the middle unplanted channel from the volume of nutrient solution in each of the treatments. The experiment was repeated once. Results of the two experiments were pooled.

Results and Discussion

The biweekly anion (Cl, NO_3, H_2PO_4 and SO_4) uptake patterns for both the biweekly harvest and the control treatments were similar and followed the same trend. Uptake of NO_3 and H_2PO_4 for each 2-week period generally increased up to 8 weeks after planting before reaching a relatively steady state uptake rate. Uptake of SO_4 and Cl each increased up to the fourth and sixth week respectively, and subsequently oscillated up and down in value through the 18th week. More Cl and NO_3 were taken up than with the other anions. These results agree with the study by Kirkby (1969) who showed that Cl and NO_3 were taken up more rapidly than SO_4. Anion uptake increased with increased plant root formation. The overall uptake patterns of the anions are in agreement with those of Schwartzkopf (1987) using a modified half-Hoagland solution in which lettuce was grown.

The cation (NH_4, K, Mg and Ca) uptake pattern as measured on a biweekly basis for both treatments also followed the same trend. K, Mg, and Ca uptake tended to be higher for the control plants than for plants in which the foliage was harvested. The uptake for these three cations oscillated from the sixth week to the eighteenth week. The nutrient uptakes were in general agreement with the findings of Mengel and Kirkby (1983) that the rate of uptake of each anion and cation specie was dependent on the magnitude of each ionic specie in the nutrient solution.

Both the mean stomatal conductance and the mean transpiration rate for control plants were higher than for those plants with biweekly foliage harvests. The comparative stomatal conductance values were 1.26 cm s^{-2} for Treatment C and 1.00 cm s^{-2} for Treatment A. The mean transpiration rates were 8.54 and 7.98 ug $cm^{-2}s^{-1}$ for treatments C and A respectively. For both treatments the results are within the range of those measured for sweet potatoes grown under ambient and elevated levels of carbon dioxide in open top chambers (Biswas et al., 1985). The higher values obtained for the control, Treatment C, may have caused the higher use of nutrient solution by these plants (170.3 L) compared to Treatment A plants (126.0 L). Since the water loss due to evaporation was taken into account, these figures represent net uptake values. Water as well as light have been reported as two factors that have the greatest influence on stomatal resistance in plants (Turner, 1974).

There were no differences in sweet potato yield components (Tables 1 and 2) for sweet potatoes between Treatment A and Treatment C. However, storage root yields tended to be higher for the control, i.e., fresh storage root weight of 482.5 g/plant as compared to 423.5 g/plant for Treatment A.

Likewise, if biweekly foliage harvests were not included in the totals, the total foliage yield tended to be higher for the control, e.g., fresh weight of 396.8 g/plant as opposed to 329.5 g/plant for Treatment A. However, if the biweekly shoot tip yields were included, the total foliage fresh weight of 433.0 g/plant in Treatment A tended to be higher than the 396.8 g/plant for the control.

Although these yield components were lower than those reported by Hill et al. (1988) for "Georgia Jet" sweet potatoes grown in NFT, the conclusions drawn that there were no differences between treatments were the same as those found by Hopkinson (1986). In field studies with sweet potatoes he found that topping treatments did not significantly affect fresh or dry storage root yield. However, the results are contrary to those reported by Gonzales et al. (1977) for field grown sweet potatoes which showed that topping reduced the storage root yields of sweet potato when shoot tips were harvested on a biweekly basis.

Table 1. Effect of biweekly topping on storage root yield components* of "Georgia Jet" sweet potato grown in NFT.

Treatment	Storage Root			
	No.	Fresh Wt. (g)	Dry Wt. (g)	Dry Matter (%)
A (Biweekly topping)	5.1	423.5	77.7	18.0
C (Control)	6.1	482.5	81.7	16.9
LSD (5%)	NS	NS	NS	NS

*Mean of eight plants.

The results of these experiments show that harvesting "Georgia Jet" sweet potato shoot tips on a biweekly basis in an NFT system for use as a green vegetable will not affect storage root yield. "Georgia Jet" sweet potato has the potential for serving as a dual purpose food — a green vegetable and a fresh storage root — for long-term manned space missions. Further research on the relationship of shoot topping frequency on storage root yields of selected sweet potato cultivars is needed for CELSS.

Table 2. Effect of biweekly topping on fibrous roots* and foliage* of "Georgia Jet" sweet potato plants grown in NFT.

Treatment	Fibrous Roots	Foliage	
	Dry Wt. (g)	Fresh Wt. (g)	Dry Wt. (g)
A (Biweekly topping)	8.8	329.5 (433.0)**	55.0 (65.9)**
C (Control)	7.9	396.8	62.1
LSD (5%)	NS	NS	NS

*Mean of eight plants
**Total foliage weight + shoot tips.

References

As-Saqui, M.A., Proc. 1st Intl. Symp., AVRDC, Shanhuan, Tianan, Taiwan, 1982, 59.

Baker, E.M.V., Proc. 7th Ann. Conf. Hydroponics. 1986. Concord, CA.

Bartolini, P.U., Proc. 1st Intl. Symp., AVRDC, Shanhuan, Tianan, Taiwan, 1982, 209.

Biswas, P.K.; Hileman, D.R.; Allen, J.R.; Bhattacharya, N.C.; Lu, J.Y.; Pace, R.D.; Rogers, H.H.; Coleman, K.B.; Eatman, J.F.; Ghosh, P.P.; Mbikayi, N.; McCrimmon, J.N.; Menefee, A., Rep. 022, U.S. DOE, Carbon Dioxide Res. Div. Off. of Energy Res., Wash., D.C., 1985, 70.

Dahniya, M.T., Proc. 1st Trien. Root Crop Symp., Int. Soc. Trop. Root Crops - African Branch, 137.

Gonzales, F.R.; Cadiz, I.G.; Gugawan, M.S., Phillipine J. Crop Sci., 1977, 2, 97.

Hill, W.A.; Loretan, P.A.; Bonsi, C.K.; Morris, C.E.; Lu, J.Y.; Ogbuehi, C.R., Comm. on Space Res. (COSPAR) XXVII Plenary Mtg., Espoo, Finland, 18-29 July 1988.

Hopkinson, S.R.A., M.S. Thesis, 1986, Tuskegee U., Tuskegee, AL.

Kirkby, E.A., British Ecol. Soc. Symp. 1969, 9, 212.

Loretan, P.A.; Morris, C.E.; Bonsi, C.K.; Hill, W.A.; Pace, R.D.; Lu, J.Y.; Biswas, P.K., 7th Int. Cong. on Soilless Culture, Flevohof, Netherlands, May 13-21, 1988.

Mengel, K.; Kirkby, E.A., 4th Ed. Intl. Potash Inst., Bern, Switzerland, 1987, 143.

Pace, R.D.; Dull, G.G.; Phills, B.R., J. Food Sci. 1985, 5, 537.

Pace, R.D.; Sibiya, T.E.; Phills, B.R.; Dull, G.G., J. Food Sci. 1985, 5, 940.

Pace, R.D.; Bonsi, C.K.; Lu, J.Y.; Loretan, P.A.; Hill, W.A.; Morris, C.E., HortSci. 1988, 23 (5), 828.

Prince, R.P.; Knott III, W.M.; Hilding, S.E.; Mack, T.L., 33rd Ann. Mtg., Amer. Astro. Soc. Preprint AAS-86-338, San Diego, CA, 1986.

Schwartzkopf, S.H., Adv. Space Res. 1987, 7(4), 89.

Turner, N.C., Plant Physio. 1974, 53, 360.

Villareal, R.L.; Tsou, S.C.S.; Lin, S.K.; Chiu, S.C., Exp. Agric., 1978, 15, 117.

EFFECT OF CHANNEL SIZE ON SWEET POTATO STORAGE ROOT ENLARGEMENT IN THE TUSKEGEE UNIVERSITY HYDROPONIC NUTRIENT FILM SYSTEM

C.E. Morris, E. Martinez*, C.K. Bonsi, D.G. Mortley,
W.A. Hill, C.R. Ogbuehi, and P.A. Loretan

G.W. Carver Agricultural Experiment Station
Tuskegee University
Tuskegee, AL

ABSTRACT

The potential of the sweet potato as a food source for future long-term manned space missions is being evaluated for the National Aeronautics and Space Administration's (NASA) Controlled Ecological Life Support Systems (CELSS) program. Sweet potatoes have been successfully grown in a specially designed Tuskegee University nutrient film technique (TU NFT) system. This hydroponic system has yielded storage roots as high as 1790 g/plant fresh weight. In order to determine the effect of channel size on the yield of sweet potatoes, the width and depth of the growing channels were varied in two separate experiments. Widths were studied using the rectangular TU NFT channels with widths of 15 cm (6 in), 30 cm (12 in) and 45 cm (18 in). Channel depths of 5 cm (2 in), 10 cm (4 in) and 15 cm (6 in) were studied using a standard NASA fan-shaped Biomass Production Chamber (BPC) channel. A comparison of preliminary results indicated that, except for storage root number, the growth and yield of sweet potatoes were not affected by channel width. Storage root yield was affected by channel depth although storage root number and foliage growth were not. Both experiments are being repeated.

* Graduate student presenting paper. Contribution No. PS015 of the George Washington Carver Agricultural Experiment Station, Tuskegee University. This research was supported by funds from the U.S. National Aeronautics and Space Administration (Grant No. NAG10-0024) and USDA/CSRS (Grant No. ALX-SP-1). We wish to thank Mr. Ralph Prince and Dr. William M. Knott III of the NASA/John F. Kennedy Space Center for technical assistance.

EFFECT OF CHANNEL SIZE ON SWEET POTATO STORAGE ROOT ENLARGEMENT IN THE TUSKEGEE UNIVERSITY HYDROPONIC NUTRIENT FILM SYSTEM

Introduction

Research on the growth and yield of food crops in a controlled environment is currently being conducted by NASA through its Controlled Ecological Life Support Systems (CELSS) program for future applications on space missions. The sweet potato is one of eight crops initially selected by NASA to be used for the CELSS program (Wheeler and Tibbitts, 1984). Studies in progress at Tuskegee University are being directed toward growing sweet potatoes hydroponically to evaluate sweet potato production potential for CELSS and to better understand the physiology of storage root enlargement.

For several years, sweet potatoes have been grown in a specially designed Tuskegee University nutrient film technique (TU NFT) system (Loretan et al., 1988b). This system uses growth channels measuring 15 cm (6 in) deep x 15 cm wide x 1.2 m (48 in) long, and a storage root yield as high as 1790 g/plant (Hill et al., 1988) has been obtained. Sweet potatoes grown hydroponically in sand and perlite in different size pots showed no significant effect from pot size (Loretan et al., 1988a). However, the storage root yield tended to increase with increased pot size.

The objectives of the present studies are to evaluate the effect of various channel widths and depths on the yield of "Georgia Jet" sweet potatoes grown in the TU NFT system.

Materials and Methods

Experiment I

Four vine cuttings (15 cm) of the "Georgia Jet" sweet potato cultivar were planted into each of three TU NFT channels. The experiment used channels of standard depth and length (15 cm [6 in] and 1.2 m [48 in], respectively) with treatments of varying widths: (a) the standard - 15 cm [6 in]; (b) 30 cm [12 in] and (c) 45 cm [18 in]. A separate reservoir (30.4 liter capacity) for the nutrient solution was used for each treatment. A modified half-Hoagland nutrient solution was delivered to the plants in each channel at a flow rate of 1 liter/min. The nutrient solution was changed every 14 days or was topped with deionized water if the volume fell to 8 liters or less before the biweekly changeover date. Nutrient solution pH was kept at 5.5 to 6.0 and solution temperature, salinity and electrical conductivity were frequently measured. The ambient temperature within the greenhouse varied between 22° and 35°C, depending on weather conditions. The daytime irradiance level ranged from 200 - 2000 umol $m^{-2}s^{-1}$. Supplemental cool white fluorescent (CWF) lighting was used on cloudy days. Carbon dioxide was at ambient level.

Experiment II

In a second experiment, "Georgia Jet" sweet potato vine cuttings (15 cm) were planted into three NASA fan-shaped channels (Prince et al., 1985). These channels have an overall length of 83 cm with

a maximum width of 42 cm at one end and a minimum width of 18 cm at the other. Three channel depth levels were used: (a) 5 cm (2 in)—standard for the Biomass Production Chamber, (b) 10 cm (4 in) and (c) 15 cm (6 in) (equivalent to the TU NFT channel depth). Methodology and growing conditions were similar to those listed in experiment I.

As the foliage grew in both experiments, the vines were trained to vertical strings dropping 1 m from above each channel. Plants were harvested 120 days after planting and storage root number and fresh weight as well as foliage fresh weights were taken. A 25 g sample of fresh storage root from each plant was dried in a 70°C oven for 48 h to provide percentage dry matter and storage root dry weight. Foliage and fibrous roots were dried in an oven at 70°C for 48 h and weighed to obtain dry weights.

Results and Discussion

The effects of three channel widths on the growth of "Georgia Jet" sweet potato are shown in Table 1. There was no effect of channel width on fresh or dry weight of foliage or storage roots. However, channel width influenced storage root number, with the 45 cm wide channel producing a significantly higher storage root number than either the 30 or 15 cm wide channels. The 45 cm channel width also tended to produce higher fresh storage root weight than the other two. Observations on the location of root enlargement within the channel showed that it took place more to the center of the channel except in the 15 cm channel where the roots made contact with the side walls. No storage roots were observed to have contacted the side walls in either the 30 cm or the 45 cm wide channels. Enlargement of the storage roots started at approximately the same distance (5 to 10 cm) from the plant stem in each treatment.

Table 1.
The effects of channel width on growth of "Georgia Jet" sweet potato plants* in a greenhouse using NFT.

Channel Width (cm)	Storage Roots			Foliage		Fibrous Roots
	No.	Fr. Wt. (g)	Dry Wt. (g)	Fr. Wt. (g)	Dry Wt. (g)	Dry Wt. (g)
45	4.8A	356.9A	79.8A	364.8A	60.0A	10.0
30	3.0B	303.0A	68.5A	319.6A	48.0A	8.0
15	2.5B	306.1A	65.5A	349.9A	46.3A	7.3

* Mean of four plants - means in the same column with the same letter are not significantly different using Duncan's Multiple Range Test at the 5% level.

The effects of channel depth on the growth of "Georgia Jet" sweet potato are shown in Table 2. The effect on storage roots was inconclusive. The number of roots tended to increase with channel depth, but there were no significant differences among channels. However, the largest fresh storage root weight (659.1 g per plant) was produced in the channel with the least depth (5 cm)—significantly higher than the 317.5 g per plant produced in the 10 cm channel. It was also higher than the 553.7 g per plant produced in the 15 cm channel depth although not significantly different. One storage root (815.7 g) in the 5 cm channel depth accounted for most of the yield in that channel. The dry storage root weights followed the same trend as the fresh weight. Even though the magnitude of the foliage weight, both fresh and dry, was in the same proportion as the storage roots, there were no significant differences among these treatments. The dry fibrous root weight also followed this trend. Thus there is no clear effect of channel depth. This may be due to an incidence of stem rot in some of the treatments. This experiment along with the experiment on channel width is presently being repeated so that the effect of channel size on the growth of "Georgia Jet" sweet potato may be clarified.

Table 2.
The effects of channel depth on growth of "Georgia Jet" sweet potato plants* in a greenhouse using NFT.

Channel Width (cm)	Storage Roots			Foliage		Fibrous Roots
	No.	Fr. Wt. (g)	Dry Wt. (g)	Fr. Wt. (g)	Dry Wt. (g)	Dry Wt. (g)
15	5.5A	553.7AB	91.0AB	561.0A	73.9A	10.5
10	3.0A	317.5B	51.1B	324.0A	50.3A	10.0
5	2.5A	659.1A	109.2A	616.0A	89.3A	13.0

* Mean of four plants - means in the same column with the same letter are not significantly different using Duncan's Multiple Range Test at the 5% level.

References

Hill, W.A.; Loretan, P.A.; Bonsi, C.K.; Morris, C.E.; Lu, J.Y.; Ogbuehi, C.R., Comm. on Space Res. (COSPAR) XXVII Plenary Mtg., Espoo, Finland, 18-29 July, 1988.

Loretan, P.A.; Hill, W.A.; Bonsi, C.K.; Morris, C.E., HortSci. 1988, 23 (5), 828.

Loretan, P.A.; Morris, C.E.; Bonsi, C.K.; Hill, W.A.; Pace, R.D.; Lu, J.Y.; Biswas, P.K., Proc. 7th Intl. Cong. on Soilless Culture, Flevohof, Netherlands, May 13-21, 1988.

Prince, R.P.; Knott, W.M. III; Hilding, S.E.; Mack, T.L., 33rd Ann. Mtg., Amer. Astro. Soc. AAS Preprint AAS-86-338, San Diego, CA, 1986.

Wheeler, R.M.; Tibbitts, T.W., NASA Contractor Report 177323. 20pp.

EXCIMER LASER INTERACTION WITH DENTIN OF THE HUMAN TOOTH

Introduction

It is well known that light amplification by stimulated emission of radiation is represented by the acronym laser. This project had its beginning in the quantum electronics department of the IBM Thomas J. Watson Research Center in Yorktowne Heights, New York. Using a excimer laser, whose frequency is in the deep ultra-violet region of the spectrum, produced many unusual conical structures within the dentin of the inner part of the human tooth.

Structure of Tooth

The structure of the tooth consists of the crown, neck, pulp cavity and root. The crown is the part of the tooth that is covered by enamel and projects beyond the gum line. The neck is the narrow area of the tooth, and the pulp cavity is that area which contains a soft vascular and sensitive organ called dental pulp. The root of the tooth is the area which is the embedded part of the tooth.

Description

Examination of the structures of the enamel reveals the following characteristics. It is the hardest, most compact part of the tooth which forms a thin layer over an exposed crown. It consists of a collection of small hexagonal rods and columns which lie parallel to each other. Dark lines mark the mode of formation of the rods (Fig. 3). The enamel's chemical composition consists of 96.5% earthy matter (phosphate with the carbonate of calcium, with traces of fluoride of calcium and phosphorous magnesium) and 3.5% animal matter.

The composition of dentin differs from that of enamel in that dentin is the calcareous part of the tooth beneath the enamel which forms the greater mass of the tooth and also covers the exposed part of the crown. Microscopic examination shows that dentin consists of a number of minute wavy branches called dentinal tubuli which are embedded in a dense homogeneous substance known as the intertubular tissue. Dentin is composed of 28% animal matter and 72% earthy matter. The cortical substance, cementum, a thin layer on the root of the tooth extends from the termination of the enamel to the apex of the root. This cortical substance chemical compound resembles bone in that it contains lacunae and canaliculi.

Method and Results

The dentin of various molar teeth were exposed to 1300 pulses to 4000 pulses using an excimer laser. The results indicate some very unique structures occurring within the dentin. The interaction of the laser light seemed to form unusual conical structures within the dentin. Using false color (when all of the gray levels have the same value, the computer will pick a particular color and the next value up or down will show as a different color) permits the eye to see detail that would not normally be visible under normal perceivable gray levels.

Conclusion

By varying the frequency of the laser one can disperse the energy and cause more bleeding in laser surgery, but not destroy the cells associated with the incision. Therefore, the healing process will virtually be without scarring. Whereas, using the infrared laser the blood loss would be less, but the healing process would tend to be longer because cells are being destroyed due to the cauterization effect of the laser. The question is, are these structures produced as an interaction with the laser or are they an intrinsic part of the structure? We are still studying the effects of the laser interaction upon dentin, and in using the EM we will be able to understand more clearly the interaction of the excimer laser upon the tooth dentin and other various biological tissue.

The Effects of Laser Interaction upon Dentin

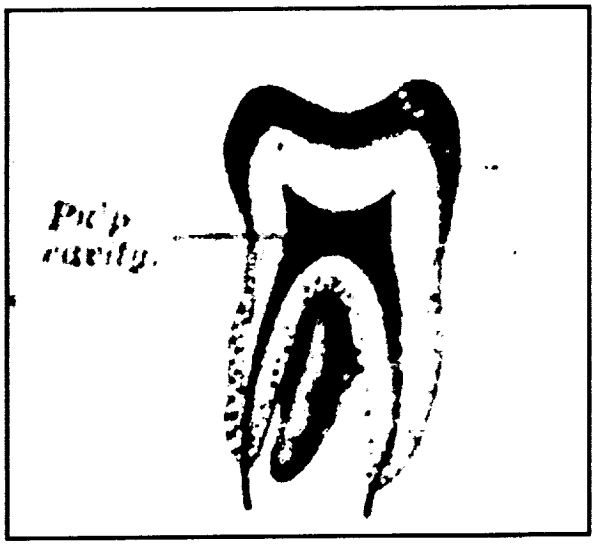

Figure 1

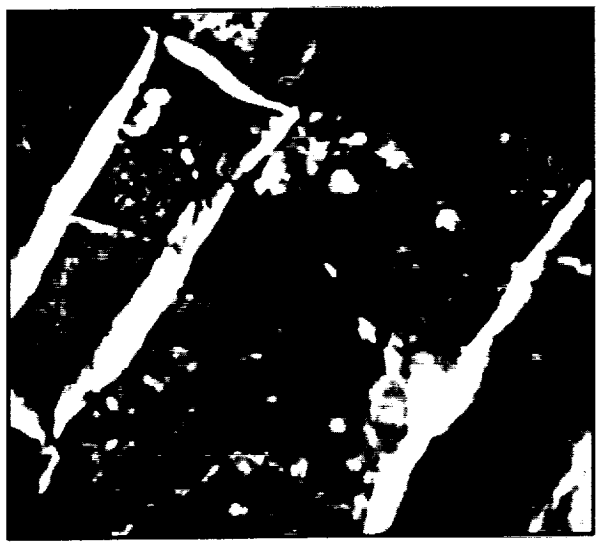

Figure 2

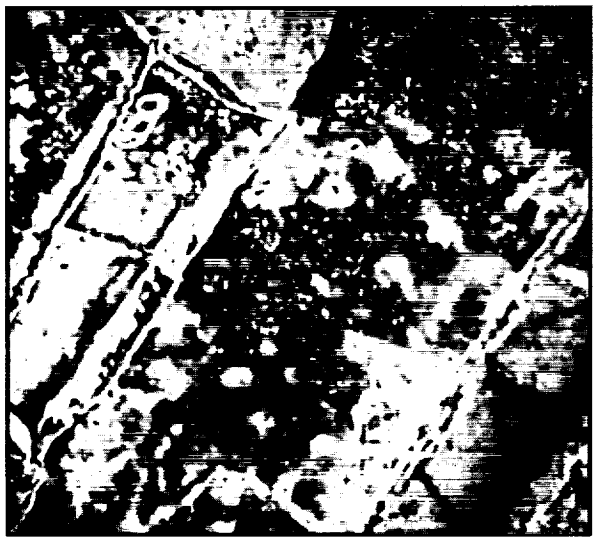

Figure 3

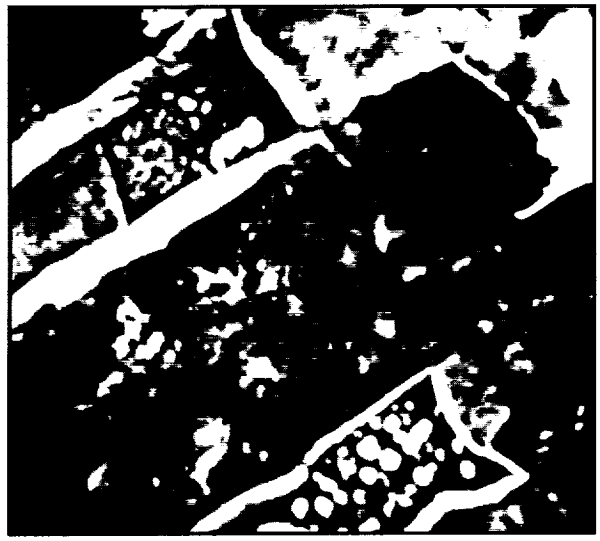

Figure 4

Figure 5

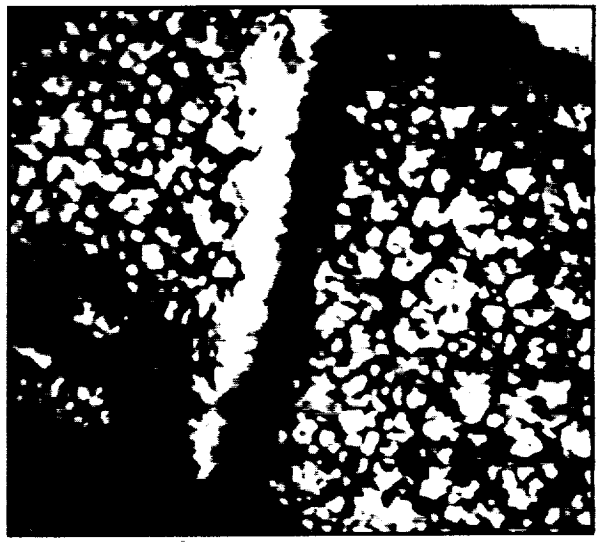

Figure 6

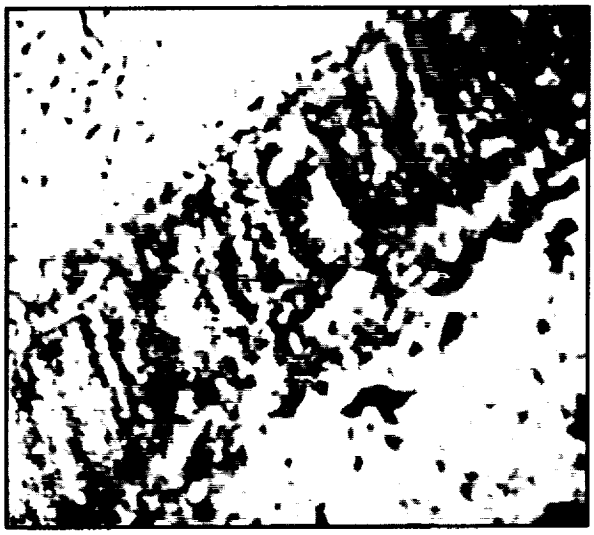

Figure 7

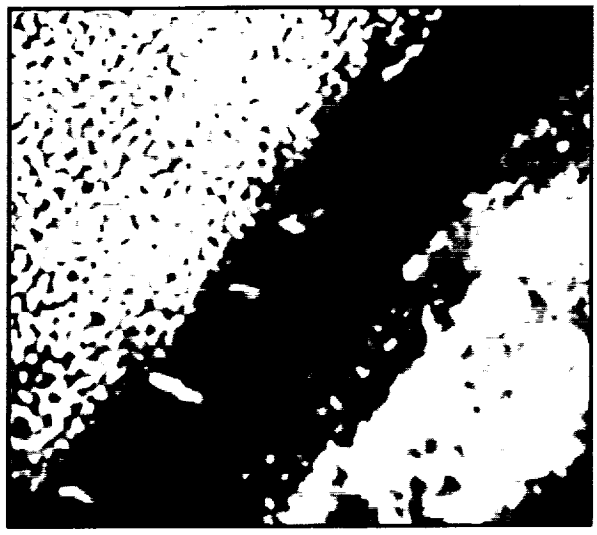

Figure 8

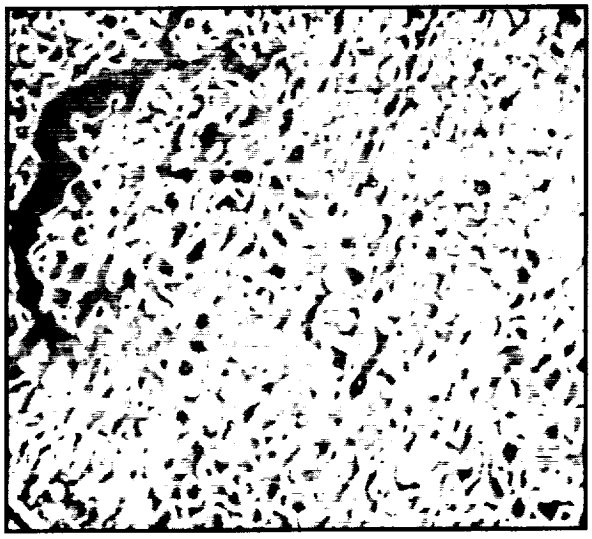

Figure 9

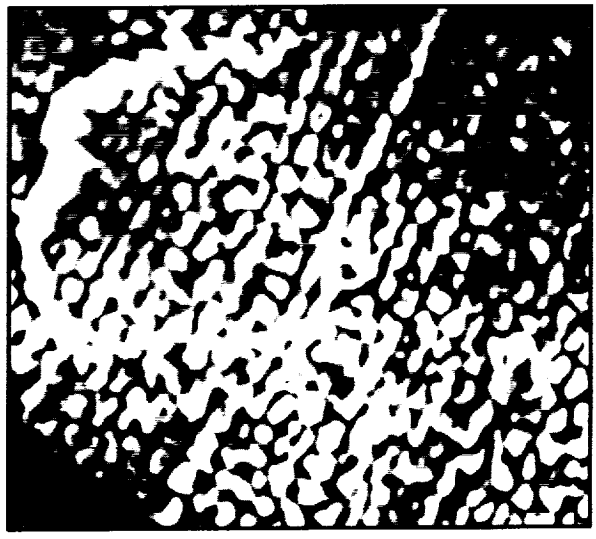

Figure 10

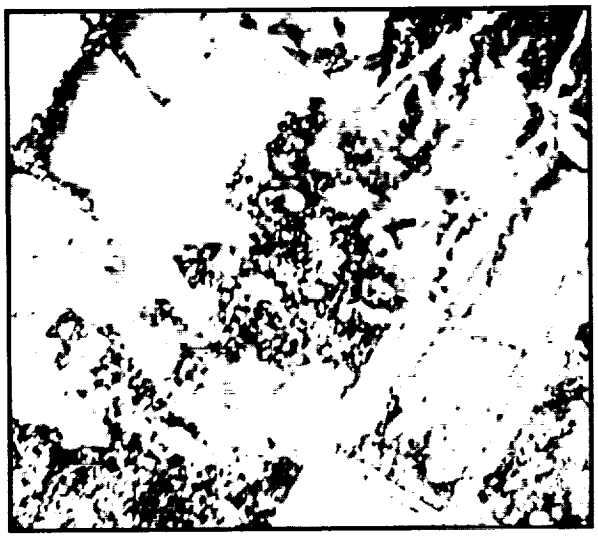

Figure 11

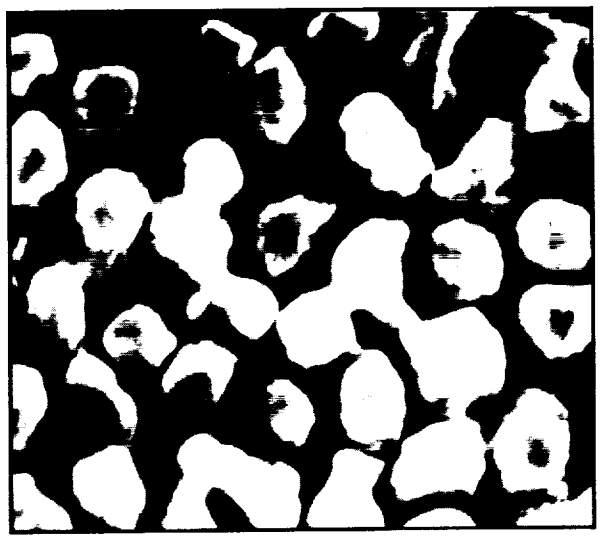

Figure 12

INTERNATIONAL FOOD PATTERNS FOR SPACE FOOD

Selina Ahmed
Department of Home Economics
Texas Southern University

Student Researchers:
Amanda Cox
Pauline V. Cornish

Technical Monitor:
Charles T. Bourland (JSC)

Introduction

The food pattern of a given group of people originates from the availability of foods in the country where they live (11). Food patterns are interwoven with the culture of the people, and are the response of individuals or groups to social and cultural pressures in selecting, consuming, and using portions of the available food supply (7,8). Food patterns are based on edible materials a culture considers to be food, as well as on the type of food production and service in a country (10).

A country's food patterns are molded by its agricultural resources, technical progress, buying power, and cultural patterns. In trying to understand the food habits of a people, one needs to learn about the country from which they come (9). The quest for space exploration is shared by cosmonauts and astronauts from American, Asian, and European countries (6). Thus, space exploration has not only become international, but also a multicultural affair. It is, therefore, necessary that scientists involved in space research investigate the multicultural backgrounds of cosmonauts and astronauts in order to learn more about food patterns of representative countries. This type of research is important in order to understand the cosmonauts' and astronauts' food habits, so appropriate menus can be developed to better serve the space explorers.

In 1982, Soviet scientist V.P. Bychkov, researched the diet of crews in Salyut-6 Orbital Space Station. He confirmed that conventional and familiar foods such as fresh fruits and vegetables have positive psychological effects as they alleviate the monotony of the processed, unconventional food common on long duration missions (5). Food consumption and psychological wellness are significantly improved by familiarity (4). Familiar foods normally enhance morale (1).

Based on the above studies, it is important to have knowledge of the food patterns of space explorers to ensure psychological well being and enhance morale. Therefore, the intent of this research is to investigate the integration of international food patterns in space nutrition programs. It is

speculated that nutritionally balanced, cross-cultural diets can be provided to meet the needs of space explorers from various cultural and ethnic backgrounds.

Statement of the Problem

The purpose of this research effort is (a) to obtain basic data on ethnic foods by studying dietary patterns and multicultural foods, and (b) to determine nutritional status of multicultural space explorers by evaluating dietary, clinical, biochemical, and socioeconomic factors.

Objectives

1. To study food patterns of selected countries' ethnic groups and cross-cultural aspects of foods' suitability for space explorers.

2. To identify appropriate foods for selected ethnic groups in terms of preparation needs, nutritional benefits, preservation, and packaging requirements.

3. To evaluate and analyze selected food items recommended for space nutrition programs.

4. To integrate selected foods into an international space food system.

Justification of the Study

The study will play a significant role in providing nutritional research for space explorers of different ethnic backgrounds. It will provide scientific background information by bringing together cross-cultural dietary and nutritional information from different ethnic groups. Results of this study will also help the health care personnel including physicians, dietitians, and nutritionists to better understand and assist patients from other cultures during illness. Also, the results will provide data which will help in the development of future food plans for long duration flights involving manned exploration to Mars and lunar base colonies.

Methodology

A literature review will determine ethnic food patterns for international crew members. Foods vary in their nutrient composition. Some have high nutrient density in relation to energy. Even ethnic foods which are familiar may not, by themselves, be nutritionally sufficient; therefore, a nutritional analysis of multicultural foods will also be conducted. The study will be conducted in four tasks (Table 1).

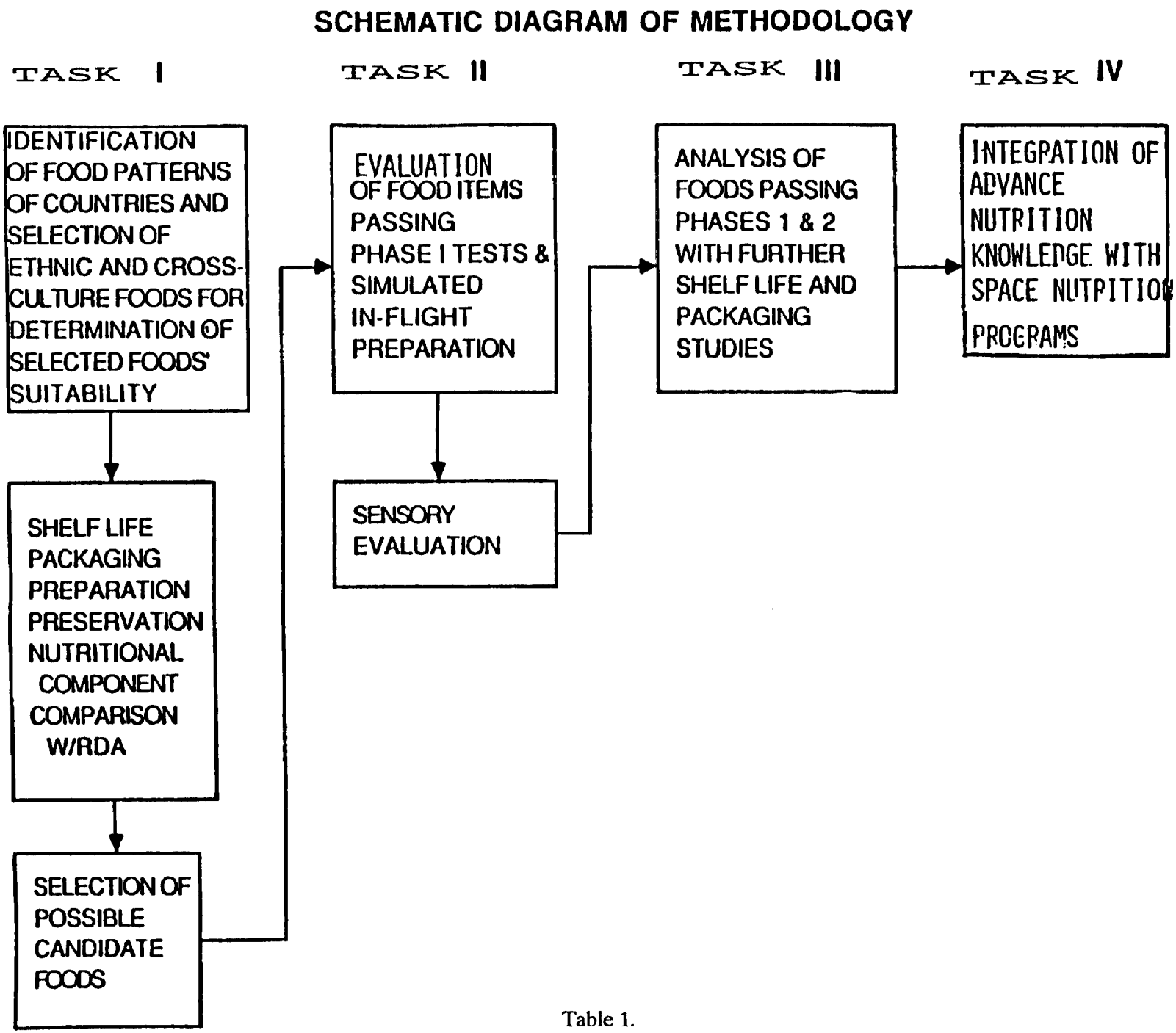
SCHEMATIC DIAGRAM OF METHODOLOGY
TASK I
TASK II
TASK III
TASK IV
IDENTIFICATION OF FOOD PATTERNS OF COUNTRIES AND SELECTION OF ETHNIC AND CROSS-CULTURE FOODS FOR DETERMINATION OF SELECTED FOODS' SUITABILITY
SHELF LIFE PACKAGING PREPARATION PRESERVATION NUTRITIONAL COMPONENT COMPARISON W/RDA
SELECTION OF POSSIBLE CANDIDATE FOODS
EVALUATION OF FOOD ITEMS PASSING PHASE I TESTS & SIMULATED IN-FLIGHT PREPARATION
SENSORY EVALUATION
ANALYSIS OF FOODS PASSING PHASES 1 & 2 WITH FURTHER SHELF LIFE AND PACKAGING STUDIES
INTEGRATION OF ADVANCE NUTRITION KNOWLEDGE WITH SPACE NUTRITION PROGRAMS

Table 1.

In task one the identification of the countries and determination of their typical dietary practices will be evaluated. Foods which provide cross-cultural satisfaction will be studied. The study will also determine food handling characteristics such as shelf life, packaging, preparation, preservation, and the nutrient content of foods from different ethnic origins.

Task two will include food preparation (in flight) and sensory evaluation by Research Guidance Panels (a mechanism to measure the acceptance of food products by using organoleptic testing).

Task I

Identification of the countries and determination of their typical dietary practices will be one of the parts of task one. Task one will also identify the foods which provide cross-cultural satisfaction and can be recommended for astronauts of different ethnic backgrounds. In order to identify food for the space food and nutrition programs, the following food handling characteristics will be considered.

A. Shelf Life Determination

Shelf life is the study of the keeping quality of food. The process involves keeping food at various desirable temperatures for different lengths of time. The maximum shelf life study will last up to 90 days for the following temperatures:

-20 degrees F frozen

40 degrees F refrigerated

70 degrees F ambient

After each shelf life study, the foods will go through acceptability tests by sensory evaluation. Food will also be tested for chemical and microbiological safety parameters. Nutritional analysis will also be considered.

B. Packaging

Packaging possibilities for the foods will be reviewed for compatibility with the Space Food Service Systems (3).

C. Preparation

Processing requirements for in-flight meal preparation will be used as a criterion in the identification of suitable foods for the space food programs.

D. Preservation

Different techniques to preserve the quality of food and retain nutritional values will be considered. Freezing, freeze drying, pre-cooking, dehydrating, etc., are all preservation methods to be evaluated in developing a menu for space food service systems for astronauts of different ethnic origin.

E. Nutritional Analysis

In order to determine the suitability of food for the space food programs, nutrition analysis is essential. It can help when planning the daily menus for the astronauts. Comparison of each complete menu with recommended dietary allowances is also necessary.

Task II

Preparation of food items passing task one tests will be examined in task two. Task two will consist of the following steps:

A. Preparation (In-Flight)

Food preparation prior to eating, e.g., cutting, peeling, adding water, chilling, and heating are the various methods of in-flight preparation to be reviewed to help select the appropriate food for the space food programs. (2)

B. Sensory Evaluation

Sensory evaluation of the foods will be conducted by technical taste panels.

Task III

The experimental foods which pass the sensory evaluation will be selected for final studies of shelf life and packaging. Foods will be packaged in appropriate containers and placed in controlled storage and evaluated at predetermined intervals.

Task IV

The ultimate goal of this study is to select suitable foods for astronauts from different ethnic backgrounds. The scientific data derived will be integrated to advance knowledge of space nutrition programs for future endeavors.

Discussion:

Based on the Johnson Space Center's selection of astronauts, the researcher selected the countries to be studied. Presently, the countries that have been selected are European countries: Sweden, West Germany, Italy, Poland, and the USSR; and Asian countries: India, Bangladesh, Pakistan, Japan, Philippines, and Thailand. The foods for these countries have also been selected.

In April 1989, ground base studies of the quality characteristics of food patterns will start. Progression of the study as indicated by the schematic diagram of methodology will be completed systematically.

Summary

The purpose of the research effort is to (a) obtain basic data on ethnic foods by studying dietary patterns and multicultural foods, and (b) to determine the nutritional status of multicultural space explorers by evaluating dietary, clinical, biochemical and socioeconomic factors.

The study will be conducted in four tasks which include identification of the countries and determination of their typical dietary practices. The study will also identify the foods which provide cross-cultural satisfaction and can be recommended for astronauts of different ethnic backgrounds. In order to identify foods for the space food and nutrition programs, the following food handling characteristics will be considered: shelf life determination, packaging, preparation, preservation, and nutritional analysis. Menu recommendations from the selected foods will also be developed.

References

1. Ahmed, S., Comparison of Soviet and U.S. Space Food and Nutrition Programs. NASA/JSC, NGT44-001-800, August, 1988.

2. Bourland, C.T., Heating Food in Space. Memo, 1985.

3. Bourland, C.T., Fohey, M.F., Rapp, R.M., and Sauer, R.L., Space Shuttle Food Processing and Packaging. Journal of Food Protection, 44:313-319, 1981.

4. Bourland, C.T., Fohey, M.F., Kloeris, V.L., and Rapp, R.M., Designing a Food System for Space Station Freedom. Food Technology. Feb. 78-81, 1989.

5. Bychkov, V.P., Ushakov, A.S., Kalandarov, S., Markaryan, M.V., Sedova, Y.E.A., Sivuk, A.K., and Khokhlova, O.S., Diet of Crews in Salyut-6 Orbital Station. USSR Report: Space Biology and Aerospace Medicine, Vol. 16, No. 2, pp. 11-15, 1982.

6. Gazenko, O.C., Man in Space: An Overview. Aviation, Space and Environmental Medicine. Dec. 53-55, 1983.

7. Krause, M.V., Mahan, L.K., Food, Nutrition and Diet Therapy, Seventh Edition, W.B. Saunders Company, pp. 334-335, 1984.

8. Lewis, J.S.; Glaspy, M.FE., Food Habits and Nutrient Intakes of Filipino Women in Los Angeles. J.Am. Diet.A. 67:122, 1975.

9. Lowenberg, M.E., Todhunter, E.N., Wilson, E.D., Savage, J.R., and Lubawski, J.L.: Food and Man, 2nd Edition, NY, John Wiley & Sons, p. 120, 1974.

10. Mitchell, H.S., Ryanbergen, H.J., Anderson, L., Dibble, M.V., Nutrition in Health and Disease, Sixteenth ed. J.B. Lippincott, Inc., 1976.

11. Robinson, C.H., Lawler, M.R. Normal and Therapeutic Nutrition, Sixteenth Edition. Macmillan Publishing Co., Inc., pp. 284-286, 1982.

12. Tobias, A.L., Thompson, P.J., Issues in Nutrition for the 1980's, Wordsworth Health Sciences Division, Monterrey, California, 1980.

IN VITRO REGENERATION OF BASELLA ALBA L.

Norris Allen Edney, Muhammad A. Rizvi
and Narjis F. Rizvi

Department of Biological Sciences
Alcorn State University
Lorman, Mississippi

ABSTRACT

Basella alba L. is a tropical vine used as a vegetable in some Asian and African countries. It has potential as a non-traditional crop for small family farms. A short day plant, it blooms during fall, provided the temperatures are mild. In the southeastern United States, the short days of fall are associated with sub-freezing temperatures, and plants are killed before blooming. In this study attempts were made to regenerate the plant using tissue culture techniques. Several trials were conducted with different media, hormones and explants. It was found that nodal segments on Gamborg medium regenerated shoots. Interaction studies of auxins and cytokinins indicated that its endogenous auxin content might be high because callus proliferated in almost all treatments and roots initiated even when the medium was not supplemented with an auxin.

IN VITRO REGENERATION OF BASELLA ALBA L.

Introduction

In recent years an increasing interest has been expressed in non-traditional crops that show promise for small American family farms (Tiwari et. al., 1988). Basella alba could be a promising new vegetable crop for small farms because it is pest and disease resistant, it has a high nutritive value, and its yield is 8 times higher than regular spinach (Yamaguchi, 1983).

Basella alba L. is a tropical vine (Bailey, 1951). It is used as a vegetable in some countries of Southeast Asia (Yamaguchi, 1983 and Tiwari et. al., 1988). Basella leaves and stems taste like spinach; therefore, it is known as "Malabar Spinach" in English (Yamaguchi, 1983). In India and Bangladesh it is known as "Poi Sag" (Tiwari et. al., 1988). In China it is called "Lok Kwa" (Yamaguchi, 1983).

Basella alba L. blooms during the short days of fall provided the temperatures are mild at nights. In Mississippi and all other parts of the southeastern United States short days are associated with sub-freezing temperatures at night. Therefore, Basella alba L. vines die before flowering.

Plant tissue culture techniques have been valuable in alleviating such problems through vegetative propagation of plants (Evans et. al. 1983). Plant regeneration in vitro is the key to practical application for most purposes using tissue culture techniques (Tomes, 1985).

Regeneration of any member of Basella alba L. has not been reported with the use of tissue culture techniques. Therefore, the purpose of this study was to investigate regeneration of Basella alba L. in vitro.

Materials and Methods

This study was conducted in three phases. The objective of phase I was to compare the performance of the three most used plant tissue culture media: Murashige & Skoog (MS), Anderson (AND) and Gamborg B5 (GB5) on callus proliferation, and root and shoot initiation on five explants: petiole, stem, meristem, leaf and node. Explant used were 0.5 cm^3 in size or segments of stem, leaf, petiole, meristem and node. All of the explants were put in Murashige and Skoog (MS), Anderson (AND) and Gamborg B5 (GB5) media after surface sterilization. Explants were sterilized as described by Thorpe (1981). MS medium had 100, 0.5, 0.5, 0.1, 2.0 and 80.0 mg/l of myo-inositol, nicotinic acid, pyrodoxine HCl, thymine HCl, glycine and adenine sulfate (Hartman and Kester, 1983). AND medium was supplemented with 4 mg/l thiamine HCl, 100 mg/l myo-inositol and 80 mg/l adenine sulfate (Hartman and Kester, 1983). GB5 medium had 10.0, 1.0, 100.0 and 80.0 mg/l of thiamine HCl, nicotinic acid, pyridoxine HCl, myo-inositol and adenine sulfate respectively in addition to basal inorganic salts (Hartman and Kester, 1983). Growth regulators for callus proliferation, shoot and root initiation trials were 0.1, 0.2, 0.4, 0.8 and 1.6 mg/l of napthaleneacetic acid (NAA) as auxin and 0.1, 0.2, 0.4, 0.8 and 1.6 mg/l of benzyl adenine (BA) as cytokinin. In every trial, one set without growth regulators was used as control. The pH of the media were adjusted to 5.7 before autoclaving. All three culture media had 30 g/l sucrose and 7 g/l agar (Thorpe, 1983). Media were autoclaved at 121°C for 20 minutes. The culture environment was maintained at 25°C and illuminated with cool white fluorescent lamps at 40 u

Einsteins/m^2/sec for 16 hours per day. After 3 weeks the cultures were evaluated by determining the size of calluses and total number of shoots greater than 5 mm in length produced per explant.

The objective of the phase II experiments was to evaluate the interactions of napthalenenacetic acid (NAA) and benzyl adenenine (BA) on callus proliferation and initiation of roots and shoots from explants selected earlier in phase I. It was 6 x 6 diallel experiment (Sondahl et. al., 1981). Dilution of NAA and BA were 0, 0.1, 0.2, 0.4, 0.8 and 1.6 ppm. Each treatment had 5 replications.

Mature vines were used as source of explants. The explants used were 3 - 5 mm segments of nodes. The explants were surface sterilized with 20% chlorox for 5 minutes and washed with distilled water 5 times. (Thorpe, 1981). Standard Gamborg B-5 medium was used as a source of nutrition for explant growth. It was supplemented with 3% sugar and 0.8% agar. After addition of NAA and BA, the pH of the medium was adjusted to 5.7 - 5.8 by NaOH and/or HCl solution. The medium was sterilized and autoclaved at 121°C at 15 lbs. PSI for 15 minutes.

Results and Discussion

Five explants: leaf, stem, meristem, petiole and nodal segments, and three media: MS, AND and GB-5 were used in phase I experiments. It was found that all explants initiated calluses but shoot initiation was restricted to a few combinations. Leaf explants on all three media showed signs of cell growth and cell elongation but did not produce a well defined callus. Stem, meristem and petiole initiated calluses on all three media are under investigation. Nodes produced calluses and proliferated shoots on GB5 and AND media but not on MS medium. In primary cultures shoot initiation occured only with the use of GB5 and AND media. Leaf, stem, meristem and petiole when used on shooting medium initiated calluses. The failure of leaf, stem, meristem and petiole explants to produce shoots on any of the media was not unprecedented. Endogenous hormones play a very significant role in the outcome of exogenous hormones on shoot proliferation (Band and Lineveger, 1986). Because of poor shooting responses on MS and AND media, further studies were made on GB5 medium only.

In the interaction trials it was found that the effective dilutions of NAA and BA for initiation of shoots ranged in between 0 - 1.6 ppm (Table 1).

Table 1:
Effect of NAA and BA in GB5 medium on shoot regeneration from nodes of Basella alba L. after two weeks of inoculation.

BA mg/1	NAA mg/1	Percent of culture with shoots
0 - 0.1	0 - 0.1	9.3
0.8 - 1.6	0 - 0.1	89.4
0.2 - 0.8	0.2 - 0.8	5.7

In the second experiment of interaction of NAA and BA it was found that calluses were observed in all of the treatments (Table 2).

Table 2:
Interaction of NAA and BA on callus formation.

BA in ppm	NAA in ppm					
0	0	0.1	0.2	0.4	0.8	1.6
0.1	1.2*	0.6	1.3	2.0	2.0	2.0
0.2	1.7	0.8	1.3	2.0	2.0	2.0
0.4	1.6	1.2	1.8	2.0	2.0	2.0
0.8	1.6	1.2	1.8	2.0	2.0	2.0
1.6	1.6	1.2	1.8	2.0	2.0	2.0

* x explant size

Shoots initiated only when NAA was in the range of 0 to 0.1 ppm. Higher concentrations of NAA inhibited shoot formation (Table 3).

Table 3:
Interaction of NAA and BA on shoot formation.

BA in ppm	NAA in ppm					
	0	0.1	0.2	0.4	0.8	1.6
0		2*				
0.1	3	3				
0.2	3	3				
0.4	3	3				
0.8	3	5		1		1
1.6	3	6				

* number of shoots/treatment

NAA favored root formation. Absence of BA was not critical for root formation. In some treatments, root initiation was found even in high concentrations of BA, but such incidence was rare (Table 4).

In phase II it was found that the favorable ratios for rooting and shooting were 0.1 - 0.2 ppm of BA/0.8 - 1.6 ppm of NAA, and 0.8 - 1.6 ppm of BA/0.1 - 0.2 ppm of NAA respectively. Media with the same ratios were used in phase III of this experiment. It was found that calluses did not respond to these treatments. Further studies are suggested to be conducted with the use of other hormones.

Table 4:
Interaction of NAA and BA on root formation.

BA in ppm	NAA in ppm					
	0	0.1	0.2	0.4	0.8	1.6
0			2	2	6	6
0.1			4	6	8	8
0.2			4	6	8	8
0.4		2*				
0.8				1		1
1.6						1

* number of roots/treatment

Literature Cited

1. Bailey, L. H. (1951). Manual of Cultivated Plants. Macmillan Co., New York. p. 367.

2. Brand, Mark H. and R. Daniel Linebeger (1986). In Vitro Propagation of Halesia Carolina L. and the Influence of Explantation Timing on Initial Shoot Proliferation. Plant, Cell, Tissue and Organ Culture: Mar. Nuj. Publisher, Netherlands.

3. Evans, D., W. Sharp, P. Ammirato and Y. Yamada (1983) Handbook of Plant Cell Culture. Macmillan & Co., New York p. 126.

4. Hartman, Hudson T., and Dale E. Kester (1983). Plant Propagation, Prentice Hall Inc., Englewood Cliffs, New Jersey.

5. Thorpe, Trever A. (1981). Plant Tissue Culture. Academic Press., Orlando, FL.

6. Tiwari, S. C., P. E. Igbokwe and J. B. Collins (1988) Malabar Spinach (Basella alba L.) MAFES Information Sheet 1321, Miss. State University, MS 29762.

7. Tomes, Dwight T. (1985). Opportunities and Limitations of Genotypic Influence on Establishment of Plant Regeneration from Callus and Cell Cultures of Crop Species in Biotechnology in Plant Science. Eds: Zaitlin, Day and Hollaender. Academic Press. London.

8. Sondahl, M. R., L. C Monaco, and W. R. Sharp (1981). In Vitro Method Applied to Coffee in Plant Tissue Culture. Ed. Thorpe. Academic Press, Orlando, FL. p. 325.

9. Yamaguchi, M. (1983). Other Succulent Vegetables. World Vegetables: Principles, Production and Nutritive Values. AVI Publication Co., Westport, CT., p. 267-368.

MANIPULATING CYANOBACTERIA: SPIRULINA FOR POTENTIAL CELSS DIET

Mahasin G. Tadros, Woodrow Smith, Peter Mbuthia and Beverly Joseph
Department of Biology
Alabama A&M University
Normal, AL

ABSTRACT

Spirulina sp. as a bioregenerative photosynthetic and an edible alga for spacecraft crew in a CELSS, was characterized for the biomass yield in batch cultures, under various environmental conditions. The partitioning of the assimalitory products (proteins, carbohydrates, lipids) were manipulated by varying the environmental growth conditions. Our experiments with Spirulina have demonstrated that under "stress" conditions (i.e. high light 160 uE m^{-2} s^{-1}, temperature 38°C, nitrogen or phosphate limitation; 0.1 M sodium chloride) carbohydrates increased at the expense of proteins. In other experiments, where the growth media were sufficient in nutrients and incubated under optimum growth conditions, the total proteins were increased up to almost 70% of the organic weight. In other words, the nutritional quality of the algal could be manipulated by growth conditions. These results support the feasibility of considering Spirulina as a subsystem in CELSS because of the ease with which its nutrient content can be manipulated.

MANIPULATING CYANOBACTERIA: SPIRULINA FOR POTENTIAL CELSS DIET

Introduction

Pursuit of our national goals in space exploration will eventually require man's long-duration tenancy of celestial vehicles and planetary bases. Requirements for life support could be met through expenditure of stored supplies and by regeneration and reuse of the waste products of human metabolism. The logistics necessary for regeneration for extended space missions are well documented (1). The primary source of all man's food and organic raw materials is solar energy. Conventional food sources consist of higher plants and animals. Unconventional food sources for human consumption are photosynthetic algae and bacteria and non-photosynthetic bacteria, yeast and fungi. Conventional food sources are highly palatable, but require a long time to produce. Algae, on the other hand, grow rapidly; their metabolism can be controlled; they produce a high ratio of edible to nonedible biomass; and their gas-exchange characteristics are compatible with human requirements. The biological components of Controlled Ecological Life Support System (CELSS) will serve as subsystems for the revitalization of air for the long term space flight.

Cyanobacteria single cell protein (SCP) has been used as a food source in various parts of the world (e.g. Mexico, China and Africa) since ancient times; in fact, dried cyanobacteria and cyanobacterial tablets are now sold in health food stores in Japan, North America and Europe because they are recognized for their nutritional value. The nutritional quality of all cyanobacteria which have been tested appears to be very high. The protein of S. maxima is easily digestible and approximately 65% of the protein is assimilable.

In order to evaluate the potential of Spirulina for a CELSS diet, it is essential to have background information on the environmental tolerance of the species. The purpose of this project was to evaluate the chemical composition of Spirulina under different growth conditions in batch cultures. This paper presents the results of one year's work.

Materials and Methods

Spirulina maxima (UTEX LB 2342) was cultured in Zarrouk medium (3). For mass culturing, algal cells were grown in bottles. Cultures were illuminated continuously by placing them in front of a bank of two cool white fluorescent lamps (40W). Light irradiation, measured at the surface of the culture bottles, was 80 uE m^{-2} s^{-1}. The cultures were grown in a water bath kept at 29-30°C by the use of a heater-thermostat combination. Cultures were grown under different conditions. Cells were collected after five days growth and analyzed for total proteins, carbohydrates and lipids.

Results and Discussion

Physiological Characterization of Cultures, under Stress Conditions: The results of analysis were expressed on the basis of organic weight (Ash Free Dry Weight: AFDW) and arerepresented in Table 1.

Light Irradiance and Temperature: Increasing the light irradiance to 120 uE m^{-2} s^{-1}, led to an increase in the total carbohydrate content and a decrease in protein content: S. Maxima 19.58%, 29.06%. Increasing the temperature of culture incubation to 38°C influenced the composition of the strain in a similar manner to the light irradiation experiment: S. maxima, 45.28%, 18.75%, for protein and carbohydrates, respectively. The culture produced a low percentage of lipids when grown in high temperature experiments. **Nutrient Limitation:** Media limited in nitrate-N and phosphate-P favored the accumulation of carbohydrate rather than protein. Nitrate and phosphate limited cultures: S. maxima had 37.52%, 35.21% carbohydrate and 21.56%, 41.25% protein. When the cultures were transferred to media limited in nitrogen and phosphate, cultures changed in color from blue to yellow-green. N-limited cultures of Anacystis nidulans (7), and P-limited cultures of Oscillatoria agardhii (8), showed elevated levels of polysaccharide storage. **Sodium Chloride:** As Zarrouk (3) media were enriched with 0.1M and 0.5M NaCl, the carbohydrate content of the cells increased, when compared to that of the control (Zarrouk: 0.01M NaCl), to 26.24%, 36.73% in S. maxima. On the other hand, the total protein decreased respectively to 52.62%, 45.64% in S. maxima. The lipid percentages showed little increase when compared to those of the complete media (control). **Bicarbonate:** When bicarbonate concentration of Zarrouk media was reduced to one quarter (4.g/L), the culture showed much difference in the chemical composition as compared with the control media except their yield was somewhat below the control. The carbohydrates increased to 38.53% when 0.03% CO_2 in air was used for aeration and to 40.23% when 1% CO_2 air was used for aeration.

It can be concluded that through manipulating environmental conditions of the algal growth, one can modify the photosynthetic products. Thus, Spirulina can be, through manipulating growth factors, used as palatable diet compared to higher plants.

Acknowledgment

This work was supported by NASA/Ames Research Center Cooperation Agreement #NCC2-501.

References

1. MacElroy, R.D., Bredt, J. CELSS, NASA CP-2378, 1985, 1.
2. Fogg, G.E. Ann. Bot., 1956, 20 265.
3. Zarrouk, C. Thesis, University of Paris (France), 1966.
4. Faucher, O., Coupal, B. Ledny, A. Can. J. Microbiol. 1979, 25, 752.
5. Goldman, J.C., Graham, S., J. Appl. Environ. Microbiol., 1981, 41, 60.
6. Lang, D.S., Brown, E.S., Appl. Environ. Microbiol., 1981, 42, 1002.
7. Lehman, M., Wober, G., Archin. Microbiol., 1976, 3, 93.
8. Riegman, R., Rutgers, M., Mur, L.R., Archin. Microbiol., 1985, 142, 66.

Table 1. Molecular Composition of Spirulina maxima

Growth Conditions	% Organic Wt. (AFDW) Protein	Carbohydrate	Lipids
*Sufficient Nutrients	69.75	11.5	4.68
High Light (160uEm-2s-1)	29.06	19.58	3.56
High Temperature (38°C)	45.28	18.75	3.75
N-limited	21.56	37.52	4.68
P-limited	41.25	35.21	5.20
Sodium Chloride 0.1M	52.62	26.25	4.68
0.1M	45.64	36.73	7.52
Bicarbonate (4.4g/L) (0.03% CO_2)	45.67	38.53	6.22
(1% CO_2)	43.52	40.23	6.53

*Experimental conditions were:
temperature 30°C; light irradiance 80uEm^{-2}s^{-1};
air flow rate 300 ml/min.;
The values shown are averages of four independent determinations.

N91-28071

SEASONAL NITROUS OXIDE FLUX FROM AN INTENSIVELY MANAGED PASTURE IN A HUMID SUBTROPICAL ECOSYSTEM

E. A. Brams and W. H. Anthony
Cooperative Agricultural Research Center
Prairie View A&M University
Prairie View, Texas

G.L. Hutchinson
Agricultural Research Service, U.S. Department of Agriculture
Northern Plains Area
Fort Collins, Colorado

G.P. Livingston
Ecosystems Science & Technology Branch
National Aeronautics & Space Administration (NASA)
Ames Research Center
Moffett Field, California

ABSTRACT

Nitrous oxide (N_2O) flux from vented chambers was measured over intensively and minimally managed bermuda grass Cynodon dactylon hay meadows in a humid, subtropical ecosystem (S.Texas) for several calendar years during scheduled sampling protocol following harvest, fertilization and rainfall events while measuring diel N_2O emissions once during each of 5 - seasonal day growth cycles which divided each calendar year. Soil pools of nitrite NO_2^-, nitrate NO_3^- and ammonia (NH_3) were measured in soil samples taken at 2 and 10 cm depths during each emission collection to determine transformations of the nitrogen pools coupled with N_20 emissions. The highest diel N_20 emission occur midday in the Spring cycle, measuring 9.0 g N/ha/d only for several weeks, while emissions dropped to <1.0 g N/ha/day during hot, dry and colder months. Intensively managed meadows (4 fertilizations and harvests per year, respectively, plus integrated pest management procedures) induced higher seasonal N_2O emissions than minimal treatment (one fertilization and harvest, respectively, per year), averaging 2.75 and 5.97 g N ha/day, respectively. Nitrous oxide emission data as responses to soil parameters (temperature and moisture) and environmental parameters (air temperatures, relative humidity, wind velocity and direction and rainfall) were also measured where air temperature, soil moisture and fertilization were the most powerful factors driving the N_2O flux.

X-RAY SENSITIVITY OF DIPLOID SKIN FIBROBLASTS FROM PATIENTS WITH FANCONI'S ANEMIA

Ranjini Kale
Biology Department
Alabama A&M University
Normal, AL

ABSTRACT

Experiments have been performed on Fanconi's anemia and normal human fibroblast cell lines growing in culture in an attempt to correlate cell cycle kinetics with genomic damage and determine their bearing on the mechanism of chromosome aberration induction. FA fibroblasts showed a significantly increased susceptibility to chromosomal breakage by x rays in the G2 phase of the cell cycle. No such response was observed in fibroblasts irradiated in the G0 phase. The observed increases in achromatic lesions and in chromatid deletions in FA cells as compared with normal cells appear to indicate that FA cells are deficient in strand break repair and also possibly in base damage excision repair. Experiments are now in progress to further elucidate the mechanisms involved.

CONSTRUCTION OF STABLE EXPLICIT FINITE-DIFFERENCE SCHEMES FOR SCHRÖDINGER TYPE DIFFERENTIAL EQUATIONS

Ronald E. Mickens
Departments of Mathematics and Physics
Clark-Atlanta University
Atlanta, Georgia

Technical Monitor
John Shoosmith
Langley Research Center

ABSTRACT

A family of conditionally stable, forward Euler finite-difference equations can be constructed for the simplest equation of Schrödinger type, namely $u_t = iu_{xx}$. Generalization of this result to physically realistic Schrödinger type equations is presented.

CONSTRUCTION OF STABLE EXPLICIT FINITE-DIFFERENCE SCHEMES FOR SCHRÖDINGER TYPE DIFFERENTIAL EQUATIONS

Introduction

Discrete finite-difference models of differential equations have been a traditional and popular technique for obtaining numerical solutions of both ordinary and partial differential equations [1,2]. An essential component of this procedure is the replacement of the derivative by its discrete analogue based on the definition of the derivative as a limit process; that is

$$\frac{dx}{dt} = \lim_{h \to 0} \frac{x(t+h) - x(t)}{h}, \tag{1}$$

and

$$\frac{dx}{dt} \to \frac{x_{k+1} - x_k}{h}, \tag{2}$$

where x_k is an approximation to $x(t_k)$ with $t_k = hk$. However, more general definitions of the derivative can be defined. As an example consider

$$\frac{dx}{dt} = \lim_{h \to 0} \frac{x(t+h) - x(t)}{\phi(h)}, \tag{3}$$

where $\phi(h)$ has the property

$$\phi(h) = h + 0(h^2). \tag{4}$$

Note that for this case the discrete replacement for the derivative is

$$\frac{dx}{dt} \to \frac{x_{k+1} - x_k}{\phi(h)}, \tag{5}$$

which, in general, differs from Eq. (2) for finite values of the step-size h.

The major implication of the above remarks is that new discrete models of differential equations can be constructed based on Eq. (3). These models have the potential for providing solutions that arise when the conventional discrete derivation of Eq. (2) is used.

As an illustration, consider the differential equation

$$\frac{dx}{dt} = i\lambda x, \qquad x(t_0) = x_0, \qquad \lambda = \text{real parameter}, \tag{6}$$

with solution

$$x(t) = x_0 \exp [i\lambda (t - t_0)]. \tag{7}$$

Application of conventional procedures [1] gives, for example, the finite-difference scheme

$$\frac{x_{k+1} - x_k}{h} = i\lambda x_k. \tag{8}$$

In contrast, consider the following exact scheme [3]

$$\frac{x_{k+1} - x_k}{\phi(h)} = i\lambda x_k, \quad x_0 = \text{given}, \tag{9}$$

where

$$\phi(h) = \frac{e^{i\lambda h} - 1}{i\lambda}. \tag{10}$$

An easy and direct calculation [4] shows that for Eqs. (6) and (8), we have for their solutions $x(t_k) \neq x_k$, while for Eqs. (6) and (9), $x(t_k) = x_k$ for all step-sizes h. Also, from Eq. (10), we obtain

$$\phi(h) = h + i\lambda h^2 + 0(h^3). \tag{11}$$

Consider the simplest Schrödinger-type equation

$$u_t = iu_{xx}. \tag{12}$$

Conventional finite-differences, using a forward Euler replacement for the time-derivative, give a scheme that is unconditionally unstable [5]. We now show how conditionally stable schemes can be constructed.

To proceed, based on the discussion presented earlier, we construct the following finite-difference scheme

$$\frac{u_m^{n+1} - u_m^n}{i\phi_1(\Delta t,\lambda)} = \frac{u_{m+1} - 2u_m^n + u_{m-1}^n}{\phi_2(\Delta x,\lambda)} \tag{13}$$

where the "denominator functions" have the properties

$$\phi_1(\Delta t, \lambda) = \Delta t + i\lambda(\Delta t)^2 + 0[(\Delta t)^3] \tag{14a}$$

$$\phi_2(\Delta x,t) = (\Delta x)^2 + 0[(\Delta x)^3] \tag{14b}$$

and λ, for the moment, is an unspecified parameter. Defining $R(\Delta t, \Delta x, \lambda)$ as

$$R \equiv \frac{i\phi_1(\Delta t, \lambda)}{\phi_2(\Delta x, \lambda)} = R_1(\Delta t, \Delta x, \lambda) + iR_2(\Delta t, \Delta x, \lambda) \tag{15}$$

we can rewrite Eq. (13) in the form

$$u_m^{n+1} = Ru_{m+1}^n + (1-2R)\,u_m^n + Ru_m^n.$$

The substitution of a typical Fourier mode

$$u_m^n = C(n)\exp[\,i\omega(\Delta x)m], \tag{17}$$

into Eq. (16) and requiring the C(n) be bounded allows the determination of the stability properties. (This concept of stability is called "practical stability" [5,6].) A straight-forward calculation shows that Eq. (16) is stable if the following condition is satisfied.

$$(R_1 - \tfrac{1}{4})^2 + (R_2)^2 \le \frac{1}{16}\,. \tag{18}$$

This relation has the interesting geometric interpretation: In the (R_1,R_2) plane, Eq. (16) is stable for points on and inside the circle of radius 0.25 centered at (0.25, 0). We will refer to the inequality of Eq. (18) as the circle condition.

For a given application, the following procedure is to be followed:

a) Select denominator functions with the properties given in Eqs. (14) and calculate R in Eq. (15).

b) Choose a point $(\bar{R}_1, \bar{R}_2)$ consistent with the circle condition of Eq. (18).

c) Determine $R_1(\Delta t, \Delta x, \lambda)$ and $R_2(\Delta t, \Delta x, \lambda)$ from Eq. (15) and set them equal, respectively to $\bar{R}_1$ and $\bar{R}_2$, i.e.,

$$R_1(\Delta t, \Delta x, \lambda) = \bar{R}_1, \quad \bar{R}_2(\Delta t, \Delta x, \lambda) = \bar{R}_2. \tag{19}$$

d) Select a value for the space-step, Δx, and solve the two relations of Eq. (19) for Δt and λ in terms of Δx. Doing this gives

$$\Delta t = f_1(\Delta x), \quad \lambda = f_2(\Delta x). \tag{20}$$

Thus, the selection of the point $(\bar{R}_1, \bar{R}_2)$, satisfying the circle condition and the relations of Eq. (20), defines completely the finite-difference scheme of Eq. (16).

As an example, consider the following denominator functions

$$\phi_1 = \Delta t + i\lambda(\Delta t)^2, \quad \phi_2 = (\Delta x)^2, \tag{21}$$

with

$$\bar{R} = \frac{1+i}{4}. \tag{22}$$

The following results are easily obtained

$$\Delta t = \frac{(\Delta x)^2}{4}, \quad \lambda = -\left[\frac{4}{(\Delta x)^2}\right], \quad \phi_1 = \frac{1-i}{4}. \tag{23}$$

and

$$u_m^{n+1} = \left(\frac{1+i}{4}\right)[u_{m+1}^n + u_{m-1}^n] + \left(\frac{1-i}{2}\right)u_m^n. \tag{24}$$

Note that everything can be expressed in terms of Δx, the space step-size; its value can be selected as desired.

A second, nontrivial example is the nonlinear Schrödinger equation

$$u_t = iu_{xx} + |u|^2 u. \tag{25}$$

A finite-difference scheme that embodies the work of this paper and also uses the nonlocal modeling of the nonlinear term [3] is

$$\frac{u_m^{n+1} - u_m^n}{\phi_1} = i\left[\frac{u_{m+1}^n - 2u_m^n + u_{m-1}^n}{\phi_2}\right] + \left[\frac{u_{m+1}^n + u_{m-1}^n}{2}\right]^* \left[\frac{u_{m+1}^n + u_{m-1}^n}{2}\right] u_m^{n+1}, \tag{26}$$

where the star (*) denotes complex conjugation, and the denominator functions $\phi_1(\Delta t, \lambda)$ and $\phi_2(\Delta x, \lambda)$ satisfy the conditions of Eqs. (14). Note that Eq. (20) is an explicit finite-difference scheme.

In summary, we have presented a new procedure to construct explicit finite-difference schemes for Schrödinger type partial differential equations. In general, we expect these schemes to be conditionally stable. This paper summarizes research that has already been published in Physics Review A, June 1989 and in the "Proceedings of the 2nd IMAC Conference on Computational Acoustics."

References

1. M.K. Jain, *Numerical Solution of Differential Equations*, Halstead Press, New York, 1984.

2. A.R. Mitchell, *Computational Methods in Partial Differential Equations*, Wiley, New York, 1969.

3. R.E. Mickens, Mathematical modeling of differential equations by difference equations, in *Computational Acoustics*, Vol. 1, D. Lee, R.L. Sternberg and M.H. Schultz, eds., North-Holland, Amsterdam, 1988.

4. R.E. Mickens, *Difference Equations*, Van Nostrand Reinhold, New York, 1987.

5. T.F. Chan, D. Lee and L. Shen, Stable explicit schemes for equations for the Schrödinger type, *Siam Journal of Numerical Analysis*, 23 (1986), 274-281.

6. R.D. Richtmyer and K.W. Morton, *Difference Methods for Initial-Value Problems*, Interscience, New York, 1967.

IMAGE DATABASES: PROBLEMS AND PERSPECTIVES

V. Naidu Gudivada
Jackson State University
Department of Computer Science
Jackson, MS

ABSTRACT

With the increasing number of computer graphics, image processing, and pattern recognition applications, economical storage, efficient representation and manipulation, and powerful and flexible query languages for retrieval of image data are of paramount importance. This paper examines these and related issues pertinent to image databases.

IMAGE DATABASES: PROBLEMS AND PERSPECTIVES

1. Introduction

With the rapid advances in the Image Processing/Pattern Recognition and Computer Graphics fields, Image Database (IDB) systems have recently attracted the attention of many researchers. The recent special issue of IEEE Transactions on Software Engineering (IEEE 88) attests to this fact. Even though there has been considerable research activity on issues such as image compression, hierarchical data structures for storing complex images, and various similarity measures for efficient retrieval of the images with partial specifications, but not until recently has serious thought been given to integrating these results and techniques into a unified framework for efficient storage, processing, and retrieval of complex images. Many of these techniques were used in several applications to varying degrees such as Desktop Publishing/Office Automation, Cartographic and Mapping Applications, Interactive Computer-aided Design (CAD), Geographic Information Systems (GIS), Spatial Database Management Systems (SDMS), Message Management Systems(MMS), and Remote Sensing (RS) of earth resources.

This paper examines some issues and techniques for designing image databases and provides a survey of some existing systems. The outline for the remainder of the paper is as follows. Section two provides a historical perspective and sets the terminology. Various existing design paradigms for image databases are examined in section three. Future outlook and conclusions are given in section four.

2. Historical Perspective and Terminology

The disadvantages of traditional file processing were recognized early in the seventies. Several database management systems (DBMS) were proposed and implemented in the later years for efficient storage, retrieval, and management of alphanumeric data. Enormous amounts of storage are required for storing images/pictures. A sharp decline in hardware prices coupled with advances in processor speeds and mass storage devices paved the way for integration of image data with alphanumeric data in several application areas. These systems capable of managing both alphanumeric and image data came to be known, depending on the application area and the extent to which facilities are provided by the system for managing image data, as Pictorial Database Systems (PDBS)(Chan 81) (Yang 87), Integrated Database Management Systems (IDMS)(Tang 81), Image Database (IDB) systems (Tamu 84), Geographic Data Processing (GDP) Systems (Nagy 79), and Geographic Information Systems (GIS)(Fran 88). Parker (Park 88) lists many other terms used synonymously with GIS. Some of these systems are not functionally distinct in the sense that some complement each other and some are supersets of others. This nomenclature problem is not uncommon for a broad and rapidly evolving discipline such as the one under discussion.

There are two basic approaches to the processing of pictorial data (Tamu 84). The first one is image processing/pattern recognition and emphasizes analysis, transformation, and recognition to yield other images or a symbolic description of the images. The second approach is computer graphics which synthesizes images from given descriptions. For computer graphics, data structures are of paramount consideration, whereas for image processing/pattern recognition, processing is of primary consideration. In other words, these two approaches vastly differ in the processing methods involved and data structures employed. Therefore, image database design concepts also differ. Graphic oriented pictorial databases are suitable for applications such as CAD/CAM which involve pictorial data of great complexity. Modeling, 3D object representations, and complex data structures/formats are of primary

concern. Image processing oriented pictorial databases are suitable for applications based on LANDSAT imagery. The primary concern here is for efficient storage techniques and use of pattern recognition techniques for retrieval. Pictorial databases refer to both graphic oriented and image processing oriented databases. Tamura and Yokoya (Tamu 84) refer to these database systems as image databases and so does this author.

Tamura (Tamu 80) classifies image database systems into five types. Type one refers to a large collection of images systematically collected and made available to several users. Remote sensing data centers databases fall into this category and require no explicit image database management system. Type two refers to databases for retrieval of secondary information such as date of acquisition, quality, altitude, etc. A conventional DBMS can be used for this type for storage and retrieval of secondary information which is inherently alphanumeric. Type three systems are characterized by the existence of a management system for imagery and map data for spatially-oriented processing. Type four systems store structural information describing pictures or scenes. Type five systems constitute a set of library images which are intended to be used as benchmarks for evaluating and comparing new algorithms. This classification is mentioned for historical interest and has no relevance for classifying today's systems.

Vector format and raster format are the two principal formats used for storing images. Applications such as cartography, topography, and spatial analysis or GIS use vector format. Spatial data are represented by using point, line or segment, and polygon data types. Applications using LANDSAT imagery use only point data type. Also, the output produced by many modern image capturing devices is inherently in raster format. Since raster format stores images as a collection of points along with their attributes, this leads to enormous storage requirements. However, several image compression techniques for compressing raster image data are reported in the literature (Yang 87) (Barn 88). Of course, compression techniques consume computational time for encoding and decoding of images. In addition to the vector and raster formats, there are several other formats (Chan 81).

3. Design Paradigms

Image data models, image data types, image data structures, mechanisms for describing image features, storage/compression techniques, and a flexible query language are integral parts of an image database system. A system to integrate and coordinate the functionalities of these components is an image database management system. In the following sections, each of the component structures is examined in detail.

3.1 Image Data Models

A data model for image databases should provide a uniform framework for handling both alphanumeric and image data. The associated management system is expected to store, retrieve, and process a large number of pictures of great complexity. There exists three main data models for managing alphanumeric data, namely, hierarchical, network, and relational models. It may seem natural to extend the concepts and techniques of conventional DBMS to bear with image database systems. This approach has two main disadvantages (Econ 83). Since conventional DBMS are geared to handle structured alphanumeric data, the resulting image databases are inefficient and cumbersome with unnatural query languages. Secondly, these query languages are very complex because they emphasize low-level descriptions of images.

Design characteristics of an image database depend on the intended functionality, types of images, and the extent of data abstraction and image data structures. An archival system for LANDSAT imagery

is more concerned about efficiency of storage and retrieval than the processing methods and data structures. On the other hand, a system for map database applications focuses on efficient data structure design, ease of update, coloring, and overlays rather than storage requirements. Some applications may impose significant data abstraction. For these applications, image features are completely symbolized and the symbolic information, not the original images, is stored and managed. On the other extreme, are the cases where the images are stored without compression and the management system simply maintains pointers to these locations. Between these two extremes are a number of other possibilities.

There are three basic approaches to image database design. The first approach is to simply extend the conventional database by adding images as a standard data type and extending the query language. ADM (Aggregate Data Manager) (Taka 80) is an example of this kind. Its architecture is based on a relational database management system, System-R. System-R's query language, SEQUEL is suitably modified to handle image data. A second approach is to add database capabilities to an existing image processing system. EIDES (ETL Image Database for Experimental Studies) (Tamu 80) and MIDAS (Multi-sensor Image Databases System) (McKe 77) are two examples of this approach. In addition to these two, there are several approaches from application fields such as geographic data processing, medical imaging, remote sensing, and fingerprint analysis (Tamu 84).

In general, a relational data model is widely used in experimental image database systems because of its mathematical simplicity. GRAIN(Graphics-oriented Relational Algebra Interpreter) and REDI(Relational Database System for Images) are two examples of early implementations (Tamu 84). Unfortunately, relational model has several shortcomings for modeling pictorial data (Moha 88). A relational model is inherently suitable for representing one-dimensional data in the tabular form but pictorial data is two-dimensional. Hierarchical structured data cannot be easily represented using a relational model. Many tables are required for representing hierarchy links. It is not possible to explicitly specify semantic information about relationships. Since most of the semantic information is distributed over several hierarchy link relations, meaning has to be guessed by the user before performing any operation.

3.2 Data Types, Data Structures, and Storage Techniques

Spatial data are inherently multi-dimensional (Oren 88). Also, notions of spatial data tend to vary from one application to another.

Geographic applications require two-dimensional data, geological applications require three-dimensional data, and some solid modeling applications require four-dimensional data. Spatial operations and representations are highly application dependent. And for this reason, many models that are implemented are application specific including query languages (Jose 88).

Image data can be viewed as a matrix of gray levels or two dimensional signals in raster format. In vector format, image data is encoded by simple data structures such as points, line segments, and polygons or regions. Quadtrees, Octtrees, and Pyramid representations are some data structures proposed for storage efficiency (Tamu 84). Cheng and others (Chen 88) recently proposed a method for compressing binary digital images using irreducible covers of maximal rectangles. Barnesley and Sloan (Barn 88) describe a method for compressing images based on fractal encoding. Only iterated function system (IFS) codes are stored rather than the original images. This approach seems promising for automatic image analysis because the combinatorial search space for feature extraction is dramatically reduced.

Orenstein and Manola (Oren 88) proposed a new approach to extend the database system functionality for spatial data modeling and query processing. Extensibility is built into their object-oriented data model, PROBE, thereby making the model flexible enough to be adapted to a different number of applications. They also show how their system can be used for spatial data modeling and querying for image database applications. Economopoulos and Lochovsky (Econ 83) have designed and implemented an image data model which represents images in terms of high-level semantic descriptions rather than a pixel-oriented description. This system is a component of a larger prototype system, Message Management System (MMS), intended for intelligent communication and processing of messages.

Joseph and Cardenas (Jose 88) describe the requirements for a generalized pictorial database management system (PDBMS) to provide data heterogeneity transparency over pictorial and non-pictorial data. The data manipulation capabilities that are expected of a generalized PDBMS are classified into six categories such as image manipulation operations, pattern recognition operations, spatial or geometric operations, function operations, user defined functions and programming language interface, and input/output operations. The proposed architecture has two database management system components, one to manage the pictorial data, called PICDMS, and the other to manage conventional data, referred to as non-pictorial database management system. Similarly, the query language has two components to manipulate and access pictorial and non-pictorial data. A notable thing about this system is that it allows a user to define his own pictorial data types in addition to the point, line, and region data types provided as standard pictorial data types.

3.3 Image Retrieval and Query Languages

There are three levels of retrieval: retrieval by an identifier, retrieval by conditional statements, and similarity retrieval by a given sample. Retrieval by an identifier corresponds to physical retrieval of an image corresponding to the given identifier. Retrieval by conditional statement is based on the image features. Image features can be precomputed or computed dynamically.

Many query languages implemented up to 1980 have been summarized (Chan 81). The majority of the query languages developed till today are command-oriented languages. Some query languages are newly designed with emphasis on registration, editing, and display of images. Other query languages are simple extensions of data manipulation languages for image file management.

Chang and Fu[Chan80] developed Query-by-Pictorial-Example (QPE), a query language for a relational database system for images (REDI). Image processing and pattern recognition techniques are used to extract structures and features from images. These extracted features are integrated and used in query processing. Original image data is retrieved and processed only when the feature data are insufficient and/or imprecise to process a query. The graphical interface for querying is similar to the well known relational query language, Query-By-Example (QBE).

PICQUERY (Jose 88) is a pictorial query processing language for PICDMS (mentioned above). PICQUERY has an open-ended design to interface with other robust PICDMS also. PICQUERY provides a fundamental shell on which user defined operations for pictorial data may be built. PSQL, a query language for the manipulation of pictorial databases, allows pictorial domains to be represented in their analog form (Rous 88). The associated database can perform direct spatial search and computation by using efficient data structures, R- and R+ trees.

The most desirable feature of a query language for image database applications is the ability to retrieve images from a large image database based on a partial description of the image content. Rabitti

and Stanchev proposed a formalism based on fuzzy set theory for this task. There are four stages involved: element recognition, segmentation object recognition, added information definition, and image clustering. During the element recognition stage, the system tries to match the image elements with the terminal symbols of an adapted grammar. Fuzzy formalism helps when the system is unable to find an exact match with the stored representations (all possible elements the system is likely to encounter are stored to start with). More than one match is assigned with different certainty factors.

Objects correspond to nonterminal symbols of the adopted grammar, and applying the production rules of the grammar recursively, objects are identified starting with the image elements. During the added information definition stage, a user can add more information to the object description. The image interpretation obtained is compared with all the given class descriptions during the last stage. The class assignment is made on the basis of distance measures.

A model based on object-oriented knowledge representation for spatial information has been reported as flexible enough to capture any type of information one wishes to represent about a given pictorial world (Moha 88). The visual user interface for map information retrieval has been reported in (Tana 88). The system is designed to reduce the semantic gap between the user's view and the system function.

4. Future Outlook and Conclusions

Image database systems started as application specific systems and are gradually evolving toward more general-purpose systems. The advances are in two specific directions based on the two basic approaches for processing of pictorial data. For the approach based on computer graphics, commercial systems such as ARC/INFO are already available and provide a uniform framework for GIS applications. Even though ERDAS is a general-purpose commercial image processing system, it is far from ideal.

Substantial research into proposing and demonstrating a unified framework for image database management systems is required. This framework is expected to provide a pictorial data model that truly provides data independence and captures all the implicit semantic information in the pictorial data. This framework is also expected to provide flexible query languages for the partial specification of queries based either on precise or imprecise image description or the image itself (specified in the format). Advances in this area will have a profound impact on providing intelligent graphical user interfaces for applications.

Acknowledgments

The author gratefully acknowledges the support received from NASA and DOE[DE-FG05-86ER75274]. The author is also thankful to Mr. Rick Galle, Stennis Space Center, and Dean Leflore and Professor Lupton at Jackson State University for their continued encouragement.

References

(Barn 88) Barnsley, M.F.; Sloan, A.D., A Better Way to Compress Images, BYTE, 1988, January, 215-223.

(Chan 80) Chang, N,; Fu, K.S., Query-by-Pictorial Example, IEEE Transactions on Software Engineering, 1980, November, 519-524.

(Chan 81) Chang, S., Pictorial Information Systems: Guest Editor's Introduction, Computer, 1981, November, 10-11.

(Chan 81a) Chang, N.S.; Fu, K.S., Picture Query Languages for Pictorial Data-Base Systems, Computer, 1981, November, 23-33.

(Chen 88) Cheng, Y.; Iyengar, S.S.; Kashyap, R.L., A New Method of Image Compression Using Irreducible Covers of Maximal Rectangles in [IEEE88].

(Econ 83) Economopoules, P.; Lochovsky, F.H., A System for Managing Image Data, Proceedings of IFIP Congress, 1983.

(Fran 88) Frank, A., Requirements for a Database Management System for a GIS, Photogrammetric Engineering and Remote Sensing, 1988, November, 1557-1564.

(IEEE 88) IEEE Transactions on Software Engineering Special Issue on Image Databases, 1988, May.

(Jose 88) Joseph, T.; Cardenas, A.F., PICQUERY: A High Level Query Language for Pictorial Database Management in [IEEE88].

(McKe 77) McKeown Jr., D.M.; Reddy, D.R., A Hierarchical Symbolic Representation for an Image Database, Proceedings of 1977 IEEE Workshop on Picture Data Description and Management, 1977, 40-44.

(Nagy 79) Nagy, G.; Wagle, S., Geographic Data Processing, Computing Surveys, 1979, June, 139-181.

(Oren 88) Orenstein, J.A.; Manola, F., PROBE Spatial Data Modeling and Query Processing in an Image Database Application, IEEE Transactions on Software Engineering, 1988, May, 611-629.

(Park 88) Parker, D.H. The Unique Qualities of a Geographic Information System: A Commentary, Photogrammetric Engineering and Remote Sensing Special GIS Issue, 1988, November, 1547-1549.

(Rous 88) Roussopoulos, N.; Faloutsos, C.; Sellis, T., An Efficient Pictorial Database System for PSQL in [IEEE88]

(Taka 80) Takao, S.; Itoh, S.; Iisaka, J., An Image-oriented Database System, Database Technique for Pictorial Applications, A. Blaser, Ed., Springer-verlag, 1980, 527-538.

(Tamu 80) Tamura, H., Image Database Management for Pattern Information Processing Studies, Pictorial Information Systems, S.K. Chang and K.S. Fu, Eds., Springer-Verlag 1980, 198-227.

(Tamu 84) Tamura, H.; Yokoya, N., Image Database Systems: A Survey, Pattern Recognition, 1984, 17, 29-43.

(Tana 88) Tanaka, M.; Ichikawa, T., A Visual User Interface for Map Information Retrieval Based on Semantic Significance in [IEEE88].

(Moha 88) Mohan, L.; Kashyap, R.L., An Object-oriented Knowledge Representation for Spatial Information in [IEEE88].

(Tang 81) Tang, G., A Management System for an Integrated Database of Pictures and Alphanumeric Data, Computer Graphics and Image Processing, 1981, 16, 270-286.

(Yang 87) Yanguang, W., The Research of Digital Picture Storage Methods for Picture Database, 38th Congress of the International Astronautical Federation, Brighton, UK, 1987, October, 1-23.

IMPLEMENTATION OF AN ALGORITHM FOR CYLINDRICAL OBJECT IDENTIFICATION USING RANGE DATA

Sylvia T. Bozeman and Benjamin J. Martin
Department of Mathematics
Spelman College
Atlanta, Georgia

ABSTRACT

This research addresses one of the problems in 3-D object identification and localization. In robotic and navigation applications the vision system must be able to distinguish cylindrical or spherical objects as well as those of other geometric shapes. An algorithm has been developed to identify cylindrical objects in an image when range data is used. The algorithm incorporates the Hough transform for line detection using edge points which emerge from a Sobel mask. Slices of the data are examined to locate arcs of circles using the normal equations of an over-determined linear system. Current efforts are devoted to testing the computer implementation of the algorithm. Refinements are expected to continue in order to accommodate cylinders in various positions. A technique is sought which is robust in the presence of noise and partial occlusions.

IMPLEMENTATION OF AN ALGORITHM FOR CYLINDRICAL OBJECT IDENTIFICATION USING RANGE DATA

Introduction

Among the various tasks assigned to the National Aeronautics and Space Administration is the investigation of space related automation and robotics. NASA has chosen to use the telerobotic system configuration as the basis for progressively studying and implementing spaceborne automation. Telerobotic systems consist of a human, a robot, a human-robot interface capability, sensors, and the accompanying computational tools. By basing research on this system structure, NASA can progressively evolve its automation capability from teleoperator, where the human is directly involved in every operation of the machine, to near autonomy, where man is only involved as a monitor of the machine's activity.

In designing automated robotic activity, it is necessary to be able to automatically (i.e., without human involvement) recognize objects, their positions, and their orientations in order to be able to grasp and manipulate them. Thus the ability to take the data from the scanning rangers and determine the composition of the image scanned and the locations of the various components is needed. Even as work progresses on the development of faster and more accurate scanners, considerable research is underway on methods for using range data in object detections and recognition. (See reference list of Faugeras and Herbert, 1986.)

In the problem of 3-D recognition and localization of objects that are rigid, a major consideration is the method of representing objects. After considerable investigation Faugeras and Herbert (1986) concluded that representation should be in terms of linear primitives, such as points, lines, and planes, although these may be derived from consideration of curved patches at intermediate stages.

The technique here employed for detecting cylinders is based on the use of external descriptors. In the case of the cylinder it is noted that in one direction the boundary should appear as straight lines. In a direction orthogonal to the first the data should fit the equation of a circle (or an ellipse in the more general case). Information on the boundary in the third orthogonal direction is not used.

The approach used in this project has been to develop the algorithm while testing it on ideal data for a right circular cylinder with the axis of the cylinder parallel to the y-axis. This condition is later relaxed to allow the introduction of an angle α that indicates the angle between the cylinder's axis and the y-axis; thus freedom of rotation in one direction is allowed. The ultimate goal is to refine the algorithm so that it is robust in noisy environments. The algorithm should also yield a high rate of accuracy when the cylinders have partial occlusions.

In approaching this problem the spirit of a comment attributed to A. Guzman is followed: "If you recognize a foot you know where (in the picture) to look for a leg..." Hence the procedure for locating cylinders in a picture has been to look first for parallel lines; then the algorithm can check for a cylinder between the lines. Therefore, the first major part of the programming project consisted of identifying edgepoints in the image and extracting lines from those edgepoints. Both tasks have been the subject of considerable research over the past 20 years. The basic methods employed in this part of the algorithm are then somewhat classical in nature.

Locating Edgepoints and Lines

The first step is to locate the pixels that are the edgepoints. At each pixel in the image a 3x3 mask centered at (i, j) is used to determine the variation on distance from the sensor in both the vertical and the horizontal directions. Note that i represents the row, j the column, and P(i, j) the range data at the pixel location (i, j). This mask is known as a basic Sobel edge detector where

$$igrad = 2(P(i-1,j)-P(i+1,j)) + P(i-1,j+1)-P(i+1,j+1) + P(i-1,j-1)-P(i+1,j-1)$$

$$jgrad = 2(P(i,j+1)-P(i,j-1)) + P(i-1,j+1)-P(i-1,j-1) + P(i+1,j+1)-P(i+1,j-1)$$

estimate the variations in the vertical and horizontal directions, respectively, at (i,j). Using these two quantities in a vector G=(jgrad, igrad) to approximate the gradient vector at (i,j), both the magnitude and direction of the greatest variation at (i,j) can be obtained. If the magnitude of the gradient,

$$k = ((igrad)^2 + (jgrad)^2)^{1/2},$$

is above some predetermined threshold value, T, then it is assumed that there is an edgepoint at (i,j). T may vary and can be selected interactively prior to runs. Using a threshold of 100 it was found that certain edgepoints around the top of the cylinder were not detected even with ideal data.

In searching for lines among the edgepoints, the gradient directional information may or may not be used. Using gradient information, the edge angle at (i,j) is found as g = arctan(igrad,jgrad).

J. Kittler [1983] has given considerable attention to the performance of the Sobel edge detector in terms of the accuracy of its magnitude and angle. He proved that the basic Sobel edge detector described above will correctly detect the true angle of the edge direction at the boundary between the object and the background in the interval $0 \leq g \leq \arctan(\frac{1}{3})$. He predicts an error of approximately 2° in direction for larger angles and an accurate magnitude only when the edge is vertical or horizontal. Davis [1987] points out that this technique loses accuracy when the edges of the objects are fuzzy.

In attempting to extract lines from among the edgepoints the Hough transform has been shown to be an effective technique. It is especially attractive in this environment because of its robust performance in noisy environments. Although it can be employed with or without the gradient information, we chose to use the gradient information in order to reduce the number of lines associated with each pixel and thereby reduce the storage requirements.

This technique for detecting collinear points dates back to 1962 with a patent issued to P.V.C. Hough. The technique is based on the fact that a line through a point (x,y) can be completely characterized by its angle (from the positive x-axis) and the length of the normal from the origin to the line. The line can be expressed using the equation

$$x_i \cos\theta + y_i \sin\theta = r. \qquad (1)$$

This approach to finding lines is based on the fact that if enough pairs (x_i ,y_i) appear in the image which give rise to the same (r, θ) pair then these points may well represent a line in the image (if they can be shown to be contiguous). Thus a "voting" system is established and a two-dimensional accumulator array is created to count the votes. When gradient information is not used the angle θ is allowed to vary independently over a 180^o range (using small increments) and each point (x_i , y_i)) can produce a value of r for each value of θ. If r lies within the limits specified by the physical dimensions of the image, the number of votes at location (r,θ) is incremented by one. When gradient information is used at each point, the only value of (r,θ) incremented for that point is the one where θ corresponds to the gradient at the point, and r is calculated using (1).

In the latter case Gorman and Clowes [1976] recommended the creation of "contributing point lists" to keep track of the points whose votes account for the value in a particular cell of the accumulator array. The data structure chosen here to accomplish this tracking was a second array, matching the accumulator array, which consisted of pointers, each pointing to the list of pairs contributing to the value at (r,θ). Once the accumulator array is filled (i.e. once the selected portion of the image has been processed) the list would contain all points found to be on or near the line specified by the parameters (r,θ).

This method works well to find the line containing line segments in the image but has two shortcomings. (1) It does not give any indication as to whether the points found are contiguous. (2) It does not give the location of line segments on the lines found. The difficulty resulting from the latter is somewhat diminished by employing the contributing point lists.

Isolating Edges and Cross-Sections of a Cylinder

Attention is now turned to analyzing the data in the parameterized space of (r,θ). Since finding consecutive pairs of parallel lines is of interest, peaks in the data taken from a cross-section of the space are sought. For a fixed value of θ, consecutive values r_1 and r_2 are sought in which the accumulation of "votes" for a line at (r_i,θ) exceeds some predetermined value M. The value M may be selected interactively and should depend on (1) the required length of a line in order to be considered meaningful, and (2) the size of the image (or subimage) being processed.

In an image of size 256x256 pixels a value of M=20 was used. The two problems that arise with this (as with any) choice of M are that (1) cylinders of less than 20 pixels in height go undetected, and (2) if less than 20 pixels are visible along the edge of the cylinder due to occlusion by other objects in the image, then the necessary matching pair of edges will not be found. If peaks appear in the parameterized data at (r_1,θ) and (r_2,θ) but for no other value of r, $r_1<r<r_2$, then a cylinder is sought between the corresponding parallel lines l_1 and l_2.

Labeling in 3-D

Since a right circular cylinder in standard position (i.e., having its axis parallel to the y-axis) has uniform cross sections whose boundaries are all circles of the same radius, the goal is to isolate a cross section of the image between the two parallel lines. The points along the visible portion of the cross

section will be tested to determine if they lie on an arc of a circle—a circle which in 3-D lies perpendicular to the plane of the image.

It is only now that the labeling of the points in the image of the 3-D space becomes important. Prior to this point in the discussion, consideration of the projection of 3-D objects onto the image plane has been sufficient. If an xy-coordinate system is superimposed onto the image, so that the origin of the system lies in the lower left corner of the image (at a background point), then each pixel location (i,j) also can be referenced as (x,y), where x=j and y=256 - i. (Figure 1.)

If a third coordinate axis z which is orthogonal to the xy image plane is added then the distance from a point R, located on an object in the scene, to the plane of the sensor can be measured along z. (Figure 1.) The grey level of each pixel in the image represents the range data and indicates the relative distance of the object from the sensor—lighter areas (higher grey levels) being closer. Thus if z=0 at R then the point R is as far as possible from the sensor. Let R be a given point on an object in the scene which appears at location (i,j) in the 2-D image. Suppose that the plane of the sensor is at a distance S from the reference background point at the origin of the coordinate system. If k is the 3-D distance at point R from the object to the sensor, then the z-coordinate of R is z=S-k. Thus, the point R can be positioned relative to the xyz-coordinate system since its x and y coordinates are the x and y coordinates of (i,j) (Figure 2).

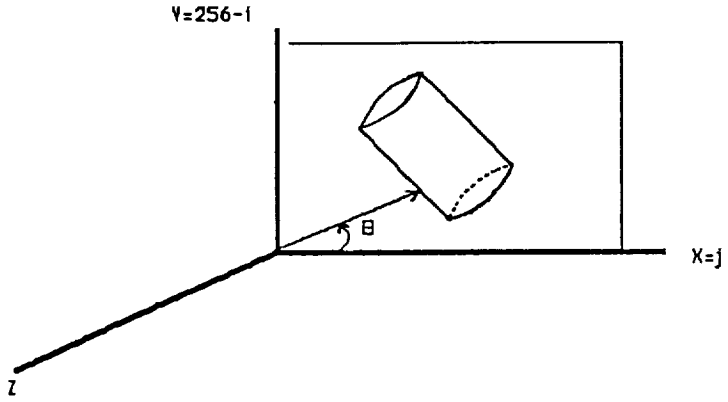

Figure 1.

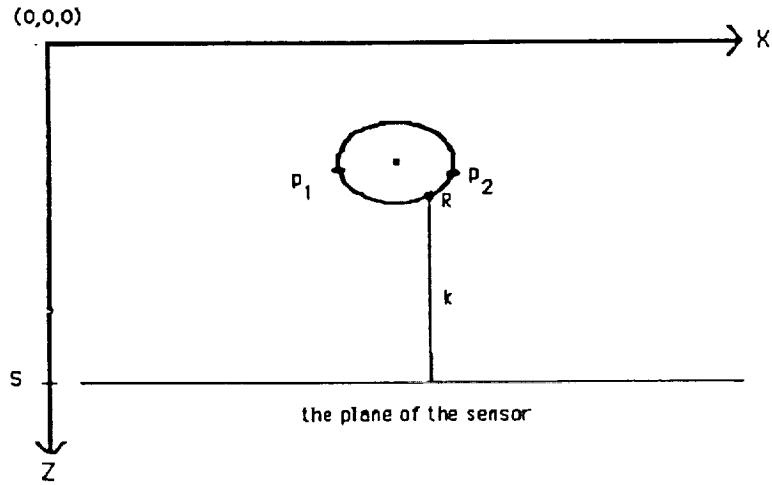

Figure 2.

Analyzing a "Slice" of the Data

In locating data which might lie on the arc of a circle between the two parallel lines l_1 and l_2 already found, a point is chosen from each of the two lines which lies on a single slice of the data. Thus we seek two points p_1 and p_2 that are endpoints of a line segment perpendicular to l_1 and l_2, so that p_1 lies on l_1 and p_2 lies on l_2. For the cylinder in a standard position such points have the same i (or y) value. Thus we need only return to the lists of contributing points corresponding to the (r,θ) values giving rise to the two lines and locate two points with the same y coordinate. (The search is made easier by ordering points as the lists are created.) In the more general case, the angle of inclination of the parallel lines can be used to determine the relationship between the y values of the two corresponding points sought.

In order to determine whether p_1 and p_2 are the endpoints of the arc of a circle in 3-D space we test the range data at these two points and points in between (on the same orthogonal slice). Denote by D this set of points. If we confine ourselves for a moment to the case of the cylinder in standard position, it is no longer necessary to consider the y direction for points on the slice. Thus each point in the image can be considered as having only x and z components (Figure 2). In this case

$$D = \{(x,y_0,z) \mid x_1 < x < x_2, \text{ where } p_1 = (x_1,y_0,z_1),\ p_2 = (x_2,y_0,z_2)\}$$

In this two-dimensional subspace the equation of a circle (whose center has y-component y_0) determined uniquely by any three points in D is sought. However, if the points of D approximate an arc all of its points must lie on, or near, the circle determined.

If we suppress the constant component, then for any point (x_i,z_i) in D,

$$(x_i - x_c)^2 + (z_i - z_c)^2 = r^2 \qquad (1)$$

if the point lies on the circle with center (x_c,y_o,z_c) and radius r. By equating two such equations using points (x_i,z_i) and (x_j,z_j) we can eliminate r and get the equation

$$2x_c (x_i - x_j) + 2z_c (z_i - z_j) = x_i^2 + z_i^2 - x_j^2 - z_j^2,$$

a linear equation in the two unknowns x_c and z_c.

Selecting m points (x_i,z_i), i=1,...,m, from D, m-1 equations in 2 unknowns can be formed as

$$2x_c (x_i - x_m) + 2z_c (z_i - z_m) = x_i^2 + z_i^2 - x_m^2 - z_m^2,\ i = 1, \ldots m - 1. \qquad (2)$$

This system of m-1 equations in 2 unknowns can be written as a matrix equation Ay=b, where A is the (m-1)x2 matrix

$$A = 2 \cdot \begin{Bmatrix} x_1 - x_m & z_1 - z_m \\ x_2 - x_m & z_2 - z_m \\ \cdot & \cdot \\ \cdot & \cdot \\ x_{m-1} - x_m & z_{m-1} - z_m \end{Bmatrix}$$

$y^T = (x_c, z_c)$, and $b^T = (x_1^2 + z_1^2 - x_m^2 - z_m^2, \ldots, x_{m-1}^2 + z_{m-1}^2 - x_m^2 - z_m^2)$. If the rank of A is 2 then the least squares problem

$$Ay = b \tag{3}$$

has a unique solution $\hat{y}$ that is determined by solving the normal equations

$$A^T A y = A^T b. \tag{4}$$

The unique solution to (4) (if it exists) is $\hat{y} = (A^T A)^{-1} A^T b$ and is simple to obtain since $A^T A$ is a 2x2 matrix.

Finally, r can be obtained using (1) and any one of the m points, although an average of the values of r found with several points is preferred.

In order to determine the accuracy of this technique the sum of the deviations, in the z direction, from the circle at each point is computed.

Thus $e = \sum_{i=1}^{m} (z_i - zp_i)$ where $zp_i = z_c + \text{Round}((r^2 - (x_i - x_c)^2)^{1/2})$. If e is small then the points of D lie on a circle with radius r and center (x_c, y_o, z_c). The size of e which is acceptable is expected to depend on r or m.

The above algorithm should be repeated to locate several circles between the two parallel lines l_1 and l_2, all having approximately the same radius and having their centers on a single line (the proposed axis of the cylinder) before concluding that a cylinder has actually been detected and localized.

Further analysis is needed to determine a priori error bounds for the solution of (4) because of the ill-conditioned problem that often results from forming the normal equations.

Given that this algorithm was tested on ideal data (rather than the noisy data from an actual sensor) the next step in this research effort is to test the robustness of the algorithm in the presence of noise. Future effort will also involve implementing this algorithm in the case when the cylinder is not in standard position but has a nonzero angle of inclination between its axis and the y-axis. The current algorithm represents a step toward an autonomous system for detection and localization of cylindrical objects in images created using range data.

References

Ballard, D.H., *Pattern Recognition*, 1981, 13(2), pp 111-122.

Davis, E.R., *Pattern Recognition Letters,* 1987, 6, pp 1-7.

Faugeras, O.D.; Herbert, M., *The International Journal of Robotics Research*, 1986, 5(3), pp 27-52.

Gonzalez, Rafael C.; Wintz, Paul, *Digital Image Processing*, 1987, 2nd ed., Reading, Mass: Addison-Wesley, pp 331-349.

Gorman, Frank and M.B. Clowes, *IEEE Transactions on Computers*, 1976, 25(4), pp 449-456.

Kittler, J., *Image and Vision Computing*, 1983, 1(1), pp 37-42.

MATHEMATICAL MODELS FOR FILM SENSITIVITY MEASUREMENTS

Ernest Hammond, Jr.
Department of Physics
Stephen Gewirtz and Osborne Parchment
Department of Mathematics
Morgan State University
Baltimore, MD

and

Gerald R. Baker
Technical Monitor
Laboratory of Astronomy and Solar Physics
Goddard Space Flight Center

ABSTRACT

The quality of the pictorial record developed from photographic material depends on the composition of the material, the procedures used in its exposure and processing as well as the nature of the physical and temporal environment extant during the creation of the record. By holding many of the variables fixed, this paper examines the effect of two environmental parameters, namely temperature and aging, on the characteristic curve of a given film. Polynomial and exponential functions are evaluated as empirical formulas for the characteristic curve, and the sensitivity of derived coefficients to the selected parameters is assessed.

are examined.

MATHEMATICAL MODELS FOR FILM SENSITIVITY MEASUREMENTS

I. Data Description and Rationale for Data Analysis

In a variety of applications of scientific photography, there is an unavoidable time lapse between film exposure and film processing. During this time, the exposed film may be subject to varying levels of ambient temperature. Such is the case, for example, when films of experiments are exposed at various times during a space mission and developed at the end of the mission. A similar scenario occurs when films are exposed at distant experimental sites and returned by common carrier to a central location for processing. In such cases the extent to which the photographic record may be affected by the aging and/or the temperature is an important consideration. The data used in this analysis was developed to assess the effect of these physical parameters on one type of common film. A description of the method used follows.

Film of the type selected was exposed for a fixed time using a light sensitivity wedge of thirty gray levels. Following exposure, the film was aged for a selected number of days at a selected temperature and then developed. The density for each gray level in the wedge was measured using a densimeter to produce data similar to that shown in Table I. For this analysis, aging periods were assigned in multiples of three days to a maximum of twenty days and the incubation temperatures were eleven and forty degrees. The development procedure was identical for all the films used in this phase of the project. The actual film used to generate the density readings used in this report was KODAK IIaO.

The density readings accurate to two decimal places, as shown, are dependable for the method as outlined. No attempt is made to correct for differences in storage times between film manufacture and film exposure. However, the supplier maintained manufacturing and shipping practices designed to minimize the effects of this factor [1].

II. Selection, Implementation and Testing of Empirical Models

The earliest researchers in the science of photography realized that a functional relationship exists between photographic densities and the exposures which produce them. F. Hurter and V. Driffield [2] originated the method of plotting density against the common logarithm of exposure to obtain empirically the characteristic curves (Figure I) so central to the theory of sensitometry. Researchers in population biology may also notice a strong similarity to the logistic growth curve.

Despite many attempts to describe this curve globally by a single mathematical formula, no satisfactory functional relationship has so far been commonly accepted as theoretically based and empirically accurate. Consequently, this study uses regression analysis on a selection of curves to represent the experimental data and presents the root mean square error resulting from each choice.

WEDGE NUMBER	DENSITY (15 days, 11°C)	DENSITY (15 days, 40°C)
0	0.22	0.31
1	0.23	0.31
2	0.24	0.32
3	0.25	0.34
4	0.27	0.38
5	0.30	0.41
6	0.35	0.51
7	0.39	0.57
8	0.46	0.66
9	0.53	0.73
10	0.62	0.82
11	0.72	0.91
12	0.78	1.00
13	0.90	1.10
14	1.03	1.19
15	1.13	1.26
16	1.25	1.35
17	1.35	1.43
18	1.47	1.56
19	1.60	1.64
20	1.68	1.69
21	1.75	1.74
22	1.82	1.78
23	1.88	1.82
24	1.93	1.91
25	1.99	1.94
26	2.03	1.97
27	2.07	2.00
28	2.11	2.03
29	2.14	2.04

TABLE I
Density Values for KODAK IIaO Film Aged 15 Days at 11, 40 Degrees Celcius.

A. Polynomial Fit by Regression Analysis

Although characteristic curves exhibit segments which appear to be approximately linear, the graph of density versus the logarithm of admissable exposures is obviously not globally a straight line. Thus an attempt to model these curves by polynomials requires them to be at least quadratic. In fact, the presence of at least one inflexion point suggests that cubics are the minimum needed if a reasonably accurate fit is to be assured. Consequently, this analysis begins with the selection of the most general cubic polynomial as a possible regression curve and proceeds to test higher degree functions until there is no perceptible change in the root mean square error computed.

The regression method for fitting a polynomial

$$P_N(X) = C_0 + C_1 X + C_2 X^2 + \ldots C_N X^N$$

to the data set (X_K, Y_K) k = 0...N, involves finding the coefficients C_K so that the expression for the least square error

$$LSE = (Y_K - P_N(X_K))^2$$

or for the root mean square error

$$RMSE = (LSE/N)$$

is minimum. This is a standard procedure in numerical or statistical analysis. The procedure results in a set of M+1 simultaneous, linear equations for the unknown coefficients. Using the Gauss-Jordan method [5] for solving such equations, the unknown coefficients which determine the best fitting polynomial are determined. The algorithms to do this were coded in Pascal and the code may be obtained by writing to the authors. Figure II shows the experimental data together with cubic and quintic regression curves.

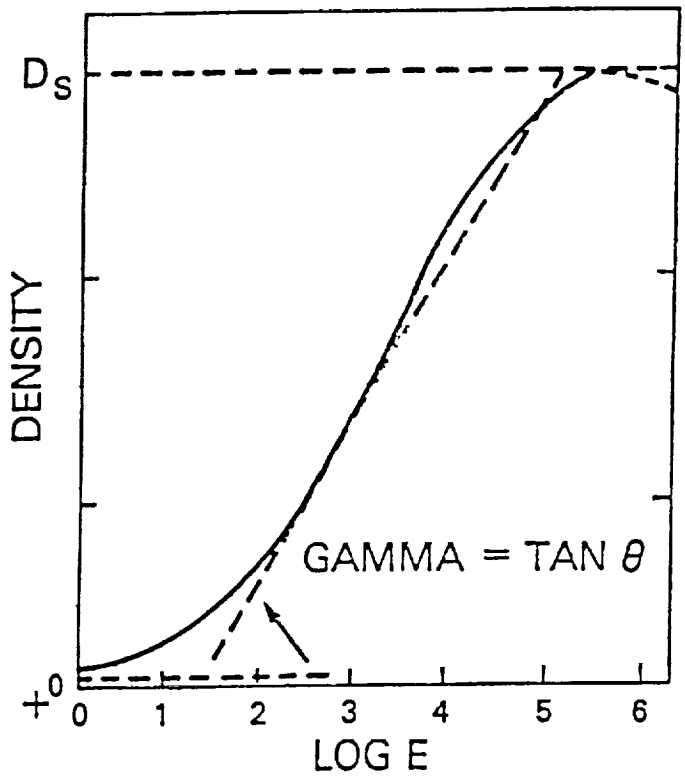

FIGURE I: Typical Characteristic Curve
Film Density vs. Log of Exposure.

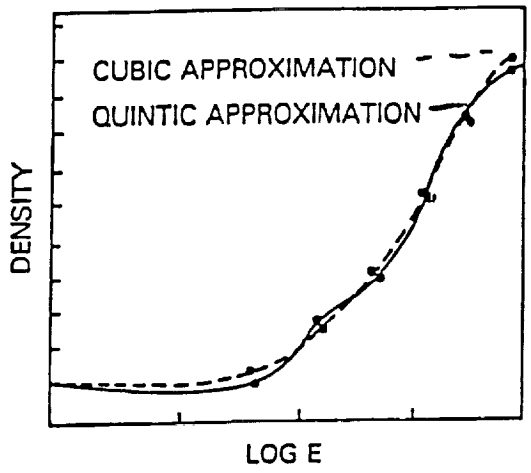

FIGURE II. Two Polynomial Approximation Curves.

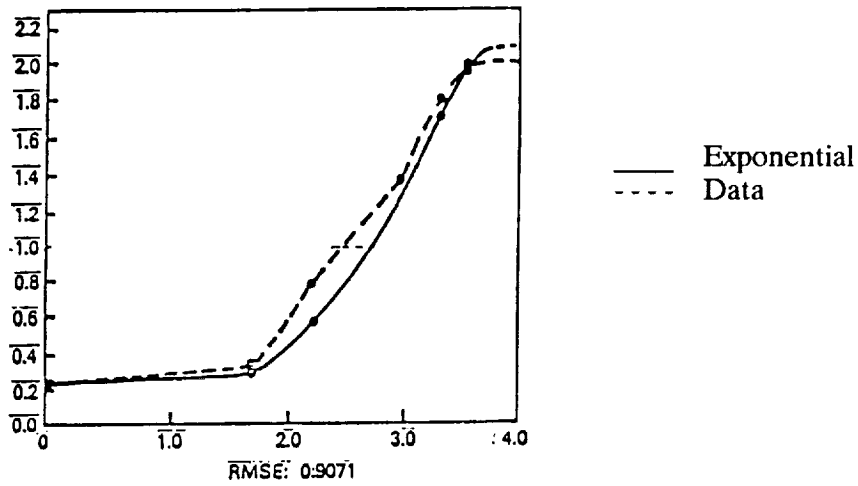

FIGURE III. Exponential Regression Fit to Data.

B. Exponential Fit by Regression Analysis

The polynomial curves derived in the preceding section produce a very good fit with the experimental sensiometric data. However, the simplest of the models considered requires the determination of four unknown coefficients. A useful question to consider is the existence of other curves capable of producing an acceptable fit with fewer adjustable constants. The general nature of the characteristic curves suggests that the rate of change of density y with respect to the logarithm of exposure x should have the form

* $dy/dx = y(a-by)$

where a and b are unknown constants. Viewing this as a differential equation for y in terms of x, we could impose the initial condition:

$y(0)$ = the fog density of the film.

Solving the resulting initial value problem using methods outlined for example in [6], yields the general solution:

** $y = a/[b + (a/y(0) - b)\exp(-ax)]$.

The problem is to determine the constants a, b from the experimental data. It will be helpful to note two relevant properties of the solutions of equation *.

Property I: For large values of x, the values of y approach the ratio a/b.

Property II: Any solution has a flexpoint at the value $y = a/(2b)$ and the rate of change at this flexpoint is $a^2/(4b)$.

The first is obvious from the solution formula **; the second can be derived by the substitution of a/(2b) for y in the right hand side of *. A reasonable assumption is that they approximated the linear portion of the characteristic curve. Using this assumption together with Property I & II gives:

$a^2/(4b)$ = slope of linear regression line

a/b = maximum density of exposed film

Consequently, the values for the constants a and b are determined by the data. Figure III compares the experimental data with the exponential regression curve derived as described above.

C. Comparision of the Models

Analysis of the approximation data shows a very good agreement of the experimental data with cubic polynomials. Although there is evident improvement resulting from the use of quintic regression curves, the changes are not significant enough to warrant the significant amount of additional computation required. Futhermore, extending mathematical approximations to accuracies beyond the error tolerance of the measuring instruments is not generally a useful exercise.

The results obtained by exponential regression show a considerably higher error when compared to the polynomial regression figures. When tempered by the fact that this method needs the determination of only two arbitrary constants compared to four and six respectively in the polynomial cases considered, the evaluation of the exponential model improves somewhat. The geometric properties of the exponential regression curve suggest better agreement for longer exposure time.

III. Conclusions and Questions for Further Study

If the commitment has been made to model the data by polynomial regression, it is clear from the study that the quintic polynomial regression provides a better fit than the same procedure applied to cubic ones. However, the increase in accuracy is not dramatic enough to justify the additional complexity and computation time required for the higher degree. Cubic splines, although not used in this analysis, are likely to provide an even better fit, but are not global polynomials although they belong locally to this class of functions. Lagrange polynomials are not practical for this model because of the high degree required to fit the data and the consequent increase in computation time.

Choosing the model by exponential regression has some theoretical appeal. However, the errors generated are an order of magnitude higher when compared to the cubic polynomial fit.

For fixed temperature, the coefficients of the respective regression curves used remained stable as functions of aging. On the contrary, for a fixed age there was significant variation in the respective coefficients as functions of temperature. Because the data was available only for three distinct temperatures, this variation is not enough to support a claim of instability of the coefficients as functions of temperature. Additional analysis with more closely spaced temperature readings would be necessary to support such a claim.

IV. References

1. Eastman Kodak Company, "Plates and Films for Scientific Photography", First Edition.

2. T.H. James & C.E.K. Mees, The Theory of the Photographic Process, Third Edition, Macmillan Company.

3. P.W. Purdom & C.A. Brown, The Analysis of Algorithms, Holt, Rhinehart and Winston.

4. R.L. Burden, J.D. Faires, Numerical Analysis, Third Edition, Prindle, Weber & Schmidt.

5. R.P. Yantis & R.J. Painter, Elementary Matrix Algebra with Applications, Second Edition, 60, Prindle, Weber & Schmidt.

6. M.R. Spiegel, Applied Differential Equations, Third Edition, 35, Prentice-Hall.

N91-28077

THE PREDICTION OF PSEUDO-RESONANCE POSITIONS IN THE SCHWINGER VARIATIONAL PRINCIPLE

Charles A. Weatherford
Roy Tucker, and Gregory Odom
Department of Physics
Florida A & M University
Tallahassee, FL

ABSTRACT

The Schwinger Variational Principle is applied to s-wave electron-hydrogen atom scattering. We show computationally, that, consistent with a recent paper by B. Apagyi, P. Levay, and K. Ladanyi[2], there are pseudo-resonances at the static exchange level of approximation, but not at the static level. We employed the T-matrix as well as the K-matrix version of the Schwinger Principle, with a real Slater basis, and obtained the same results in both. We are able to identify the origin of the pseudo-resonances as resulting from singularities in the separable potential that is effectively employed in the Lippman-Schwinger equation from which the Schwinger Variational Principle can be derived. The determination of the pseudo-resonance parameters from the separable potential is computationally inexpensive and may be used to predict the pseudo-resonance parameters for the scattering calculations so that they may be avoided.

THE PREDICTION OF PSEUDO-RESONANCE POSITIONS IN THE SCHWINGER VARIATIONAL PRINCIPLE

Rationale

The present work is a computational study of electron scattering from atomic hydrogen in its ground electronic state. We are studying this system using the Schwinger Variational Principle (SVP). This system has been studied many times before at a very high level of accuracy. [1] It is not our intent to study e^- + H just for the cross section data that result, but rather to study this system as a model system to explore some of the subtle aspects of the SVP. We are primarily interested in electron-molecule collisions where L^2 basis set methods, such as the SVP, have shown the greatest utility, especially for processes such as electronic excitation and dissociative recombination.

However, there are a number of problems that are encountered in using the SVP. In particular, two recent papers [2,3] have shown that, contrary to the prevalent belief [4], the SVP does encounter pseudo-resonances, even in the simple s-wave e^- + H system, so long as the exchange effect is included. Indeed, it is necessary to have an energy dependent potential in order to see these pseudo-resonances. At the static level, the pseudo-resonances are not encountered in the SVP, in contrast to the Kohn Variational Principle [5] (KVP) where they are encountered even at the static level.

This fact apparently led many researchers [4,6] to conclude that the SVP did not suffer from the occurrence of pseudo-resonances. The argument that was used to explain the assumed non-occurrence of pseudo-resonances in the SVP is based on the paper of Adhikari and Sloan [7] who show that the derivation of the SVP, from the Lippman-Schwinger equation by taking the variations of the wavefunction and deleting second order terms, is equivalent to approximating the exact potential in the Lippman-Schwinger equation, by the projection of the exact potential onto an L^2 basis set, thus producing a finite rank separable approximation to the exact potential. It was then argued that the SVP implementation was equivalent to solving the Lippman-Schwinger equation exactly for a certain separable potential, and since the solution was exact, no spurious resonances would occur in the solution. This, as it turned out, was true, but a somewhat subtle flaw in the argument leads to pseudo-resonances anyway. We shall presently elaborate.

These false resonances are non-physical. This is especially troubling since resonance processes have turned out to be the predominant mechanism by which molecules are excited and by which molecules dissociate upon scattering by electrons. It is, therefore, extremely important to distinguish the real resonances from the pseudo resonances.

Thus, in order to study the origin and characteristics of these resonances, it is fortuitous to encounter them in so simple a system as s-wave e^- + H, at the static exchange level [2] (static + exchange potential). We therefore decided not only to repeat the calculation of Ref. 2, but also to perform the calculation using the T-matrix approach, as well as the K-matrix approach, in contrast to the authors of Ref. 2 and 3. In doing so, several interesting aspects of the use of the SVP were studied and the origin of the pseudo resonances was explained.

Sketch Of The Theory

The theory for the K-matrix version of the calculation is given rather completely in Ref. 1. We shall just limit our description of the theory to certain fundamental points that are useful to define the differences in our work from Ref. 1 and to facilitate the explanation of our conclusions. We are solving the time-independent Shrödinger equation, for electron-H atom scattering, which, in atomic units, is

$$H\Psi(\vec{r_1},\vec{r_2}) = E\Psi(\vec{r_1},\vec{r_2}) \tag{1}$$

where H is the Hamiltonian operator given by

$$H = -\frac{1}{2}\nabla_1^2 - \frac{1}{2}\nabla_2^2 - \frac{1}{r_1} - \frac{1}{r_2} + \frac{1}{|\vec{r_1} - \vec{r_2}|} \tag{2}$$

and where Ψ is the system wavefunction. We then employ the basic idea of the close-coupling method which is to expand the total wavefunction Ψ in target states. [2,5] We then obtain, in standard fashion of the close-coupling method, the following static exchange equation for the continuum orbital F

$$(\nabla^2 + k^2)F(\vec{r}) = U(\vec{r})F(\vec{r}) + (-1)^s \langle \hat{K} | F \rangle \tag{3}$$

where k is the projectile momentum, U is the static potential, and $\hat{K}$ is the exchange kernel. The symbol s is 0 for singlet scattering and 1 for triplet scattering. F of Eq. (3) is required to satisfy the standard time-independent scattering boundary conditions [5] of incoming plane waves and outgoing spherical waves.

We then expand the continuum orbital in partial waves according to

$$F(\vec{r}) = \sum_{l,m} f_l(r) Y_l^m(\theta,\phi). \tag{4}$$

We just keep the $l = 0$ term in Eq. (4); hence, we are considering only s-wave scattering. Thus the model is simple but realistic. Then, the partial s-wave continuum orbital f, satisfies the K-matrix boundary conditions given by

$$\lim_{r\to\infty} f(r) = A^{(K)} G^{(1)}(kr) + B^{(K)} G^{(2)}(kr) \tag{5}$$

where the K-matrix is given by

$$K = tan(\delta) = B^{(K)}/A^{(K)}. \tag{6}$$

The T-matrix boundary conditions are given by

$$\lim_{r\to\infty} f(r) = A^{(T)} G^{(1)}(kr) + B^{(T)} H^{(+)}(kr) \tag{7}$$

where the T-matrix is given by

$$T = e^{i\delta}\sin(\delta) = B^{(T)}/A^{(T)}. \tag{8}$$

The $G^{(1)}$ and $G^{(2)}$ are related to the spherical Bessel functions by

$$G^{(1)}(kr) = krj_0(kr) \tag{9}$$

and

$$G^{(2)}(kr) = -krn_0(kr) \tag{10}$$

where j_0 is the $l = 0$ regular Bessel function and n_0 is the $l = 0$ irregular spherical Bessel function. Also, $H^{(+)}$ is the Hankel function of the first kind given by

$$H^{(+)}(kr) = G^{(1)}(kr) + iG^{(2)}(kr). \tag{11}$$

The static exchange differential equation for s-wave scattering is then changed into an integral equation, in standard fashion, which is called the Lippman-Schwinger equation, and is given by

$$f(r) = w^{(1)}(r) -$$

$$(-1)^s \frac{1}{k} \int_0^\infty dy\, [w^{(1)}(r_<)w^{(2)}(r_>)]_{r,y} \int_0^\infty dx\, V^s(y,x)\, f(x) \tag{12}$$

where the w functions are related to the Gs by

$$w^{(1)}(r) = G^{(1)}(kr)$$

$$w^{(2)}(r) = G^{(2)}(kr) + \beta G^{(1)}(kr) \tag{13}$$

where $\beta = 0$ for the K-matrix case and $\beta = i$ for the T-matrix case. In Eq. (12), V^s is the sum of the static and exchange potential so that

$$V^s(y,x) = U(x)\delta(x-y) + (-1)^s \hat{K}(x,y) \tag{14}$$

Then, we have[2]

$$D = -\frac{1}{k}\langle w^{(1)}|V^s|f\rangle \tag{15}$$

where D is either the K- or T-matrix depending on the form of w^2 in Eqs. (12) and (13).

Then we expand f in a Slater basis set

$$\phi_n(\alpha,r) = r^{n-1}e^{-\alpha r} \tag{16}$$

according to

$$f(\alpha,r) = \sum_n C_n \phi_n(\alpha,r) \tag{17}$$

We then proceed in a standard fashion which may be taken from Ref. 6 or 7 or from many other places. We then obtain the following set of working equations:

$$D = -\frac{1}{k} \vec{C} \underline{M}^{-1} \vec{C} \tag{18}$$

where

$$C_m = \langle w^{(1)} | V^s | \phi_m \rangle \tag{19}$$

and

$$M_{mn} = \langle \phi_m | V^s - V^s \hat{g} V^s | \phi_n \rangle \tag{20}$$

In Eq. (21), $\hat{g}$ is the reduced Green's function operator. Its form can be inferred by rewriting Eq. (12) in Dirac notation

$$|f\rangle = |w^{(1)}\rangle + \hat{g} V^s |f\rangle \tag{21}$$

and comparing Eq. (21) and (12).

Results and Conclusions

The $\underline{M}$ of Eq. (18) can be written as

$$\underline{M} = \underline{M}_R + \beta \underline{M}_I \tag{22}$$

where $\beta = 0$ if we are using the K-matrix form and $\beta = i$ if we are using the T-matrix form. One of the surprising results of the present work is that $\underline{M}_I$ is explicitly singular and cannot be inverted. This does not mean that $\underline{M}$ is singular, since we can use the following results. If, in general,

$$\underline{M} \equiv \underline{A} + i\underline{B} \tag{23}$$

and

$$\underline{M}^{-1} \equiv \underline{C} + i\underline{D} \tag{23}$$

then

$$\underline{C} = [\underline{A} + \underline{B}\underline{A}^{-1}\underline{B}]^{-1} \tag{24}$$

and

$$\underline{D} = -\underline{C}\,\underline{B}\,\underline{A}^{-1} \tag{25}$$

However, if $\underline{B}$ is singular, then, as the size of the matrices increases, the accuracy with which $\underline{M}^{-1}$ can be computed decreases until the inverse is no longer accurate. In fact, for any matrix size, the inverse is somewhat corrupted. The accuracy of the inverse computation can be tested by constructing the unit matrix. Also, the results can be compared with the K-matrix result where there is no $\underline{M}_I$. The agreement between the phaseshifts decreases as the basis set size increases. On a 64 bit word length computer, however, the agreement was still eight significant figures for a 15x15 matrix. We would like to note that we attempted to alleviate this problem by using an orthogonalized basis set instead of the ϕs of Eq. (16). This improved the agreement between the K-matrix and the T-matrix phaseshifts by one to two significant figures, but did not alleviate the problem. The conclusion to be drawn from these results seems to be that there is no point in using the T-matrix form if real basis functions are to be used.

Pseudo-resonances are encountered, just as in Ref. 2, for both the K-matrix and T-matrix forms. A surprising result, however, was that $\underline{M}_R$ is not singular until the energy is very near the pseudo-resonance energy. You have to be right on top of the pseudo-resonance energy before you lose the ability to compute $\underline{M}_R^{-1}$. This is quite different from our experience with the Kohn anomalies. [8] The explanation for this and for the existence of the pseudo-resonances can be understood by considering the argument given above in the Rationale for the supposed non-existence of the pseudo-resonances in the SVP. The finite rank potential that is substituted into the Lippman-Schwinger equation is given by

$$V^{sep} \approx V^s \,|\vec{\phi}\,\rangle \underline{\Delta} \langle \vec{\phi}\,|\, V^s \tag{26}$$

where

$$\underline{\Delta}^{-1} = \langle \vec{\phi}\,|\, V^s \,|\vec{\phi}\,\rangle \tag{27}$$

If V^s is energy independent (static potential), then V^{sep} is well behaved. If V^s is energy dependent, then there are going to be energies where $\underline{\Delta}$ does not exist. In other words, the phase shift that we are computing is indeed the exact phase shift for the separable potential V^{sep}. The problem is, the separable potential is non-physical at energies where $\underline{\Delta}$ does not exist.

We have now investigated the energy dependence of $\underline{\Delta}$ to see if the energies where pseudo-resonances occur are related in an identifiable way to the energies where the separable potential does not exist. The central result of this paper is the finding that they are exactly the same energies. Thus, we can predict the energy positions of the pseudo-resonances before we run the scattering calculation, and thus avoid the troublesome energies. This ability is aided by the fact that the pseudo-resonances are very narrow and become more narrow as the basis set size increases.

Acknowledgments

This work was supported by NASA Grant NCC 2-492 and by a grant of computer time from the Florida State University Supercomputer Computations Research Institute.

References

1. Callaway, J., Phys. Rep. 1978, 45, 89.

2. Apagyi, B.; Levay, P.; and Ladanyi, K., Phys. Rev. A, 1988, 37, 4577.

3. Ladanyi, K.; Levay, P.; and Apagyi, B., Phys Rev. A, 1988, 38, 3365.

4. Rescigno, T; McKoy, V.; and Schneider, B., editors, *Electron - Molecule and Photon - Molecule Collisions,* Plenum, 1979, page 103.

5. Nesbet, R.K., *Variational Methods in Electron - Atom Scattering Theory*, Plenum, 1980.

6. Watson, D.K., and McKoy, V., Phys. Rev. A., 1979, 20, 1474.

7. Adhikari, S.K., and Sloan, I.H., Nucl. Phys. A, 1975, 241, 429.

8. Weatherford, C.A., Int. J. Quant. Chem. S, 1982, 16, 277.

GROWTH AND CHARACTERIZATION OF CRYSTALS FOR IR DETECTORS AND SECOND HARMONIC GENERATION DEVICES*

Ravi B. Lal, Ashok Batra, M.S. Rao, S.S. Bhatia** and K.P. Chunduru**
Department of Physics
Alabama A&M University
Huntsville, AL

and

Ron Paulson
EDO Corporation/Barnes Engineering Division
Shelton, CT

and

Tripty K. Mookherji
Teledyne Brown Engineering
Huntsville, AL

ABSTRACT

Two types of materials, L-Arginine Phosphate (LAP) and doped Triglycine Sulfate (TGS), are examined for their growth characteristics and relevant properties for second harmonic generation and IR detector applications respectively.

* Work supported by Center for Commercial Crystal Growth in Space, Potsdam, N.Y., a NASA Sponsored Center for Commercial Development of Space (CCDS) - Clarkson University.

** Graduate Students.

GROWTH AND CHARACTERIZATION OF CRYSTALS FOR IR DETECTORS AND SECOND HARMONIC GENERATION DEVICES

A. L-Arginine Phosphate Crystals

Introduction

LAP is considered to be a potential new material for efficient second harmonic generation for an Nd:YAG laser. It is phase matchable with conversion efficiency between 3 to 4 times that of potassium dihydrogen phosphates (KDP). It has a high damage threshold (about 50 times of KDP) and a high figure of merit (40 times of KDP). Being a fairly new material, little data are available in the literature on growth parameters under which optical quality crystal can be grown from solution. In this section, characteristics of LAP solution and growth kinetics of LAP crystals grown under different conditions are described. The preliminary results of second harmonic conversion efficiency of LAP Crystals in comparison with KDP are also discussed.

Experimental Procedures and Results

The compound L-arginine phosphate, which is not commercially available, was synthesized in the laboratory. L-arginine and phosphoric acid were mixed in stoichiometric ratio and dissolved in deionized water. The mixture was stirred and heated to dissolve homogeneously. The chemical reaction can be presented as $C_6 H_{14} N_4 O_2 + H_3 PO_4 \rightarrow C_6 H_{16} N_4 O_3 \cdot H_3 PO_4$. The solution was kept at room temperature for evaporation. The self nucleated crystallites of LAP compound were formed and were removed from solution and dried. In order to find that the compound was in fact LAP, a powder sample was prepared and packed into a thin cell formed by two glass slides. The sample was illuminated with a 1064nm Nd:YAG laser and the second harmonic output from the sample which was green in color, was observed (corresponding to 532 nm wave length). This confirmed the formation of an L-arginine phosphate compound. Since no data were available about the solubility of LAP in water, it was determined at various temperatures. The details of the method are described elsewhere (1). The solubility data for LAP compound are presented in Table I.

Table I
Data for Solubility of LAP in Water

S.No.	Temperature (°C)	Solubility (gm/100 gm of Water)
1	28.0	13.93
2	35.0	20.04
3	40.0	25.66
4	45.0	32.32
5	50.0	40.02

The index of refraction of a solution is a sensitive indicator of the concentration. The measurements of the refractive index of LAP solution were made using an Abbe refractometer with a temperature controlled sample stage, and white light. Fig. 1. shows the index of refraction of the saturated solution as a function of temperature. The growth of crystals from the solution depends on various parameters: temperature of growth, degree of supersaturation, character of solution and hydrodynamic conditions. In the present work, in order to find the optimum conditions under which optical quality crystals can be grown, character of solution (pH) and hydrodynamics conditions were varied, keeping other conditions constant. The crystals were grown using temperature lowering techniques in a modified crystallizer (1,2). It was found that the morphology and optical quality of the LAP crystal changes with the pH of the solution. The optical quality crystals with prismatic morphology were grown from solution with optimum pH. At the optimum value of the pH of the solution, it was found that rotating the seeds between 17-26 rpm does not affect significantly the morphology and optical quality of the crystals. Single crystals of LAP, cut and polished, were placed in an Nd:YAG laser beam (1064nm) and the second harmonic was recorded at 532.2nm. The conversion efficiency of LAP samples was comparable with that of KDP. The lower value may be due to small thickness and bad polish. Further work to understand the growth mechanism and optical studies are in progress. The most important task, reducing growth time and increasing the growth rate in the desired direction, is also in progress.

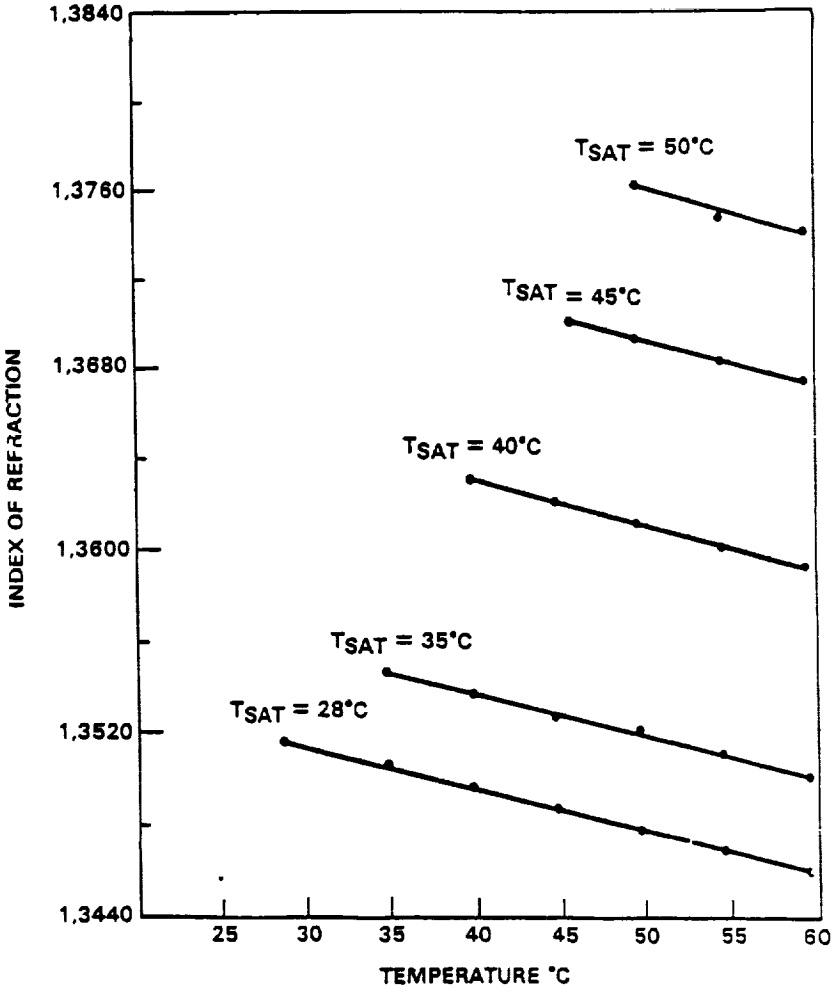

Figure 1. Index of Refraction Versus Temperature for LAP Solution.

B. Triglycine Sulfate Crystals

Introduction

TGS is a well known ferroelectric material and is widely used for i.r. detection at room temperature in scientific, medical, and commercial applications. It is the most sensitive material among available pyroelectric materials. However, it has a strong tendency of depoling (T_c = 49° C) due to temperature and mechanical shocks, causing degradation of the detector performance. In order to improve the pyroelectric properties and check depoling, various dopants have been tried. In this section, growth and characteristics of doped TGS crystals are described. The results are compared with a pure TGS crystal.

Experimental Procedure and Results

Triglycine sulfate crystals were grown using the reciprocating crystallizer designed and fabricated in the workshop of the Physics Department (2,3). The seed crystals with the desired amount of dopants were grown by slow evaporation. The detail of the method of growing crystals, growth kinetics and characterization techniques for electrical and detector properties are described elsewhere (3,4). The detectors were fabricated and tested at EDO Corporation / Barnes Engn. Div., Shelton, CT. The results of measurement for material characteristics are presented in Table II. It can be inferred from the table that the figure of merit of TGS crystals doped with L-alanine and simultaneously doped with L-alanine and cesium is higher than that of the pure TGS crystal. Moreover, L-AL+Cs doped TGS crystals are relatively harder and easier for sample handling and processing. The detector characteristics of doped TGS crystals are presented in Table III. It is shown that Detectivity (D*) of L-alanine doped crystals is higher than for other crystals investigated. It is probably the best value reported so far in the literature. The amount of dopant and conditions of growth chosen resulted in uniform incorporation of L-alanine in the crystal, as can be seen from the values of D* obtained for five detectors fabricated on one chip.

Conclusion

The present studies demonstrate that large optical quality LAP crystals can be grown by a solution cooling technique in a reciprocating crystallizer. However, studies to understand the role of the character of the solution (pH and dopants) on the crystal growth and optical quality of LAP crystals are required.

From the work on TGS crystals, it can be concluded that L-alanine and Cs+L-alanine doped crystals are attractive for pyroelectric infrared detector applications.

Acknowledgments

The authors would like to thank Lloyd Sharp and Keith Land for technical assistance, P. Chandra Sekhar for helping in optical studies, and R.S. Adhav of Quantum Technology, Inc. for supplying the KDP crystals.

TABLE II
MATERIAL PARAMETERS OF TGS CRYSTALS

CRYSTAL	PYROELECTRIC COEFFICIENT, p ($nc/cm^2\ °C$)				DIELECTRIC CONSTANT e'				FIGURE OF MERIT p/e' ($nc/cm^2\ °C$)			
TEMP°C	30	35	40	45	30	35	40	45	30	35	40	45
TGS	53	70	98	170	48	64	106	250	1.1	1.09	0.92	0.68
TGS + Ce	37.2	53	84	150	61	76	115	350	0.61	0.7	0.73	0.42
TGS + Cs	43	64	85	155	67	84	120	300	0.64	0.76	0.70	0.52
TGS + LA	38	44	80	172	30	37	48	62	1.2	1.48	1.6	2.7
TGS + Cs + LA	55	134	200	315	38	41	54	69	1.44	3.26	3.7	4.5

TABLE III
DETECTOR CHARACTERISTICS

SAMPLE	CELL NO.	RESPONSIVITY (V/W) 1000 K/BLACKBODY		NOISE (nV/Hz)		D* (1000K,f,1) $x10^8$	
		15 Hz	90 Hz	15 Hz	90 Hz	15 Hz	90 Hz
NO. 1 (TGS)	20930	1×10^3	160	260	80	7.7	4.0
	20944	1×10^3	160	170.5	56	12.0	5.5
NO. 2 (TGS + L-ALANINE)	20752	1×10^3	160	190	65	11.0	5.0
	20885	1×10^3	160	167	60	11.8	5.3
	20963	950	160	190	66	12.0	5.2
	20803	1×10^3	160	175	60	13.5	5.6
	20941	1×10^3	160	167	54	12.3	5.7
NO. 3 (TGS + Cs + L-ALANINE)	20986	1×10^3	150	560	140	3.35	2.05
	20924	850	130	280	92.5	6.25	3.0
	20980	890	140	760	170.5	2.20	1.6

References

1. Bhatia, S., M.S. Thesis, AL A&M University, AL; 1988.

2. Aggarwal, M.D.; Lal, R.B., Rev. Sci. Inst. 772, 54(6), 1983.

3. Banan, M. M.S. Thesis, AL A&M University, AL; 1986.

4. Lal, R.B.; Aggasrwal, M.D.; Batra, A.K.; Kroes, R.L., Final Technical Report, NAS8-32945, 1987.

JACKSON STATE UNIVERSITY'S CENTER FOR SPATIAL DATA RESEARCH AND APPLICATIONS: NEW FACILITIES AND NEW PARADIGMS

Bruce E. Davis
Gregory Elliot
Jackson State University
Jackson, MS

ABSTRACT

Jackson State University recently established the Center for Spatial Data Research and Applications, a Geographical Information Systems (GIS) and remote sensing laboratory. Taking advantage of new technologies and new directions in the spatial (geographic) sciences, JSU is building a Center of Excellence in Spatial Data Management. New opportunities for research, applications, and employment are emerging. GIS requires fundamental shifts and new demands in traditional computer science and geographic training. The Center is not merely another computer lab but is one setting the pace in a new applied frontier. GIS and its associated technologies are discussed.

The Center's facilities are described. An ARC/INFO GIS runs on a Vax mainframe, with numerous workstations. Image processing packages include ELAS, LIPS, VICAR, and ERDAS. A host of hardware and software peripherals are used in support. Numerous projects are underway, such as the construction of a Gulf of Mexico environmental data base, development of AI in image processing, a land use dynamics study of metropolitan Jackson, and others. A new academic interdisciplinary program in Spatial Data Management is under development, combining courses in Geography and Computer Science. The broad range of JSU's GIS and remote sensing activities is addressed. The impacts on changing paradigms in the university setting and in the professional world conclude the discussion.

THE JACKSON STATE UNIVERSITY CENTER FOR SPATIAL DATA RESEARCH AND APPLICATIONS: NEW FACILITIES AND NEW PARADIGMS

We are in an era of rapid technological change and few fields have seen such dynamic evolution as computer technology. Many disciplines are benefiting from the remarkable advances that are emerging, but the spatial (geographic) sciences seem to be profiting extraordinarily well. In particular, the new specialty of GIS (Geographical Information Systems) is experiencing an international growth of over thirty-five percent per year, which opens the door for new directions in research and applications and new markets for employment. Because of GIS, novel operational and philosophic paradigms are being introduced into numerous disciplines. Jackson State University (JSU) has embraced GIS technology and is developing a unique center of excellence in spatial data analysis and applications. This paper presents Jackson State's efforts and plans. A brief explanation of GIS and associated technologies is given, followed by discussion of JSU's GIS infrastructure and activities. Intrinsic in the presentation are the changes in educational, research, and applications directions that are arising from these technological advances. In particular, we emphasize the dynamic paradigms that are sure to have long-reaching influence in the profession. (Note: herein GIS refers to the broad range of computer spatial techniques and technologies rather than to a specific package of mapping routines.)

GIS and Remote Sensing

GIS is a computerized methodology for collection, organization, analysis, and display of geographic data. Far more than simple computer mapping it provides sophisticated techniques for manipulating geographic data. First, GIS is a spatial data base, an ideal inventory structure from which diverse forms of information can be stored and extracted. Any type of data that can be located ("georeferenced") can be used, e.g., maps, imagery, census information, etc. From there data can be extracted in "raw" form for direct readout or combined with other data sets to produce new information.

More important is the analytical capability of GIS, especially considering the graphics functions for mapping. Data from various scales and formats of maps can be combined (overlaid) to assess relationships previously impossible to determine. Buffer zones of select size can be built around features for proximity analysis. Many other "tricks" are available for manipulating data either graphically or within the data base. Each generation of data forms a new base from which to perform analysis.

Remote sensing imagery (photographic or digital) from aircraft or satellites forms an important data resource for GIS. Unlike traditional airphoto depositories where imagery is stored on rolls of film in canisters for occasional visual inspection, modern remote sensing techniques convert landscape scenes to digital format. Once in the computer, a plethora of processing procedures is available for extracting new information not perceivable in the original imagery.

Satellite data, for example, are obtained in several distinct bands or channels of the electromagnetic spectrum, each channel providing unique views of a scene. Digital manipulations can be applied to each band to derive a variety of data. When composited in different combinations, synergetic renditions can result. Many versions of the original imagery are obtainable.

GIS also has advantages for map production, e.g., ease, rapidity, and flexibility. Traditional pen and ink methods of cartography are too limiting in terms of time and design agility. For example, map size reproduction can be changed quickly and easily, typically via a simple computer instruction. Segments of the digital coverage can be separated and mapped. Also, the range of data to be used is selectable, from the full set (maximum discrimination) to a more simple (generalized) classification. Efficient and flexible productivity is a primary characteristic of GIS.

Other advantages are apparent. Statistical reports can be produced automatically, describing the quantitative and qualitative nature of each viewed feature. Map storage no longer needs physical equipment such as large cabinets or racks. Data can be shared over long distances rapidly, easily, and cost effectively. In effect, GIS offers highly efficient and flexible methods and technologies to innovate the spatial data world.

Jackson State University

Jackson State is developing a Center of Excellence in Spatial Data Management to take advantage of the many research and market opportunities afforded by GIS technology. JSU is particularly well-suited to such innovation because of several advantages: (1) Having considerable computation power, major GIS and remote sensing packages can be facilitated without additional expensive investment. (2) With a large computer science (CS) faculty, a substantial human resource base exists. (3) Having the largest computer science enrollment of any HBCU, an excellent student resource base and a foundation to establish an academic program are in place. This is particularly true given the extraordinary enthusiasm exhibited by students thus far.

(4) A relative vacuum exists in the state and region concerning GIS, thus giving an unparalleled opportunity to the institution having prescience. (5) Probably the most important factor has been the presence of an administration, from the top down, with remarkable foresight, ambition, vision, competence, and cooperation in emplacing a new direction in the university setting. Therefore, JSU is building a substantial and exceptional program in the new spatial technologies from which it can become a prominent and pace-setting leader.

Central to the center of excellence concept is JSU's new Center for Spatial Data Research and Applications (CSDRA). The CSDRA (also referred to as the Center) is a GIS and remote sensing lab providing the setting for research, educational, and professional out-reach efforts in the spatial sciences. Described below are its facilities and equipment, major research efforts, academic developments, professional activities, and plans.

Facilities, Equipment and Staff: Housed in the new science building, the CSDRA contains most of the GIS and remote sensing equipment. The nucleus of the GIS infrastructure is a Vax cluster ARC/INFO, the premier international system. It uses a powerful mapping graphics package integrated with a relational database program. Three Tektronix workstations serve as the primary interfaces, but numerous other graphics terminals are used as secondary workstations. Micro-based ERDAS is also used.

Image processing software consists of NASA's ELAS and LIPS, Jet Propulsion Laboratory's VICAR, and ERDAS, all functionally linked to ARC/INFO for direct feed of imagery to a mapping base. A 40" Calcomp color electrostatic plotter and two Tektronix color inkjet plotters serve as the primary hardcopy devices. Mapping data entry is performed on a large digitizing tablet and with an

Eikonix scanning digitizer. A host of peripheral equipment supports operations, e.g., microcomputers, film recorder, etc.

CSDRA staff consists of a principal investigator, Center director, lab manager, a project manager, five CS faculty, three systems technicians, and several clerical personnel. Twelve research assistants and four workstudy staff form the student help. The academic program (to be discussed) will be supported by two new faculty, one in computer science and the other in geography. Adjuncts from local GIS and remote sensing operation agencies serve as program associates.

Projects: Two major funded research projects, begun in late 1987, formed the initial and primary efforts of the Center. The Department of Interior's Minerals Management Service (MMS) initiated a project to develop GIS in its operations, to build a Gulf of Mexico environmental database, and to assist in various research and applications tasks. MMS is responsible for off-shore mineral leases and mineral extraction activities, so its basic duties are ideally suited to GIS methodologies.

The first task was to construct a lease block data base to serve as the base map and data for subsequent informational needs. Over 30,000 blocks are distributed in the Gulf and each has unique identifiers that must be quickly recalled and used either graphically or in the relational data base. GIS's ability to relate to either graphics or tabular data is a critical asset for MMS needs. Other MMS tasks include mapping of Alaska off-shore blocks and data, mapping of coral reefs and offshore structures, digitizing of shallow geology, and data base preparation to support oil spill accidents off Florida.

The National Aeronautics and Space Administration (NASA) has aimed primarily at image processing (IP) but is also interested in using remote sensing in support of GIS. One of the major projects is the inventory and analysis of metro Jackson, Mississippi urban dynamics—land use, demographic factors, quality of life, environmental impacts, and application of artificial intelligence (AI) and expert systems to identification of undeveloped lands. Remote sensing from NASA aircraft will cover the city with large and medium scale color infrared photography and digital scanner data. Imagery is the principal data source but associated contemporary and historic information is employed for comprehensive coverage.

Other NASA assignments consist of a variety of data conversion and programming tasks, publication of a nation-wide remote sensing facilities survey, assistance in development of an academic program and associated specialized training, construction of a publication data base to support numerous GIS and remote sensing needs, and provision of overall guidance in the establishment of the center of excellence. Other smaller projects are under consideration (see Plans below).

Academic Programs: One of the major new paradigms to emerge from GIS is the development of a truly interdisciplinary methodology in the spatial sciences. A new (Fall, 1990) interdisciplinary academic graduate and undergraduate program in Spatial Data Management (tentative title) is under development. The undergraduate program consists of courses in both the departments of Computer Science (Science and Technology Division) and Urban Affairs/Geography (Liberal Arts Division), forming a concentration in both disciplines. A graduate concentration in CS will be part of the information science direction. Courses in GIS, remote sensing, spatial analysis, and traditional applications and systems are used. Projects, theses, and an intern option provide practical experience. One thesis has been completed and two are underway. The JSU spatial data program is distinctive in the American university system in that it integrates two traditionally segregated departments—Geography and CS. Unique in HBCUs, JSU's GIS-based academic program is approached only by a very small number of higher education institutions. New directions and new educational paradigms are being

established. Both geographers and computer specialists must redefine their approaches to the management and analysis of spatial data, but the potential rewards can be tremendous.

Professional Activities: CSDRA personnel have been instrumental in instituting a state-wide alliance of GIS and spatial data users—the Mississippi GIS Association. It provides a linkage among academic, public, and private users of GIS or geographic data. A newsletter is to be published and several activities for community out-reach are planned, including surveys of systems and relevant data bases in the region. A coastal branch was begun recently and other divisions are under discussion.

Presentations and publications on several themes have been produced. Fundamentals of marine GIS were established. Future directions of GIS and associated fields, particularly the contributions of computer science advances, have been presented. A national survey of remote sensing has been published. Numerous papers have been given and several publications are in process.

Plans: Two other major projects are pending (summer initiation planned): economic mineral mapping of northeast Mississippi and institution of a county GIS operation. Additional small formal and informal research and applications activities are under discussion. For example, GIS is a perfect mechanism for design and creation of thematic atlases and a quality of life atlas for the state has been proposed.

Jackson State's GIS program has only begun and it is difficult to predict the specific directions that will be taken. The themes mentioned will continue to be important but other interests may be pursued. As expertise and capabilities build, one desirable direction is the application of GIS to Third World development, particularly Africa. Preliminary contacts with relevant agencies have begun, e.g., the United Nations Environmental Program's Global Resource Information Database (GRID).

Enhancement of the academic program has high priority. As the initial strategy develops, more depth will be added in terms of courses and faculty. New disciplines will be included. Equally important will be increased opportunities for student hands-on experience, either in the Center or in additional internship locations. Because GIS is a practical application, we feel that it is essential that properly trained graduates have functional credentials.

Purpose

As a progressive institution, JSU is interested in cutting-edge advances in many disciplines, but GIS is perhaps one of the most exciting and productive new fields to emerge from technologic progress. To embrace the GIS field is a logical and forward step in institutional evolution. To date, only a few schools offer training beyond an introductory course and broad, strong programs like the one at JSU are largely absent on the academic scene. However, the strengths, potential, and market for GIS is not a secret, for it has become entrenched in several disciplines in the last few years; it is only a matter of short time before analytical computer mapping becomes a standard curriculum item. By taking a lead at this relatively early stage, JSU stands to become broadly noted, not only among HBCUs, but on the national scene as well. That purpose alone suffices as relevant support for contemporary development of GIS at Jackson State.

The market potential for GIS-educated personnel is tremendous, especially given the very high growth rate of the field and shortage of qualified personnel. It takes little to become marketable today (usually a little experience or a course in GIS), but enhanced training (dedicated program with

specialized directions) will ensure high promise of professional success for graduating seniors or masters. This is specifically valid for minorities, who are vastly underrepresented in the field. Thus, marketability is a major purpose for initiating a center of excellence.

One of the primary reasons that GIS and its related fields are doing so well is that more and more types of data are becoming "spatialized", i.e., tagged to location. Once the locational attribute has been identified, GIS can apply its many capabilities to produce information heretofore unavailable. There is little wonder that sales of GIS software and hardware are increasing internationally at over thirty-five percent per year. This is another substantial support for JSU's activities.

Paradigms

As used here, "paradigm" denotes a model of thinking or acting, a philosophic or practical basis for operating in a prescribed manner, or a fundamental logic or motivation for development of values and social or professional behavior. Paradigms guide, often tell, how to proceed and what to expect. However, paradigms change—society evolves and ideas go through "life cycles", from birth and infancy through maturity to old age and eventually, death. Scientific paradigms are especially sensitive to technologic and social changes and may have relatively brief lives. Paradigms in computer science have rather particularly short life expectancies.

GIS is much more than a technologic advance; it is establishing new ways of doing new things with spatial data. New paradigms in scientific and social training, analysis, and applications are under construction. Disciplines and professions are undergoing radical transformations; change is inevitable. For example, as JSU's Geography program plans for reinvigoration of its techniques courses in preparation for the spatial data management concentration, a detailed budget must be furnished. The "shopping list" of cartographic supplies does not include drafting equipment, press-on lettering, or any of the paraphernalia commonly found in traditional mapping labs. We plan to begin at the digital level and build from there. The rationalization (i.e., new paradigm) is that the professional world is much more interested in modern training than in old style techniques.

Another paradigm under development is that no longer can a single discipline provide the necessary breadth that is demanded by employers today. The market is best for those who have both technical skills and a broad understanding of what to do with the new techniques. The most viable GIS training involves both operations and applications. We have accepted that premise and are designing programs to accommodate the CS major and the applications disciplines. There can be pockets of resistance in interdisciplinary or trans-divisional programs (the new paradigm), but the vision that is making JSU a leader in the field recognizes the necessity of different paths for different destinations.

Despite reluctance to overstate, it is difficult to exaggerate the potential that exists in this new approach to the use of geographic information. Jackson State University is at the forefront of initiating and instituting important new paradigms not only in the educational universe, but in the applications world. As an HBCU, JSU is responsible for an added dimension of substantiating the role and mission of minorities. The wealth of possibilities, the richness of potential, and the inevitability of new horizons are apparent; JSU intends to be at the front, providing avenues for all. Clearly, we are at an age of new paradigms.

SOLUTION GROWTH OF TRIGLYCINE SULFATE (TGS) CRYSTALS ON THE INTERNATIONAL MICROGRAVITY LABORATORY (IML-1)*

R.B. Lal, A.K. Batra, and Li Yang**
Department of Physics
Alabama A&M University
Huntsville, Alabama

and

W.R. Wilcox
Clarkston University
Potsdam, New York

and

J.D. Trolinger
MetroLaser
Irvine, California

ABSTRACT

An experiment has been planned for the International Microgravity Laboratory (IML-1) to be launched around February, 1991. Crystals of triglycine sulfate (TGS) will be grown by low temperature solution crystal growth technique using a multiuser facility called Fluid Experiment System (FES). A special cooled sting technique of solution crystal growth will be used where heat is extracted form the seed crystal through a semi-insulating sting, thereby creating the desired supersaturation near the growing crystal. Also, a holocamera will be used to provide tomography of the three dimensional flow field and particle image dispacement velocimetry to monitor the convective flows.

* Work supported by NASA contract NAS8-36634.

** Graduate Student

SOLUTION GROWTH OF TRIGLYCINE SULFATE (TGS) CRYSTALS ON THE INTERNATIONAL MICROGRAVITY LABORATORY (IML-1)

Introduction

In the Spacelab-3 flight flown in 1985, the Fluid Experiment System (FES) was used to conduct crystal growth experiments to help in the understanding of the solution growth of crystals in a micro-gravity environment. This paper describes the reflight of the FES on the IML-1 mission to be flown on Spacelab mission in early 1991, with different objectives and a refined optical system. The objectives of the experiment are 1) to grow crystals of TGS using a modified version of the Fluid Experiment System (FES), 2) to study the holographic interferometry tomography of the fluid in three dimensions, and 3) to study the fluid motion due to g-jitter by measuring the fluid velocity using simple multiple exposure holography of tracer particles and to study the influence of g-jitter on the growth rate of TGS crystals.

Importance of TGS

Triglycine Sulfate (TGS) is a good model material for solution crystal growth. TGS crystals can be grown at considerably low temperatures like 30-45° C, TGS solution is transparent and so holographic techniques can be used to study the fluid properties, considerable ground based work has been completed, and it is easy to handle. Apart from this, TGS has technological importance for pyroelectric infrared detectors which require no cooling as compared to quantum detectors. The present devices have detectivities (D*) from 5×10^8 - 1×10^9 $cm\ Hz^{1/2}$ / watt. This is about an order of magnitude away from the theoretical value for a pyroelectric bolometer operating at room temperature. This difference is expected to be due to the dielectric loss in the material.

Growth of Crystals Using FES and Cooled Sting Technique

During the IML-1 mission TGS crystals will be grown from an aqueous solution using a specially developed technique of cooled sting[2]. Many crystals of TGS have been grown in the laboratory using the cooled sting technique and the growth rate is monitored using a three axes movement telemicroscope. During the IML-1 mission, two experimental runs are planned where the saturation temperature of the TGS solution will be around 45°C. In the first experiment a polyhedral seed with (010) orientation will be used; in the second experiment a similar seed with (001) orientation will be used.

In the absence of convection, crystal growth from solution will rapidly become slower as the adjacent solution layer is depleted in solute, unless the growth in temperature is lowered to compensate. However, if the temperature is lowered too fast, the growth rate will reach a level where sovent inclusions are formed. To accomplish a uniform growth rate, the temperature is lowered at a programmed rate. This can be done by programming down the walls of the growth cell. However, in reduced convection or in the absence of convection, only change of temperature of the walls would require a

long time to inwards towards the crystal. On the other hand, controlling the temperature of the sting in intimate contact with the crystal should allow the growth rate to be held constant. Details of this have been given earlier[3]. Details of the flight growth cell are given in fig. 1.

Planned Crystal Growth Runs on IML-1 Mission

The first crystal growth run will be for a period of about 1 day. During this run, the fluid flow in three dimensions will be studied. To achieve this, TGS solution will be seeded with small particles that can be imaged by holography to show the direction and velocity of fluid movements. The present plans include the use of polystyrene microballons added to the fluid as tracer particles. In this run a seed crystal of TGS with (010) orientation will be used. The data from the first run will be used to grow a high quality single crystal during the second run that will last several days. No tracer particles will be used during this run, because they would contaminate the crystal by forming inclusions and other defects. A three dimensional view of the crystal and flow field can be recorded by applying holographic optical elements to the crystal growth cell. Tomography is made possible by passing light through the FES windows at three different angles. Studies have shown that this will be sufficient to extract three dimensional density data from the field of the type anticipated. Details of the optical holography system are published elsewhere[4].

On the IML-1 mission, the accelerations that cause convection and disturb crystal growth will be carefully monitored. In addition to an internal FES accelerometer that measures accelerations above 5 Hz, the Space Acceleration Monitoring System (SAMS) has two accelerometers located near the FES crystal growth cell and one more mounted in the Spacelab aisles. This special set of accelerometers measures low-frequency (0 to 5 Hz) vibrations that are harmful to crystal growth experiments.

Analysis of the Crystals

Considerable ground-based data have been generated for TGS crystals grown by a similar technique. After the mission the grown crystal will be returned to our laboratory for extensive analysis of their structure and electrical and other physical properties, including their infrared detection characteristics. The space-grown crystals will be compared with crystals grown by commercial companies. The detector characteristics of the ground crystals and later for the flight crystals will be measured at EDO/Barnes Engineering Division, Shelton, Connecticut.

Acknowledgments

The authors would like to thank The National Aeronautics and Space Administration, Office of Microgravity Science and Applications for the support of this work through a contract. Thanks are also due to Rudy Ruff, William Witherow, David McIntosh, Todd Macleod, and David Johnston of NASA/Marshall Space Flight Center for their continued support during the preparation of this experiment.

References

1. Yoo, Hak-Do, Wilcox, W.R., Lal, R.B., and Trolinger, J.D. J. Crystal Growth, 1988, 92, 101.

2. Lal, R.B., Aggarwal, M.D., Kroes, R.L., and Wilcox, W.R., Phys. Status. Sol(a). 1983, 80, 547.

3. Liu, L.C., Wilcox, W.R., Kroes, R.L., and Lal, R.B., in Material Processing in the Reduced Gravity Environment of Space, Ed G. Rindone (North-Holland, Amsterdam, 1982) p. 389.

4. Trolinger, J.D., Tan, Hung., and Lal, R.B., International Congress on Applications of Lasers and Electro-Optics (ICALEO), San Diego, CA, Nov 9, 1987.

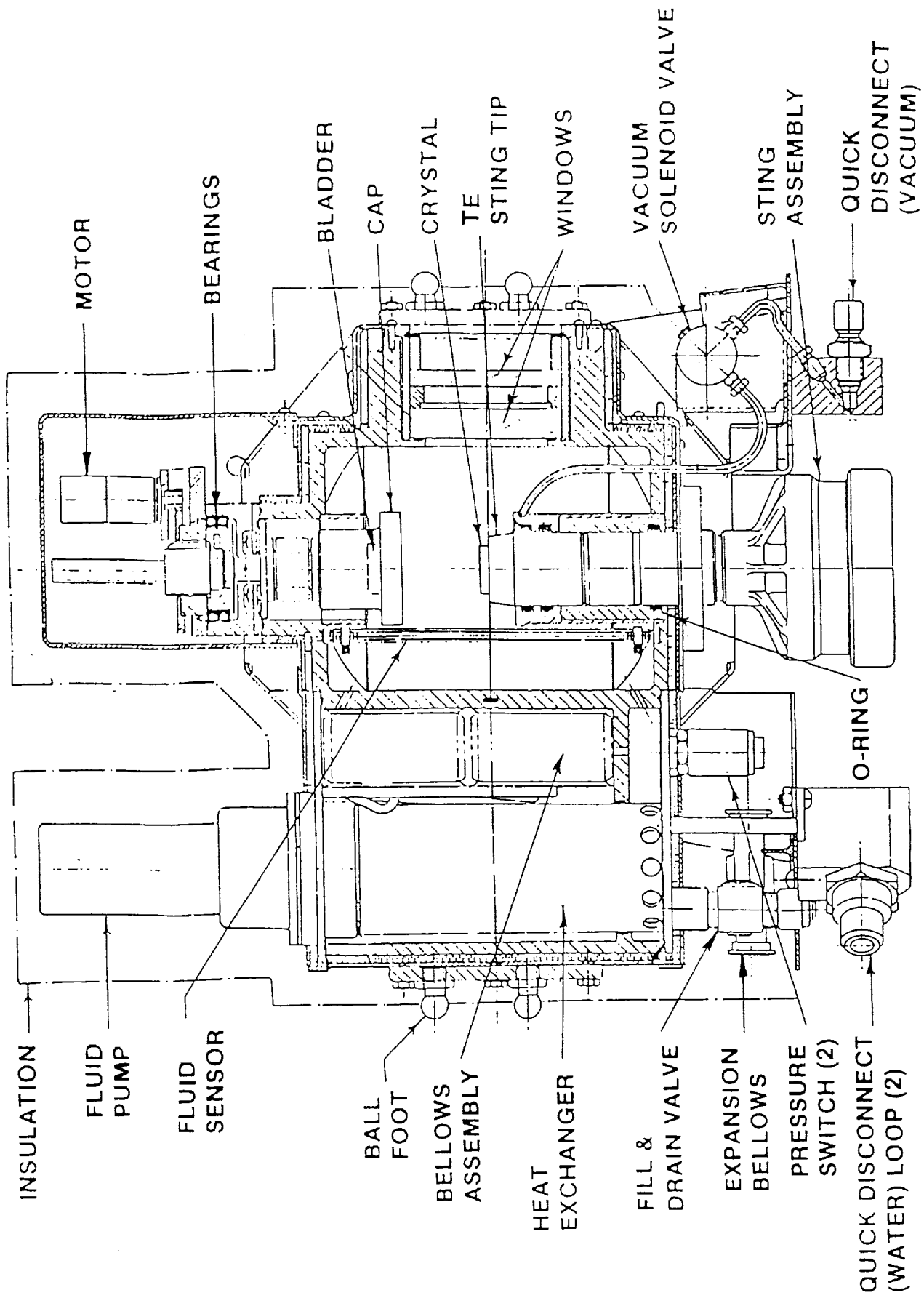
FES TEST CELL
MOTOR
BEARINGS
BLADDER
CAP
CRYSTAL
TE
STING TIP
WINDOWS
VACUUM SOLENOID VALVE
STING ASSEMBLY
QUICK DISCONNECT (VACUUM)
O-RING
INSULATION
FLUID PUMP
FLUID SENSOR
BALL FOOT
BELLOWS ASSEMBLY
HEAT EXCHANGER
FILL & DRAIN VALVE
EXPANSION BELLOWS
PRESSURE SWITCH (2)
QUICK DISCONNECT (WATER) LOOP (2)

Figure 1.

A STUDY OF SPATIAL DATA MANAGEMENT AND ANALYSIS SYSTEMS

Clyde Christopher
Jackson State University
Jackson, Mississippi

and

Richard Galle
Stennis Space Center
NSTL, Mississippi

ABSTRACT

The Earth Resources Laboratory of NASA's Stennis Space Center is a center of space related technology for earth observations. It has assumed the task, in a joint effort with Jackson State University, to reach out to the science community and acquire information pertaining to characteristics of spatially oriented data processing.

A STUDY OF SPATIAL DATA MANAGEMENT AND ANALYSIS SYSTEMS

1. Introduction

During the past 15 years much computer software has been developed for handling spatial data. A number of centers have been set up for processing spatial data, all with different configurations. Some studies have been conducted to collect and disseminate data on software in this area. Scientists at the Earth Resources Laboratory (ERL) were interested in knowing the software and hardware characteristics in such centers. Additionally, they wanted to know with what centers those who are actively engaged in spatial data processing are communicating. This information is to be shared with scientists in those centers so that all will be fully aware of the state-of-the-art software and hardware for spatial data processing.

2. Methodology

The desired information was collected by means of a survey. The survey instrument was designed by Christopher and Galle with approval from proper authorities. Part I asked for background information including names of adminnistrators, primary mission, list of principal application areas, and a list of representative projects currently supported at that facility.

Part II requested data processing methodology. First, it asked for a listing of hardware devices devoted to spatial data processing including the host computer, display devices, digitizers, disk drives, tape drives, plotters, etc. Next, it asked for a list of software packages currently supported by the facility, including compilers, GIS systems, statistical packages, data base management systems, etc. Finally, it asked with what other facility they were linked and what communication package is being used.

Part III is a request for data characteristics. The survey asks what types of data are used (Landsat, TM, AVHRR, Soils Maps, etc.), what are the sources, how is it input for processing, what is its internal format (Raster, Vector, Etc.), and what CAD related capabilities are available for editing the data sets.

Part IV asked for data analysis characteristics. It specifically asked what types of data processing (statistical, analytical, expert system decision making, polygon declaration, model structuring) supports the applications at that installation. Also, it asks whether there is merging or overlaying of data and what steps are taken in the processing life cycle.

Part V, the concluding section, asked for representative research which has been undertaken at the facility in the area of spatial data processing and, also, the research objectives which are needed.

The survey was first mailed under a cover letter dated July 10, 1987. A second copy was mailed to those facilities that had not responded by September 8, 1987. The survey was mailed to 349 different installations. Completed forms were received from 115 installations. A survey instrument worded so that all answers could be given by checking the correct item probably would have yielded a higher number of responses. However, that type of instrument would not have yielded as much detailed information as the one used.

The data will be used to build a data base with appropriate query language so that local users will have access to it. Hopefully, problems in communication will be solved, providing access to this data on a nationwide basis.

3. Results

A. Background Information. The survey was sent to basically three types of organizations: 1) government agencies, 2) private industry, and 3) educational institutions. In addition to supplying names of key contact personnel at the installation this section of the survey provided us with a statement of the primary mission of the installation and a list of ongoing projects. The government and industrial organizations said they were involved in research in remote sensing and in analyzing terrain and giving technical advice on use of land and water resources. The educational institutions are involved in training students in the use of remote sensing as well as research in that area.

No two installations listed the same project. Typical projects were: "Land use of 13 county region of Tennessee", "Training in forestry and wetlands remote sensing techniques", and "produce 7 1/2 foot wetland maps of the United States". Some indicated that project titles are not available to the public.

The principal application area is an important response in this section. These ranged from "land use classification" to "geological engineering". However, the most frequent responses were "remote sensing", "image processing", "GIS", or some combination of these.

B. Data Processing Methodology. Computer systems used to process spatial data range from microcomputers to mainframes. The most frequently listed microcomputers are the IBM PC-AT and APPLE II PC. In the minicomputer class the VAX 11/780 is most used. In the largest class an Amdahl V7/V8 was listed by one installation. The Prime 9650 was listed by several installations.

TABLE 1. Host Computer(s)

Model	Number of Installations
Microvax II	15
Apple IIc	2
Amdahl (5860/V7/V8)	3
Harris (1000, 500, 800)	3
VAX (8200, 11/730, 11/750, 11/780, 11/785)	36
Hewlett-Packard 9000	2
IBM PC (ATXT)	12
SUN	3
PDP 11/70	8
Concurrent (Perkin Elmer)	5
Prime (400, 550, 750, 465, 9755, 9650, 2655, 2275, 6350, 250, 9955)	32
Data General	4
Gould 32/27	5
IBM (3013, 3081, 3084, 4361, 4381)	11
Zenith 248	3
MASSCOMP 5600	5
AT&T (3B5, 3B2)	3

TABLE 2. Operating Systems

Software	Number of Installations
RIPS	1
VMS	39
VOS 6.1	2
UNIX	11
PRIMOS	30
MVS	7
RT-11	3
MS-DOS	6
MPX	4
RSX-11M	2
OS-32	5
VM/CMS	3
VORTEX	2
AOS	2
ULTRIX	1

TABLE 3. Digitizers

Model	Number of Installations
GTCO	15
Hitachi	4
CALCOMP 9100	32
Altek	23
Goegraphics	5
Summagraphics	6
Perkin Elmer (concurrent)	1
Talos	5
NUMONICS	3
Intergraph	2
Tektronix	7

TABLE 4. Display Devices

Model	Number of Installations
Tektronix	58
Comtal	11
De Anza	3
ADAGE	2
Visual 500	8
CALCOMP	2
Lexidata	6
Hewlett-Packard	3
Intergraph	2
ERDAS	3
Hitachi	3

The type of compilers available depends upon the model of computer and the memory size. Some installations list Fortran, only. Pascal and C are also frequently listed. Many installations listed all three of the above languages, but Fortran was listed most frequently. Other languages used inclined Lisp, Prolog, BASIC, SCAN, COBOL, MODULA2, Ada, and PL/1.

Among the image processing and GIS systems listed, ELAS and ARC/INFO were most frequent. Others in the order of occurrance were RIPS., ORSER, GRASS, ERDAS, MOSS, SYNERCOM, and ODYSSEY.

TABLE 5. Image Processing Software

Model	Number of Installations
ELAS	30
RIPS	6
COS	3
ARC/INFO	45
GRASS	6
ERDAS	22
MOSS	10
SYNERCOM	2
ORSO	2
ATLAS	2
Intergraph	2
EROS	2

Some installations indicated that their processing involves statistical analyses and they named the statistical package that is available on their system. SAS, SPSS, GLIM, BMPD, MINITAB, OSIRIS, NAG, VECTOR, MATH 77, SSPLIB, IMSL and Microstat were among the packages named.

Database management systems were as varied as statistical packages. However, some who responded did not name a DBMS. One installation stated that it has as in-house information storage and retrieval system. The usual response was one or more of the familiar ststems such as Datatrieve, INFO, PC INF, RBASE, Dbase III, ORACLE, BASELINE, CDOS, SMARTSTAR, SPIRES, or INGRES.

TABLE 6. Data Base Management Systems

Software Package	Number of Installations
DBASE II or III	20
Datatrieve	5
INFO	36
SMARTSTAR	1
ORACLE	7
BASELINE	1
RBASE	5
Prime-INFORMATION	4
SPIRES	1
OPS-83	1
CDOS	1
INGRES	4

Some large installations at government sponsored organizations indicated that they are connected with state or regional offices through some type of communication link. In general, the educational institutions have local networks. This was the case with several other installations as well, but there were those who indicated that they have no networking.

C. Data Characteristics. Landsat, TM and MSS data are the most used data in the installations that responded. However, a great variety of data types are used. AVHRR, Soils Maps, SPOT, and GOES were frequently named in the survey. Most installations named several types. Some other types listed were land use maps, USGS topographic maps, ACZCS, census, transportation networks, streams and rivers, watershed and aerial photos. The primary sources of data were EROS, NASA, USGS, SPOT Image Corporations, and virtually all map sources.

TABLE 7. Data Types

Data Type	Number of Installations
LANDSAT (MSS AND TM)	72
AVHRR	24
Soils Maps	41
Land Use Maps	12
Census	10
SPOT	21
GOES	6
SIR-B	2
USGS Topographic Maps	18

As a rule digitizers and magnetic tapes are used to input data for processing. Floppy disks were frequently listed as input media. Video cameras, optical disks, and keyboards were each listed by at least two installations.

TABLE 8. Data Input Scheme

Input Media	Number of Installations
Digitizer	84
Magnetic Tape	86
Magnetic Disk	21
Optical Disk	3
Keyboard	9
Scanning	6
Digital Camera	6

The internal format for data was given as raster or vector or both. CAD related capabilities at various installations include scroll, zoom, draw, density slice, classification, cut, paste, and paint.

TABLE 9. Input Format

Characteristic	Number of Installations
Raster	86
Vector	72
Gridded	4

D. Data Analysis Characteristics. In answer to the question on analysis of data during processing, we found that a majority of installations do a statistical analysis. Several installations use the data in decision making for expert systems. A few installations are doing polygon declarations. A small number indicated that they are merging data sets and at least one installation is overlaying data. Some installations were cooperative in sharing with us the steps in the processing life cycle, not an easy task.

E. Conclusion. In this section some installations listed some research efforts that are ongoing in special areas. A non-conclusive list of these follows:

1) Incorporation of the SOI-5 soil interpretation records into ARC/INFO

2) Incorporate spatial data (GIS) into a decision support system

3) GRASS G&D functions

4) Link between S and GRASS

5) Hydrologic modeling, flood damage analysis

6) Image texure recognition

7) Geometric rectification, image animation

8) Map display techniques

9) Digital image processing-both spectral and spatial analysis

(Notes. The researchers acknowledge assistance in this project from the following: Pauline Frances, Systems Analyst; Jeanette Lewis, Laboratory Coordinator; Andrew Ward, Kimberly Wallace, Rickey Myers, Jody B Hasten, and Shelton James, students; Jackson State University.)

N91-28082

ANALYSIS OF CURED CARBON-PHENOLIC DECOMPOSITION PRODUCTS TO INVESTIGATE THE THERMAL DECOMPOSITION OF NOZZLE MATERIALS

James M. Thompson and Janice D. Daniel
Department of Chemistry
Alabama Agricultural and Mechanical University
Huntsville, Alabama

ABSTRACT

This paper describes the development of a mass spectrometer/thermal analyzer/computer (MS/TA/Computer) system capable of providing simultaneous thermogravimetry (TG), differential thermal analysis (DTA), derivative thermogravimetry (DTG) and evolved gas detection and analysis (EGD and EGA) under both atmospheric and high pressure conditions. The combined system has been used to study the thermal decomposition of the nozzle material that constitutes the "throat" of the solid rocket boosters (SRB).

ANALYSIS OF CURED CARBON-PHENOLIC DECOMPOSITION PRODUCTS TO INVESTIGATE THE THERMAL DECOMPOSITION OF NOZZLE MATERIALS

Introduction

Since the development of the first themrobalance by Honda in 1915, thermal analysis has become an important instrumental method in understanding the behavior of non-metallic materials. The method is especially important in understanding the properties of polymeric materials. For instance, the procedure has been used in determining the flexibility, impact strength, resistance to wear, oxidative stability, amount of additive, and cure time of polymeric materials. Thermal analysis also plays an important role in solving production and quality control problems and it has become an indispensable tool in thermal studies of strategic materials.

The workers in this laboratory have developed an MS/TA/Computer system which has been used to study the thermal decomposition of the nozzle material that constitutes the "throat" of the solid rocket boosters (1-5). This material consists of a carbon cloth impregnated with a modified phenolic resin in which certain additives have been added. The uncured prepreg material is built up in layers to form the throat of the solid rocket booster and then cured in place. Thermal stability of this cured material is most important in materials evaluation and in component failure analysis.

Prior to beginning this work, several workers had reported the coupling of a mass spectrometer with a thermoanalyzer (6-16). Relying on this information, a Balzers QMG-511 quadrupole mass spectrometer has been successfully coupled with a Mettler thermoanalyzer (TA-2). In addition, the mass spectrometer has been interfaced with a microcomputer. This has resulted in a versatile instrument system whereby mass spectral data on decomposition gases may be rapidly acquired and processed under programmed conditions. Data from the mass filter and other units of the spectrometer may be digitally transferred to the computer whereupon mass spectral data are generated and displayed on the CRT and/or produced as hard copies. The combined system is also capable of providing simultaneous TG, DTA, DTG as well as partial pressure changes when studies are carried out under vacuum conditions.

While commercial thermoanalyzers are capable of providing valuable thermal information, these instruments are usually incapable of providing information on the identity of decomposition products. Obviously, such information represents an important complement to the traditional thermal data and is often useful in expanding our understanding of the thermal behavior of materials.

The Mass Spectrometer/Computer Interface

The mass spectrometer/computer interface has been achieved using the Teknivent Microtrace™ system (Teknivent Corp.). This turnkey system consists of a dual card interface-controller and the software necessary to control, acquire and process data from the QMG-511 quadropole mass spectrometer. The interface card plugs into the BF-511 buffer of the mass spectrometer, while the controller card plugs into an IBM-AT (or one of the compatible systems). The MS/TA Computer system, which is schematically shown in figure 1, is capable of continuous or disjointed spectrum scanning up to 1023

atomic mass units (amu). All data are presented in real time on a color or monochrome CRT. Multitasking features allow simultaneous data acquisition and processing. The system is also capable of functioning as the front panel of the console unit allowing the operator to set and adjust twenty one (21) parameters of the mass spectrometer from the keyboard of the computer. Other features include keyboard control of all tuning parameters, the ability to monitor up to 28 selected ions simultaneously, top acquisition speeds of up to 1000/amu/sec, subtraction of background gases, scaling, translation and normalization of data. The capability to search a mass spectra data base is an optional feature.

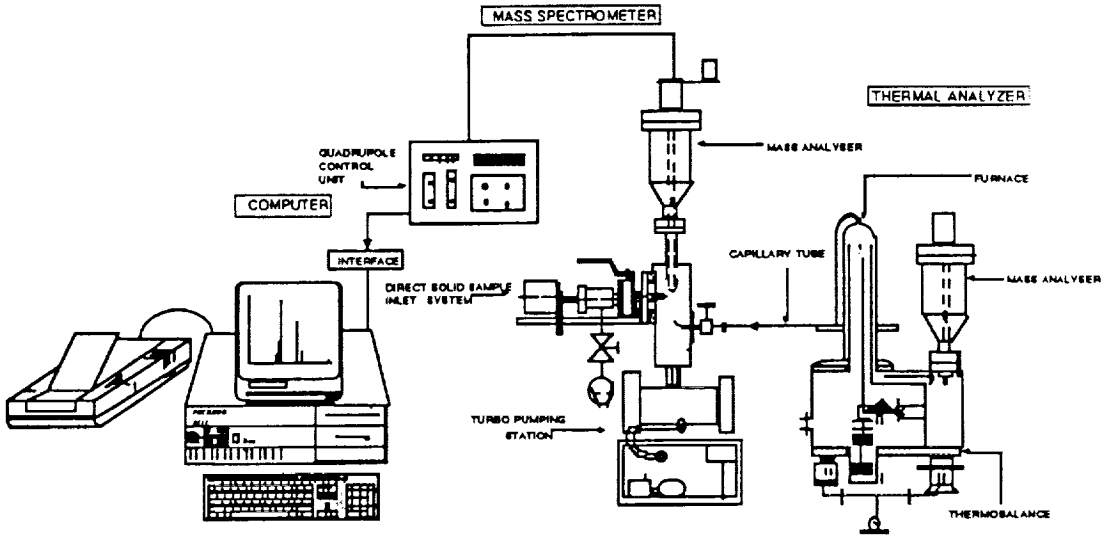

Figure 1. A Schematic Diagram of the Combined MS/TA/Computer System.

Through joint efforts with the Teknivent Corporation, low cost modifications have been made to the software and electronic interface of the Microtrace™ unit so that thermal data may also be obtained from the Mettler TA-2 thermoanalyzer. As a result of these modifications, the combined MS/TA/Computer system is able to acquire, monitor and process (in real time) TG, DTA, DTG, temperature and partial pressure data simultaneously with mass spectral data. By implementing these modifications, the need to re-plot weight loss vs. temperature curves has been eliminated; thermal data among different nozzle material samples may now be compared at the computer; weight loss curves may be superimposed upon mass chromatograms and hard copies of all data generated. Thermal data may also be monitored by the strip chart recorder of the TA-2 unit.

Again, through joint efforts with Teknivent, a second IBM-AT compatible microcomputer has been outfitted with a remote processing unit. Thus, data collected using the dedicated computer may now be transferred to the remote unit and processed. Overall, these modifications have increased production and facilitated data interpretation. The installation of the Teknivent Microtrace™ unit has vastly enhanced the capability of the MS/TA system to acquire and process mass spectrometric data on decomposition gases.

The MS-TA-Computer system has also been modified to allow partial pressure curves to be generated as part of the data provided by the thermal analyzer. This modification becomes significant when thermal decompositions are conducted under vacuum conditions.

Another major enhancement to the MS/TA/Computer system includes the addition of a second mass analyzer which occupies a permanent position in the chamber of the thermobalance (figure 2). Prior to installing this second unit, it was necessary to transfer the mass analyzer from the vacuum chamber of the mass spectrometer to the chamber of the thermobalance when evolved gas studies were desired under high vacuum conditions. This cumbersome procedure often required a retuning of the resonance frequency generator, a procedure which was awkward and time consuming. With the second analyzer in place, evolved gas studies can now be undertaken under both atmospheric and high vacuum conditions at any pressure between with only a transfer of cables.

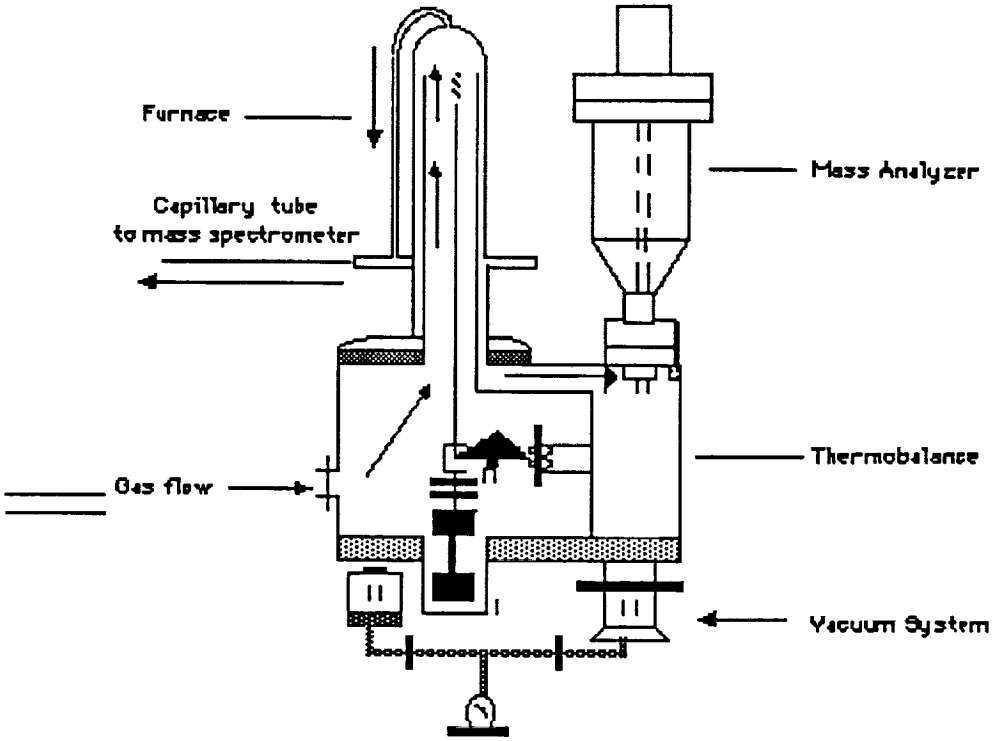

Figure 2. A Schematic Diagram of the Thermobalance of the Mettler Thermoanalyzer Showing the Second Mass Analyzer in the Vacuum Chamber.

Determination of the Accuracy and Reliability of the MS/TA/Computer System

The decomposition of $CaC_2O_4 \cdot H_2O$ has been studied by several workers (17-27) and its thermal decomposition profile is well known. Consequently, it was decided to use this material to determine the reliability and accuracy of the mass spectrometer unit of the combined system. In determining the accuracy and reliability of the unit, a sample of $CaC_2O_4 \cdot H_2O$ was placed in a 0.45 ml platinum crucible, and in a second identical crucible was placed an Al_2O_3 reference standard. Both materials were placed on the DTA sample holder and the sample and reference heated between 25 - 1000°C by the middle range temperature furnace. As the decomposition gases evolved, they were pulled into the chamber of the mass spectrometer through a heated capillary tube (figures 1 and 2). During the entire heating period, evolved gases between amu 1-55 were monitored using the computer/Teknivent system.

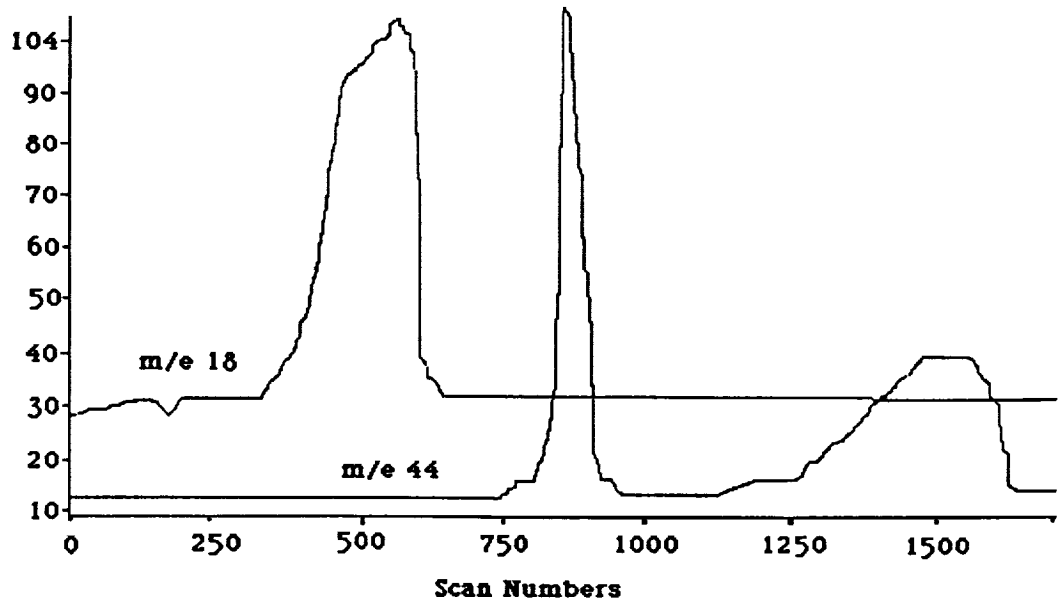

Figure 3. The Overlaid Mass Chromatograms for m/z 18 and 44 from the Thermal Decomposition of $CaC_2O_4 \cdot H_2O$ under Atmospheric Conditions (Note: the CO formed in the Second Decomposition Step Reacts with O_2 in the Air to form CO_2; thus, CO is Not Observed).

Based on the overlaid mass chromatograms shown in figure 3, three gas evolutions were observed as shown below. The first evolution consisted of water, followed by CO (which reacts with O_2 to produce CO_2). The last decomposition produced CO_2.

$$CaC_2O_4 \cdot H_2O \text{ ----------> } CaC_2O_4 + H_2O$$

$$CaC_2O_4 \text{ ----------> } CaCO_3 + CO$$

$$CaCO_3 \text{ --------> } CO_2 + CaO$$

The nature of the gases, their order of evolution, and the temperatures corresponding to each evolution were consistent with repeated values, thus confirming the accuracy and reliability of the system.

The Thermal Decomposition of Nozzle Material (FLX-D) Under Atmospheric Pressure Between 25 - 1000°C

A 106.55 mg powdered sample of nozzle material (called FLX-D) was placed in a 0.45 ml platinum crucible and positioned on the thermocouple crucible holder. The crucible holder is designed so that the "hot junction" of the thermocouple is in direct contact with the bottom of the crucible. The furnace was mounted over the sample and both sample and reference heated between 25 - 1000°C at a linear temperature rate of 8°C/min. The chamber of the mass spectrometer was monitored under computer control for fragment ions between 5-200 mass units. The thermal decomposition was conducted using

a non-discriminating gas inlet valve (figure 4) and a special dual side arm quartz furnace (figures 1 and 2). The non-discriminating inlet valve is a two stage pressure reduction gas inlet valve that allows the evolved gases to enter the chamber of the mass spectrometer without changing the ratio of the gaseous components or the chamber pressure. One end of a heated (200°C) one meter stainless steel capillary tube (with a diameter of 0.15 nm) was attached to the side-arm of the furnace and the other end to the non-discriminating gas inlet valve. The decomposition gases were swept out of the furnace by a stream of dry air which traveled through the thermobalance up the inner tube and to the side arm of the furnace (figure 2). Once the gases reached the side arm of the furnace, they were pulled through the heated stainless steel tube by a rotary vane pump attached to the non-discriminating valve. From the stainless steel capillary, the gases entered the non-discriminating valve and moved into the vacuum chamber of the mass spectrometer. In the chamber, the gases were ionized by electron impact and the positive ions accelerated into the quadropole filter where they were separated and detected in normal fashion.

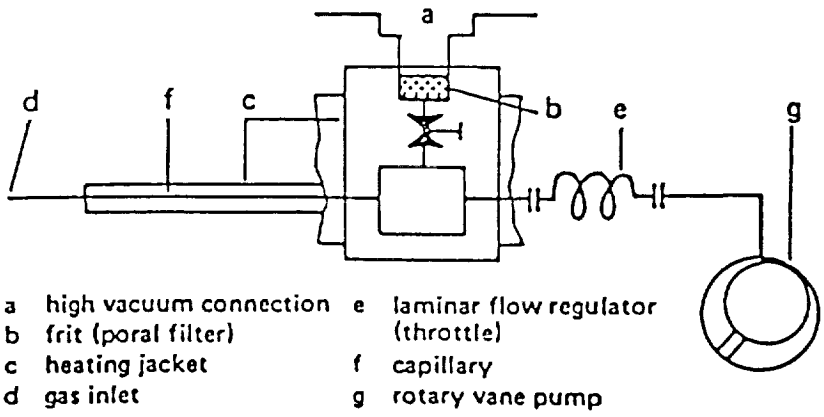

Figure 4. Schematic Diagram of the Non-Discriminating Gas Inlet System (Balzers High Vacuum Systems).

Discussion

Soon after heating, the nozzle material sample underwent a small weight loss which was attributed to either surface or occluded water as indicated by the bar chart in figure 5, the replotted TG curve in figure 6 and the overlaid mass chromatograms in figure 7. The water loss reached its maximum intensity near 375°C. Also, near 375°C, CO_2 was observed and its presence was evident for the remaining of the heating cycle (figure 7). No other evolved gases were observed.

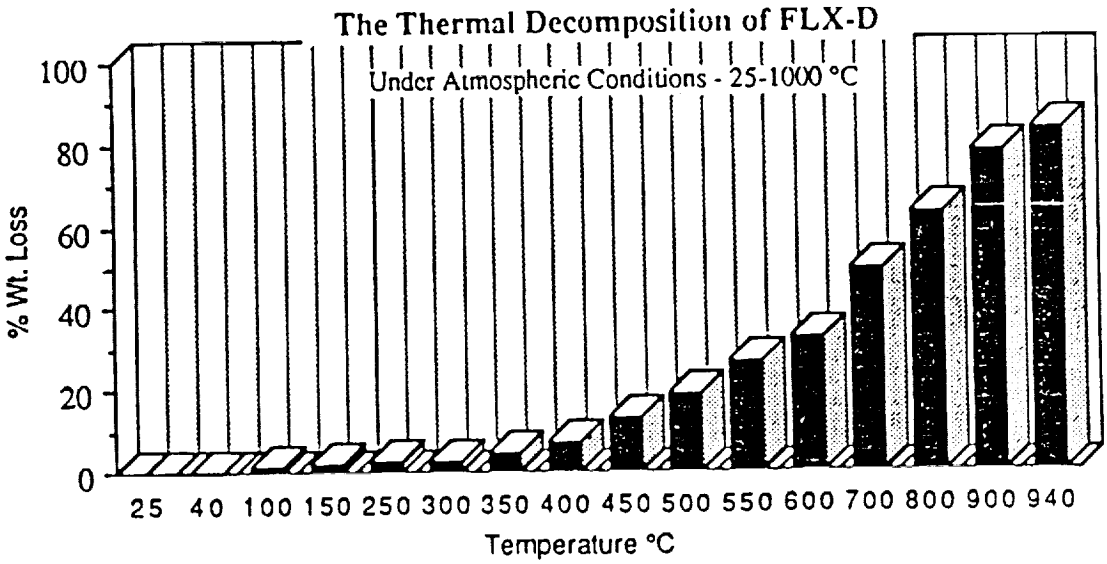

Figure 5. Bar Chart Showing the Thermal Decomposition of FLX-D Under Atmospheric Conditions Between 25 - 1000°C.

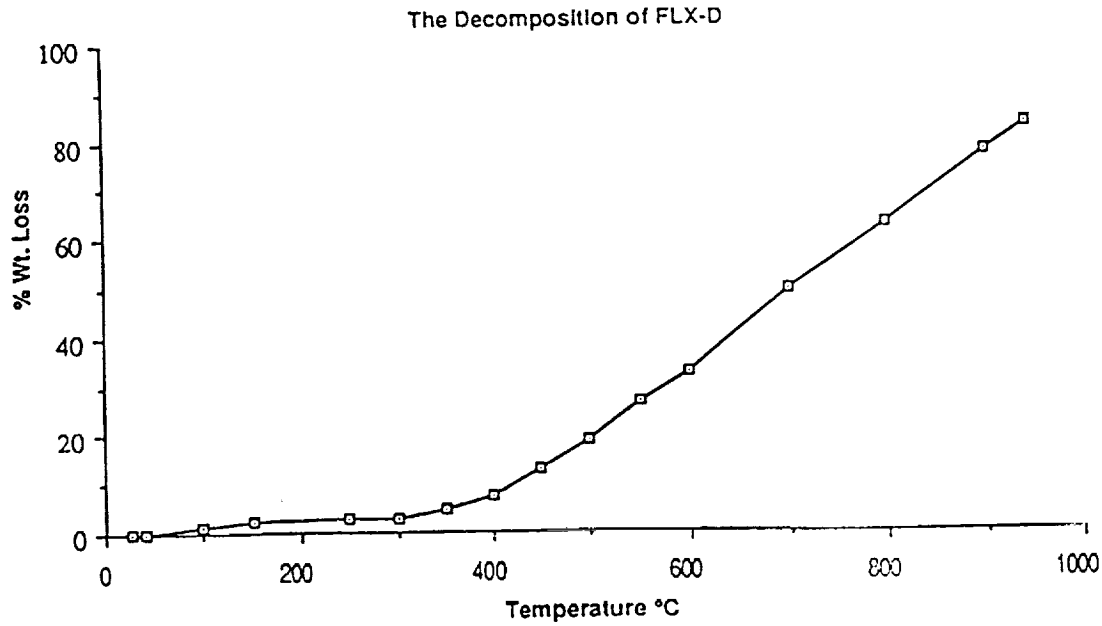

Figure 6. Replotted TG Curve, Showing the Thermal Decomposition of FLX-D Under Atmospheric Conditions Between 25 - 1000°C.

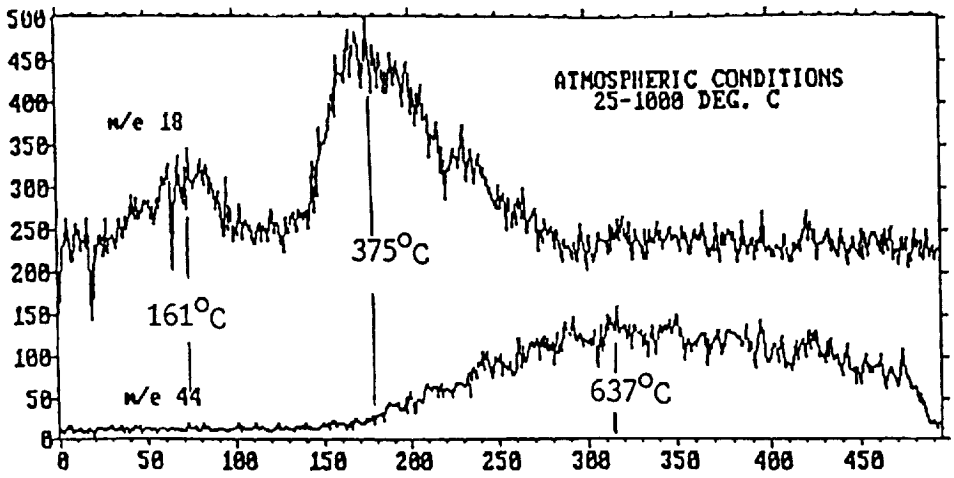

Figure 7. The Overlaid Mass Chromatograms for m/z 18 and 44 from the Thermal Decomposition of the FLX-D Nozzle Material Between 25 - 1000°C Under Atmospheric Conditions.

Evolved Gas Studies Between 35 −300°C Under High Vacuum Conditions.

The study of evolved gases under high vacuum conditions was conducted using the MS/TA/Computer system shown in figure 1; however detection of the decomposition gases was carried out using the mass analyzer which had been installed in the chamber of the thermobalance (figure 2).

Each of the seven nozzle material samples which were the object of this study was reduced to powder form, weighed and placed in a platinum crucible. An Al_2O_3 reference material was placed in an identical crucible and both sample and reference were placed on the DTA thermocouple. Sample size was kept to a specific weight level so as to maintain a pressure at the mass analyzer of no higher than 10^{-4} torr. Beyond this pressure, the proportionality between ion current and sample concentration is no longer valid. The standard middle temperature range furnace was sealed over the sample and reference and both the furnace chamber and chamber containing the mass analyzer were evacuated to approximately 1 - 5 x 10^{-6} torr using a pumping system consisting of both rotary and diffusion pump. Once the approximate vacuum had been reached, the sample and reference were heated between 25 - 1000°C at a linear rate of 5°C/min. Just prior to heating the sample, the mass spectrometer was placed under computer control to receive the mass spectrometric data output. The furnace pressure, temperature, DTA, TG, and DTG were monitored using the strip chart recorder located on the control unit of the thermoanalyzer, while the decomposition gases were monitored at the CRT. Evolved gas studies were carried out under programmed control between 10-200 amu using the Teknivent Microtrace™ system. During data acquisition the total ion current (TIC) curve and ion masses at m/z 18, 28, 32, and 44 were selected for direct monitoring.

Discussion

As indicated by figure 8 and Table 1, all seven samples of nozzle material underwent small weight losses between 25°C and approximately 300°C, under both atmospheric and high vacuum conditions. These initial weight losses were relatively small, ranging between 3.1 and 4.5% of the total weight of

the sample (Table 1). Under high vacuum conditions, major decompositions of the nozzle material occurred near 350°C and near 300°C under atmospheric conditions.

Of the seven samples, FLX-D was arbitrarily selected for evolved gas studies between 25 - 300°C. On heating, the sample lost approximately 3.1% of its original weight as shown by the replotted TG curve in Figure 9. This weight loss did not include a 0.02% weight loss which was observed during pump down.

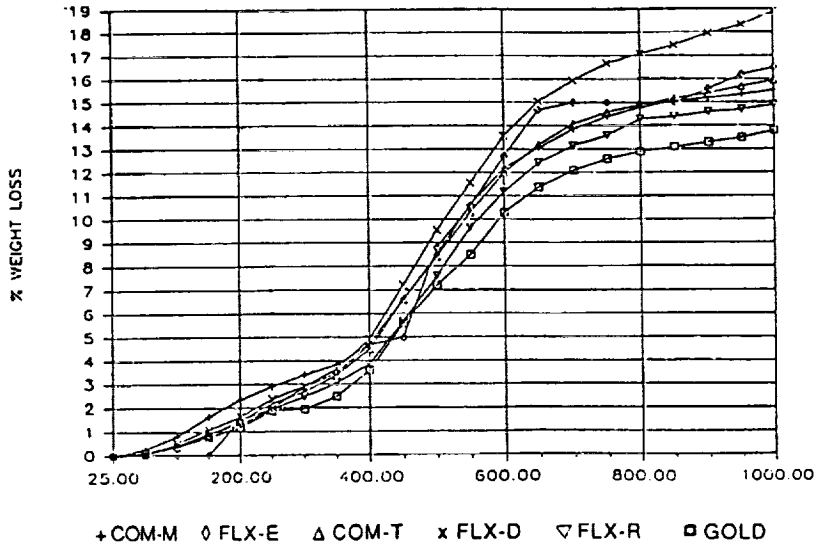

Figure 8. A Series of TG Curves Showing the Small Weight Loss of Different Nozzle Material Samples Between 25 - 1000°C When Thermally Decomposed Under High Vacuum Conditions.

Table 1. Percent Weight Loss of Several Samples of the Nozzle Materials When Thermally Decomposed Between 25°C and 300°C Under High Vacuum Conditions.

Sample	Temperature of First Weight Loss (°C)	% Weight Loss
COM-M	(35-40) - 240	3.9
FLX-R	40-180°C	4.0
FLX-E	(30-40) - 190	4.2
GOLD	35 -200b	4.1
COM-T	(35-40) - 150	3.1
COM-A	30-190	4.5

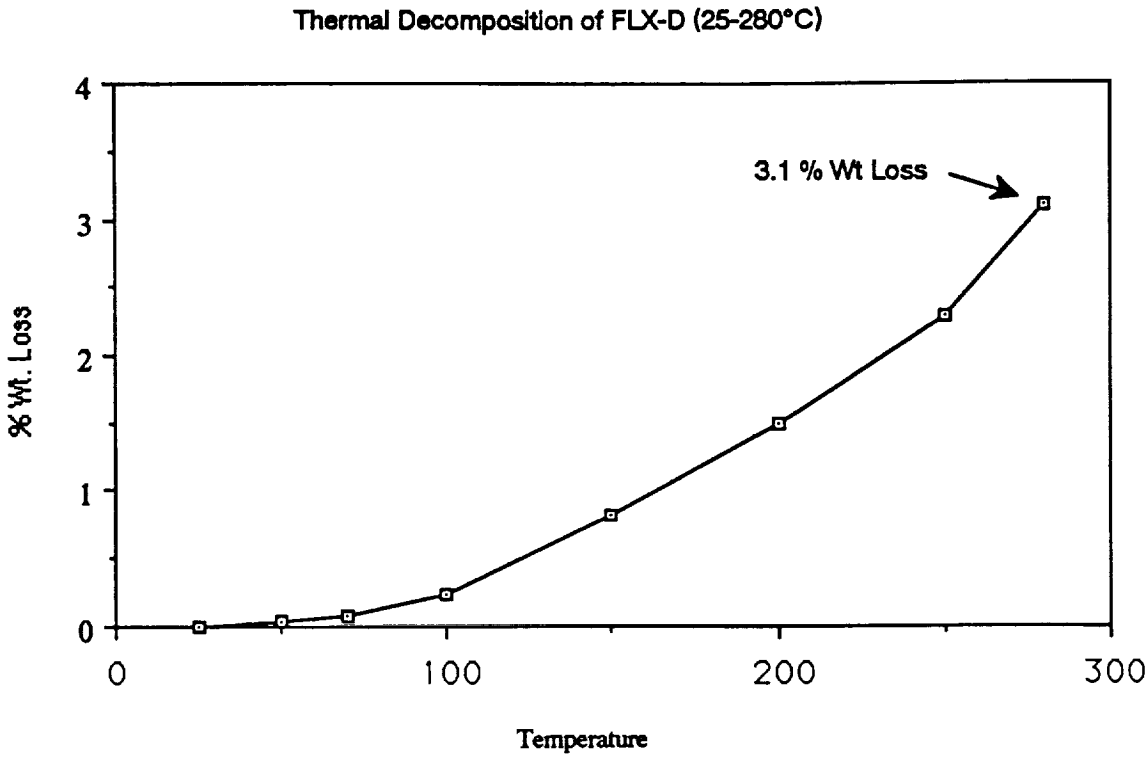

Figure 9. The Replotted TG Curve for the Thermal Decomposition of FLX-D Under High Vacuum Conditions Between 25 - 1000°C.

An Analysis of the Evolved Gases Resulting From the Decomposition of FLX-D Nozzle Material Between 25 - 300°C Under High Vacuum Conditions

The Total Ion Current -FLX-D

The total ion current (figure 10) was uneventful, revealing a slight but continuous increase in total ion abundance between the 25 - 300°C heating cycle.

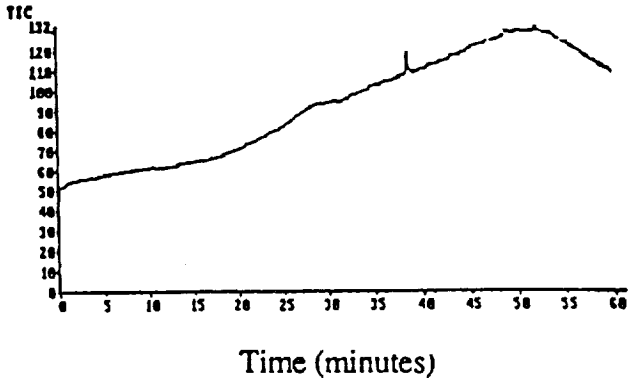

Figure 10. The Total Ion Current for the Thermal Decomposition of FLX-D Nozzle Material Between 25 - 300°C Under High Vacuum Conditions.

Mass 18

Based on a comparison of figures 11-14, the chromatogram corresponding to mass 18 revealed the largest overall increase in ion abundance, suggesting that the major weight loss of the FLX-D nozzle material during the 25 - 300°C heating cycle was due to water. The abundance of the m/z 18 ion over the heating range was sufficiently high that it partially influenced the overall shape of the TIC curve (compare figures 10 and 11). The suggestion that water constitutes the major weight loss of the FLX-D sample between 25 - 300°C was also supported by an analysis of the mass spectral histograms.

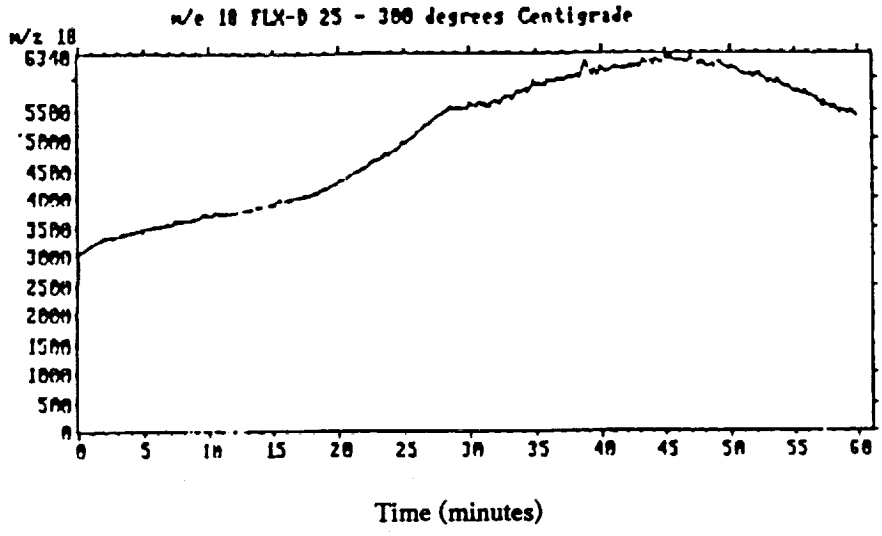

Figure 11. The Mass Chromatogram of m/z 18 (H_2O^+) Obtained from the Thermal Decomposition of the FLX-D Nozzle Material Between 25 - 300°C Under High Vacuum Conditions.

Mass 28

The m/z 28 mass chromatogram (figure 12) revealed only a slight increase in overall abundance between 25 - 300°C. However, near 150°C, the abundance of the ion began to increase and reached a maximum near the 300°C temperature limit. Based on separate studies which are not reported here, the mass 28 ion appears to have resulted, at least in part, from the fragmentation of isopropyl alcohol (5). This contention is based on observations that the m/z 28 ion and certain other fragments were common to both the evolved gases of the FLX-D sample and to the mass spectrum of isopropyl alcohol. These fragment ions appeared at m/z 27, 29, 31, 41, 42, 43, 44 and 45 (base peak in the mass spectrum of isopropyl alcohol). In addition, the shapes of the mass chromatograms corresponding to these ions revealed a distinct commonalty, suggesting that they probably resulted from the fragmentation of a common parent ion which may very well have been isopropyl alcohol. Still, the relative abundance of the mass 28 fragment (as indicated by the counts on the vertical y-axis) suggests that more than one mass 28 fragment may be implicated. Structural possibilities for the m/z 28 ion include CO^+, $H_2C = CH_2$, and N_2^+.

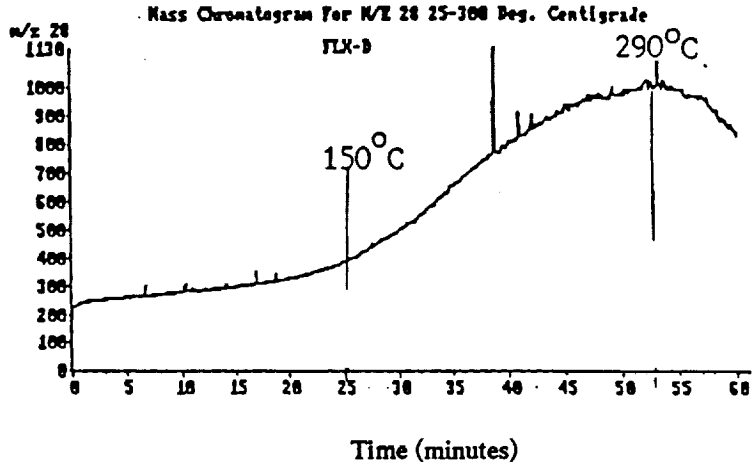

Figure 12. The Mass Chromatogram for m/z 28 Obtained from the Thermal Decomposition of the FLX-D Nozzle Material Between 25 - 300°C Under High Vacuum Conditions.

Mass 32

The mass 32 chromatogram (which is believed to be O_2^+) is shown in figure 13. Among the ions shown by the chromatograms in figures 11-14, this ion revealed the lowest increase in overall abundance over the 25 - 300°C heating range, suggesting the production of only a relatively small amount of O_2.

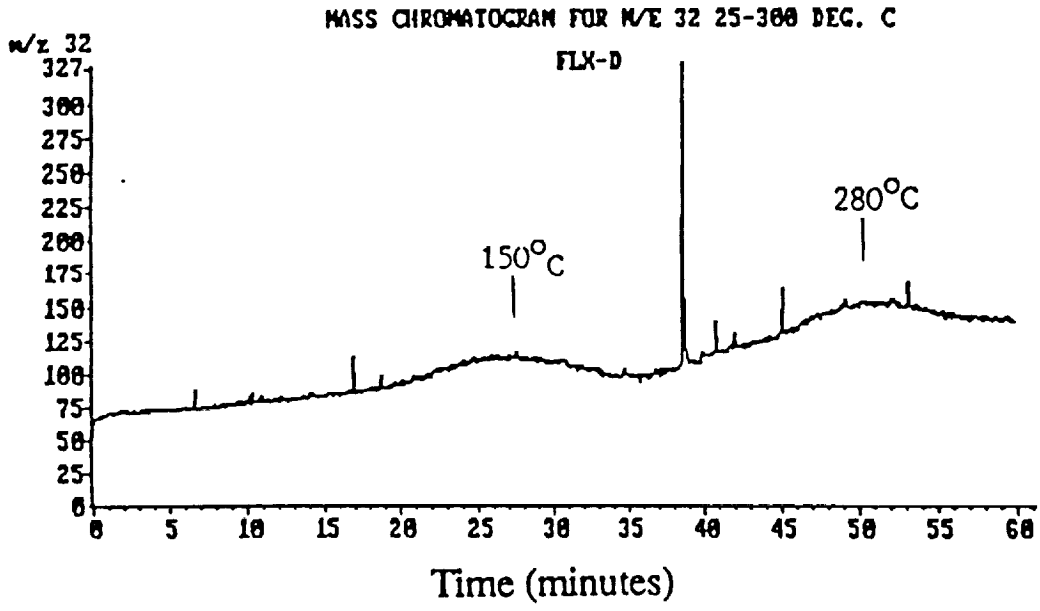

Figure 13. The Mass Chromatogram for m/z 32 (O_2^+) Obtained from the Thermal Decomposition of the FLX-D Nozzle Material Between 25 - 300°C Under High Vacuum Conditions.

Mass 44

The chromatogram represented by mass 44 (figure 14) was almost devoid of ion activity until about 125°C. Between 125 and 170°C, a relatively sharp increase in abundance was observed. Near 170°C, the overall abundance of the ion decreased just slightly, followed by a relatively sharp increase which continued for the duration of the heating period. The presence of the mass 44 ion is consistent with the fragmentation of isopropyl alcohol and may represent, at least in part, the following "isopropyl" fragment or some modification thereof.

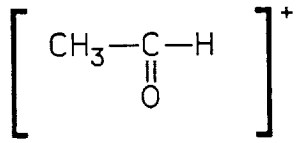

m/z 44

Fragment ions detected at m/z 15 (CH_3^+) and m/z 45 (shown below) also offer support to the argument that isopropyl alcohol is implicated in the thermal decomposition of the nozzle material. It should also be mentioned that the most abundant fragment ion in the mass spectrum of isopropyl alcohol is m/z 45.

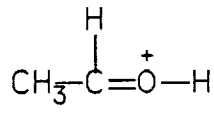

m/z 45

As mentioned, other ions corresponding to the fragmentation of isopropyl alcohol were observed in the decomposition gases of FLX-D. These ions were located at m/z 19, 27, 29, 30, 38, 42, 43. A conclusive identification of the structure of the m/z 44 fragment must await a study of the nozzle material using TG/FTIR.

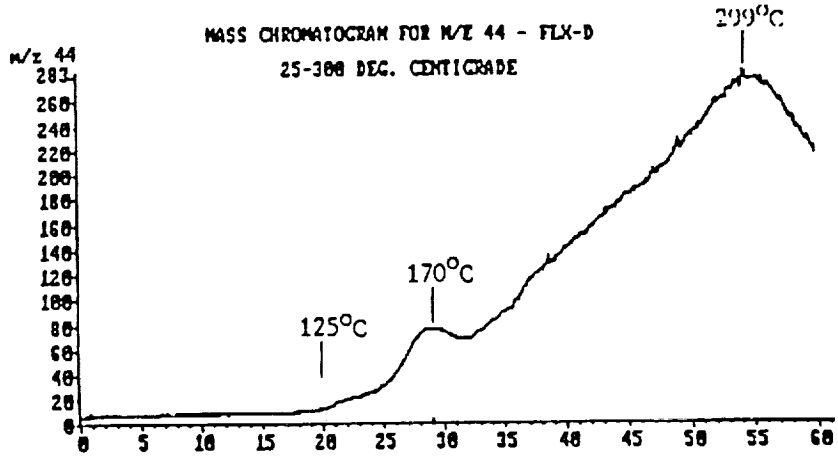

Figure 14. The Mass Chromatogram of m/z 44 Obtained from the Thermal Decomposition of the FLX-D Nozzle Material Between 25 - 300°C Under High Vacuum Conditions.

An Analysis of the Evolved Gases Resulting From the Decomposition of FLX-D Nozzle Material Between 300 - 1000°C Under High Vacuum Conditions

After obtaining evolved gas data on the FLX-D sample between 25 - 300°C, the same sample was heated between 300 - 1000°C (without cooling) and evolved gas data acquired and processed under computer control as previously described. The sample was scanned 1488 times between a mass range of 10-3000 amu at a rate of 5,478 seconds per scan, making a total heating time of approximately 140 minutes. During data acquisition, the TIC curve (Figure 15) and mass chromatograms corresponding to masses 18, 28, 32 and 44 were again monitored (figures 16-19).

The Total Ion Current

As expected, the total ion current (figure 15) obtained for the 300 - 1000°C run was totally different from what was observed for the 25 - 300°C run (compare figures 10 and 15). In addition, the maximum number of counts were larger for the 300 - 1000°C run, suggesting, as expected, that decomposition at the higher temperature range was more pronounced. For the 300 - 1000°C run the TIC curve (figure 15) revealed two levels of high ion abundance near 450 and 590°C. Beyond 590°C, there was a decrease in ion abundance, reaching a minimum near 850°C. Between 850 - 1000°C, the ion current was almost level.

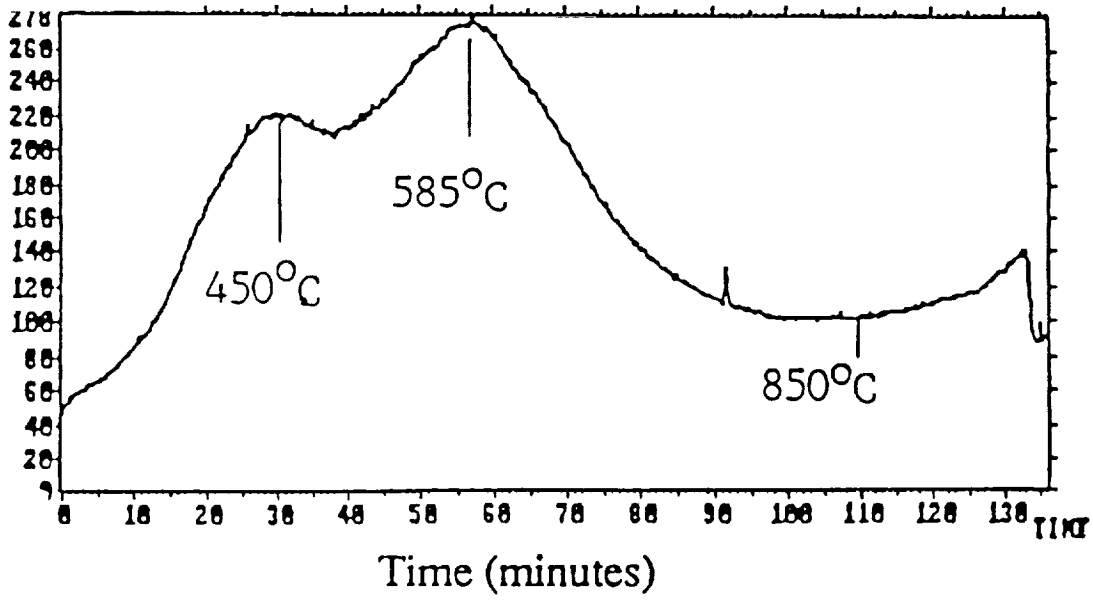

Figure 15. The Total Ion Current (TIC) for the Thermal Decomposition of FLX-D Under High Vacuum Conditions Between 300 - 1000°C.

Mass 18

The mass 18 fragment which is believed to be due to H_2O^+ was so abundant during the decomposition that it caused the mass chromatogram to go off scale near 450°C and reappear near 650°C (Figure 16). Based on the mass 18 chromatogram, it appears that water is also the major decomposition product between 300 - 1000°C, just as it was for the 25 - 300°C study. Thus, water appears to be the major overall decomposition product.

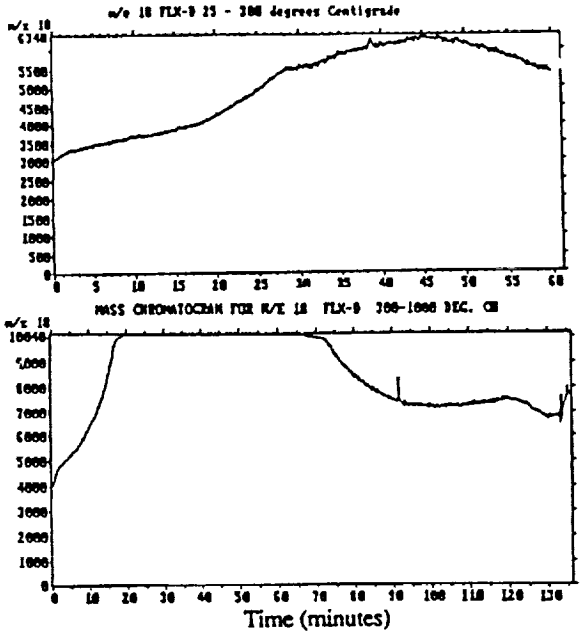

Figure 16. The m/z 18 Mass Chromatogram for the Thermal Decomposition of the FLX-D Nozzle Material Between (a) 25 - 300°C and (b) 300 - 1000°C Under High Vacuum Conditions.

It is believed that an amine curing agent is involved in the fabrication of the nozzle material, thus the mass 18 fragment may also include fragments attributed to NH_4^+

Again, the mass 28 chromatogram (figure 17) is believed to be related, at least in part, to the fragmentation of isopropyl alcohol. Structural possibilities include N_2^+, and $CH_2 = CH_2^+$ with CO^+ and/or $CH_2 = CH_2^+$, probably resulting from the decomposition of isopropyl alcohol. The abundance of this ion peaked near 595°C, followed by a fairly sharp drop.

Again, the overall abundance of the mass 32 ion (figure 18) was much smaller than for m/z 18, 28 or 44, reaching a maximum between 435 to 575°C

The mass 44 chromatogram (figure 19) revealed a number of peaks and valleys indicating changes in the relative abundance of the ion during the 300 - 1000°C heating cycle. The increase in abundance continued beyond the 300°C temperature limit of the first study, reaching a maximum near 435°C.

Other Fragment Ions Observed for the Thermal Decomposition of FLX-D Between 300 - 1000°C Under High Vacuum Conditions

Recognizing the versatility of the Teknivent Microtrace™ data collecting system, it was decided to recall from the acquired data, the mass chromatograms of all major fragments observed between the 10-300 amu limits. This resulted in a total of 114 fragment ions of varying relative abundances. Efforts to identify a number of these fragments have been reported elsewhere (5). Because of space limitations, discussion is prohibited in this paper.

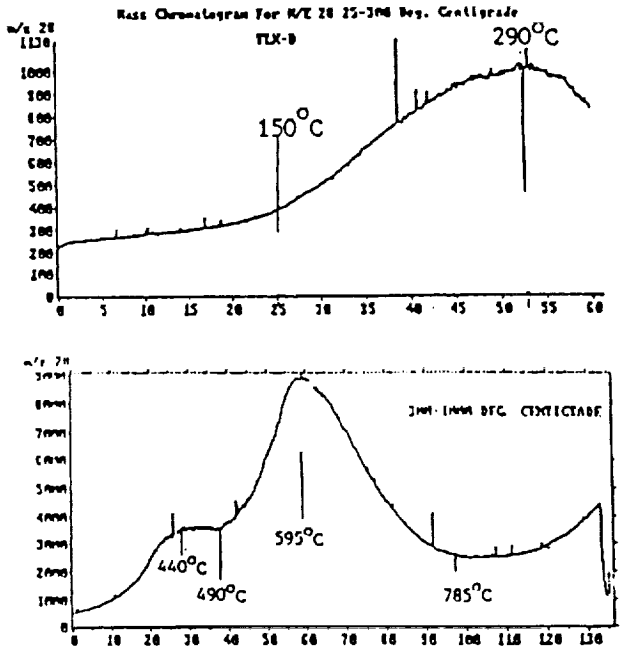

Figure 17. The m/z 28 Mass Chromatogram for the Thermal Decomposition of FLX-D Under High Vacuum Conditions Between (a) 25 - 300°C and (b) 300 - 1000°C.

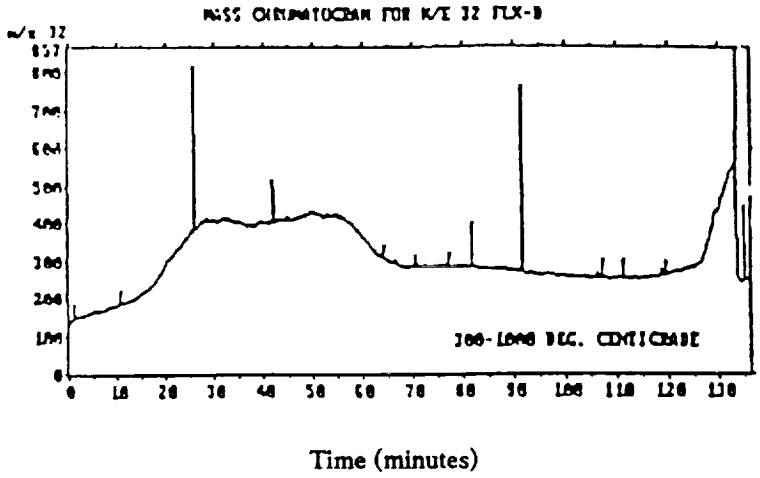

Figure 18. The m/z 32 Mass Chromatogram for the Thermal Decomposition of FLX-D Under High Vacuum Conditions Between 300 - 1000°C.

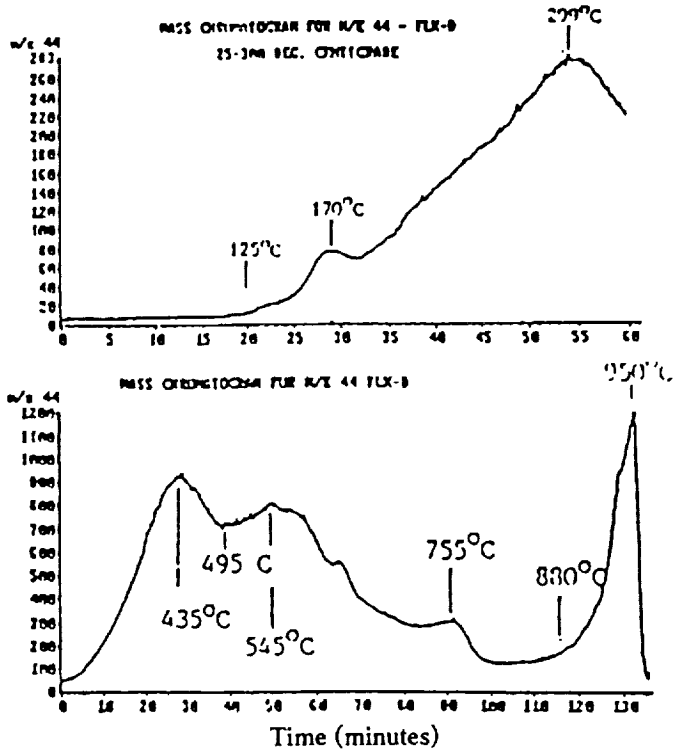

Figure 19. The m/z 44 Mass Chromatogram for the Thermal Decomposition of FLX-D Under High Vacuum Conditions Between (a) 25 - 300°C and (b) 300 - 1000°C.

Conclusions

The MS/TA/Computer system as presently configured has been shown to be a useful and reliable instrument for understanding the thermal decomposition of the nozzle material of the solid rocket booster as well as other non-metallic materials. However, as with any instrument system there are certain inherent limitations, most of which relate to the inability of the present system to make distinctions among different structures of identical masses. The problem becomes even more acute as efforts are made to make structural assignment to fragments of high molecular masses. FTIR/TG data would provide functional group analysis and would aid in the resolution of these structural problems.

The ideal system for studying evolved gas would be a combined TG/MS/FTIR system which has not yet been developed (28). A rough schematic of such a system is shown in figure 20.

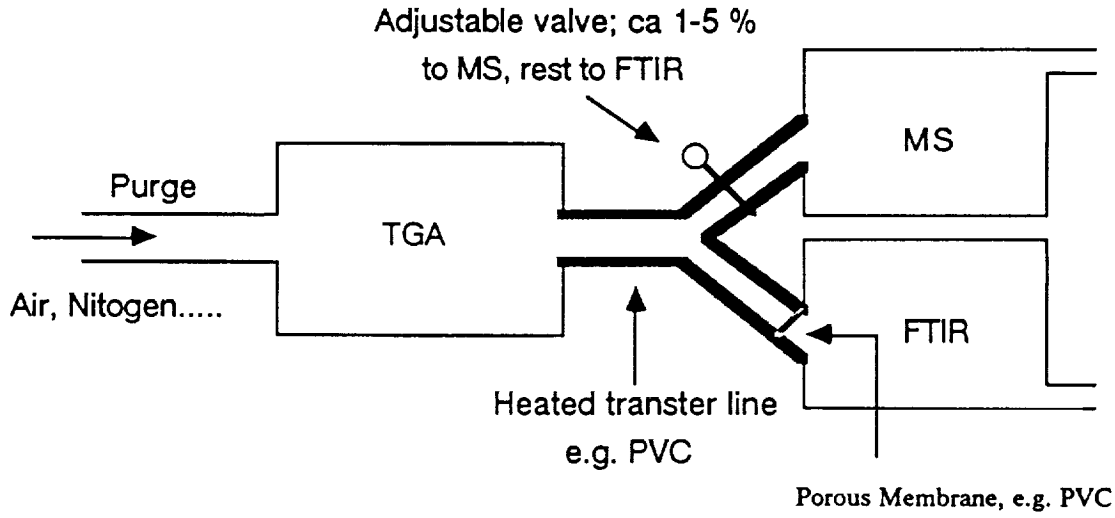

Figure 20. Rough Schematic of a Potential TG/MS/FTIR System (re-drawn from ref. 28).

Literature Cited

1. Thompson, J.M., Laboratory Automation of a Quadropole Mass Spectrometer, Faculty Fellowship Program, NASA Contractor Report No. 170942, December, 1983.

2. Thompson, J.M., A Computer Controlled Mass Spectrometer System for Investigating the Decomposition of Non-Metallic Materials, Faculty Research Program, NASA Contractor Report No. NASA CR-171317, January, 1984.

3. Thompson, J.M., A Thermoanalytical-Mass Spectrometer Investigation of the Nozzle Material That Constitutes the Throat of the Solid Rocket Boosters, First Annual Contractor Report No. NAS 8-36299.

4. Thompson, J.M., Nozzle Materials Investigation, Second Annual Contractor Report, NAS 8-36299, June, 1988.

5. Thompson, J.M., Evolved Gases and Thermal Profiles-A Comparative Study of Nozzle Material, Third Annual Contractor Report, NASA8-36299, January, 1989.

6. Zitomer, F., Anal. Chem., 40, 1091 (1968).

7. Wilson, D.E., and F.M., Thermal Analysis, R.F. Schwenker and P.D. Garn, Editors, Academic, new York 1969, Vol. 1, p. 295.

8. Gibson, E.K., and S.M. Johnson, Themochem. Acta., 4, 49 (1972).

9. Chang, T.L., and T.E. Mead, Anal Chem., 43, 534 (1971).

10. Mettler Thermal Techniques, Series T-107.

11. Langer, H.G., R.S. Gohlke, and D.H. Smith, Anal. Chim. Acta., 32, 405 (1965).

12. Wiedemann, H.G., Thermal Analysis, R.F. Schwenker and P.D. Garn, Editors, Academic, New York 1969, Vol. 1, p. 229.

13. Wendlandth, W.W., and T. M. Southern, Anal. Chim. Acta., 32, 405 (1965).

14. Redfern, J.P., B.L. Treherne, M.L. Aspimal, and W.A. Wolstenolme, 17th Conference of Mass Spectrometry and Allied Topics, Dallas, Texas, May 1969.

15. Gaulin, C.A., F. Wachi, and T.H. Johnson, Thermal Analysis, R.F. Schwenker and P.D. Garn, Editors, Academic, New York, 1969, Vol. 2, p. 1453.

16. Dunner, W. and H. Eppler, Advanced Coupling Systems for Thermoanalyzers With Quadropole Mass Spectrometers, the 4th International Congress on Thermal Analysis (ICTA), Budapest, July 1974.

17. Angeloni, F.M., Differential Thermal Analysis Studies on the Mechanism of the Thermal and Oxidative Decomposition of Calcium Oxalate, Ph.D. Dissertation, The University of Akron, 1976, Dissertation Abstracts International, Vol. 37/05-B.

18. Chang, J., A Study of the Decomposition of Calcium Oxalate, Ph.D. Dissertation, The Pennsylvania State University, 1965, Dissertation Abstracts International, Vol. 26/08.

19. Freeman, E.S., Non-Isothermal Reaction Kinetics: The Dehydration of Calcium Oxalate Monohydrate and Thermal Decompositions of Calcium Carbonate on the Solid State, Ph.D. Dissertation, Rutgers University, 1961, Dissertation Abstracts International, Vol., 22/01.

20. Szekely, T., Varhegyi, F. Till, P. Szabo and E. Jakab, Kinetic Reaction of the Thermal Decomposition of Calcium Oxalate and Calcium Carbonate, J. Anal. Appl. Pyrolysis., 11, p. 71-81, (1987).

21. Ninan, K.N., Thermal Decomposition Kinetics: Effects of Sample Mass on the Thermal Decomposition Kinetics of Calcium Oxalate monohydrate, Thermochim Acta, 74, No. 1-3, p. 143-50.

22. Ninan, K.N., and C.G.R. Nair, Thermochim Acta, 30, no. 1-2 (1979).

23. Nair, C.G.R., and K.N. Ninan, Thermochim Acta, 23, No. 1, p. 161-9 (1978).

24. Gurrier, S., G. Siracusa and R. Cali, J. Therm. Anal., 6, no. 3, p. 293-8 (1974).

25. Dollimore, D., T.E. Jones and P. Spooner, J. Chem Soc., 17, p 2809-12 (1970).

26. Nerad, I., S.Vitkova and I. Prokks, J. Therm. Anal., 33, No. 1, p. 291-5 (1988).

27. Gadalla, A.M., Thermochim. Acta, 74, No. 1-3, p. 255-72 (1984)

28. Prime, R.B., NATAS NOTES, Vol. 19, No. 4, p. 48 (Winter 1987-88).

3-(BROMOACETAMIDO) - PROPYLAMINE HYDROCHLORIDE: A NOVEL SULFHYDRYL REAGENT AND ITS FUTURE POTENTIAL IN THE CONFIGURATIONAL STUDY OF S1-MYOSIN

Prasanta Sharma
Miles College
Birmingham, AL

and

Herbert C. Cheung
Department of Biochemistry
University of Alabama at Birmingham
Birmingham, AL

ABSTRACT

Configurational study of S1-Myosin is an important step towards understanding force generation in muscle contraction. Previously reported NMR studies have been corroborated by us. We have synthesized a novel compound, 3-(Bromoacetamido) - Propylamine Hydrochloride, and its potential as a sulfhydryl reagent provides an indirect but elegant approach towards future structural elucidation of S1-Myosin. Our preliminary investigation has shown that this compound, BAAP, reacted with S1 in the absence of MgADP and the modified enzyme had a 2-fold increase in Ca-ATPase activity and no detectable K-EDTA ATPase activity. Reaction of BAAP with S1 in the presence of MgADP resulted in a modified enzyme which retained a Ca-ATPase activity that was about 60% of unmodified S1 and had essentially zero K-EDTA ATPase activity. Sulfhydryl titration indicated that about 1.5 and 3.5 -SH groups per S1 molecule were blocked by BAAP in the absence and presence of MgADP, respectively. When coupled to a carboxyl group of EDTA, the resulting reagent could become a useful -SH reagent in which chelated paramagnetic or luminescent lanthanide ions can be exploited to probe S1 conformation.

3-(BROMOACETAMIDO) - PROPYLAMINE HYDROCHLORIDE: A NOVEL SULFHYDRYL REAGENT AND ITS FUTURE POTENTIAL IN THE CONFIGURATIONAL STUDY OF S1-MYOSIN

Introduction

Myosin Subfragment 1 is the globular head of myosin and contains two sets of functional sites that are essential for force generation in muscle contraction. These are the two actin-binding sites and the single nucleotide-binding site at which ATP is hydrolyzed. One current model of contraction[1] proposes that force generation results from structural changes occurring in the S1 region of myosin while myosin is still attached to actin. Considerable attention has been paid to the structure of S1 in intact myosin or myofibrils as well as isolated S1 and structural changes that occur in S1 resulting from interaction with actin and nucleotides.

Among the various tools used in the study of proteins, NMR has been used successfully for proteins of molecular weights less than 20K. For larger macromolecules, however, the spectra are accompanied by broad, poorly-resolved overlapping NMR signals. Nevertheless, recent high-resolution NMR has provided valuable information on structural changes that proteins undergo under varied conditions.[2]

Within the context of structural studies of S1 in solution, in the present work ^1H NMR spectra were observed both with and without the addition of chemical denaturants. The spectra were then set against a computer-simulated random-coil spectrum[3] (Fig.1) and the derived assignments compared against previously published results[4]. The present NMR data seem to be in general agreement with those previously reported.

S1 contains two reactive thiols (SH_1 and SH_2) located at Cys 707 and Cys 697 of the heavy chain which are readily alkylated by a number of sulfhydryl reagents[5]. The chemically-modified protein provides a model in which structural information can be obtained. Modification of one -SH group (SH_1) of S1 typically activates the Ca-ATPase by a factor of 2-3 and suppresses the K-EDTA ATPase activity[6]. When both SH_1 and SH_2 are blocked, both types of ATPase activity are abolished[7]. Early studies indicated that the two -SH groups can be crosslinked or chelated by several bifunctional alkylating agents[8] suggesting considerable flexibility of the polypeptide backbone between Cys 697 and Cys 707. The equilibrium separation between SH_1 and SH_2 was determined by measuring the extent of fluorescence resonance energy transfer between probes covalently attached to the two thiols[9]. The measured distance was found to be sensitive to MgADP. Other workers have also investigated S1 conformation by using several extrinsic fluorescent probes[10].

A different approach to the use of fluorescent probes for distance measurements was provided by Mears and coworkers[11], who synthesized para-substituted derivatives of 1-phenyl ethylenedinitrilotetraacetic acids in which the substituents are NO_2, NH_2, N_2^+, $HNCOCH_2Br$, etc. Once attached to a protein, the tetraacetate groups can be exploited to chelate cation possessing suitable spectroscopic or radioactive properties for structural studies of the host protein. In particular, lanthanide ions can be used for this purpose. In preliminary studies we were unable to selectively modify SH_1 of subfragment 1 and to obtain the desired degree of ATPase activation. This lack of success led us to synthesize an aliphatic EDTA analog with sulfhydryl reactivity. In this report we describe the synthesis of a precursor of such an analog, 3-(Bromoacetamido)-propylamine hydrochloride, and its reaction with SH_1 and SH_2 of S1.

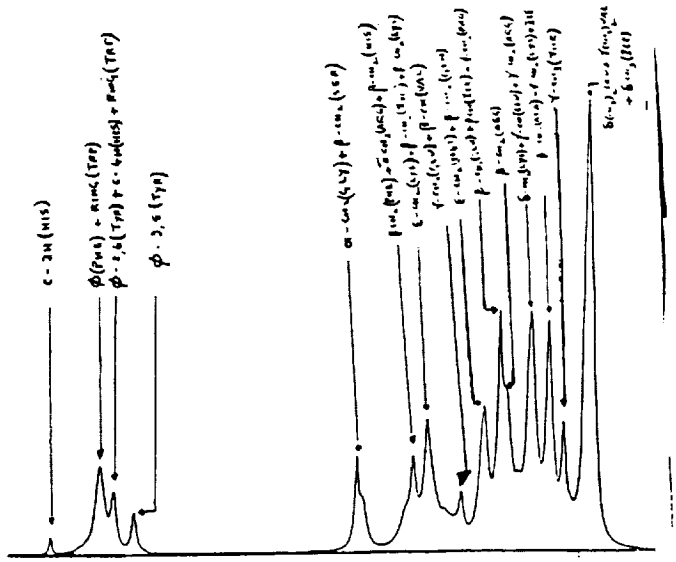

Figure 1C.
Computer simulated NMR spectra.

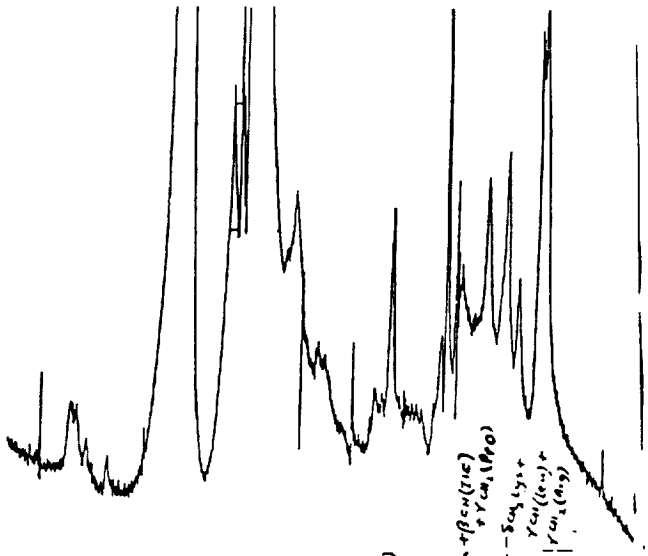

Figure 1B.
S1/ Phosphate Buffer (^2H_2O) - denatured with 8M urea.

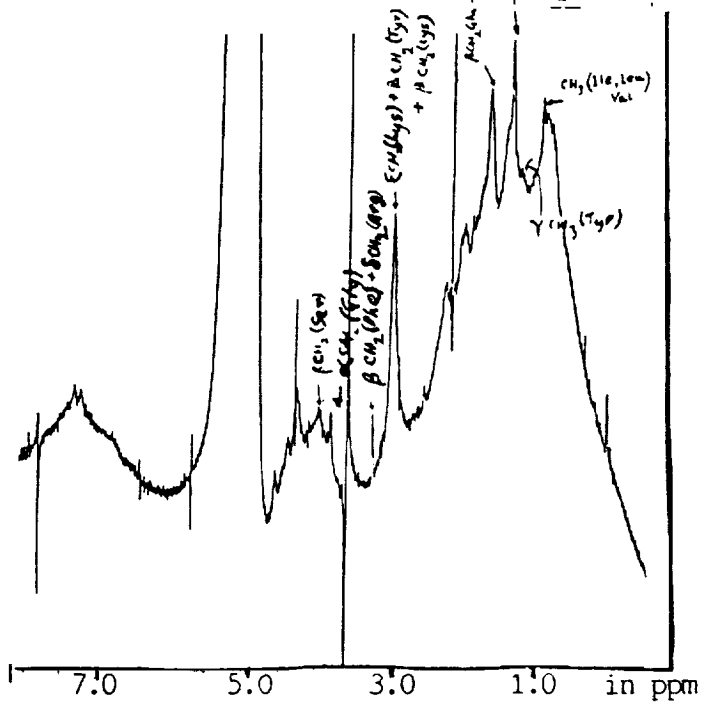

Figure 1A.
S1/ Phosphated Buffer (^2H_2O) - native.

Experimental

Synthesis of BAAP.

An indirect method for synthesis of bromoacetamidoalkylamines has been reported[12]. Though direct monoacylation of diamines has proved to be difficult[13], in our present work we have obtained the product, the reaction being carried out at a relatively low temperature. To 2.5 mL of 1,3 diaminopropane (0.03 mol), in a small volume of dry chloroform, was added dropwise 2.47 mL bromoacetylchloride (0.03 mol) while stirring in an atmosphere of nitrogen. The reaction was carried out in the presence of dry ice/ acetone. The sticky white precipitate that formed was separated and extracted overnight with chloroform under ice-cold conditions. On evaporating to dryness, the chloroform extract yielded a white crystalline solid (m.p. 113-115°C). TLC tests with ninhydrin and 4-(4-Nitrobenzyl) pyridine established the purity of the product. ^{1}H NMR profile corresponded to four methylene resonances (4.1-1.7 ppm) and a downfield component (7.1 ppm) resulting from the exchange of the amide proton.

Microanalysis data (Table 1) correspond to the empirical formula $C_5H_{12}BrClON_2$ (FW 231.6). The molar extinction coefficient of a sample of BAAP in dimethyl sulfoxide was determined (E_{277} = 4.4×10^3).

Table 1. Microanalysis of BAAP.

	% C	% H	% N	% Halogen
Calculated	25.93	5.22	12.10	49.81
Microanalysis	26.03	5.11	11.96	50.16

Protein Preparation.

Myosin was obtained from rabbit skeletal muscle by a method described by Flamig and Cusanovich[14]. The procedure involved extraction of freshly-ground back and leg muscles with a phosphate buffer, pH 7.5 containing 0.3 M KCl for 1 hr. The precipitate was dissolved in 0.5 M KCl and subsequently reprecipitated. Subfragment 1 was obtained by digestion of myosin with α-chymotrypsin, followed by purification on a DEAE-cellulose (DE-52) column[15]. The S1 concentration was estimated from a molecular weight of 115,000 and an extinction coefficient of $E_{280}^{1\%} = 7.5$ cm^{-1} [16].

Reaction of S1 with BAAP.

S1 was labeled at SH_1 with a 1.5-fold molar excess of BAAP in a buffer containing 60 mM KCl and 50 mM Tris at pH 7.8 (Buffer A). Prior to labeling, the protein solution (130 μM) was dialyzed in Buffer A in the presence of 1 mM DTT. Any residual DTT was subsequently removed by extensive dialysis with Buffer A. Appropriate quantities of 5 mM BAAP (dissolved in Buffer A) were added to S1 followed by incubation in the dark under ice-cold conditions for 18-20 hr. Any unreacted probe was subsequently removed by exhaustive dialysis in Buffer A. The percentage of protein sites labeled was calculated by measuring the absorbance of a sample of labeled protein at 280 nm and subtracting the optical density derived for an equivalent concentration of protein at this wavelength. The Lowry method[17] was used to determine protein concentration in labeled S1 to avoid optical interference from the label.

For SH_2 modification, SH_1-modified S1 was incubated with a 4- and 50-fold molar excess of BAAP (3 mM) and MgADP, respectively, under ice-cold conditions in the dark for 38-40 hr. Ca and K-EDTA ATPase activities were determined by measuring the release of inorganic phosphate using a modification of the Fiske-Subbarow method as previously described[5]. The thiol content was determined using Ellman's method[18]. S1 (0.1 mL of 30-50 μM) was added to 2.6 mL of a freshly-prepared urea solution (9.0 M Urea, 10 mM EDTA, 50 mM Tris, 0.1 M KCl, pH 8.0) and the absorbance was measured at 412 nm. After approximately 15 minutes 0.3 mL of freshly-prepared DTNB (1 mM DTNB, 0.1 M KCl, 10 mM phosphate, pH 7.0) was added and the absorbance at 412 nm was followed until there was no further increase in absorbance. A molar extinction coefficient of 13600 at 412 nm was used for DTNB.

NMR

Sample buffer containing 50 mM KCl, 12 mM phosphate, 1 mM NaN_3 in ^2H_2O at p ^2H 7.0 was passed through a column packed with chelex. S1 in sample buffer was next dialyzed against 330 mM EDTA in buffer followed up by dialysis against several changes of buffer at 4°C. Denatured samples were prepared by adding 8M Urea (^2H). The ^1H NMR spectra were obtained on a Bruker WH-400 spectrometer operating in the FT mode. A typical sample consisted of 0.4 ml S1 (90 μM) in the presence of TSP, an internal standard. The H^2HO resonance was saturated with a homonuclear decoupling phase. All spectra were recorded at 4°C.

The ^1H NMR spectra of BAAP in $CDCl_3$ were recorded in a Nicolet -300-W.B. FT NMR spectrometer.

Results and Discussion

The relative ATPase activities of native and modified S1 and their sulfhydryl content are reported in Table 2. Modification of the SH_1 site was evidenced by a two-fold increase in Ca-ATPase while the corresponding K-EDTA ATPase activity was completely abolished. Comparison of the data on the third row of Table 2 indicated that the second site (SH_2) was labeled.

Table 2. Comparison of relative ATPase activities between native and modified S1 and the corresponding loss in the number of free sulfhydryl groups.

Sample	Relative ATPase activities[a]		Loss of -SH Groups per mole of S1 [a]
	Ca(%)[b]	K-EDTA(%)[c]	
1. S1-unmod	100	100	-
2. S1-(1) BAAP	207	0	1.48
3. S1-(1,2) BAAP	61	4	3.43

(a) The data are obtained by averaging over two samples.
(b), (c) 100% Ca-ATPase and K-EDTA ATPase activities correspond to 1.07 and 2.68 moles Pi mg-1 min-1, respectively.

Overall, preliminary biochemical tests indicate that BAAP is a monofunctional SH-coupling reagent. It has a relatively short span (10.80 ± 0.03 Å)[19] and appears reasonably specific for myosin SH_1 and SH_2. It should be possible to link BAAP via its terminal amino group to a carboxyl group of EDTA. Such a compound should still possess sulfhydryl reactivity and is expected to chelate paramagnetic or luminescent lanthanide ions such as Tb (III). The chelated cation provides a spectroscopic signal that may be useful for elucidating the structural properties of the protein by luminescence or NMR methods.

Acknowledgement

This work was supported in part by AR31239 from the U.S. National Institute of Health.

References

1. Huxley, H.E. and Kress, M., J. Muscle Res. Cell Motil., 1985, 6, 153.
2. Jardetzky, O. and Roberts, G.C.K., NMR in Molecular Biology, 1981, Academic Press, New York.
3. McDonald, C.C. and Phillips, W.D., J. Am. Chem. Soc., 1969, 91, 1513.
4. Prince, P.; Trayer, H.R.; Henry, G.D.; Trayer, I.P.; Dalgarno, D.C.; Levine, B.A.; Cary, P.D. and Truner, C., Eur. J. Biochem., 1981, 121, 213.
5. Cheung, H.C.; Gonsoulin, F. and Garland, F., J. Biol.Chem., 1983, 258, 5775.
6. Sekine, T. and Kielley, W.W., Biochim. Biophys. Acta, 1964, 81, 336.
7. Yamaguchi, M. and Sekine, T., J. Biochem., 1966, 59, 24.
8. Burke, M. and Reisler, E., Biochemistry, 1977, 16, 5559
9. Cheung, H.C.; Gonsoulin, F. and Garland, F., Biochim. Biophys. Acta, 1985, 832, 52.
10. Dalbey, R.E.; Weiel, J. and Yount, R.G., Biochemistry, 1983, 22, 4696.
11. Stryer, L.; Thomas, D.D. and Mears, C.F., Ann. Rev. Biophys. Bioeng., 1982, 11, 203.
12. Lawson, W.B.; Leafer, M.D.; Tewes, A. and Rao, G.J.S., Hoppe- Seylors Z. Physiol. Chem., 1968, 349, 251.
13. Moore, T.S.; Boyle, M. and Thorn, V.M., J. Chem. Soc., 1929, 132, 39.
14. Flamig, D.P. and Cusanovich, M.A., Biochemistry,1981, 20, 6760.
15. Weeds, A.G. and Taylor, R.S., Nature (London), 1975, 257, 54.

16. Wagner, P.D. and Weeds, A.G., J. Mol. Biol., 1977, 109, 455.

17. Lowry, O.H.; Rosebrough, N.J.; Farr, A.L. and Randall, R.J., J. Biol. Chem., 1951, 193, 265.

18. Elman, G.L., Arch. Biochem. Biophys., 1959, 82, 1970.

19. This value was computed from interatomic distances taken from the CRC Handbook of Chemistry and Physics, 58th Edition, 1977-78.

Abbreviations: S1, chymotryptic subfragment-1 of myosin; BAAP, [3-(Bromoacetamido)- Propylamine hydrochloride]; DTT, dithiothreitol; DTNB, 5,5'-dithiobis(2-nitrobenzoic acid); TSP,[3-(Trimethylsilyl)propionic acid, Na salt); S1-(1) BAAP, subfragment-1 modified with BAAP at SH_1; S1-(1,2) BAAP, subfragment-1 modified with BAAP at SH_1 and SH_2.

ELLIPSOMETRIC MEASUREMENT OF LIQUID FILM THICKNESS

K.J. Chang
Department of Chemistry
Alabama A&M University
Huntsville, AL

and

D.O. Frazier
Marshall Space Flight Center, NASA
Huntsville, AL

ABSTRACT

The immediate objective of this research is to measure liquid film thickness from the two equilibrium phases of a monotectic system in order to estimate the film pressure of each phase. Thus liquid film thicknesses on the inside walls of the prism cell above the liquid level have been measured ellipsometrically for the monotectic system of succinonitrile and water. The thickness varies with temperature and composition of each phase.

The preliminary results from both layers at 60° angle of incidence show nearly uniform thickness from about 21°C to 23°C. The thickness increases with temperature but near 30°C the film appears foggy and scatters the laser beam. As the temperature of the cell is raised beyond room temperature it becomes increasingly difficult to equalize the temperature inside and outside the cell. But the fogging may also be an indication that solution, not pure water, is adsorbed onto the substrate.

Nevertheless, our preliminary results suggest that ellipsometric measurement is feasible and necessary to measure more accurately and rapidly the film thickness and to improve thermal control of the prism walls.

ELLIPSOMETRIC MEASUREMENT OF LIQUID FILM THICKNESS

Introduction

Considerable interest in monotectic systems within NASA and in materials science in general during the last decade or so is evidenced by the large number of publications on this subject. A few of them are listed in the reference section.[1,2,3,4] Succinonitrile is a transparent organic compound and freezes like metals with small entropies of melting.[5]

The monotectic system of succinonitrile-water has been subjected to considerable investigations not only due to its transparency but also due to a convenient temperature range to work with for its solution and solidification. Its upper consolution temperature of near 56°C and monotectic temperature of close to 19°C make the system[2] nearly ideal for various experiments.

In our current investigation attempts have been made to estimate the thickness of liquid films formed on the inner wall of a prism cell from each of the two separate layers: water-rich and succinonitrile-rich layers of the monotectic system. Several other monotectic systems including succinonitrile-ethanol, succinonitrile-glycerol and succinonitrile-phenanthrene will be subjected to similar investigations. The reason for this study is to assess Cahn's critical wetting theory[6] in a quantitative manner by determining solid-liquid interfacial tension input to Young's equation

$$\gamma_{L_2S} = \gamma_{L_1S} + \gamma_{L_1L_2} \cos\theta$$

where θ is the contact angle and γ is the interfacial energy corresponding to the interface denoted by the subscript pair. The liquid film from these solutions may be formed by condensation of the vapor or by van der Waals adsorption of the liquid along the wall. Thus, it becomes necessary to estimate partial pressures of each component for each solution equilibrated at different temperatures. This task is pursued by Frazier and coworkers[7] at the Marshall Space Flight Center.

Experiment

Since ellipsometric measurement of film thickness requires refractive indices of medium, liquid and substrate, it is absolutely imperative that these values be available or estimated accurately at the particular wavelength, in our case, 632.8 nm of He-Ne laser. Unfortunately these quantities are not available and therefore must be estimated with some degree of accuracy at various temperatures.

Refractive indices are very sensitive to temperature[8] and composition of the liquid. Therefore, index measurements were made using two different devices, a prism spectrometer and the ellipsometer with He-Ne laser. There was some variance between the two apparatuses, as shown in Table 1, which may be due to thermal sensitivity of the prism spectrometer. The table was not completed for all the listed temperatures due to the lack of temperature control device for the prism spectrometer. Thermal control stability on the solution in the prism cell was ± 0.1°C, although it was difficult to achieve this stability on the prism wall at temperatures other than ambient temperature. This was the case because circulation of the bath water around the wall on which film thicknesses were measured would not be permitted since it would obstruct the measurement.

Table 1. Indices of Refraction for Succinonitrile-rich Phase

T°C	Ellipsometer	Prism Spectrometer
18.9	1.42114	
19.2		1.42043
19.6		1.42069
19.9	1.41871	
21.0		1.42017
22.0		1.41945
24.0	1.41990	
24.6		1.41763
25.5		1.41661
26.0	1.42003	
28.0	1.41416	
29.0	1.41135	
30.0	1.41096	
31.0	1.41036	

For the ellipsometric work, prism cells of three different angles of incidence were specifically designed for refractive index and thickness measurements. As stated earlier, the inner wall temperature of the prism could not be controlled as accurately as the solution temperature in the cell. Refractive indices of water from the literature[8] are compared with those estimated ellipsometrically in our experiment in Table 2. The agreement between the two is excellent near room temperature. In this measurement the refractive index of the cell prism glass was assumed constant over the temperature range.

Table 2. Indices of Refraction for Water

T°C	Ellipsometer	Ref. 8*	Deviation %
16.0	1.32880	1.33245	0.3
18.0	1.32977	1.33229	0.2
22.0	1.33197	1.33194	0.002
25.0	1.33119	1.33165	0.03
29.0	1.33099	1.33121	0.02
40.0	1.32970	1.32977	0.005

*Temperature was rounded to 3 digits for this table.

The manually operated ellipsometer (leased from the Marshall Space Flight Center) has been used very extensively, but is very time-consuming and tedious. A temperature shift during a long reading period was entirely possible unless the room and the water jacket were at the same ambient temperature.

Preliminary Result

Liquid film thickness and refractive indices are presented in Figs. 1 and 2 for the monotectic system of succinonitrile and water (SN-water) at the 60° incident angle. Both water-rich and succinonitrile-rich (SN-rich) phases show variation of thickness with temperature. Variations are small between 21° and 23°C. At higher temperatures, film thickness increases, while at lower temperatures thickness decreases. The two layers gave rise to the same thickness near the monotectic temperature. Formation of foggy film as the cell temperature was raised beyond room temperature may indicate precipitation of the conjugate phase within the adsorbed film itself if indeed the film composition is similar to the liquid solution composition, rendering the film quite foggy. The fogging is one of the most consistent problems that should be dealt with. Similar results were obtained with the cells of different glass and angles of incidence.

In calculation of thickness, experimental values of index of refraction for the solution phases obtained in this lab were used. No literature data are available for the solution. Measurements were usually made on a large drop of the phase placed at the floor corner away from the prism wall to minimize capillary migration of the liquid along the wall. Condensation of the vapor onto the wall is the main mechanism of film formation when the wall is not in contact with the sample solution. This allows use of the Gibbs adsorption equation to determine film pressure of liquid films formed from adsorbed phase.

The variation of the index with temperature for both conjugate phases of each succinonitrile-water solution is as anticipated because at higher temperatures there will be more homogeneous mixing between the two components. This trend was shown by both the hollow-prism spectrometer and the ellipsometer. Thus, the succinonitrile-rich phase has a decreasing index as the temperature is raised. In fact, the graph of indices, Fig. 1, is a combination of two separate data from the prism spectrometer and ellipsometer. The result is rather remarkable for the two entirely different instruments. On the other hand, the index of the water-rich phase varies very little with temperature near 23° to 25°C but slowly decreases again above this temperature range. Under nearly identical conditions, variance between the two spectrometers is usually less than 0.1%, still a remarkable agreement.

A preliminary calculation of film pressure was also attempted by utilizing the estimated film thickness and partial pressure data[7] for the two components, succinonitrile and water, obtained elsewhere. The result was obviously too large when the specific surface was replaced by the total inner walls (24 cm^2) of the sample cell. Since for the flat surface of prism glass specific area has not been defined, some new parameters need to be defined and estimated for the Gibbs adsorption equation to calculate film pressure. One parameter under consideration in our laboratory is the quantity defined as the total empty volume of the cell divided by the total inner surface area of the available space.

Conclusion

Much work remains to be done including more precise control of the sample cell and accurate measurement of film thickness with a fully automated ellipsometer system. This system requires a new design of prism cells so that the difficulty of observing liquid film formation on the vertical wall can be eliminated. The liquid film itself on the cell ceiling will be less dependent on any capillary adsorption of liquid. Partial pressures and composition of each component vapor phase should also be estimated.

Acknowledgements

We gratefully acknowledge the funding support of the National Aeronautics and Space Administration for this work and for their loaning of the ellipsometer.

References

1. Ang, C.Y.; Lacy, L.L.; NASA TMX-64956, 1975; Glles, S.H.; Markworth, A.J.; NASA TM-78125, Nov., 1977; Kaukler, W.; Frazier, D.O.; Facemire, B.; NASA TM-82581, April, 1984.

2. Smith, J.E.; Frazier, D.O.; Kaukler, W.; Scripta Metall. 1984, 18, 677.

3. Frazier, D.O.; Facemire, B.; Fanning, U.S.; Acta Metall., 1986, 34, 63.

4. Rai, U.S.; Sing, O.; Sing, N.; Can. J. Chem., 1987, 65, 2639.

5. Jackson, K.A.; Hunt, J.D.; Acta. Metall., 1965, 13, 1212.

6. Cahn, J.W.; J. Chem. Phys., 1977, 66, 3667.

7. Frazier, D.O.; Coworkers; Private Communications, Marshall Space Flight Center, Alabama 35812.

8. Stanley, E.M.; J. Chem. Eng. Data, 1971, 16, 454.

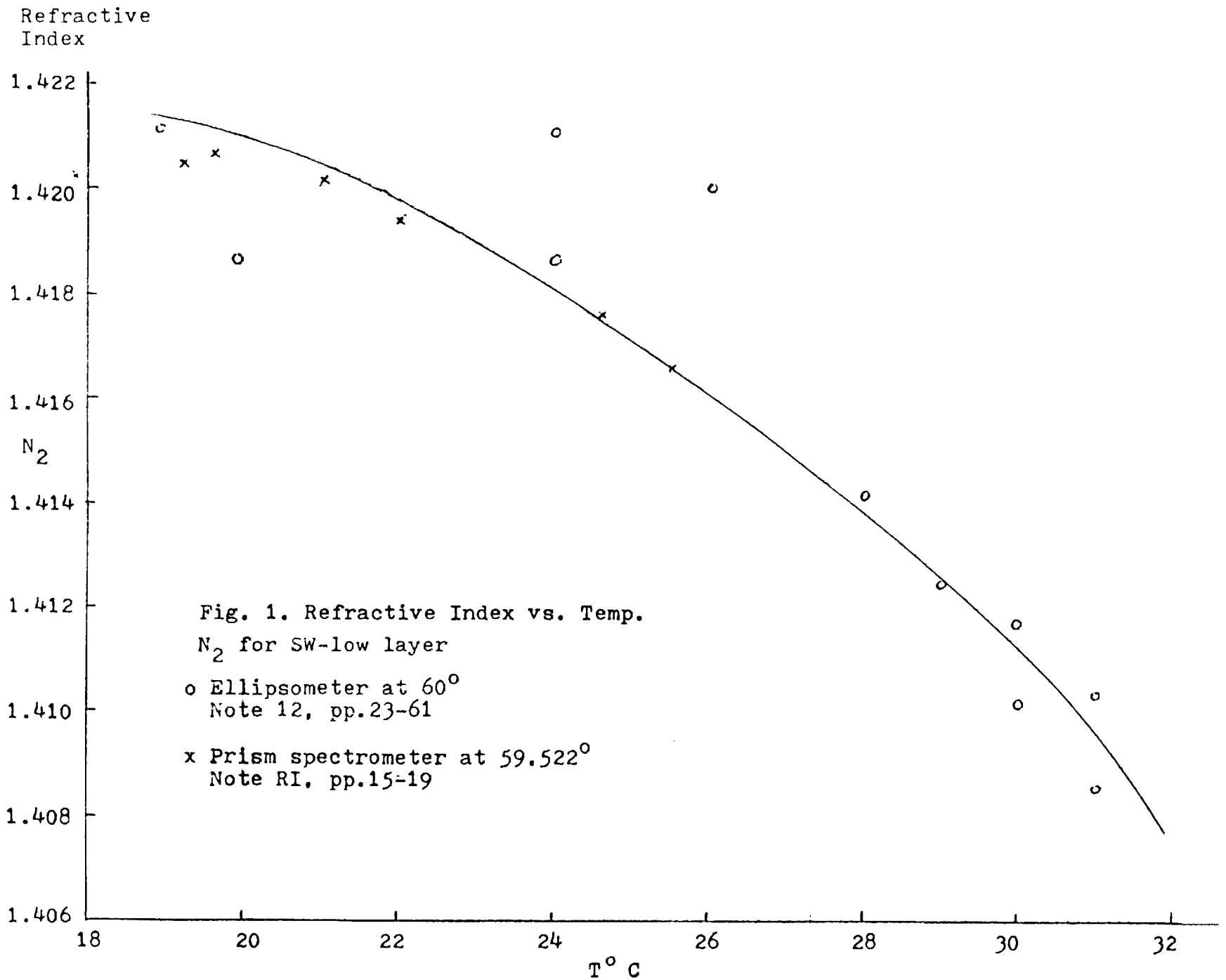

Fig. 1. Refractive Index vs. Temp.

N_2 for SW-low layer

o Ellipsometer at 60°
Note 12, pp.23-61

x Prism spectrometer at 59.522°
Note RI, pp.15-19

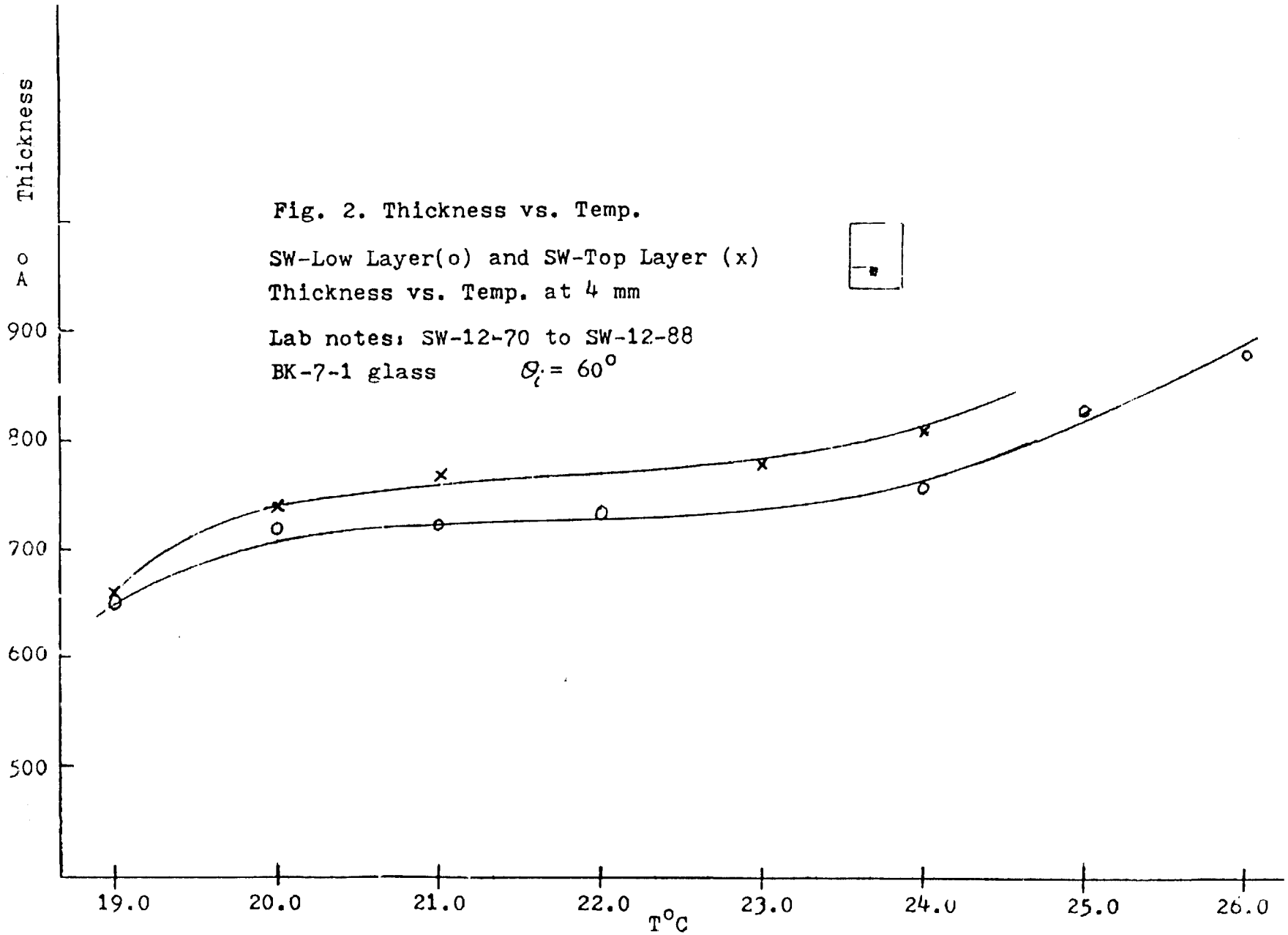

Fig. 2. Thickness vs. Temp.

SW-Low Layer(o) and SW-Top Layer (x)
Thickness vs. Temp. at 4 mm

Lab notes: SW-12-70 to SW-12-88
BK-7-1 glass $\theta_i = 60^\circ$

THE FORMATION AND STUDY OF TITANIUM, ZIRCONIUM AND HAFNIUM COMPLEXES

Bobby Wilson, Sam Sarin, Laverne Smith and Melanie Wilson
Department of Chemistry
Texas Southern University
3100 Cleburne
Houston, Texas

ABSTRACT

Research involves the preparation and characterization of a series of Ti, Zr, Hf, TiO, and HfO, complexes using the poly(pyrazolyl)borates as ligands. The study will provide increased understanding of the decomposition of these coordination compounds which may lead to the production of molecular oxygen on the moon from lunar materials such as ilmenite and rutile. These model compounds are investigated under reducing conditions of molecular hydrogen by use of a high temperature/pressure stainless steel autoclave reactor and by thermogravimetric analysis.

Introduction

Currently, there is considerable interest in the United States in producing molecular oxygen from lunar ores to be used as fuel and in life support systems for space travel. Ilmenite ($FeTiO_3$) and rutile (TiO_2) are both abundant on the moon. Reduction of these ores to produce the pure metal and molecular oxygen is most desirable. Even though several technically different approaches are reported in the literature, none is acceptable for use on the moon.

A survey of the literature on research concerning the use of ilmenite and rutile in the generation of O_2 and Ti brings us to the following conclusions: (1) There is evidence of a lack of research in the above stated direction because of the focus of many industrial firms is the extraction and use of pure TiO_2 and Ti in other processes with no attention being given to the recyclability and energy efficiency of oxygen production(1). However, on the positive side, a variety of these processes do appear to be adaptable to lunar processing, with the modification of these chemical processes. The real bonus of lunar processing is the inert atmosphere, which is very conducive for the production of ultra pure titanium. Because of the considerable amount of energy and time wasted in the earth processes to effect high temperature vacuum annealing of titanium, reduction in a lunar environment becomes even more attractive (2). For example, the Plasma Reduction Process which occurs at 25000 to 35000 K with hydrogen is clean when there are no leaks from the environment (3). The reactions may be written as follows:

$$TiO_2 + 2H_2 \longrightarrow Ti + 2H_2O$$

$$2H_2O \longrightarrow 2H_2 + O_2$$

One solution to the improvement of the TiO_2 reduction is the development of appropriate catalysts that will enhance a lunar process. These catalysts must be chemically stable, or be converted into species which are stable under the conditions required to reduce TiO_2 or $FeTiO_3$ to Fe, Ti and O_2 which may be quite severe. The primary purpose of this research is to prepare and characterize a series of Ti, Zr, Hf, TiO and HfO complexes using the poly(pyrazolyl) borates as ligands.

The poly(pyrazolyl)borates, anions of the general structure $(H_nB\,(Pz)_{4-n})^-$, (where n=0,1 or 2) can be made to function as a bidentate ligand, a tridentate ligand of C_{3v} symmetry analogous to the cyclopentadienide anions, and even as a tetradentate (bis-bidentate) ligand with appropriate control substituents (see Scheme 1 (4-7)). The formation of transition metal complexes with these ligands allows for the option of varying the form (group attachment) of the ligand that is used in the preparation of the coordination complex. The aim is to determine the importance of altering the molecular weight and size of the poly(pyrazolyl)borate and to correlate the chelate effect on complex formation. The decomposition temperature of the enclosed metal complex should have a profound effect upon the metallurgical aspects of the lunar material. Thermogravimetric analyses are currently under study on selected samples under an inert atmosphere in an effort to correlate decomposition temperature with speciation.

SCHEME I

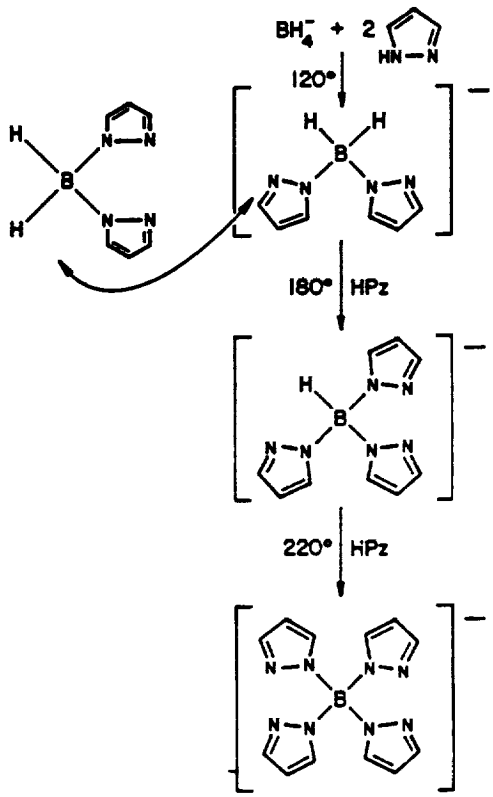

Experimental Details

Since the compounds synthesized during this study were sensitive to air and moisture, all syntheses and subsequent handling of the compounds were conducted under vacuum or in an inert atmosphere. Samples and solutions were prepared in a nitrogen-filled glove box.

Materials

Titanium tetrabromide and titanium tetraiodide (97%), obtained from Alfa Inorganic Products, were used as received. Potassium borohydride (98%) and pyrazole, which were obtained from Fisher Scientific, were also used as received. Analytical grade methylene chloride was purchased from Fisher Scientific Company and dried by refluxing for 24 hours over calcium hydride.

Preparation

Ligand - the following reaction gives rise to potassium dihydrobis(pyrazolyl)borate, $K(H_2B(Pz)_2)$:

$$KBH_4 + 2HPz \text{ ----> } K(H_2B(Pz)_2) + 2H_2$$

The potassium dihydrobis(pyrazolyl)borate was prepared by mixing potassium borohydride (45 g, 1 mole) with pyrazole (272 g, 4 moles) in a one-liter round bottom flask equipped with a magnetic stirrer, thermometer and vent line. The pyrazole was carefully melted by means of an oil bath at 90°C. When the contents of the flask were sufficiently molten to allow magnetic stirring, the mixture was stirred and heated to 120°C. Potassium borohydride dissolved slowly with the evolution of hydrogen. After 24 hours, only a few small particles of KBH_4 were still floating in the melt. These particles were removed mechanically. The melt was poured into 500 ml of toluene, stirred until it cooled to room temperature, and filtered. The filter cake was washed three times with 150 ml portions of hot toluene and then air dried, yielding 140 g of white solid with a melting point of range of 171 - 172°C (8).

Metal Complexes

Preliminary results are consistent with the following reactions on preparation of the titanium complexes:

$$TiX_4 + 2K[H_2B(Pz)_2] \text{ ----> } TiX_2[H_2B(Pz)_2]_2 + 2KX$$

$$TiX_4 + 4K[H_2B(Pz)_2] \text{ ----> } Ti[H_2B(Pz)_2]_4 + 4K$$

(where X = Br and I)

Results and Discussion

Compounds of early transition metals in oxidation state IV are extremely sensitive to oxygen and/or moisture. Therefore, it is essential that all manipulations of these complexes be effected under inert conditions. Since these compounds require special working conditions, relatively few have been prepared and fully characterized. We feel that the poly(pyrazolyl)borate anions with their good chelating abilities and uni-negative property afford an excellent opportunity to increase our knowledge in this area of inorganic chemistry. It is known that the choice of ligands influences the stereochemistry of the metal ions. Small donors decrease the steric repulsions and tend to favor the higher coordination numbers. Large donors tend to favor lower coordination because of the increase in steric repulsions. This series of ligands allows us to test both trends without changing the donor atoms or charge on the ligand. It is also known that the ionic radii increase from titanium(IV) to hafnium(IV) (8,9). These complexes will be investigated under inert conditions by use of nuclear magnetic resonance, vibrational spectra, and x-ray powder diffraction and GC/Mass Spectrometry. It is aimed to elucidate the structure and to ascertain the mode of bonding in the products obtained by the reactions of the metal halides and oxyhalides with potassium dihydrobis(pyrazolyl)borate, potassium hydrotris(pyrazolyl)borate, and potassium tetrakis(pyrazolyl)borate.

References

1. Vilk, W.; Stotler, H.H., Journal of Metals, 1970, 22, 50.
2. Chase, J.D.; Skrivan, J.F., AlChE Symposium Series, 1979, 75, 38.
3. McLaughlin, W.J., "Plasma Reduction of Titanium Dioxide," U.S. Patent 3,429,691, 1969.
4. Asslani, S.S.; Rahbornochi, R.; Wilson, B., Inorg. Chem. Lett., 15, 59 (1959)
5. Trofimenko, S., J. Amer. Chem. Soc., 1966, 88, 1842.
6. Trofimenko, S., J. Amer. Chem. Soc., 1967, 890, 3270.
7. Trofimenko, S. Chem. Rev., 1972, 72, 497.
8. Calderon, J.L.; Cotton, F.A.,; Shaver, A., J. Organometal. Chem., 1972, 37, 127.
9. Bagnell, K.W.; Edwards, J.; Preez, J.G.H.; Warren, T.F., J. Chem Soc. (Dalton), 1975, 140.

KAON - NUCLEUS SCATTERING

Byungsik Hong, Warren W. Buck and Khin M. Maung
Department of Physics
Hampton University
Hampton, Virginia

Technical Monitors
John W. Wilson and L.W. Townsend
NASA Langley Research Center
Hampton, Virginia

ABSTRACT

Two kinds of number density distributions of the nucleus, harmonic well and Woods-Saxon models, are used with our t-matrix that is taken from the scattering experiments to find a simple optical potential. The parameterized two body inputs, which are kaon-nucleon total cross sections, elastic slope parameters, and the ratio of the real to imaginary part of the forward elastic scattering amplitude, are shown. The eikonal approximation was chosen as our solution method to estimate the total and absorptive cross sections for the kaon-nucleus scattering.

KAON - NUCLEUS SCATTERING

For the scattering of the high energy incoming particle, particulary a meson, by a nucleus, it is expected that the situation can be considered in terms of its scattering by the constituent nucleons of the nucleus individually. This means the many body problem may be reduced to a collection of the two body interactions.

One of the successful scattering frameworks is the multiple scattering theory. A simple picture of the scattering of elementary particles by a nucleus is to view the scattering in terms of the projectile interactions with each single constituent of the nucleus (single scattering). There may be other terms contributing to the scattering such as the projectile interacting with two consecutive constituents (double scattering). Similarly there are contributions from three, four, and more successive scatterings. The formalisms using this picture are called multiple scattering theories.[1,2,3] It is clear from this description that the scattering from a nucleus is determined from the amplitude for the scattering of the projectile from a single target constituent, i.e., a two body scattering amplitude.[4]

A general multiple scattering theory for scattering between two nuclei (neglecting three body interaction) has previously been developed by Wilson.[4,5] The reaction for the heavy ion projectile which is the previous application of Wilson's theory was well developed by Wilson et al.[6] And the application to the antiproton, antideuteron and antinuclei was also done by Buck et al.[7] giving good agreement with the available experimental data.

A successful feature of multiple scattering theories manifests itself when combined with the optical model. This allows the optical potential for elementary particle scattering from a nucleus to be determined from more fundamental quantities such as the two body scattering amplitude and the target number density function.

$$W(R) = A \int d^3r' \rho_A(\mathbf{r}')\, t\,(e,\mathbf{r}' - \mathbf{R}) \tag{1}$$

where R is the distance between the origin and projectile particle, r' is the separation between the origin and the considered target constituent, A is the target mass number, e is the kaon-nucleon kinetic energy in the center of the mass frame, ρ_A is the target number density, and t is the energy dependent kaon-proton transition amplitude obtained from scattering experiments. The origin was taken at the center of the mass of the target nucleus. In the eikonal context, the scattering amplitude for the kaon-nucleus scattering is given by

$$f\,(k,\theta) = \frac{k}{2\pi i} \int d^2b e^{i\,\mathbf{q}\cdot\mathbf{b}} [e^{i\chi\,(\mathbf{b},k)} - 1] \tag{2}$$

where

$$\chi(\mathbf{b},k) = -\frac{1}{2k}\frac{2\mu}{\hbar^2} \int_{-\infty}^{\infty} W\,(\mathbf{b},z)dz \tag{3}$$

is the eikonal scattering phase shift function, b is the impact parameter, and μ is the reduced mass of the K-nucleus system. Using the above scattering amplitude and the optical theorem, we can obtain the total and absorption cross section expressed as follows:

$$\sigma_{total} = 2\int d^2b\,[1 - e^{\mathrm{Im}\chi(\mathbf{b},k)}\cos(Re\chi(\mathbf{b},k))] \tag{4}$$

and

$$\sigma_{absorption} = \int d^2b\,[1 - e^{-2Im\chi(\mathbf{b},k)}]. \tag{5}$$

The number density ρ_A of nuclear matter can be extracted from the corresponding charge density ρ_C by assuming [7]

$$\rho_C(r) = \int \rho_N(r')\rho_A(r + r')\,d^3r' \tag{6}$$

where ρ_C is the nuclear charge distribution, ρ_N is the nucleon charge distribution, and ρ_A is the nuclear single particle density. ρ_N was taken to be the usual Gaussian function

$$\rho_N(r) = \left(\frac{3}{2\pi r_N^2}\right)^{3/2} exp\left(-\frac{3r^2}{2r_N^2}\right) \tag{7}$$

with the nucleon root-mean-square charge radius set equal to the proton value of $0.87fm$[12].

For nuclei with $A<20$ we used an harmonic well form of ρ_C as

$$\rho_C(r) = \rho_0[1 + \gamma(\frac{r}{2})^2]exp(-\frac{r^2}{a^2}) \tag{8}$$

with the charge distribution parameters γ and a listed in Table I. Substituting Eq.(7) and Eq. (8) into Eq.(6), we get

$$\rho_A(r) = \frac{\rho_0 a^3}{8s^3}\left[1 + \frac{3\gamma}{2} - \frac{3\gamma a^2}{8s^2} + \frac{\gamma a^2 r^2}{16s^4}\right] exp\left(-\frac{r^2}{4s^2}\right) \tag{9}$$

where

$$s^2 = \frac{a^2}{4} - \frac{r_N^2}{6}. \tag{10}$$

For target nuclei with $A \geq 20$ we choose a Woods-Saxon form of charge distribution

$$\rho_C(r) = \rho_0\left[1 + exp\left(\frac{r - R}{c}\right)\right]^{-1} \tag{11}$$

where the parameters R and c are given by

$$R = r_{0.5} \tag{12}$$

and

$$c = \frac{t_c}{4.4} \tag{13}$$

and $r_{0.5}$ is the radius at half-density with t_c representing the skin thickness. Values for R and t_c are also shown in table I. If we substitute Eqs. (7) and (11) into Eq. (6), we'll see the nuclear single particle density that is also of Woods-Saxon form with the same R, but different normalization coefficient, ρ_0, and surface thickness. The latter is given (in fm) by

$$t_A = [5.08 r_N \, ln \, (\frac{3\beta - 1}{3 - \beta})]^{-1} \tag{14}$$

and

$$\beta = exp \, (2.54 \frac{r_N}{t_c}). \tag{15}$$

We choose the kaon-nucleon scattering amplitude to be the function of momentum transfer q as

$$f(q) = \frac{k}{4\pi} \sigma_T (i + \alpha) e^{-B_q{}^2/2} \tag{16}$$

where k is the wave number of the kaon-nucleon system, σ_T is the kaon-nucleon total cross section, α is the ratio of the real to imaginary part of the forward elastic scattering, and B is the slope parameter. Then the t-matrix in the coordinate space is

$$t(r) = -\sqrt{\frac{e\hbar^2}{2\mu'}} \sigma_T (i + \alpha) \frac{1}{(2\pi B)^{3/2}} e^{-r^2/(2B)} \tag{17}$$

where e is the total kinetic energy in the c.m. frame and μ' is the reduced mass of the colliding particles. We compared our scattering amplitude, Eq. (16), with the experimental data of the K^+p differential cross section taken from Ref.13 and show the results in Figs. 1 and 2. In the case of the kaon-nucleus scattering, the comparison to our calculation utilizing eikonal scattering amplitude, Eq. (2), with the experimental data [9] for C^{12} are displayed in Figs. 3 and 4. The optical potentials coming from the above informations for K^+ and K^- projectiles and C^{12} target are shown in Figs. 5 and 6.

The total cross sections of the $K^{\pm}$- proton system may be fitted by the following form:

$$\sigma_T = \sigma_b \, (P_K^{Lab}) + \sum_i g_i \, (P_K^{Lab}) \tag{18}$$

where P_K^{Lab} is the corresponding kaon laboratory momentum in GeV/c and the unit of σ is mb. The typical form of $g_i \, (P_K^{Lab})$ is that

$$g_i\,(P_K^{Lab}) = \frac{m_i}{[(P_{R_i} - P_K^{Lab})\frac{2}{n_i}]^2 + 1} \tag{19}$$

where P_{R_i} is the resonance momentum of the ith peak and m_i and n_i are the constants which have to be determined from the data.

Eq. (18) actually corresponds to the superpostion of Breit-Wigner formulae where $\sigma_b\,(P_K^{Lab})$ is a non-resonant background. Our fitting constants in the resonance energy range are displayed in table II. The background functions are fitted by

$$\sigma_b\,(P_K^{Lab}) = 23.2e^{-0.003P_K^{Lab}} \tag{20}$$

for $K^- p$ scattering and

$$\sigma_b\,(P_K^{Lab}) = 16.8 - \frac{1}{P_K^{Lab}} \tag{21}$$

for $K^+ p$ scattering. When P_K^{Lab} is less than 0.7 GeV/c in $K^- p$ scattering, we used the following function:

$$\sigma_T = 172.38e^{-2.0(P_K^{Lab} + 0.1)}. \tag{22}$$

In the more high energy region, the empirical formulae for Kp system are given by

$$\sigma_T = 20.18 + \frac{24.63}{P_K^{Lab}} \tag{23}$$

when $P_K^{Lab} > 20GeV/c$ in $K^- p$ system and

$$\sigma_T = 16.8 - \frac{0.22}{P_K^{Lab}} \tag{24}$$

when $P_K^{Lab} > 5GeV/c$ in $K^+ p$ system.

The fitting formulae which we used for $K^\pm - N$ systems are Eq. (25) through (28). For $K^- n$ scattering,

$$\sigma_T = -1033.0 + 1060.0P_K^{Lab^{-0.03}} + 28.0lnP_K^{Lab} \tag{25}$$

when $P_K^{Lab} \geq 2.5GeV/c$ and

$$\sigma_T = 23.91 + 17.0e^{-(P_K^{Lab} - 1.0)^2/0.12} \tag{26}$$

when $P_K^{Lab} < 2.5GeV/c$. And for $K^+ n$ scattering,

$$\sigma_T = 18.4 + 175.0P_K^{Lab^{-7.85}} + 0.2ln^2P_K^{Lab} - 0.75lnP_K^{Lab} \tag{27}$$

when $P_K^{Lab} \geq 2.5 GeV/c$ and

$$\sigma T = \alpha\,(18.0 + 3.0e^{-(P_K^{Lab} - 1.2)^2/0.08}) \tag{28}$$

when $P_K^{Lab} < 2.5\ GeV/c$. The constant α is equal to 1 when $P_K^{Lab} \geq 1.2 GeV/c$ and 0.94 when $P_K^{Lab} < 1.2 GeV/c$.

We determined the fitting formulae of slope parameter, B, in the range of $0.1 \leq |t| \leq 0.4 (GeV/c)^2$. The resultant formulae are shown below.

$$B = 7.3 \tag{29}$$

for $K^- p$ scattering and

$$B = -24.3 + 7.0 ln\,(s + 50.0) \tag{30}$$

for $K^+ p$ interaction. The square of the momentum transfer t $(GeV/c)^2$,, and the invariant mass squared, $s(GeV/c^2)$, are two convenient Mandelstam variables.

Our parameterized formulae, α, for $K^- p$ and $K^+ p$ scattering, respectively, are as follows.

$$\alpha = -\frac{0.32}{1.0 + 0.9 P_K^{Lab^2}} \sin\{\frac{5\pi}{2}(P_K^{Lab} - 0.2)\} \tag{31}$$

for $K^- p$ scattering and

$$\alpha = -1.86e^{-(P_K^{Lab} - 0.1)^2/0.41} - 0.44 \tag{32}$$

for $K^+ p$ interaction where P_K^{Lab} is the kaon laboratory monentum in GeV/c.

The total and absorptive cross sections for $K^{\pm} - Al^{27}$ scattering using the harmonic well and Woods-Saxon single particle densities are shown in Figs. 7 and 8. Although we cannot evaluate the exact error due to the scaricty of experimental data, we expect that our calculation reasonably represents the situation, because of the good agreement between our calculation and the experimental data of other quantities such as the differential cross sections of kaon-proton and kaon-nucleus scattering.

In case of $K^+ p$ scattering our scattering amplitude was quite reasonable. Moreover, the calculation of the differential cross section gave us more accurate result as the energy of projectile went higher. For $K^{\pm} - C^{12}$ scattering the differential cross sections are estimated lower than the experimental results. It may be natural because we used a very simplified, non-relativistic optical potential. At the very forward angle the experiments show us the differential cross sections rise very rapidly, but the calculations converge smaller values. This comes from the fact that we have neglected the contribution of Coulomb interaction which is the long range interaction in the optical potential.

The total and absorptive cross sections for K^- - nucleus scattering were bigger than those of K^+ - nucleus scattering. This, of course, indicates that K^- meson interacts with nucleons stronger than K^+ meson. According to the quark model, K^+ resonant peak requires the formation of five-quark

objects which have never been found, but the $K^- N$ interactions are so strong that the cross sections are roughly comparable to those of nucleon-nucleon scattering.

K^+ -nucleus total cross section shows almost perfect linear dependence of A and K^- - nucleus total cross section also represents linearity of A at high energies, but exhibits a little complexity at low energies. Other things that we can give attention to are that the absorptive cross section of K^+ - nucleus scattering depends on $A^{0.82}$ linearly, but K^- - nucleus absorptive cross section does not show fairly good linear dependence of $A^{0.82}$ as in the case of total cross section at relatively low energies. The linear dependence of $A^{0.82}$ of absorptive cross section tells us that the nucleus is not perfectly black to the kaon projectile.

The results of this work will be used in the hadron transport computer code at NASA Langley Research Center (Ref. 18).

References

1. Watson, K.M., Phys. Rev. 1953, **89**, 575

2. Frank, R.M.; Gammel, J.L.; Watson, K.M., Phys. Rev. 1956, **101**, 891

3. Watson, K.M., Phys. Rev. 1957, **105**, 1388

4. Wilson, J.W., A Dissertation for Ph.D, 1975

5. Wilson, J.W.; Phys. Lett. B 1974, **52**, 149

6. Wilson, J.W.; Townsend, L.W., Can. J. Phys. 1981, **59**, 1569

7. Buck, W.W.; Norbury, J.W.; Townsend, L.W.; Wilson, J.W., Phys. Rev. C 1986, **33**, 234

8. Aguilar-Benitez, M. *etal.*, "Particle Properties Data Booklet", North-Holland, Amsterdam, April 1986

9. Marlow, D.; Varnes, P.D.; Colella, N.J.; Dytman, S.A.; Eisenstein, R.A.; Grace, R.; Takeutchi, F.; Wharton, W.R.; Bart, S.; Hancock, D.; Hackenberg, R.; Hungerford, E.; Mayes, W.; Pinsky, L.; Williams, T.; Chrien, R.; Palevsky, H.; Sutter, R., Phys. Rev. C 1982, **25**, 2619

10. Siegel, P.B.; Kaufmann, W.B.; Gibbs, W.R., Phys. Rev. C 1984, **30**, 1256

11. Goldberger, M.L.; Watson, K.M., "Collision Theory", John Wiley & Sons, New York, 1964

12. Borkowski, F.; Simon, G.G.; Walther, V.H.; Wendling, R.D., Z. Phys. A 1975, **275**, 29

13. Price, LeRoy R.; Barash-Schmidt, Naomi; Benary, Odette: Bland, Roger W.; Rosenfeld, Arther H.; Wohl, Charles G., " A Compliation of K^+N Reactions" , Lawrence Radiation Laboratory, University of California, Berkley, California, UCRL-20000 K^+N, Sept. 1969

14. Giacomeli, G., "Total Cross Section Measurement", Pergamon Press, Ltd, New York, 1970

15. Baldini, A.; Flaminio, V.; Moorehead, W.G.; Morrison, D.R.O., Landolt-Börnstein New Series I/12a and I/12b, "Total Cross-Sections for Reactions of High Energy Particles", Springer Berlin Heidelberg, 1988

16. Perl, Martin L., "High Energy Hadron Physics", John Wiley & Sons, Inc., 1974

17. Lusiguoli, M.; Restignoli, M.; Violini, G.; Snow, G.A., Nuovo Cimento 1966, **45**,A792

18. Wilson, J.W.; Townsend, L.W.; Chun, S.Y.; Lamkin, S.L.; Ganapol, B.D.; Hong, B.S.; Buck W.W.; Khan, F.; Cucinotta, F.A.; Nealy, J.E., "BRYNTRN; A baryon transport model", NASA TP-2887, Feb. 1989.

Table I.
Nuclear charge distribution parameters from electron scattering data taken from Ref. 8.

Nucleus	Distribution	γ or t_c (fm)	a or R (fm)
H^2		0	1.71
He^4	HW	0	1.33
Li^7	HW	0.327	1.77
Be^9	HW	0.611	1.791
B^{11}	HW	0.811	1.69
C^{12}	HW	1.247	1.649
N^{14}	HW	1.291	1.729
O^{16}	HW	1.544	1.833
Ne^{20}	WS	2.517	2.74
Al^{27}	WS	2.504	3.05
Ar^{40}	WS	2.693	3.47
Fe^{56}	WS	2.611	3.971
Cu^{64}	WS	2.504	3.05
Br^{80}	WS	2.306	4.604
Ag^{108}	WS	2.354	5.139
Ba^{138}	WS	2.621	5.618
Pb^{208}	WS	2.416	6.624

Table II.
Kaon-nucleon total cross section parameters

	i	P_{R_i} (GeV/c)	m_i (mb)	n_i (GeV/c)
Kp	1	0.8	11.	0.21
	2	1.05	27.	0.2
	3	1.60	9.	0.35
	4	2.30	4.	1.
	5	3.50	4.30	2.
K^+p	1	0.80	-4.	0.40
	2	1.30	2.50	1.

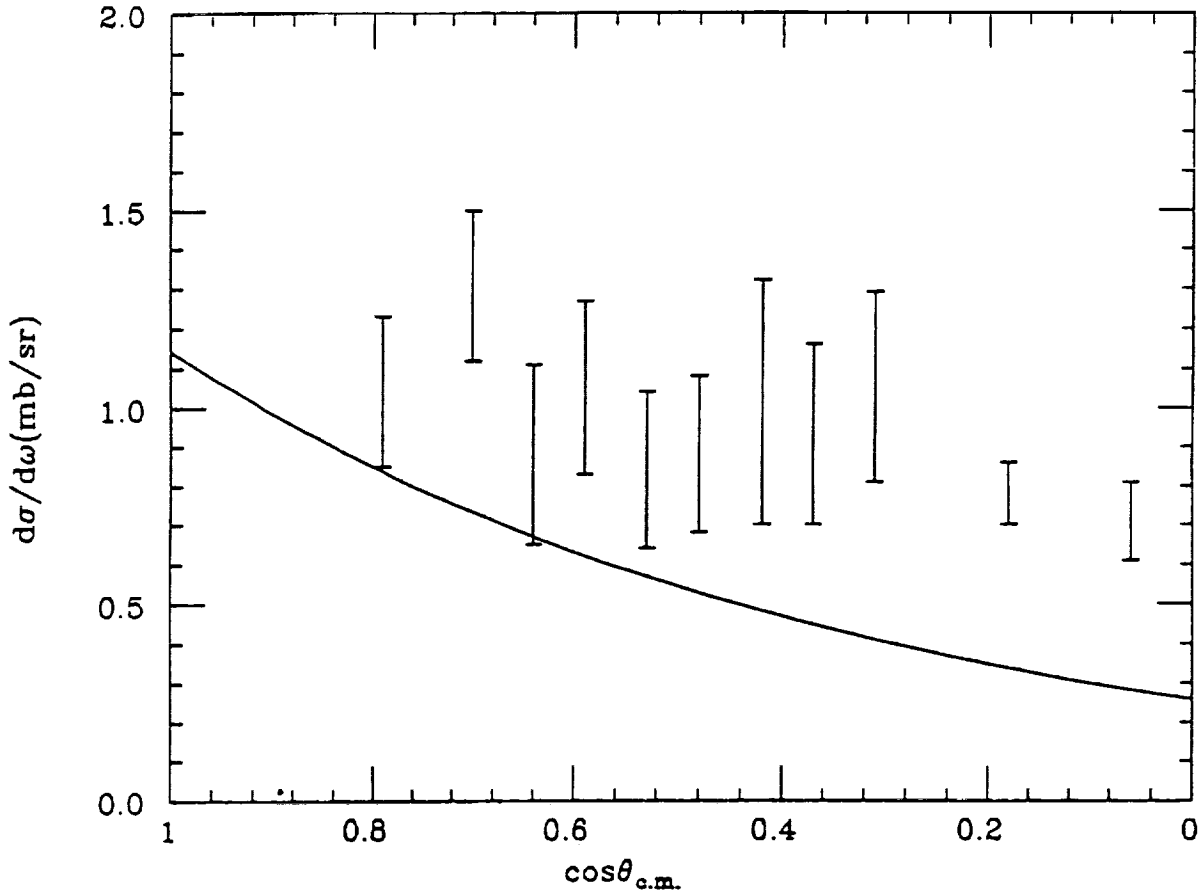

Figure 1. Differential cross section of K^+p scattering at 503 MeV

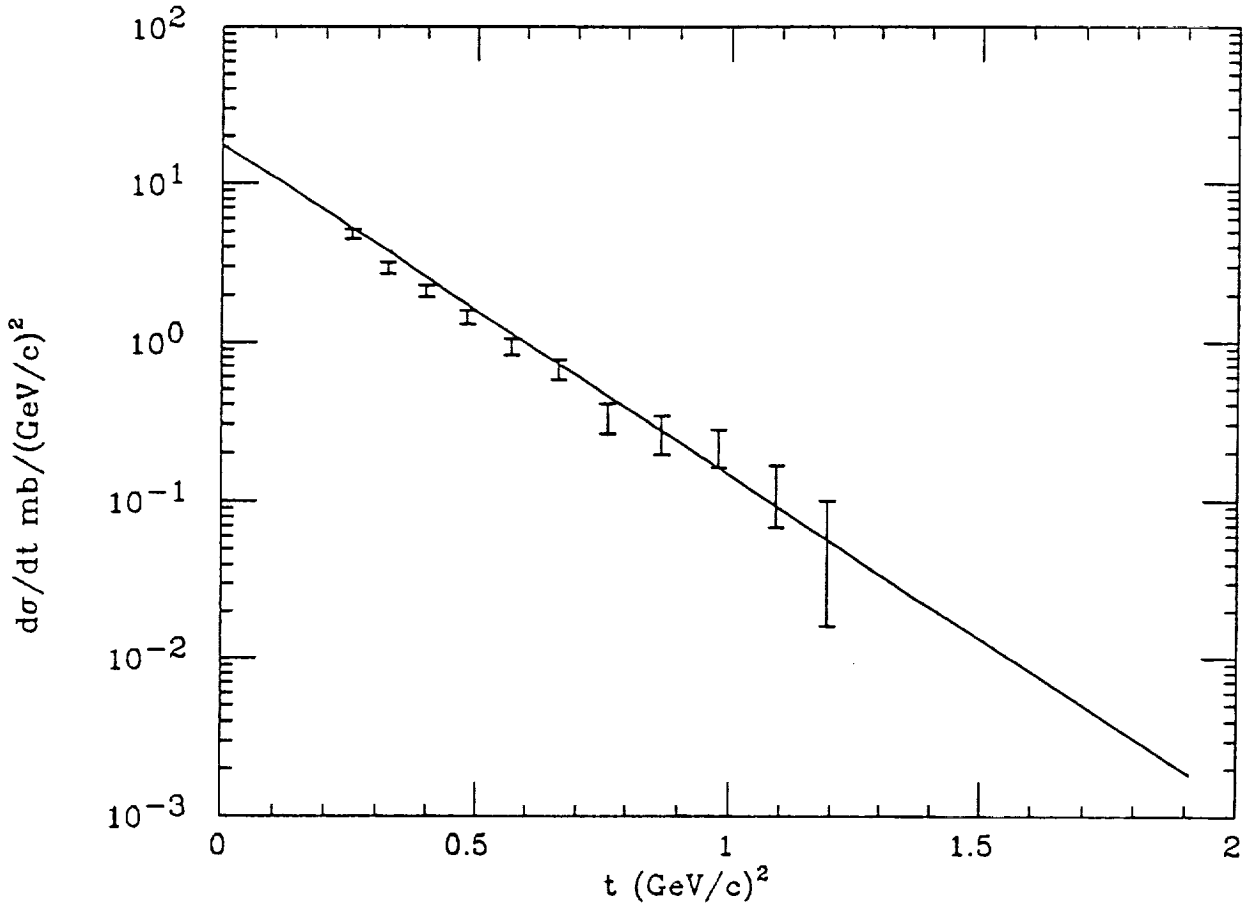

Figure 2. Differential cross section of K^+p scattering at 6324.9 *MeV*

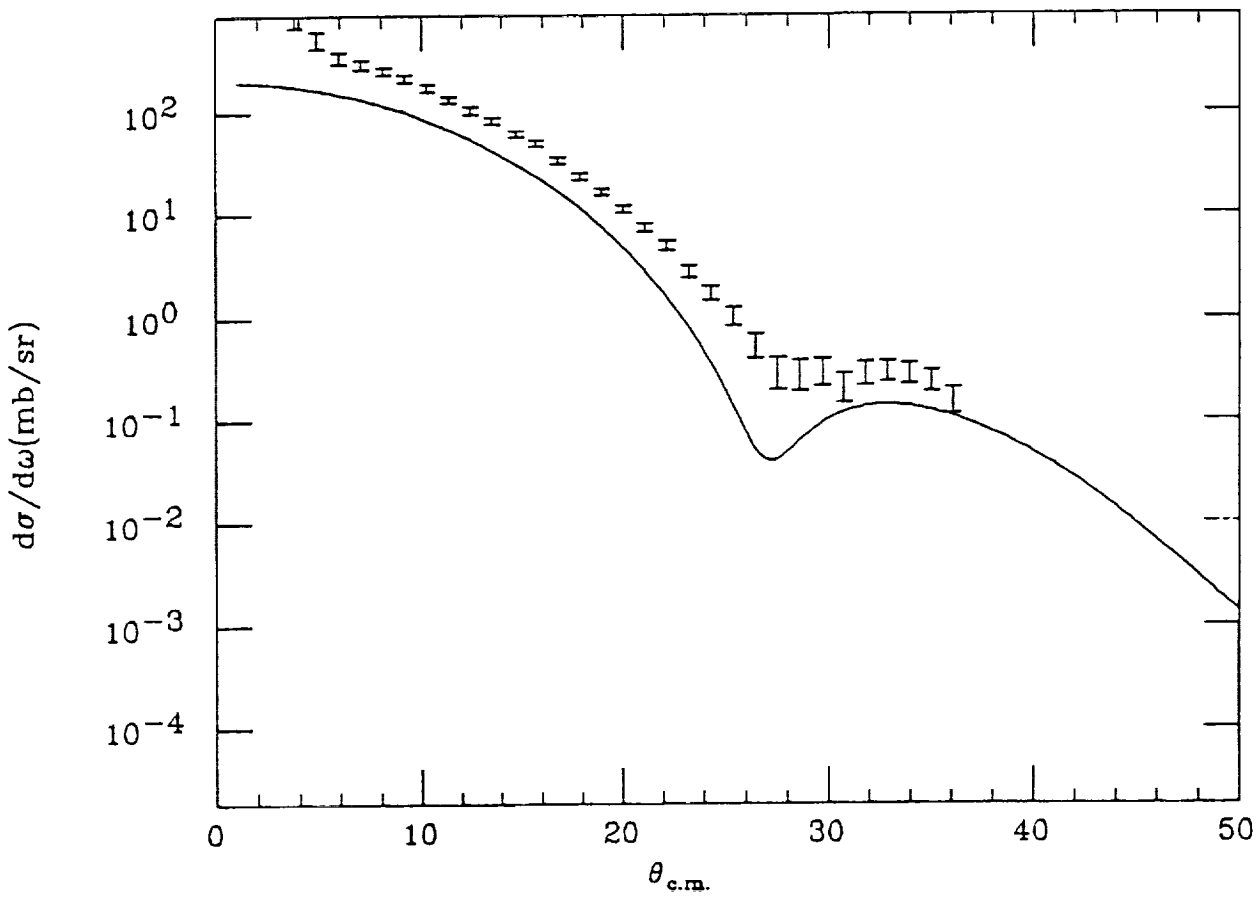

Figure 3. Differential cross section of K^+C^{12} scattering at 800 *MeV/c*

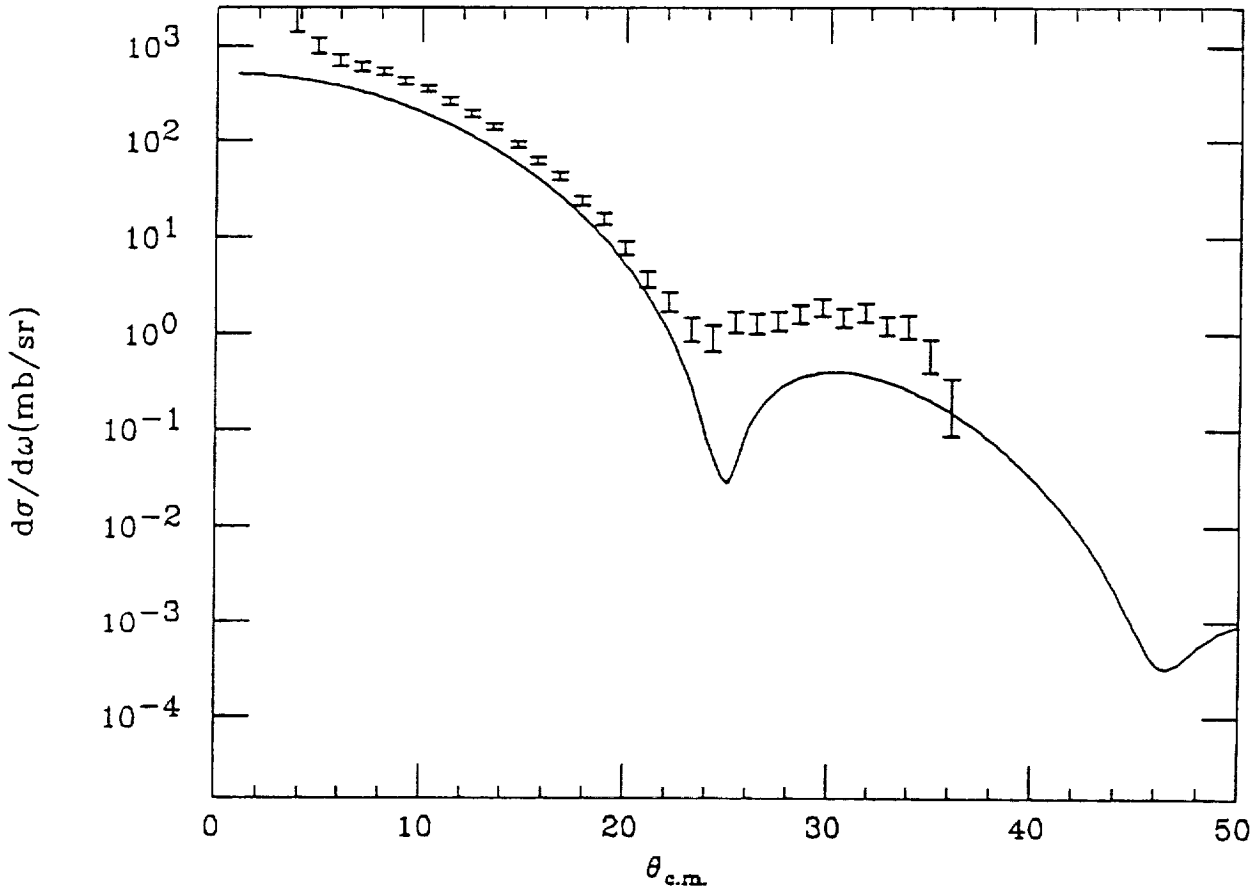

Figure 4. Differential cross section of $K^- C^{12}$ scattering at 800 *MeV/c*

Q-3

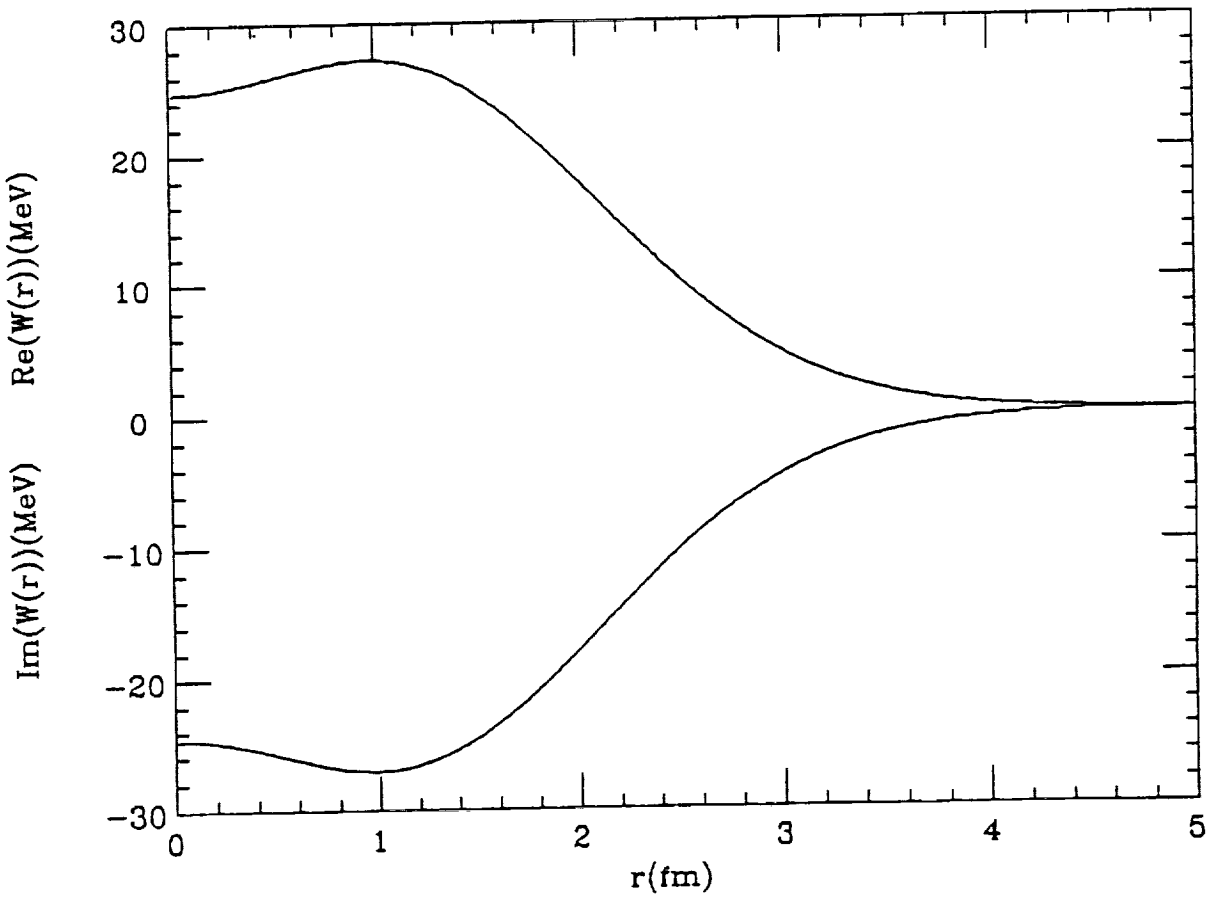

Figure 5. Optical potential for K^+C^{12} at 800 *MeV/c*

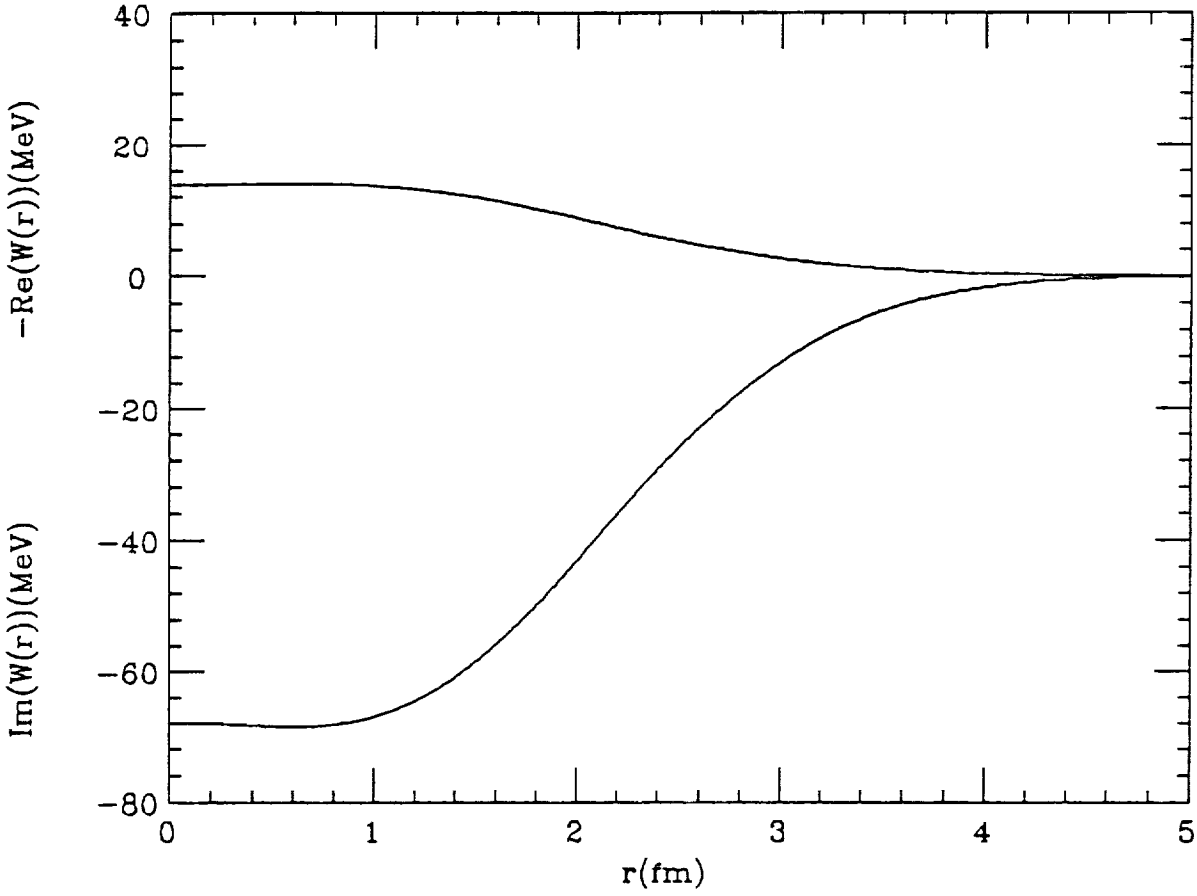

Figure 6. Optical potential for $K^- C^{12}$ at 800 *MeV/c*

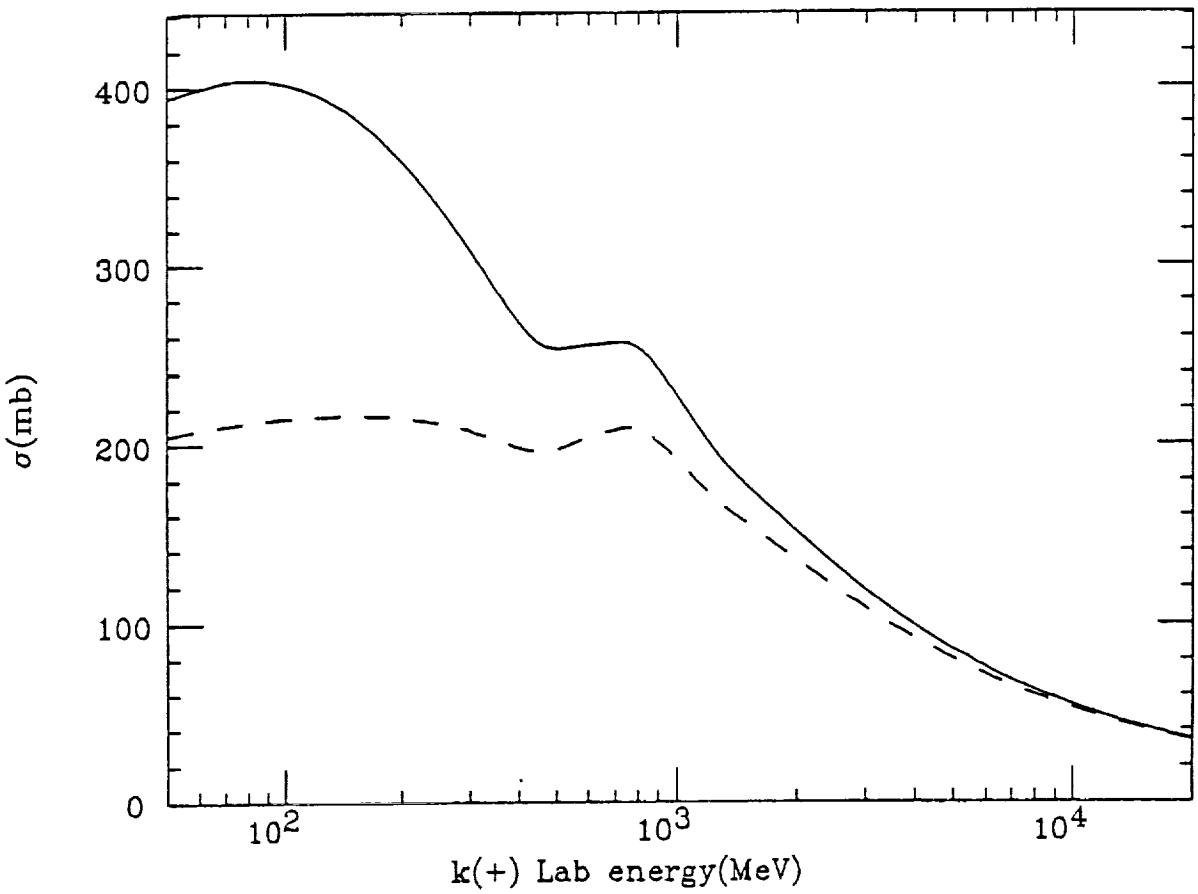

Figure 7. Total (solid) and absorptive (dashed) cross sections for K^+Al^{27}

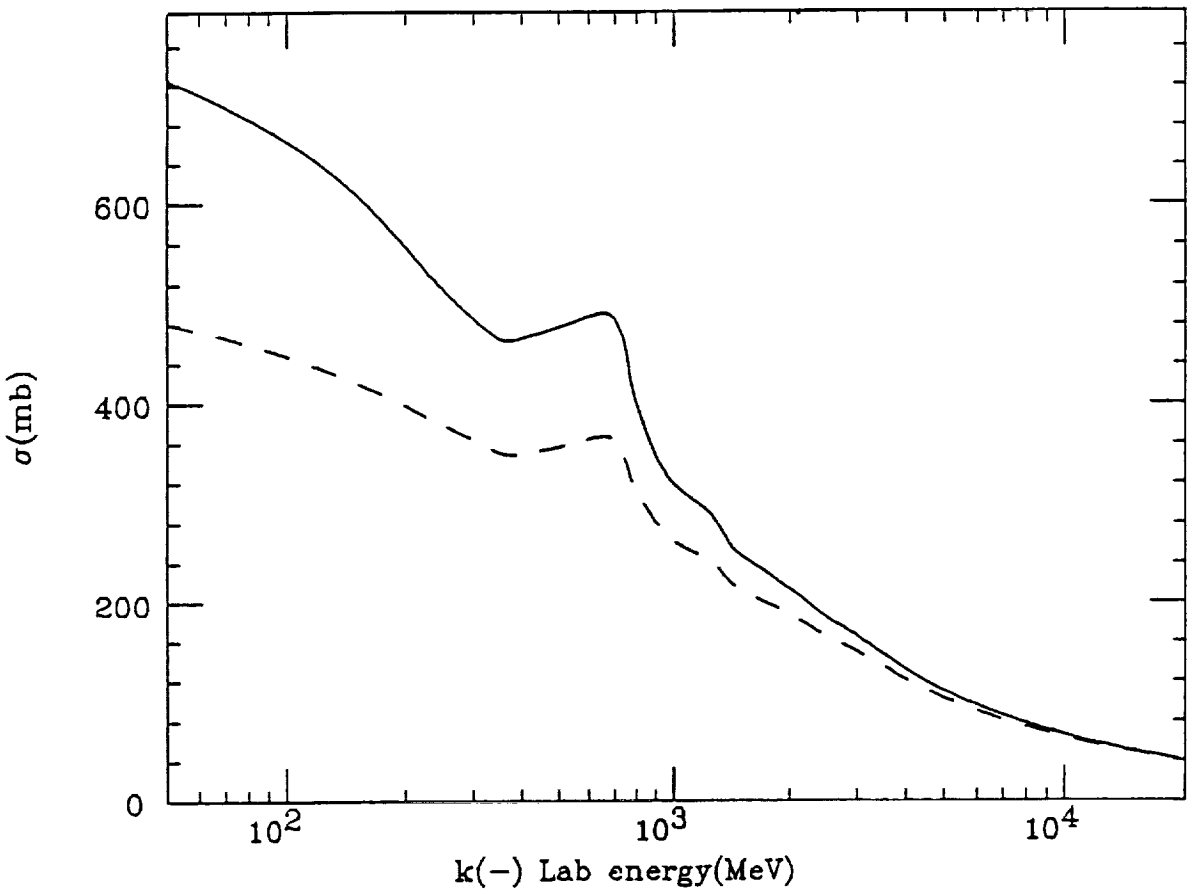

Figure 8. Total (solid) and absorptive (dashed) cross sections for $K^- Al^{27}$

N91-28087

PHASE CONJUGATION BY DEGENERATE FOUR WAVE MIXING IN DISODIUM FLUORESCEIN SOLUTION IN METHANOL*

524-25
J6605
P.9

H. Abdeldayem, P. Chandra Sekhar, P. Venkateswarlu and M.C. Geroge
Department of Physics
Alabama A&M University
Normal, Alabama

ABSTRACT

Organic dyes are known to show resonant type of non-linear optical properties, including phase conjugation. In our present work, disodium fluorescein in methanol is used as an organic non-linear medium for degenerate four wave mixing at 532 nm to see the intensity dependence of the phase conjugate signal at different concentrations of the solution. It is observed that the maximum reflectivity of the signal occurs in a concentration range of 5×10^{-3} g/cm^3 to 1.2×10^{-2} g/cm^3. It is also observed that the intensity of the signal drops suddenly to less than half of its maximum outside the concentration range mentioned above.

An investigation of the phase conjugate signal intensity by changing the delay time between probe signal and the forward pump signal is also examined.

Briefly discussed is the possibility of population grating in dye liquids as a source of enhancing the third order susceptibility besides the other techniques mentioned in reference[4].

The experiment is done by beam splitting the second harmonic (532 nm) of Nd:YAG laser, Q-switched at 20-pulses/sec. (pulse width ~8ns and ~200 mJ per pulse).

approximate

*Supported by NASA Grant No. 2-356-14-3300-390.

PHASE CONJUGATION BY DEGENERATE FOUR WAVE MIXING IN DISODIUM FLUORESCEIN SOLUTION IN METHANOL

Introduction

Phase conjugation by degenerate four wave mixing (DFWM) has shown considerable promise as a technique of generating high fidelity phase conjugate signals. The only difficulty which limits its use is its low efficiency. Because of that, a great deal of research work is concentrated on finding the proper and most efficient nonlinear media with the highest possible third order susceptibilities to improve the efficiency.

In an earlier experiment[6], Caro and Gower obtained a DFWM signal which decreased and vanished if the path difference was greater than the coherence length, showing that their signal was purely due to DFWM. On the other hand, Basov et. al[8] obtained stimulated Brillouin Scattering from two pump beams even with a path difference much larger than the coherence length of the laser. Seeded Brillouin Scattering has also resulted in phase conjugation of two incoherent beams[9].

Recently, considerable interest has been generated in the study of organic dye solutions as efficient nonlinear media. A class of highly efficient organic dyes with a wide and flexible range of operating conditions has become known.

The purpose of our experiment is to pick up an organic dye as a nonlinear medium for our DFWM experiments to investigate the possible mechanisms which are responsible for phase conjugation. Disodium fluorescein was chosen among several other organic dyes as a candidate for our experiment based on the idea that it showed a relatively strong phase conjugate signal, using a frequency doubled Nd:YAG laser (532nm), Q-switched at 20 pulses/sec (pulse width ~8 ns and ~200 mJ/pulse), although its absorption spectrum in ethanol shows only a small tail beyond 525 nm.

Mechanisms for DFWM:

When mutually coherent laser beams interfere in an absorbing medium, the interference pattern heats the medium nonuniformly. The nonuniform heating causes density variations in the medium, consequently an index of refraction grating, which Bragg scatters a read beam into the conjugate wave signal, is formed.

It is believed[1] that in the initial few picoseconds after the energy has been deposited, the medium has not yet had time to expand, the density is thus constant and any index change is due to the intrinsic variation in the index of refraction with temperature at constant density. Subsequently, sound waves produced by the nonuniform heating propagate across the medium and begin the expansion process. Finally, the sound waves damp out and the usual thermally induced grating[2] becomes dominant.

Besides the thermal grating mechanism, there are other possible mechanisms which are also responsible for producing nonlinear susceptibility like saturable absorption[3] and the optical Kerr effect[4].

In addition to these different mechanisms, one may also examine the energy level structure of a typical dye molecule, shown in Fig. 1[5], where the first excited singlet state is generally higher than the lowest triplet state. Since dye molecules are large, the vibrational and rotational levels in any electronic state are too numerous and too closely spaced, and the spread of these levels is large. Further, the excited singlet states are not well separated from one another. All the dye molecules in the excited states relax quickly by nonradiative interactions to the lowest singlet state S_1. This is the only state which has been observed to fluoresce and has, in most of the cases, lifetimes of the order of a few nanoseconds. The upper singlet states are not known to fluoresce and they relax to the S_1 state in times of the order of picoseconds. There are two other competing processes for relaxation of the molecules from S_1 in addition to the spontaneous emission to the ground state. Although singlet to triplet state transitions are generally forbidden, relaxation to triplet levels is still possible. The triplet state T_1 has a lifetime of a few microseconds which is large compared to the life time of the S_1 state.

The possible excitation to the triplet state T_1, which is of a relatively longer lifetime, may result in a population grating which should be considered as an extra mechanism which will contribute to the third order nonlinearity and Bragg scattering of the phase conjugate signal.

Experiment

The experimental set up is as shown in Fig. 2 in which the frequency doubled Q-switched Nd:YAG laser (532 nm) is split to obtain ~20% as a probe beam A_3 and the rest as two equally intense and counter propagating pump beams A_1 and A_2. The phase conjugate signal is seen as a beam counter propagating to A_3, the intensity of which is first observed at different concentrations of the disodium fluorescein in methanol in a 1 cm thick cuvette. The experimental results obtained are as expected (Fig. 3). At relatively low concentrations the number of the dye molecules are not enough to form a strong grating to reflect the signal. As the concentration increases to the optimum one, $\sim 7 \times 10^{-3}$ g/cm^3 in this specific case, the grating is good enough to reflect a relatively powerful phase conjugate signal. At higher concentrations up to 20×10^{-3} g/cm^3 the curve shows a weaker phase conjugate signal.

The decay in the phase conjugate signal at high concentration can be attributed to two factors: (1) The fluorescence quenching where the fluorescence emitted by some molecules are absorbed by others in the medium. This contributes to heating the medium quickly. The rise in temperature inhibits the formation of the grating and hence the medium becomes less efficient. (2) The heat increase in the cell causes the medium to boil. The hydrodynamic motion of the liquid tends to wash out the grating and reduces its efficiency.

The dependence of the phase conjugate signal on the delay time between the probe and the forward pump is shown in Fig. 4. Since the phase conjugate signal is thought to be due mainly to the grating which is formed by the interference pattern of the two coherent beams, A_1 and A_3, one expects that if the path difference between the beams is larger than the coherence length of the laser, which is ~1 cm (0.03 ns delay time), the signal should vanish. Surprisingly, the phase conjugate signal is detected even for a path difference of more than 360 cm (12.0 ns delay time) (Fig. 5). This result is probably attributable to the presence of stimulated scattering. Similar results are obtained for the same sample in a smaller cell of 1 mm thickness. Preliminary experiments with a single beam show that stimulated back-scattering signals can be obtained from pure ethanol, acetone and methanol. Experiments on stimulated scattering in dye solutions are now in progress to clarify this situation.

In summary, we discussed a population grating as a mechanism for the index grating in liquids, along with the previously mentioned ones. In addition, our experimental results show that the phase conjugate signal through DFWM could be superimposed on a signal due to stimulated scattering.

Acknowledgments

The authors wish to thank NASA for a grant and a fellowship (Grant No. 2-356-14-3300-390).

References

1. R.C. Desai, M.D. Levenson and J.A. Barker, Phys. Rev. A 27, No. 4, P.1968 (1983)

2. G. Martin and R.W. Hellwarth, Appl. Phys. Lett., Vol. 34, p.371 (1979).

3. R.L. Abrams and R.C. Lind, Opt. Lett., Vol. 2, P. 94 (1978); Opt. Lett. Vol. 3, p. 205 (1978).

4. D.M. Bloom and G.C. Bjorklund, Appl. Phys. Lett. Vol. 31, p. 592 (1977)

5. P. Venkateswarlu, M.C. George, H. Jagannath, Y.V. Rao, G. Chakrapani and A. Miahnahri, A report on Optical Studies in Laser Dyes, submitted to Ballistic Missile Defense Systems Command, Huntsville, Alabama 35807, from Alabama A&M University, Physics Department, October, 1985.

6. R.G. Caro and M.C. Gower, Appl. Phys. Lett. 39 (11) December 1981.

7. R.G. Caro and M.C. Gower, IEEE J. of Quantum Electronics, Vol. QE-18, No. 9, September, 1982.

8. N.G. Basov, I.G. Zubarev, A.B. Mironov and A. Yu Okulov, Sov. Phys. JETP 52(5). P. 847, November, 1980.

9. T.R. Loree, D.E. Watkins, T.M. Johnson, N.A. Kurnit, and R.A. Fisher, Opt. Lett., Vol. 12, No. 3, P. 178, March, 1987.

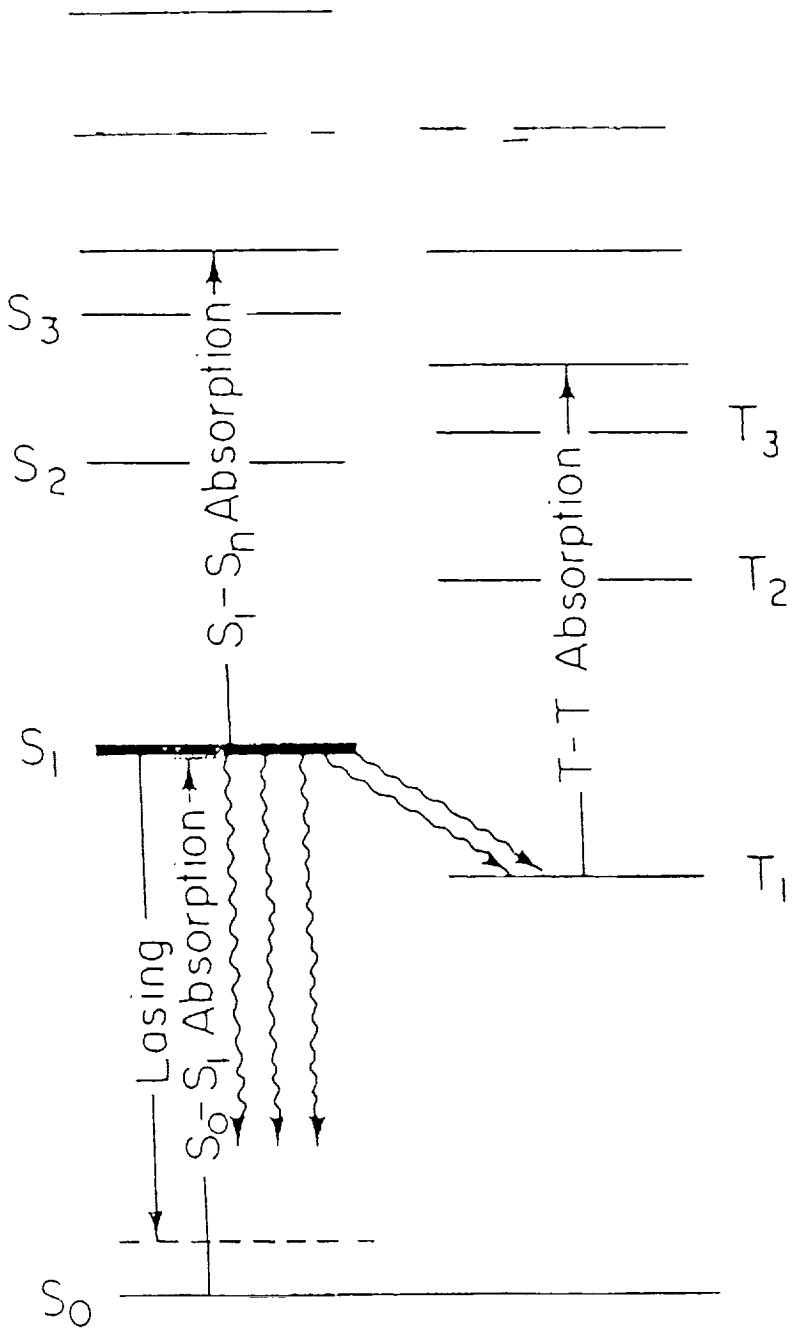

Figure 1. Energy level diagram of a dye molecule.

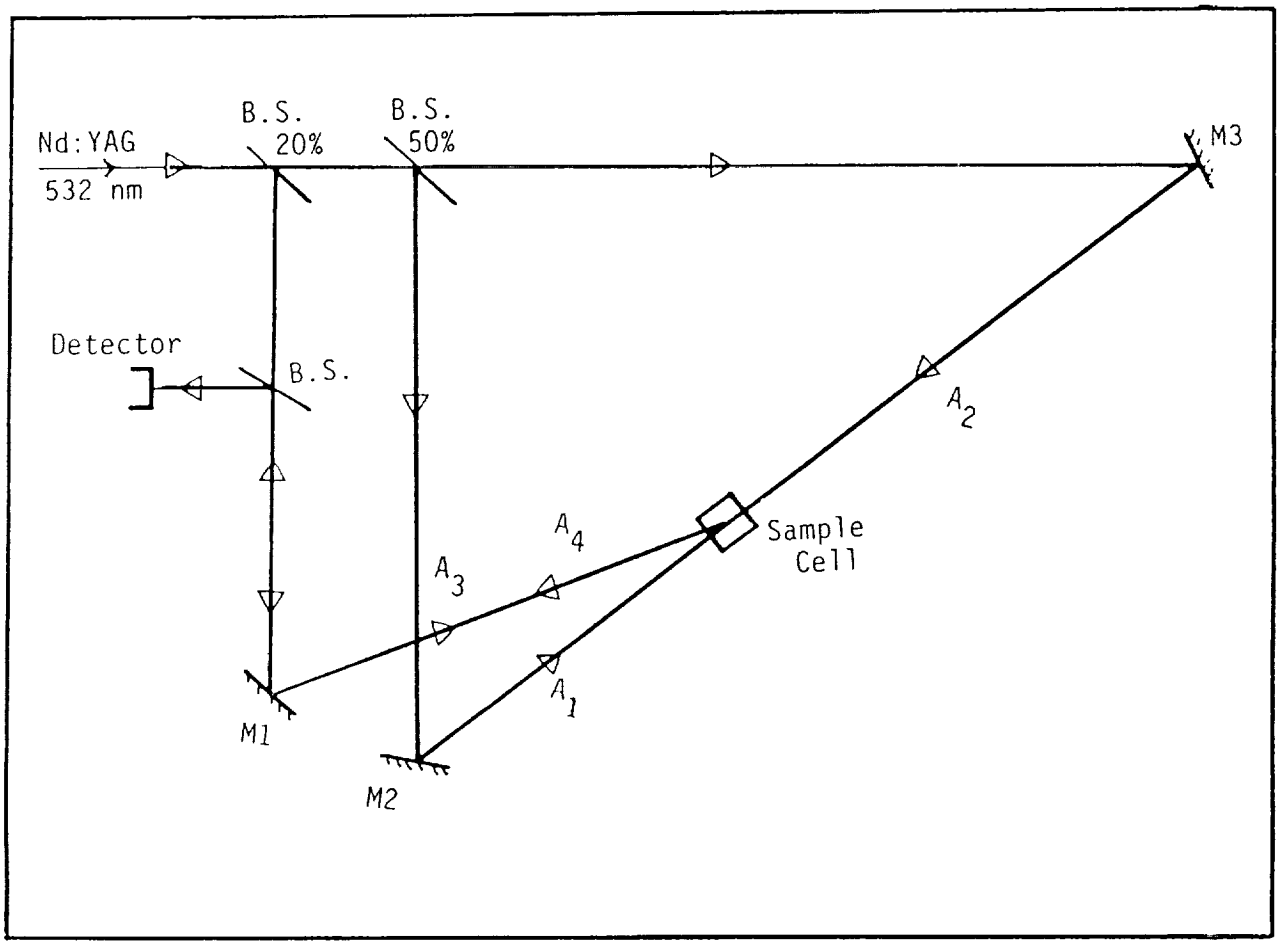

Figure 2. Experimental Layout: BS: Beam splitters M: Mirrors
A_1, A_2: Pump Beams, A_3: Probe, A_4: Phase Conjugate.

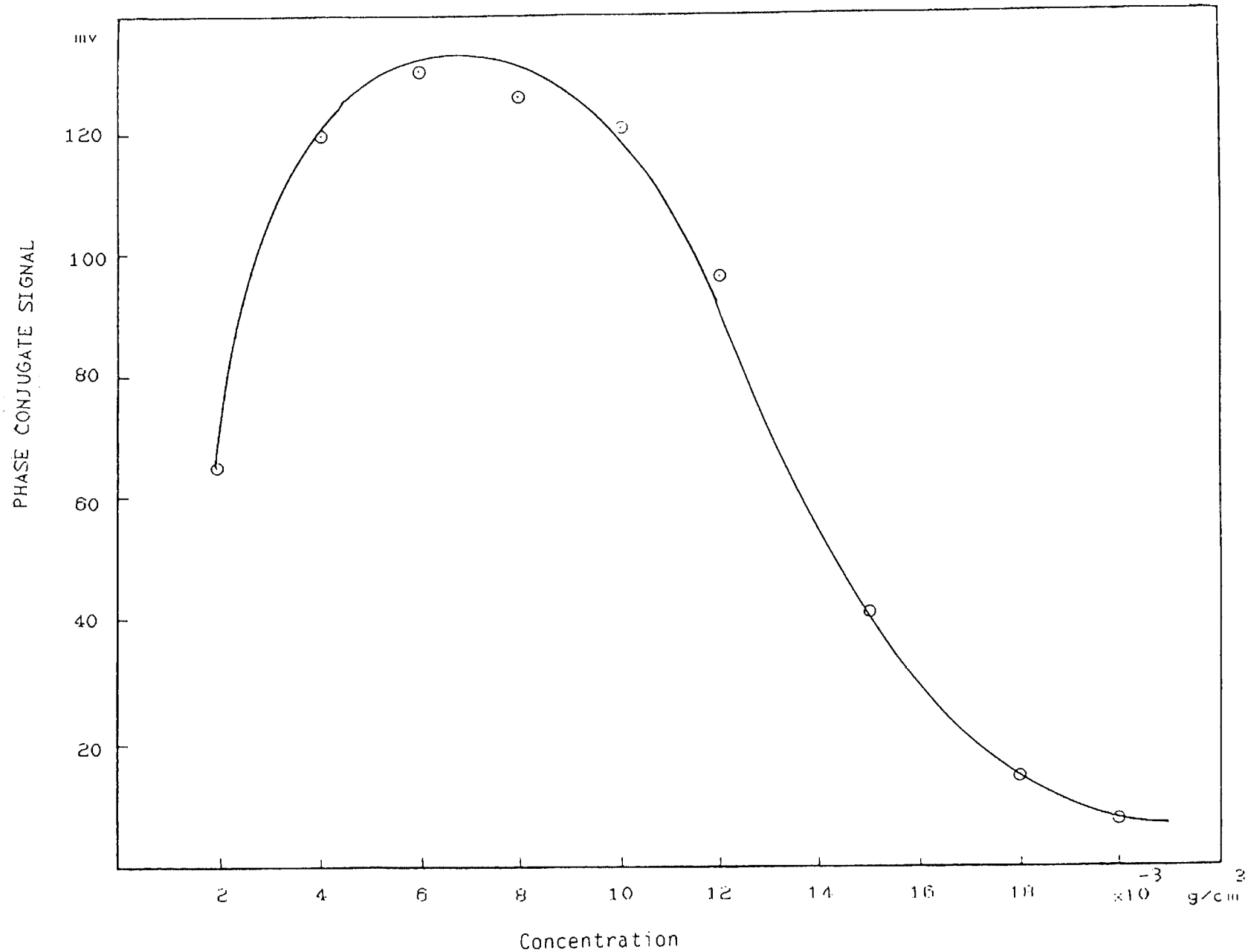

Figure 3. Dependence of phase conjugate signal on concentration of disodium fluorescein.

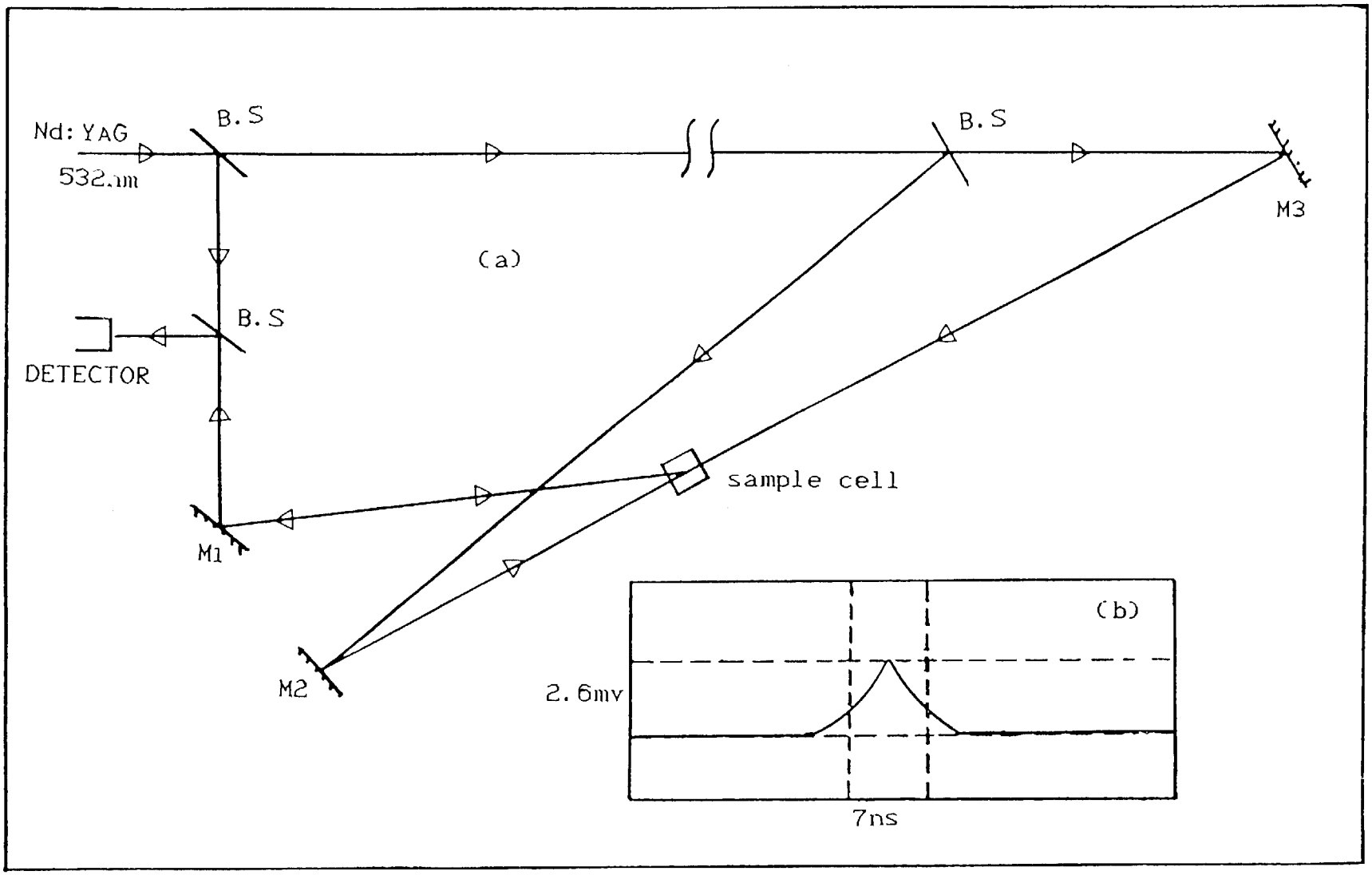

Figure 4. (a) The experimental layout with the pump beam #1 (A_1) delayed.
(b) The phase conjugate signal obtained at 12.2ns delay with respect to the probe (A_3)

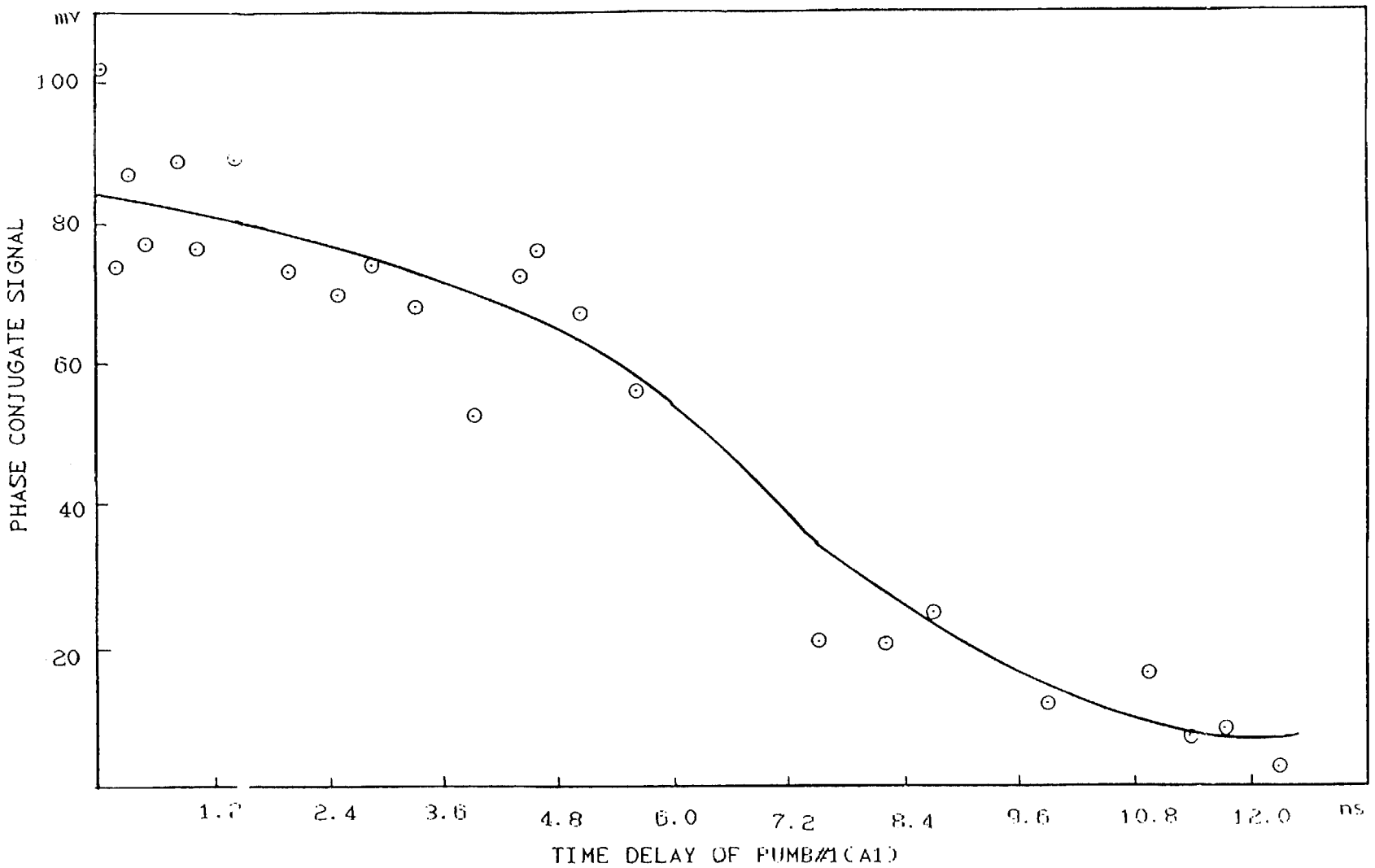

Figure 5. Dependance of the phase conjugate signal on the delay time of the pump beam (A_1).

N91-28088

POLAROGRAPHIC STUDY OF CADMIUM 5-(Hydroxy-2-(Hydroxymethyl)-4H-Pyran-4-one COMPLEX

S25-25
26606
P-17

Ray F. Wilson and Robert C. Daniels
Department of Chemistry
Texas Southern University
Houston, Texas

ABSTRACT

A polarographic study has been carried out on the products formed in the interaction of cadmium(II) with 5-Hydroxy-2-(Hydroxymethyl)-4H-Pyran-4-one, using varying conditions of pH, supporting electrolyte, and concentration. Measurements using the differential pulse method show that cadmium(II) exhibits a molar combining ratio of complexing agents to cation ranging from 1 to 1 to 3 to 1 depending on the pH and the supporting electrolyte employed.

POLAROGRAPHIC STUDY OF CADMIUM 5-(Hydroxy-2-(Hydroxymethyl)-4H-Pyran-4-one COMPLEX

Introduction

Polarography has been applied variously to the quantitative determination of cadmium in different supporting electrolytes (1). The presence of relatively high concentrations and toxicity of cadmium in process wastewaters which contain phenolic type compounds resulting from coal gasification and liquefaction (1,2) gives rise to a need to study further the coordination chemistry of this metal. Further, the study of the polarography of cadmium could add to the understanding and ascertainment of this element as a possible trace metal in selected lunar like materials. A polarographic study of the interaction of selected organic complexing agents should add to the understanding of cadmium solution chemistry.

This study was undertaken to investigate the formation constants and determine the stoichiometry in a solution of the interaction of cadmium(II) with 5-Hydroxy-2-(Hydroxymethyl)-4H-Pyran-4-one, commonly called kojic acid. The polarographic data obtained using the differential pulse method revealed that the cadmium(II) exhibits complexes ranging from 1 to 1 to 3 to 1 molar ratio of complexing agent to cadmium. The formation constants for the cadmium complexes are supporting electrolyte and pH dependent.

At sufficiently negative potentials, simple and complex ions of cadmium are reduced at the dropping mercury electrode and dissolve in the mercury to produce an amalgam on the surface of the mercury drop. For a reversible electrode reaction involving complex metal ions, Kolthoff and Lingane (3) have shown that the half-wave potentials of metal ions are generally shifted to more negative values by complex ion formation. Further, these authors (3) have derived the relationship for calculating both the formation constant and the coordination number for metal complexes based on this negative shift as a function of the concentration of the complexing agent employed. Thus, according to Kolthoff and Lingane (3) reactions

$$M^{n+} + ze = M^{(n-z)+}$$

and

$$M^{n+} + xR^{-y} = MR_x{}^{(n-xy)}$$

give

$$E_{1/2}{}^{c} - E_{1/2}{}^{m} = \frac{-0.0591}{z} \log K_f - \frac{-0.0591x}{z} \log C_R \qquad (1)$$

where M^{n+}, $M^{(n-z)+}$, R^{-y}, $MR_x{}^{(n-xy)}$, $E_{1/2}{}^{c}$, $E_{1/2}{}^{m}$, and K_f, respectively represent the metal ion in oxidation state one, metal ion in state two, complexing agent, metal complex (where x is the coordination number of the metal ion), halfwave potential for the complex, half-wave potential for the simple metal ion, and the formation constant for the complex.

Theory of Phenolic Differential Polarography

Phenolic type compounds are generally strong complexing reagents because in the ionized form they have three pairs of electrons and a negative charge. Further, the stability of metal phenol complex ions is changed markedly by adjusting the pH of the solution. According to the law of mass equilibrium the ionization of phenol type compounds in aqueous media may be represented as follows:

$$RH_i = R^{i-} + iH^+ \tag{2}$$

and correspondingly, phenolic metal complex ion formation can be written in the following manner:

$$M^{n+} + xRH_i = [MR_x]^{(n-ix)+} + ixH^+ \tag{3}$$

The formation constant expression for the above reaction is

$$K_f = \frac{([MR_x]^{(n-ix)^+})(H^+)^{ix}}{(M^{n+})\ (RH_i)^x} \tag{4}$$

For a reversible reduction, at the dropping mercury electrode, to the metallic amalgam state of a complex ion of a metal that is soluble in mercury, one may represent the reaction as follows:

$$[MR_x]^{(n-ix)^+} = M^{n+} + xR^{i-} \tag{5}$$

$$M^{n+} + Hg + ze = M(Hg) \tag{6}$$

$$[MR_x]^{(n-ix)^+} + Hg + ze = xR^{i-} + M(Hg) \tag{7}$$

where equation 7 is the sum of equations 5 and 6.

Assuming the activities of mercury and the amalgam to be constant or unified and that molar concentrations may be employed in place of activities in dilute solutions within a moderate concentration range, one may reasonably propose that for phenolic complex ion solutions at constant temperature

$$E_{1/2} = f(\ln C_R, pH) \tag{8}$$

where C_R and C_H are the molar concentrations of the complexing agent and hydrogen ion respectively. Thus within the range of experimental data

$$dE_{1/2} = \left(\frac{\partial E_{1/2}}{\partial \ln C_R}\right)_{pH} dC_R + \left(\frac{\partial E_{1/2}}{\partial pH}\right)_{\ln C_R} dpH. \tag{9}$$

Kolthoff and Lingane (3) have shown previously that the effect of complexing agents on the half-wave potential at the dropping mercury electrode is generally to make the half-wave potential more negative. Similarly, based on equations 5 and 6, respectively, the reduction of the simple metal ions and the corresponding complex phenol metal ion at the dropping mercury electrode, one may express the simultaneous effect of complexing agent and pH on the half-wave potential as follows:

$$E_{1/2}^{c} = E_{c}^{o} - \frac{0.0591}{z} \log \frac{([MRx]^{(n-ix)^{+}})}{(R^{i-})^{x}} \tag{10}$$

$$E_{1/2}^{s} = E_{s}^{o} - \frac{0.0591}{z} \log (M^{n+}) \tag{11}$$

$$E_{1/2}^{c} - E_{1/2}^{s} = E_{c}^{o} - E_{s}^{o} - \frac{0.0591}{z} \log \frac{([MR_x]^{(n-ix)^{+}})}{(R^{i-})^{x}(M^{n+})} \tag{12}$$

where the subscripts c and s refer to the complex and simple metal ions, respectively, and the superscript o refers to the standard potential of each reaction. The substitution of the molar concentration ratio of the complexing agent ion from equation 4 or 4a into equation 11 gives

$$E_{1/2}^{c} - E_{1/2}^{s} = E_{c}^{o} - E_{s}^{o} - \frac{0.0591}{z} \log K_f \frac{(RH_i)^{x}}{(H^{+})^{ix}(R^{i-})^{x}}. \tag{13}$$

upon combining the $E_c^o - E_s^o$ and the $-0.0591 \log K_f$ terms in equation 13, one obtains equation 1:.

$$E_{1/2}^{c} - E_{1/2}^{s} = \frac{-0.0591}{z} \log K_f \frac{-0.0591}{z} \log \frac{(RH_i)^{x}}{(R^{i-})(H^{+})^{ix}} \tag{14}$$

where

$$E_{1/2}^{c} - E_{1/2}^{s} = \frac{-0.0591}{z} \log K_f \frac{-0.0591}{z} x \log \frac{(RH_i)}{(R^{i-})} \frac{-0.0591ix}{z} \log \frac{1}{(H^{+})} \tag{15}$$

$$E_{1/2}^{c} - E_{1/2}^{s} = \frac{-0.0591}{z} \log K_f \frac{-0.0591}{z} x \log \frac{(RH_i)}{(R^{i-})} \frac{-0.0591ix}{z} pH \tag{16}$$

Based on the above equation both pH and concentration of the complexing agent will cause the half-wave potential, $E_{1/2}^{c}$, of phenolic complexes to shift to more negative potentials. Moreover, it should be noted that neither the concentration of the metal complex nor the simple metal ion is a factor in equation 15; thus $E_{1/2}^{c}$ is not a function of these ions. However, equation 4 shows that the ratio of the concentration of complex to simple ion

$$\frac{[MR_x]^{(n-ix)^{+}}}{(M^{n+})} = K_f \frac{(RH_i)^{x}}{(H^{+})^{ix}} \tag{4a}$$

is proportional to the ratio of complexing agent to hydrogen ion. Thus $E_{1/2\,c}$ is an implicit function of the above ratio and not the concentration of the complex or simple metal ions. If the stability of the phenolic complex ion is a function of pH, then, based on equation 15, as the pH of a series of solutions containing a fixed amount of complexing agent approaches an upper limiting value, the $E_{1/2}$ of the solution should approach a limit of maximum half-wave potential $E_{1/2\,cm}$. Similarly, as the pH of the series approaches a lower limit, the $E_{1/2}$ of the solutions should approach a limit of minimum half-wave potential, $E_{1/2(sm)}$, the $E_{1/2}$ of the simple metal ion. At any constant pH, the magnitude of the quantity $E_{1/2(cm)} - E_{1/2(sm)}$ essentially corresponds implicity to the relative amounts of the complex and simple

metal ions in the solution. The molar concentrations of complex ions and simple ions should be equal at $\partial E_{1/2}/\partial pH^2 = 0$.

Firstly, the above discussion and theory show that the complexing agent and the pH simultaneously cause the half-wave potentials of phenolic complex ions to shift to more negative potentials, and, secondly, that differential polarographic study of the complex ion chemistry of these ions requires carefully controlled conditions of pH in excess, complexing agent concentration. A third consequence of the aforementioned theory is that a plot of $E_{1/2c} - E_{1/2s}$ or $E_{1/2c}$ vs. pH should give a graph with asymptotic lower and upper limits, a plot of $d(\Delta E_{1/2})/dpH$ vs. pH should give a parabolic plot, and a plot of $d^2(\Delta E_{1/2})/dpH^2$ vs. pH should give a graph with both a positive and a negative area.

In order to test the aforementioned theory, a cadmium complex in our laboratory was selected for study.

Experimental

Apparatus and Reagents. All polarographic measurements were obtained at 25°C employing a Sargent-Welch Voltammetric Analyzer Model 7000 Microprocessor. All data were collected using the differential pulse method (2) over the range -0.300 to -0.900 volt using a scan rate of 0.002 volt per second, a drop time of one second, and an excitation energy of 0.02 volt. All solutions were purged with N_2 for 10 minutes.

Standard solutions of cadmium(II) chloride in water were prepared from EM Science atomic absorption standards traceable to National Bureau of Standards. All other reagents employed in this study were reagent grade chemicals.

The effect of complex formation on the polarographic wave of the cadmium(II) complex was determined as follows: To a series of 50 ml volumetric flasks were added the desired volumes of standard cadmium(II) solution, the volume supporting the electrolyte required to give optimum buffer concentration, and varying concentrations of the chelating agent, and the solutions were diluted to volume with water. $Na_2B_4O_7$ supporting electrolyte was employed, and dilute aqueous NaOH or HNO_3 was added drop wise prior to dilution to obtain the final desired pH. These solutions show reproducible differential pulse peaks (used in place of half-wave potentials) within the region of -0.300 to -0.900 volts.

The kojic acid was purified as follows: The chelating agent was recrystallized after being dissolved in boiling ethanol mixed with finely divided charcoal. This solution was filtered while hot and allowed to recrystallize in a refrigerator at about 5°C. After discarding the alcohol, the chelating agent was dried and stored in a dessicator. The white crystallized solid gave a sharp melting point at 153°C.

Discussion

Differential pulse polarographic measurements obtained in these studies show that cadmium(II) reacts with excess chelating agent to form a 1 to 1, 2 to 1 and 3 to 1 cadmium to reagent products. The ionic strength and the activity coefficients of the reducible complex and the complexing agent were

assumed to be constant over the concentration range studied. Thus on rearranging, equation 16 becomes

$$\log K_f = -x\log C_R/C_R^{i-} - ix\,pH\,\frac{z}{0.0591}(E_{\nu_{2c}} - E_{\nu_{2m}}) \quad (17)$$

and on differentiation, equation 18 is obtained since $E_{\nu_2}^m$ for the simple metal ion is a constant.

$$\frac{\Delta E_{\nu_{2c}}}{\Delta pH} + 0.0591\,x\,\frac{\Delta\log C_R/C_R^{i-}}{\Delta pH} = \frac{-0.0591ix}{z} \quad (18)$$

at constant C_R/C_R^{i-}

$$\frac{\Delta E_{\nu_{2c}}}{\Delta pH} = \frac{-0.0591ix}{z} \quad (19)$$

and at constant pH, equation 16 becomes equation 1

$$\log K_f = x\log C_R + \frac{z}{0.0591}(E_{\nu_{2m}} - E_{\nu_{2c}})$$

which was used to calculate the formation constant for the cadmium(II) complexes. Since $E_{\nu_2}^m$ for the simple metal ion is a constant, knowing that cadmium(II) is reduced to cadmium metal at the dropping mercury electrode (4) corresponding to a two electron reduction, one can calculate x the molar combining ratio of complexing agent to the central metal ions for varying conditions of pH supporting electrolyte, etc.

Graphical and tabular data are shown in Figures 1 through 5 and Tables 1 through 9 for the systematic study of several cadmium(II) kojic acid complex ions. These results indicate that the composition and stabilities of the cadmium complex ions formed in these interactions, in the presence of excess chelating agent, depend on optimum conditions of pH and the nature of the supporting electrolyte. Figure 1 shows that all of the cadmium complex ions studied are reversibly reduced at the dropping mercury electrode. Graphical representations (Figure 2) and the data in Tables 1, 2, and 3 indicate that the stability and molar combining ratio of kojic acid to cadmium in ammonium hydroxide-ammonium chloride supporting electrolyte decreases as the pH increases. At pH = 8.38, the molar combining ratio of kojic acid to cadmium is 2 to 1. At pH ≥ 9.88, the molar ratio is 1 to 1.

In an attempt to obtain some understanding of the separate ligand ion effect in the aforementioned interactions, sodium borate was selected as a non-competing supporting electrolyte. The data in Tables 4, 5, 6, and 7 and Figure 3, employing sodium borate as a non-complexing supporting electrolyte, show that the molar-combining ratio of kojic acid to cadmium is 2 to 1 and does not depend on the pH of the solution in the pH range 9.8 to 10.8. The composite of these data, Tables 1 through 7, suggest that the ammonia molecule and/or the hydroxide ion may compete with kojic acid when relatively large concentrations of the three are present in the same solution. Data for the effect of pH at constant complex ion concentrations in borate medium are shown in Table 9 and Figure 5 as predicted.

The complexing effect of ammonium hydroxide on cadmium(II) in sodium borate supporting electrolyte is shown in Table 8 and Figure 4. Based on the magnitude of the formation constants in the two support-electrolytes, in the absence of knowing the exponential order of the mass law equations,

the cadmium ammine complex appears to be less stable than the cadmium kojic acid complex. The proposed cadmium ammonium hydroxide interaction in sodium borate supporting electrolyte is

$$Cd^{+2} + 3NH_4OH = [Cd(NH_3)_3(OH)]^+ + H^+ + 2H_2O$$

which indicates that cadmium exhibits a coordination number of 4 and a combining ratio of 3 to 1 of ammonium hydroxide to cadmium. Further, assuming kojic acid to be a bidentate ligand, one would expect kojic acid to cadmium interaction to give a combining ratio of 2 to 1 corresponding to a coordination number of 4. At a pH $\leq$8.38, in ammonium hydroxide-ammonium chloride buffer, the combining ratio of kojic acid to cadmium is 2 to 1. In the interval 8.38$\leq$pH$\leq$9.88, non-whole number combining ratios are obtained which suggest a mixture of complex species, resulting from competing complexation between kojic acid and ammine and/or hydroxide. At a pH$\leq$9.88, a combining ratio of 1 to 1 of kojic acid is obtained which suggests that the composition of the complex becomes constant.

Acknowledgment

The authors wish to express their sincere thanks to the United States National Aeronautics and Space Administration and the U.S. Department of Energy for grants which supported this study.

References

1. Drummond, C.J., Noceti, R.P., et. al., Envir. Prog., 40, 26-32 (1985).

2. Drummond, C.J., Noceti, R.P., et. al., Envir. Prog., 1, 73-78 (1982).

3. Kolthoff, I.M. and Lingane, J.J., "Polarography," 1, 2nd., Interscience Publishers, N.Y., (1952), pp. 189-234.

4. Rubinson, K.A., "Chemical Analysis," Little, Brown, Con., (1987), p. 413.

5. Meites, L., "Polarographic Techniques," Interscience Publishers, N.Y. (1967), p. 268.

6. Kolthoff, I.M. and Lingane, J.J., "Polarography," 2, (1952) p. 475-511.

TABLE 1

Cadmium(II) Micromolar	Kojic Acid Millimolar	Diffusion Current Nanometers	Half-Wave $E_{\frac{1}{2}}$, Volts	Formation Constant
89	0	34	-0.623	
89	0.79	34	-0.610	5.74×10^5
89	1.74	33	-0.630	5.72×10^5
89	3.16	35	-0.645	5.57×10^5
89	5.01	34	-0.657	5.66×10^5
89	10.00	34	-0.674	5.36×10^5
89	25.00	34	-0.698	5.52×10^5
89	54.95	34	-0.717	5.07×10^5

Supporting Electrolyte: 0.08 M NH_3/NH_4Cl Avg. $K_f = 5.52 \times 10^5 \pm 0.24$

Coordination Number: 2 pH: 8.38

TABLE 2

Cadmium(II) Micromolar	Kojic Acid Millimolar	Diffusion Current Nanometers	Half-Wave $E_{\frac{1}{2}}$, Volts	Formation Constant
89	0	34	-0.666	
89	0.79	35	-0.670	1.74×10^3
89	1.74	34	-0.679	1.58×10^3
89	3.16	34	-0.687	1.62×10^3
89	5.01	34	-0.693	1.66×10^3
89	10.00	33	-0.702	1.66×10^3
89	25.00	34	-0.714	1.70×10^3
89	54.95	34	-0.724	1.70×10^3

Supporting Electrolyte: 0.2 M NH_3/NH_4Cl $K_f = 1.67 \times 10^3 \pm 0.05$

Coordination Number: 1 pH: 9.88

TABLE 3

Cadmium(II) Micromolar	Kojic Acid Millimolar	Diffusion Current Nanometers	Half-Wave $E_{\frac{1}{2}}$, Volts	Formation Constant
89	0	34	-0.704	
89	0.79	34	-0.688	3.63×10^2
89	1.74	33	-0.698	3.63×10^2
89	3.16	34	-0.706	3.70×10^2
89	5.01	34	-0.712	3.72×10^2
89	10.00	34	-0.721	3.77×10^2
89	25.00	34	-0.733	3.80×10^2
89	54.95	34	-0.743	3.82×10^2

Supporting Electrolyte: 0.4M $NH_3 - NH_4Cl$ $K_f = 3.72 \times 10^{-2} \pm 0.006$

Coordination Number: 1 pH: 10.15

TABLE 4

Cadmium(II) Micromolar	Kojic Acid Millimolar	Diffusion Current Nanometers	Half-Wave $E_{\frac{1}{2}}$, Volts	Formation Constant
89	0	34	-0.527	
89	5.01	33	-0.572	1.33×10^6
89	13.80	33	-0.598	1.34×10^6
89	20.40	34	-0.607	1.27×10^6
89	50.10	35	-0.630	1.23×10^6
89	100.00	34	-0.647	1.17×10^6
89	199.50	34	-0.665	1.20×10^6

Supporting Electrolyte: 0.04 M $Na_2B_4O_7$ Avg. $K_f = 1.25 \times 10^6 \pm 0.07$

Coordination Number: 2 pH: 7.00

TABLE 5

Cadmium(II) Micromolar	Kojic Acid Millimolar	Diffusion Current Nanometers	Half-Wave $E_{\frac{1}{2}}$, Volts	Formation Constant
89	0	34	-0.535	
89	5.01	34	-0.614	1.90×10^7
89	13.80	34	-0.640	1.90×10^7
89	20.40	35	-0.650	1.90×10^7
89	50.10	34	-0.673	1.90×10^7
89	100.00	34	-0.691	1.94×10^7
89	199.50	34	-0.708	1.84×10^7

Supporting Electrolyte: 0.04 M $Na_2B_4O_7$ Avg. $K_f = 1.90 \times 10^7 \pm 0.03$

Coordination Number: 2 pH: 8.00

TABLE 6

Cadmium(II) Micromolar	Kojic Acid Millimolar	Diffusion Current Nanometers	Half-Wave $E_{\frac{1}{2}}$, Volts	Formation Constant
89	0	34	-0.558	
89	5.01	34	-0.632	1.28×10^7
89	13.80	33	-0.658	1.29×10^7
89	20.40	35	-0.669	1.39×10^7
89	50.10	34	-0.692	1.39×10^7
89	100.00	34	-0.710	1.42×10^7
89	199.50	34	-0.727	1.34×10^7

Supporting Electrolyte: 0.04 M $Na_2B_4O_7$ Avg. $K_f = 1.35 \times 10^7 \pm 0$ 06

Coordination Number: 2 pH: 9.00

TABLE 7

Cadmium(II) Micromolar	Kojic Acid Millimolar	Diffusion Current Nanometers	Half-Wave $E_{\frac{1}{2}}$, Volts	Formation Constant
89	0	33	-0.574	
89	5.01	34	-0.633	3.98×10^6
89	13.80	34	-0.658	3.69×10^6
89	20.40	35	-0.669	3.98×10^6
89	50.10	34	-0.692	3.98×10^6
89	100.00	33	-0.710	4.08×10^6
89	199.50	34	-0.727	3.86×10^6

Supporting Electrolyte: 0.04 M $Na_2B_4O_7$ Avg. $K_f = 3.93 \times 10^6 \pm 0.15$

Coordination Number: 2 pH: 10.00

TABLE 8

Cadmium(II) Micromolar	Ammonium Hydroxide Millimolar	Diffusion Current Nanometers	Half-Wave $E_{\frac{1}{2}}$, Volts	Formation Constant
89	0	34	-0.544	
89	30.00	34	-0.572	3.23×10^5
89	50.00	34	-0.591	3.11×10^5
89	100.00	34	-0.618	3.22×10^5
89	150.00	34	-0.634	3.24×10^5
89	200.00	34	-0.645	3.34×10^5
89	251.19	34	-0.654	3.38×10^5

Supporting Electrolyte: 0.04 M $Na_2B_4O_7$ $K_f = 3.25 \times 10^5 \pm 0.096$

Coordination Number: 3 pH: 9.8 to 10.8

TABLE 9

Cadmium(II) Micromolar	Kojic Acid Millimolar	$Na_2B_4O_7$ Millimolar	pH	Diffusion Current Nanometer	Half-Wave $E_{\frac{1}{2}}$, Volts
89	13.7	30.0	2.00	34	-0.528
89	13.7	30.0	3.00	34	-0.530
89	13.7	30.0	4.00	34	-0.532
89	13.7	30.0	5.00	34	-0.534
89	13.7	30.0	6.00	35	-0.562
89	13.7	30.0	6.50	34	-0.581
89	13.7	30.0	7.00	36	-0.605
89	13.7	30.0	7.50	34	-0.635
89	13.7	30.0	8.00	33	-0.655
89	13.7	30.0	8.50	34	-0.663
89	13.7	30.0	9.00	34	-0.667
89	13.7	30.0	9.50	35	-0.667
89	13.7	30.0	10.00	34	-0.667
89	13.7	30.0	10.50	34	-0.669
89	13.7	30.0	11.00	34	-0.667

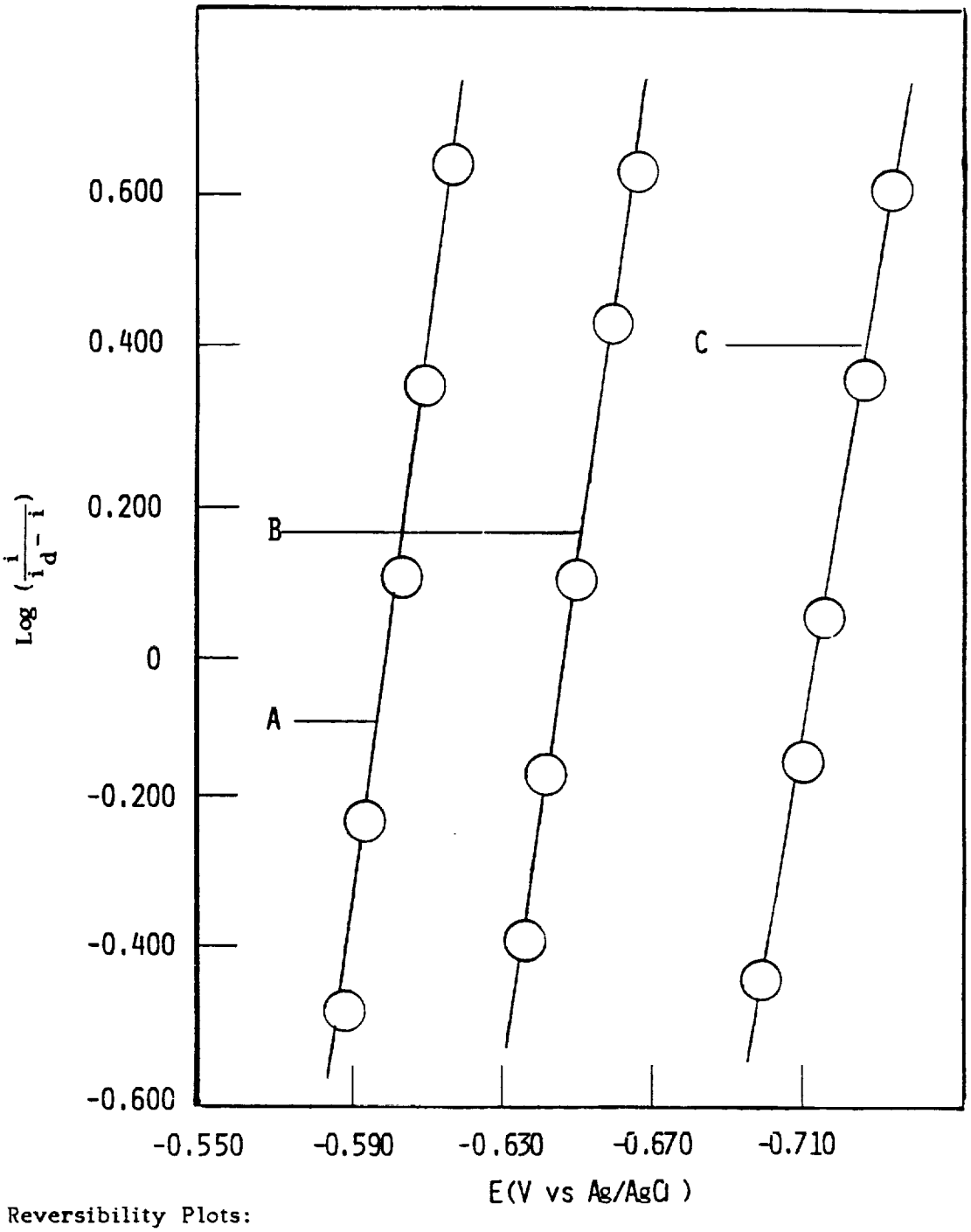

Reversibility Plots:

A — pH - 8.00 - 0.04m $Na_2B_2O_4$ + 89um Cd(II) + 13.8m Mol Kojic Acid

B — pH - 10.15 - 0.04m $Na_2B_2O_4$ + 89um Cd(II) + 100m Mol NH_4OH

C — pH - 8.38 - 0.08m NH_3/NH_4Cl + 89um Cd(II) + 13.8m Mol Kojic Acid

Figure 1

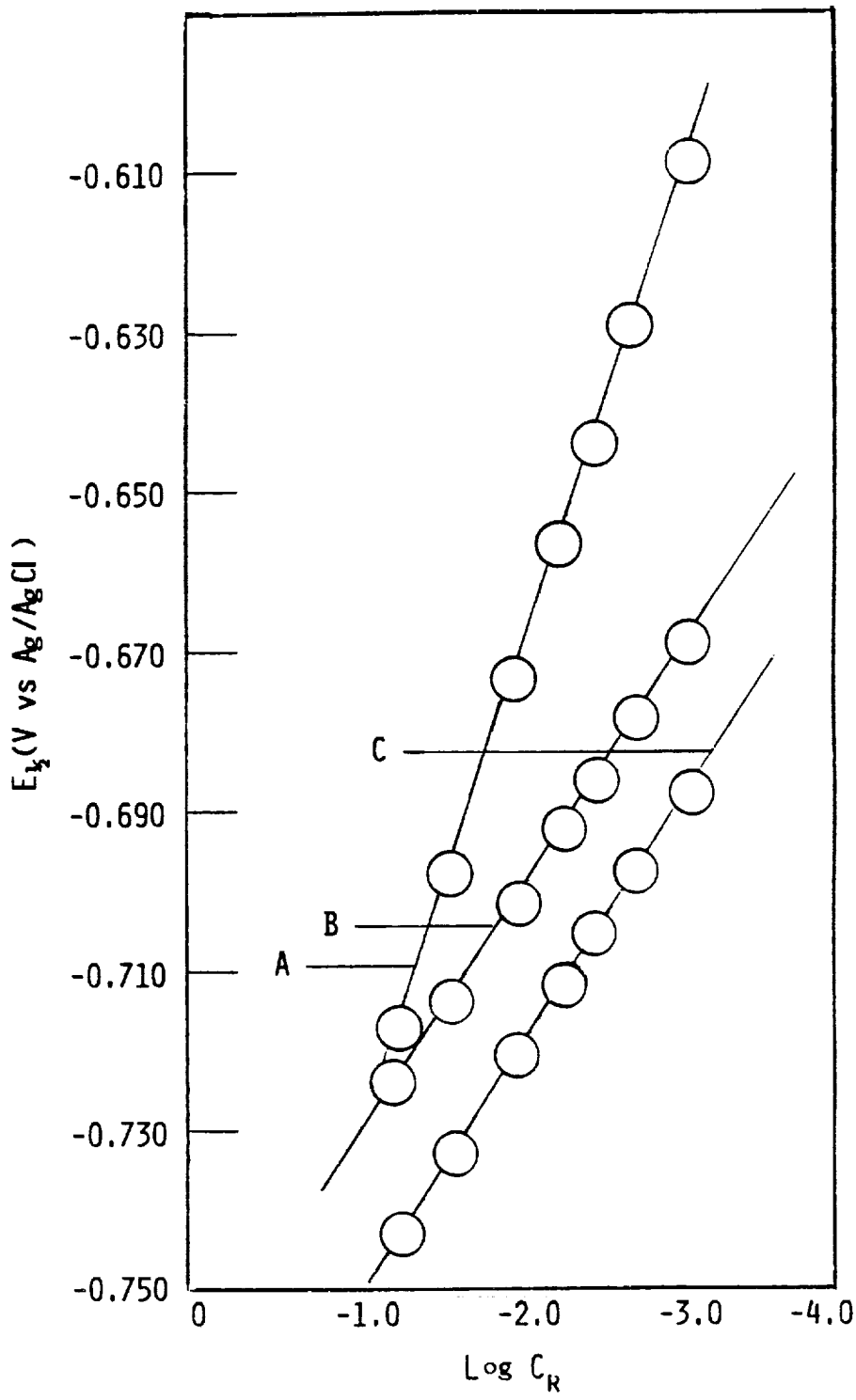

Effects of Complexing Agent Concentration on the Half-Wave Potential of Cadmium in 0.4M NH_3-NH_4Cl at (a) pH-8.38; (b) pH-9.88; (c) pH-10.15

Figure 2

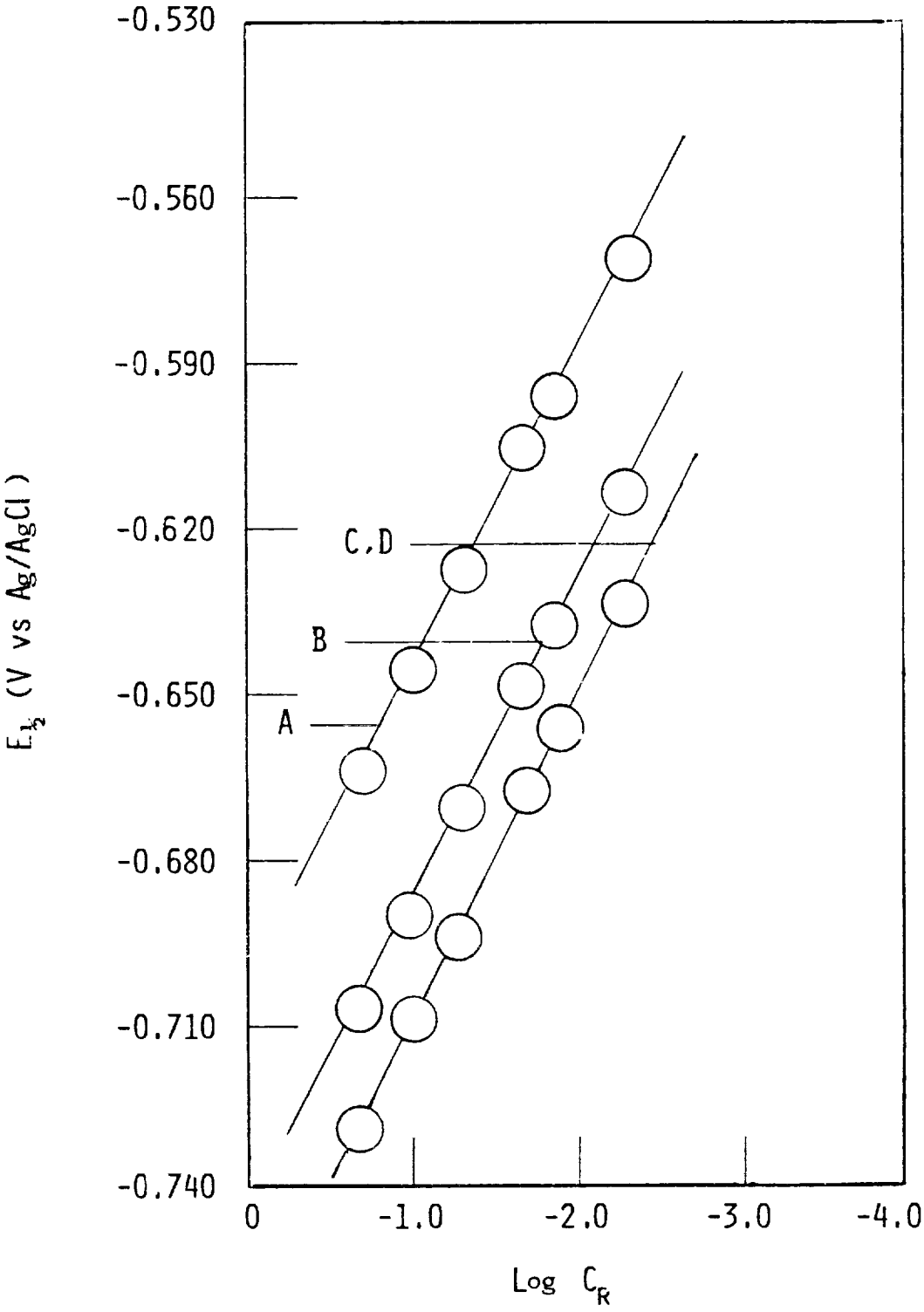

Effects of Complexing Agent Concentration on the Half-Wave Potential of Cadmium in 0.04 M $Na_2B_4O_7$ at (a) pH-7; (b) pH-8; (c) pH-9 and pH-10

Figure 3

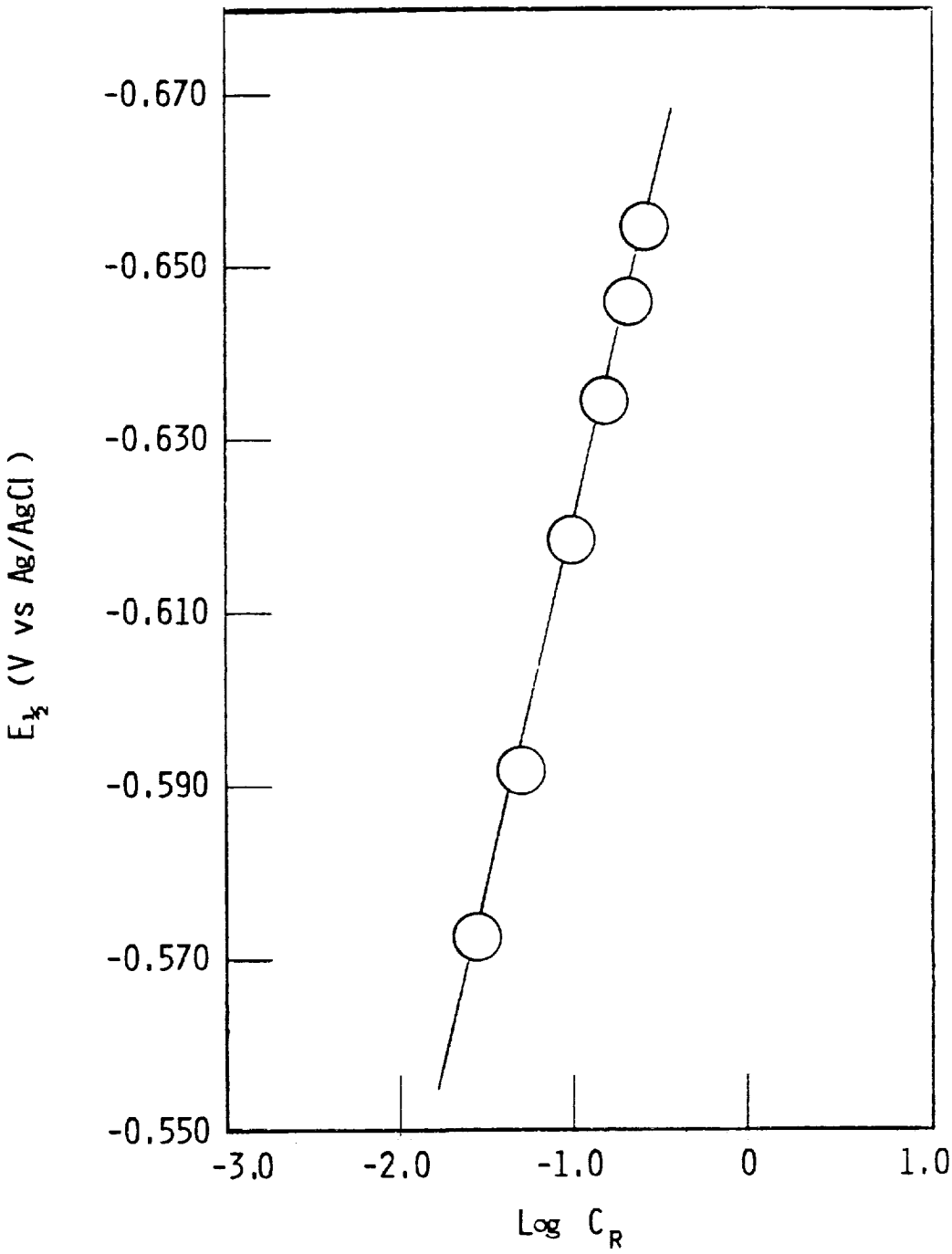

Effects of Complexing Agent Concentration on the Half-Wave Potential of Cd(II) in 0.10 M NH_4OH

Figure 4

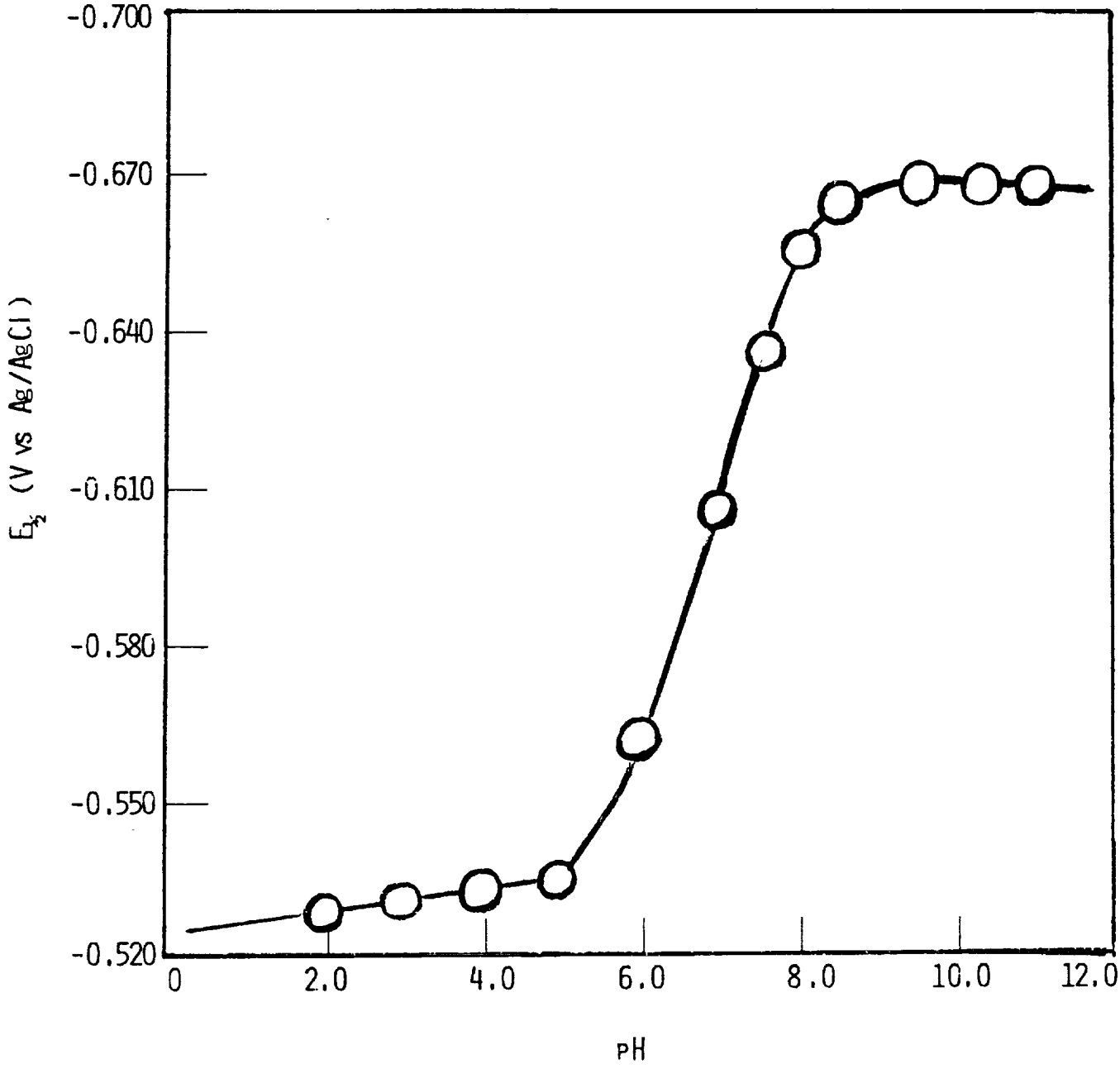
-0.700
-0.670
-0.640
-0.610
-0.580
-0.550
-0.520
$E_{1/2}$ (V vs Ag/AgCl)
0
2.0
4.0
6.0
8.0
10.0
12.0
pH

Figure 5

N91-28089

PURIFICATION, GROWTH AND CHARACTERIZATION OF $Zn_xCd_{1-x}Se$ CRYSTALS

E. Silberman, A. Burger, W. Chen, D. O. Henderson,
S. H. Morgan, J. M. Springer and Y. Yao

Physics Department
Fisk University
Nashville, TN

ABSTRACT

We report here on the purification of starting materials which were used in growth of $Zn_xCd_{1-x}Se$ (x=0.2) single crystals using the traveling solution method (TSM). Up to 13 cm long single crystals and as grown resistivities of $6X10^{12}$ohm.cm could be achieved. Infrared and Raman spectra of $Zn_{0.2}Cd_{0.8}Se$ are also presented and discussed.

6 x 10 (exp 12)

isotherm

PURIFICATION, GROWTH AND CHARACTERIZATION OF $Zn_xCd_{1-x}Se$ CRYSTALS

Introduction

The existence of the $Zn_xCd_{1-x}Se$ single crystal system was demonstrated as early as 1951 (1) and its potential for optoelectronic applications is due to the possibility of obtaining variable energy gaps from 1.74 to 2.67 eV. The materials are interesting as phosphors for color TV applications (2) and, more recently, the lasing properties of $Zn_xCd_{1-x}Se$ single crystals, for x=0.33, were reported (3).

Growth of medium resistivity crystals of $Zn_xCd_{1-x}Se$ has been demonstrated in the past using the temperature gradient solution zoning (TGSZ) method (4). Following this development, $Zn_xCd_{1-x}Se$ has been proposed (5) as an alternate material to CdSe for room temperature nuclear radiation detection because replacement of Cd by Zn in the crystal lattice results in an increased energy band gap and a higher resistivity material, which is a prerequisite for such an application. Crystal growth using the traveling solution method (TSM) was sucessfully applied to the growth of tellurides (6,7), resulting in low contamination and good crystalline perfection. It was therefore interesting to determine the possibilities of this method in the case of selenides, which involve higher growth temperature and pressure.

In this paper we present the steps completed in our research program, which include: the purification of raw materials; the crystal growth using the traveling solution method (TSM), which, to the best of our knowledge, is the first attempt to use this technique for the growth of selenide crystals; and the characterization of the as-grown crystals by electric measurements and by Raman and infrared spectroscopy.

Experimental

a)Purification. CdSe commercial reagents (Alfa, 99.999% purity on a metal basis, and General Electric, electronic grade) were subjected to repeated vacuum sublimations at 700 and 1000°C. Unlike Cd and Zn, Se is not commercially available in high enough purity and therefore we used Se of 99.999% purity (Johnson Matthey) which was further purified in a laboratory built zone refiner.

b)Crystal growth. Up to 40 g of raw material composed of Zn and Cd having 99.9999% purity (Cominco), in the desired composition, together with a stoichiometric amount of Se of 99.999% purity (Johnson Matthey) were loaded in a quartz reaction ampule. The ampule was vacuum sealed at 10^{-5} torr, mounted in a laboratory designed and built rocking furnace, and then the temperature was increased slowly (100°C/day) up to 900°C. After two weeks the reaction was completed and the charge was used as starting material, together with 10% additional Se, in the crystal growth experiment. The crystal growth ampule had an internal diameter of 1 cm and was 26 cm long. The crystal growth system included a three zone furnace mounted on a vertical translational stage. The middle zone was narrow, (approx. 5 cm) with the highest temperature slowly (10°C/min) increasing to 1170°C, while the upper and lower zones were kept at 970°C. The ampule was static and the furnace was moved upwards at 0.5 to 2 cm/day.

c) Characterization. Samples were prepared by cleaving the crystal along the a or c planes, followed by grinding and polishing to the desired thickness. Lapping and etching were performed in a solution containing 10% bromine in methanol. Electric contacts were applied using aquadag paint or by vacuum evaporation of Au. A SPEX Model 1403 Double Spectrometer and a Coherent Model Innova 90 Ar laser (514.5 nm, 800 mW) were used to record the Raman spectra. The Fourier transform infrared spectra were recorded in the 400- 4000 cm^{-1} range using a Bomem DA.3 FT-IR spectrometer.

Results and Discussion

The diffuse reflectance infrared Fourier transform (DRIFT) spectra of the raw material, CdSe powder purchased from two different vendors, have shown the presence of peaks which can be assigned to the sulphate group. The reaction of $CdSO_4$ with H2Se is one common way to synthesize CdSe, and the presence of an unreacted residue of $CdSO_4$ could be the explanation for these impurity bands. DRIFT spectra of repeated vacuum sublimed powders showed that the SO_4^{-2} bands disappeared, due probably to thermal decomposition. However, the method was probably not sufficiently efficient in removing the sulphur impurity. CdSe crystals grown using this purification method have shown a new band appearing at 540 cm^{-1}, which was attributed to sulphur impurity induced modes (8). We have therefore used the synthesis from Zn, Cd and Se elements as preparation of the starting material for crystal growth using TSM. Up to 13 cm long single crystals could be grown using the above technique. Fig. 1 shows an infrared transmittance spectrum obtained from a 0.5 mm thick sample. The absence of any major band around 540 cm^{-1} proves that synthesis from elements results in $Zn_xCd_{1-x}Se$ crystals having less S impurity. We did not observe a broad band, such as the one seen in the 500 to 1200 cm-1 region in Bridgman grown CdSe (8), which was attributed to infrared absorption by free carriers in non-stoichiometric (Cd-rich), low resistivity crystals. The I-V curve of an as-grown $Zn_{0.2}Cd_{0.8}Se$ sample is shown in Fig. 2. From the slope of the graph we can calculate a resistivity of $6X10^{12}$ ohm.cm, which is the highest reported for this class of ternary compounds (4).

The vibrational properties of $Zn_xCd_{1-x}Se$ were studied using Raman scattering and the spectra are shown in Fig. 3. The general features agree with a previous study (9) where crystals were in the x=0.4 to 1 composition range. From Valakh et al. (9) spectra and from our spectra it can be concluded that $Zn_xCd_{1-x}Se$ belongs to the one-mode type of crystals in which the frequency of the LO-phonon changes continuously versus crystal composition.

More work is under way to calibrate these LO frequencies against actual composition as determined by chemical analysis, which will enable us to use Raman measurements for determinations of Zn/Cd molar ratio distributions along the crystalline boule.

Acknowledgment

The research was sponsored by NASA, Grant no. NAG8-113.

References

1. S. Forgue, R. Goodrich and A. Cope, RCA Rev., 1951, 12, 335.
2. W. Lehmann, J. Electrochem. Soc. 1966, 113, 449.
3. J. Khurgin, B.J. Fitzpatrick and W. Seemungal, J. Appl. Phys. 1987, 61(4), 1606.
4. A. Burger and M. Roth, J. of Cryst. Growth, 1984, 70, 7.
5. A. Burger and M. Roth, I.E.E.E. Trans. Nucl. Sci., 1985, 32, 556.
6. R. Triboulet and Y. Marfaing, J. Electrochem. Soc., 1973, 120/9, 1260.
7. R. Triboulet and G. Didier, J. Cryst. Growth, 1975, 28, 29.
8. A. Burger, D. Henderson, S. Morgan and E. Silberman, to be published.
9. M. Ya. Valakh, M. P. Lisitsa, G. S. Pekar, G. N. Polysskii, V. I. Sidoprenko, and A. M. Yaremko, Phys. Stat. Sol. (b), 1982, 113, 635.

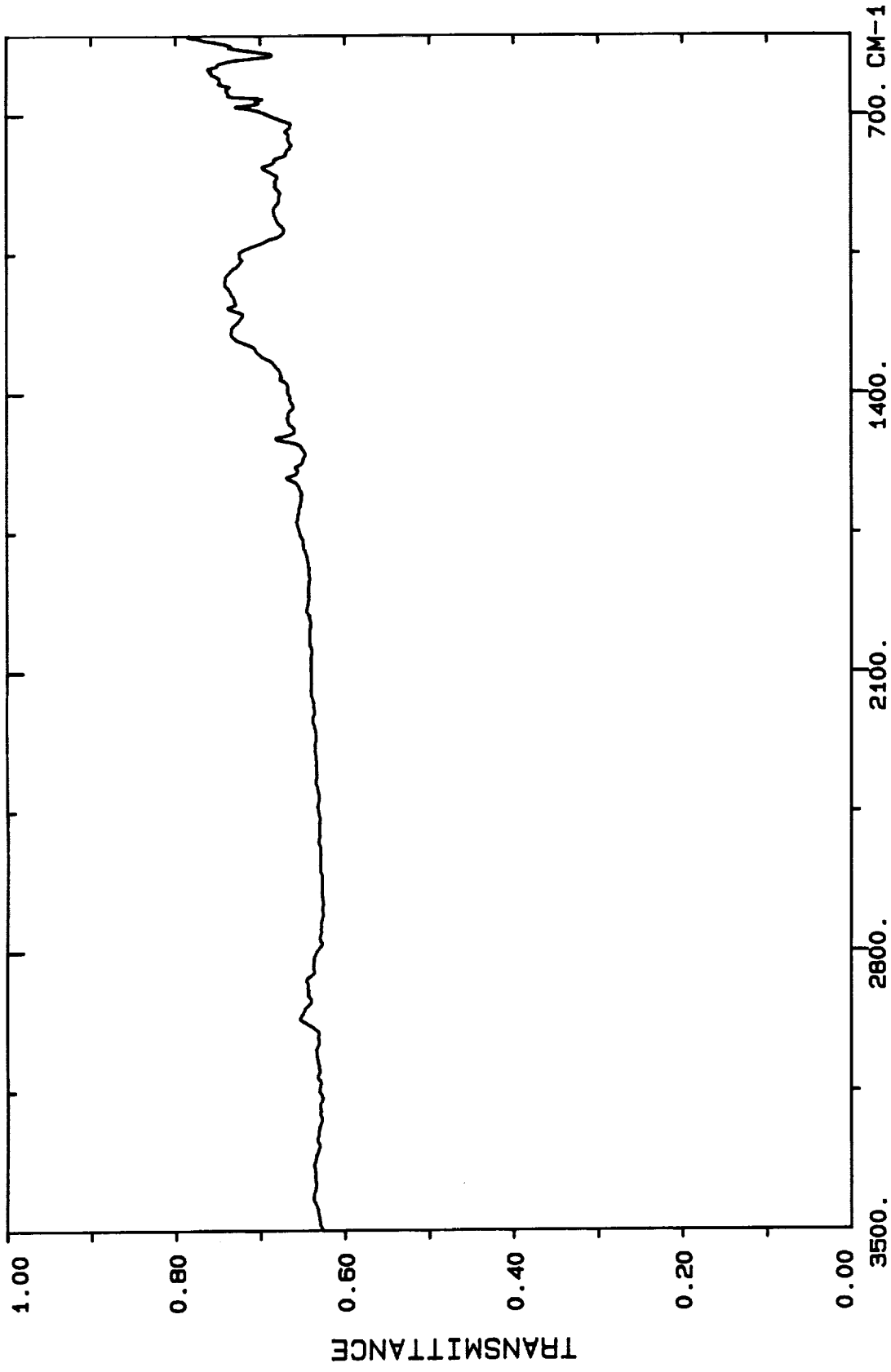

Figure 1.
Infrared transmittance spectrum from a 0.5 mm thick $Zn_{0.2}Cd_{0.8}Se$ single crystal.

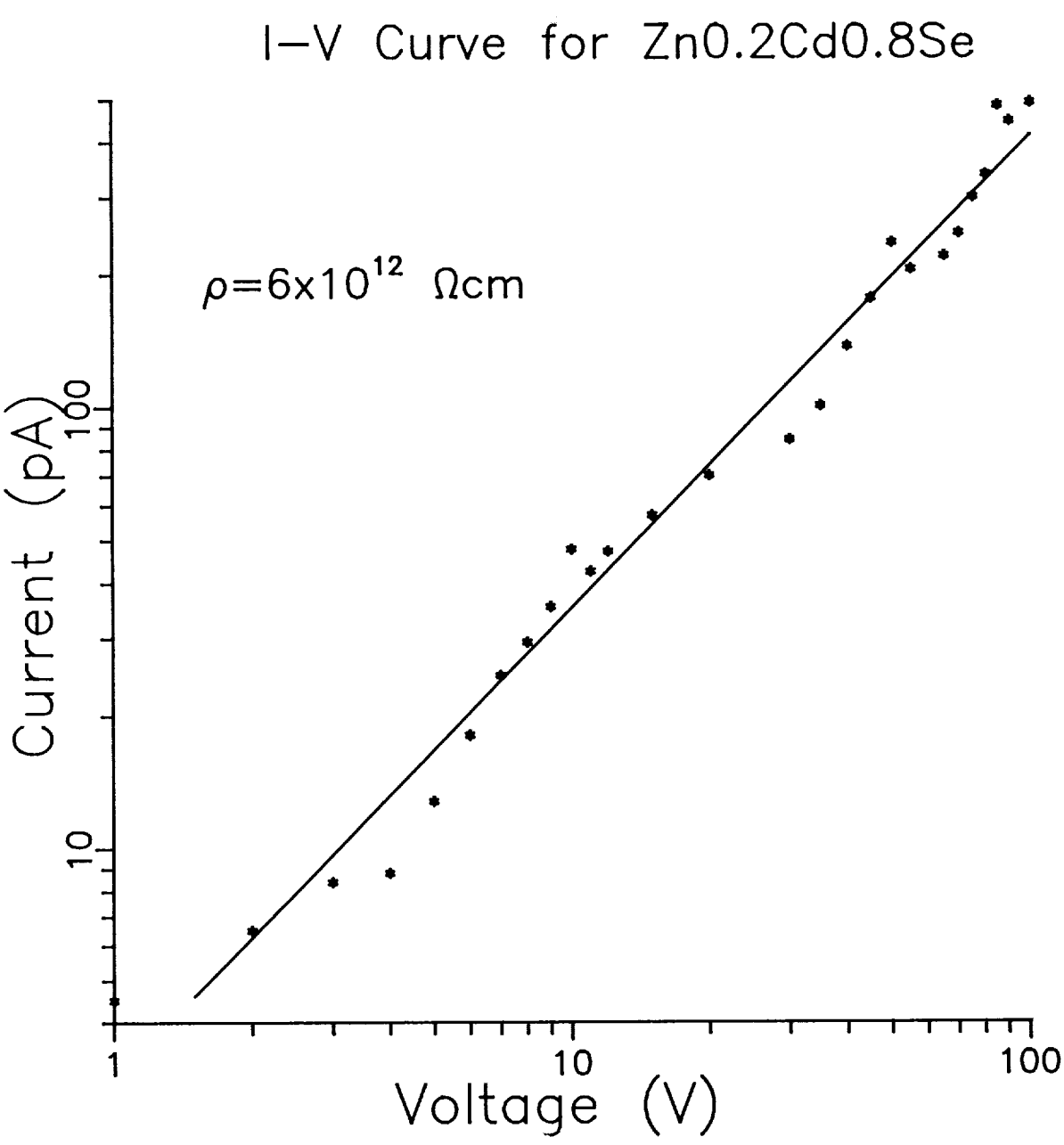

Figure 2.
The I-V curve of an as-grown $Zn_{0.2}Cd_{0.8}Se$ sample, 0.15 cm thick, 0.06 cm^2 contact area.

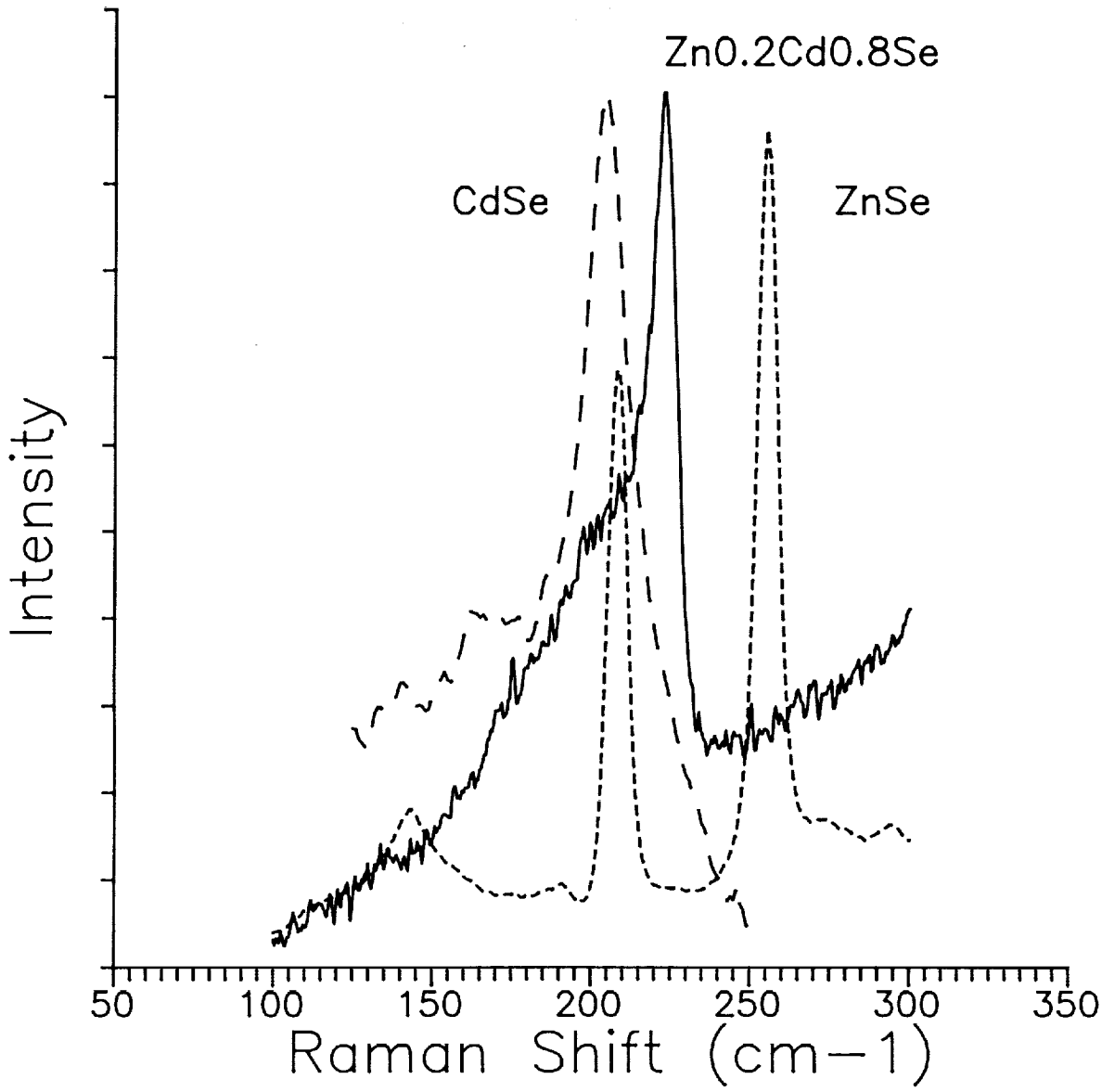

Figure 3.
Raman scattering spectra for CdSe, $Zn_{0.2}Cd_{0.8}Se$ and ZnSe single crystals.

A SCANNING ELECTRON MICROSCOPY STUDY OF THE MACRO-CRYSTALLINE STRUCTURE OF 2-(2,4-DINITROBENZYL) PYRIDINE

Jacqueline Ware and Ernest Hammond,Jr.
Morgan State University
Baltimore, MD

and

Gerald R. Baker
Technical Monitor
Laboratory of Astronomy and Solar Physics
Goddard Space Flight Center

ABSTRACT

The compound, 2-(2,4-dinitrobenzyl) pyridine, was synthesized in the laboratory; an introductory level electron microscopy study of the macro-crystalline structure was conducted using the scanning electron microscope (SEM). The structure of these crystals was compared with the macro-structure of the crystal of 2-(2,4-dinitrobenzyl) pyridinium bromide, the hydrobromic salt of the compound which was also synthesized in the laboratory. A scanning electron microscopy crystal study was combined with a study of the principle of the electron microscope.

A SCANNING ELECTRON MICROSCOPY STUDY OF THE MACRO-CRYSTALLINE STRUCTURE OF 2-(2,4-DINITROBENZYL) PYRIDINE

Theory of Color Change

Sandy colored crystals of the 2-(2,4-dinitrobenzyl) pyridine have the unusual property of turning a deep blue color when exposed to sunlight. The deep blue color can then revert again to sandy color when kept in the dark. This color change from sandy to deep blue takes only a few minutes; however, the color change from deep blue back to sandy takes about one day in the dark. Observations show that the interconversions are reversible an unlimited number of times. The phenomenon is explained by the formation of a tautomeric form by the action of light.

In the presence of light the sandy colored dinitro compound rearranges to the deep blue colored acid-nitro tautomer. In doing so, the sandy colored compound undergoes intramolecular hydrogen bonding. A proton (H+) is transferred from the methyl group to the oxygen of the nitro group. This results in extended conjugation of multiple bonds in the blue tautomer (shown in the encircled group). This chromophore is responsible for producing the color in the blue tautomer.

Visible ultraviolet spectroscopy, providing information of conjugation, confirms that the blue tautomer has a greater degree of conjugation. Maximum absorption of radiation is expected to take place at a longer wavelength for the compound with the greater number of conjugated multiple bonds. Maximum absorption occurs at a wavelength of 248 nm for the sandy compound and 567 for the blue compound.

Superiority of the Electron Microscope Over the Light Microscope

The macro-crystalline structures of the photochromic compound, 2-(2,4-dinitrobenzyl) pyridine and its salt, 2-(2,4-dinitrobenzyl) pyridinium bromide, were studied using the scanning electron microscope (SEM). The SEM along with a high speed-camera was used to magnify, photograph, study, and compare the small details of the macro-structure of the crystals. It is the overwhelming superiority of the electron microscope that allows the observation of minute details, such as the inner structure of tiny crystals (note micrograph 3.8), which exceeds the scope of the light microscope.

The principle of this 20th century invention reveals its high degree of superiority over the light microscope. With the optical microscope, it is the wave length of light that places an ultimate limit to the resolution or the smallest distance between two points at the object that can be seen separately through a microscope. The overwhelming superiority of the electron microscope is due to the fact that the wavelength of the electron can be many thousand times smaller than the wavelength of light.

Whenever the size of an object in front of a wave is about the same size as the wavelength of the wave, the wave will bend or diffract around it. To project the outline of an object on a screen, one must use a wave whose wavelength is very small compared with the object. Visible light has a wavelength of about 0.5×10^{-6}m so it is hard to see the outline of a body whose diameter is about 0.5×10^{-6}m. The

electron can have a wavelength of 10^{-10}m so the outline of an atom whose diameter is 10^{-10}m is barely perceptible for this wavelength. Electrons will form a sharp shadow of viruses having a diameter of about 10^{-6}m, while visible light will diffract around them. A small wavelength gives the most accurate measurement of a body's position. The behavior of electrons in this manner is an example of the wave-particle duality set forth by Louis de Broglie in 1924.

The more powerful lens microscope can magnify an object only about 2,000 times its own diameter. An electron microscope magnifies about 200,000 times, or 100 times as much as an ordinary microscope. This image can also be photographed and magnified to approximately 800,000 times the original diameter, or 400 times as much as a regular microscope magnifies. The electron microscope has a theoretical resolution of about 3A which is about the distance between atoms in solids. The scanning tunneling electron microscope can attain an amazing vertical resolution of about 0.1A. At the same time, the great depth of focus, which is about 300 times that of a light microscope, endows images of objects with a life-like, three dimensional quality. This is lacking in the light microscopes of the same magnification. Operation at the ultimate peak of performance requires a well-experienced microscopist.

Principle of Electron Microscopes

Electrons are strongly scattered by all forms of matter including air. Therefore, the electron microscope must be evacuated to about 10^{-4}mm Hg (10^{-7}atmospheric pressure). The lenses cannot be material in nature. They are electric or magnetic fields, which are symmetrical about the axis of the instrument. The source of electrons is housed in the electron gun which shoots beams of electrons toward the object. The electron source relies on high temperatures to enable a fraction of the free electrons in the cathode material to overcome the barrier of the work function and leave. In effect, the electrons are "boiled out" of the cathode material. The electron source is an incandescent, hairpin-shaped filament of tungsten (W) or lanthanum hexaboride (LaB_6), surrounded by electrodes which accelerate and collect the electrons in a narrow, intense beam. The electron gun can operate at voltages of 1-100kV.

Highly accelerated beams of electrons from the electron gun are focused by the electron lens into a tiny spot. The electric or magnetic field, or a combination thereof, which comprises the lens, acts upon an electron beam in a manner analogous to that in which an optical lens acts upon a light beam.

The condenser and objective or probe-forming electron lenses serve to demagnify the image of the crossover, the narrowest cross section of the beam from the electron gun. The condenser lens determines the beam current, and the probe-forming lens determines the final spot size of the electron beam which impinges upon the sample. The electron beam is focused by the electromagnetic field of the magnetic lens as the electrons travel down the column or bore of the lens.

In the axially symmetrical condenser lens, solenoid windings of copper wire are used to induce a magnetic field (when traversed by electric current). The solenoid windings are surrounded by an iron mantle, except for a gap in the iron core representing the distance between the north and south pole pieces of the lens. The magnetic strength of the lens is stronger by the presence of the iron core than in its absence. At the gap, the concentrated magnetic field forms the electron lens having a focal length of one eighth to about one sixteenth of an inch, which is inversely proportional to the strength of the lens. The lens height is 10-15 cm in a 30 Kv SEM. The strength (or intensity of the magnetic field) of the magnetic lens in the gap is proportional to the flow of current through the lens, as well as the number of turns in the solenoid winding.

Production of a minimum electron spot size begins with the reduction of the electron beam at crossover (50 um for a tungsten hairpin) to a greatly reduced scale. An electron image of the crossover passes through the condenser lens, and it is focused to a smaller intermediate diameter. The distance the electrons are focused is varied by changing the strength of the condenser lens system. If the current is increased, then the strength of the lens increases, and the demagnification increases (the focused spot gets smaller). Also, the divergence of the electron ray from the focused spot will increase. Less beam current will enter the final probe-forming lens, to obtain a minimum probe size which improves resolution. The condenser lens can be focused to allow most of the electron beam to pass through the aperture of the objective lens, to obtain maximum beam current and signal. Consequently, one can decide between maximum beam and current signal, or lose current but have minimum probe size for optimum resolution.

In the scanning electron microscope a fine electron beam is focused on a thick specimen and the pattern of the reflected electrons is displayed on a television-like image tube. A mechanical stage allows scanning of the object. The image can be photographed on regular photographic film. However, the problems and complexities of high-voltage electron microscopes limit their application.

Scanning Electron Microscopy Crystal Study

Sample preparation for observation in the electron microscope involved mounting the sample on a specimen stub with silver paint, and coating the crystal sample with a thin film of conducting material of gold-palladium by the process called sputter coating. This was done to eliminate or reduce the electric charge which can build up in a non-conducting sample when scanned by a high-energy electron beam. The coating provides a conducting path and should help eliminate the problems associated with charging.

The electron micrographs show the expected variations in crystal shapes, sizes, and lengths for crystals not grown in a controlled environment. Micrograph 1.1, for example, shows crystals of various shapes and sizes at low magnification.

The samples were coated by the process of sputter coating. By this process, an energetic ion or neutral atom of argon gas accelerates towards and strikes the surface of the negatively biased gold-palladium target and imparts momentum to the atoms. Some of the atoms of the target may receive enough energy in the collision to break bonds with neighboring atoms and be carried away from the solid, if the velocity imparted to them is sufficient. Electrons are ejected from the negatively charged target, discharging a glow normally associated with sputter coating. As the electron accelerates towards the positive anode, under the influence of an applied voltage, it may collide with a gas molecule, leaving behind an ion and an extra free electron. The positive ions then accelerate towards the negatively biased gold-palladium target where they cause sputtering as the atoms lying near the surface of the target are ejected in this collision and sputtered onto the sample as a thin film deposit of gold-palladium.

Micrograph 1.1 shows one of the advantages of sputter coating. The target atoms, after collision, are traveling in all directions as they sputter coat on the surface of the sample. In this way, the target atoms are able to "go around corners" and achieve a complete coating without the need of rotating or tilting the sample. An artistic pile-up of crystals can be adequately coated by sputter coating.

Some disadvantages of sputter coating can be seen in micrographs 3.4 and 3.8. These include thermal damage due to heat of radiation from the target and electron bombardment of the sample.

Another potential problem is surface etching. It is attributed to either stray bombarding gas ions, or metal particles hitting the surface with sufficient force to erode it away. In micrograph 3.2 the crystal in the center contains many small holes sometimes found in sputter coated samples. At a magnification of about 2,000, micrograph 3.8 shows surface erosion and sample destruction at a pitted area. It is not known for certain whether the very small holes found in sputter coated samples, examined at high resolution, are the result of surface etching or just thermal damage. Thermal damage, when it occurs, is manifested as melting, pitting, and in extreme cases, complete destruction of the sample. But this is thought to be mainly due to the sample being subjected to inordinately high power fluxes.

Thermal damage can also be caused by excessive heating in the electron microscope, which results in specimen or sample movement and instability to breakdown and destruction. It is manisfested as blisters, cracks, and holes in and on the surface of the sample.

Micrograph 3.9 exhibits beam damage by the appearance of blisters on the surface of the crystal specimen. The blistering effect is only obtained, or at least seen, under higher magnifications of about 2,000 or greater. A vertical fracture near the lower center of micrograph 3.9 may be due to beam damage. Hair-like fibers extend from one side of the fracture to the other as the crystal breaks and melts under the heat of the electron beam, resulting in sample breakdown and destruction. Problems of thermal damage can be reduced by working at lower beam currents. Sample heating from the probe current in the picoampere range is expected not to be a problem for samples in the SEM. An alternative is to coat with a thin film of copper, aluminum, silver, or gold.

Crystals of the protonated compound (hydrobromic salt of the photochromic compound), 2-(2,4-dinitrobenzyl) pyridinium bromide, can be seen in micrograph 4.13. In comparison, the gold-palladium coated sample of salt crystals appear to be wider and flatter than the crystals of the unprotonated photochromic compound. The width of the long, wide, diagonal crystal in the lower right of micrograph 4.13 is 53 microns. Holes in the crystals of the salt compound are smooth and precise. Inner layers are not found in the holes of the salt crystals, as can be found in the unprotonated photochromic compound from which they were prepared. Additionally, the salt crystals do not exhibit properties of photochromism.

An interesting outcome of the study is the detection of inner layers in the macro-crystalline structure of the photochromic compound, 2-(2,4-dinitrobenzyl) pyridine. A very interesting layering effect is seen in the crystal on the right side of micrograph 1.4. The long horizontal crystal on the right, in micrograph 3.2, is similarly layered. However, the former appears to have more inner layers as compared to the hollow appearance of the latter. Micrograph 2.11 is that of an uncoated crystal sample, and exhibits a great deal of charging. Nevertheless, thermal damage has exposed many inner layers of the crystal. These layers are calculated to be less than 1.7 microns in thickness.

The relationship of the inner layers to the color change for these photochromic crystals remains to be determined. Additional study may reveal a relationship between layering phenomenon and the color change, along with the action of light, by which the compound is able to undergo intramolecular hydrogen bonding, allowing it to rearrange to the deep blue tautomeric form. Layers of 2-(2,4-dinitrobenzyl) pyridine as thin as 0.015 mm have been crystallized between fused silica plates.[2] Layers of crystalline films reduced to 0.004 - 0.008 inches thick can be investigated by transmission microscopy for the study of structure and structural defects.

Lastly, several potential areas of usefulness of the photochromic compound, 2-(2,4-dinitrobenzyl) pyridine, exist in the deformation of dye laser pulses,[4] in the photographic screen stencil printing process,[1] and in information storage.[3]

Acknowledgments

The contributions of Professor Ernest Hammonds and Dr. Roosevelt Shaw to this project are gratefully acknowledged.

References

1. Brynko, C., et. al., "Photographic Screen Stencil Printing Process", Chemical Abstracts, 10th Collective Index, 93: 177283r.

2. Clark, W.C., et. al., "Phototropic Properties of 2-(2,4-dinitrobenzyl) Pyridine", Chemical Abstracts, 6th Collectine Index. (1957-61), 51-55.

3. Cowan, D.O., and Drisko, R.L., Elements of Organic Photochemistry.

4. Garness, J.I, et. al., "Apparatus for deformation of dye laser pulses...", Chemical Abstracts, 10th Collective Index, 91:11997K.

Micrograph 1.1

Micrograph 1.4

Micrograph 2.11

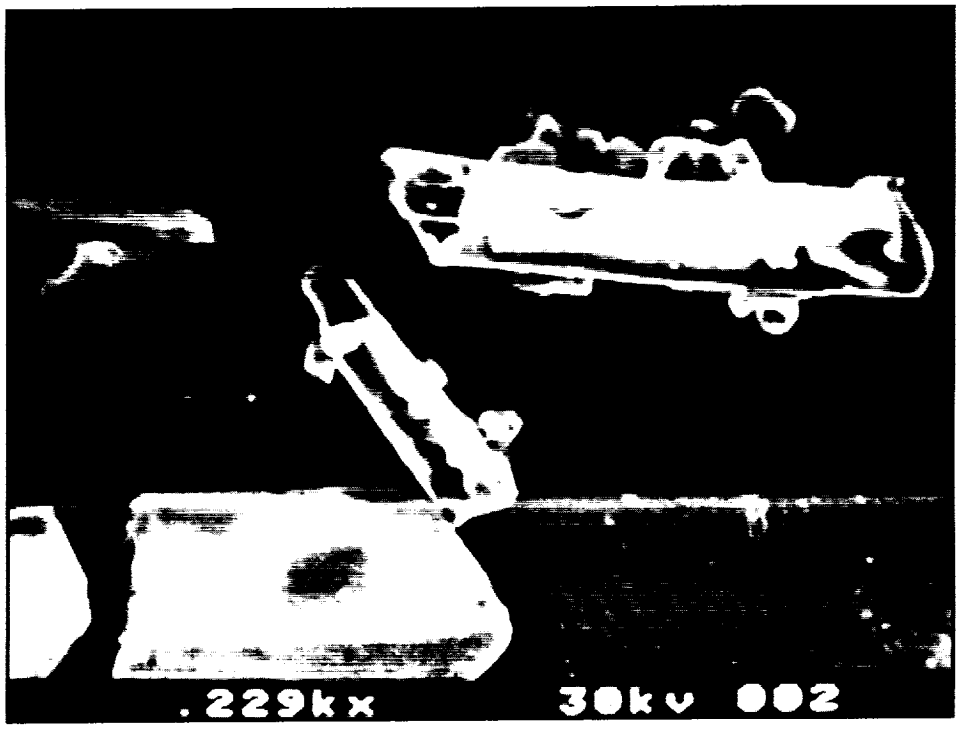

Micrograph 3.2

Micrograph 3.4

Micrograph 3.8

ORIGINAL PAGE
BLACK AND WHITE PHOTOGRAPH

Micrograph 3.9

Micrograph 4.13

STRUCTURES OF CYANO-BIPHENYL LIQUID CRYSTALS

Yuan-Chao Chu, Tung Tsang and E. Rahimzadeh
Department of Physics and Astronomy
Howard University
Washington D.C.

and

L. Yin
Technical Monitor
NASA Goddard Space Flight Center
Greenbelt, Maryland

ABSTRACT

The structures of p-alkyl-p′-cyano-bicyclohexanes, $C_nH_{2n+1}(C_6H_{10})(C_6H_{10})CN$ (n−CCH), and p-alkyl-p′-cyano-biphenyls, $C_nH_{2n+1}(C_6H_4)(C_6H_4)CN$ (n−CBP), have been studied. It is convenient to use an x-ray image intensification device to search for symmetric x-ray diffraction patterns. Despite the similarities in molecular structures of these compounds, very different crystal structures have been found. For the smectic phase of 2CCH, the structure is close to rhombohedral with threefold symmetry. In contrast, the structure is close to hexagonal close-packed with two molecules per unit cell for 4CCH. Since intermolecular forces may be quite weak for these liquid crystals systems, it appears that crystal structures can change considerably when the alkyl chain length is slightly altered. Different structures have also been found in the crystalline phases of n-CBP for n=6 to 9. For n=7 to 9, the structures are close to monclinic. The structures are reminiscent of the smectic-A liquid crystal structures with the linear molecules slightly tilted away from the c-axis. In contrast, the structure is quite different for n=6 with the molecules nearly perpendicular to the c-axis.

STRUCTURES OF CYANO-BIPHENYL LIQUID CRYSTALS

p-alkyl-p'-cyano-bicyclohexane (n-CCH), $R(C_6H_{10})(C_6H_{10})CN$, and p-alkyl-p'-biphenyl (n-CBP), $R(C_6H_4)(C_6H_4)CN$, are new classes of liquid cystals[1,2], where C_6H_4 is the phenyl ring, C_6H_{10} is the saturated cyclohexane ring, R may be any alkyl (C_nH_{2n+1}) group, and n is the number of carbon atoms in the alkyl chain. These molecules have long rod-like shapes. Extensive investigations have already been reported for the structures of a variety of these liquid crystals. For the CBP systems, there are stronger interactions between the molecules due to the double bonds in the phenyl rings. The smectic-A structures are commonly observed for these compounds with n=8,10,12 where the CBP molecules are tilted with respect to the smectic layers.[3] The ratio between the smectic layer spacing and the molecular length is about 1.4. In contrast, the molecular interactions are relatively weak for the CCH systems. The smectic phase structures are apparently unstable for 7CCH and higher members. For lower values of n, great varieties of structures have been observed for the smectic phases.[4]

Because of the important roles of both the alkyl chain lengths (n) and the ring systems, we have studied the structures of these systems in our present work. Because of the weak intermolecular forces, the crystallization processes are rather slow. We are able to obtain single-domained samples in capillary tubes by slow cooling from the less-ordered phase at higher temperature. Nevertheless, the spatial orientation of the domain inside the capillary depends on the direction of the initial nucleation and is therefore rather arbitrary. With the sample mounted on a goniometer, we have found it convenient to use an x-ray image intensification device to search for symmetric diffraction patterns visually while the goniometer is rotated.

The x-ray image intensification device was developed by Yin and collaborators at NASA Goddard Space Flight Center.[5,6] The diffracted x-rays are converted into visible light images by a rare-earth phosphor as shown in Fig. 1. The visible light is then coupled via fiber optics to a microchannel-plate

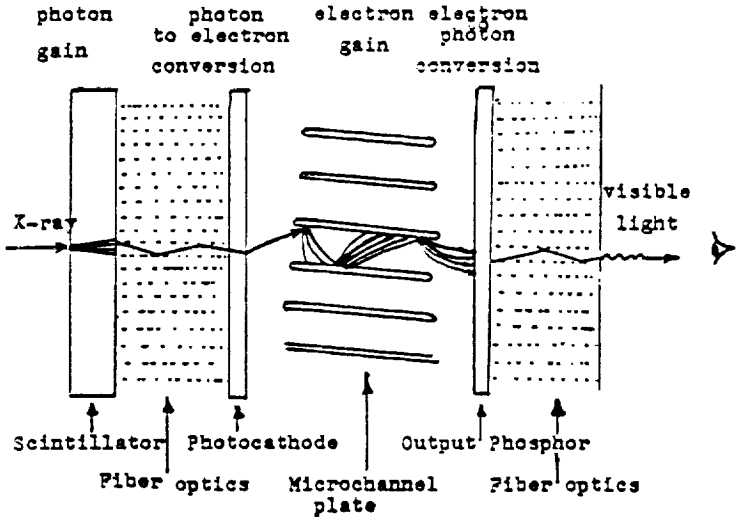

Figure 1. X-ray image intensification system.

image intensifier whic intensifies the visible light signal with a luminous gain of $\sim 10^5$. Because of the high luminous gain, the intensified visible light output can be viewed directly, photographed, or coupled to other video devices. The transmission Laue spots on the output screen can be easily viewed in subdued room light while the sample is being rotated. Hence this is a convenient technique to study the liquid crystals whose molecular alignments inside the capillaries are not known.

The X-rays are produced by a copper anode tube with a nickel filter, usually operating at 22kV and 500 watts. After collimation, the X-ray beam is directed onto the liquid crystal sample which is placed in a thin-walled capillary tube installed on a two-axis goniometer. The goniometer is enclosed in a container so that the sample may be heated or cooled in an air stream with controlled temperature. The X-ray image intensification device, which is small and compact, is placed in the forward scattering direction about 4 cm from the sample. The diffraction pattern displayed on the output screen may be recorded by a Polaroid camera. The calibration is accomplished by placing standard lead grids (with circular and with rectangualr grid patterns) over the scintillation screen. The angular resolution is about 0.03°. It should be noted that the diffraction spots can come from both the characteristic CuKα radiation (wave length of 1.54Å) and the white radiations with shorter wave lengths from the copper anode. The former spots tend to have higher intensities. These two types of spots may be more clearly distinguished by lowering the X-ray tube voltage. There would be much larger reductions in the intensities of white radiation spots as compared to the CuKα radiation spots. Because of the low crystalline orders and large molecular fluctuations in liquid crystals, diffraction spots are observable only in the forward scattering direction within a few degrees of the incident X-ray direction. It is, therefore, necessary to measure several diffraction patterns for various goniometer orientations and then express the scattering vectors of these different orientations in terms of a common set of unit vectors arbitrarily fixed in the crystal.

For the smectic phase of 4CCH, we have used the X-ray image intensification device to search for symmetric diffraction patterns. These patterns are shown on the left side of Fig. 2. Patterns of sixfold symmetry are shown in (a) and (b). Changing the goniometer angles resulted in patterns with twofold symmetry as shown in (c) and (d) where the incident X-ray direction is perpendicular to the c-axis with sixfold symmetry. These results indicate a hexagonal close-packed structure for the smectic phase of 4CCH with c=31Å and a=b=5.7Å. The packings of the molecules are sketched on the right side of Fig. 2. The unit cell parameters a and b are nearly the same as the molecular diameter. The parameter c is slightly less than twice the molecular length ($\sim$17Å).

It is surprising to find that the smectic phase structure of 2CCH is quite different from 4CCH despite the similarities in their molecular structures. Again, we have used the X-ray image intensification device to search for symmetric diffraction patterns. A diffraction pattern with threefold symmetry is sketched in Fig. 3(a). The incident X-ray direction is coincident with the direction of the threefold axis. At other goniometer angles, the diffraction patterns shown in Figs. 3(b), (c) and (d) have been observed. The incident X-ray directions for these patterns are tilted about 16° from the threefold axis and are distributed symmetrically about the threefold axis. These results indicate that the smectic phase structure of 2CCH is close to rhombohedral with a=b=c=12.5Å and the common angle of 28° between pairs of these units' cell vectors. These vectors are 17° away from the threefold axis direction.

These experiments indicate that the liquid crystal structures can change considerably even when their molecular structures are only slightly altered. This may be a consequence of the weak intermolecular forces in these systems. The effects of the alkyl chain length n may also be important.

Different structures have also been found for the crystalline phases of n-CBP for n=6 to 9. For 8CBP, several typical diffraction patterns are shown in Fig. 4. After some searching with the X-ray image intensification device, a clean symmetric pattern of four spots has been found as shown in Fig. 4(a) (the

shaded circle is the beam stop). This pattern demonstrates the monoclinic symmetry of the lattice. When the X-ray beam is more than 3° away from the monoclinic c-axis, the diffraction spots are usually observed in pairs only, as shown in Figs. 4(b), (c) and (d). These results indicate that the crystalline phase structure of 8CBP is close to monoclinic with a=b=5.5Å, c=37Å, $\alpha=\beta=90°$ and $\gamma=99°$. There are two molecules per unit cell. The unit cell parameters a and b are comparable to the molecular diameter. The parameter c is slightly less than twice the molecular length ~21Å. This structure is similar to the hexagonal close-packed structure except that the angle γ is 99° instead of the standard value of 120°. Similar structures have been found for 9CBP (a=b=4.9Å, c=27Å, $\gamma=110°$) and 7CBP(a=7Å, b=6Å, c=30Å, $\gamma=133°$). These structures are reminiscent of the smectic-A liquid crystal structures with molecules tilted slightly away from the c-axis. In contrast, the structure is quite different for 6CBP with a=19Å, b=9Å, c=6Å, $\gamma=148°$. The molecules are nearly perpendicular to the c-axis. Our experimental results have demonstrated that the crystal structures can change considerably when the alkyl chain length n is altered.

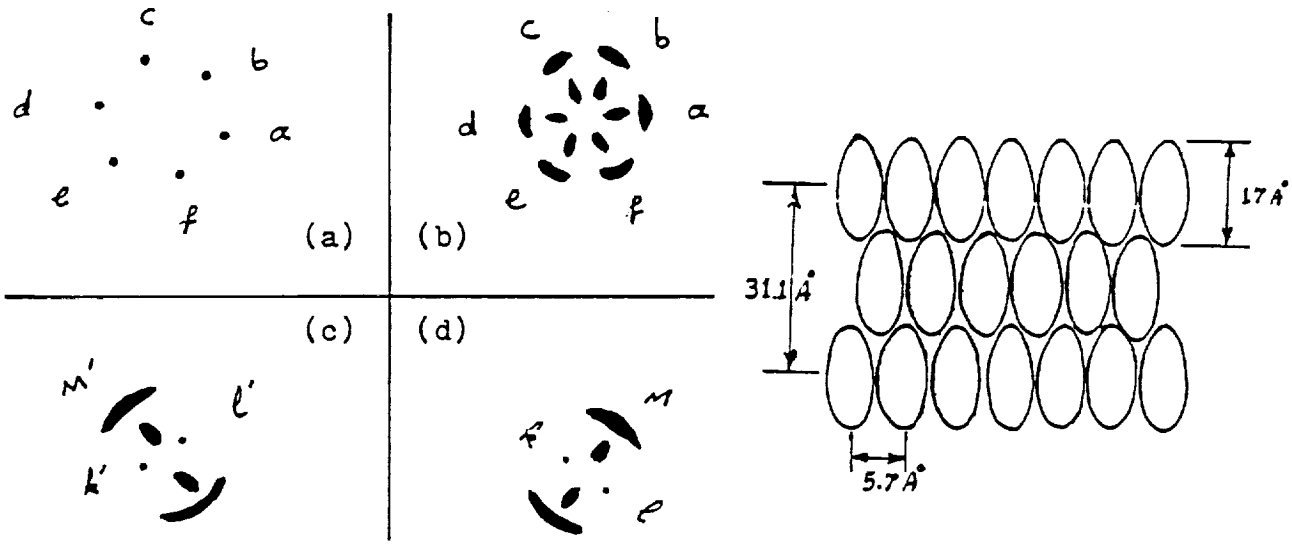

Figure 2. Left: Sketch of diffraction patterns of smectic phase of 4CCH.
(a)(b) X-ray beam along the sixfold c-axis., (c)(d) X-ray beam perpendicular to sixfold axis.
Right: Sketch of the molecular packing (c-axis in the perpendicular direction).

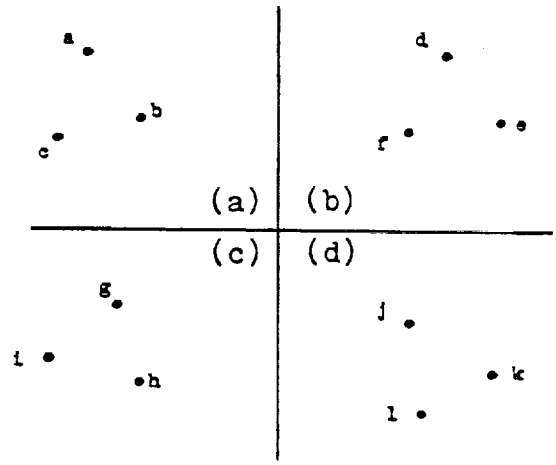

Figure 3. Diffraction patterns of smectic phase of 2CCH from CuKα X-rays. (a) X-ray beam along threefold axis; (b)(c)(d) X-ray beams 16° away from the threefold axis and 120° apart azimuthally.

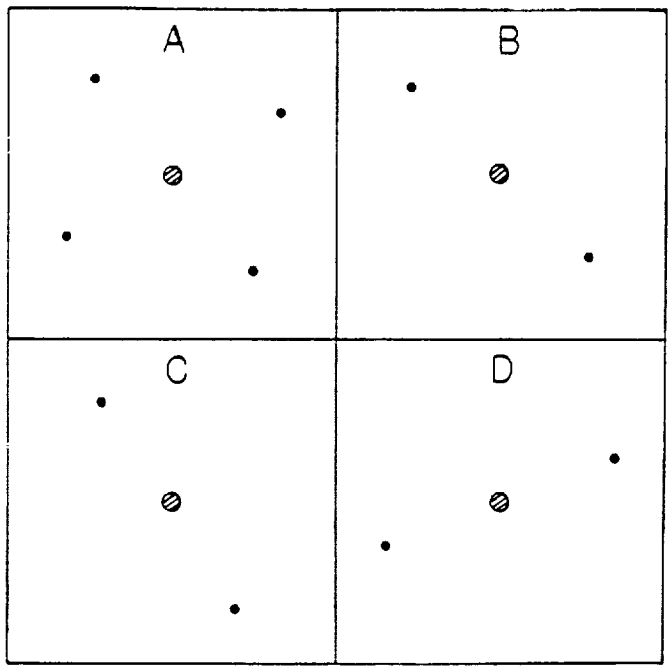

Figure 4. Diffraction patterns of the crystalline phase of 8CBP from CuKα X-rays. (a) incident X-ray along monoclinic c-axis, (b)(c)(d) incident X-rays 3°, 16°, 14° away from c-axis.

The partial financial support by the National Aeronautical and Space Administration grant NAG-5-156 is gratefully acknowledged. We thank Dr. L. Yin of NASA Goddard Space Flight Center (Greenbelt, Maryland) for many useful discussions.

References

1. L. Pohl, R. Eidenschink, J. Krause and D. Erdmann, Phys. Letters A60, 421 (1977).

2. L. Pohl, R. Eidenschink, J. Krause and G. Webe, Phys. Letters A65, 169 (1978)

3. G.J. Brownsey and A.J. Leadbetter, J. Physique Lettres 42, L135 (1985).

4. A.J. Leadbetter, J.C. Frost, J.P. Gaughan, G.W. Gray and A. Mosley, J. Physique 40, 375 (1979).

5. L. Yin, J.I. Trombka and S.M. Seltzer, Nuclear Instrum. and Methods 158, 175 (1979); 172, 471 (1980).

6. D.Y. Chung, T. Tsang, L. Yin and J.R. Anderson, Rev. Sci. Instrum. 52, 1112 (1981).

STUDIES OF SUPERCONDUCTING MATERIALS WITH MUON SPIN ROTATION

M.R. Davis and C.E. Stronach
Physics Department
Virginia State University
Petersburg, VA

W.J. Kossler, H.E. Schone, and X.H. Yu
Physics Department
College of William and Mary
Williamsburg, VA

Y.J. Uemura and B.J. Sternlieb
Physics Department
Columbia University
New York, NY

J.R. Kempton
TRIUMF
4004 Wesbrook Mall
Vancouver, BC
Canada

J. Oostens
Physics Department
University of Cincinnati
Cincinnati, OH

and

W.F. Lankford
Physics Department
George Mason University
Fairfax, VA

STUDIES OF SUPERCONDUCTING MATERIALS WITH MUON SPIN ROTATION

ABSTRACT

The muon spin rotation/relaxation technique has been found to be an exceptionally effective means of measuring the magnetic properties of superconductors, including the new high temperature superconductor materials, at the microscopic level. The technique directly measures the magnetic penetration depth (type II SC's) and detects the presence of magnetic ordering (antiferromagnetism or spin-glass ordering has been observed in some HTSC's and in many closely related compounds). Extensive studies of HTSC materials have been conducted by the Virginia State University - College of William and Mary - Columbia University collaboration at Brookhaven National Laboratory and TRIUMF (Vancouver). A survey of LaSrCuO, YBaCaCuO systems shows an essentially linear relationship between the transition temperature T_c and the relaxation rate σ. This appears to be a manifestation of the proportionality between T_c and the Fermi energy, which suggests a high energy scale for the SC coupling, and which is not consistent with the weak coupling of phonon-mediated SC. Studies of LaCuO and YBaCuO "parent" compounds show clear evidence of antiferromagnetism. $YBa_2Cu_{3-x}CO_xO_7$ shows the simultaneous presence of spin-glass magnetic ordering and superconductivity. The three-dimensional SC, $(Ba,K)BiO_3$, unlike the layered CuO-based compounds, shows no suggestion of magnetic ordering. Experimental techniques and theoretical implications will be discussed.

STUDIES OF SUPERCONDUCTING MATERIALS WITH MUON SPIN ROTATION

The Muon Spin Rotation Technique

The use of the positive muon as a probe of condensed matter was first suggested by Garwin, Lederman and Weinrich in their 1957 paper describing their experimental observation of parity violation in muon production and decay. [1] The positive muon is one of a number of light positive ions which have been used to probe condensed matter. These include the positron (e^+), hole (h^+), muon (μ^+), pion (π^+), proton (p^+), deuteron (d^+) and triton (t^+). The muon is the least easily produced of all these particles, but the details of its behavior in condensed matter are far more easily discerned than for any other particles. This is because of subtleties in the nature of the weak interaction. Because of the parity violation inherent in the μ^+ production,

$$\pi^+ \rightarrow \mu^+ + \nu_\mu ,$$

muons resulting from pion decay are 100% polarized in the center-of-mass frame. Consequently, by appropriate momentum selection (with magnets) one can obtain a nearly 100% polarized muon beam regardless (within reasonable limits) of the momentum of the source pions.

In like manner the muon decays into a positron through the weak interaction,

$$\mu^+ \rightarrow e^+ + \nu_e + \bar{\nu}_\mu .$$

The positrons are emitted asymmetrically with respect to the muon spin, and with considerable kinetic energy (average: 35 MeV).

Data are taken with an apparatus such as the one our group uses at the Alternating Gradient Synchrotron of Brookhaven National Laboratory (Figure 1). Signals in scintillators 1,2 and M5 with no signals in F6 indicate that a muon has stopped in the sample, which is in a thin-walled container (usually a cryostat). Signals in A4 and A3 (or in F7 and F8) indicate the emission of a positron in the backward (or forward) direction. The muon signal starts a clock, a positron signal stops it, and two histograms (backward and forward) are accumulated. A pair of magnet coils provides an external transverse field. The muons precess at a rate directly proportional to the magnetic field they sense, and this precession signal decays at a rate which depends upon the variance in the magnetic field observed by all the muons in the ensemble.

The data are fit to a function of the general form:

$$N(t) = No\ e^{-t/\tau} \quad [1 + A\ G_x(t) \cos(\omega t + \phi)] + B ,$$

where τ = 2.2 microseconds (mean muon lifetime), A is the e^+ anisotropy, $G_x(t)$ is the depolarization function, ω is the precession rate, ϕ is a geometrical phase angle, and B is random background. A, $G_x(t)$ and ω are usually the quantities of physical interest.

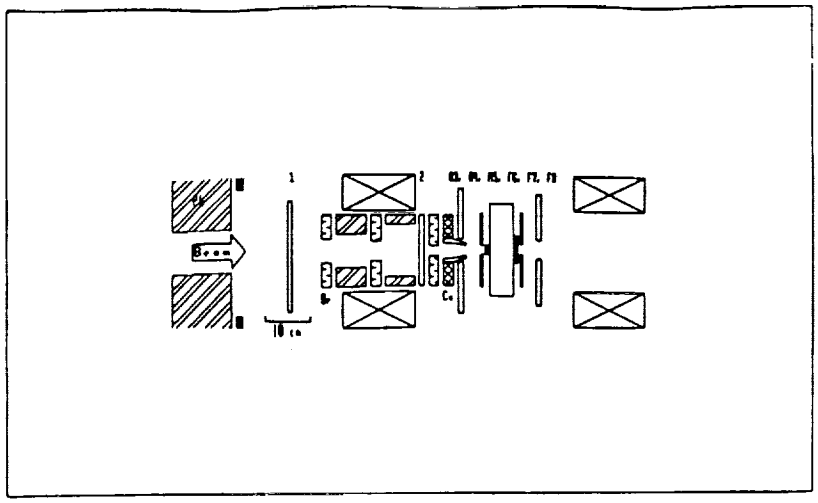

Figure 1.
Muon Spin Rotation Apparatus at the AGS Brookhaven National Laboratory.

MuSR Studies of HTSC Materials

The high-temperature copper-oxide-based superconductors discovered since the initial breakthrough on LaSrCuO by Bednorz and Müller, [2] which have transition temperatures ranging from about 40K up to about 125K, are some form of type II superconductors. Type II's have a surface-to-volume energy relation which favors the intrusion of external applied magnetic fields in flux quanta which generally take on a uniform triangular geometry. This produces a variation in the internal magnetic field sensed by microscopic probes implanted into the material, such as μ^+. This variation produces a depolarization of the muon spin precession, as in Figure 2, which shows the experimental asymmetry we obtained in $YBa_2Cu_3O_7$, both above and below its transition temperature. From the depolarization rate observed in the superconducting state, the magnetic penetration depth can be calculated. By combining the values from μSR with more conventional measurements, the superconducting charge carrier density and the effective mass of the carriers (m^*/m_e) may also be determined.

The variation in the magnetic field in a type II sample is given by

$$B(x) = B_o \exp(-x/\lambda_L)$$

Our data show that, to a good approximation, the depolarization rate σ is proportional to T_c. Relating this to the penetration depth gives

$$\sigma \propto \lambda_L^{-2} \propto n_s/m^* \propto T_c.$$

This suggests that the carrier density n_s plays a major role in determining T_c. Furthermore, this relation appears to be inconsistent with standard Bardeen-Cooper-Schrieffer (BCS) theory, and suggests a high energy scale for the coupling mechanism. [4] Such a high energy scale is found in models based on a large transfer integral between the oxygen and neighboring Cu atoms, [5] and is also expected in the resonating-valence-bond picture. [6]

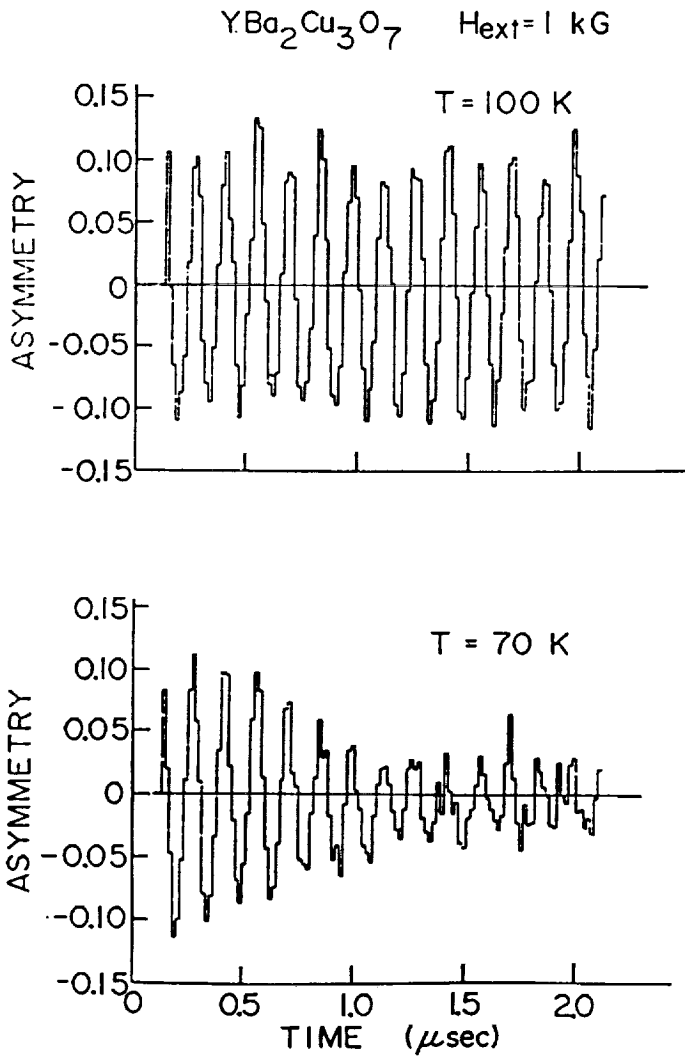

Figure 2. Asymmetry in normal (top) and superconducting (bottom) $YBa_2Cu_3O_7$.

Magnetic Ordering in HTSC Materials

Muon spin rotation also serves as an exceptionally effective probe of magnetic ordering in materials at the microscopic level, and we have utilized this aspect of μSR to observe magnetic ordering in materials very closely related to HTSC materials. A prime example of this is our study of $LaCuO_{4-y}$, which is "parent" to the HTSC LaSrCuO. Figure 3 shows our data taken with zero external field on LaSrCuO (top) and La_2CuO_{4-y} (Bottom). No oscillations are present in the top case, but they are clearly observed in the lower plot. This indicates the presence of antiferromagnetism with a moment per Cu atom of about 0.5 Bohr magneton. [7] A similar experiment done at TRIUMF on oxygen-depleted $YBa_2Cu_3O_{7-y}$ shows similar antiferromagnetic ordering in that material. [8] These results suggest a close relationship between superconductivity and magnetic ordering in the new CuO-based HTSC materials, which is opposite to all experiences with conventional superconductors (heavy-fermion materials which have superconducting phases show close relations between SC and magnetism in some cases also).

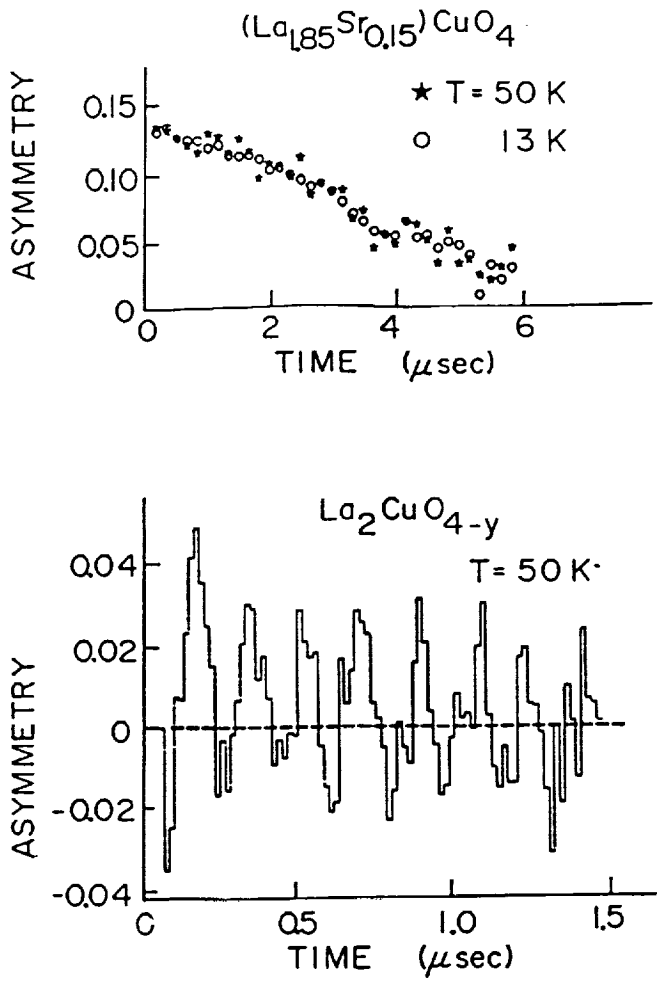

Figure 3. Zero-field asymmetry in LaSrCuO and $LaCuO_{4-y}$.
AFM is observed in the lower spectrum.

A study of YBaCuO doped with Co, $YBa_2Cu_{3-x}Co_xO_7$, shows simultaneous SC and magnetic ordering, in this case the spin-glass variety in which magnetic moments are frozen into random but static orientations. For x = 0.1, for example, the depolarization rate begins to rise at about 40K, indicating the onset of SC, while the initial polarization begins to decrease at about 30K, indicating the onset of spin-glass ordering. Figure 4 shows how the SC transition temperature T_c and the magnetic ordering transition temperature T_m vary with Co concentration. There is a clear overlap of SC and spin glass ordering. We suspect that this does not violate the Meissner effect because the two effects are probably occurring in microscopically distinct regions of the sample, such as alternating planes.

In light of the magnetic ordering present in materials closely related to the essentially two-dimensional CuO perovskite HTSC's, we studied three-dimensional perovskite superconductors which do not contain Cu, (Ba,K) BiO_3. These showed no evidence for magnetic ordering, [9] which suggests that these materials are probably not likely candidates for record-setting values of T_c.

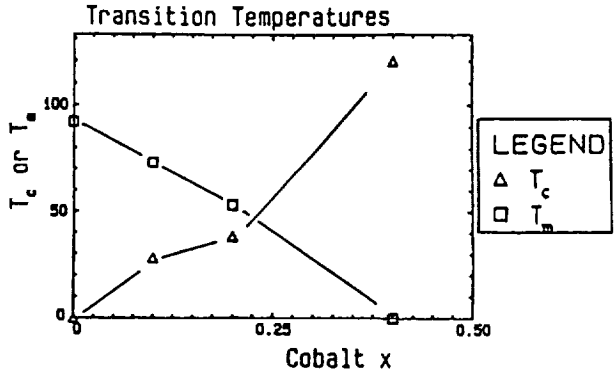

Figure 4.
Transition temperatures as functions of Co concentration in $YBa_2Cu_{3-x}Co_xO_7$.

Acknowledgments

This work was supported in part by NASA grant NAG-1-416, NSF grant DMR-8503223, and US DOE contract 76-A002-CH00016. Our colleagues at TRIUMF are supported by the National Science and Engineering Research Council of Canada. Special thanks to R.S. Cary for assistance in producing this document.

References

1. Garwin, R.L.; Lederman, L.M.; Weinrich, M., Phys. Rev. 1957, 105, 1415.

2. Bednorz, J.G.; Müller, K.A., Z. Physik 1986, B64, 189.

3. Kossler, W.J.; Kempton, J.R.; Yu, X.H.; Schone, H.E.; Uemura, Y.J.; Moodenbaugh, A.R.; Suenaga, M.; Stronach, C.E., Phys. Rev. 1987, B35, 7133.

4. Uemura, Y.J.; Emery, V.J.; Moodenbaugh, A.R.; Suenaga, M.; Johnston, D.C.; Jacobson, A.J.; Lewandowski, J.T.; Brewer, J.H.; Kiefl, R.F.; Kreitzman, S.R.; Luke, G.M.; Riseman, T.; Stronach, C.E.; Kossler, W.J.; Kempton, J.R.; Yu, X.H.; Opie, D.; Schone, H.E., Phys. Rev. 1988, B38, 909.

5. Emery, V.J., Phys. Rev. Lett. 1987, 58, 2794.

6. Anderson, P.W., et al., Phys. Rev. Lett. 1987, 58, 2790

7. Uemura, Y.J.; Kossler, W.J.; Yu, X.H.; Kempton, J.R.; Schone, H.E.; Opie, D.; Stronach, C.E.; Johnston, D.C.; Alvarez, M.S.; Goshorn, D.P., Phys. Rev. Lett. 1987, 59, 1045.

8. Brewer, J.H.; et al., Phys. Rev. Lett. 1988, 60, 1073.

9. Uemura, Y.J.; et al., Nature 1988, 355, 151.

A 10-WATT CW PHOTODISSOCIATION LASER WITH IODO PERFLUORO-TERT-BUTANE

Bagher Tabibi and Demetrius D. Venable
Department of Physics
Hampton University
Hampton, VA

ABSTRACT

$t-C_4F_9I$ has been successfully tested as a lasant in a solar-simulator-pumped laser system and produced a 14-W CW output. The pump-to-laser efficiency was determined to be three times that of the commonly used $n-C_3F_7I$.

A 10-WATT CW PHOTODISSOCIATION LASER WITH IODO PERFLUORO-TERT-BUTANE

Introduction

NASA has been investigating the feasibility of direct solar-pumped laser systems for power beaming in space.[1] Among the various gas, liquid and solid laser systems being proposed as candidates for solar-pumped lasers,[2-4] the iodine photodissociation gas laser has demonstrated its potential for space application.[5-8]

Of immediate attention is the determination of system requirements and the choice of lasants to improve the system efficiency. The development of an efficient iodine laser depends on the availability of a suitable iodide which has favorable laser kinetics, chemical reversibility, and solar energy utilization. Among the various alkyliodide lasants comparatively tested in a long-pulse system, perfluoro-tert-butyl iodide, $t-C_4F_9I$, was found to be the best.[9] However, the operating conditions for the laser medium in a continuously pumped and continuous-flow iodine laser differ considerably from those in the pulsed regime. [10] Therefore, this experiment reports the results of CW laser performance from $t-C_4F_9I$.

Perfluoro-n-propyl iodide, $n-C_3F_7I$ is used for comparison in this study because of its universal use in photodissociation iodine lasers.

Solar-Pumped Iodine Laser

Successful excitation of an iodine laser by a solar-simulator was first reported in 1980 [5]. The active media for such lasers are CF_3I, or C_3F_7I, and are generally described by the formula RI, where R stands for the radical CF_3, C_3F_7, C_4F_9, or C_6F_{13}. The absorption bands of these iodides are in the UV part of the solar spectrum (250-300 nm). Resulting photodissociation produces excited I^* atoms with the reaction

$$RI + h\nu_s \rightarrow R + I^*(5^2P_{1/2}).$$

Lasing occurs because of the atomic transitions

$$I^*(5^2P_{1/2}) \rightarrow I(5^2P_{3/2}) + h\nu_L,$$

where

$$\lambda_L = \frac{c}{\nu_L} = 1.315\mu m.$$

The quantum yield of the excited iodine atoms, I^*, the most important quantity in the laser kinetics, was measured to be near unity for most alkyliodides.[10] (See Table 2.)

Four other processes which occur following the photodissociation are also important and must be considered: the collisional deactivation of I^*, by the parent molecule RI according to $I^* + RI \xrightarrow{(Q_1)} I + RI$; the recombination process of $R + I^* \xrightarrow{(K_1)} RI$; the dimerization $R + R \xrightarrow{(K_3)} R_2$; and formation of molecular iodine $I + I + M \rightarrow I_2 + M$ or $I^* + I + M \rightarrow I_2 + M$. These reactions are the important loss mechanisms for the iodine laser system.

$t-C_4F_9I$ Laser

Perfluoro-tert-butyl iodide, $t-C_4F_9I$, is attractive for direct solar-pumped laser medium because of two important properties. First, the photodissociation absorption peak is centered at 288 nm which is red-shifted by 15 nm from the 275 nm absorption center of $n-C_3F_7I$ (see Fig. 2). This red-shift and the broader half-width (see Table 1) increase the solar spectrum utilization and result in a higher photodissociation rate. The photodissociation rate of the solar-pumped iodine laser can be calculated from[11]

$$\gamma = \frac{1}{hc} \int \sigma S_\lambda \lambda \, d\lambda$$

where h is Planck's constant; c is light velocity, σ is absorption cross-section, S_λ is solar spectral irradiance and λ is wavelength. A calculation using the data for air mass zero (AMO) solar spectral irradiance [12] provides $\gamma(n-C_3F_7I) = 0.83 \times 10^{-3}\ s^{-1}$ and $\gamma(t-C_4F_9I) = 2 \times 10^{-3}\ s^{-1}$ which is 2.4 times higher for $t-C_4F_9I$ when compared with $n-C_3F_7I$.[11] The photodissociation rate was calculated for $t-C_4F_9I$ in comparison with that for CF_3I.[11] The second advantage for this gas is the absence of extremely small contributed reactions which lead to the direct loss of radicals.[13] Particularly, recombination reaction of radicals R between each other, observed for the other iodides, are strongly inhibited for $t-C_4F_9I$.[13-15] Other kinetic rate coefficients were found to be similar to those for the $n-C_3F_7I$ molecules.[14] (See Table 2.) Therefore, the photodissociation of $t-C_4F_9I$ by solar radiation could lead to a stationary concentration of the radicals, I atoms, and I_2 molecules.

Experiment

The present experiment used the laser system of reference 6 which used the iodide, $n-C_3F_7I$, so that comparative evaluation to the $t-C_4F_9I$ could be made directly. Figure 1 shows a schematic of the experiment. A Vortek Industrial model 107 arc lamp [6] with a 0.2-m-long arc length was used as the solar-simulator. The lamp was capable of electrical input powers up to 150 kW. However, only 75 kW was used in this experiment. Considering the ~45% conversion efficiency, as claimed by Vortek Industry, a maximum of ~34 kW of visible and near-infrared radiant power could be achieved.

The arc lamp and the laser tube were optically coupled on the conjugate focal lines of a water-cooled elliptical cylindrical reflector of polished aluminum. The suprasil laser tube had a 20-mm ID and 0.45 m length. The gain medium was shadowed by the side plates of the reflector. The total pumping power used in this experiment was ~13 kW.[6] Equivalent pumping power density was 994 solar constants (1 solar constant equals 1.35 kW/m^2) on the surface of the laser tube. The pumping power density was varied by adjusting the arc current. The emission spectrum of the Vortek solar simulator was similar to the air mass zero solar spectrum and is given in reference 6.

The laser cavity consisted of a 70% output mirror and a maximum reflectivity rear mirror. The cavity length was 0.9 m, and a pyroelectric power meter was used to monitor the laser power output.

The lasant supply is shown in Figure 1. The flow of $t-C_4F_9I$ vapor was longitudinal and maintained by a pressure differential between the heated evaporator and the liquid nitrogen cooled condenser containing iodide. To obtain sufficient flow rates of $t-C_4F_9I$, the evaporator had to be heated because the vapor pressure of $t-C_4F_9I$ was only 76 Torr at room temperature which is about 5 times lower than that of $n-C_3F_7I$ (350 Torr).

The photoabsorption of $t-C_4F_9I$ was accurately measured by spectrophotometry and is compared to that of $n-C_3F_7I$ in Figure 2. Photoabsorption, vapor pressure, and heat capacity parameters for $t-C_4F_9I$ and $n-C_3F_7I$ are summarized in Table 1. Note that the high heat capacity of $t-C_4F_9I$ is advantageous for maintaining reduced lasant temperatures with high power, cw operation.

Results

CW laser operation from $t-C_4F_9I$, unlike the $n-C_3F_7I$, requires some technical efforts leading to high purity of the iodide and a large surface area of evaporator to achieve sufficient flow rate and corresponding pressure in the laser tube. $t-C_4F_9I$ is solid at room temperature and melts at 60°C. The maximum vapor pressure of $t-C_4F_9I$ obtainable with flow from a room temperature evaporator was only a few Torr and fell down to zero within a few seconds because of insufficient compensation of evaporation cooling in the reservoir. In order to increase the flow, the pressure was increased by heating the reservoir and the laser tube to 45°C. The vapor pressure of $t-C_4F_9I$ increased to 30 Torr but fell to 10 Torr and lower within one minute. Thus, the period of CW output from $t-C_4F_9I$ was limited to a few seconds in this experiment by the limitation of the amount of iodide and its evaporational cooling.

Figure 3 shows a typical oscillogram of the CW power output of $t-C_4F_9I$ (lower trace). The upper trace is the pressure of $t-C_4F_9I$ inside the laser tube during a lasing period of ~ 20 s. To recycle back to the initial pressure, it was necessary to shut down the flow of iodide by the controllable valve (see Figure 1) for almost 3 minutes to compensate for insufficient thermal dissipation of the evaporational cooling in the reservoir. A maximum power output of ~ 14 W CW was achieved for ~ 20 s with a flow rate and a vapor pressure of 2700 SCCM and ~ 19 Torr, respectively.

To compare the CW output of $t-C_4F_9I$ to that of $n-C_3F_7I$ another set of experiments was performed for both iodides under the same operational conditions of flow rate, flow velocity, and pressure. The results of the tests for the two iodides pumped by different simulator arc currents are shown in Figure 4. The flow rate and the vapor pressure of $n-C_3F_7I$ were constant at 900 SCCM and 6 Torr, respectively, throughout the tests, but those of $t-C_4F_9I$ unavoidably decreased from 1200 to 700 SCCM and from 9 to 5 Torr, respectively. The measurements were made from low to high arc currents. In spite of the reduced flow rate of the $t-C_4F_9I$, more than a three-fold increase in the power output was measured.

CW Laser from the Mixture of $t-C_4F_9I$ and $n-C_6F_{13}I$

To maintain the flow and pressure of $t-C_4F_9I$ throughout the lasing period we attempted to mix it with $n-C_6F_{13}I$ which is liquid at room temperature and has much lower vapor pressure than $t-C_4F_9I$ (see Table 1). We dissolved equal amounts of $t-C_4F_9I$ in $n-C_6F_{13}I$ until it reached saturation. The idea was to speed the heat conduction by stirring the liquid mixture.

The absorption band of the mixture of equal amounts of each iodide was measured by the OMA spectral analyzer (see Table 1). The mixture had a 285 nm absorption peak and 85 Torr vapor pressure at room temperature. This mixture was used for the CW laser. The conditions of the experiment were kept the same as for the pure $t-C_4F_9I$. A typical oscillogram of CW output from the mixture of $t-C_4F_9I$ + $n-C_6F_{13}I$ (1:1) is shown in Figure 5 (lower trace). The upper trace is the pressure of the mixture inside the laser tube during the lasing period of 4.6 minutes. Evidently, the lasing period for the mixture increased considerably in comparison to that for pure $t-C_4F_9I$. A maximum power output of 11.5 W was achieved with a pressure of 25 Torr and a flow rate of ~4300 SCCM. The results of these tests indicate some usefulness of the mixing of $t-C_4F_9I$ in $n-C_6F_{13}I$ to maintain the flow rate and the pressure during the longer lasing time period but the mixture is less efficient than pure $t-C_4F_9I$.

It is important to note that the power output of this mixture after treatment with $Na_2S_2O_5$ + Ag, which acts as an I_2 absorbing agent, decreased by half from the power output of the first run. The treatment period was about one week. The power output of the third run of the mixture which was chemically treated for a longer period of about one month still decreased. The measurement of the absorption band of the used mixture demonstrated an absorption peak of 275 nm indicating the presence of iodides other than $t-C_4F_9I$ in the medium.

Conclusion

The iodide $t-C_4F_9I$ was successfully tested in a solar-simulator-pumped CW laser. Its efficiency (pump-to-laser) was measured to be three times that of the commonly used iodide $n-C_3F_7I$. $t-C_4F_9I$ also demonstrated a higher chemical reversibility than that of $n-C_3F_7I$. However, some technical efforts are required for obtaining and maintaining high flow rates and pressures throughout the CW laser operation.

References

[1] R.J. DeYoung, G.D. Walberg, E.J. Conway, and L.W. Jones, "A NASA High-Power Space-Based Laser Research and Applications Program", NASA Langley Research Center, NASA-SP-464, Langley AFB, VA (1983).

[2] A.L. Golger and I.I. Kliniovski, "Lasers Pumped by Solar Radiation (review)", Sov. J. Quantum Electron, vol. 14, No. 2, pp 164-179 (1984).

[3] R.T. Schneider, V.H. Kurzweg, J.D. Cox, and N.H. Weinstein, "Research on Solar Pumped Liquid Lasers", Univ. Florida, Gainsville, FL., rep. No. NAG-1-135 (1983).

[4] M. Weksler and J. Shwartz, "Solar-Pumped Solid-State Lasers", IEEE J. of Quantum Electron, Vol 24, No. 6, pp 1222-1228 (1988).

[5] J. H. Lee, Willard R. Weaver, Appl. Phys. Lett. 39, (1981) 137.

[6] J.H. Lee, M.H. Lee, and W.R. Weaver, Proceeding of the International Conference on Lasers '86, (1986) 150.

[7] J.H. Lee, B.M. Tabibi, D.H. Humes, and W.R. Weaver, "High-Power, Continuously Solar-Pumped and Q-Switched Iodine Laser", AIP Conf. Proc. 172, Advances in Laser Science III (1988) 109.

[8] R.J. DeYoung, G.H. Walker, M.D. Williams, G.L. Schuster, and E.J. Conway, IECEC, Philadelphia, PA., August 10-14, 1987, Paper 879038.

[9] B.M. Taibibi, J.H. Lee and W.R. Weaver, "Performance on Perfluoro-alkyl Iodides in a Long Gain-Length Laser", Bull. Am. Phys. Soc. 31 (1986) 1756.

[10] T.L. Andreeva, G.N. Birch, I.I. Sobelman, V.N. Sorokin, and I,I, Struck, "Continuously Pumped Continuous-Flow Iodine Laser", Sov. J. of Quantum Electron, 4, (1977) 2150.

[11] V. Yu Zaleskii, Kvantovaya Elektron. (Moscow) 10, 1097 (1983).

[12] J.R. Carter, H.Y. Tada, "Solar Cell Radiation Handbook", Jet Propulsion Lab., CIT, Pasadena, California, (1973) 2-2.

[13] T.L. Andreeva, G.N. Birch, I.I. Sobelman, V.N. Sorokin, and I.I. Struck, Sov. J. Quantum Electron 7, (1977) 1230.

[14] L.S. Ershov, V. Zaleskii, V.I. Sokolov, Sov. J.Q., 8, (1978) 494.

[15] J.H. Lee, J.W. Wilson, T. Enderson, W.R. Weaver, D.H. Humes, and B.M. Tabibi, Optics Comm. 53, 356 (1985).

Appendix A: Human Resources

Graduate students continue to be trained in this area of research at the University. To date, five students have completed theses and four students are enrolled. Eight of the nine MS students are American citizens and seven of the nine are considered members of an underrepresented minority in physics. Table A1 lists students and thesis titles.

GRADUATE STUDENT TRAINEES

STUDENT	THESIS TITLE	DATE
Gill Lee (NASA-GRTP)	A Parametric Study of the Threshold Pump Power of a Direct Solar Simulator Pumped C_3F_7I Laser	'84
Kenneth Preston	A Study of Selected Dyes for Enhancement of Lasing Using the Converter Technique	'86
Julie Williams	Solar Simulator Pumped Waveguide Amplifier for Dye Laser	'87
Won Yi	UV Dye Lasers Pumped by Hypocycloidal Pinch Plasmas	'87
Todd Pilot	Solar Simulator Waveguide Dye Amplifier Under a Long Excitation Pulse	'88
Lamarr Brown	Nd:YAG and Nd:Cr:GSGG as Candidates for Solar Simulator Pumped Solid State Laser	'89
Vincent Jones	Comparison of t-C_4F_9I and C_3F_7I for Direct Solar Pumping	*
Abdulaziz Gambo	???	*
Clarence Wells (US Military)	???	*

Note: 8 of the 9 MS students are American citizens.
7 of the 9 MS students are considered under-represented minorities in physics.

Table 1. Characteristic Parameters of Iodides.

Temperature Iodide [torr]	Absorption Peak, λ[nm]	C_V Δλ[nm] [J/Mole^{0}K]	C_P [J/mole^{0}K]	Absorption Cross Section, $\sigma_{max}[10^{-19}cm^2]$		Room Vapor Pressure
t-C_4F_9I	288	50		4.8 ±		
0.05		76		181	189	
n-C_3F_7I	273	42		6.6 ±		
0.1		350		146	154	
n-$C_6F_{13}I$	272	42		6.0 ± 0.5		~16
t-C_4F_9I + n-$C_6F_{13}I$	285	- -		---		85

Table 2. Kinetic Parameters for Iodides.

Parameter	t-C_4F_9I	n-C_3F_7I
Quantum Yield	0.88	0.98
K_2, cm^3/s	6.0×10^{-12}	8.0×10^{-12}
K_3, cm^3/s	≈0	2.0×10^{-12}
Q_1, cm^3/s	2.9×10^{-16}	3.0×10^{-17}

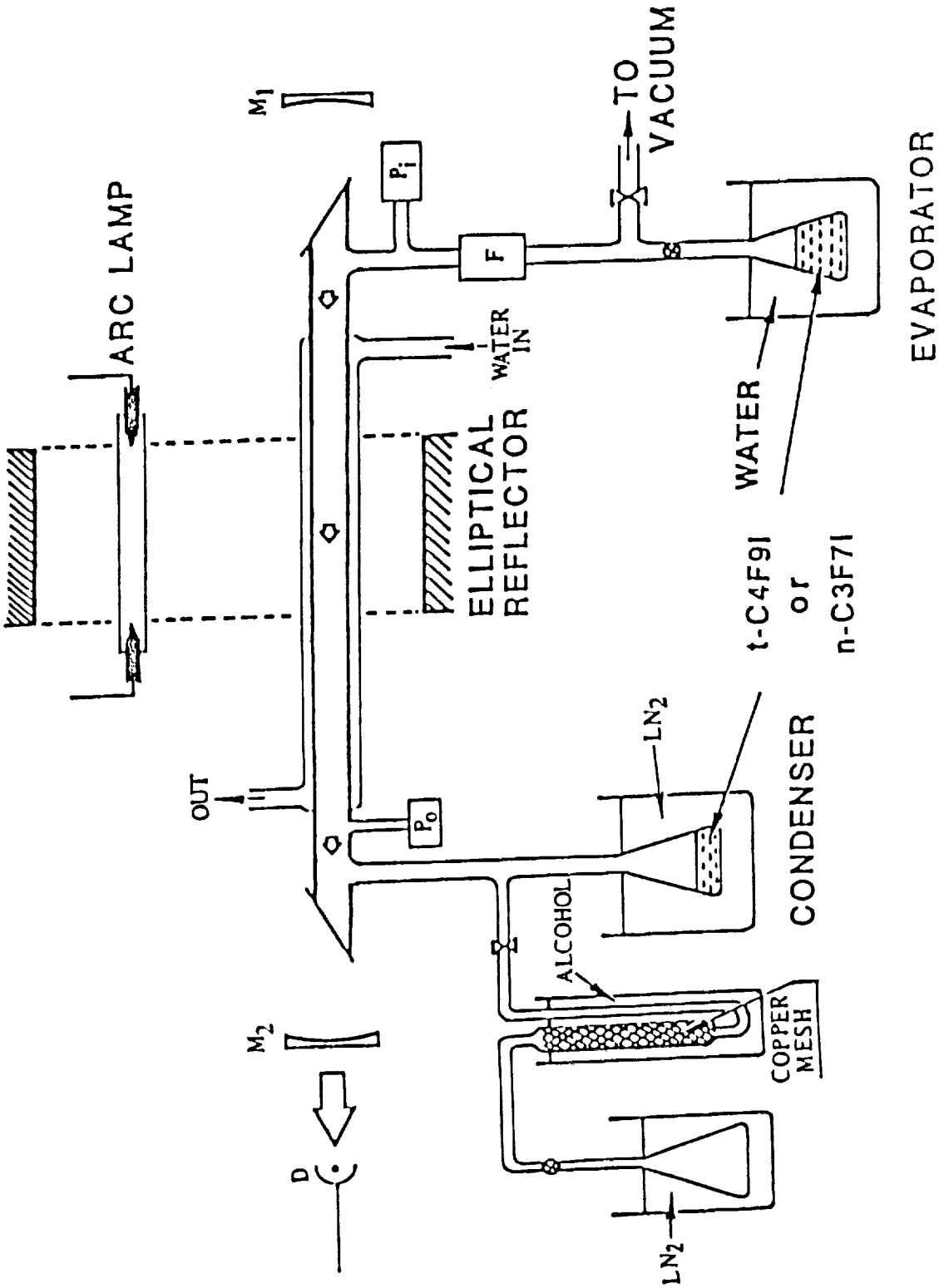

Figure 1. CW solar-simulator-pumped laser experiment.

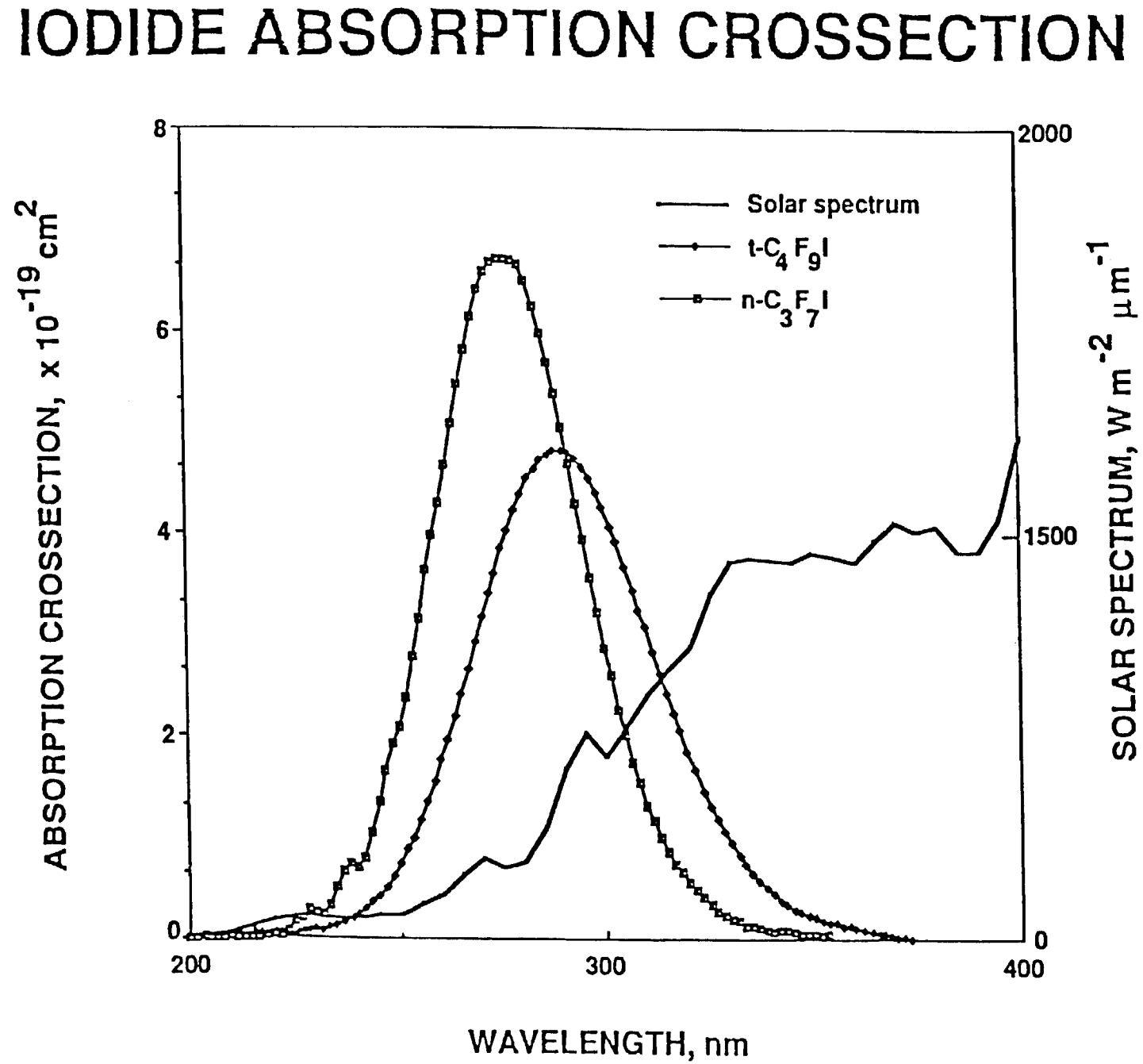

Figure 2. Absorption cross-section of iodides.

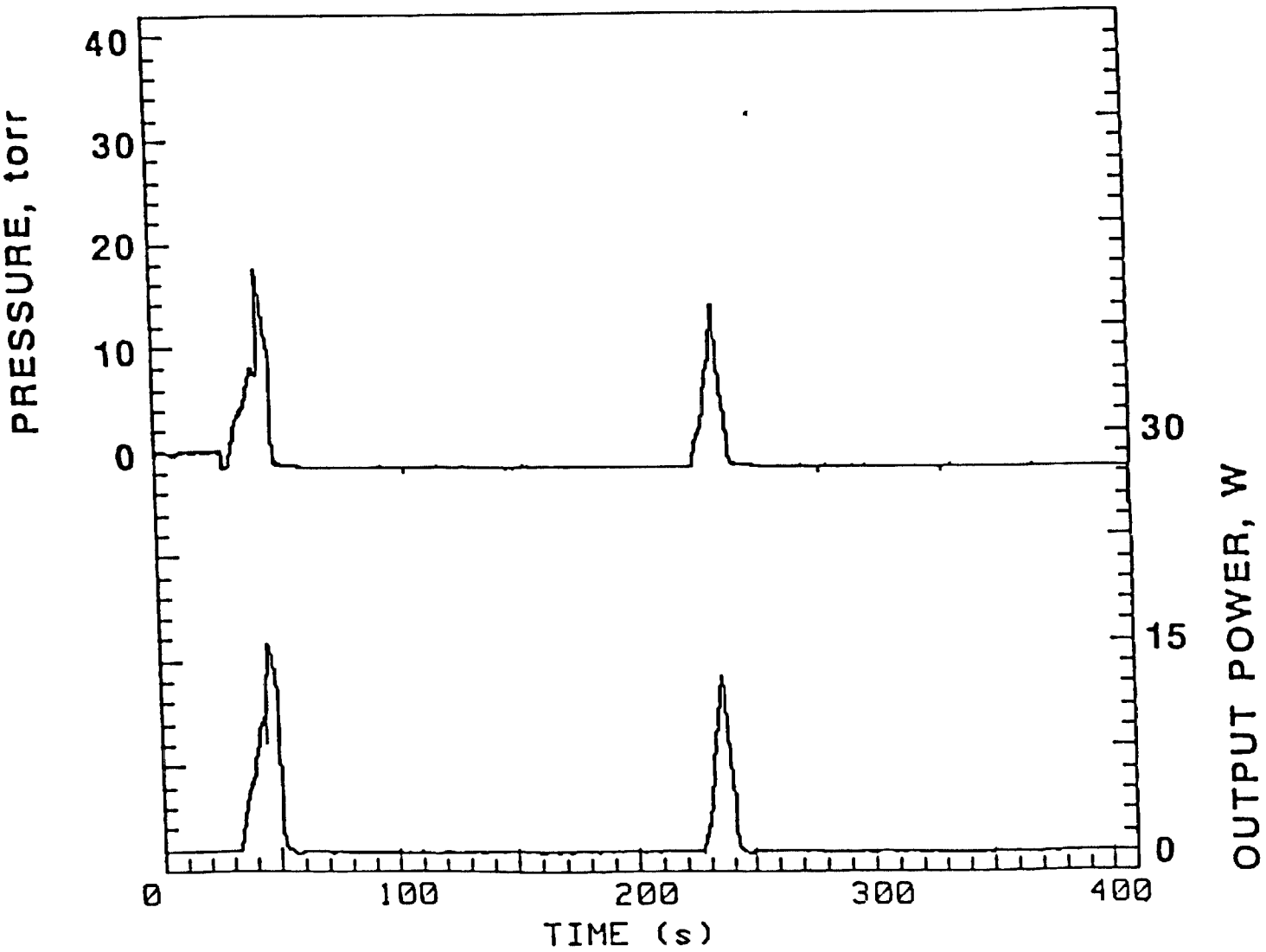

Figure 3. Oscillogram of CW output from t-C_4F_9I (lower trace) and its pressure (upper trace).

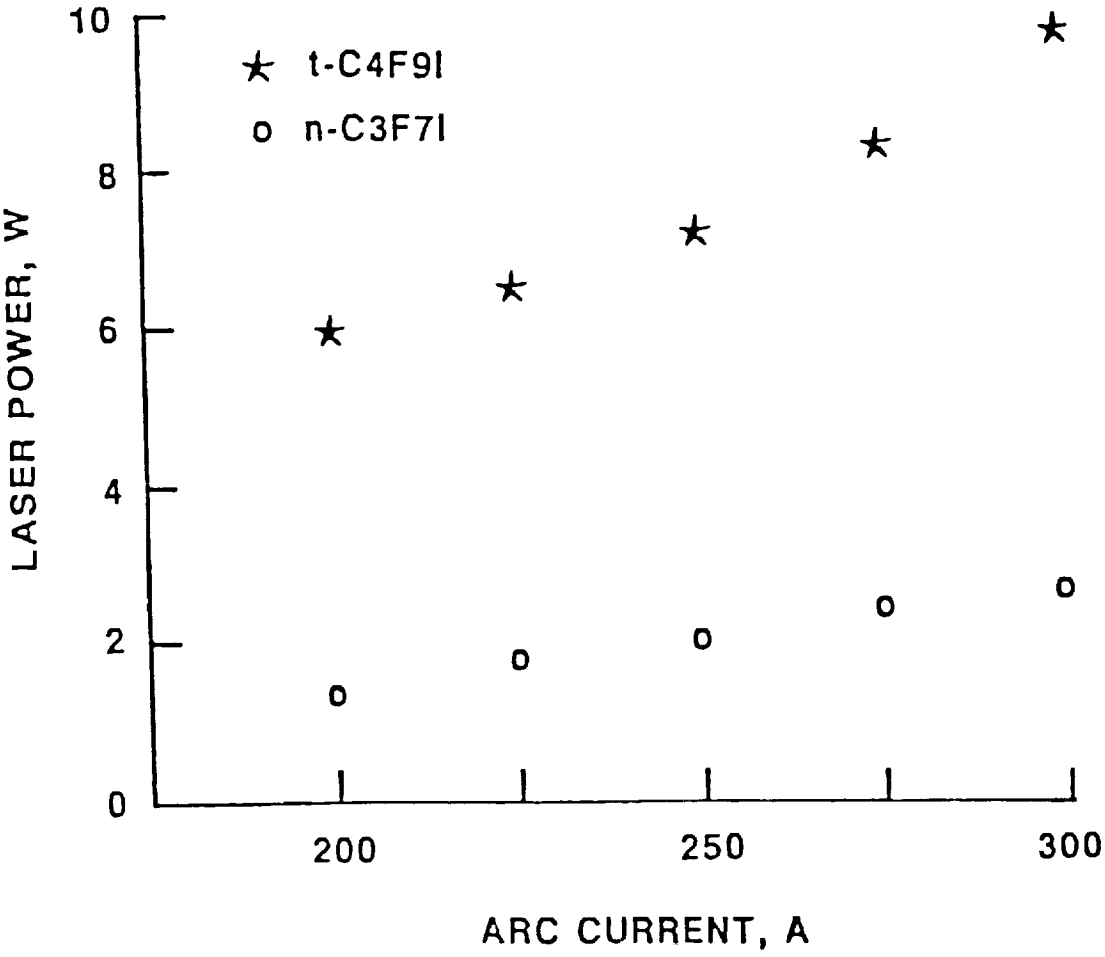

Figure 4. CW power output vs. the arc current.

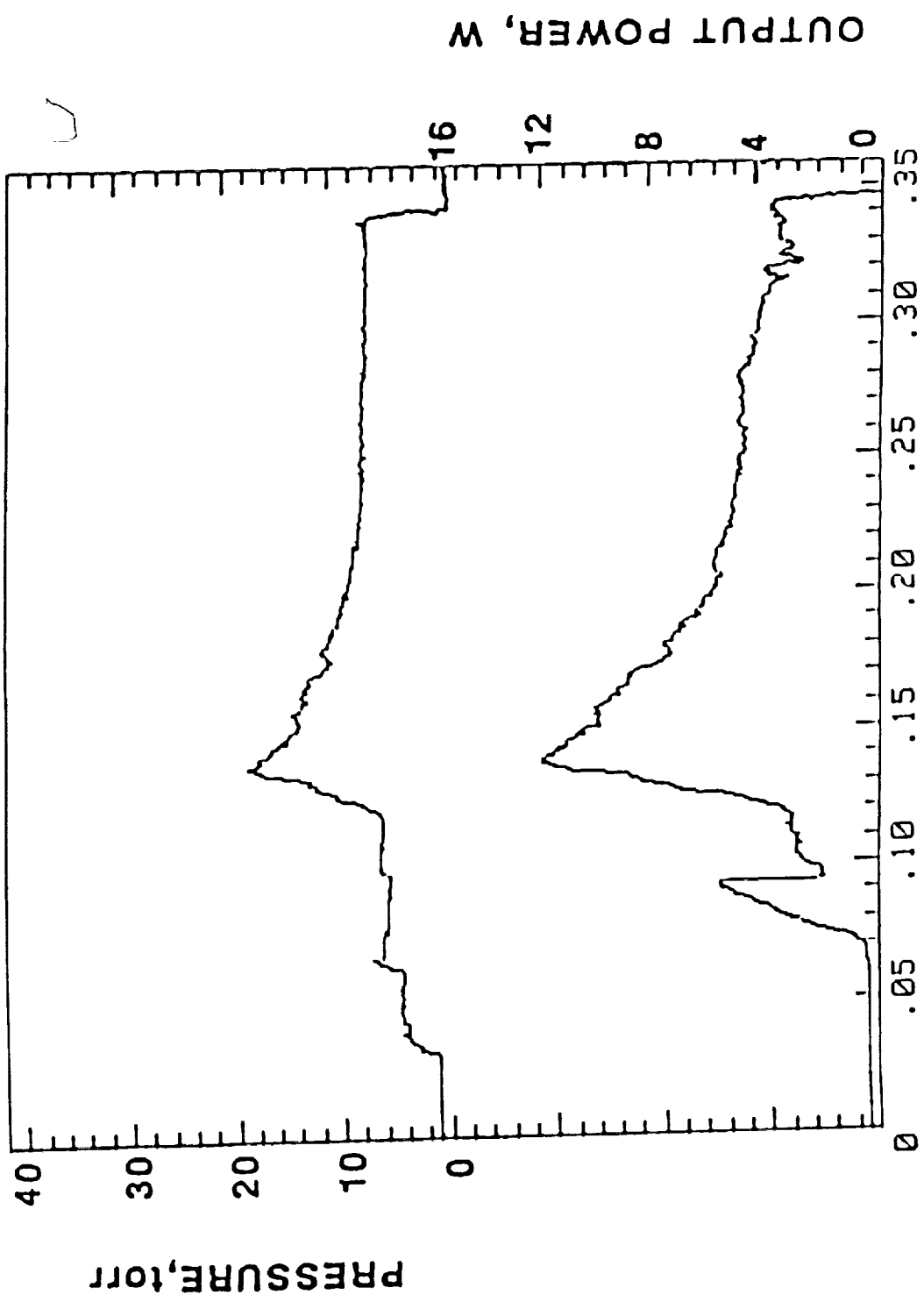

Figure 5. Oscillogram of CW output from a mixture of t-C_4F_9I and n-$C_6F_{13}I$.

THE UV PHOTOCHEMISTRY OF $C_2 N_2$

Joshua B. Halpern and Samuel A. Barts
Department of Chemistry
Howard University
Washington, DC

ABSTRACT

The absorption, emission and photodissociation yield spectra of $C_2 N_2$ have been measured in the 220 and 210 nm region near the 4_0^1 and $1_0^1 4_0^1$ bands of the $A^1\Sigma^- \leftarrow X^1\Sigma^+$ system. The emission spectrum showed very few lines which appeared in the absorption spectrum. Moreover the emission had 660 ns lifetime and, at 210 nm a very large electronic emission quenching rate. We used laser induced fluorescence to measure the relative yield of CN radicals as a function of photolysis wavelength. This spectrum seemed to follow the absorption spectrum below the dissociation threshold. Energy in the CN fragments appeared to be statistically distributed.

THE UV PHOTOCHEMISTRY OF $C_2 N_2$

Introduction

Cyanogen is a photochemically important molecule found in the atmosphere of Titan, and perhaps in other astronomical systems. We have discovered that this molecule has a strong and distinctive emission spectrum that can be used for remote detection.

Cyanogen is also an extremely simple tetra-atomic system in which predissociation can be studied. Potential energy surfaces have been calculated for all of the excited states which means that models of dissociation dynamics can be tested in detail.

Experimental

The apparatus was similar to that described in Reference [1]. $C_2 N_2$ from Matheson was purified by freeze-thaw cycling. The gas flow from a 3 liter reservoir was controlled by a Granville-Phillips fine metering valve and introduced into the cell through a hypodermic needle. The pressure was monitored by a MKS Model 200 capacitance manometer of a cold cathode gauge.

The excitation source was a Spectra Physics PDL-2 dye laser pumped by a DCR-11 Nd-YAG system. Light from the dye laser was frequency doubled in a KDP crystal and Raman shifted in about 10 atmospheres of hydrogen gas. For this experiment third and fourth anti-Stokes shifted beams were used. Since the doubled light is 100% polarized, all of the Raman shifted beams will be fully polarized. The intensity of the dye laser beam ranged between 25 and 60 μJ depending on the dye gain curve and dye used. The energy contained in each pulse of the photolysis beam ranged from a few to perhaps a hundred microjoules.

Emission from $C_2 N_2$ was detected directly through an unfiltered 11 stage EMR VUV photomultiplier. The signal was integrated by a PAR Model 160 boxcar analyzer.

CN fragments were detected by laser-induced fluorescence (LIF) excited by Molectron DL-II dye laser pumped by UV400 Nitrogen laser. The roughly 200 μJ beam was expanded, attenuated by neutral density glass filters and passed through a thin film glass polarizer to eliminate any elliptical character. Care was taken that the LIF signal was unsaturated. The electric vector of this dye laser beam was parallel to that of the photolysis laser. The overlapping laser beams passed through the experimental cell in opposite directions. The LIF signal was monitored about 100 μs after the photolysis pulse. This delay eliminates the effect of any changes in the nascent CN distribution as the photolysis wavelength was changed. The nitrogen pumped dye laser was tuned to resonance with the R(7) line of the CN $B^2\Sigma^+ \leftarrow X^2\Sigma^+$ violet system. LIF was monitored by an EMI 9558 photomultiplier tube looking through a 388 nm bandpass filter. The photomultiplier was placed perpendicular to the plane of the laser beams and the electric vector of the photolyzing light. The fluorescence signal was integrated in one channel of a PAR Model 162 boxcar analyzer. The intensity of the dye laser beam was measured by picking off a reflection and sending it into a photodiode.

The experiments were controlled by an IBM PC\XT microcomputer based data acquisition system constructed in our laboratory. The firing of the lasers and the dye laser scanning was controlled by the microcomputer.

Absorption spectra were measured directly on a Cary 2390 UV-VIS-NIR spectrophotometer or by measuring the far UV light intensity before and after the cell using scintillators to convert the light frequency into regions that can be detected by two Si photodiodes.

Results

Figure 1 shows an absorption spectra measured on the Cary 2390 spectrophotometer between 200 and 230 nm. The lower half of the diagram shows the difference between spectra measured at 20 and 70°C when the cell was heated by water from a thermostated bath. This identifies lines that originate in excited vibrational states and aids in the assignment of the vibrational bands. Figure 2 shows an absorption spectrum taken in the 220 nm region with a higher resolution instrument [2].

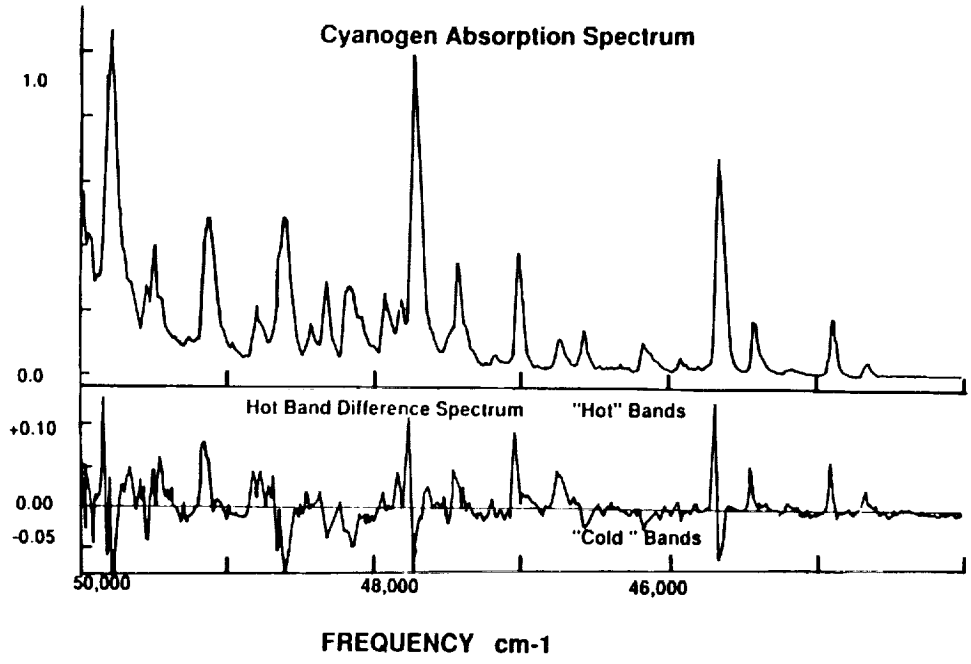

Figure 1

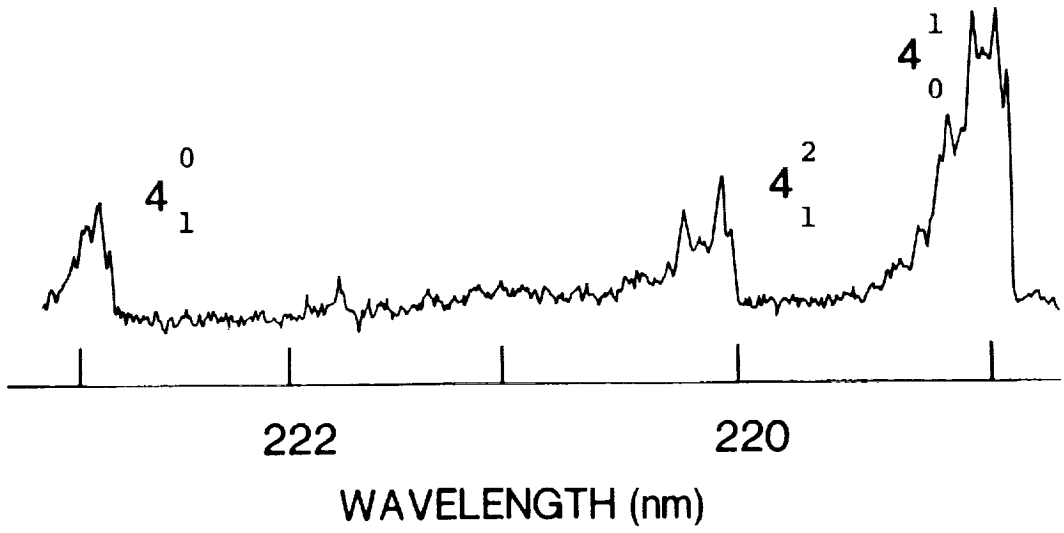

Figure 2

Figure 3 shows the spectrum of total emission following laser excitation in the 220 nm region. Attempts to detect CN fragments from photodissociation were unsuccessful although we were able to detect fragments if we used the much weaker 200 nm fourth anti-Stokes beam. This confirms the bond energy measurements of Eres and McDonald [3] which predicted that the dissociation threshold would be 212.76 nm. The emission spectrum does not match the absorption spectrum in all detail. The ratio of intensities between the 4_0^1 and 4_1^2 bands is somewhat different from that seen in absorption as is the shape of the bands. The emission lifetime obtained at the peak of the 4_0^1 band is 660 ns. Figure 4 shows the fluorescence spectrum obtained when the dye laser is fixed on the Q bandhead of the 4_0^1 line.

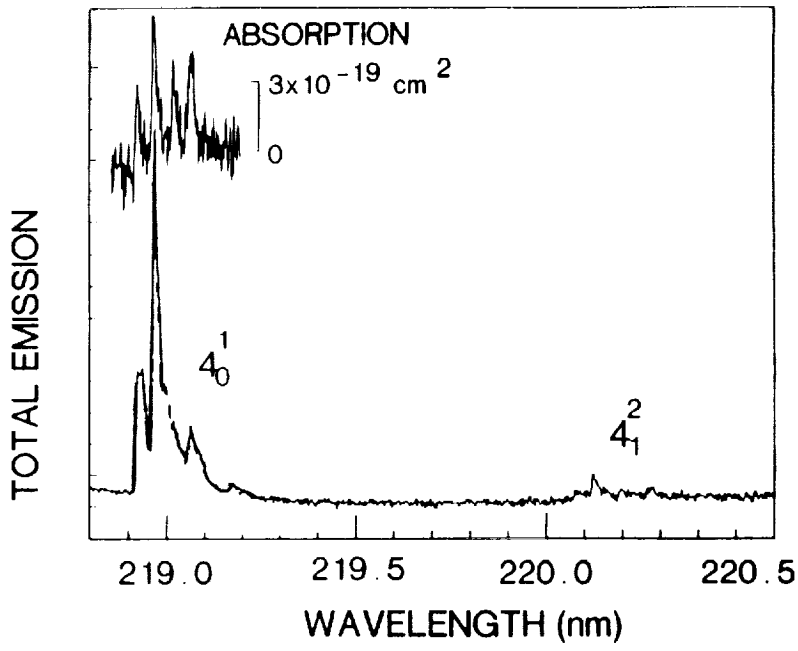

Figure 3

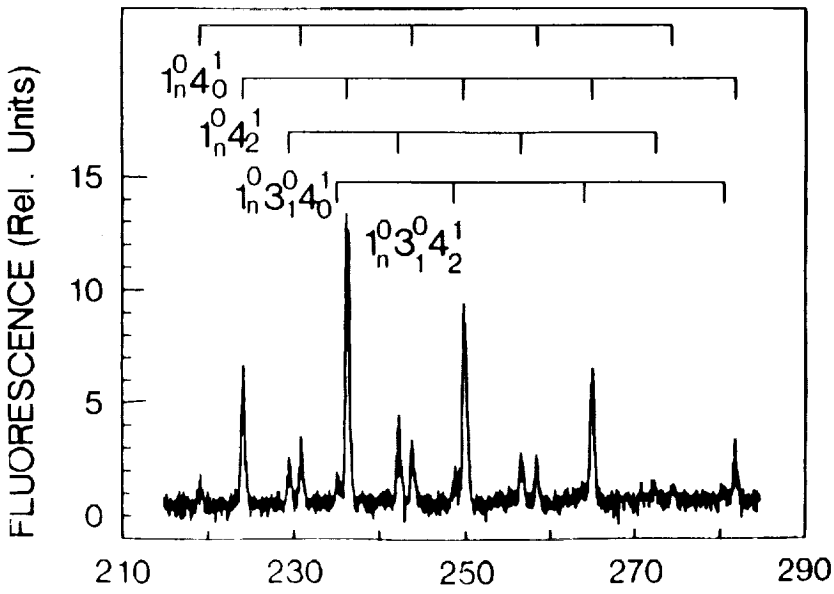

Figure 4

Figure 5 shows the absorption spectrum measured between 206.4 and 211 nm. Figure 6 shows the yield of CN fragments in the same region. The relative yield of CN was measured as a function of photolysis wavelength by (LIF). The photolysis yield generally follows the absorption spectrum as would be expected in any predissociation. Figure 7 shows the emission spectrum measured in the same region. Only a few peaks are observed. Note that the signal from the $1_0^1 4_0^1$ band extends far above the top of the scale. The insert in Figure 7 shows the $1_0^1 4_0^1$ band attenuated by a factor of 50. Structure can be seen on the red side of the emission at higher gain. We have measured the lifetimes of the emission excited in this band as a function of pressure. A Stern-Volmer plot of the measured decay rates is shown in Figure 8.

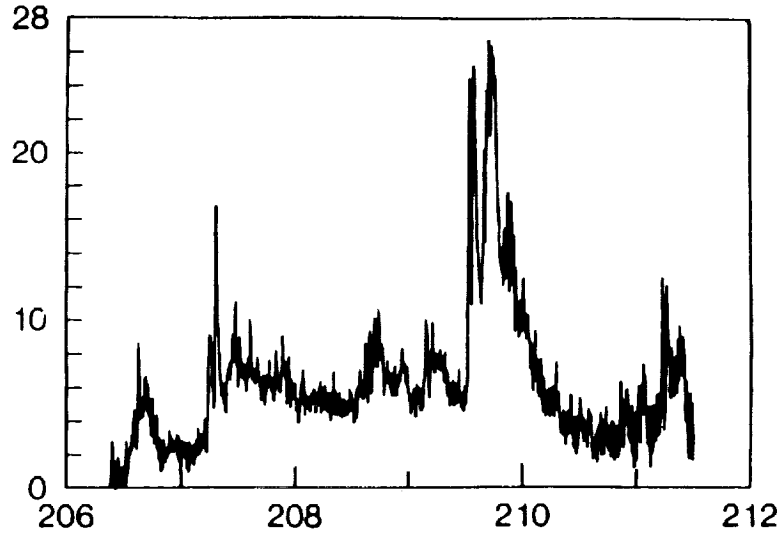

Figure 5

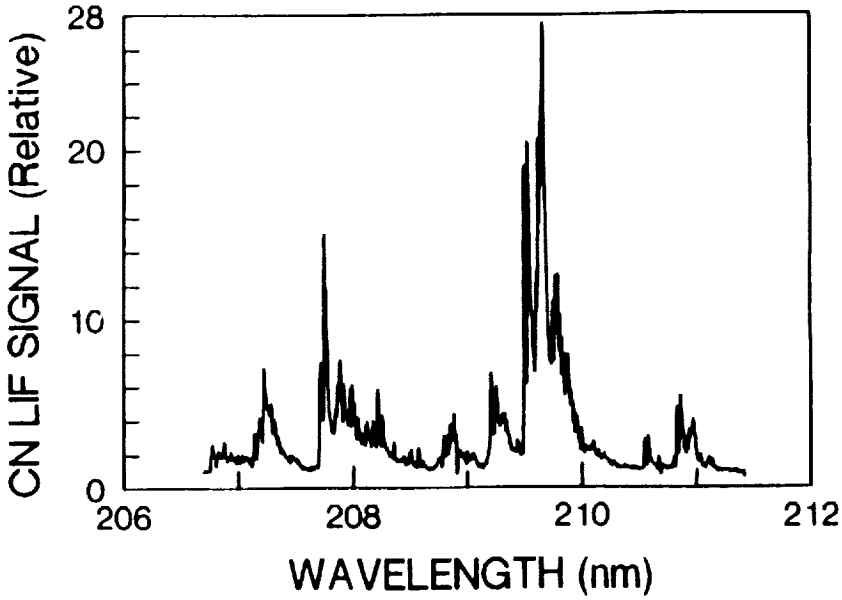

Figure 6

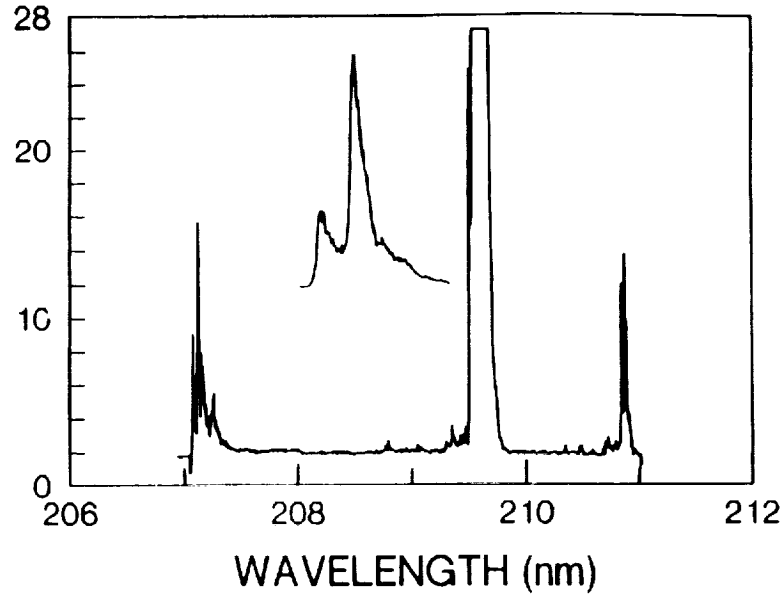

Figure 7

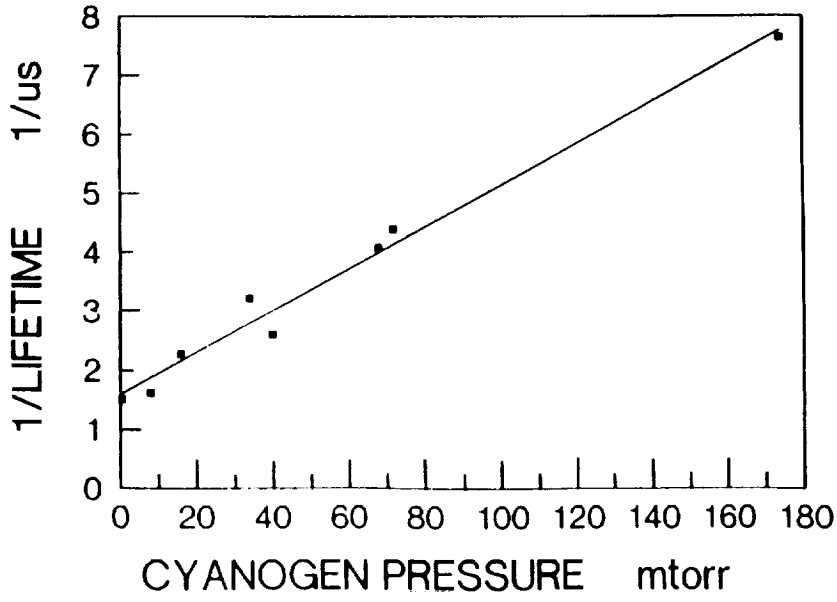

Figure 8

Figure 9 shows the fragment yield spectrum between 200 and 202 nm corresponding to excitation of the $1_0^2 4_0^1$ transition. The right hand half of Figure 10 shows the emission spectrum in the $1_0^2 4_0^1$ region as compared to that from the 4_0^1 region. There is a factor of several thousand difference in the intensities of the emissions.

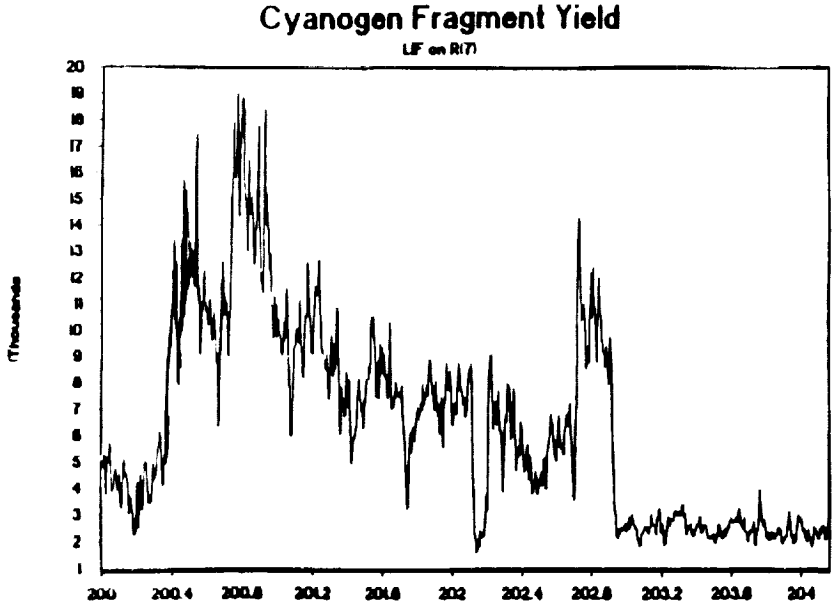

Figure 9

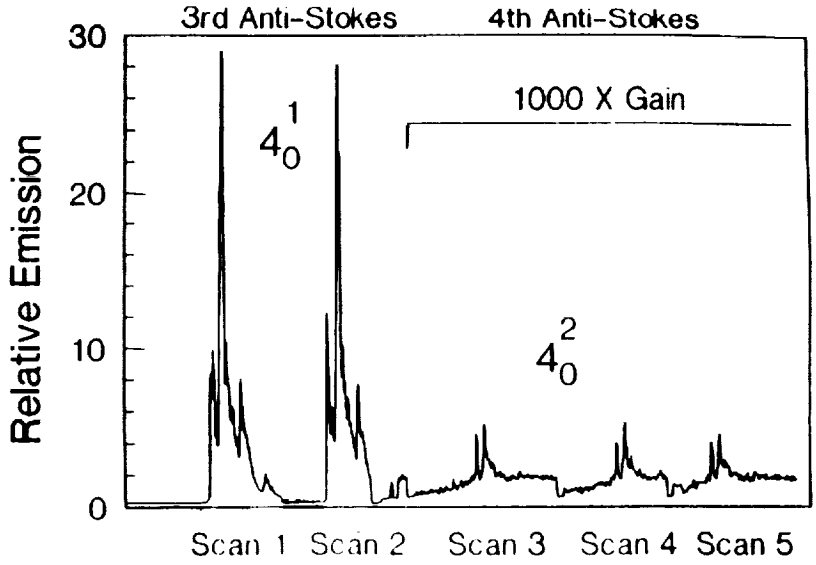

Figure 10

Discussion

Figure 11 is a linear correlation diagram from Reference 4. These observations can be qualitatively explained with the following model: C_2N_2 is excited from the ground $X^1\Sigma^+$ state into the $A^1\Sigma^-$ state. At excitation energies below the dissociation limit the molecule simply fluoresces and returns to the ground state. This is shown conclusively by the fluorescence spectrum as explained in Reference 1. After excitation above the dissociation limit there is a competition between fluorescence, dissociation (where energetically possible) and crossing over to a lower triplet system. Emission can also occur from this triplet system back down to the ground state. The correlation diagram indicates that the $A^1\Sigma^-$ state cannot directly dissociate to ground state CN fragments in the linear configuration. While this restriction would be relaxed in a bent configuration it is also possible that dissociation occurs through a crossing to the $a^3\Sigma_u^+$ system which correlates with ground state fragments. The barrier in the linear configuration can be avoided if the molecule bends.

Future experiments will attempt to elucidate this mechanism and add quantitative detail to this qualitative model. Experiments to be done include measurement of the fluorescence spectra below the dissociation limit. This will allow us to elucidate the mechanism of dissociation. Second, we will compare the intensity of emission with that from known pressures of NO, allowing us to calculate quantum yields for all processes. This will allow us to map the state density of the emitting triplet state and provide a clock for measuring photodissociation rates.

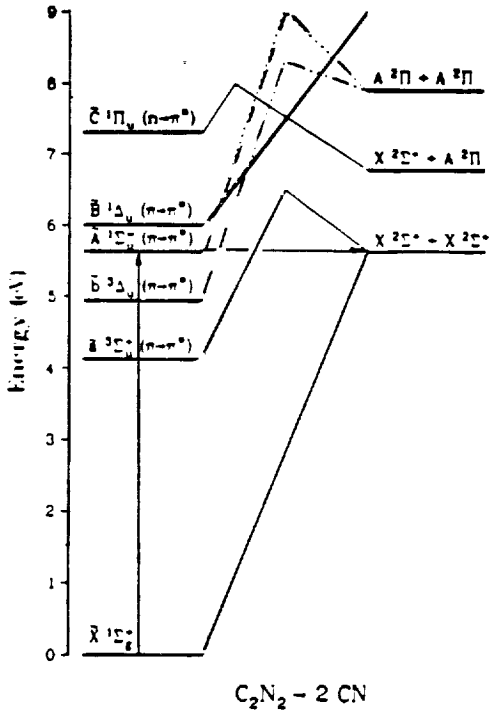

Figure 11

Conclusion

The study of cyanogen $C_2 N_2$ photolysis has produced several important results. First, significant emission was observed from $C_2 N_2$ following excitation to both bound and unbound states. This emission has not previously been reported. If, as has been suggested, cyanogen is a minor constituent of astronomical objects the intensity of this emission would be the measure of the cyanogen concentration. Second, we made initial measurements of the competition between emission and dissociation.

Acknowledgments

Parts of this work were supported by NASA under Grant NAG-5071 and a grant of money from the Howard University Research Development program. S.A. Barts was supported by a Danforth Foundation Fellowship.

1. J.A. Russell, I.A. McClaren, W.M.Jackson and J.B. Halpern, J. Phys. Chem., **91** (1987) 3248.

2. Taken with the assistance of Dr. Alan Laufer at NIST.

3. D. Eres, M. Gurnick and J.D. McDonald, J. Chem. Phys., **81** (1984) 5552.

4. Dateo, C.; Thesis, University of California, Berkeley, 1987.

ENCOURAGING THE PURSUIT OF ADVANCED DEGREES IN SCIENCE AND ENGINEERING: TOP-DOWN AND BOTTOM-UP METHODOLOGIES

Anthony B. Maddox
Massachusetts Pre-Engineering Program and
Brandeis University Computer Science Department

Renée P. Smith-Maddox
Massachusetts Pre-Engineering Program and
Brandeis University Heller Graduate School

Benson E. Penick
Benson Penick & Associates

ABSTRACT

This paper describes the MassPEP/NASA Graduate Research Development Program (GRDP)[1] whose objective is to encourage Black Americans, Mexican Americans, American Indians, Puerto Ricans, and Pacific Islanders to pursue graduate degrees in science and engineering. GRDP employs a **top-down** or goal-driven methodology through five modules which focus on research, graduate school climate, technical writing, standardized examinations, and electronic networking. These modules are designed to develop and reinforce some of the skills necessary to seriously consider the **goal** of completing a graduate education.

GRDP is a community-based program which seeks to recruit twenty participants from a pool of Boston-area undergraduates enrolled in engineering and science curriculums and recent graduates with engineering and science degrees. The program emphasizes that with sufficient information, its participants can overcome most of the barriers perceived as preventing them from obtaining graduate science and engineering degrees.

Our experience has shown that our top-down modules may be complemented by a more **bottom-up** or event-driven methodology. This approach considers **events** in the academic and professional experiences of participants in order to develop the personal and leadership skills necessary for graduate school and similar endeavors.

---

[1]The MassPEP/NASA GRDP is supported by the National Aeronautics and Space Administration (NASA) Office of Equal Opportunity Programs under Training Grant NGT 22-005-900 and administered by the Massachusetts Pre-Engineering Program (MassPEP). We gratefully acknowledge GRDP staff and participants for their comments and perspectives.

ENCOURAGING THE PURSUIT OF ADVANCED DEGREES IN SCIENCE AND ENGINEERING: TOP-DOWN AND BOTTOM-UP METHODOLOGIES

Introduction

As the United States becomes more technology-based, there is a corresponding growth in the demand for technically-trained people. Some recent demographic projections indicate that approximately 0.75 million technical positions may go unfilled at the beginning of the 21st century. Many of these positions will require research-oriented master's and doctoral degrees, which are increasingly being awarded to individuals who are not citizens of the United States. One way to increase our national resource of technical people is to encourage Americans from racial and ethnic populations who are underrepresented in technical disciplines to pursue engineering and science degrees and careers.

For the past 10 years, the Massachusetts Pre-Engineering Program (MassPEP) has been successfully encouraging Boston and Cambridge middle and high school students from these populations to study engineering and science. Recently, more than 80 percent of MassPEP participants have attended college, many selecting technical majors. Since the Fall of 1986, MassPEP and the National Aeronautics and Space Administration (NASA) have collaborated on the Graduate Research Development Program (GRDP). The goal of GRDP is to encourage Black Americans, Mexican Americans, American Indians, Puerto Ricans, and Pacific Islanders (hereafter referred to as our target population) to pursue research-oriented graduate degrees in engineering and science.

Top-Down Program Design

GRDP employs a **top-down** or goal-driven methodology through five modules which focus on research, the graduate school process, technical writing, standardized examinations, and electronic networking. These modules are designed to develop and reinforce some of the skills necessary to seriously consider the **goal** of completing a graduate education. GRDP modules were also designed to disseminate information needed when applying to and completing graduate programs in a wide range of technical disciplines.

The modular activities of the GRDP curriculum were generated directly from the program objectives, which are the **subgoals** of the program. They were designed to achieve the objectives over a twelve-week period with four-hour meetings scheduled on Saturday of each week. To accommodate scheduling disparities, GRDP does not emphasize the structure of regular meeting attendance, but instead, places an emphasis on effective time management within the constraints of other commitments.

The objective of the **RESEARCH** module is to expose each participant to the process of developing a technical research proposal. Each participant generates a 5-10 page proposal including abstract and bibliography in an area of interest. An oral presentation is given in an open forum which may include representatives from academia, industry, and government as well as GRDP staff and participants. Generally, undergraduate research opportunities are seized by upperclassmen who have

developed relations with faculty or have exhibited exceptional academic ability. Factors such as social isolation and academic performance can prevent our target population from developing these necessary faculty relationships thus curbing an interest in research. GRDP offers an opportunity to explore a technical research topic of interest.

The **SEMINAR** module's objective is to help each participant develop perspectives on various research opportunities and apply for research internships, admission to graduate research programs, and financial support. Pursuit of a research-oriented experience is illustrated as a planned sequence of activities guided by a thorough investigation of technical interests and objectives. Attention is given to specific strategies, heuristics, and personal development issues. The module's agenda is supported by a booklet published by GRDP entitled **Graduate School in Science and Engineering: IT PAYS TO GO** and discussions with invited speakers. Participants are asked to submit applications to at least two research internship or graduate programs and financial aid sources. All application fees are reimbursed by GRDP.

Success in graduate school involves: (1) academic performance, (2) understanding departmental agendas and procedures, and (3) successfully interacting with colleagues and faculty. GRDP participants learn about the explicit and implicit details of applying to and being successful in graduate programs. There are opportunities for participants to discuss and examine various aspects of the graduate school process. Topics include: matching one's skills with particular academic institutions, the application process, financial support, tenured versus non-tenured advisors, oral versus written qualifying and comprehensive examinations, etc.

The objective of the **COMMUNICATION** module is to provide each participant with practice and experience with communicating written and oral technical information and opportunities to discuss technical issues. Occasionally the module's format includes class discussions pertaining to racial and ethnic issues which can affect graduate students. The result is a completed research proposal and an oral presentation with visual aids. Some undergraduate engineering and science curriculums do not include many courses on writing, though written communication is an essential part of an engineering or science career. GRDP gives its participants the opportunity to develop the writing skills which are necessary for graduate school applications, research reports and papers, etc.

The Graduate Record Examination (**GRE**) module's objective is to reinforce each participant's skill in taking the GRE. Practice GRE General Tests are administered by GRDP while each participant is offered the option of taking an Educational Testing Service (ETS) administered GRE General or Subject Test. Participants are responsible for completing two examinations and the verbal, quantitative, and analytical sections of past examinations as in-class assignments. There are also opportunities to freely discuss individual or group concerns about the GRE. All GRE registration fees are reimbursed by GRDP. The rationale is that if practice improves GRE scores, the chances of being accepted into graduate school also improve.

The objective of the **COMPUTER** module is to reinforce the use of computers as an essential means to support research and as an effective means to maintain professional networks for each participant. Participants have the opportunity to use electronic bulletin boards and mail to reinforce networking. The major concern of GRDP participants is that the program will interfere with their academic or work schedules. Computer-based communications allow staff and participants to interact when personal contact is not possible. This "electronic mentoring" also helps participants and staff become more familiar with the use of computers, terminals, and modems.

Participants

GRDP is a community-based program which seeks to recruit twenty participants from a pool of Boston-area undergraduates enrolled in engineering and science curriculums and recent graduates with engineering and science degrees. We have found that recent graduates, those who have received their degrees within the past five years, have been the most consistent participants in GRDP. Two possible reasons are that: (1) their employment schedules do not interfere with GRDP activity as much as the academic schedules of undergraduates and (2) their experience has shown them the value of an advanced degree.

Admission

Recent graduates are accepted for admission if they have a bachelor's or master's degree in engineering or science. Undergraduates (excluding freshmen) are admitted as long as they meet the minimum academic requirements for their academic institution. One of the strongest messages sent by the program was that there is no reason not to consider a graduate degree in engineering or science. GRDP is committed to showing its participants how they could use a variety of strategies for overcoming many apprehensions based on their academic or personal histories. Though GRDP maintains that standardized examination scores and other factors such as research experience may strengthen an average undergraduate record, we acknowledge that there are few substitutes for above average academic performance.

Benefits

In addition to paying graduate school application and GRE fees, GRDP provides the use of a modem and personal computer or terminal for networking. This has proven to be helpful to participants who access computers regularly in their work or studies. A $200 stipend is also awarded to participants who complete two GRE examinations, give an oral presentation on their written research proposal, and submit two research internship or graduate school applications. For partial completion of program activity, a pro-rated amount is awarded based on accomplishments within each module.

GRDP participants who apply to a graduate school or a research laboratory are reminded that visiting an institution or facility may enhance an applicant's chances of being offered a desired opportunity. To underscore this point, GRDP reimburses or advances travel expenses to visit a research laboratory or graduate school before or after being offered a position, respectively. These travel grants are limited and the GRDP staff helps participants plan to maximize the travel resources allotted to them. GRDP establishes contact with an administrator, professor, scientist, engineer, or student who may assist the participant in assessing opportunities at the institution or facility. A one-page trip summary of the visit is a responsibility of the participant. Travel is arranged so that academic commitments may be maintained.

GRDP participants who are juniors and accept an internship at a research facility are eligible for GRDP research internship support. On an individual basis, GRDP attempts to provide the difference between a research internship salary and a non-research salary, up to a designated maximum. Brief progress reports or research papers are required to receive the grant throughout the summer.

Staff

The Boston metropolitan area has provided GRDP with a diverse staff. Each staff member is or has been a graduate student, most in technical disciplines, and has a part-time association with GRDP. For staff which are currently graduate students, GRDP has the secondary benefit of providing them with support for their graduate education. In the three-year history of GRDP, two staff members have been awarded NASA fellowships.

GRDP staff members have had a variety of experiences. Some have had experience in industry. Others were born outside of the United States (Jamaica, Guyana, Japan, Panama). We have had single parents as well as married couples with adult or pre-school children. GDRP thus provides participants with social as well as professional role-models.

GRDP's Competition

Encouraging the target populations to pursue degrees requiring technical and quantitative skills has been difficult but generally successful. It appears that as a result of attrition at the undergraduate level, a relatively small number of individuals from the target populations receive undergraduate degrees in engineering and science. It is from this small pool that candidates for graduate-level degrees are generally selected.

This pool is also the recruiting source for business and industry. Individuals with undergraduate science and engineering degrees command high salaries from employers seeking people with state-of-the-art skills for various technical positions. Annual salary offers approaching the middle $30,000 range are not uncommon. Large starting salaries deter many from continuing on to graduate school. Unlike professional fields such as medicine, law, or dentistry, engineering practice generally does not require an advanced degree or licensure. Though professional registration for engineers is often encouraged, many laws allow employers to assume the legal responsibilities for engineering practice. Consequently there is less incentive to attend graduate school.

Bottom-Up Methodologies

Our experience has shown that our top-down modules may be complemented by a **bottom-up** or event-driven methodology. This approach considers **events** in the academic and professional experiences of participants as a means to guide the development of the personal and leadership skills necessary for graduate school and similar endeavors. We have learned that it is important for GRDP to understand more about each individual participant. To help accomplish this, each staff member serves as a mentor to a participant. Each mentor decides when and how much information to share with other staff about their participant. We often find that similar issues and problems surface in different modules and we become better equipped to deal with them when they are discussed in an open manner.

Our conclusion is that the best strategy for encouraging our target population to consider graduate school is to foster individual interaction with them. It is important for us to understand many of the issues that cause participants to investigate or reject graduate school. These issues include family and

employment pressures, self-esteem and confidence problems, research interests, indecisiveness, academic burnout, etc.

Results

From the approximately 50 people who have participated in GRDP, five have applied to graduate programs. Two have successfully been admitted to graduate school. One individual is employed with a master's degree, and is pursuing her doctorate part-time. She is also the instructor for the program's GRE module. The other participated in GRDP since her junior year and is enrolled full-time in a master's degree program with fellowship support. Two of the remaining three applicants are awaiting decisions on admission and financial aid. One individual was unsuccessful in gaining admission for graduate study. We believe that this was mainly due to her not actively seeking admission for graduate study until the second semester of her senior year. Four of the five were females of Black and/or Hispanic origin who had majored in engineering. The remaining individual was a Black male who majored in engineering technology.

We do not base the success of GRDP solely on the numbers of individuals who attend graduate school. We believe that for undergraduates to include GRDP in their weekly activities is significant. Since GRDP offers no direct benefit to academic pursuits, and offers a modest stipend, participation is an indicator of interest in graduate school. We have had several undergraduates who could not accommodate GRDP in earlier program years, return to GRDP seeking admission.

Quite often we have been told by our participants that GRDP serves as means for social interaction. They felt that GRDP was a comfortable environment where issues could be discussed candidly and straightforward answers and comments could be expected. We were not surprised that our recent graduates would share this perspective. There is limited support provided for our target population by employers. We did not expect this response from undergraduates who were associated with academic, professional, and social support organizations internal and external to their academic institutions. Apparently the existence of sophisticated social avenues for undergraduates does not reduce the need for programs similar to GRDP.

Future Issues

There are several important issues which will be explored in future program years. First, it is not easy to identify how GRDP has had an effect on its participants; for example, whether GRDP supports existing intentions or promotes non-existing aspirations to pursue graduate degrees. Knowing the difference could lead to program designs which allow a program's resources to be used more efficiently and effectively.

Second, profiles need to be established to detect common characteristics of those who attend graduate school and those who do not. We believe that specific identification of factors beyond employment and salaries which cause selection of employment over graduate study would be helpful in deciding how to suggest graduate study earlier in a student's academic career. For example, we need to discover why: (1) fewer males in the target population appear to be applying to graduate school and (2) fewer females apply to technical graduate schools.

Third, an effort is needed to expand the scope of such programs to include more disciplines which are underrepresented by racial and ethnic populations. Many of the details illustrated in this paper may apply for various types of graduate programs. Techniques and strategies which are generally applicable will be very useful for attracting students to graduate programs.

Summary

From our experiences with GRDP, we have summarized some of the important aspects of the program:

1. **Program setting**. Programs such as GRDP benefit from being housed in academic settings. In large metropolitan areas such as Boston, where there are several academic institutions, a community-based program has the opportunity to attract a diverse undergraduate student population. It also attracts recent graduates from nearby business and industry. University environments also allow recent graduates to become reacclimated to academic surroundings. Commitments from administrative personnel for meeting space, laboratory tours, computer resources, etc., are easier to secure.

2. **Diverse participants**. One of the most receptive audiences for the message of graduate school is the recent graduate. These individuals have the advantage of having experience as a way to measure the importance of a graduate degree. Recent graduates may also be able to influence undergraduates through associations developed within the program. First-year graduate students who continue to require mentoring and skill development should also be invited to participate in programs such as GRDP.

3. **Mentoring**. Mentoring relationships are essential for success in structured and competitive environments. The lack of role models at the graduate level in science and engineering departments often does not allow undergraduates to have the exposure they need. The same can be true in industry where there may not be scientists and engineers who are visible to younger employees. Therefore, the selection of a staff which includes role models who have had experience in graduate school has been critical. The fact that the staff has had experience in both industry and academia has been a plus to the program.

4. **Admissions**. A rolling admissions policy has been essential to the success of the program. Our efforts to structure the program around self-initiative as opposed to a schedule was not only necessary, but provides the participant with a first-hand opportunity to learn to manage the resources necessary to complete the graduate school process. Our admission procedure has increased the workload on staff members, but it has allowed us to attract and retain individuals as soon as they discover the program and its benefits.

5. **Information**. GRDP attempts to maintain an environment where a participant may match his or her level of preparation, skills, and commitment with his or her desire to attend and complete graduate school. The program provides a forum for asking questions about graduate school and the politics of the graduate school process while allowing the participant to simulate different aspects of the graduate school process. There is a constant flow of information in the form of articles, books and presentations which are available to anyone, including non-GRDP participants.

JPL INITIATIVE ON HISTORICALLY BLACK COLLEGES AND UNIVERSITIES

L. Allen, P. Forte and M. H. Leipold
Jet Propulsion Laboratory

I. Background

Executive Order #12320 of September 15, 1981, established a program designed to significantly increase the participation of historically black colleges and universities (HBCUs) in Federal programs. Because of its geographical remoteness and position as a contractor operated center, JPL had not participated in grant and training programs with the HBCUs. In recognition of our responsibility to the national commitment on behalf of the historically black colleges and universities, this paper describes an initiative with effective, achievable guidelines and early progress for a better and more productive interaction between JPL and the HBCUs.

While responding to the Federal mandate, the JPL initiative contributes to our University research base and our ability to recruit capable engineers and scientists. The historically black colleges and universities are staffed with motivated, competent and experienced scientists and engineers and graduate students. They have performed excellent research for other NASA centers. It is in the interest of JPL to tap this capability in meeting our research needs. Therefore, key elements of this initiative provide efficient mechanisms to allow for the granting of research funds to enable consulting, fellowships, academic part time, and summer employment for faculty and graduate students and to provide a means for JPL employees to attend these schools. This will provide the opportunity for students to learn, about both technology and JPL.

II. Program Content

Numerous areas of interaction with the historically black colleges and universities have been identified and are being implemented. They have two broad objectives, research interactions and faculty/student interactions. Plans and progress to date for each specific area are summarized below.

1. Research Grants

The fundamental mechanism for promoting research at the HBCUs is through a grant. Although JPL is barred from directly issuing grants due to our contractor status, a mechanism has been established to allow NASA to issue grants in our behalf. If funding for a grant is available entirely at NASA Headquarters, the grant is issued directly by NASA with JPL named as the technical monitor. If JPL wishes to release funds to use on a grant, JPL returns those funds to NASA and NASA similarly issues a grant and names JPL as technical monitor.

The responsibility for providing grant money and identifying research areas is with the Technical Divisions at JPL in concert with JPL's program offices. Through informal discussion and announcements of opportunity, appropriate HBCUs are apprised of the need for work. In making JPL research

interests known to HBCUs, emphasis is placed on individual-to-individual interfacing. Contacts among technical personnel and visits between institutions are encouraged. The HBCUs will respond with unsolicited proposals to accomplish the work, as germane to their academic needs and focus. We also submit to NASA a correct, exciting, and timely description of the Laboratory and its needs for inclusion in the NASA Initiative with Historically Black Colleges and Universities.

Review criteria have been pre-established and are included in information to prospective applicants to ensure that they have a prior understanding of the bases for evaluating their proposals. They include technical and programmatic relevance to JPL's objectives, scientific or engineering merit, qualifications of the investigator, qualifications of the investigator's institution, and overall cost. After review, the proposals, evaluations, and evaluation summaries are returned for further action - either a request to the Grants Program Analysis Officer, NASA Code U, for a grant award or a letter declining the proposal.

Funds are provided from one or more of the following four possible sources; 1) Redirection of JPL funds through the appropriate NASA headquarters program office to Code U, 2) Transfer of uncommitted NASA Headquarters program office funds to Code U, 3) Matching or enabling funds provided by NASA Headquarters EEO, Minority University Program, Code U, or 4) Other NASA program offices, centers or other government agencies. Upon receipt of the proposal and summary, Code U first obtains NASA program office concurrence that the proposed project is appropriate. Technical and administrative monitoring of the grant is the responsibility of JPL.

For each grant, there is a task manager who is responsible for coordinating all technical administrative and monitoring activities with the appropriate program office. Semi-annual and annual technical status reports are required of the grantee to assist in monitoring the grantee's progress.

At present, slightly over 20 proposals and white papers have been received and reviewed. Of these, six have been selected for funding and their status ranges from under negotiation to funding in place. Most of the the remaining proposals are still under consideration, frequently in a continued effort to develop necessary funding.

2. Technical Clinics

Claremont College in Claremont, California has, for many years, operated a Mathematics Clinic and an Engineering Clinic for JPL. These clinics were established to give undergraduate and graduate students experience with "real-world" problems in math. To make use of the clinic, an organization (company, government agency, etc.) contracts with a clinic to perform research on a particular problem. The clinic utilizes undergraduates under the guidance of a professor to seek the solution to the problem. This provides an excellent educational experience for students while making low cost talent available to the contracting organization. Further, it allows the student and contracting organization to better know each other.

While these clinics are sponsored by JPL, they are available to the rest of NASA and to industry. It is in JPL's interest to maintain close contact with the clinic through a guidance committee in order to assure a close interaction between JPL and the school's faculty and staff.

It is our intent to encourage the establishment of clinics at the HBCUs as appropriate to the school's area of interest. JPL's role is to sponsor the establishment of the clinic through the use of research grants as well as the sponsoring of actual clinic problems. We envision clinics in spectroscopy,

remote sensing, materials, and computer science. At present, no specific working relationships have been identified.

3. Equipment Loan

An existing NASA program makes unused JPL equipment available to colleges and universities in support of their research programs. Most elements of the transfer of equipment to support a grant at an HBCU by JPL are covered under existing procedures. In addition to this provision for loans, equipment which has been transferred to a school in support of a grant may frequently be abandoned in place at the conclusion of a research grant. The existence of a Memorandum of Understanding between JPL and a specific HBCU normally contains a statement advocating equipment transfer as a goal. This may also serve as a mechanism for transfer of equipment. In addition to assisting JPL and HBCUs in the administrative aspects of a transfer, this inititive may be able to assist in the financial aspects of transfer costs and instructions on equipment operation to the HBCU staff. As part of this initiative, a group at JPL working with data visualization problems has begun the transfer of film readers and software for Video Imaging Communication and Retrieval to Jackson State University. This capability at Jackson State is expected to result in continued joint efforts between the two groups.

4. Facilities Use

An existing NASA program allows colleges and universities to use JPL facilities on a non-interference basis for the enhancement of their research programs. Again, the JPL Initiative provides a mechanism for specific attention to the needs of HBCUs.

5. Personnel Loan Program

Another potential interaction is a personnel loan program whereby JPL employees are sponsored as visiting faculty at an HBCU. This employee spends one to two years at the candidate school performing teaching and research duties. Ideally, a research grant accompanies the employee to allow JPL sponsored research to be accomplished by a JPL employee and his/her students. The approval and awarding process for these grants follows the procedures outlined earlier.

The HBCU would normally provide support for the teaching/research activities including supplies and course expenses, equipment (leasing only), transportation expenses (related to University work), student assistant wages, and applicable university burden costs. A Memorandum of Understanding (MOU) between the JPL employee and the cognizant JPL organization detailing the terms is normally required.

At present, Dr. Kofi Apenyo from JPL is on loan to the Dolphus E. Milligan Research Institute of the Atlanta University Center. He will be teaching and doing research on database query systems for about 2 years.

6. Cooperative Education

Utilizing a highly successful existing program, undergraduate students are invited to take part in co-op programs. This program provides practical experience for students and develops a bonding between those students and JPL. Cooperative education programs are now in place between JPL and several schools. These programs will be extended to other schools as appropriate.

The Cooperative Education Program is designed to give undergraduate students an opportunity to prepare for a career with on-the-job training as a supplement to classroom instruction. Periods of classroom-related, fully paid employment alternate with periods of full-time study. In addition, work experience is supplemented by weekly meetings of Co-op students including information on projects in progress at the Lab and tours of various Lab facilities, as well as career and skill-development programs. These latter learning experiences serve both to broaden the student's technical base as well as provide an understanding of operating procedures at JPL.

In order for a student to be eligible for the JPL Cooperative Education program he/she must be enrolled in a Cooperative Education Program at a college or university with whom JPL has a signed Co-op agreement, be in good academic standing, have at least a 3.0 grade-point average on a 4.0 scale, and meet the regular JPL employment criteria. Work assignments are normally designed so that they may be completed during a six month time period and include scientific, technical, or administrative assignments. The difficulty and responsibility of the task depends on the position, experience, and interest. In addition, students are given the opportunity to learn new technical fields and organizational procedures.

Included are salary and a weekly housing allowance for eligible students. Limited funds may be available to support the hiring of minorities and women and every effort is made to ensure that a majority of the Co-op employees are females and/or minorities. All school expenses are the responsibility of the student.

JPL has had a small number of students from HBCU's as co-op students each year from the 4 HBCUs involved. These numbers are expected to increase as this initiative becomes fully effective.

7. Summer Employment

An existing summer employment program has provided a rich work experience for hundreds of students. Unlike the co-op program, this effort is not specifically tied to a course of instruction and is available to graduate students and faculty. It provides learning opportunities for participants as well as direct benefit to JPL for work conducted. Because the HBCU schools are outside of California, special provision for travel and housing expenses is made to make the program more attractive. The existing summer program budget is augmented by Minority Office funds to assure that HBCU hiring goals are realistically met. The intent is to enhance and increase the capabilities of minority scientists in JPL's hiring pool. This assists in the recruitment of college graduates as regular Laboratory employees. Not infrequently, summer faculty positions have been filled by professors in science, engineering, and business administration from universities where JPL frequently recruits.

College-level students are preferred, particularly those majoring in science, engineering and business administration. Student summer employees must have plans to return to school in the fall. Candidates from schools where the Laboratory regularly recruits are given preference. The minimum hiring age is sixteen. Salaries are based on a set salary structure in accordance with the student's academic standing at the beginning of summer.

Here as with the co-op program, the number of students involved is expected to increase as knowledge of our program is disseminated throughout the HBCU's.

8. Faculty Resident Program

A Faculty Exchange Program to employ faculty on leave or sabbatical for 6 months to one-year periods has been established. This provides an excellent opportunity for HBCU faculty to learn about us and for us to establish long-term ties to HBCUs.

This program is designed to further the interaction with HBCUs in the employment of faculty members in Laboratory research or project activities while in residence at JPL. Selected faculty members spend one or more academic units (quarter or semester) at the Laboratory working in an area of their choice and expertise, as part of an existing JPL team/group. This arrangement is renewable for up to two years.

Interested faculty members submit curriculum vitae to the Manager of Historically Black Colleges and Universities Initiative, together with a brief description of the activity they would like to be associated with as well as an endorsement from their dean or department head. JPL then circulates the applicant's material to potentially interested Laboratory organizations. Pre-established contacts between faculty and JPL staff greatly enhance successful selection. JPL positions are open to any bona fide faculty member for whom an appropriate position can be identified. Faculty interactions with an HBCU are also facilitated through existing programs such as the NASA Summer Faculty Fellowship. This program is NASA- wide and JPL is involved. It invites engineering and science educators who have interests in common with a professional peer at JPL to spend ten weeks during the summer on research here.

At present, no faculty have been placed at JPL under this Initiative.

9. Minority Fellowship Program

The Minority Fellowship Program is instituted as a JPL Affirmative Action Program to 1) provide JPL under-represented minority employees with an attractive opportunity to acquire an undergraduate or graduate college degree, 2) provide an employment incentive to attract newly graduated minority scientists, engineers, and administrative personnel, and 3) improve our level of interaction with HBCUs through direct contact between JPL employees and HBCU staff.

To meet these goals, the Minority Fellowship Program provides a full fellowship to deserving candidates. This includes full tuition and salary and benefits during full-time study at an HBCU. Fellowships are awarded for a maximum of five years. To assure that the employee has high career potential at JPL, that there is a reasonable chance that he will pursue a long-term career at the Laboratory and that he has a reasonable chance of successfully completing a degree program, the following conditions for candidacy apply:

1) The employee must pursue a course of instruction in a technical or administrative discipline that is appropriate for employment at JPL;
2) The employee must have at least 2 years of experience at JPL;
3) The employee must have completed at least 2 years of college;
4) The employee must have exhibited a high potential for a successful career at JPL;
5) The employee must demonstrate financial need; and
6) The employee must be willing to agree to 3 years work at JPL after completing his degree.

Appointments are made by a committee established by the assistant laboratory director. This committee administers, coordinates and monitors the program. Fellows must make consistent, appro-

priate and significant progress toward their degree objective, and progress is regularly reviewed. If a Fellow's progress is deemed to be below reasonable expectations in terms of attendance, grades, etc., appropriate remedial action is recommended.

Award of a fellowship is contingent upon the candidate being accepted by the proposed college or university within six months following selection. Acceptance prior to application for the program is preferred and enhances the applicant's chance for a fellowship.

The first group of applicants is being reviewed at this time for inclusion under this element of the initiative. The number is expected to be small, only 2 to 4, because of the limited funds available to support this part of the initiative.

10. Operation Pipeline

The intent of this activity is to outline a long-range development program to increase interest of local minorities in the math and science fields, leading to eventual graduation from an HBCU in a field related to the work of the Laboratory. JPL has participated in a very successful program with Elliot Middle School in Pasadena, California. In an extension to that program, we are pursuing a "pipeline" program that monitors and helps the progress of gifted students identified at Elliot and other schools as they progress toward college. Besides enrichment programs and summer or part-time employment at JPL, students are eligible for scholarships made available by HBCUs to fund their study at an HBCU. In most cases, this element does not introduce new activities, but serves as a continuous thread tying the various existing activities together and applying them to individual students.

Major program goals are to (1) develop student interest in math and science, 2) provide training for minorities who exhibit potential for success in the fields of science and math, 3) provide some financial support for needy and deserving minority students, and 4) provide a pool of talented minorities at JPL who have both experience and supporting education.

As an addition to the existing JPL Outreach Program to improve science teaching at the grade school level in our local area, a joint effort involving the University of the District of Columbia is under negotiation.

III. Technical Interchange Workshop

As part of the Initiative, JPL sponsors an Annual Technical Interchange Workshop involving the HBCUs taking part in the JPL program. Held at JPL, the Workshop primarily focuses upon the research grants and clinics. As appropriate, Workshop sessions also review and discuss progress in faculty and student interaction programs. It is the intent of JPL that the Workshop also be available as a forum to discuss the challenges of HBCUs as they work toward a strengthened competitive status in taking part in NASA and JPL work. The purpose of this conference is to:

1. Encourage annual interaction between faculty at historically black colleges and universities (HBCUs) and JPL personnel involved in sponsored research;
2. Familiarize JPL personnel with HBCU research capabilities; and
3. Further develop NASA supported HBCU research.

The conference also provides a forum to discuss, evaluate, and recommend appropriate changes in JPL/HBCU research interactions.

The initial conference occurred in May 1988. JPL personnel involved in this orientation included personnel from sections where research interests exist; contract management staff; recruitment staff, and other appropriate laboratory individuals. The second is planned for June 13 and 14, 1989. A number of additional schools are expected to take part this year.

IV. Supporting Organization

A division-level manager in the Technical Divisions serves as manager of the JPL HBCU initiative. This position is presently filled by Dr. Martin H. Leipold who acts as advocate to the technical divisions and program offices, provides information for and assures correct reporting to NASA, and monitors the performance of the varied activities. He is assisted by an Initiative Administrator, Mr. Paul Forte, who is responsible for generating required reports and coordinating initiative activities with managers from the Administrative Divisions.

The office of the Director at JPL has appointed a Steering Committee to review the actions taken or to be taken in the HBCU program and to provide guidance in the proper operation and functioning of the program at JPL and NASA. This committee reports on the activities being conducted as a part of the total HBCU Program. It is presently chaired by Dr. A. Zygielbaum.

The Initiative Manager and Administrator generate and distribute an annual plan showing important dates covering the mechanics of the initiative and establishing goals for participation by Laboratory organizations.

LINCOLN ADVANCED SCIENCE AND ENGINEERING REINFORCEMENT (LASER) PROGRAM

Dr. Willie E. Williams, Director
Physics Department
Lincoln University
Lincoln University, Pa

ABSTRACT

Lincoln University, under the Lincoln Advanced Science and Engineering Reinforcement (LASER) Program, has identified and successfully recruited over 100 students for majors in technical fields. To date over 70% of these students have completed or will complete technical degrees in engineering, physics, chemistry, and computer science. Of those completing the undergraduate degree, over 40% have gone on to graduate and professional schools.

This success is attributable to well-planned approaches to student recruitment, training, personal motivation, retention, and program staff. Very closely coupled to the above factors is a focus designed to achieve excellence in program services and student performance.

Future contributions by the LASER Program to the pool of technical minority graduates will have a significant impact. This is already evident from the success of the students that began the first year of the program. With program plans to refine many of the already successful techniques, follow-on activities are expected to make even greater contributions to the availability of technically trained minorities. For example, undergraduate research exposure, broadened summer and co-op work experiences will be enhanced.

This program is supported in part by the Office of Naval Research, National Aeronautics and Space Administration, and the Department of Education under grant #N00014-83-G-0082, Grant #NGT-90020, and Grant #P120B80021, respectively.

LINCOLN ADVANCED SCIENCE AND ENGINEERING REINFORCEMENT (LASER) PROGRAM

Introduction

LASER is a program sponsored by the National Aeronautics and Space Administration (NASA), Office of Naval Research (ONR), and the Department of Education (DOE) to explicitly encourage minority students to pursue engineering and science studies. The program was established in 1980 by NASA and Lincoln University as a joint effort to increase the number of students entering careers in engineering. Since then, the program has been expanded to include Physics, Mathematics, Computer Science and Chemistry majors. Lincoln was chosen as the site for the program because of its long history of providing students with the preparation skills needed to succeed in science and engineering careers. The program consists of summer and academic year components in an overall effort to prepare talented students for a course of study leading to a B.S. degree in Chemistry, Physics, Biology, Mathematics, or Computer Science or a dual degree: a bachelor of science in engineering and a bachelor of arts in liberal arts. Students are annually recruited nationwide to fill the twenty slots available.

The summer program provides the opportunity for participating students to begin their early course of study in an environment that has support services for success. Class sizes are small to provide the opportunity for students to work closely with instructors. In addition, special math, writing, and reading labs are maintained to provide additional help as needed. Each student is assigned a faculty advisor and counselor to offer academic and career guidance.

The program also provides the opportunity to work and interact with engineers and scientists. In subsequent summers, NASA, ONR, and other agencies provide employment with an opportunity to gain first hand knowledge of the careers in science and engineering.

LASER participants receive financial support to cover the cost of normal college expenses such as room and board as well as tuition for the summer program. In addition, the student receives a stipend to help cover his or her personal expenses.

The remainder of the paper provides a detailed discussion of the program components and review of the program's successes.

Philosophy

The LASER Program is a quest for excellence! In these times of diminishing quality and expectations, the LASER Program still stands for excellence and the best one can be. Like its acronym, the LASER Program is a very narrowly focused project aimed at producing an excellent and outstanding group of young men and women for careers in science and engineering. It is no accident that the expectations are so high. Each student is hand-picked based on high school performance, academic potential, natural ability, drive and motivation. Each student selected becomes a member of a select group that will make a major contribution to the world of engineering and related fields. From the very

outset the founders of the LASER Program designed a concept of excellence in every aspect of the program and conveyed it to the students accepted into the program.

Students are expected to achieve their highest potential. No second rate work or efforts are tolerated. Everyone must strive to be the very best he or she can as a student, as a person, as a human being. Nothing less than each student's individual best effort is ever accepted. The student's foremost concern must be achieving good grades in all course work. A "C" grade is not satisfactory, only "A" and "B" are grades worthy of a LASER student.

Students serve as role models of excellence in math and science and throughout the entire university. The LASER student is with few exceptions the best in all his or her classes and extra-curricular activities. He or she is a leader, setting goals and standards to be met by all.

Achievement and success in the LASER Program represent the collective efforts of LASER students, parents, staff, the Director and other university officials, all striving for excellence. In fact, excellence in LASER can only come as a result of this collective effort. The achievement of excellence is the single most important goal that runs throughout the LASER Program. All activities, tasks and specific objectives are set up to help achieve this excellence.

Program Objectives

Objective 1: To seek out and identify future minority scientists and engineers to meet the future requirements of our technical society.

The hallmark of LASER over the years has been an ability to understand the needs of students and, through the application of special aid and support, money, and technical skill, devise means to assist these young men and women to become successful. However, if one does not have an understanding of the student needs, no amount of money or technical skill will result in successful students.

A good understanding of the student requirements does not just happen. It takes hard work and a thorough understanding of the students themselves. One must deal actively and prudently with the environment that the students come from, as well as the environment that students find themselves in while attending the program. One must insure that the student involvement with the local environment is controlled and does not become counter productive for overall program goals.

Objective 2: To help LASER students achieve success by providing opportunities for advancement based on their academic performance, recognizing their individual achievements, and insuring the personal satisfaction that comes from a sense of accomplishment in their work.

One can take pride in the students and people in the LASER Program, their performance, and their attitude toward their jobs and toward the program. The LASER Program has been built around these individuals, the personal dignity of each, and the recognition of personal achievements.

The general policies and attitudes of the staff toward students and the people that work with them are more important than any specific person. Staff and student relationships will be good only if people have faith in the motives and integrity of their supervisors and the program management. On the other hand, relations will be poor if they do not.

Administrative Overview

Organization

The LASER Program is organized into four major efforts. The first of these involves the identification, recruitment, and training of minority students for careers in science and engineering. The second and equally important component of these efforts is the student reinforcement and retention activities. After careful analysis,the focus here is to provide the all important support system each student requires to be successful. This represents the bulk of the effort to date. The third component is the introduction of research and development experiences as well as exposure to national facilities like NASA, Fermi Lab, Stanford Accelerator Lab, Bell Labs, etc.The final component of the program tries to address the required facilities and equipment needed to maintain current, and when possible state-of-the-art, experience and exposure to emerging science and engineering concepts.

ORGANIZATION CHART

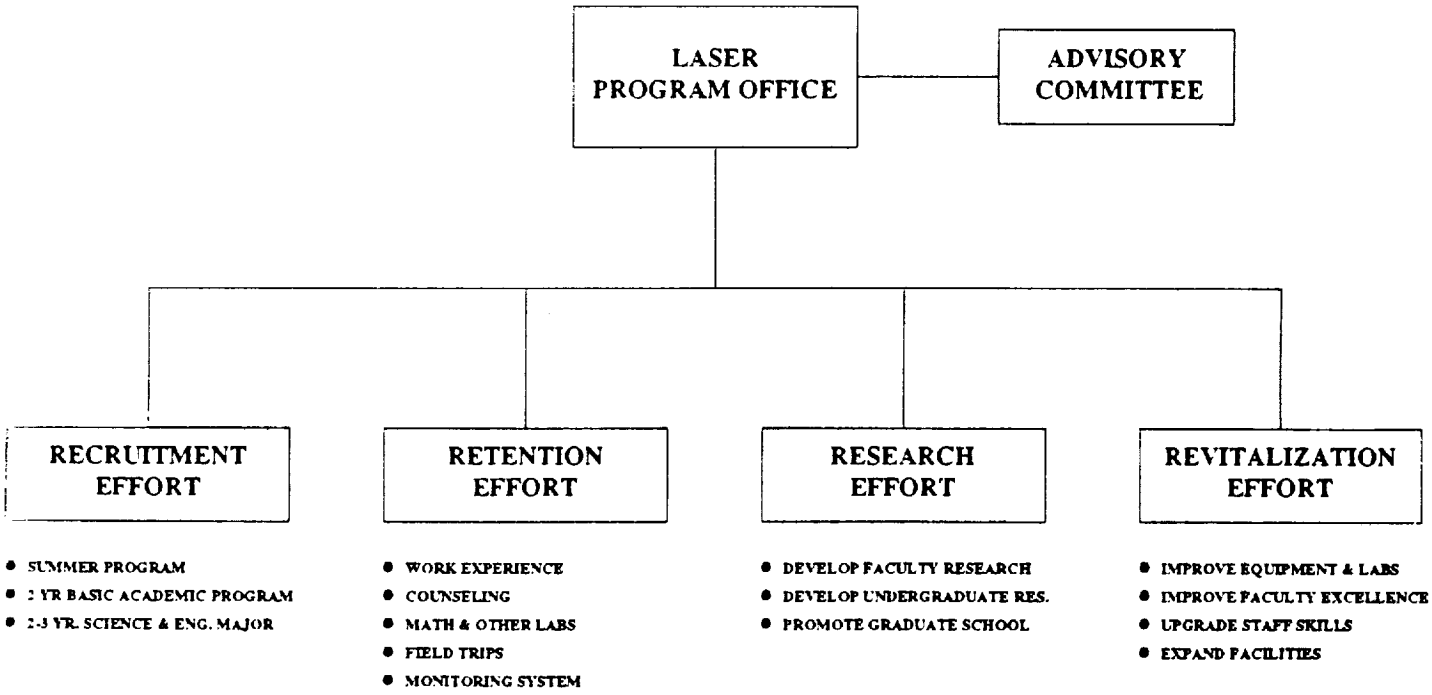

Participants

Students are recruited nationwide for the program. However, major efforts are concentrated within a radius of about 150 miles beyond the campus. Such areas as Baltimore, Philadelphia, New York, and Washington are target cities. The number of participants sought range form 12 up to 20, depending on the amount of available funding during a given year. The number 12 is regarded as the minimum number to be cost effective. Table 1 below summarizes the results for the past several years.

TABLE 1

	1981-82 Group I	1982-83 Group II	1983-84 Group III	1984-85 Group IV	1985-86 Group V	1986-87 Group VI	1987-88 Group VII	1988-89 Group VIII	TOTAL
	#	#	#	#	#	#	#	#	#
MALE	12	13	5	12	10	5	9	5	71
FEMALE	8	1	4	7	6	3	6	9	44
TOTAL:	20	14	9	19	16	8	15	14	115

Recruitment

The multi-approach is used in recruiting students for the program. The approach utilizes science faculty, admission personnel, high school counselors, science and math teachers, alumni and the media.

Extensive use is also made of mailings to alumni, high schools, and other groups. During the Fall term, letters and materials are sent to all known alumni on the East Coast. The mailing describes the program and requests their support in identifying potential candidates. During the same time high school science and math teachers are also mailed similar materials seeking their help in recommending students for the program.

Limited media exposure is provided for the program on a few local radio stations and in several newspapers. Occasionally, the program is able to receive TV coverage on one of the local community service programs.

Participant Selection

Each potential participant is required to complete both a program and university application, provide three (3) letters of recommendation, a high school transcript, and SAT scores.

Upon receipt of the LASER application and materials, the student is invited for an on-campus interview. The main purpose of the interview is to allow for a close review and evaluation of the student's abilities, academic potential, strengths and weaknesses. A team of 3 to 5 people spend from 45 to 90 minutes talking with each student. From the interview each student is rated on six items that are considered important to the student's success in the program.

Following the interview, students are required to complete the math placement test. This is an ETS test designed to evaluate the student's skills in algebra and pre-calculus. Based on their performance, students are placed in one of several math courses: algebra, pre-calculus or calculus. Normally, only those students testing into calculus are considered for the program. However, the final decision on selection is made by the director only after careful review of all the information available on a given student. Generally, with the exception of math background, no single item is the sole basis for selection.

Faculty and Staff

The pertinent program staff consists of a director, secretary, and an advisory committee. In addition, one or more assistants to the director, counselors, parents, course instructors, student tutors, and resident advisors are utilized during the course of the program.

Curriculum

The curriculum for this program is based on very specific requirements needed to complete technical programs in science and engineering. Most of these requirements have been worked out with participating science departments and engineering schools. The actual courses are in our science and pre-engineering curriculum.

The academic phase of the initial year of the program begins in the summer. During this period, students complete first year pre-engineering requirements in mathematics (calculus) and physics, as well as a survey course in engineering sciences taught by the project director and other engineers and scientists. At the conclusion of this summer trimester, students have earned approximately 18 credit hours. These students continue their studies in the fall.

Student Outcomes

The overall goal of the LASER program is to improve students' interest in and ability to pursue a technically-oriented education that leads to a career (or at least a degree) in engineering or a related science field. Thus, the entire program has been designed and implemented to achieve that end. The significant accomplishments of the project are summarized under the headings listed below and in Table 2.

Undergraduate Degrees Awarded

The most significant results of this project is the number of technical graduates. The program has had 34 students complete degree programs. Of this total, over 70% completed degrees in one of several technical areas. Expected graduates for the 1988-89 academic year will include 8 physics majors, 8 chemistry majors, and 1 electrical engineer.

TABLE 2
LASER PARTICIPANTS STATUS (RETENTION/TRANSFERS/GRADUATION)

		Number of Students Retained With Years Since Entry										
Year	#	1	2	3	4	5	6	Trans	Eng	Tech	Non	Grad
1981-82	20	20 (110%)	17 (85%)	9 (45%)	6 (30%)	1 (5%)	0	6 (30%)	5 (25%)	14 (70%)	3 (15%)	5 (25%)
1982-83	14	10 (71%)	5 (36%)	5 (36%)	4 (29%)	1 (7%)	0	5 (36%)	4 (29%)	8 (57%)	1 (7%)	2 (14%)
1983-84	9	9 (100%)	8 (89%)	6 (67%)	4 (44%)	3 (33%)	0	1 (11%)	1 (11%)	7 (78%)	0	0
1984-85	19	18 (95%)	18 (95%)	18 (95%)	10 (53%)	5 (26%)		3 (16%)	2 (11%)	14 (74%)	0	6 (32%)
1985-86	16	16 (100%)	14 (88%)	11 (69%)	8 (50%)		6 (30%)	4 (25%)	5 (31%)	1 (6%)	0	
1986-87	8	8 (100%)	8 (100%)	7 (88%)								
1987-88	17	16 (94%)	16 (94%)									
1988-89	15	14 (93%)										

Trans represents the # of students that have transfered. Eng represents the # of students that are Engineering graduates or persisting. Tech represents the # of students that are Technical graduates or persisting. Non represents the # of students that are Non-technical graduates or persisting. Grad represents the # of students that are in graduate school.

The LASER concept is successfully adding to the number of minorities completing undergraduate degrees in science and engineering. By the close of the 1988-89 academic year, the program expects to have graduated 13 B.S. engineers; 28 B.S. physicists; 6 B.S. chemists and 8 M.S. level scientists and engineers.

Graduate and Professional Programs

Equally impressive has been the project's success in encouraging students to seek advanced degrees in a wide variety of areas. A total of 14 students have enrolled in some type of advanced studies. Of this total, 80% are completing degrees in one of several technical areas that include engineering, physics, and chemistry, or non-technical areas such as psychology.

During 1988, three (3) students were selected as recipients of national fellowships from the Office of Naval Research and Oakridge Associates. Yvette Bell and Octavia Blount received ONR Fellowships that year, while Lori Thomas and Yvette Bell received Oakridge Fellowships.

Participants

The program has over 40 participants this academic year. Ten (10) of these participants are currently completing degrees at other colleges. Eight (8) of the ten students are pursuing degrees in engineering. In addition to the above students, a large number of students will be completing their studies at Lincoln. Over 80% of the students are pursuing technical degree programs.

A MODEL SUMMER PROGRAM FOR HANDICAPPED COLLEGE STUDENTS

Anne B. Nissen
Gallaudet University
Washington, D.C.

During the summer of 1988, the Goddard Space Flight Center was the site of a new NASA project called "A Model Summer Program for Handicapped College Students." Directed by Gallaudet University, the project's aim was to identify eight severely physically disabled college students — four from Gallaudet University and four from local historically black colleges and universities (HBCUs) — majoring in technical fields and to assign them technical projects related to aerospace which they would complete under the guidance of mentors who were full time employees of Goddard.

Gallaudet University is unique. It was founded in 1864 by an Act of Congress under President Abraham Lincoln and became the only liberal arts college in the world for the deaf. Located in northeast Washington, D.C., Gallaudet is just a twenty minute drive from Goddard. Virtually all its undergraduates are deaf or hard of hearing. A large percentage have additional disabilities including visual and mobility impairments. While at Gallaudet, deaf students are not handicapped, for virtually all the staff and faculty use sign language. Also commonplace to make collegiate life more accessible are TDDs (Telecommunication Devices for the Deaf), flashing lights (to complement bells and sirens), and captioned movies and television. Gallaudet is the only university in the world to have a deaf president.

Even as Galluadet provides a non-handicapping environment, so too can the workplace create an environment for disabled people that is enabling, comfortable, and accommodating. Towards this end, the model summer program at Goddard was established.

The greatest challenge of the project was locating students who met the project's four criteria for participation. This task tended to be difficult because offices offering services to handicapped students are not well established at the majority of HBCU's contacted. Students were required to:

1. be enrolled at Gallaudet or an HBCU;
2. be making progress toward a BA/BS degree in a technical or scientific field;
3. have a respectable grade point average; and
4. have a severe disability.

The pool for eligible applicants is exceedingly small. Few severely disabled minority young people are enrolled at four-year colleges. Furthermore, persons with disabilities do not traditionally select majors in scientific and engineering fields. The reasons for this situation are many:

1. While growing up, frequently the focus by the family and social services was on coping with the child's disability. Little thought was given to preparing the child for a career.

2. In many high schools, disabled students were waived from the science requirement due to inaccessibility to the lab, and real or imaginary dangers perceived by parents, teachers, and administrators.

3. There were few role models in the scientific or technical fields for the disabled student.

These combined factors severely limit the number of candidates for the program. We expect that the pool of candidates will grow as students are encouraged to explore the possibility of a future in a technical or scientific field while they are still in elementary school. Furthermore, the laws now require that all students receive an equal access to education.

Other factors complicate the placement of students in the work environment. Many disabled students have had little, if any, prior work experience and are reluctant to seek a work experience: issues of transportation, communication or accessibility often may seem overwhelming.

On the other hand, many organizations hesitate to consider severely disabled candidates because the organizations themselves feel uncomfortable and do not understand the abilities of these people who are different from the typical applicant.

Thus, with these issues in mind, Goddard Space Flight Center and Gallaudet University designed a model ten week program which provided:

1. support, resources, and training to supervisors and co-workers through workshops and individual assistance;

2. accessible housing at Gallaudet and accessible transportation for the students;

3. a mentor from Goddard for each student;

4. bi-weekly sign language classes for all interested Goddard employees;

5. an actual technical project for each student to work on;

6. on-site seminars on various technical topics for all participating students;

7. sign language interpreters for all training seminars;

8. a full-time coordinator who arranged the seminars, taught the sign language classes, handled the logistical issues, and met with the students as a group each week to evaluate and examine their experiences.

Was the program a success? Although we were unable to fill all four slots designated for the HBCU students because of the aforementioned reasons, seven students participated: five were from Gallaudet,

one was from the University of the District of Columbia, and one was from Bowie State College in Bowie, Maryland. Five of the seven had GPAs of 3.0 or higher. All were severely handicapped and majored in math and/or computer science.

The participants were almost unanimous in stating they received much more than they had expected. They were especially surprised at how challenging the tasks were for which they were responsible. Most did not expect to be treated so professionally: One participant stated "For the first time I was able to work on projects with other professionals...I learned so much!"

Almost all the participants responding listed improvement in their technical skills and an increase in self confidence as their primary growth areas. Other areas of growth listed included improvements in human relationship skills and the ability to handle responsibility. One participant summed it up best: "I felt positive about myself...I learned so much that my brain almost exploded." Another student said "I felt so good and proud to work for NASA."

As for the supervisors' reactions to the students:

* Six of the seven supervisors involved in the project want to be included in the coming year's project.

* Five of the seven participating students would "definitely" be hired if a position became available.

Other positive outcomes of the program:

* Three of the seven students are still working at NASA, one as a stay-in-school, and the other two are enrolled in Goddard's co-op program.

* Twenty-three employees studied sign language so that they are able to communicate more effectively with their summer co-worker and other permanent deaf employees.

* One of the participants made a presentation about her NASA experience to a group of about 200 Gallaudet freshmen who were considering a major in the Computer Science, Physics, Engineering, or Math fields. At that presentation the freshmen were also given information about the various ways they might be considered for employment at a NASA facility.

* Three Gallaudet participants made presentations about their experiences at a meeting of 50 Co-op interns.

* The success of this project and examples of student participants' accomplishments have been used by Gallaudet faculty in advising other Gallaudet students about career opportunities and skill requirements.

* A group of 15 deaf high school students participating in a Young Scholars Program at Gallaudet toured Goddard Space Flight Center and visited the deaf college students at their worksites.

Summing up the first year's program, the project was a threefold success:

* Disabled students received important technical work experience.

* Goddard was sensitized and exposed to the abilities of physically-challenged persons and became more aware of a new pool of talent.

* Younger students, high school and entering freshmen or sophomores, were encouraged by older students' positive experiences related to the technical opportunities offered by NASA.

According to almost all participants, the model program was a success. It will be repeated during the summer of 1989 at Goddard.

A SUCCESSFUL INTERVENTION PROGRAM FOR HIGH ABILITY MINORITY STUDENTS

Winson R. Coleman
Director - Science and Engineering Center
College of Physical Science, Engineering and Technology
University of District of Columbia
Washington, D.C.

Among professional occupations in the United States, non-Asian minorities are least represented in science and engineering fields. Minorities represented at least 20% of the total population, but less than 2% of the doctoral degrees in science and engineering are awarded to non-Asian minorities. If we trace the process that produces Black, Hispanic, and Native American scientists and engineers back one step further, we continue to find underrepresentation. Within the college-age population, blacks make up 14%, Hispanics constitute 6.4% and Native Americans constitute 0.6%. However, only 5% of the full-time college students majoring in engineering are Black, only 4.5% are Hispanic, and only 0.4% are Native American (Engineering and Manpower Commission 1987). The Bureau of Labor Statistics predicts that over the next decade, civilian employment of scientists and engineers has the potential to grow by 40%. Further, projections for the year 2000 indicate that 100,000 fewer B.S. and B.A. degrees will be awarded than were awarded in 1984 (Devarics 1987). The latter projection takes into consideration the overall declining proportion of all 18-year old college students. Within this shrinking pool of 18-year old potential college students will be an increasing proportion of Blacks and Hispanics. In order to change the educational patterns for minority youth, we must take an intense look at the factors that affect the science and mathematics performance of minorities. Further, we must examine and document, with the intent of replicating, the work of programs that are successful at producing minority scientists and engineers. The fundamental concern at this time appears to be the quality of precollege experience because research has shown that lack of precollege preparation is the single most important cause of underrepresentation of minorities in science and engineering careers. For many years, intervention programs have attempted to improve the quality of the minority precollege experience by latter year intervention in grades eleven and twelve. Later efforts, such as this one, have concentrated on earlier years. The vast majority of these programs have operated with little or no emphasis placed on the formal evaluation of their efforts. Casual evaluations (e.g., George 1987; Wellington 1984), however, have shown that many of the students involved in such programs have gone on to pursue studies in quantitative fields. That intervention programs are effective is widely accepted but not rigorously documented. The mechanisms these programs have developed need to be identified and their potential for broader use evaluated. The ultimate goal of such studies would be to provide the different educational communities with a set of proven cost-effective state-of-the-art mechanisms designed to increase participation and success of minority students in science and mathematics-related courses. One such intervention program is the Saturday Academy program for high ability minority students in the Washington, D.C. area. The purpose of this study is to provide a description of the Saturday Academy with the intent of making it available to personnel who are considering the development of similar projects and to examine the effect of participation in the program on high school graduation rates, college enrollment and choice of quantitative major.

Description of the Saturday Academy Program

Located on the campus of the University of the District of Columbia the program operated in 1987-88 on a direct cost budget of $68,063, funded primarily by the National Aeronautics and Space Administration (NASA), and serviced 282 students (approximately $242 per student). Participants are students who have been identified as academically talented, primarily seventh, eighth, and ninth graders from the metropolitan Washington, D.C. area. To be selected for this program, first students must have an overall B-average or better. Second, the students must be recommended by their math/science teacher or counselor. Third, students must have a parent or guardian willing to attend two Saturday sessions and an orientation session. Finally, the student must agree to the program's mandatory attendance requirements - more than one unexcused absence results in dismissal from the program. The Saturday Academy is designed to provide enrichment experiences for academically talented minority youth without cost to them. These experiences are in creative mathematics, electrical engineering, and computer science. The program has been in existence since September 1982.

Electrical Engineering Component

The engineering component is designed to introduce the participants to the world of electrical engineering in an organized scientific manner. For the most part this is accomplished by first introducing basic theory of electricity in terms of current and voltage and the instruments that measure these quantities. Secondly, the various components used in electrical construction are introduced through theory and observation. Students are also given specific instruction in soldering, reading schematic diagrams, and in identifying components such as resistors, diodes, capacitors, integrated circuits and transistors. They then go on to construct light generators, sound generators and/or transistor radios and robots.

Computer Science Component

The computer science component is designed to help program participants become computer literate. Most participants do not have access to personal computers at home and have limited access at their regular schools. Instruction begins with teaching the present limitations of the computer and its internal structure. Participants learn to program in BASIC; they access the university's Vax 8650, Vax 11-780 or IBM 4341 with a modem or by direct link. IBM PC's are also available to participants. More advanced students are instructed in PASCAL.

Mathematics Component

This component provides students with abstract and semi-abstract experiences in what the program calls non-numerical mathematics. The end result of such experiences is designed to be the student's acquisition of application, analysis, and synthesis skills. All students work with group tables and the construction of mathematical systems. They learn operations in bases other than base 10, 3-dimensional explorations, and basic set theory. Advanced students study trigonometric and geometric concepts.

Evaluation

In an attempt to evaluate the Saturday Academy Program, all persons involved were given an opportunity to give input. Parents (or guardians) of the current participants, participants, and program teachers were asked to complete questionnaires. Administrative personnel were interviewed and project reports were examined. Results of these surveys and interviews will be made available during the actual presentation. Also included in the evaluation were alumni of the Saturday Academy Program. Eighth and ninth grade participants in the 1982 program and ninth grade participants in the 1983 program formed the experimental population. There were 180 students in the population. Of the 180 students, 69 students were still living at the same address and/or still had the same telephone number as when they were participants in the program or were accessible through other accessible participants. The experimental group was made up of these 69 Saturday Academy alumni. Telephone contact was made with the homes of each of the 69. If the former participants were not available, information was obtained from parents or guardians; information was not accepted from siblings or others. Questions, read from a prepared survey form, were asked about high school graduation, enrollment in college and choice of college major. One hundred and thirty four students were in the control population. All control population students were ninth graders in 1983. They were identified as having the same profile as the Saturday Academy participants with regard to performance in high school course work and recommendations of teachers and/or counselors. No parental participation was required of the control group; this factor may have an effect which limits the generalizability of this study. Of the 134 control population students, 50 (37%) were still living at the same address and/or still had the same telephone number as they had in 1983 or were accessible through other accessible control group students. The control group was made up of these 50. Control group students were contacted by telephone in the same fashion as were the experimental group members. A tally was kept on the number of each students in each group completing high school, enrolling in college and choosing a quantitative major. The results are given below.

The program had a significant effect on the three variables; the effect was, however, more pronounced for males than for females.

	Experimental Group vs. Control Group		
VARIABLES	EXPERIMENTAL P_1	CONTROL P_2	DIFFERENCE $P_1 - P_2$
high school graduation	.99	.76	.23
college enrollment	.91	.46	.45
quantitative major	.45	.20	.25

Discussion

Several common themes emerged in the evaluation by the various groups: the effectiveness of hands-on activities, the necessity for improvement in some aspects of instruction, the desirability of including career information and field trips. Parents mentioned that more black males should be recruited, a particularly crucial factor given the success of the program with males. The study of the alumni of the program shows that it was successful in improving high school graduation rates, college enrollment rates, and the rate of selection of a quantitative major. The program had substantially greater effect on male participants than on female participants. Moreover, substantially more than half of the participants were female. This highlights a feature that distinguishes the participants of this program from the white participants of most science and mathematics programs in the United States, where generally females are underrepresented. Colleges and universities sometimes see intervention programs as recruitment devices. Thus it is of interest to note that of the students in this study (experimental and control), thirteen chose to attend the University of District of Columbia. Nine of these 13 were Saturday Academy alumni. The results of this investigation serve to document the success which this intervention program has enjoyed with respect to encouraging non-Asian minority students to prepare themselves for quantitative careers. It is not possible to point to an intervention program that can trace its successful influence through the participants' sophomore year in college. Further research, however, is needed to track these same students through their college graduation and into graduate school and/or careers. Such studies would then determine the proportion of intervention programs students that i) graduate from college; ii) graduate with a quantitative degree; iii) complete a graduate degree; iv) complete a graduate degree in a quantitative field; and v) enter a career field requiring quantitative expertise. In-depth interviews with alumni who chose quantitative majors should inquire as to whether they found some part of the Saturday Academy program particularly helpful. Longitudinal studies of later alumni are also needed; the program should encourage all alumni to continue their contact throughout their college studies.

Research is also needed with controls for the parental involvement factor. Other influential variables to be studied include the students' academic performance and socio-economic factors.

References

Dervarics, Charles. "White House Urges More Minority Participation in Math and Science", Black Issues in Higher Education, 1987, 4, 5.

Engineering Manpower Commission, *Engineering Manpower Bulletin: Minorities in Engineering*, Washington, DC.: American Association of Engineering Societies, 1987.

Hayden, Linda, *The Impact of an Intervention Program for High Ability Minority Students.* American University, 1988.

George, Y., Chu-Clewell, B., and Watkins, N. "Lessons for HBCUs from Precollege Mathematics and Science Programs." Paper presented at the U.S. Dept. of Education White House Initiative on Historically Black Colleges and Universities, Washington, D.C., 1987.

Wellington, R.G. "Subsequent Academic and Career Development of Participants in Selected NSF Student Science Training (Pre-college) Programs," 1974, DDJ-74-09447.34/10A: 6478.

N91-28100

THE WOMEN IN SCIENCE AND ENGINEERING SCHOLARS PROGRAM

Etta Z. Falconer and Lori A. Guy
Spelman College
Atlanta, Georgia

ABSTRACT

The Women in Science and Engineering Scholars Program provides scientifically talented women students, including those from groups underrepresented in the scientific and technical work force, with the opportunity to pursue undergraduate studies in science and engineering in the highly motivating and supportive environment of Spelman College. It also exposes students to research training at NASA Centers during the summer. The program provides an opportunity for students to increase their knowledge of career opportunities at NASA and to strengthen their motivation through exposure to NASA women scientists and engineers as role models. An extensive counseling and academic support component to maximize academic performance supplements the instructional and research components. The program is designed to increase the number of women scientists and engineers with graduate degrees, particularly those with an interest in a career with NASA.

THE WOMEN IN SCIENCE AND ENGINEERING SCHOLARS PROGRAM

The Women in Science and Engineering Scholars Program was initiated in 1987 as a cooperative effort between Spelman College and NASA. The program provides scientifically talented women from groups underrepresented in the scientific and technical work force with the opportunity to pursue undergraduate studies in science and engineering in the highly motivating and supportive environment of Spelman College.

The goal of the Women in Science and Engineering Scholars Program or the WISE Scholars Program is to increase the number of women, including minority women, entering scientific and technical careers. The specific objectives are:

1. To identify high ability women students from underrepresented groups and to provide the students with an opportunity to pursue undergraduate study in engineering and science.

2. To enable high ability women college students to maintain academic excellence in scientific and technical studies.

3. To motivate and encourage students to pursue scientific and engineering careers.

4. To provide research training for selected students both in the undergraduate setting and at NASA Centers.

5. To motivate and prepare students to earn graduate degrees in science and engineering.

Scholars are actively recruited and are selected by a competitive process. Preference is given to students residing close to NASA Centers. Selection criteria include high potential and achievement in science and mathematics as measured by college entrance examinations and the high school record, and an interest in pursuing a career in science or engineering. Scholars are selected by a committee of Spelman faculty and staff, the NASA Center Equal Opportunity Officers, and the NASA Agency wide Federal Women's Program Manager.

Currently, there are 13 sophomore and 15 freshman Scholars. Each Scholar has a sponsoring NASA Center. The Equal Opportunity Officers and the Federal Women's Program Managers at NASA installations have a primary role in the development of the students. The NASA Centers and the number of students sponsored are given below.

NASA CENTERS AND WISE SCHOLARS

Ames Research Center	3
Goddard Space Flight Center	4
Jet Propulsion Laboratory	2
Johnson Space Center	4
Kennedy Space Center	3
Langley Research Center	4
Lewis Research Center	4
Marshall Space Flight Center	2
Stennis Space Center	2
TOTAL	28

Scholars pursue majors in electrical or aerospace engineering through the Dual Degree Engineering Program, physics, mathematics, or another scientific or engineering major related to the mission of NASA and the work of the sponsoring NASA Center. In the Dual Degree Engineering Program a student spends three years at Spelman and two at Georgia Tech, Rochester Institute of Technology, Boston University, or Auburn University, earning degrees from both Spelman and the engineering institution.

A three-day Orientation Conference was held prior to the beginning of the Fall semester for the Freshman WISE Scholars, parents, NASA officers, Spelman administrators and faculty and program supporters. The objectives of the conference were to provide a detailed explanation of the program, including the role of NASA, and to make certain that student and parents understand their responsibilities and the various support mechanisms available to help students meet program requirements. The conference was valuable in providing an opportunity for the Scholars to become acquainted with NASA officers and the WISE program staff. It was particularly effective in creating a bonding of the Scholars which has been instrumental in their academic success.

The Academic Year

The students take a strong sequence of science and mathematics courses leading to a major in science or engineering. The following courses are required of every Scholar.

Honors Analysis I, II (Calculus of One Variable)
Analysis III (Calculus of Several Variables)
General Chemistry I, II
Mechanics and Heat
Electricity and Magnetism
FORTRAN or Pascal
Honors English I, II
Independent Study/Research

Freshman Scholars take a schedule of challenging courses, including Honors Mathematics, Honors English, and chemistry. Engineering majors also take Introduction to Engineering and Engineering Graphics. Honors Mathematics is offered on three levels and students are assigned mathematics courses based on placement examination scores. Honors Mathematics provides an introduction to research methods through the requirement of at least one paper or project reflecting independent work, library research, and oral and/or written presentation. Freshmen also enroll in a special Study Skills and Critical Thinking Seminar. Additional courses from the required general studies complete the schedule.

Sophomore Scholars take Mechanics and Heat, and Electricity and Magnetism, along with appropriate mathematics courses. General studies and major courses such as Computer Systems, Linear Algebra, or Organic Chemistry complete the schedule.

Academic Support and Counseling Component

The director serves as academic advisor during the first two crucial years and maintains close contact with instructors of Scholars in order to take necessary intervention action to assure student success. Early identification of potential problems in science and mathematics courses is made by requesting student progress reports during the semester from their instructors.

Tutorials are an important part of the Academic Support Program. Tutors are provided for students in mathematics, chemistry, physics, and computer science. Tutors are graduate students or upper-level undergraduates of exceptional ability and achievement. The graduate tutor in mathematics conducts a group session for freshmen who are taking Honors Quantitative Reasoning I, Honors Quantitative Reasoning II, or Honors Analysis I. The session is designed to develop the ability of the students to work in small, productive groups. The tutor moves from one group to another offering assistance as needed. The graduate student is also available at other hours to provide individual tutoring.

In chemistry, a graduate tutor conducts a required group tutorial session for two hours. Difficult but basic topics are emphasized by the tutor, and questions are taken from the group. The tutor is also available for individual tutoring. In physics, an undergraduate senior provides individual or small group tutoring. Students are encouraged to attend tutorial sessions as a means of enhancing learning. Individual tutoring is provided in computer science.

All freshman and most sophomore Scholars live in the same dormitory, the Living Learning Center. A special graduate residential assistant is available to provide counseling and to give assistance during the evenings, nights and weekends. Students also attend group meetings with the director during the year for the purpose of assessing progress, determining problem areas, and providing support. Each freshman Scholar has a sophomore Scholar who serves as her Big Sister. The students are matched by major and the Big Sister provides advice, support and friendship.

Freshmen attend a seminar in Study Skills and Critical Thinking. The non-credit course meets once a week for a semester and covers topics such as study and test-taking skills, time management, and techniques for studying the sciences. The seminar is taught by a college counselor and guest lecturers.

Each semester a woman scientist or engineer from NASA spends two days on campus as the NASA Lecturer. She gives several talks and conducts an informal session for the WISE Scholars. Through the visit a strong statement is made that women can achieve in science and engineering.

Research Experiences

Scholars engage in a 10-week research experience at the sponsoring NASA Center each summer. Each student is required to submit a paper upon return to Spelman and to give a presentation of her work. The following presentations were given this semester:

Inertial Reference Package
Detector Array
Computer Research at Stennis
Fuel-Rich Catalyst Combustion
Model for Research of LCG
Investigation of Space Adaptation Syndrome
Computer-Aided Design for Large Advanced Space Systems
The Attitude Heads by Display Prototype
Controlling Indoor Pollution
Zirconium Ignition Test
Thermal Cycling Effects on Crack Densities in the Space Station

The following report by WISE Scholar Lori Ann Guy is representative of the summer research component of the program.

Computer-Aided Design for Large Advanced Space Systems

The Large Advanced Space Systems Computer-Aided Design and Analysis Program (LASS) has the capability of modeling intricate structures that are too complex to be built by most existing computer-aided design software packages. Last summer under the direction of Melvin Ferebee, Jr. of NASA Langley Research Center, I developed expertise in the use of LASS and created a model of a space platform in order to validate the program.

LASS includes several antenna synthesizer programs and corresponding databases for each configuration. The configurations are: a box-ring, a box truss, a hoop and column, a radial rib, a tetrahedral truss, and a default database. Each database contains the information necessary to create an antenna or model. Once a configuration has been specified, the appropriate synthesizer must be activated. The synthesizer is the part of the program that creates the antenna that will be used for analysis. The size and design of the antenna must be specified after the synthesizer is activated.

Following the selection of the desired antenna for the model of the space station, the execution of the corresponding synthesizer resulted in an output of a model file, a database file, and a set of mass properties. Next, a translator program which writes a universal file of the structure was executed. It contained all of the structure, geometry, and data sets pertaining to the model. It was necessary to specify whether the antenna would be added to an existing model during the writing of an universal file.

The universal file creates a permanent group of the individual models which is useful in allowing the user to manipulate all of the nodes of the antenna as a whole structure. While writing the universal file, the user has the ability to translate and/or rotate the model.

Modifications of the physical structure and analysis of the physical and material properties were made to the various models of the space station by using other programs. An internal program translated the modifications into a NASTRAN output file, which in turn had to be translated into a format suitable for use in the LASS program. Then the General Truss Synthesizer (GTS) was used to make final changes in the model and to review its components. GTS has two input categories - a listing of the values for the structural model in addition to those of a tetrahedral truss, and a second category which may require additional changes in order to identify antennas other than a tetrahedral truss. GTS writes the elements and nodes of the model to a file which contains the structural and geometric data of the elements in the model. Finally GTS outputs information about synthesizers including the number of nodes and elements contained in the model, the types of elements (beams, cables, or rods), and data on physical and material properties.

Following the viewing of the GTS output for the models of the Space Station, the Thermal Analysis program was executed. This program specified the orbit and material properties of the model and then computed temperatures and heat rates. This data was also translated into an analysis data set in a universal file that could be read into another program.

Several antennas were designed and analyzed as trial cases in order to validate the program before the actual modeling of the space platform. LASS is an excellent tool for modeling large and intricate structures and with modifications, will become an essential tool in the design process of space craft.

Outcomes

An early evaluation based on the outcomes of the first year indicates that the program is successful. Thirteen of the original 15 Scholars are still in the program. The average GPA of the returning students was 3.3.

Fourteen Scholars made the honor roll at least one semester last year and 11 made the honor roll for both semesters. Two students were among the 15 Dual Degree Engineering students of all levels from the Atlanta University Center institutions who received outstanding student awards at the Annual Awards Banquet. Seven students received honor pins at the affair.

The WISE Scholars Program has given a high visibility to NASA on the campus. It has created a core of high potential minority women students who share common interests and goals in science and engineering. There is a sense of enthusiasm and confidence in the Scholars which has had a positive effect on other science and engineering students. The Scholars are already interested in pursuing graduate degrees and are determined to succeed.

AN ANALYSIS OF THE MOON'S SURFACE USING REFLECTED ILLUMINATION FROM THE EARTH DURING A WANING CRESCENT LUNAR PHASE

Ernest C. Hammond, Jr., and Maggie Linton-Petza
Department of Physics
Morgan State University
Baltimore, MD

and

Gerald R. Baker
Technical Monitor
Laboratory of Astronomy and Solar Physics
Goddard Space Flight Center

ABSTRACT

There have been many articles written concerning the lunar after-glow, the spectacular reflection from the moon's surface, and the possible observation of luminescence on the dark side of the moon. The researcher, using a 600 mm cassegrain telescope lens and Kodak 400 ASA T-Max film, photographed the crescent moon whose dark side was clearly visible by the reflected light from the earth. The film was digitized to a Perkin-Elmer 1010M microdensitometer for enhancement and enlargement. The resulting pictures indicate a completely different land pattern formation than observed during a full moon. There is an attempt to analyze the observed structures and to compare them to the pictures observed during the normal full moon. There are boundaries on the digitized dark section of the moon that can be identified with structures seen during the normal full moon. But, these variations do change considerably under enhancement.

AN ANALYSIS OF THE MOON'S SURFACE USING REFLECTED ILLUMINATION FROM THE EARTH DURING A WANING CRESCENT LUNAR PHASE

Introduction

There have been many articles written about the lunar afterglow, the spectacular reflection from the moon's surface and the possible observation of luminescence on the dark side of the moon. Using a 600 mm Cassegrain telescope lens and Kodak 400-ASA T-Max film, we have photographed the crescent moon, whose dark side was clearly visible by the reflected light from the earth. The film was then digitized to a Perkin-Elmer 1010-M microdensitometer for enhancement and enlargement.

Method

We began with an actual negative taken with a 600 mm Cassegrain telescopic lens. The resulting image was then digitized using the microdensitometer. This project of photographing the major luminary next to the sun has given us an opportunity to test both hard and software in digitizing photographic films (Figure I).

Figure I.

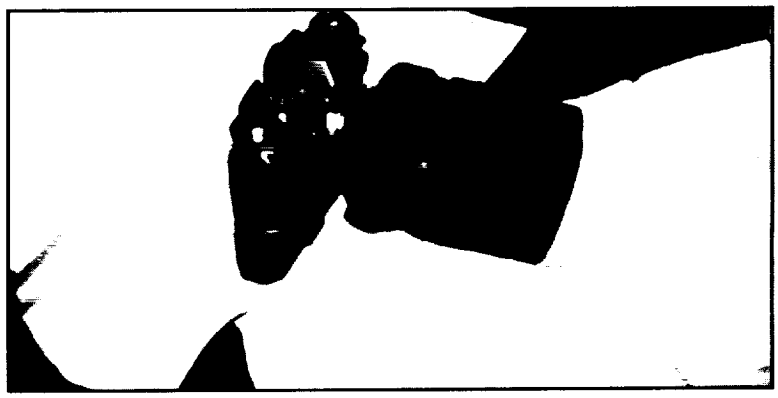

Results

After digitizing using the microdensitometer, an outline of cratering was produced along with the flat plain areas. The light part represents the flat plains, with minimal cratering (Figure II).

Figure II.

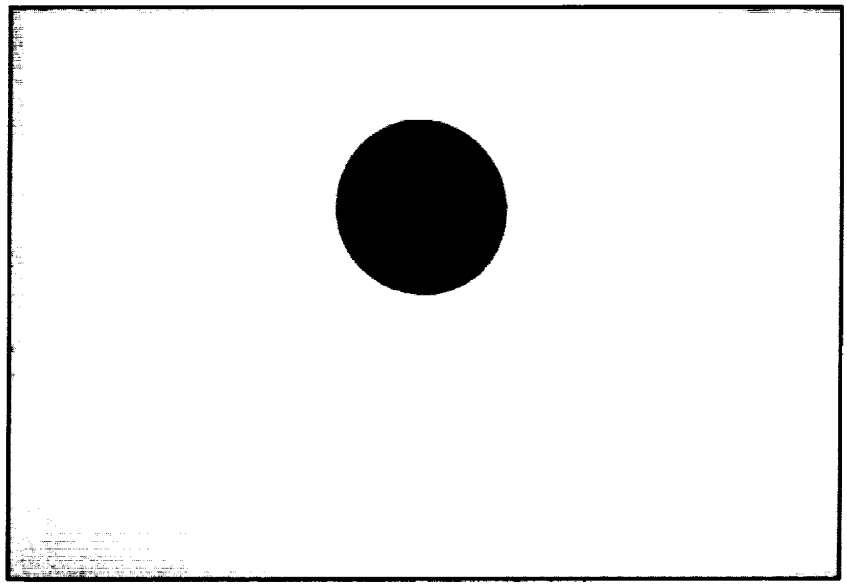

Figure III represents pseudo or false coloring of the moon. Every color represents a different gray level value. One should note, in particular, that the limb around the moon seems to be brighter than most of the interior. It is also noteworthy, that with pseudo coloring, there are structures within the maras or seas that are invisible in the black and white enhanced views (Figure III).

Figure III.

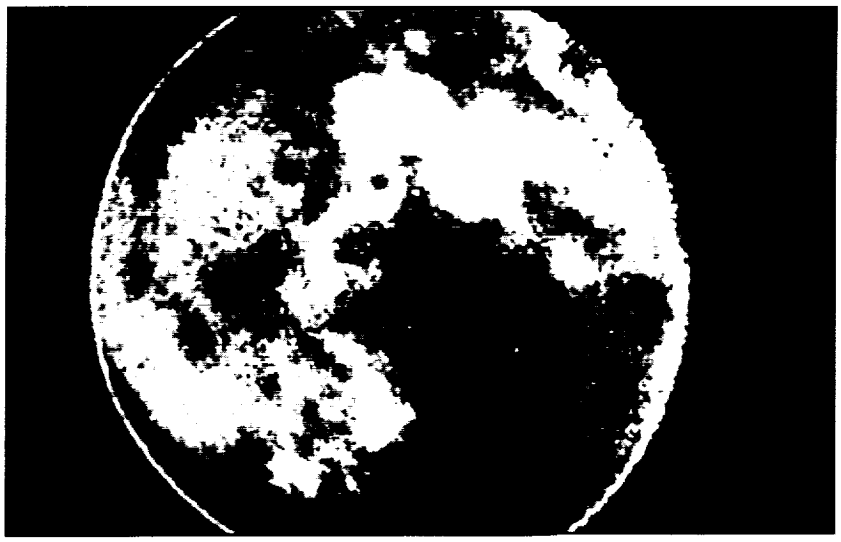

Changing the pseudo color pixel values again will produce dramatic changes within the so-called "lunar seas". Given value determination, we suspect that all blue or red values can tell us something about the mineral content of the surface, if we could know the reflectivity of certain minerals.

Photographs of some of the lunar rocks that the astronauts brought back from the moon, should help identify mineral contents on various parts of the moon (Figure IV).

Figure IV.

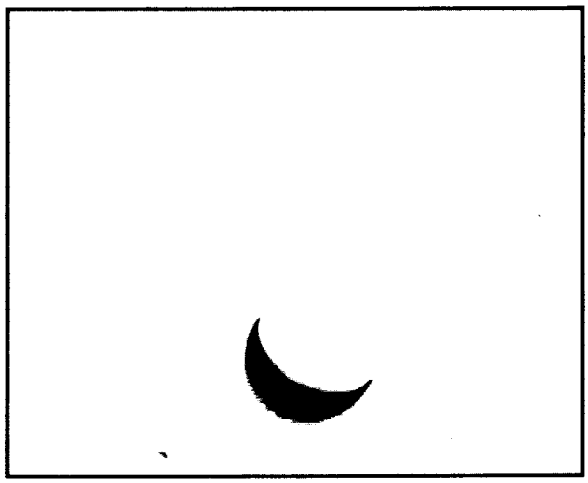

Further study of this technique, with an appropriate telescopic instrument, will permit us to review the moon's surface in a way that would be very beneficial and enlighting, and would provide a substantial amount of information about the local cratering areas (Figure V).

Figure V.

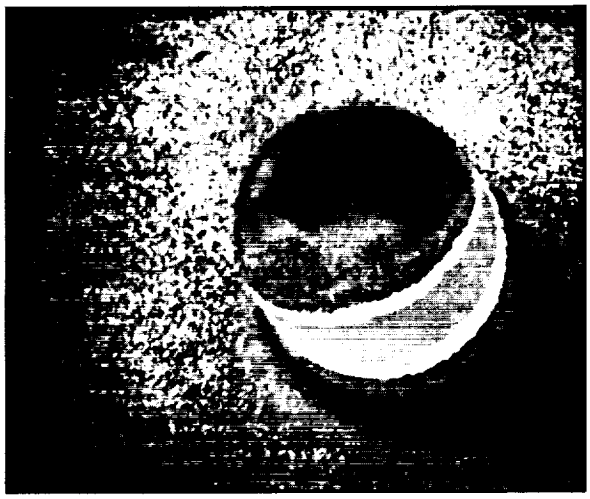

Figure VI represents the zoom capability of looking at the center of the moon, representing an area of 20-square miles. The dark areas represent craters and the flat areas represent plains (Figure VI).

Figure VI.

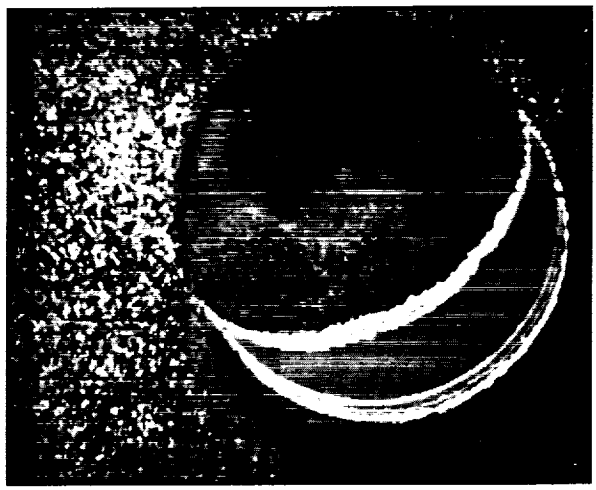

When one applies false color to this magnified view of the surface, one can clearly see cratering and other structures associated with the same values, along with even greater changes within the interface between the plain and cratering area. The resolution is bad primarily due to the grain size of the film (Figure VII).

Figure VII.

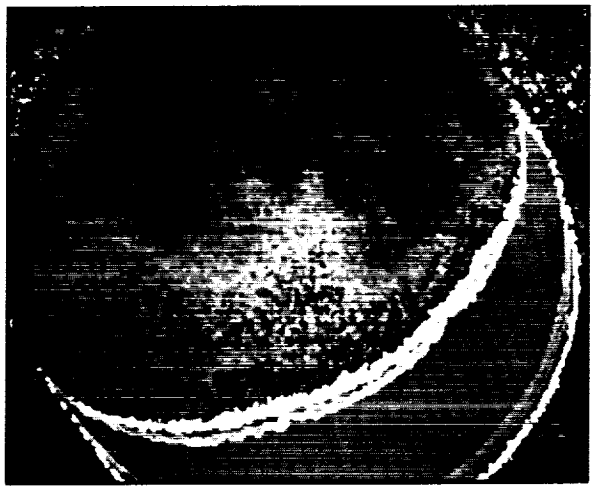

Looking at the moon illuminated by earth shine, the dark area represents the reflected light from the sun and the grayish area represents the reflected light from the earth. Let us consider the enhancement on the slide as the earth's reflected light illuminating the moon (Figure VIII).

Figure VIII.

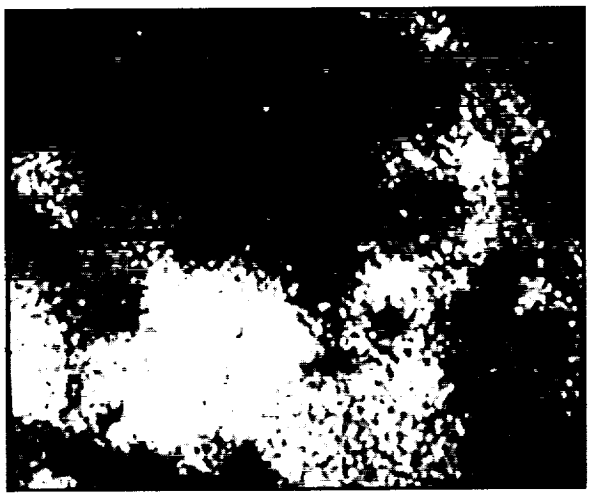

A computer zoom of the interface between the waning crescent and the dark side of the moon produces the image seen in Figure IX. One can see cratering, as well as a glow along the limb of the moon. The craters appear as small blobs along the interface between the sunlit part of the moon during this waning crescent.

Figure IX.

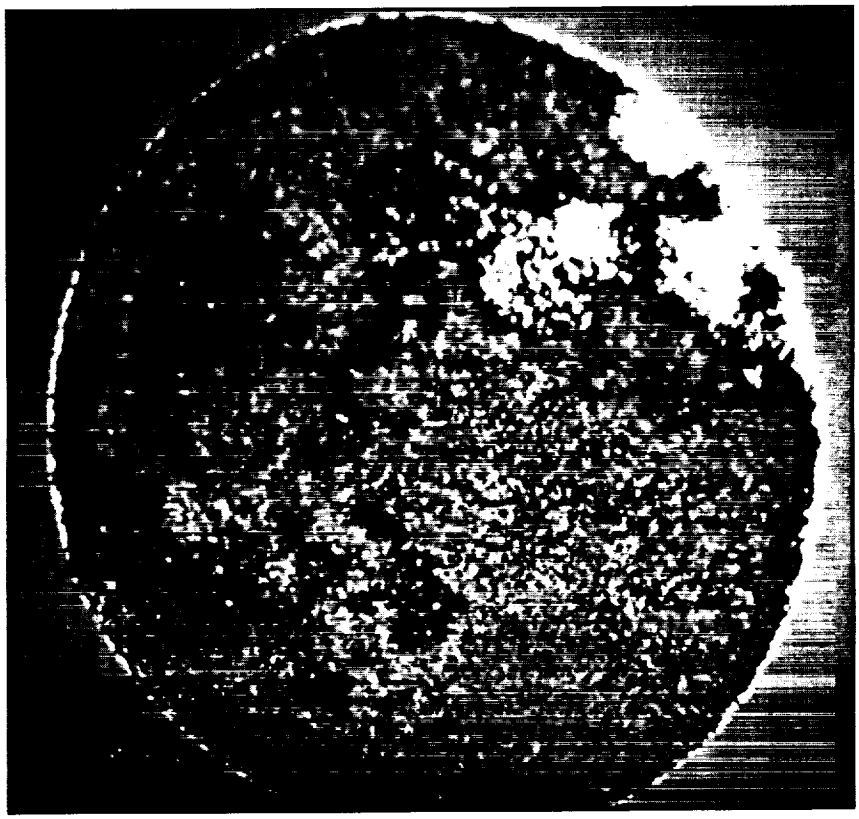

Figure X is a view of the entire moon with its dark side partially illuminated by the light reflected off the earth's surface and atmosphere. Note that the pattern observed is considerably different from those patterns observed when the full disk of the moon was shown. Notice also the ridges and lines that run throughout the surface of the moon, which the eye perceives very differently than when the moon is full (Figure X).

Figure X.

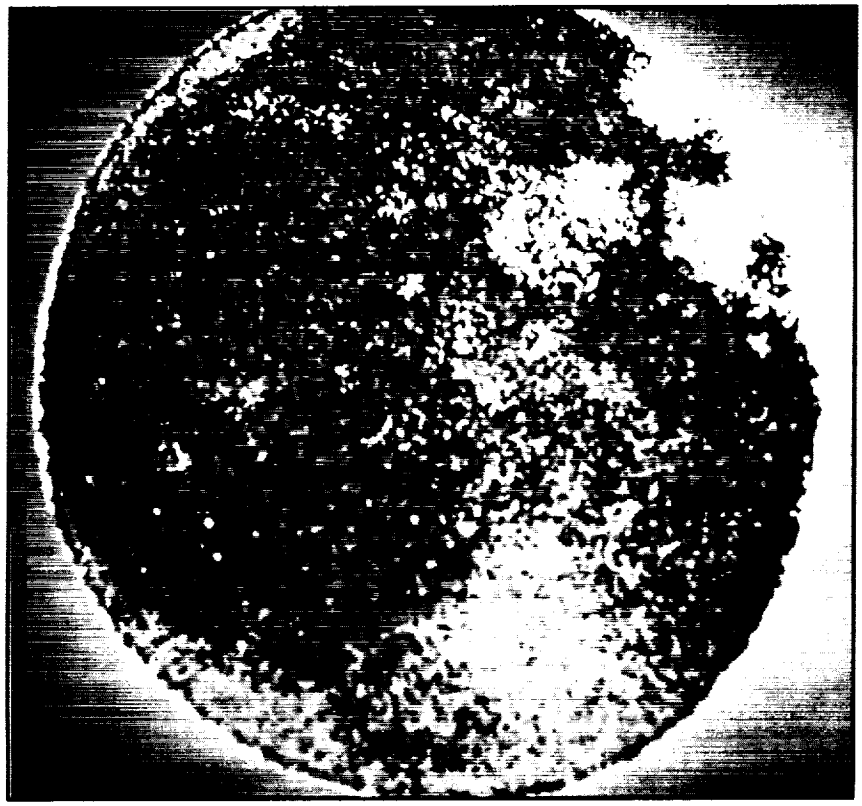

By using false color, one can clearly show patterns and structures which are not seen during the full moon. Also, lens problems within the Cassegrain lens give us some optical flaring effects. However, one of the more interesting aspects is that we can use this technique of pseudo coloring to show lines equal in light intensity.

Conclusion

Careful evaluation of the slides reveals cratering from the same value of the moon. Increased intensity of light on the surface opposite the sun is also noted at the upper limb of the moon. But even more important, the entire pattern on the dark side of the moon is totally different from the pattern observed when the moon is full. We want to continue to explore the pattern differentials, to see if there is any potential to identify mineral content based on the reflected light from the earth and sun.

A DENSITOMETRIC ANALYSIS OF IIaO FILM FLOWN ABOARD THE SPACE SHUTTLE TRANSPORTATION SYSTEM STS #3, 7 AND 8

Ernest C. Hammond, Jr.
Morgan State University
Baltimore, Maryland

ABSTRACT

Since the United States of America is moving into an age of reusable space vehicles, both electronic and photographic materials will continue to be an integral part of the recording techniques available. Film as a scientifically viable recording technique in astronomy is well documented. There is a real need to expose various types of films to the Shuttle environment. Thus, the purpose of this study is to look at the subtle densitometric changes of canisters of IIaO film that were placed aboard the Space Shuttle #3 (STS-3).

A DENSITOMETRIC ANALYSIS OF IIaO FILM FLOWN ABOARD THE SPACE SHUTTLE TRANSPORTATION SYSTEM STS #3, 7 AND 8

Introduction

Since the first major use in Skylab in 1974, scientists have used over 400 rolls of photographic film in the space environment to obtain sensitometric data. The present research team prepared 3 canisters of IIaO film along with packets of color film from the National Geographic Society, which were then placed on the Space Shuttle #3 (STS-3). The ultimate goal was to obtain reasonably accurate data concerning the background fogging effects on IIaO film as it relates to the total environmental experience. This includes: the ground based packing and loading of the film from Goddard Space Flight Center to Cape Kennedy; the effects of solar winds, humidity, and cosmic rays; the Van Allen Belt radiation exposure, various thermal effects, reentry and off-loading of the film during take-off, and 8 day, 3 hour 15 minute orbits. The development and analysis of the returned film constitute the basis of this report. The objective of this experiment was to examine the total densitometric change caused by all of the above factors.

The Laboratory for Solar Physics and Astronomy, Goddard Space Flight Center, has been using large quantities of IIaO film in its rocket and space shuttle flights. Next year, during the Ultra Violet Image Telescopic Experiment, the UIT is launching a payload which will be using 70 millimeter IIaO film. Thus, it was a requirement for the laboratory to quantitatively determine the aging effects associated with the sensitometric images on film.

IIaO film for this experiment (Figures 2 & 3) was obtained from the same roll of Kodak film Mfg. date 5-76-A5J. The film was loaded into specially prepared aluminum anodized packages that would fit aboard the Space Shuttle's Getaway Special Container. One roll of film was cut from the same stock and maintained as the control. The control film was maintained at a temperature of 22 degrees Centigrade at Goddard Space Flight Center. After the mission, the three rolls of IIaO film were shipped back to the Small Payload Section of the Laboratory for Astronomy and Solar Physics. One film and the control film were developed as Set I, while the other IIaO sample film was developed as Set II.

Using a MacBeth Densitometer, measurements were obtained form the film every 2 centimeters, developing 3 columns of data. Significant differences were found when samples were compared with the control. Sample A and Sample B had a 5.26% increase in density or fogging background, while the film developed shortly after its arrival at Goddard Space Flight Center displayed a 3.8% increase in the density or the fogging background.

An analysis of the data for each sample film aboard the Space Shuttle (Figures 5, 6, & 7) indicates variation in intensity with respect to the fogging levels as a function of position on the film. There is a tendency of more random variation toward one end of the film, but the actual orientation in the Space Shuttle is unknown. A possible theory is that the high energy cosmic rays had penetrated the aluminum film cartridges aboard the Space Shuttle causing certain secondary reactions that produce variations towards one end of the film due to the wrapping procedure used in placement of the film in the canister. Other theories suggest thermal effects cause density variations. It is known that aluminum containers tend to innately fog various UV films along with the wrapping geometry of the film within the canister.

Densitometric Response of IIaO Film Flown on STS-7

Three canisters of 35mm IIaO film were flown on STS-7 in a getaway special canister in cooperation with NASA's Plasma Physics Branch and the Naval Research's Solar Astronomy Branch. The results indicate a high degree of thermal aging during the space shuttle mission.

The future requirements for film used aboard the space lab and on the UIT (Ultra Violet Imaging Telescope) will include the following. Some ultraviolet films may have to be exposed directly to the particular vacuum of space at those altitudes, thus giving rise to concern of metallic outgasing of chemicals that may do permanent damage to the film's emulsion. The IIaO film being used on the UIT will not be exposed directly to space, but may be exposed to ionospheric fields associated with a low orbiting space shuttle. The major factor that can cause fogging is thermal exposure.

Experimental Set-Up

Using a sensitometer, a continuous roll of IIaO film was exposed for ten seconds using a General Electric Lamp 328 at 195 ma + 3 ma with a 10 - 18 hour calibration burn in time. The film was placed in three 35 mm canisters, sealed in air and attached to the getaway special canister containing other special ultraviolet films. The film was loaded in the canister approximately 22 days before the launch of the Space Shuttle Columbia.

Discussion

During the loading or pre-flight launch, post-flight analysis (Figure 8) indicates that the IIaO film had been exposed to some type of thermal aging effects. The exact nature of these effects was not apparent as we examine the temperature profiles for STS-7. But there is a concern that the rapid increase in temperature from approximately -15 °C to a temperature of +22 °C in an hour and a half after touchdown of the shuttle could explain the exaggerated thermal aging effects. There is another real concern which is associated with the fact that the shuttle landed on the West Coast, and the automatic temperature cut-off control was turned off approximately three days before the shuttle arrived at Cape Kennedy where the getaway special canister containing the film was unloaded.

Analysis of terrestrial thermal and aging effects produced similar curves as observed in this experiment, but the slopes of the individual curves tended to vary dramatically. In conclusion, there were observed densitometric changes in comparing the control films and the flight film, though both had been developed at the same time as the flight film received from STS-7.

Experimental Set Up for STS-8

This research team was able to use one of the canisters to place four rolls of IIaO film of STS-8, one roll of Illford G5 nuclear emulsion, and one roll of a new batch of IIaO. The Naval Research Laboratory setup was using a very sensitive ultraviolet film to study the effects of space on the ultraviolet emulsions. The shuttle orbit was low enough to expect some minimum cosmic ray damage to the film as well as tracks on the nuclear emulsion film. The Getaway Special was aligned in the bay of the shuttle with bay portals pointed to the earth for cooling purposes as shown in figure 9.

The temperature profiles for STS-7 and STS-8 were very similar, going from a temperature of approximately 23 degrees centigrade before launch to a temperature of -22 degrees centigrade during the flight. This increased the density of the wedges. The major differences between STS-7 and STS-8

occurred because STS-7 had to land in California where the automatic temperature control devices and appropriate air conditioning units for the shuttle cargo were not present. Once the shuttle had landed, one can measure the dirunal temperature variations (Figure 8). Terrestrial experiments have shown that less dense wedges produce densitometric increases as the temperature increases (Figure 12) over a number of days. The diagram shows the effects of the first 3 step wedges including the aging effect of the background at 32 degrees. The lowering of the temperature decreases the slope of the family curves for each of the darker step wedges. Figures 11 & 14 (aging effects) show the slope variation at 21 degrees and at 32 degrees over a 90-day period.

A most interesting effect occurs at the darker patterns. They tend to drop in density, while the lighter patterns tend to increase in density. Furthermore, the IIaO film seems to perform nonlinearly for temperature values above 67 or 68 degrees (Figure 13). The least dense step wedges tend to show dramatic increases in density above 68 degrees Centigrade while the darker wedges show a reduction of temperature above 70 degrees. The slopes of these films are increased further when the ambient temperatures seem to increase.

A brief examination of the aging effects will assist us in understanding the observed effects on the film caused by exposure to the space environment of the shuttle (Figure 14). We used a microdensitometer to contrast and compare the terrestrial film as well as the shuttle flight film (Figure 15). Using this technique we were able to calculate the signal to noise ratio for flight as well as for control film. On board STS-8 the signal to noise ratio increased while the control film decreased. The signal to noise ratio computed for STS-7 shows that at higher exposure the signal to noise ratio is less than for the flight films (Figure 16). But at lower exposures the control and flight film seem to have larger signal to noise ratios (Figure 17). This difference may be caused by additional thermal activity within the canister as shown in Figure 17 and the lack of appropriate air conditioning equipment at the California landing site.

Signals to Noise Ratio of Aging Film

Analysis of the signals to noise ratio for IIaO film aged 8, 9, 21, 17, and 71 days indicates that a certain amount of aging reduces the signal to noise ratio over the short term, but will increase the signal to noise ratio over long periods of time (Figure 18).

An examination of the interaction of protons of varying dosages and energies indicates that the very light wedges are very sensitive to proton interaction with the emulsion while the very dark patterns tend to be less sensitive to very high MEV protons (Figure 19). MEV vs. dosage figures were obtained by using the Harvard University Cyclotron.

Using the Harvard University Cyclotron, we bombarded the IIaO film with alpha particles, (Figure 18) searching for parallel interactions in the space shuttle due to cosmic rays as from the cyclotron. We bombarded the IIaO film using the alpha particles at 47 MEV, 79 MEV and 153 MEV for the 6.8 rad dosage. We expected to see similar results when we examined the films from the shuttle. But we did not see such effect (Figure 19). There is a difference in the front part of the curve, but the toe and the shoulders did not seem to respond; as a result we do not think that there was any dramatic cosmic ray activity (Figure 20A).

Microdensitometric Analysis

When comparing similar step wedges that have been aged from 3 to 71 days, one can immediately see an increase in granularity. However, this is not consistent for all step wedges as it is for the middle wedges. The denser the wedges, the more one observes the converse of less granularity. Furthermore, as aging occurs, granular definition between step wedges seems to decrease, while other step wedges under densitometric aging will produce a heavier granularity indicative of increased grain structure.

Microdensitometric Comparison of Control Vs. Flight Film

The control film of STS-8 for step wedges 3 has larger grain structure than the flight film. Similarly on STS-8 strip 4, a new batch of IIaO film indicates a slight increase of granularity toward the darker wedges (Figure 24). Conversely, the least dense step wedge controls are heavier than the traces for the flight film (Figure 25). Microdensitometric traces of step 4 and strip 4 tend to illustrate very small changes. Finally, traces from STS-8 again show greater granularity for the flight film than for terrestrial controls (Figure 27).

A new approach to the examination of the IIaO film emulsion is the use of the scanning electron microscope to investigate surface grains and their structure. Varying the voltage of the probe electrons, we are able to examine grain structure under the surface of the emulsion at the proper accelerating voltage of the electrons. All the IIaO films were coated with gold palladium using standard sputtering techniques.

Using about 1,000X Magnification (Figure 27), it became very evident that the energy of the electrons within the scanning electron microscope striking the emulsion is very crucial in terms of the viewing of the grain structure. What we want to do in the future is to look at the aged film and see exactly how these grains change (Figure 28).

We found that a working voltage for SEM ISI SS 40 somewhere between 2 kilovolts and 10 kilovolts is sufficient to produce clear images without flaring. The flaring of the image from the SEM produces a 4-8% increase in the total area of the grain under investigation from direct measurements of the micrograph.

But as the energy of the electrons increases, one notices that there is a flare effect, each grain spreading out brightly (Figure 29). Then one begins to see some of the grains beneath the surface of the emulsion. So using this scanning electron technique, we can examine some of the grains just below the surface if the charging voltage is appropriate.

We also attempted to look at the wedges under the electron microscope. The extreme left represents the least dense, and the extreme right represents the most dense. (Figures 33, 34, 35 & 36 A&B). Of course, as the density increases, the size of these grains seems to decrease. Using this technique, one can measure with ease and acquire some statistical understanding (Figure 38).

Qualitative analysis techniques of energy dispersion reveal a very large silver peak along with traces of copper sodium and sulfur and argon peaks as shown in Figure 38. These trace element peaks are associated with the elements used in the development process and other materials in the emulsion.

Reciprocity Failure of IIaO Film

Reciprocity failure was examined for IIaO spectroscopic film. The failure was examined over two ranges of time from one second to thirty-one seconds and one minute to 180 minutes. The variation of illuminance was obtained by using thirty neutral density filters. A standard sensitometric device imprinted the wedge pattern on the film as exposure time was changed. Our results indicate reciprocity failure occurring for higher density patterns within the first minute. Multiple failure occurs at 13, 30, 80, and 180 minutes.

Materials and Methods

Twenty-seven wedge patterns were placed on IIaO spectroscopic film in total darkness using a light sensitometer with a 24 hour burn in time for the bulb. Each film section was exposed to the light sources for a specific period of time. Time intervals were the following: 1-30 seconds and 1-11, 15, 19, 22.5, 25, 27, 30, 35, 40, 45, 58, 90, 125, and 180 minutes respectively.

The film was then developed using Kodak D-19 developer, rapid fixer, hypo-clearing agent and photo-flo solutions. The following development procedure was used for each film section: In absolute darkness, and a water bath at a temperature of 20c + 1.5c, one section of film was placed in Kodak D-19 developer and gently agitated for four minutes using a specific soak and agitating pattern. It was washed in water for 30 seconds, shaken, then placed in Kodak rapid fixer solution, using the exact same pattern of agitation and soaking, and gently agitated for four minutes. It was then removed, rinsed in water for 30 seconds, washed in water for one minute, then hung to dry. After developing, the optical densities of the wedge patterns were read using a MacBeth Densitometer.

Results

An examination of the reciprocity failure for the 1 to 30 second exposure periods (i.e., a separate wedge pattern that was exposed to an amount of light from 1 to 30 seconds sequentially) reveals that for two separate batches of film whose histories of use were different, there is some reciprocity failure occurring at the darker wedge patterns. While an examination of the very light patterns further shows the trend of reciprocity failure at the 30th and 31st seconds, it should be noted that the very darkest patterns have a marked decrease in reciprocity failure around the 30 second interval, with other variations occurring at 10, 15 and 19 seconds consistently with each variation of the pattern.

An examination shows that reciprocity failure minimum points occur at 13 minutes, 20 minutes, 30 minutes, and 90 minutes, with a less defined failure at +80 minutes. The middle density wedges indicate the same reciprocity failure points occurring at the same time. The darkest wedges show remarkable stability for the first 10 minutes exposure, but dramatic failures occur at 11 and 20 minutes. Very dramatic reductions occur at 30 minutes.

Conclusion

For exposure times of 30 to 31 seconds, darker wedges experience failure more than light wedge patterns. This indicates that the lighter wedges are less sensitive to Reciprocity Failure at short exposure times. As the exposure time increases, there appear to be some migration of grains in the darker wedges; especially the last three columns which gave an appearance that a double exposure had occurred. There is also an increased darkening of the film with increased exposure times. Fogging of the film is prevalent at 30, 45, 58, 90, and 180 minutes, again with increased exposure times. An examination of the reciprocity

failure from 1 to 180 minutes completely demonstrates the following: (a) The reciprocity failure minimum points are at 13 minutes, 20 minutes, 30 minutes, and 90 minutes, whereas, less defined failure occurs at 11 minutes. The light and middle density wedges showed this result. Darker wedges (b) show remarkable stability for the first 10 minutes of exposure, but reductions occured at 11 minutes, 20 minutes, and dramatic reductions at 30 minutes.

Summary

The results of these studies have implications for the utilization of the IIaO spectroscopic film on future shuttle and space lab missions. These responses to standard photonic energy sources will have immediate applications in a terrestrial or extraterrestrial environment with associated digital imaging equipment.

The author is indebted to Gerry Baker and Al Stober of the Small Payloads Section of the Laboratory for Solar Physics and Astronomy for their hours of discussion and support. Special thanks to Dr. Dan Klingsmith of the interactive Astronomical Data Analysis Facility, also of the Goddard Space Flight Center, Greenbelt, Maryland for his patient assistance during the imaging processing of these films. Very special thanks to Kevin Peters, Sean Gunther, Lisa Cunningham, and Deborah Wright for their careful assistance during the development process.

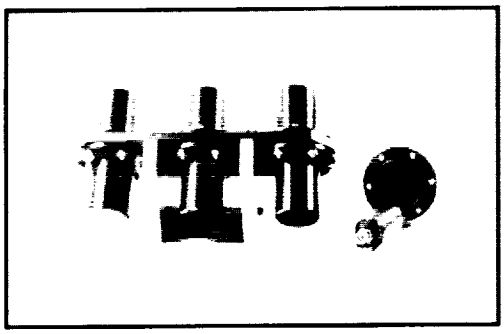

Figure 2

Figure 3

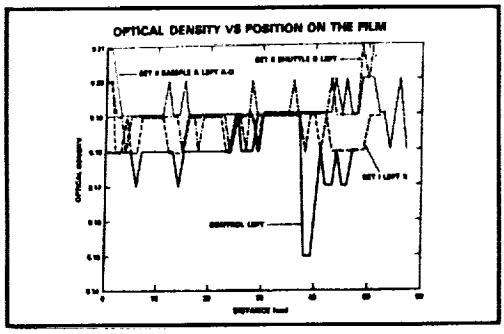

Figure 5

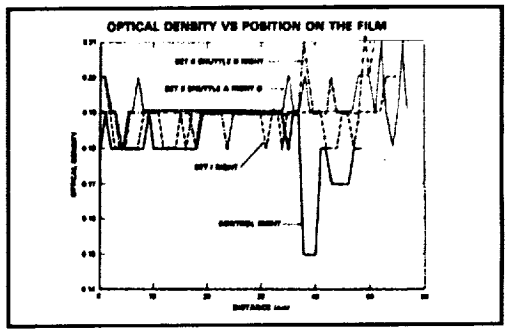

Figure 6

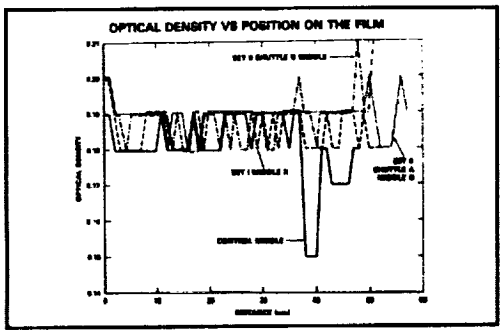

Figure 7

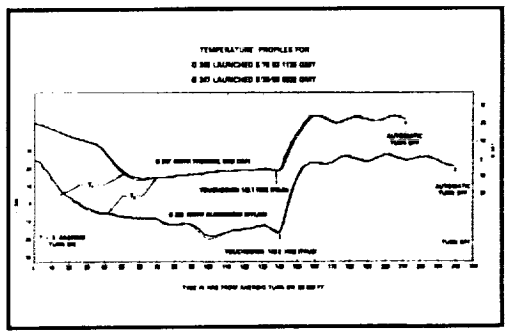

Figure 8

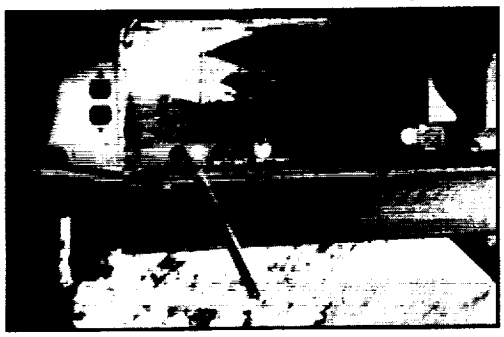

Figure 9

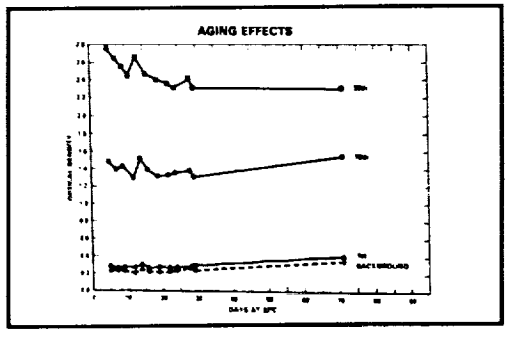

Figure 11

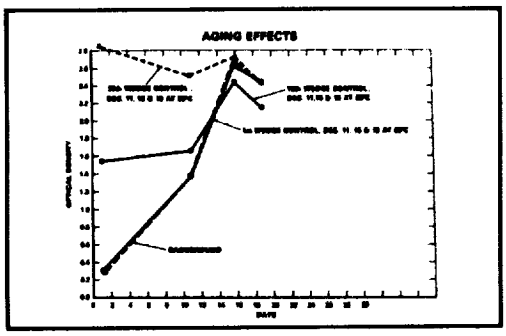

Figure 12

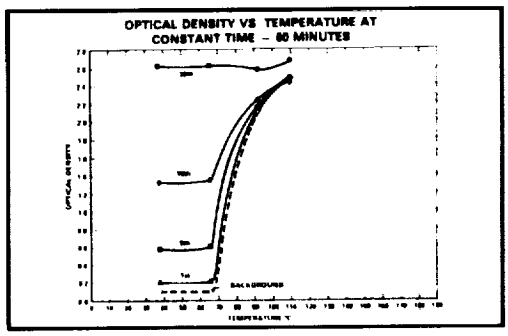

Figure 13

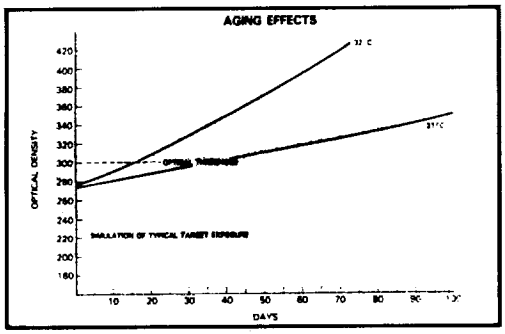

Figure 14

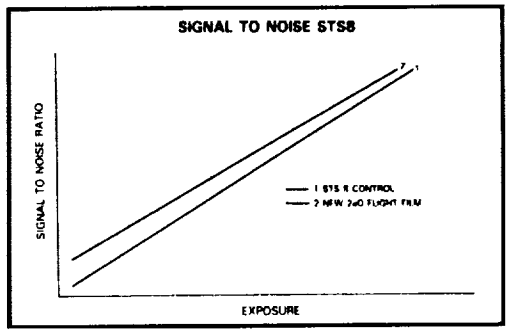

Figure 15

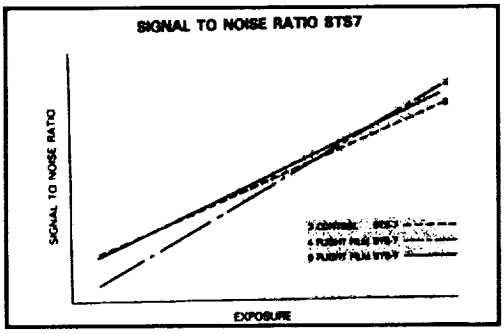

Figure 16

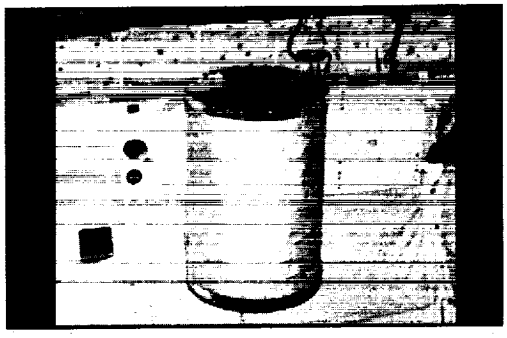

Figure 17

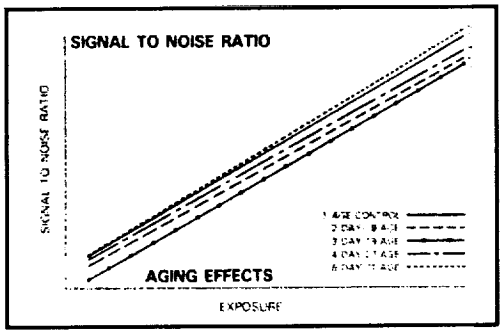

Figure 18

ORIGINAL PAGE IS
OF POOR QUALITY

ORIGINAL PAGE
BLACK AND WHITE PHOTOGRAPH

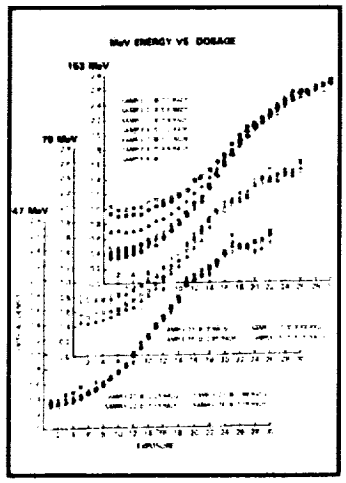

Figure 19

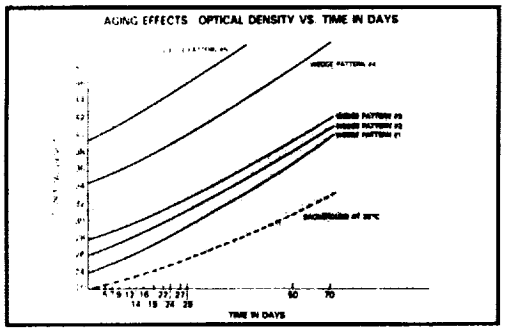

Figure 20 A

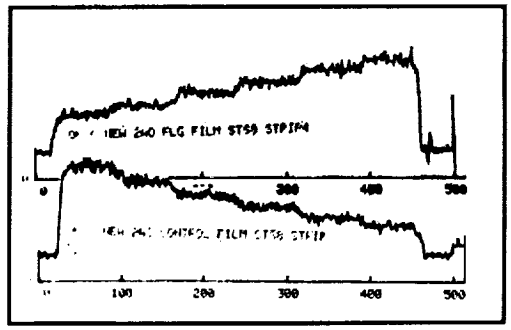

Figure 24

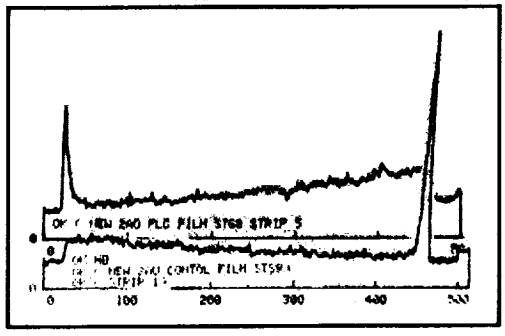

Figure 25

Figure 27

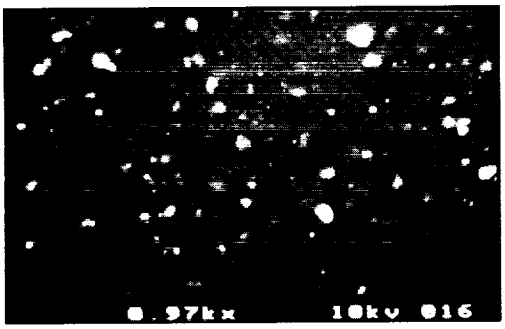

Figure 28

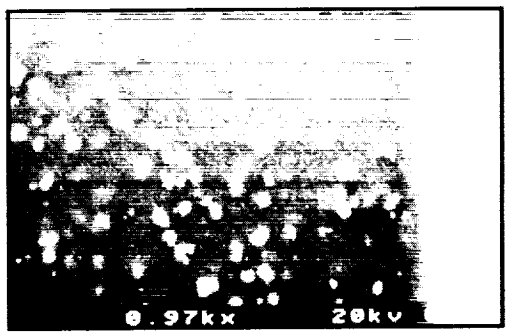

Figure 29

Figure 33

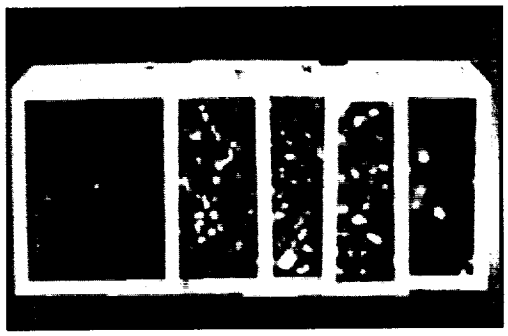

Figure 34

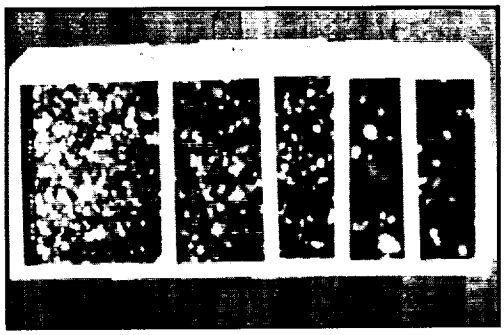

Figure 35

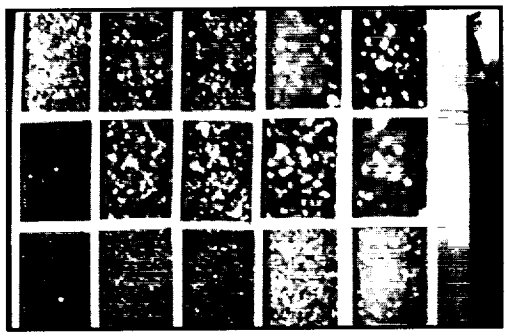

Figure 36 A

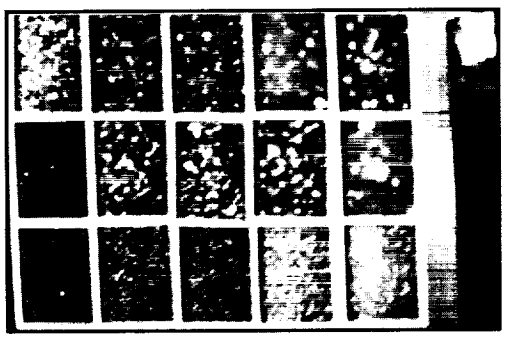

Figure 36 B

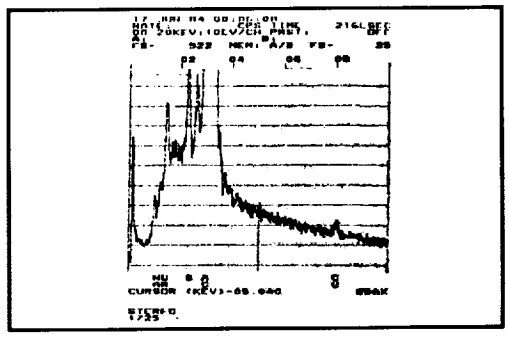

Figure 38

MÖSSBAUER SPECTROSCOPY AND SCANNING ELECTRON MICROSCOPY OF THE MURCHISON METEORITE

Christopher L. Brown, Frederick W. Oliver, and Ernest C. Hammond, Jr.
Morgan State University
Baltimore, Maryland

and

Gerald R. Baker
Technical Monitor
Laboratory of Astronomy and Solar Physics
Goddard Space Flight Center

ABSTRACT

Stones from heaven, better known as meteorites, provide a wealth of information about the solar system's formation, since they have similar building blocks as the Earth's crust but have been virtually unaltered since their formation. Some stony meteorites contain minerals and silicate inclusions, called chondrules, in the matrix. Utilizing Mössbauer spectroscopy, we identified minerals in the Murchison meteorite, a carbonaceous chondritic meteorite, by the gamma ray resonance lines observed. Absorption patterns of the spectra were found due to the minerals olivine and phyllosilicate. We used a scanning electron microscope to describe the structure of the chondrules in the Murchison meteorite. The chondrules were found to be deformed due to weathering of the meteorite. Diameters varied in size from 0.2 to 0.5 mm. Further enhancement of the microscopic imagery using a digital image processor was used to describe the physical characteristics of the inclusions.

MÖSSBAUER SPECTROSCOPY AND SCANNING ELECTRON MICROSCOPY OF THE MURCHISON METEORITE

Introduction

Today we know most meteorites are extremely primitive remnants of the formation of the solar system 4.6 billion years ago. They provide a valuable record of that event. In order to distinguish between meteorites in terms of physical and chemical composition, scientists have divided meteorites into three broad classes. They are iron meteorites, stony meteorites, and stony-iron meteorites. Furthermore, these meteorites contain minerals and metallic components.

The Murchison meteorite fell in Australia in 1969. The Murchison is a rare type of meteorite called a carbonaceous chondrite. The carbonaceous chondrites are of interest because complex organic chemicals, including amino acids, have been found in them and it is possible that they may hold clues to the process by which life originated on Earth. Carbonaceous chondrites are also the least altered samples we have of the material which formed our solar system.

Utilizing Mössbauer spectroscopy, we may study the iron composition in carbonaceous meteorites without altering the sample by chemical analysis. By comparing the Mössbauer spectra with those of known terrestrial minerals, one can identify the iron minerals present in the sample and indicate the state of the iron.[1-3] We used this technique to identify iron-containing minerals in the Murchison meteorite.

Scanning electron microscopy may be used to derive information about the nature of stony meteorites. A scanning electron microscope was used to describe the shape, composition, crystal structure, and physical characteristics of the Murchison meteorite. Using electron microscopy in combination with digital image processing methods, the structural organization of the meteorite was determined.

Theory

The general principle of the Mössbauer effect is based on the nuclear gamma ray resonance. The effect is a method of attaining recoil-free emission and resonant absorption of nuclear gamma rays by placing the gamma ray source in a solid crystal lattice. An absorption spectrum is obtained when gamma rays from this crystalline source are transmitted through an absorber and measured as a function of velocity of the source. As a consequence, it is possible to detect the very small line shifts and splitting which result from the presence of magnetic and electric fields surrounding the absorbing nucleus. The splitting of the spectra are due to magnetic (Zeeman) splitting and quadrupole splitting.[4] It is also possible to measure a parameter called the isomer shift, which is just the difference in the source, S, and absorber, A, transition energies. The quadruple splitting is the velocity difference between double peaks. The isomer shift, quadrupole splitting, and magnetic splitting of the iron (Fe) have been calculated for many minerals. In order to identify which minerals are present in a sample, measurements are made of the isomer shift, quadrupole splitting, and magnetic splitting and comparison is made with spectra of known minerals. Ferromagnetic compounds are distinguished by six line patterns and paramagnetic compounds have one or two line patterns.[5]

The scanning electron microscope is a multi-lens system. The versatility of the scanning electron microscope for the study of solids is derived in large measure from the rich variety of interactions which the beam electrons undergo in the sample. The primary beam enters the sample and undergoes elastic scattering: 30 percent emerges from the surface of the sample as backscattered electrons and secondary electrons. The microscopist uses this information to determine other information about the nature of the sample - shape, diameter, composition, and physical characteristics of the material.[6]

Experimental Procedures

The techniques employed in sample preparation are those of standard Mössbauer spectroscopy and electron microscopy. For the Mössbauer spectrometer measurements, a 42.3 mg sample of the Murchison meteorite was pulverized into a fine powder. Sample preparation included using epoxy to shape the sample into a disk. The sample was placed in a chamber and the test run at room temperature. An Fe foil standard was also run at room temperature. The Mössbauer effect in Fe was used to determine the iron minerals present in the Murchison. A Canberra multi-channel analyzer was used to store and analyze the data. A Mössbauer computer program using least square analysis was used to calculate the peaks of the spectra. The data were fitted to Lorentzian lines.

To determine the structure and composition of the Murchison, the SX-30 scanning electron microscope (SEM) was used. A 13 mg sample of the meteorite was cut into small chips. The sample was sputter-coated with gold-palladium, mounted on a stage, placed in a chamber, and the SEM focused for optimum image sharpness. The Murchison meteorite is a unique type of meteorite known as a carbonaceous chondrite, consisting of chondrules within a matrix. The SEM was used to examine these chondrules' shape, size and diameter. Further enhancement of the SEM images, using a digital image processor was used to describe the silicate inclusions. Two high resolution monitors were used to display the digitized images by way of a computer program.

Data Analysis

Mössbauer Results

In the Mössbauer spectrum of the Murchison meteorite, the predominant absorption lines are of two non-magnetic patterns. The lines may be identified by comparison with reference spectra of iron compounds expected to be present in stony meteorites. The two most intense lines of the Murchison spectrum were found to correspond to the 2-lined patterns of the minerals olivine,$(Mg,Fe)_2 SiO_4$, and a phyllosilicate. There was evidence of ferromagnetic materials; however, they were not very pronounced. The magnitude of the isomer shift was found to be $+.87 \pm 0.01$ mm/s for the olivine. The quadrupole splitting for the olivine was found to be 3.20 ± 0.01 mm/s.

SEM Results

The stony meteorites are composed of a silicate material similar to the Earth's crustal rocks and are difficult to distinguish from ordinary rocks. When the Murchison was examined under the SEM, it

was found to contain chondrules embedded in a black crust. However, in the Murchison meteorite very few of the chondrules were found to be really spherical; most appeared to be sintered together and/or plastically deformed. The chondrules in the Murchison were found not to have a uniform composition. Instead, they could possibly be composed of different minerals packed together. Structural examination of an individual chondrule at a magnification of 11.6 kx showed layers on the surface. The chondrules may be composed of minerals, other than olivine and phyllosilicates, densely packed together. The chondrules in the Murchison matrix have diameters in the range of 0.2 to 0.5 mm.

Conclusion

Mössbauer spectroscopy and scanning electron microscopy are analytical methods that have been successfully applied to the analysis of meteorites. The Mössbauer effect has been investigated as a method to identify iron in stony meteorites without altering the meteorite chemically. Computer analysis of the gamma ray resonance lines indicates the iron minerals present to be predominantly olivine, $(Mg,Fe)_2\ SiO_4$, and phyllisilicates. The relative abundances of minerals are nearly the same as in the Earth. The Mössbauer spectrum showed magnetic components; however, they were not very pronounced.

The SEM study showed that some of the chondrules in the matrix are spherical and deformed. Although they appear to be clustered together, their diameters range from 0.2 mm to 0.5 mm. Based on the classification of Wiik[7], our results indicate the Murchison to be type II carbonaceous chondrite and definitely of primitive material since chondrules are typical of primitive meteorites.

References

1. Herr, W. and Skerra, B. "Mössbauer Spectroscopy Applied to the Classification of Stone Meteorites," Meteorite Research (P.M. Millman ed. Symposium, Vienna, (1968), pp.108-118.

2. Sprenkel-Segal, E.L. ed. "Mössbauer Analysis of Iron in Stone Meteorite" Geochimica et Cosmochimica, (1964), Vol. 28, pp. 1913-1931.

3. Oliver, F.W. and Isuk, E., "Mössbauer Study of the Allende Meteorite" Meteoritics, (1984), Vol. 19, pp. 26-26.

4. Beiser, A., *Concepts of Modern Physics*. Columbus, Ohio, Bell and Howell Co., 1985, pp. 189-210.

5. May, Leopold, ed. *An Introduction to Mössbauer Spectroscopy*, New York, Plenum Press, 1979.

6. Goldstein, J.I., *Scanning Electron Microscopy and X-Ray Microanalysis.* New York, Plenum Press, 1981.

7. Wiik, H.B., Gechim. Cosmochim. Acta. (1956), Vol. 9, p. 279.

SOLVING THE BM CAMELOPARDALIS PUZZLE

Mathias Teke
Department of Mechanical Engineering
Tennessee State University
Nashville, Tennessee

Michael R. Busby
Center of Excellence in Information Systems
Tennessee State University
Nashville, Tennessee

Douglas S. Hall
Dyer Observatory
Vanderbilt University
Nashville, Tennessee

John Davis
Technical Monitor
NASA/Marshall Space Flight Center

ABSTRACT

BM Camelopardalis (=12 Cam) is a chromospherically active binary star with a relatively large orbital eccentricity. Systems with large eccentricities usually rotate pseudosynchronously. However, BM Cam has been a puzzle since its observed rotation rate is virtually equal to its orbital period indicating synchronization. All available photometry data for BM Cam have been collected and analyzed. Two models of a modulated ellipticity effect are proposed, one based on equilibrium tidal deformation of the primary star and the other on a dynamical tidal effect. When the starspot variability is removed from the data, the dynamical tidal model was the better approximation to the real physical situation. The analysis indicates that BM Cam is not rotating pseudosynchrnously but is rotating in virtual synchronism after all.

SOLVING THE BM CAMELOPARDALIS PUZZLE

BM Camelopardalis (= 12 Cam) is an SB1 in which a K1 giant orbits its unseen companion star in an eccentric 80-day orbit. The K1 giant shows strong emission in its H and K lines of Ca II, so it is chromospherically active (Abt, Dukes, and Weaver 1969). The photometric variability, produced by longitudinally concentrated starspot regions, was discovered by Eaton et al. (1980). Hall and Osborn (1986) analyzed the photometric variability and found two periodicities, 0.3% faster than and 1.0% slower than the $80^{d}.174469$ orbital period, presumably caused by two starspot regions at different latitudes. Hall (1986) calculated that, if the K1 giant is rotating pseudo-synchronously, the photometric period should be $45^{d}.2 \pm 2^{d}.5$. He noted that it was a disturbing coincidence to have the observed rotation rate virtually equal to the orbital period. If the rotation is not pseudosynchronous, then any period faster than or slower than 45 days would be possible, with no reason for 80 days to be preferred. This is the BM Cam puzzle.

To solve this puzzle we collected all available photometry. The 1979 and 1980 photometry discussed by Eaton et al. (1980) was not published but was available in our files. Fernandes (1983) published some 1983 photometry. We had in our files photometry from the years 1980 through 1985, obtained by 15 different observers and sent to us for analysis. Photometry obtained between 1983 and 1987 by the 10-inch automatic telescope in Arizona will be published by Boyd, Genet, Busby, Hall, and Strassmeier (1989). The preliminary analyses by Nelson et al. (1987) and by Strassmeier, Hall, Boyd and Genet (1989) were based on subsets of these data. We also had access to 1988 photometry obtained by the Vanderbilt 16-inch automatic telescope on Mt. Hopkins (Hall 1988). The analysis in this paper is restricted to the V-band data, which was the most extensive. All telescopes except that of Fernandes used the same comparison star, HR 1688. To compensate, we added $-0^{M}.995$ to his differential magnitudes.

One source of photometric variability which should be exactly in phase with the orbital period is the ellipticity effect (Morris 1985). That, however, should produce <u>two</u> maxima and <u>two</u> minima during each orbital cycle and thus show up in a periodogram at P = 40 days. A periodogram of the entire data set showed the most power around 80 days, very little around 40 days.

In the discussion which follows m = magnitude, e = orbital eccentricity, w = angle of periastron measured from the ascending node of the spectroscopic primary in the direction of its orbital motion, M = mean anomaly, v = true anomaly, a = orbital semi-major axis, d = distance between star centers, and R = stellar radius.

Then it occurred to us that the ellipticity effect should be modulated by the varying star-to-star separation in this eccentric orbit. The giant star should experience greater tidal deformation at periastron and less at apastron. This should be a strong effect because it depends on the cube of the ratio R/d (Russell and Merrill 1952). If w is near 90° or 270°, then the light curve should show a maxima of equal height but minima of unequal depth. Abt, Dukes, and Weaver had found $w = 72°.5$, not far from 90°, so we formed the tentative hypothesis that this modulated ellipticity effect could explain at least one of the strong 80-day periodicities.

To quantify this hypothesis, we considered two versions. The first assumes that the long axis of the tidally distorted star always points towards the other star and that the effect on the light curve, in magnitude units, is proportional to $(R/d)^3$. This would correspond to the theory of equilibrium tides. The second assumes that the long axis of the tidally distorted star rotates uniformly in time, i.e., directly

proportional to the mean anomaly, and that the effect on the light curve varies uniformly in time between the two extremes, i.e., between the maximum effect at d = a(1-e) and the minimum effect at d = a(1+e). This would correspond to the theory of dynamical tides. Both versions have the same cos 2ϕ dependence, where ϕ is the angle between the line of sight and the long axis of the tidally elongated star. Thus, in both versions, the ellipticity effect vanishes at $\phi = 45^\circ, 135^\circ, 215^\circ,$ and 225°.

For the first version, the change in magnitude produced by the ellipticity effect is given by

$$\Delta m = k\ (d/a)^{-3}\ \cos 2\phi, \tag{1}$$

where $\phi = v + w - 90^\circ$ and the usual equations of the two-body problem can be used to compute d and v as functions of time.

For the second version, the change in magnitude produced by ellipticity is given by

$$\Delta m = k\ (\alpha + \beta \cos M)\ \cos 2\phi, \tag{2}$$

where now $\phi = M + w - 90^\circ$. In this equation

$$\alpha = \tfrac{1}{2}\ (f_p + f_a) \tag{3}$$

$$\beta = \tfrac{1}{2}\ (f_p - f_a) \tag{4}$$

and

$$f_p = (1 - e)^{-3} \tag{5}$$

$$f_a = (1 + e)^{-3} \tag{6}$$

Note that, in this second version, there is no need to compute v or d as functions of time.

In both versions the coefficient k would correspond approximately to the coefficient A_2 as defined by Russell and Merrill (1952). In the case of a circular orbit, where d = a in equation (1) or e = 0 in equation (2), one would get $k = A_2$.

To try this hypothesis on BM Cam we proceeded by iteration. The observed magnitudes were plotted modulo; the known orbital period and means were taken in bins 0.02 phase units wide. There was considerable dispersion within each bin, of course, because of the other variability present in the system with supposedly different periodicities. We were encouraged that the resulting mean light curve had roughly the expected shape: two nearly equal maxima and two quite unequal minima. Then this mean light curve was subtracted from the observed magnitudes and the residuals examined.

The residuals showed something we recognized as variability produced by starspots. Within each observing season there was a roughly sinusoidal variation with a period similar to but significantly different from the orbital period. That period was about $82^d.5$ up through 1984.5 and about $81^d.0$ after that, with a half-cycle phase shift also around 1984.5. The amplitude of this roughly sinusoidal variation changed dramatically: up to a maximum of $0^M.15$ at 1981.3, down to a minimum of $0^M.03$ at 1984.0, up to another maximum of $0^M.15$ at 1985.6, and possibly decreasing thereafter. In addition, the average light level changed significantly from year to year, covering a range of $0^m.06$.

The next step of the iteration was to find analytical expressions to approximate this starspot variability. An assumed sinusoid required as its parameters the mean light level, the epoch of light minimum, the period, and the amplitude. Additionally, we allowed the mean light level to increase or decrease linearly with time.

The starspot variability was then removed from the original observed magnitudes with these analytical expressions. These residuals, which we presume contain only the ellipticity effect, were then fit in turn with equations (1) and with equation (2). Both fits yielded P, k, e, and w. The period P enters as a parameter when we convert Julian date into mean anomaly.

Results with equation (2) were superior, in the sense that the sum of the squares of the residuals reached a much smaller minimum. We take this as indication that the theory in the second version is a better approximation to the real physical situation. The parameters are presented in Table I with their formal standard errors and compared to the corresponding elements of the Abt, Dukes, and Weaver (1969) solution to the spectroscopic orbit.

Table I

Derived Elements

element	photometric	spectroscopic
P(orb.)	$79^d.93$ $\pm$ .05	$80^d.174469$ $\pm$ .000003
e	0.25 $\pm$ .03	0.35 $\pm$ .02
w	$95^\circ.0$ $\pm$5.0	$72^\circ.5$ $\pm$3.0
k	$0^M.018$ $\pm$ .002	——

The difference between the two determinations of the orbital period amounts to 5 standard errors and thus poses an apparent conflict. The spectroscopic determination was supposedly uncertain by only $\pm 0^d.00003$, but we can show that it could be significantly in error. The solution of Abt, Dukes, and Weaver (1969) was based on 13 radial velocities obtained in 1966, 1967, and 1968 plus three radial velocities obtained long before, in 1916 and 1917. That long 50-year baseline gave them their high

precision but depended critically on proper phasing. The three old velocities fell coincidentally at very nearly the same phase and had about the same velocity, namely V_r = -8.km/sec. If one places them on the falling slope of the radial velocity curve rather than the rising slope, one could have gotten orbital period of $80^d.04$ or $80^d.79$. The first of these would differ from our photometric determination by only 2 standard errors.

The difference between the two determinations of w amounts to 3 standard errors and thus poses another apparent conflict. There is, however, an easy explanation for this discrepancy, namely apsidal motion. The $22^\circ.5$ increase in w between 1967 and 1984 would correspond to an apsidal motion period of 272 years. Theory shows that the rate of apsidal motion is proportional to the fifth power of the ratio R/a. Since that ratio must be large in any binary with an observable ellipticity effect, it is expected that apsidal motion in BM Cam would be relatively rapid, i.e., measurable within a few decades.

The period of the photometric variation produced by the starspots is a measure of the rotation period of the K1 giant. The fact that it differs only a few percent from the orbital period indicates that BM Cam is not rotating pseudosynchronously but is rotating in virtual synchronism after all. From this we might conclude that the theory of pseudosynchronism does not apply when dynamical tides phase-locked with the orbital period are more important than the equilibrium tides.

This investigation is not quite finished. We need to improve the analytical representation of the starspot variability by allowing the amplitude of the assumed sinusoidal variation to increase or decrease linearly with time within each season. We need to repeat the iterative process a few more iterations, and we need to compute the theoretically expected apsidal motion period, which will require a determination or estimate of the orbital inclination and the mass ratio, neither of which is known directly for a single-lined spectroscopic binary nor for a non-eclipsing ellipsoidal variable.

Acknowledgments

The Vanderbilt 16-inch telescope was obtained with NSF research grant AST 84-14594 and the analysis in this paper was supported by NASA research grant NAG 8-111.

References

Abt, H.A., Dukes, R.J., and Weaver, W.B. 1969, Ap. J. **157**, 717.

Boyd, L.J., Genet, R.M., Busby, M.R., Hall, D.S., and Strassmeier, K.G. 1989, Ap. J. Suppl., in preparation.

Eaton, J.A., Hall, D.S., Henry, G.W., Landis, H.J., McFaul, T.G., and Renner, T.R. 1980, I.B.V.S. No. 1902.

Fernandes, M. 1983, B.A.V. Rundbrief **32**, 119.

Hall, D.S. 1986, Ap. J. **309**, L83.

Hall, D.S. 1988, in *Automatic Small Telescopes*, edited by D.S. Hayes and R.M. Genet (Mesa: Fairborn Press), in press.

Hall, D.S. and Osborn, S.A.G. 1986, in *Cool Stars, Stellar Systems, and the Sun*, edited by M. Zeilik and D.M. Gibson (Berlin: Springer-Verlag), p.84.

Morris, S.L. 1985, Ap. J. **295**, 143.

Nelson, E.R., Boyd, L.J., Genet, R.M., Hall, D.S. 1987 in *Cool Stars, Stellar Systems, and the Sun,* edited by J.L. Linsky and R.E. Stencel (Berlin: Springer-Verlag), p. 497.

Russell, H.N. and Merrill, J.E. 1952, Contrb. Princeton Univ. Obsv. No. 26, chapter IV.

Strassmeier, K.G., Hall, D.S., Boyd, L.J., Genet, R.M. 1989, Ap. J. Suppl. **69**, 141.

AEROSOL SPECKLE EFFECTS ON ATMOSPHERIC PULSED LIDAR BACKSCATTERED SIGNALS

S.R. Murty
Alabama A&M University
School of Engineering and Technology
Normal, Alabama

The effects of refractive turbulence along the path on the aerosol speckle field propagation and on the decorrelation time are studied for coherent pulsed lidar systems.

Introduction

Lidar systems using atmospheric aerosols as targets exhibit return signal amplitude and power fluctuations which indicate speckle effects. [1,2] The speckle effects are manifested statistically as Rayleigh-distributed amplitude and exponentially distributed power of the backscattered signals. The signals from the various scatterers which make up the target combine to form a speckle pattern at any point along the backscattered beam. The speckle size is $\approx \lambda z/b$, where z is the range from the target, λ is the wavelength, and b is the radius of the illuminating beam on the diffuse target. Therefore, as the beam size on the diffuse target increases, the speckle size at the receiver decreases. Since the field across a speckle pattern is produced by the addition of a number of signals of random phase, the speckle pattern changes as each particle moves, thereby generating spatial and temporal changes in intensity. The particles move primarily due to atmospheric turbulence, and the changes in the speckle pattern are caused by the velocity turbulence in the illuminated region of the atmosphere which contributes to the backscattered signal at the receiver. For a pulsed laser, the backscatter region of the atmosphere is $ct_p/2$ around the range point where t_p is the pulse duration and c is the speed of light.

In addition to producing signal intensity fluctuations, aerosol-generated speckle causes a decorrelation of the backscattered signals, as the aerosols are free to move about relative to each other along the beam axis and transverse to it. The resulting decorrelation time determines the temporal window of the return signal from which the power spectrum can be calculated to obtain wind speed.

A laser beam experiences fluctuations in intensity and a reduction in coherence due to propagation in the refractive turbulence of the atmosphere between the telescope range point as shown in Fig. 1. Consequently the received signal characteristics are affected by a combination of refractive turbulence and speckle effects. The objective of this paper is to examine the effects of refractive turbulence along the path on the aerosol speckle field propagation and of the decorrelation time.

Churnside and Yura [3] have developed the basic theoretical formulation of the spatiotemporal correlation function for the aerosol return-signal field. Ancellet and Menzies [4] presented results of measurement using a pulsed TEA CO_2 laser and found a decorrelation time of 2-2.5 μ s over a 1.3-km range. Laser pulses shorter than ~150ps are broadened due to atmospheric turbulence, but the pulse spreading and wander in turbulence decrease as the pulse becomes longer. [5,6] In this work, the pulse is represented as a Fourier integral, and we make use of the two-frequency mutual coherence function to study propagation of the aerosol speckle field.

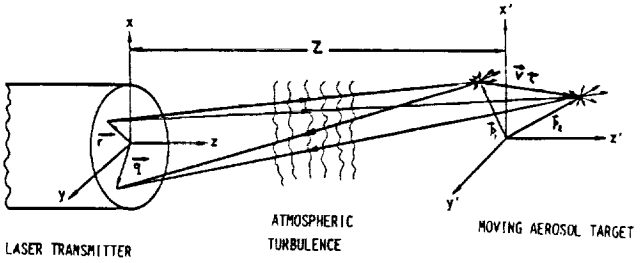

Fig. 1. Sketch of pulsed lidar propagating through atmospheric turbulence using moving aerosols as a target.

Analysis

The transmitter and receiver are assumed to be colocated having a common telescope aperture diameter d. The laser transmitter is assumed to be pulsed with a pulse duration t_p and a transmitted power $P_T(t)$ at time t. The complex field of the pulse propagating in the turbulent medium at any range point z is given by

$$U_I(z,\mathbf{p},t) = \int_{-\infty}^{\infty} A(\omega) u_I(\mathbf{p},k,t) \exp(i\omega t) d\omega, \tag{1}$$

where $A(\omega)$ is the Fourier spectral amplitude, u_I is the monochromatic field amplitude at a distance z from the transmitter, $\mathbf{p}$ is a 2-D transverse vector in the aerosol target plane, and k is the optical wave number. Using the paraxial approximation and the extended Huygens-Fresnel principle, [7] u_I can be expressed as

$$u_I(\mathbf{p},k,t) = \frac{k \exp(ikz)}{2\pi i z} \int d^2\mathbf{r} u_T\left(\mathbf{r},t-\frac{z}{c}\right) \times \exp\left[\frac{ik}{2z}(\mathbf{p}-\mathbf{r})^2 + \psi(\mathbf{r},\mathbf{p},k,t)\right]. \tag{2}$$

In Eq. (2), $\mathbf{r}$ is a transverse vector in the transmitter plane, $\psi(\mathbf{r},\mathbf{p},k,t)$ is the sum of the logamplitude and phase perturbation experienced by a spherical wave propagating from $\mathbf{r}$ to $\mathbf{p}$ through the atmospheric turbulence, and u_T represents the field amplitude at the transmitter given by

$$U_T(r,t) = \left[\frac{2P_T(t)}{\pi a^2}\right]^{1/2} \exp\left[-\left(\frac{1}{a^2}+\frac{ik}{2}\right)r^2\right] \tag{3}$$

where a is the beam radius at exp(-2) intensity, and f is the geometric focus of the telescope.

The complex field $U_I(z,\mathbf{p},t)$ is assumed to be backscattered at range z by an atmospheric aerosol present in the illuminated volume. The scattered pulse propagates back to the receiver through atmospheric turbulence, and its field is given by

$$U_s(\mathbf{q},t) = \int_{-\infty}^{\infty} A(\omega) u_s(\mathbf{q},k,t) \exp(i\omega t) d\omega, \tag{4}$$

where the monochromatic wave field $u_s(\mathbf{q},k,t)$ is given by [9]

$$u_s(\mathbf{q},k,t) = \frac{S(k)}{z} u_I\left(\mathbf{p},k,t - \frac{z}{c}\right)) \times \exp\left[ikz + \frac{ik}{2z}(\mathbf{q}-\mathbf{p})^2 + \psi(\mathbf{p},\mathbf{q},k,t)\right]. \tag{5}$$

In Eq. (5), $\mathbf{q}$ is a transverse vector in the receiver plane and S(k) is the monochromatic backscatter coefficient of the aerosol.

The pulse is assumed to have a center carrier angular frequency ω_0 and optical wavenumber k_0 and is narrowband. It is convenient to write Eq. (4) as

$$U_s(\mathbf{q},t) = \exp[i(\omega_0 t - k_0 z)] \int_{-\infty}^{\infty} d\omega A(\omega + \omega_0) \times u_s(q, \omega + \omega_0, t) \exp(i\omega t). \tag{6}$$

During a small time interval of <1 ms, the aerosol position is assumed to change due to a radial velocity v_z, a transverse velocity $\mathbf{V}_T$ to a new position given by the following relations:

$$z_\tau = z(t+\tau) + z(t) + v_z \tau;$$

$$\mathbf{p}_\tau = \mathbf{p}(t+\tau) = \mathbf{p}(t) + \mathbf{V}_T \tau.$$

The backscattered field at time $t + \tau$, is given by

$$U_s(\mathbf{q},t+\tau) = \exp[i\omega_0(t + \tau - z_{v_c})] \int_{-\infty}^{\infty} A(\omega + \omega_0) \times u_s(\mathbf{q}, \omega + \omega_0, t + \tau) \times \exp[i\omega(t + \tau - z_{v_c}) d\omega, \tag{7}$$

and the monochromatic wave field at time and $t + \tau$ is given by

$$u_s(\mathbf{q},\omega,t+\tau) = \frac{kS\exp(2ikz_\tau)}{2\pi i z^2}\int dr^2 u_T\left(\mathbf{r},t+\tau-\frac{2z}{c}\right)$$

$$\times\exp\left[\frac{ik}{2z}(\mathbf{p}_\tau-\mathbf{r})^2+(\mathbf{q}-\mathbf{p}_\tau)^2\right]$$

$$+\Psi(\mathbf{r},\mathbf{p}_\tau,k,t+6\tau)+\Psi(\mathbf{p}_\tau,\mathbf{q},k,t+\tau). \qquad (8)$$

The cross-product of the received fields at time t and $t+\tau$ is given by

$$U_s(\mathbf{q}_1,t)\,U_s^*(\mathbf{q}_2,t+\tau) = \int_{-\infty}^{\infty} d\omega_1 \int_{-\infty}^{\infty} d\omega_2 A_e(\omega_1)$$

$$\times u_s(\mathbf{q}_1,\omega_1,t)\,A_e(\omega_2)\,u_s^*(\mathbf{q}_2,\omega_2,t+\tau)$$

$$\times\exp[i(\omega_1-\omega_2)t], \qquad (9)$$

where $A_e(\omega) = A(\omega+\omega_0)$.

Equation (9) will be ensemble-averaged over the propagation path for refractive turbulence and over the illuminated volume for velocity turbulence to obtain the pulse spatiotemporal correlation function. This process is represented by double angular brackets, and the correlation function of the received optical fields is given by

$$\ll U_s(\mathbf{q}_1,t)U_s^*(\mathbf{q}_2,t+\tau)\gg = \int_{-\infty}^{\infty} d\omega_1 \int_{-\infty}^{\infty} d\omega_2 A_e(\omega_1)A_e^*(\omega_2)$$

$$\times\Gamma(\mathbf{q}_1,\mathbf{q}_2,\omega_1,\omega_2)$$

$$\times\exp[i(\omega_1-\omega_2)t], \qquad (10)$$

where $\Gamma(\mathbf{q}_1,\mathbf{q}_2,\omega_1,\omega_2) = \ll u_s(\mathbf{q}_1,\omega_1,t)u_s(\mathbf{q}_2,\omega_2,t+\tau)\gg$ is a two-frequency mutual coherence function. The determination of the effects of aerosol speckle, refractive turbulence, and pulse shape are now dependent on the evaluation of the function Γ.

Ensemble Averaging

Following Churnside and Yura [3] for the averaging over velocity turbulence, the aerosol velocities are assumed Gaussian-distributed within the inertial subrange, and we obtain the expected value of the mutual coherence function as

$$\Gamma(\mathbf{q}_1,\mathbf{q}_2,\omega_1,\omega_2) = \int_{-\infty}^{\infty} dv_z \int_{-\infty}^{\infty} d^2\mathbf{v}_T \int dz d^2\mathbf{p}$$

$$\times u_s(\mathbf{q}_1,\omega_1,t)\,u_s^*(\mathbf{q}_2,\omega_2 t+\tau)$$

$$\times P(v_z)P(\mathbf{V}_T)/V. \qquad (11)$$

In Eq. (11), V is the illuminated volume, and the probability density functions of the velocity components are given by

$$P(v_z) = \frac{1}{\sqrt{2\pi}\sigma_z} \exp\left[-(v_z - \bar{v}_z)^2/2\sigma_z^2\right],$$

$$P(\mathbf{V}_T) = \frac{1}{2\pi\sigma_T^2} \exp\left[-(\mathbf{V}_T - \bar{\mathbf{V}}_T)^2/\sigma_T^2\right],$$

where $\bar{v}_z$, $\bar{\mathbf{V}}_T$ and σ_z^2, σ_T^2 are the means and variances of the wind components along the z axis and transverse to it.

The ensemble average over path turbulence is given by

$$\begin{aligned}\langle u_s(\mathbf{q}_1,\omega_1,t)\, u_s^*(\mathbf{q}_2,\omega_2,t+\tau)\rangle = {} & \frac{k_1k_2S(\omega_1)S(\omega_2)}{(2\pi z^2)^2} \exp[2i(k_1-k_2)z \\ & -2ik_2v_z\tau]\int\int d^2\mathbf{r}_1 d^2\mathbf{r}_2 u_T\left(\mathbf{r}_1,t-\frac{2z}{c}\right) \\ & \times u_T^*\left(\mathbf{r}_2,t+\tau-\frac{2z}{c}\right)\exp\left[\frac{ik_1}{2z}(\mathbf{p}-\mathbf{r}_1)^2\right. \\ & +\frac{ik_1}{2z}(\mathbf{q}_1-\mathbf{p})^2 - \frac{ik_2}{2z}(\mathbf{p}+\mathbf{V}_T\tau-\mathbf{r}_2)^2 \\ & \left.-\frac{ik_2}{2z}(q_2-\mathbf{p}-V_T\tau)^2\right] \\ & \times H(\mathbf{q}_1,\mathbf{q}_2,\mathbf{r}_1,\mathbf{r}_2,k_1,k_2), \end{aligned} \tag{12}$$

where H is the fourth-order mutual coherence function given by

$$\begin{aligned} H = {} & \langle\exp[\Psi(\mathbf{p},\mathbf{r}_1,k_1,t) + \Psi(\mathbf{p},\mathbf{q}_1,k_1,t) + \Psi^*(\mathbf{p}+\mathbf{V}_T\tau,\mathbf{r}_2,k_2,t+\tau) \\ & +\Psi^*(\mathbf{p}+\mathbf{V}_T\tau,\mathbf{q}_2,k_2,t+\tau)\rangle. \end{aligned} \tag{13}$$

The change in the aerosol position has very little effect on the refractive turbulence encountered along the path for small τ and will be neglected in evaluating the mutual coherence function, which can be written as [8]

$$\begin{aligned} H = {} & \exp\left[-(1/2)(D_{12}-D_{13}+D_{14}+D_{23}+D_{34}-D_{24}+D_{34})\right. \\ & \left.+2C_{X_{12}}+2C_{X_{34}}\right]. \end{aligned} \tag{14}$$

In Eq. (14) $D_{ij} = D(|\mathbf{r}_i - \mathbf{r}_j|)$ is the two-frequency wave structure function of a point source given by [10]

$$D(\rho) = 2(\rho/\rho_0)^{5/3} - 2\Delta_{12}^2/\Omega^2,$$

$$\rho_0 = (0.545 k_0 C_n^2 z)^{-3/5},$$

$$\Omega^{-2} \simeq 0.39 k_0 C_n^2 L_o^{5/3} z, \quad \Delta_{12} = |k_1 - k_2|/k_0, \tag{15}$$

where L_0 is the outer scale of turbulence, c is the speed of light, and C_n^2 is the turbulence structure constant assumed uniform along the path. $C_{xij} = C_x(|\mathbf{r}_i - \mathbf{r}_j|)$ is the two-frequency covariance of the logamplitude of a point source given by [11]

$$C_{xij} = 0.132\pi^2 k_1 k_j z C_n^2 \int_0^1 dt \int uu^{-8/3} J_0$$

$$\times [u|(\mathbf{r}_i - \mathbf{r}_j)(1-t)|] \sin\left[\frac{u^2 t(1-t)z}{2k_1}\right]$$

$$\times \sin\left[\frac{u^2 t(1-t)z}{2k_j}\right]. \tag{16}$$

The integrations of Eq. (12) are lengthy and cannot be performed in closed form. We present the approximate results in this work for the simplified case of a collimated beam and negligible transverse velocity component and consider points along the beam axis. It is also assumed that $\Delta_{12} \ll 1$, and we make use of a quadratic approximation for the structure function. With these simplications, the integrations of Eq. (12) can be carried out, and the result is

$$\langle u_s(o,\omega_1,t)\, u_s^*(o,\omega_2,t+\tau)\rangle = \frac{2S^2F^2}{a^2z^2(1+F^2+2a^2/\rho_0^2)\pi}$$

$$\times \left[P_T\left(t - \frac{62z}{c}\right) P_T\left(t + \tau - \frac{2z}{c}\right)\right]^{1/2}$$

$$\times \exp\left\{ i(\omega_1 - \omega_2) T_d - (\omega_1 - \omega_2)^2/\Omega^2 \right.$$

$$- (k_1 - k_2) p^2/2z - 2\left(\frac{k_0 a^2}{2z}\right) p^2 /$$

$$\left. \left[1 + \left(\frac{k_0 a^2}{2z}\right)\right]^2 2ik_1 z - 2ik_2 z\tau \right\}, \tag{17}$$

where $F = k_0 a^2/2z$ is the Fresnel number of the source, T_d si the time delay given by

$$T_d \approx \frac{F}{ck_0}\left(\frac{1 + a^2/\rho_0^2}{1 + F^2 + 2a^2/\rho_0^2}\right), \tag{18}$$

the coherence bandwidth is given by

$$\Omega^{-2} \approx 0.39 C_n^2 L_o^{5/3} z/c^2, \tag{19}$$

and L_o is the outer scale of the turbulence, and c is the speed of light. It may be noted that the pulse broadening is inversely proportional to the coherence bandwidth. We will now carry out integrations indicated in Eq. (11) over the velocity spectrum and sensing volume V and replace $S^2\ N/V$ by the aerosol backscatter coefficient β, where N is the total number of aerosols within the volume V. The result is

$$\Gamma(o,o,\omega_1,\omega_2,) = \int \frac{\beta}{2z^2} \left[P_T\left(t\frac{2z}{c}\right) P_T\left(t + \tau - \frac{2z\tau}{c}\right) \right]^{1/2}$$

$$\times \exp\left[i(\omega_1 - \omega_2) T_d - (\omega_1 - \omega_2)^2/\Omega^2\right.$$

$$\left. + 2i(k_1 - k_2) z - 2ik_2 \bar{v}_z \sigma_z \tau - 2\sigma_z^2 k_2^2 \tau^2\right] dz. \tag{20}$$

The integrations over ω_1 and ω_2 are carried out for a Gaussian pulse with frequency spectrum given by

$$A(\omega) = (2\pi\sigma_\omega^2)^{-1/2} \exp[(\omega - \omega_0)^2/2\sigma_\omega^2],$$

where σ_ω is the bandwidth of the pulse. The variables are changed using $2\omega'_0 = \omega_1 + \omega_2$, $\delta = \omega_1 - \omega_2$.

The spatiotemporal correlation function is calculated for a Gaussian transmitted power distribution given by

$$P_T(t) = \frac{E}{\sqrt{\pi} t_p} \exp(-t^2/t_p^2),$$

where E is the total energy in the pulse, and the pulse width is related to bandwidth as $t_p = \sqrt{2}\sigma_\omega^{-1}$. The integration over z is performed designating arbitrarily the time of peak power by t = 0, and the result is

$$\ll U_s(o,t)U_s^*(o,t+\tau)\gg = \frac{c\beta E}{2z_0^2}\,\frac{\Omega}{(\Omega^2+4\sigma_\omega^2)^{1/2}}\,\frac{\tau_e}{(\tau_e^2+t_p^2)^{1/2}}$$

$$\times\frac{1}{1+6F^2+2a^2/\rho_0^2}\exp\Big[-2\sigma_z^2 k_0^2\tau^2$$

$$-\frac{\sigma_\omega^2}{4}(\tau^2+2\bar{v}_z\sigma_z\tau/c)^2-\frac{\tau_e^2}{\tau_e^2+t_p^2}$$

$$\times\left[\frac{\tau^2}{4t_p^2}+\frac{\tau^2/4+(T_d+\bar{v}_z\tau/c)^2}{\tau_e^2}\right]$$

$$-i(\omega_0\tau+2k_0\bar{v}_z\tau)\Big], \qquad (22)$$

where $\tau_e^2=\sigma_\omega^{-2}+4\Omega^{-2}$ and z_0 is the range. Equation (22) is the main result of this paper, which exhibits the effects of refractive path turbulence on pulse spreading and aerosol speckle. The first term in the exponential gives the decorrelation effect due to velocity turbulence along the beam of the axis; the second and third terms give the effect of refractive turbulence and velocity turbulence on pulse broadening and its contribution to the decorrelation of aerosol scattered signals.

Discussion

The spatiotemporal correlation function obtained by Churnside and Yura [3] has been extended to include the spectral effect of pulsed signals and refractive turbulence along the propagation path. An approximate result for a collimated beam along the beam axis is presented in Eq. (22) for the combined effects assuming a quadratic approximation for the structure functions. These approximations permit us to bring out explicitly the effect of time delay T_d and coherence bandwidth Ω on the correlation function.

We consider a long path wind-measuring pulsed lidar having a pulse duration of 100 ns operating at 9.1 μm wavelength. The path length is assumed as 100 km through a turbulent atmosphere with $C_n^2 = 6.4\times10^{-15}\ \mathrm{m}^{-2/3}$ corresponding to a clear day in the lower atmosphere with an outer scale length $L_0 = 100$m and $\sigma_z = 1$ m/s. The beam radius at exp(-2) intensity is taken as 1 m, which gives the Fresnel number of the source as F = 3.45. The transverse coherence length for this path is $\rho_0 = 0.0465$m.

The coherence bandwidth Ω and the time delay T_d corresponding to these parameters are $\Omega = 4.1\times10^{11}$ rad/s and $T_d = 1.65\times10^{-14}$s. Using these values, we obtain $\sigma_\omega = 1.4\times10^{10}$ rad/s and $\tau_e = 70.9$ ns. These time scales are shorter than the correlation time of the order of 1μs corresponding to moderate turbulence-induced aerosol dephasing, and the effect of pulse broadening is negligible for this case. When the correlation time due to aerosol dephasing approaches the nanosecond range, pulse broadening effects need to be considered.

This work is supported by NASA grant NSG 8037. It is a pleasure to acknowledge the discussions with James W. Bilbro of NASA Marshall Space Flight Center.

References

1. R.M. Hardesty, R.J. Keeler, M.J. Post, and R.A. Richter, "Characteristics of Coherent Lidar Returns from Calibration Targets and Aerosols," Appl. Opt. **20**, 3763 (1981).

2. P.H. Flamant, R.T. Menzies, and M.J. Kavayaa, "Evidence for Speckle Effects on Pulsed CO_2 Lidar Signal Returns form Remote Targets," Appl. Opt. **23**, 1412 (1984).

3. H. Churnside and H.T. Yura, "Speckle Statistics of Atmospherically Backscattered Laser Lights," Appl. Opt. **22**, 2559 (1983).

4. G.M. Ancellet and R.T. Menzies, "Atmospheric Correlation Time Measurements and Effects on Coherent Doppler Lidar," J. Opt. Soc. Am. A **4**, 367 (1987).

5. C.H. Liu and K.C. Yeh, "Pulse Spreading and Wandering in Random Media," Rad. Sci, **14**, 925, (1979).

6. I. Sreeivasiah, A. Ishimaru, and T.S. Hong, "Two Frequency Mutual Coherence Function and Pulse Propagation in a Random Medium: An Analytic Solution to the Plane Wave Case," Rad. Sci. **11**, 775 (1976).

7. R.F. Lutomirski and H.T. Yura, "Propagation of a Finite Optical Beam in an Inhomogeneous Medium," Appl. Opt. **10**, 1652 (1971).

8. H.M. Lee, J.F. Holmes, and J.R. Kerr, "Statistics of Speckle Propagation Through the Turbulent Atmosphere," J. Opt. Soc. Am. **66**, 1164 (1976).

9. H.T. Yura, "Mutual Coherence Function of a Finite Cross-Section Optical Beam Propagating in a Turbulent Medium," Appl. Opt. **11**, 1399 (1972).

10. R.L. Fante, "Electromagnetic Beam Propagation in Turbulent Media: An Update," Proc. IEEE **68**, 1424 (1980).

11. A. Ishimaru, "Temporal Frequency Spectra of Multifrequency Waves in Turbulent Atmosphere," IEEE Trans. Antennas Propag. **AP-20,** 10 (1972).

AUTOMATED ASSEMBLY IN SPACE

S. Srivastava, Professor
Bowie State University

Suren N. Dwivedi, Professor
West Virginia University

Gary Jones, Manager
Goddard Space Flight Center
Greenbelt, MD

Toh Teck Soon, Reddy Bandi, Soumen Banerjee, and Cecilia Hughes
Student Assistants
Bowie State University
Bowie, MD

ABSTRACT

The installation of robots and their use for assembly in space will create an exciting and promising future for the U.S. Space Program. The concept of assembly in space is very complicated and error prone and it is not possible unless the various parts and modules are suitably designed for automation.

This paper develops certain guidelines for part designing and for an easy precision assembly. Major design problems associated with automated assembly are considered and solutions to resolve these problems are evaluated in the guidelines format. Methods for gripping and methods for part feeding are developed with regard to the absence of gravity in space. The guidelines for part orientation, adjustments, compliances and various assembly construction are discussed. Design modifications of various fasteners and fastening methods are also investigated.

In phase 2, a smart menu driven user friendly software will be developed containing all these guidelines and rules. Finally, this software will be implemented and its performance will be evaluated. Some examples will be considered and tested using the guidelines and/or software.

AUTOMATED ASSEMBLY IN SPACE

Introduction

In the coming years, the first permanently manned space station, which will perform such tasks as collection of data from distant stars, repairing satellites and manufacturing of extremely pure pharmacological products, will be launched. The space robots will be designed in such a way that they would assemble the space station itself, perform satellite repairing and testing, and various extra vehicular activities (EVA) under the control commands given from the earth station. Almost total reliance upon space robots in the space station will free astronauts for accomplishing more significant tasks including taking advantage of unforeseen opportunities, solving unexpected problems, occasionally saving a mission, supervising machines and acquiring, integrating and interpreting multisensory data.

The concept of assembly in space seems quite complicated, unproductive and error prone unless various parts and modules are suitably designed for automation from the beginning.

This paper basically focuses on the development of such guidelines and rules for the design of products that will be assembled in space. The parts once designed with these considerations will be easily assembled by simple telerobots, programmed robots or manually, without any error and in shorter time. It will also reduce the need for complicated grippers and end-effectors to monitor the assembly process.

In addition, these proposed modifications that are incorporated into the design of a part facilitate easy handling, omit orientational ambiguities and require simple assembly steps by robots. What is more important about these guidelines is their applicability under the prevailing condition of zero gravity in space.

Development of Guidelines and Rules

1. Design for Part Handling and Gripping

The gripping of the components to be assembled is the most difficult part of assembly by robots in space. If the components are not gripped properly, they can become projected missiles and damage vital equipment as well as the spacecraft and the astronauts. While designing the products and the grippers, care should be taken so that when the components are moved, their movements are secure, verifiable and failsafe.

For higher productivity in assembly by robots in space, the design of the general purpose gripper is a critical factor. The design emphasis and functional requirement of grippers used in industries and space are different in some respects. The object escaped from the end-effector would take off with a velocity in an arbitrary direction determined by the robot motion, transforming it into a potentially harmful projectile. The grip provide by the end-effector has necessarily got to be failsafe. This requirement translates into considerations such as positive grasp (see Fig. 1), low friction grasping surfaces, sensory verification, zero back-drivability, and extreme gripper strength. Furthermore, the issue of compliance in space robotic gripping should be considered. Compliance has to be incorporated either in the object, fixture, gripper, or the arm. In the majority of the cases vacuum suction and magnetic pick will be used for part handling (see Fig. 2).

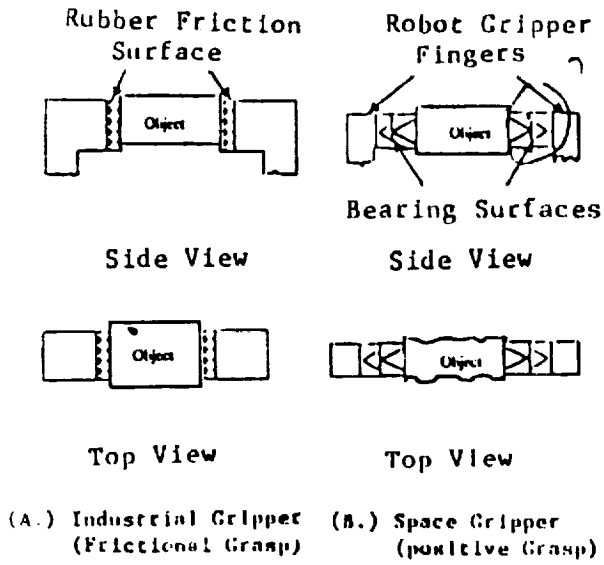

Figure 1

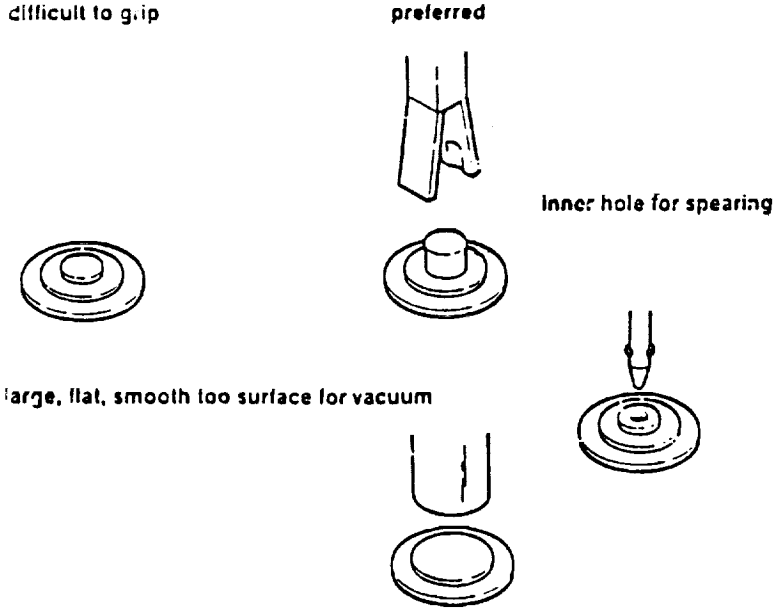

Figure 2

2. Design for Part Feeding and Orientation

There are several key concerns when considering design for proper part feeding and orientating. Parts coming to the assembly station are usually bulk components. They are fed along a suitable conveyor-media (a conveyor box) and will be latched between two fixed ends in the space ship, and thus avoiding the parts swimming in space.

First, part dimensions should be designed to facilitate automation. It is very difficult to automatically orient parts that have dimensions that differ by only a small amount. The obvious alternative is to make these parts' dimensions either identical or their differences more pronounced.

Second, a part should be designed so that symmetry is the priority. It will be a lot easier for a robot to handle a symmetrical part than an asymmetrical part (see Fig. 3). Sometimes asymmetry also makes part orientation easier (see Fig. 4).

Designs should be created so that they do not conflict. This includes avoiding such feeding problems as tangling, nesting, shingling, wedging and jamming. Springs must have closed end loops. Tangling problems are reduced by eliminating protrusions or closing off holes that are unnecessary on the parts (see Fig.5). Parts that travel on a conveyor should be thick enough so that they do not have a tendency to shingle, or start stacking on one another. Additional care should be taken with angles so that the parts do not tend to wedge with each other (Fig.6).

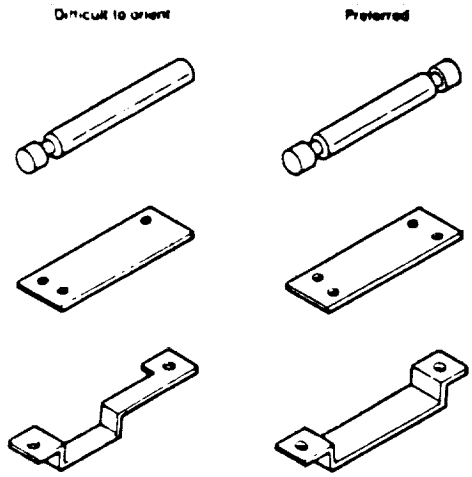

Figure 3

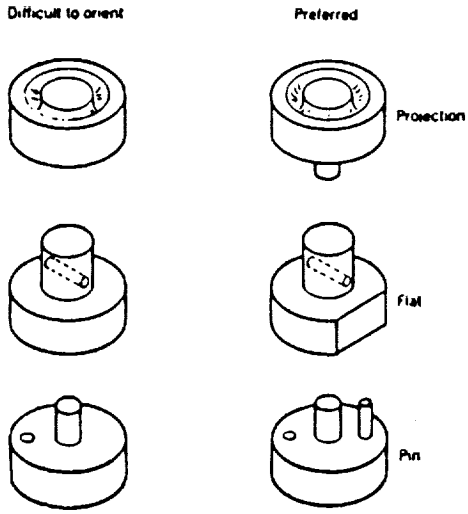

Figure 4

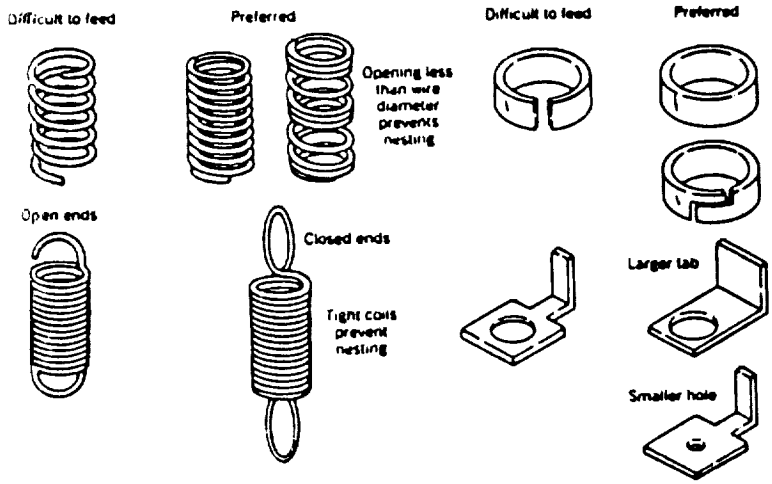

Figure 5

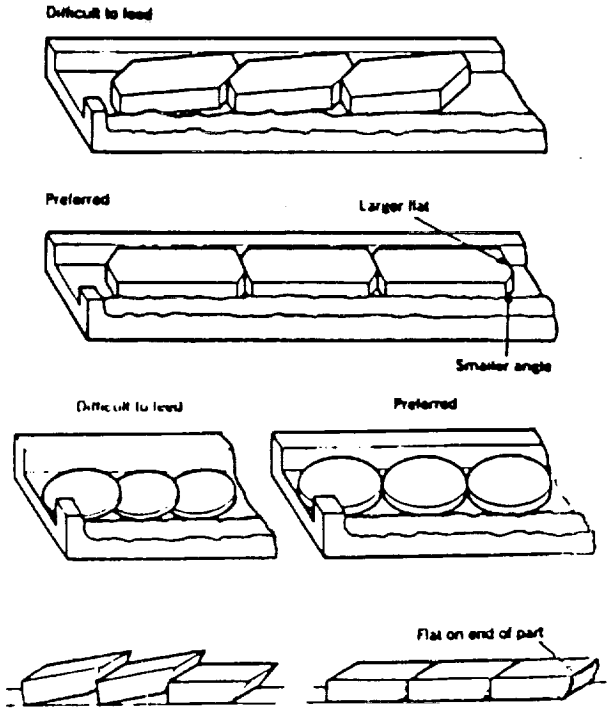

Figure 6

3. Design for Part Fastener

Fastening is one of the most time consuming operations in the assembly. This can be alleviated by using integral fasteners and building the fasteners right into the product, and using snaps and latches built in to fasten parts quickly, without the necessity of extra fastening parts. If screws were to be used in fastening, using the screw with built-in washers, and reducing the screws in number and variety in any component would help. (see Fig.7).

The methods of assembly including mechanical fastening, staging, kiting, and soldering techniques. Devices for feeding and orienting should all be evaluated in order to reduce time of assembly/disassembly.

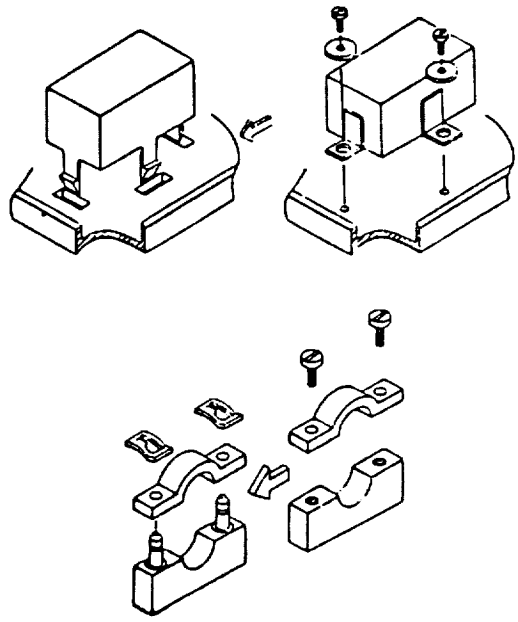

Figure 7

4. Design for Minimum Number of Parts

Economizing on the number of parts either by redesigning or elimination can produce dramatic results for assembly in space. This can only happen if a concentrated effort is made to design equipment which require a minimum number of parts. Fewer parts are advantageous to the assembly cycle, assembly costs, system costs, material costs, and warehousing costs; and in many cases provide a higher quality product (Fig.8).

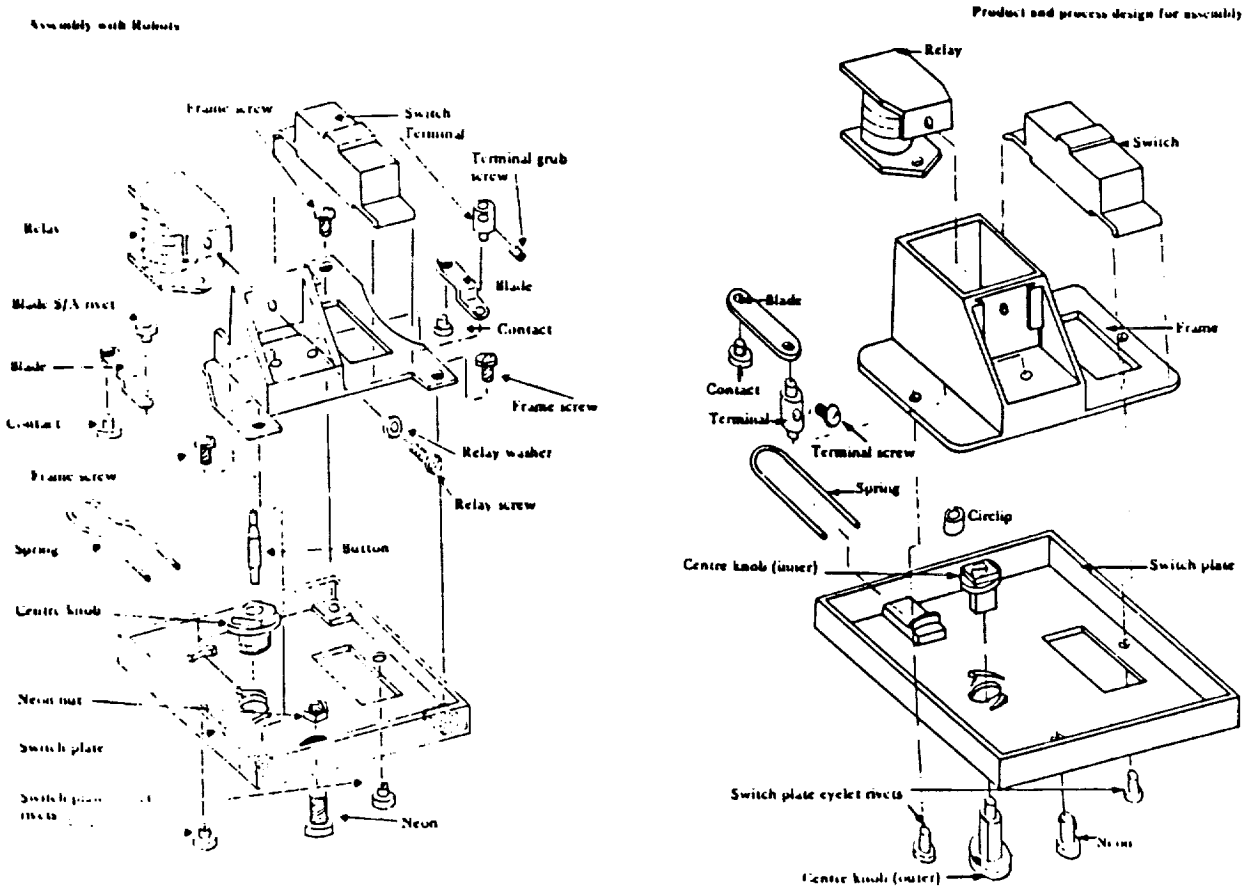

Figure 8

5. Design for Modular Assembly

A strictly structural approach should be taken for assembly of equipment. Designing a product in modules is advantageous. Subassemblies may be built in different areas. Modules may be tested and repaired before final assembly. Model variations can be accomplished at the subsystem level. This system will also make it easier for servicing the part. In addition, assemblies can take place from any direction but must be in optimal sequence (Fig. 9).

6. Design for Minimum Part Variations

When product variation is low, commonality of parts is high. However, if follow on products maintain a family resemblance, the assembly of the product will be greatly simplified, and cost effectiveness and quality for assembly in space will naturally follow(Fig. 10).

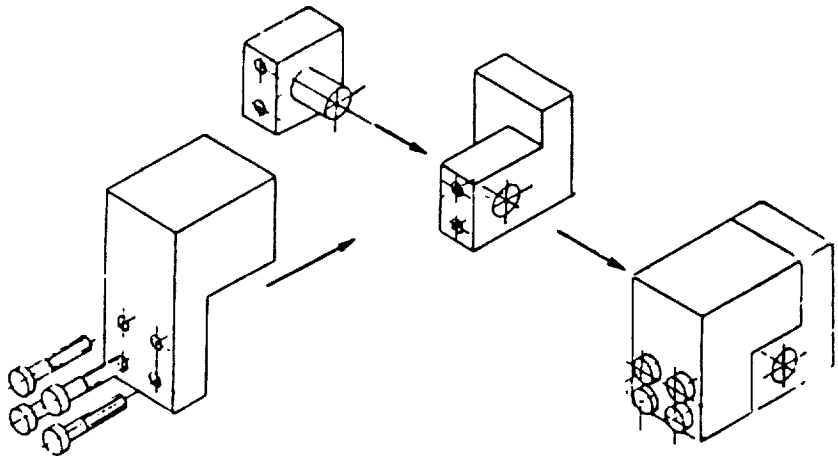

Figure 9

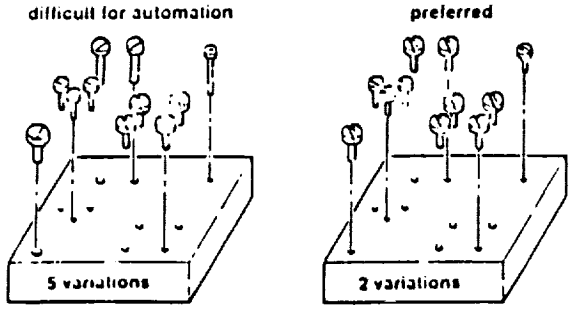

Figure 10

Benefits of Guidelines and Rules

The direct benefits of the space assembly products include: Facilitating automatic assembly with ease, reduction or elimination of the need for expensive electronics normally required for precise positioning, allowing relaxed positioning tolerance, reduction in downtime of assembly equipment by reducing wedging, jamming and damaging of parts, increased productivity with humans functioning as managers rather than as operators, increased responsiveness to innovation since the automated station will become more flexible and adaptable, lower cost of operations with highly automated systems which will run at peak efficiency, uniform quality control, greater autonomy with machine intelligence to support monitoring and control of station systems, thereby lessening reliance on ground support,

improved reliability, the ability to perform with robots and teleoperators tasks which are unsuitable to humans alone, for instance, the assembly of large structures, and a reduced need to expose humans to hazardous conditions existing in space.

Conclusion

In conclusion, it can be said that assembly by robots in space will be a very interesting research area. It will help in establishment of a station in outer space to assemble and launch satellites and spacecraft automatically. The space station will also be capable of testing, servicing, refueling and recovering a space shuttle or satellite by teleoperation from the ground. Automated assembly in space stations can also be used for various material processing and manufacturing. The key feature of manufacturing in space is the extended period of weightlessness that is permitted in its low gravity environment. Thus, these guidelines will be helpful in automizing the tasks of the space industry by properly designing various containers, etc., suitable for robotic handling.

References

1. Mahalingam, S., Sharifi, M., Dwivedi,S.N. and Vranish, J., "Special Challenges of Robotic Gripping in Space", Pro. IEEE Comp. Soc. 20th Southeastern Conf. on Systems Theory, pp. 581-586, March 1988.

2. Vranish, J.M., "A Quick Change Gripper for Robots", Robot Grippers, Springer Verlag, pp. 277-298, 1986.

3. Robert-Bunch, W. and Vranish, J.M., "Split Rail Parallel Gripper", RI/SME Robots 9 Conf, June 1985.

4. Salisbury, J.K., "Teleoperator Hand Design Issues", Proc. IEEE Int. Conf. on Robotics and Automation, pp. 1924-1928, 1987.

5. Tournassoud, P., Lozano-Perez, T. and Mazer, E., "Regrasping", Proc. IEEE Int. Conf. on Robotics and Automation, pp. 1355-1360, 1986.

6. Craig, J.J. and Raibert, M., "A Systematic Method for Hybrid Position/Force Control of a Manipulator", Proc. IEEE Comp. Software Applications Conference, 1979.

7. Cutcosky, M.R., "Robotic Grasping and Fine Manipulation", Kluwer Publishers, 1985.

8. Van der Loos, H. F. M., "Design of a Three-fingered Robotic Gripper", The Industrial Robot, International Fluidic Services, Bedford, England, Vol. 5, No. 4, pp. 179-183, Dec. 1978.

9. Chen, F. Y., "Gripping Mechanism for Industrial Robots - An Overview", Mechanism and Machine Theory, Vol. 17, No. 5, pp. 299-311, 1982.

10. Analysis of Large Space Structure Assembly, Essex Corporation. Huntsville, Alabama.

11. Preliminary Program Plan for the Space Station Flight Telerobotic Servicer Program, Prepared by Goddard Space Fight Center for the Office of NASA Headquarters, Washington, D.C., p. 6, 1987.

12. Nevins, J.L., "Exploratory Research in Industrial Modular Assembly", R-800, Charles Starks Draper Laboratory, Inc; March 1974.

ELECTRODE EROSION IN LOW POWER ARCJET THRUSTERS*

A. Ghosh and P. Ray
School of Engineering and Architecture
Tuskegee University, AL

ABSTRACT

Low power arcjet thrusters (0.5 to 3kW) are currently being considered for North-South station keeping of geosynchronous communications satellites. The erosion mechanisms of cathodes in these thrusters are not well understood. The experimental set-up to produce a steady state electric arc in a gas flow is described and some preliminary theoretical results on cathode erosion are presented.

*Work supported by NASA Grant NAG3-726

ELECTRODE EROSION IN LOW POWER ARCJET THRUSTERS

Introduction

The power available for auxiliary propulsion on communications satellites currently ranges from 0.5 to 3kW. Low-power arcjet thrusters are being developed for North-South station keeping of these satellites. These devices convert electrical energy to thermal energy by heat transfer from an arc discharge to a propellant gas and subsequently from thermal energy to directed kinetic energy by expanding the gas through a nozzle. Arcjet thrusters offer more than 50 percent increase in specific impulse over state-of-the-art auxiliary propulsion [1]. Significant mass savings can thus be achieved for these spacecrafts using auxiliary propulsion.

Extensive work has been done in the last few years in understanding the interaction between various parameters of the low-power constricted arcjet thrusters [2-4]. This has resulted in significant advances in the performance of these devices. A 1000-hr life test (500 cycles of 2-hr duration) at a specific impulse of about 450 sec and about 1.2kW power level was recently successfully completed [5].

It was observed from this test that a burn-in period spanning over several cycles existed before a stable and consistent thruster operation was obtained. The burn-in period was characterized by voltage excursions, some of which were rapid while others were step changes. A rapid increase in steady state arc voltage was observed during the burn-in period, indicating rapid cathode tip recession.

To maintain the arc, the cathode emits electrons through an extremely complex process which makes it one of the key components in the arcjet thruster. One result of an arc discharge is the loss of cathode material ejected in the form of vapor jets at high velocities. The arc termination at the cathode is characterized by the formation of molten areas called spots, which can be highly mobile. It is presumed that the voltage fluctuations observed during the burn-in period are caused by the motion of the arc spot at the cathode tip. The objective of this research is to understand the mechanisms of cathode erosion in the low-power constricted arcjet thrusters by using both experimental techniques and theoretical analysis.

Experimental Setup

An experimental assembly to generate an open dc arc has been fabricated. The arc is established in an argon environment at or below one atmosphere pressure. Initial studies have been made to gain an understanding of the arc ignition and maintenance processes and to get preliminary information on electrode erosion. A schematic drawing of the experimental system is shown in Fig. 1.

The cathodes used are 3.2 mm diameter, 2 percent thoriated tungsten rods ground to a 30° half angle tip. For preliminary arc characteristic studies and mass loss information, the anode inserts used are finely polished bolt heads made of various materials such as low carbon steel, aluminum, brass and titanium. Cathode and anode holders are designed in a way so that the electrode inserts can be replaced quickly.

The cathode is put inside a brass electrode holder and held in place by a brass screw clamp. The brass electrode holder is made to thread into the copper cooling jacket. The cathode tip would typically extend about 2 cm from the brass holder.

The anodes are threaded directly into the copper cooling jacket. The inlet and outlet connections to the cooling water jackets are fitted with thermocouples to monitor temperatures of water circulated through the electrode assemblies.

The distance between the cathode and the anode can be set precisely by the use of a micrometer head. The rotation of the micrometer spindle is translated into a linear motion of the cathode assembly, thereby adjusting the gap width to the desired value. The gap width generally ranges from 1 to 5 mm.

A current-controlled, voltage-regulated dc power source (Sorenson Power Supply) with a maximum capacity of 18 A at 600 V is used to provide the power. Initial testing has been done in the range of 5 to 15 A arc current.

The test chamber which contains the arc is a pyrex cross. To start the arc ignition process, vacuum is first obtained by the use of a roughing pump. Argon is then forced into the pyrex test chamber to increase the pressure to the desired level.

The arc is started at about 200 V by separating the electrode contacts. After the arc is initiated, the voltage across the arc drops to approximately 40 V. For the ballast resistance, a set of 1 kW, 1 ohm resistors are used. The resistors could easily be added to or removed from the system. It was found that a combination producing 2 ohm of resistance provided adequate stability to the arc.

The measured voltage-current characteristics confirm the observed trend that the arc voltage decreases as the current increases. The arc voltage also tends to increase as the distance between the electrodes increases. The mass loss is observed to range from 1 to 40 μ g/C depending on the material and the arc power level.

Theoretical Analysis

A preliminary theoretical parametric study of the cathode processes of a low-current electric arc was done. The independent parameters were the cathode fall potential, work function of the electrode material, atomic mass of the electrode material and thermal conductivity. The dependent variables were the electron current density, the ion current density at cathode spot, the ratio of ion current to total current, the electric field in the cathode fall region and the temperature of the cathode spot.

The cathode temperature was found to be related to the cathode spot radius, a, the heat flux, Q, and the thermal conductivity, K. It is given by the relationship:

$$T_c = a.Q/K. \qquad (1)$$

The heat flux was related to ion current density, J_i; cathode fall potential, U_c, and work function, φ, by

$$Q = J_i . (U_c - \varphi) . \qquad (2)$$

The cathode spot radius can be written as a function of arc current, I, and arc density, J.

$$a = (I/\pi J)^{1/2}. \tag{3}$$

Defining $\nu = J_i/J$, one gets

$$a = (I\nu/\pi J_i)^{1/2}. \tag{4}$$

Hence,

$$T_c = (I\nu J_i)^{1/2}.(U_c - \varphi)/(\pi^{1/2} K). \tag{5}$$

The erosion of the cathode can be calculated by assuming that the ion bombardment raises the temperature of the cathode spot beyond the melting point of the cathode material. The cathode mass removal rate, m, is given by

$$m = \nu (U_c - \varphi)/[(L + C_s (T_s - T_r) + C_l (T_c - T_s)] \tag{6}$$

where L is the latent heat of fusion of the cahtode material, C_s and C_l are the specific heats of cathode in solid and liquid state respectively, T_r is the room temperature and T_s is the melting point of the cathode material.

Discussion

An experimental assembly to generate an open arc in an argon environment has been fabricated and is operating satisfactorily. In the next phase of this research, we plan to incorporate an arcjet thruster into this assembly and study the cathode spots through the use of optical spectroscopy, high speed photographic techniques and scanning electron microscopy.

From the theoretical analysis it was found that the ion current density plays a crucial role in determining the cathode spot temperature and cathode spot size. For an ion current density ranging from 1×10^9 A/m^2 to 1×10^{10} A/m^2, the cathode spot temperature varies between 2000°K to 6000°K. The cathode spot size varies between 4μm to 150μm for the given range of ion current density. The rate of cathode erosion is dependent on the cathode spot temperature as well as on the melting point of the cathode material. The erosion rates are in the range of tens of micrograms per coulomb and these values correspond well to the erosion rates that have been observed with electric arcs.

References

1. Stone, J.R., "Recent Advances in Low Thrust Propulsion Technology", Paper No. AIAA-88-3283. (1988).

2. Hardy, T.L.; Curran, F.M., "Low Power dc Arcjet Operation with Hydrogen/Nitrogen/Ammonia Mixtures", Paper No. AIAA-87-1948. (1987).

3. Haag, T.W.; Curran, F.M., "Arcjet Starting Reliability: A Multistart Test on Hydrogen/ Nitrogen Mixtures", Paper No. AIAA-87-1061, (1987).

4. Curran, F.M.; Haag, T.W., "Arcjet Component Conditions Through a Multistart Test", Paper No. AIAA-87-1060, (1987).

5. Curran, F.M.; Haag, T.W., "An Extended Life and Performance Test of a Low Power Arcjet", Paper No. AIAA-88-3106, (1988).

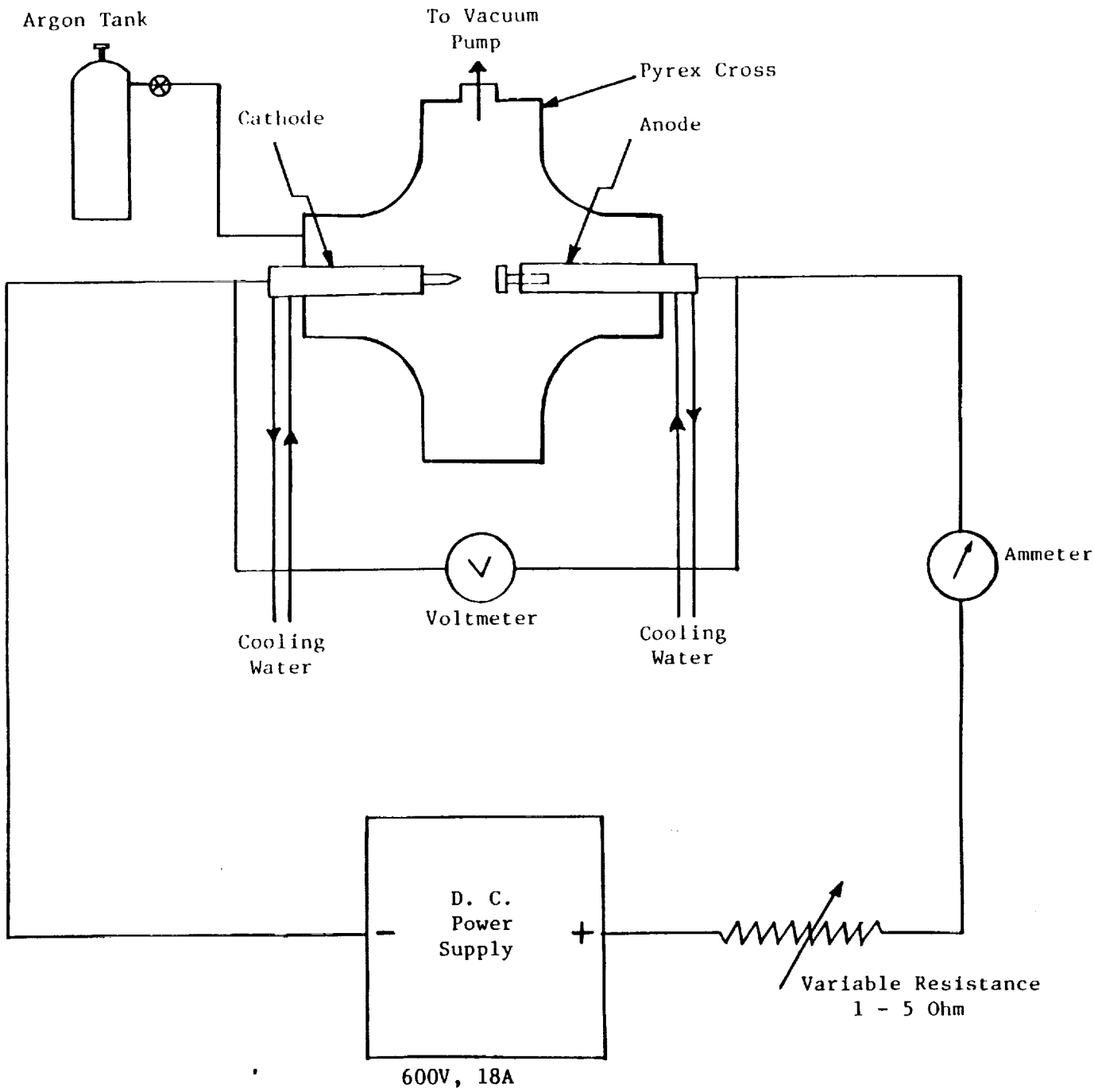

Figure 1. Schematic drawing of the arc discharge experimental system.

EVALUATION OF ON-BOARD HYDROGEN STORAGE METHODS FOR HYPERSONIC VEHICLES

A. Akyurtlu, J.F. Akyurtlu, A.A. Adeyiga, and S. Perdue
Department of Engineering
Hampton University
Hampton, Virginia

and

G.B. Northam
NASA/Langley Research Center
Hampton, Virginia

ABSTRACT

Hydrogen is the foremost candidate as a fuel for use in high speed transport. Since any aircraft moving at hypersonic speeds must have a very slender body, means of decreasing the storage volume requirements below that for liquid hydrogen are needed. The total performance of the hypersonic plane needs to be considered for the evaluation of candidate fuel and storage systems.

To accomplish this, a simple model for the performance of a hypersonic plane follows. To allow for the use of different engines and fuels during different phases of flight, the total trajectory is divided into three phases: subsonic-supersonic, hypersonic and rocket propulsion phase. The fuel fraction for the first phase is found by a simple energy balance using an average thrust to drag ratio for this phase. The hypersonic flight phase is investigated in more detail by taking small altitude increments and calculating the thrust, drag, fuel fraction and the effective specific impulse of each increment. This approach allowed the use of flight profiles other than the constant dynamic pressure flight. The effect of fuel volume on drag, structural mass and tankage mass was introduced through simplified equations involving the characteristic dimension of the plane. The propellant requirement for the last phase is found by employing the basic rocket equations.

The candidate fuel systems such as the cryogenic fuel combinations and solid and liquid endothermic hydrogen generators are first screened thermodynamically with respect to their energy densities and cooling capacities and then evaluated using the above model.

EVALUATION OF ON-BOARD HYDROGEN STORAGE METHODS FOR HYPERSONIC VEHICLES

Introduction

Hydrogen is the foremost candidate as a fuel for use in high-speed transport. The National Aerospace Plane program has been recently initiated by NASA and the Department of Defense (DOD) for developing hypersonic/trans-atmospheric vehicles for takeoff from conventional airport runways to orbit, or for rapid, long-distance, intercontinental aerospace transportation. For this purpose, air-breathing hydrogen-fueled supersonic combustion ramjet (scramjet) engines are being developed for speeds of Mach 5 to 25.

The main difficulty encountered in the use of hydrogen as a high-speed aircraft fuel is the space requirement for its on-board storage. If hydrogen is stored as a liquid, it requires about four times the volume to produce the same amount of energy as conventional fuels. This is especially important for supersonic and hypersonic aircraft which need to have slender designs.

The main aim of the present study is to identify and evaluate the storage media capable of increasing the hydrogen storage density (mass of hydrogen stored per unit storage volume) to a level higher than that of liquid hydrogen (approximately 70 kg/m^3 of hydrogen).

Evaluation Criteria

During hypersonic flight, besides providing propulsion, the fuel has to contribute to structural and engine cooling. In addition, combustibles other than hydrogen in the storage system may serve as rocket fuel in space flight or may be burnt to provide power for the aircraft subsystems. Therefore, the hydrogen storage density, and the heats of combustion of hydrogen and other combustibles in the storage system are important parameters for the evaluation of possible storage systems.

It should be realized that for any improvement in hydrogen storage density a certain penalty has to be paid in terms of increased gross lift-off mass, decreased specific impulse, or increased cost and complexity of tankage, fuel feed systems and technology development. These effects depend on, among others, the flight trajectory, whether the plane will be designed as a launch vehicle or as a hypersonic transport plane, the structural design of the plane, the types of engines to be used, and the switchover Mach numbers for the engines. Only the first two of these effects are considered in the present evaluation. To account for them, differences in the effective specific impulses and the payload capacities are taken to be the additional evaluation criteria.

Since actual design and flight data for the National Aerospace Plane (NASP) do not exist, a need for a mathematical model for the purpose of evaluating the effective specific impulses and payload capacities, especially in the hypersonic range, was strongly felt.

As a result, in order to provide a tool for the comparison of different fuel storage systems, a very simplified model was written for the SSTO flight of the NASP.

Since the main aim is not to obtain a quantitative description of the performance of a hypersonic vehicle but only to compare the performances of two vehicles with different fuel storage systems, no attempt was made to evaluate various structural and flight parameters. Instead, these were left as adjustable parameters. Initially, only the hypersonic segment of the flight trajectory was considered[1].

Simplifying assumptions such as isentropic compression, constant pressure combustion and isentropic expansion to ambient pressure were used in the evaluation of the engine performance. At this step, engine geometry was assumed not to change with the type of fuel or storage system. Thrust-to-drag ratio for a baseline liquid hydrogen plane was left as an adjustable parameter. The required fuel fraction was calculated using the simplified analysis of Jones and Donaldson[2].

The thrust structure mass, thermal protection mass, fuel tankage mass, engine mass and drag for the vehicle were expressed in terms of a characteristic dimension which was iteratively calculated from the specified mean thrust to drag ratio. Conditions at the combustion chamber exit were obtained by interfacing with the NASA/Lewis Chemical Equilibrium Program CEC. Isentropic frozen expansion to ambient pressure was assumed after complete, constant pressure combustion.

Preliminary Results

Percent changes in the payload capacity and the effective specific impulse with respect to the cryogenic LH2 vehicle were computed to aid in the comparison of different fuel systems. The results indicated that if liquid methane is used as fuel, it would result in a 22% less payload capacity and 10% lower effective specific impulse. But, if a mixture of 83% hydrogen and 17% by mass methane is used, the corresponding reductions in payload capacity and effective specific impulse were 3% and 0.7%, respectively. A sample endothermic fuel, cyclohexane, was also tested. If only the hydrogen extracted from cyclohexane is used as fuel negative payloads are obtained. On the other hand, the effective specific impulse increased by 7% due to decreased drag. This indicated that unless the benzene obtained after the extraction of hydrogen from cyclohexane is used as fuel for a later stage of flight, it will not be possible to use cyclohexane as a hydrogen storage medium.

Modified Model

The preliminary results indicated that in order to be able to evaluate complex fuel systems the model should be modified to enable the use of different fuels for different stages of flight. Furthermore, there is a strong indication that the air-breathing propulsion will not be sustained up to orbital velocities and the last stage of flight will be rocket propelled.

The outcome of the considerations is the second generation model. Its information flow diagram is shown in Appendix A.

In this model the total SSTO flight is considered in three stages: (1) subsonic-supersonic AB propulsion; (2) hypersonic AB propulsion; and (3) rocket propulsion. The hypersonic AB phase is further divided into small segments for which a different dynamic pressure and climb angle can be specified. Thus, for this phase a specified flight profile can be approximated.

For the subsonic-supersonic AB propulsion phase, an average thrust-to-drag ratio is specified and the initial to final mass ratio for this phase is calculated using Jones and Donaldson's analysis.

A more detailed analysis is performed for the hypersonic AB propulsion phase in order to obtain an effective specific impulse profile. At the engine inlet, isentropic compression is assumed. Chemical equilibrium conditions for a complete, constant pressure combustion is obtained by calling relevant subroutines of the NASA/Lewis Chemical Equilibrium program (CEC). Exit velocities are then calculated assuming isentropic, frozen expansion to ambient pressure. Engine inlet size is fixed by specifying an initial thrust-to-drag ratio for hypersonic flight and assumed not to change. The thrust structure mass and the engine mass is taken to be proportional to the gross lift-off mass of the vehicle. Thermal protection mass and the mass of propellant tanks are expressed in terms of a characteristic dimension of the vehicle following Dorrington's approach.[3] Equipment mass is assumed to be independent of flight and vehicle characteristics. Total drag is assumed to depend on the square of the characteristic dimension which is in turn a function of the total propellant volume. The mass ratio for each segment is calculated using a modified version of Jones and Donaldson's analysis[2], and therefore requires information on thrust-to-drag ratio. For this reason, the characteristic length is found by an iterative procedure in which the propellant volume is estimated; characteristic length, drag and total propellant mass is calculated and a new propellant volume is obtained.

During the rocket phase extending up to orbital velocity, it is assumed that the specific impulse is constant at 455 seconds and any variation is accommodated in the velocity losses.

Conclusion

A modified computer model is obtained to evaluate relative performances of hypersonic vehicles with different fuel systems.

The candidate fuel systems such as the cryogenic fuel combinations, gelled fuels, and solid and liquid endothermic hydrogen generators were screened thermodynamically with respect to their energy densities and cooling capacities. Some sample results are presented in Appendix A. These systems will be evaluated using the new computer model with respect to their relative payload capacities and effective specific impulses with the possibility of integration of air-breathing and rocket phase propellants. The critical issue is the availability of data on the NASP and the various propulsion systems, especially on the new integrated engines in various stages of development. For example, cryogenic fuels may start the air-breathing propulsion with LACE engines (or its derivatives) while endothermic hydrogen generators will probably employ engines with some type of turbine propulsion. Also, combustion of certain fuels in some engine types may not be technically feasible. Integration of the cooling duty to propulsion requirements should be the topic of further study.

Bibliography

1. Akyurtlu, A.; Akyurtlu, J.F.; Adeyiga, A.A.: "Evaluation of On-Board Storage Methods for High Speed Aircraft," First Annual Report on the project NAG-1-767 submitted to NASA Langley Research Center, January 29, 1988.

2. Jones, R.A. and Donaldson, C. duP: Aerospace America 25(8), 32-34, 1987.

3. Dorrington, G.E.: "Optimum Combined-Cycle Propulsion Systems for Earth-to-Orbit Transportation," paper presented at Joint Propulsion Conference, Boston, July 11-13, 1988.

Nomenclature

AFR	Air flow rate for the vehicle with candidate fuel system
AFRH	Air flow rate for LH2 vehicle
AIN	Engine inlet area for the vehicle with candidate fuel system
AINH	Engine inlet area for LH2 vehicle
C	Drag coefficient for the planes (a function of TETA only)
CR	Air inlet compression ratio
DV	Velocity increment for rocket propulsion phase
DZ	Altitude increment
E2,E1	Final and initial total energies for a flight segment defined by E = V2/2 + gZ
EP	Propulsion efficiency
ERP	Error criterion for the convergence of propellant volume calculations
F	Air to fuel mass ratio for the vehicle with the candidate fuel
FD	Drag for the vehicle with the candidate fuel system
FDH	Drag for the LH2 vehicle
FH	Air to fuel mass ratio for the LH2 vehicle
FT	Thrust of the vehicle with the candidate fuel system
FTH	Thrust of the LH2 vehicle
IEFF	Effective specific impulse for the vehicle with the candidate fuel system
IEFFH	Effective specific impulse for the LH2 vehicle
IFH	Fuel specific impulse for the LH2 vehicle
IFS	Fuel specific impulse for the vehicle with the candidate fuel system
ISR	Specific impulse for the rocket propulsion phase
L	Characteristic length of the vehicle
M	Mach number
MA	Switchover Mach numbers
MCI	Mach number at the combustion chamber inlet
MD	Dry mass of the vehicle
ME	Engine mass
MF	Vehicle mass with the candidate fuel system
MFH	LH2 vehicle mass
MFT	Thrust structure mass
MPF	Payload mass of the vehicle with candidate fuel system
MPH	Payload mass of the LH2 vehicle
MR	Final to initial mass ratio of the vehicle with the candidate fuel system, for a specific flight segment

MRH	Final to initial mass ratio of the LH2 vehicle for a specific flight segment
MRR	Final to initial mass ratio for rocket propulsion phase
MSS	Equipment mass
MTNK	Propellant tank mass
MTOT	Gross lift-off mass
MTPS	Thermal protection mass
P	Pressure
PCI	Combustion chamber pressure
Q	Dynamic pressure
QF	Heat of combustion of propellant
RHO	Density
RHOF	Density of the candidate fuel for hypersonic AB propulsion
RHOF1	Density of the fuel for subsonic-supersonic AB propulsion
T	Temperature
TCI	Temperature at combustion chamber inlet
TDR	Thrust to drag ratio
TDRM	Mean thrust to drag ratio
TETA	Climb angle
V	Velocity
VE	Exit velocity
VORB	Orbital velocity
VPF	Propellant volume for the vehicle with the candidate fuel system
VPFAB	Propellant volume for AB propulsion
VPH	Propellant volume for the LH2 vehicle
VPRO	Rocket phase oxidant volume
Z	Altitude

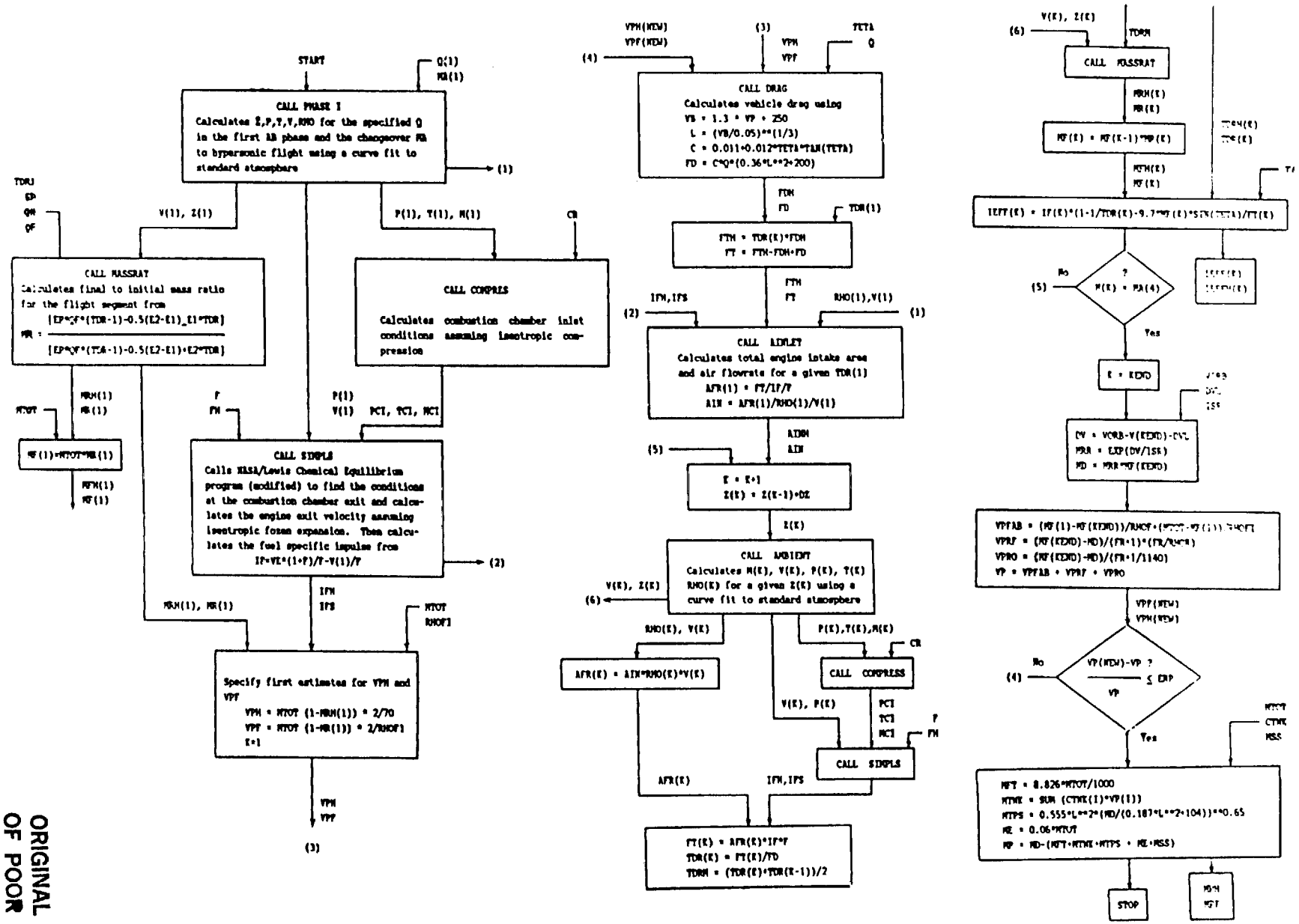

Appendix A

Information Flow Diagram of the Computer Program for the Evaluation of the Performance of Hypersonic Vehicles.

END-EFFECTOR - JOINT CONJUGATES FOR ROBOTIC ASSEMBLY OF LARGE TRUSS STRUCTURES IN SPACE: A SECOND GENERATION

William V. Brewer
School of Science and Technology
Jackson State University
Jackson, MS

in association with

Langley Research Center
Hampton, VA

ABSTRACT

Attachment of strut to node can be accomplished with a variety of mechanisms: references [1,2,3,4]. All require extensive standoff elements (called scars) added to the nodes. These increase packaging volume for the nodes by as much as 300%. First generation designs also tend to be either heavy or expensive due to complex parts. This investigation focuses on screw thread mechanisms as the simplest and most easily manufactured of alternatives. Torque and rotational motion must be transmitted across the strut to end-effector interface accomplishing the joining process and establishing a specified preload. Four drive mechanisms are considered: worm, helical, bevel, and differential gears. All are developed with the following criteria in mind.

1. Preload: 250 to 500 lbs.

2. Envelopes: 1.0" strut; 2.5" node (reduce violation of specified diameters to a minimum)

3. Cost Reduction: reduce part complexity, diversity and count; increase "off the shelf" part fraction

4. Feedback mechanisms: incorporate in strut design

END-EFFECTOR - JOINT CONJUGATES FOR ROBOTIC ASSEMBLY OF LARGE TRUSS STRUCTURES IN SPACE: A SECOND GENERATION

Introduction

Current designs, a first generation intended for robotic assembly, have given priority to the ease and certainty of the assembly process under less than ideal conditions with a minimum of sensory feedback. As a consequence they are either heavy or expensive and all exhibit a relatively low packaging density. Low packaging density is caused by extensive "scars" applied to the node, increasing its envelope diameter by as much as 150% . Strut envelopes are violated to a lessEr extent with diameters increased by 25% or more. This smaller percentage is still a significant problem owing to a much higher fraction of the packaged volume represented by struts. As structures in space become larger, packaging density becomes an important consideration.

Objectives

Develop end-effector - joint conjugates that do not violate the envelopes of a 2.5" diameter node or a 1.0" diameter strut.

Reduce cost by:

increasing the fraction of "off the shelf" parts;
reducing part complexity, diversity and count.

Incorporate feedback mechanisms as an integral part of the overall scheme.

Discussion

Attachment of strut to node can be accomplished with a variety of mechanisms: references [1, 2, 3, 4]. All require extensive scars or standoff elements added to the node. These permit compliance when a strut must be fitted between nodes whose separation distance is either greater or smaller than the length. Two methods that do not require standoffs are the screw thread and conical wedge (concrete anchor) [5]. They allow the node separation distance to be too great, but depend on distortion of the truss in the case when the distance is too small. The present effort is designed around the screwthread as the simplest and most easily manufactured of all alternatives.

Torque and rotational motion must be transmitted across the strut to end-effector interface accomplishing the joining process and establishing the requisite 250 to 500 lb. preload. Four drive mechanisms were considered: worm gear, helical gear, bevel gear and differential gear. A strut-end design based on the differential gear was developed because it is the most compatible with the drive mechanism used on a first generation end-effector currently under fabrication. Torque capacities of available differential gears that would fit within the 1" envelope could not overcome friction in the screw-threads generated by the requisite 250 lb. preload. Helical gears provide a much better basics for achieving the objectives of a 2nd generation based on screwthread assembly. Part complexity, count and cost are all reduced. Attaching a left-hand helical gear to the bolt shaft so that it "travels" with the bolt has an additional advantage: axial thrust will always assist in driving the bolt in the desired direction.

The traveling helical assembly (Fig. 1) was integrated into a strut-end design (Fig. 2) that incorporates features which assist in the assembly process.

Capture of the node by a robotically manipulated strut-end can be assisted by active feedback mechanisms, parts of which are embedded in the strut-end (Fig. 3) or by passive spring loading devices (Fig. 4) without feedback. Active feedback is interfaced with the end-effector by means of a probe inserted thru a slot in the strut envelope and into a receptacle drilled in a non-rotating axial "traveler". This probe can assist in axial translation of the bolt as well as in reading its location and the axial force applied to it.

References

[1] Gralewski, M., "Development of Joint Connector Model and Associated End Effector Concept for Automated Assembly of Large Space Truss Structures", Contract No. NASI-17536, Doc. No. 36230-114, Astro Aerospace, Carpenteria, CA 93013-2993, 2/29/88

[2] Final Report, "... same as title above ...", Response to AS&M RFP 18235-39-092887, Honeybee Robotics, New York, NY 10002, 1988

[3] Everman, M. R.,"Final Report on the ASMI End Effector", AECR88336/429, Able Engineering Company, Goleta CA 93116-0588, 3/11/88

[4] Stout, D. A., "Joint Connector Concept", D-300-01-001, Jewett Automation, 2/8/88

[5] Wesselski, C. J.,"Space Station Lock Joint", Div/Off ES22, Johnson Space Center, Houston, TX

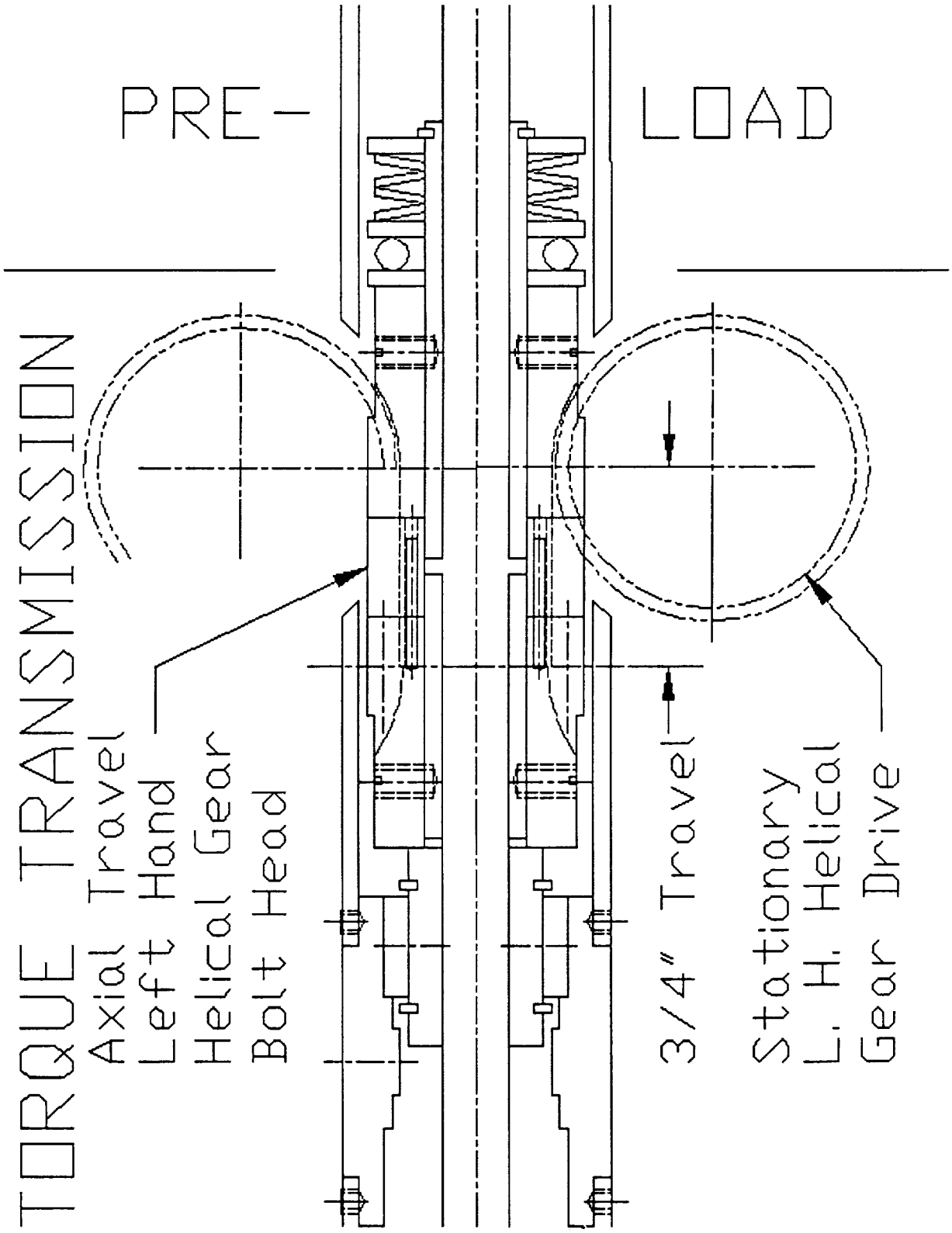
TORQUE TRANSMISSION
Axial Travel
Left Hand
Helical Gear
Bolt Head
PRE-
LOAD
3/4" Travel
Stationary
L. H. Helical
Gear Drive

Figure 1.

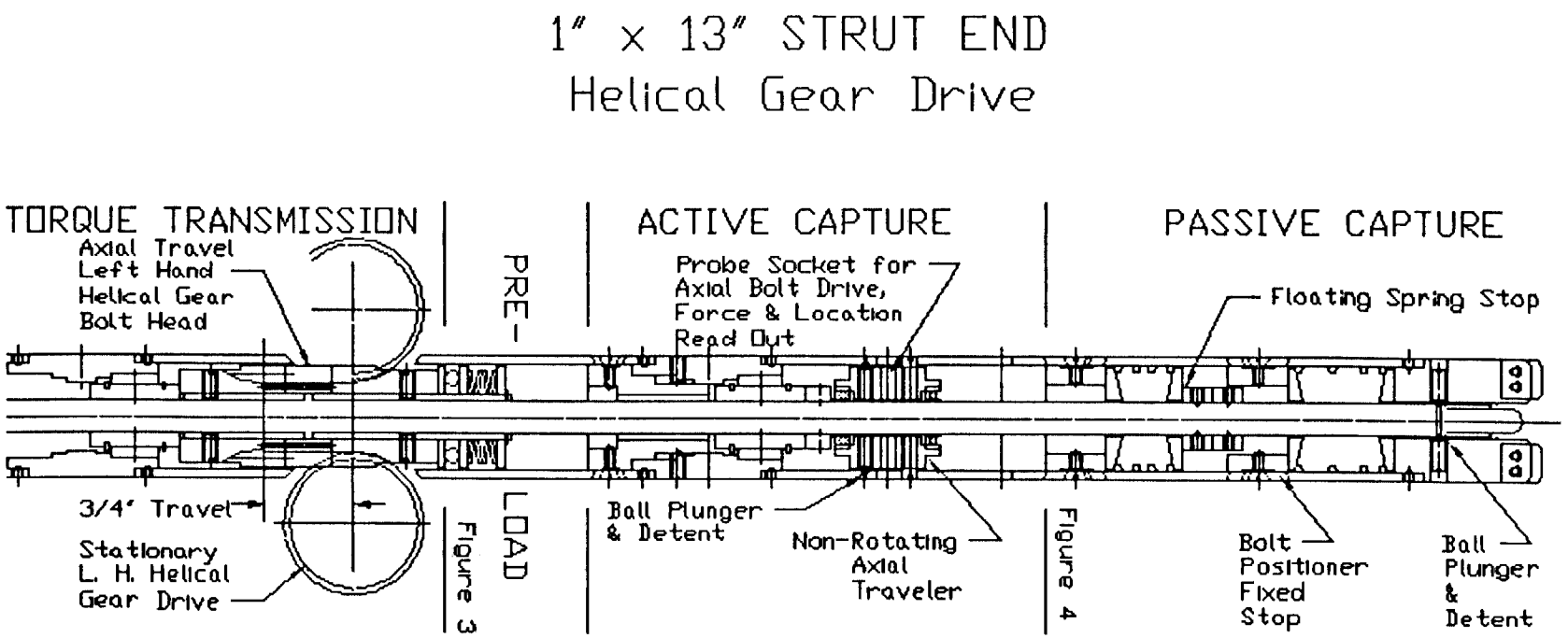
1" x 13" STRUT END
Helical Gear Drive
TORQUE TRANSMISSION
Axial Travel
Left Hand
Helical Gear
Bolt Head
3/4" Travel
Stationary
L. H. Helical
Gear Drive
PRE-
LOAD
Figure 3
ACTIVE CAPTURE
Probe Socket for
Axial Bolt Drive,
Force & Location
Read Out
Ball Plunger
& Detent
Non-Rotating
Axial
Traveler
Figure 4
PASSIVE CAPTURE
Floating Spring Stop
Bolt
Positioner
Fixed
Stop
Ball
Plunger
&
Detent

Figure 2.

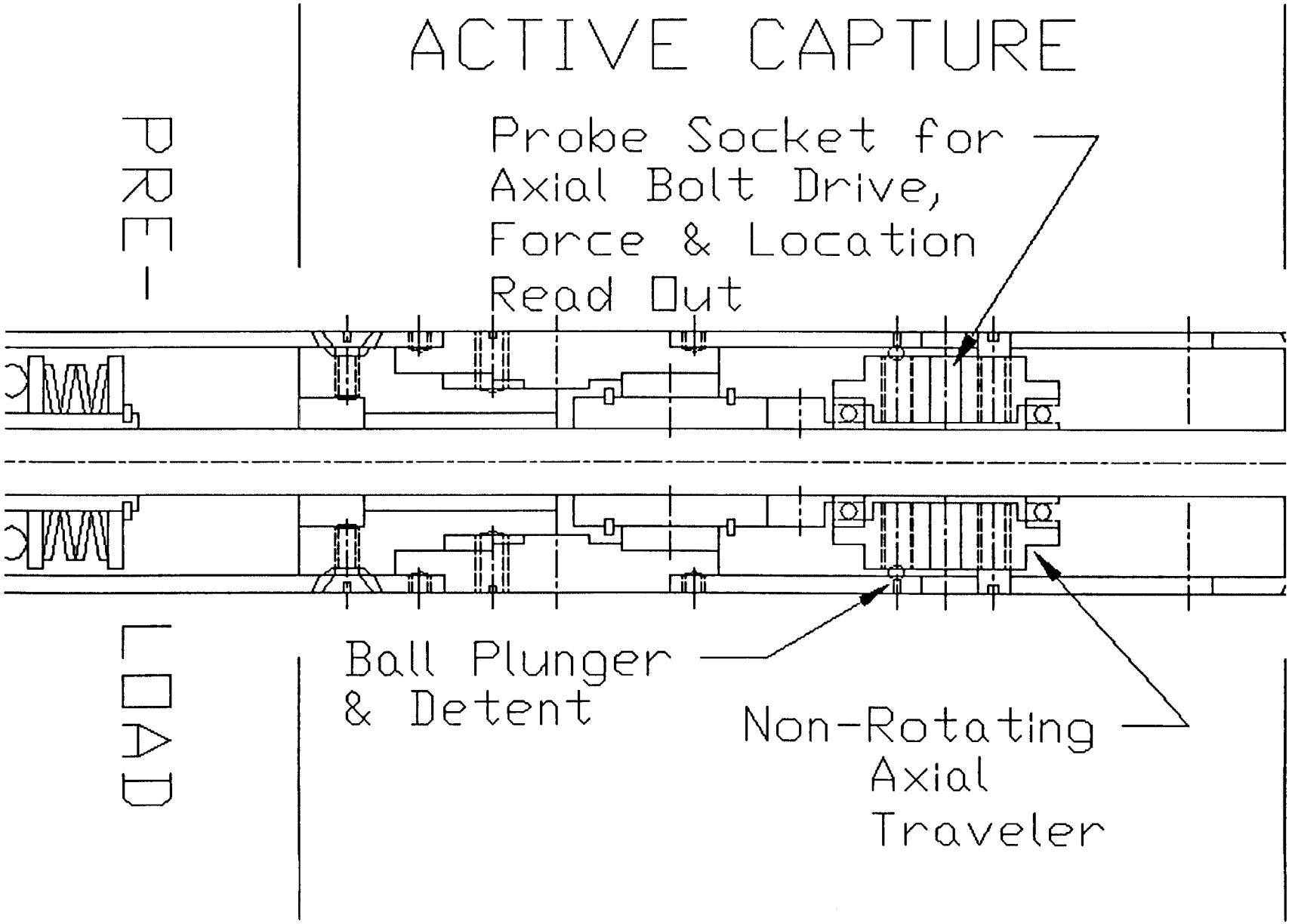
ACTIVE CAPTURE
PROBE
Probe Socket for
Axial Bolt Drive,
Force & Location
Read Out
LOAD
Ball Plunger
& Detent
Non-Rotating
Axial
Traveler

Figure 3.

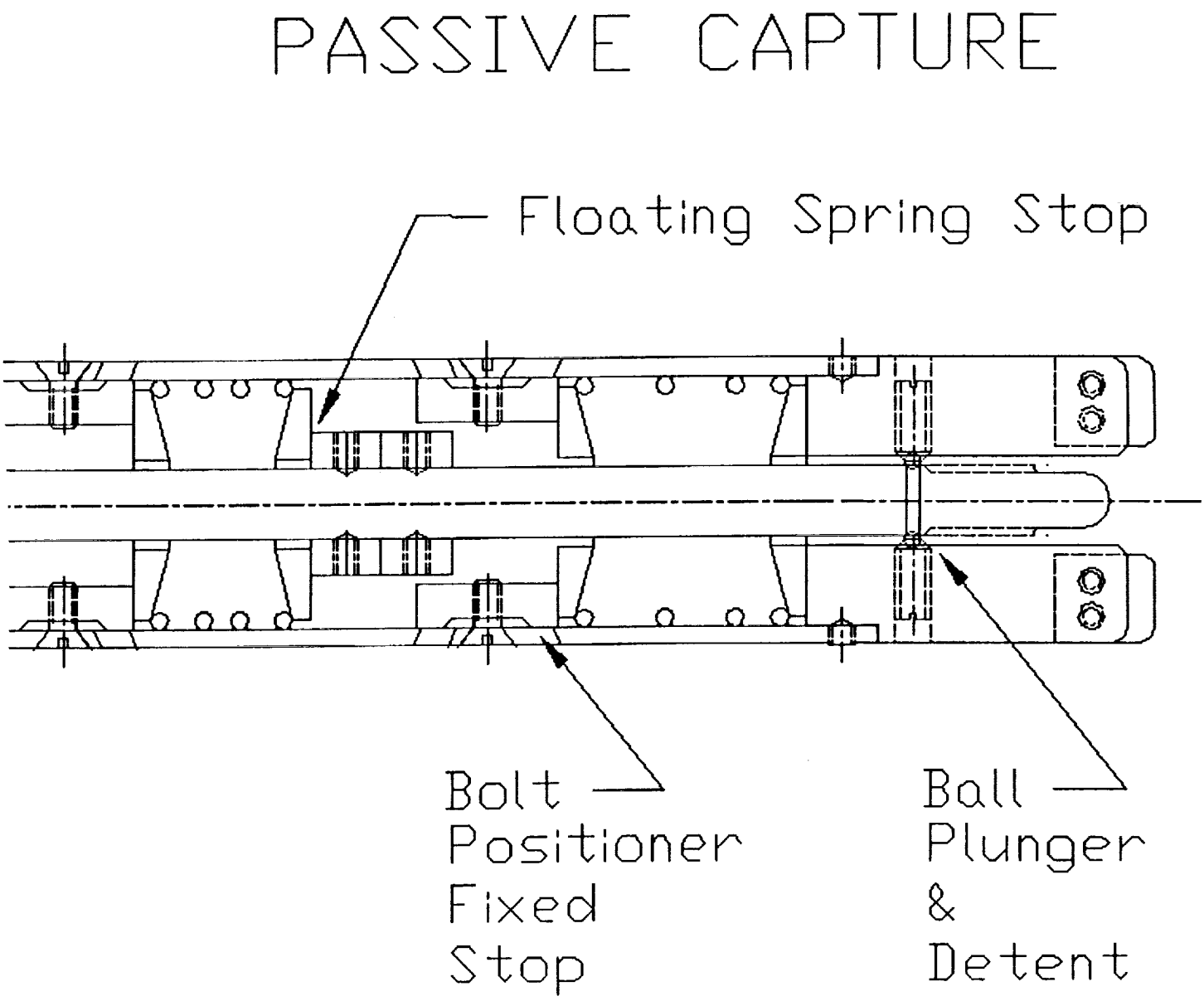
PASSIVE CAPTURE
Floating Spring Stop
Bolt
Positioner
Fixed
Stop
Ball
Plunger
&
Detent

Figure 4.

MARS SURFACE BASED FACTORY: PHASE II - TASK 1C COMPUTER CONTROL OF A WATER TREATMENT SYSTEM TO SUPPORT A SPACE COLONY ON MARS

Dr. John Fuller, Warsame Ali, and Danette Willis
Department of Electrical Engineering
Prairie View A&M University
Prairie View, Texas

ABSTRACT

In a continued effort to design a surface based factory on Mars for the production of oxygen and water, the Design Group at Prairie View A&M University made a preliminary study of the surface and atmospheric composition on Mars and determined the mass densities of the various gases in the Martian atmosphere. Based on the initial studies, the design group determined oxygen and water to be the two products that could be produced economically under the Martian conditions.

Studies were also made on present production techniques to obtain water and oxygen. Analyses were made to evaluate the current methods of production that were adaptable to the Martian conditions. The detailed report (Phase 1- Mars Surface-Based Factory: A Preliminary Design) was contained in an Interim Report submitted to NASA/USRA in August of 1986.

Even though the initial effort was the production of oxygen and water, we found it necessary to produce some diluted gases that can be mixed with the oxygen produced to constitute "breathable" air.

In Phase II - Task 1A, The Prairie View A&M University team completed the conceptual design of a breathable air manufacturing system, a means of drilling for underground water, and storage of water for future use. The design objective of the team for the 1987-88 academic year (Phase II-Task 1B), was the conceptual design of an integrated system for the supply of quality water for biological consumption, farming, residential and industrial use. The design has also been completed.

Phase II - Task 1C is the present (1988-89) task for the Prairie View Design Team. This is a continuation of the previous task.

The continuation of this effort is the investigation into the extraction of water from beneath the surface and an alternative method of extraction from ice formations on the surface of Mars if they are accessible.

In addition to investigation of water extraction, a system for computer control of extraction and treatment will be developed with emphasis on fully automated control with robotic repair and maintenance. It is expected that oxygen and water producing plants on Mars will be limited in the amount of human control that will be available to man large and/or isolated plants. Therefore, it is imperative that computers be integrated into plant operation with the capability to maintain life support systems and analyze and replace defective parts or systems with no human interface.

MARS SURFACE BASED FACTORY: PHASE II - TASK 1C COMPUTER CONTROL OF A WATER TREATMENT SYSTEM TO SUPPORT A SPACE COLONY ON MARS

Introduction

The Design Group at Prairie View A&M University is designing a computer control system for a water treatment plant to support a colony on Mars. The system is being developed with emphasis on fully automated control, robotic repair and maintenance. It is expected that the water producing plant on Mars will be limited in the amount of human control that will be available to man the plant. Therefore, it is imperative that computers be integrated into plant operation with the capability to maintain the water system and analyze and replace defective parts or systems with no or limited human interface.

Methods to extract water from beneath the surface of Mars are also being investigated. It is believed that water exists on Mars in polar ice deposits and in permafrost layers (ground ice). There is also evidence that water exists underneath the permafrost zone. The Prairie View Design Team is investigating ways of extracting and treating the water for human consumption and protein production. To carry out the described task, teams were formed to investigate problems, and design necessary equipment and implementation procedures for the four areas of drilling for water, plant control, computer interface and maintenance. Figure 1 shows the structure of the design team as developed for the 1988-89 academic year. The project will be completed in the summer of 1989. As this project continues, the focus will shift to the production of proteins for human consumption.

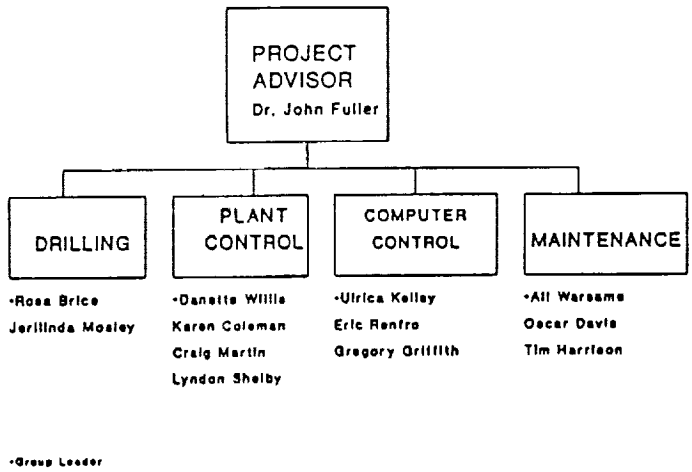

Figure 1

Drilling for Water

The success or failure of any attempt to colonize the planet Mars will largely depend on the availability of the most important life sustainer, water. Not only is water important for life but also any meaningful self-sustained technological advancement on Mars will be based on water as a process fluid. It is therefore imperative that every attempt be made to locate an adequate supply of water on Mars.

Mars is presently too cold to support oceans or any form of stable liquid water on its surface. The mean ambient temperature is -25 degrees Celsius. It is believed that there are ice deposits or permafrost beneath the surface of Mars. The thickness of the zone containing ground ice is about 10 to 30 cm. More water may exist underneath the permafrost zone.

In order to assess the amount of water on the planet other than by mere estimation, some form of drilling must be done.

The study of the composition of the Martian soil is very important in determining its drillability. A survey of the Martian soil has been conducted through the exploration by the Viking Landers. The soil is composed of different elements such as silicon, iron, phosphorus, calcium, aluminum, thallium, and sulfur. The debris analyzed by the Viking Landers showed silicon oxides in abundance of approximately 45 percent by weight.

One other important factor to consider in the design of the drilling unit is the drilling rate. The drilling rate is a function of several variables, the most important of which are the rock drillability, the weight on the bit and the extent of cleaning the hole. The effect of the weight on the bit is of great importance to our design since the gravity on Mars is substantially less than that on Earth.

The drilling process will involve boring a hole by using a rotating bit to which a downward force is applied. The bit is supported and rotated by a hollow stem composed of high-quality steel, through which a drilling fluid is circulated. The fluid leaves the stem at the bit, thereby cooling and lubricating the cutting structure. By flowing across the cutting surface, the drilling fluid drags cuttings from the hole stem annulus. This process will form the basis for the design of the drilling unit.

Plant Control and Computer Control

The integrated water treatment plant consists of several processes, such as a suspended solids removal unit, ultrafiltration unit, and reverse osmosis unit, which have parameters that need to be monitored or controlled. These parameters include flow rate, temperature, pressure, and conductivity. Therefore, devices such as sensors, transmitters, and control valves must be employed.

To facilitate the need of automated control, a personal computer would be used to maintain and run the entire water system. The electronic sensors, transmitters, and control valves along with analog to digital and digital to analog converters will communicate with the personal computer.

Through the use of one or more microprocessors, RS232 serial cables and/or fiber optics along with analog to digital converters, the above devices will be integrated with each other.

The purpose of the A/D and D/A converters will be to interpret the analog signals being sent from the sensors and convert them to digital signals to be analyzed by the computer. If an adjustment needs

to be made within a process, the computer will send a signal to a valve (actuator) to make the proper adjustment. The microprocessors that are being investigated are the Intel 8086, Motorola 68000 and the Z80.

Maintenance

The initial habitation of Mars will require machining and maintenance for space applications. Machining and maintenance on Mars is complicated due to the following factors: the absence of atmosphere, light is not diffused or scattered, the natural space environment consists of intensive light and dark periods, small number of persons, and the lack of machining parts. The factory communication network system will consist of an industrial microcomputer cell control, computer interface units, a robotic controller, vision, and a computer numerical control machine (CNC lathe).

Robotics for space applications have been proposed for increased productivity, improved reliability, increased flexibility, higher safety and for the performance of automating time consuming tasks. If a malfunction takes place within the system, it takes almost twenty minutes to receive a signal from Earth. This signal instructs the machine on how to recover from the fault. So, it is necessary to have an emergency plan that can start automatically right after the shutdown of the plant.

Vision/sensing is projected to include the fusion of multi-sensors ranging from microwave to optical with multi-mode capability to include measuring capability for position, attitude, recognition and motion parameters. [1]

The objective of using a CAD/CAM system on a CNC lathe machine is to produce machine parts on Mars, and it is planned to modernize the computer numerical control (CNC) lathe by developing a software system on a personal computer. The CAD/CAM system is able to take all the data from design programs and convert the information to numerical control (NC) programs which are used on the CNC lathe.

The design programs are written in Basic language on a personal computer. The CAD/CAM software system is developed in Fortran language. By using software packages the need of punched tape for the CNC lathe and blueprints of the design drawings are eliminated. As a result, the complete automation from design to manufacturing for the CNC lathe is achieved. The sample design program is shown in Figure 2, the sample of a manufactured work piece is shown in figure 3, its horizontal tool path cutting is shown in Figure 4, and its NC program is shown in Figure 5.

The computer graphics method using basic language to generate CNC program offers the following advantages:

1. It is safer. A problem, such as the cutting tool colliding with the chuck of an engine lathe, would provide a genuine hazard to a user trying out a CNC program. With the CAD/CAM program, the problem is eliminated.

2. It is economical. Besides saving all of the scrap work that would have been produced in the actual situation, CAD/CAM program allows the limited machine tools to be utilized.

3. It is psychologically more satisfying. The major advantage of using this CAD/CAM system is to generate a CNC program.

Recommendations for Future Research

The following are recommended areas for future development:

1. Develop the CAD/CAM software package of the CNC lathe for threading operation.

2. Comprehending all errors and malfunctions that can take place between the personal computer and the CNC lathe.

3. Testing the system by a set of design programs to produce mechanical parts.

4. Design a plant prototype with simulation of all system parameters.

5. Study the Martian moon, Phobos, as an alternate source of water.

6. Raise fish on the planet Mars for life support.

References

1. Kumar, Krishen; "Space Robotic Vision System Technology." International Conference and Exhibit, Houston, Tx. October 16-21, 1988.

2. Ali, Warsame; "Development of a CAD/CAM System on An EMCO-5 CNC Lathe", Master Thesis at Prairie View A&M University, December 1986.

3. EMCO-5 CNC Lathe Manual, 1986.

4. Haberle, Robert; "The Climate of Mars."


```
10  ' piece of iron ==============================
20 SCREEN 1,0 :CLS : KEY OFF : DEFINT A-Z
30 LINE (48,39)-(132,39),1
40 LINE (48,39)-(48,121),1
50 LINE (48,121)-(132,121),1
60 LINE (132,39)-(132,121),1
70 LINE (132,50)-(155,50),2
80 LINE (132,110)-(155,110),2
90 LINE (155,50)-(155,110),2
100 LINE (155,57)-(199,57),3
110 LINE (155,103)-(199,103),3
120 LINE (199,57)-(199,103),3
122 LINE (132,39)-(132,50),1
124 LINE (132,121)-(132,110),1
126 LINE (155,110)-(155,103),1
128 LINE (155,50)-(155,55),1
130 LET X1=48 : X2=199
140 LET Y=80
150 FOR I=X1 TO X2 STEP 21
160 LINE (I,Y)-(I+10,Y),1
170 LINE (I+15,Y)-(I+16,Y),2
180 NEXT I
190 END

Ok
```

Figure 2

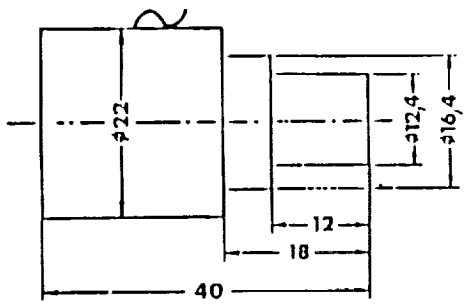

Figure 3

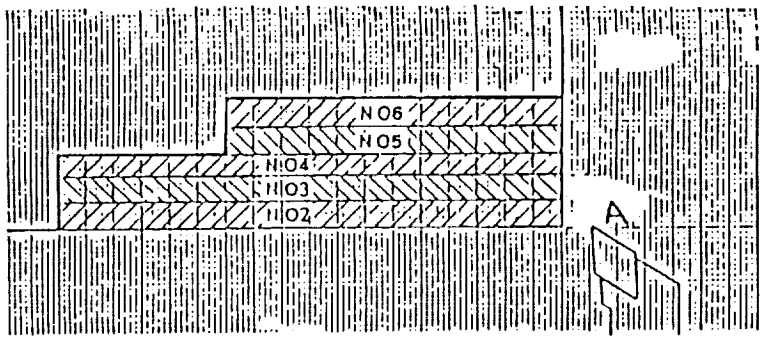

Figure 4

N	G	X (BLU)	Z (BLU)	F (mm/min)
00	00	-500		
01	01	00	-400	
02	04	-100	-1900	400
03	04	-200	-1900	400
04	04	-280	-1900	400
05	04	-380	-1300	400
06	04	-480	-1300	400
07	22			

BLU=0.01 mm

Figure 5

SERVOMOTOR-LINKED ARTICULATED VERSATILE END EFFECTOR (SLAVE^2)

Abayomi J. Ajayi-Majebi, William A. Grissom,
Brian Wingard and Derrick Walker

Manufacturing Engineering Department
Central State University
Wilberforce, Ohio

ABSTRACT

A strategy is presented for the design and construction of a large master/slave-controlled, five-finger robotic hand. Each of the five fingers will possess four independent axes each driven by a brushless DC servomotor and, thus, four degrees-of-freedom. It is proposed that commercially available components be utilized as much as possible to fabricate a working laboratory model of the device with an anticipated overall length of approximately three feet (0.9 m). The fingers are to be designed to accommodate proximity, tactile, or force/torque sensors imbedded in their structure. In order to provide for the simultaneous control of the twenty independent hand joints, a multilevel master/slave control strategy is proposed in which the operator wears a specially instrumented glove which produces control signals corresponding to the finger configurations and which is capable of conveying sensor feedback signals to the operator. Two dexterous hand master devices are currently commercially available for this application with both undergoing continuing development. A third approach to be investigated for the master control mode is the use of real-time image processing of a specially patterned master glove to provide the respective control signals for positioning the multiple finger joints.

SERVOMOTOR-LINKED ARTICULATED VERSATILE END EFFECTOR ($SLAVE^2$)

Design Objectives

Development is underway to design and construct a large, five-finger, anthropomorphic, master/slave-controlled, robotic hand. The envisioned device would be larger and more powerful than the human hand while possessing sufficient dexterity to closely mimic the fingering and grasping configurations of its human counterpart. Control signals would be generated by a master glove worn by the operator. The device has been assigned the acronym, $SLAVE^2$ for, "Servomotor-Linked Articulated Versatile End Effector," reflecting the planned master/slave control mode and the use of an individual electric servomotor to drive each joint.

Anticipated commercial applications include handling of hazardous wastes, munitions, or large radioactive or chemically contaminated objects. Fire fighting, construction, demolition, disaster clean-up, and rescue operations might provide additional applications for a large, dexterous end effector operated remotely under master/slave control.

A rapid prototype R&D strategy utilizing off-the-shelf components wherever possible is being employed for the development of the $SLAVE^2$ laboratory prototype. A key goal of the strategy is to minimize development time and costs by eliminating long lead times for design and construction of individual components. Thus, commercial availability of components, including the electric servomotors and power transmission mechanisms to drive the individual finger joints, will dictate size, weight, payload and finger length of the hand assembly. Based upon this consideration and current design estimates, it is anticipated that the initial working laboratory model will be approximately four-times human size with an overall hand length of approximately three feet (0.9 m) and an individual fingertip clamping force of 10-12 pounds (44 - 53 N). It is expected that the finger will have a typical length of about 18 inches (46 cm) and weigh approximately 15 pounds (6.8 kg). Initial estimates indicate that a frequency response of 0.5 Hz can be achieved.

Proposed Robotic Hand Design

Mechanical Configuration

A mechanical hand configuration possessing four fingers and a thumb is contemplated. Each of these five members will have four joints or degrees-of-freedom. More specifically, for each finger/thumb member three joints would provide flexion and extension (and possibly hyperextension) and a fourth joint would allow abduction and adduction. This would give the hand a total of twenty degrees of freedom and provide sufficient dexterity to closely replicate the gripping and fingering actions of a human hand.

The goal of the first year of the development effort currently underway is to develop a working laboratory prototype of a single four degree-of-freedom finger. Initial emphasis has been placed upon the selection of the most desirable mechanical configuration for the compound knuckle joint which must provide for both flexion/extension and abduction/adduction angular motions. In arriving at a

prototype design a number of different mechanical configurations were considered before selecting the arrangement shown in the sketch of Figure 1. This configuration features coincident flexion/extension and ab/adduction axes and provides for the drive motors for these two axes to be mounted on the stationary palm rather than on the moving finger.

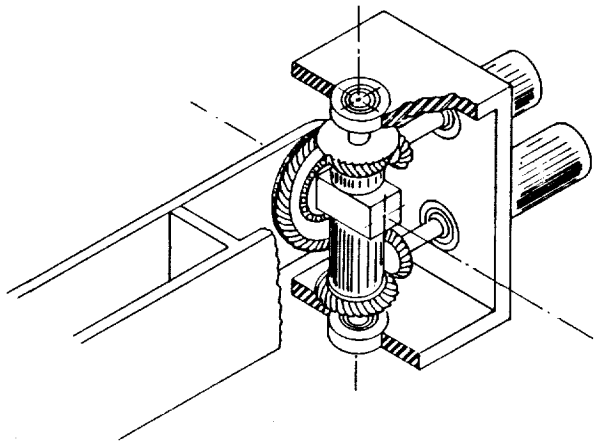

Figure 1 - Compound Axis Knuckle Joint Configuration

Drive Component Selection

The selection of the drive components to power the finger joints was governed by a desire to achieve optimum performance and compactness while utilizing commercially available components to the greatest extent possible. Thus, an attempt was made to balance the load capacity of the servomotors, gear reducers, and right angle drive units. In this regard, when evaluated on the basis of torque capacity-to-density (weight and compactness), the right angle drive units surprisingly proved to be the limiting factor in achieving greater payloads.

Servomotors

Each of the twenty joints is to be directly driven by an independent brushless DC servomotor and integrated speed reducing mechanism. Although practical brushless DC servomotors are a relatively recent development triggered by advances in solid state electronics and permanent magnet technology, units are now available from a number of major manufacturers. The selection of 24 volt DC brushless motors from the Inland Motor Division of Kollmorgen Corporation was based upon high torque-to-density ratios and the convenient operating voltage range. The brushless DC type of servomotor duplicates the external performance of a conventional DC motor without utilizing a commutator or brushes. This is possible because solid-state electronic switching replaces the conventional brush commutation switching process. A second major difference is that the wound member, or armature, reverses its role and relative position from rotor (rotating member) and inner component in the conventional DC motor, to stator (stationary member) and outer component in the brushless motor.

These two differences lead to a number of significant advantages from the brushless DC motor with respect to performance, safety and reliability [1,2]:

1. No brushes to wear out: increased reliability, reduced maintenance requirements.
2. No commutator bars to oxidize: ability to sit idle for years without loss of performance.
3. Absence of brush arcing: safer in the presence of fumes, dust, paint spray, etc.
4. Speeds up to 80,000 RPM are practical.
5. Less radio-frequency interference.
6. Easier cooling of windings with fins or cooling jacket: extended operating range.
7. Smaller diameter, more compact.
8. Reduced inertia: increased acceleration and improved control.

Power Transmission

Electric motors characteristically produce relatively low torque in the low speeds range. This is true as well for brushless DC motors, and preliminary calculations indicate that torque multiplication (or speed reduction) rates of about 100:1 will be required to achieve the desired robotic hand strength. To meet this requirement, the patented harmonic drive gearing device available from the Harmonic Drive Division of the Emhart Machinery Group, Wakefield, MA, has been identified.

The unique design of the harmonic drive with three simple concentric components yields the following advantages for robotics gear reduction applications:

1. Exceptionally high torque and power capability in a small package.
2. Essentially zero backlash.
3. Efficiencies as high as 90%.
4. Ratios as high as 320:1 in a single reduction with much higher ratios achieved by compound stages.
5. Concentric input and output shafts.
6. No radial loads since torque is generated by a pure couple; this simplifies the supporting structure requirements.
7. Resists back driving, providing a measure of braking.

Drawbacks of the harmonic drive are that it is relatively compliant exhibiting a soft windup characteristic in the low torque region, and that it produces a small, sinusoidal positional error on the output. This error varies inversely with the pitch diameter at a predominant frequency of twice the input speed. Additionally, an amplitude modulation typically occurs twice per output revolution.

A detailed explanation of the operating principles is given in the "Harmonic Drive Designers Handbook" [3] along with load and accuracy ratings, operating life expectancies and installation and servicing guidelines.

In view of the need to maintain a slender aspect ratio in the design of the finger configuration, it is necessary to utilize a right angle drive mechanism to provide torque about an axis perpendicular to the axis of the servomotor-harmonic drive assembly. For this purpose spiral bevel gears manufactured by the Arrow Gear Company of Downers Grove, Illinois, were selected. This type of gearing features efficient and smooth operation and relatively high strength.

Electronic Programmable Controllers

With the many degrees of freedom required for dexterous robot hands, the problem of control and demand on computing escalates. The simplest approach is to use a local control loop for each joint. However, for precise motion control, a coordinated motion for all joints is essential for an efficient design.

For master-slave operation, where the coordination is achieved by the action of a human in the loop, the coupling between the fingers is neglected. Currently, a number of high performance servomotor controllers are commercially available. These controllers are designed to be programmable and installed in personal computers.

The Galil DMC/600 series Advanced Motion Controller has been selected to fulfill this role in the finger prototype development. The DMC/600 is a fully programmable servo motion controller contained on an IBM PC compatible card. It controls the motion of up to three DC motors with incremental encoder feedback. Modes of motion include independent or vector positioning, contouring, jogging and homing. A FIFO buffer allows fast pipelining of instructions. The DMC/600 contains a digital filter with an integral gain term for eliminating position error at stop. Several error handling features are available including automatic shut-off for excessive position error, limit switch inputs, emergency stop inputs and programmable torque limits.

Dexterous Hand Masters

The proposed master/slave control mode calls for the operator to wear a specially instrumented dexterous hand master. This device must produce control signals capable of directing the servomotor actuators of the robotic slave hand into correspondence with the respective positions of the human operator's hand joints. Plans call for consideration of three different dexterous hand masters to carry out this control function. Two such devices, the A. D. Little "Sarcos Dexterous Hand Master" and the VPL Research "DataGlove" are currently commercially available though both are undergoing continuing development. Their application will be discussed briefly in the following paragraphs together with a third approach utilizing real-time image processing of a special optically patterned master glove.

Arthur D. Little, Inc. of Cambridge, Massachusetts [4,12] offers a Sarcos Dexterous Hand Master. The device utilizes mechanical linkage assemblies secured to the individual finger digits by means of flexible ring-like bands. Built-in hall effect potentiometers translate the various linkage motions into electrical signals which can be correlated to the individual finger joint movements.

VPL Research of Redwood City, California markets the DataGlove [5-7], an ingenious glove-like dexterous hand master that senses hand gesture position and orientation in real time. The device utilizes fiber-optic cables sandwiched between a stretchable inner glove and a cloth outer glove. Each joint

motion to be detected requires a separate fiber-optic cable laid in a parallel path running across the joint and looping back so that both free ends are anchored in an interface board mounted near the wrist. At one end of the cable is a light emitting diode source and at the other a phototransistor. The segments of the cable which rest over the joint are specially treated so that the light escapes when the joint is flexed. The greater the degree of bending, the greater is the loss of transmitted light. This effect can be detected by the phototransistor and calibrated to provide angular measurements with a resolution of one degree. A data acquisition rate of 60 times per second is used.

A third method suggested for the master control mode is the use of a master glove imprinted with a special color-coded optical pattern. In this approach, the respective control signals for positioning the multiple finger joints would be extracted from the glove image. Potentially, the patterned glove could be lighter, better fitting, less cumbersome, and less expensive than either the A. D. Little Sarcos Dexterous Hand Master or VPL DataGlove. The authors are not aware of any commercially available devices of this nature or any researchers who have applied this approach to date.

Acknowledgments

Funding is being provided by NASA Grant No. NAGW 1336, Jet Propulsion Laboratory Contract No. 958292, and an Ohio Board of Regents Research Challenge grant. Mr. James Aliberti of Kennedy Space Center and Dr. Edwin P. Kan of Jet Propulsion Laboratory are serving as technical monitors. The NASA support was achieved through the efforts of Dr. Yvonne B. Freeman of NASA Headquarters.

References

1. McCormick, Malcolm, "A Primer On: Brushless DC Motors," MECHANICAL ENGINEERING, New York, NY, Vol. 110, No. 2, February 1988, pp. 52-57.

2. TORQUE MOTOR ENGINEERING HANDBOOK, Clifton Precision, Litton Systems, Inc., Clifton Heights, PA, 1986, Section 3.

3. HARMONIC DRIVE DESIGNER'S HANDBOOK, Harmonic Drive Division, Emhart Machinery Group, Wakefield, MA, 1986.

4. "A. D. Little/Sarcos Dexterous Hand Master," product brochure, Arthur D. Little, Inc., Cambridge, MA, 1988

5. "VPL Research DataGlove Model 2 System," product brochure, VPL Research Inc., Redwood City, CA, 1987.

6. Foley, J. D., "Interfaces for Advanced Computing," SCIENTIFIC AMERICAN, New York, NY, Vol. 257, No. 4, October 1987, pp. 127-135.

7. Fisher, S. S., "Telepresence Master Glove Controller for Dexterous Robotic End-Effectors," INTELLIGENT ROBOTS AND COMPUTER VISION - FIFTH

IN A SERIES, Proceedings of SPIE-The International Society for Optical Engineering, Vol. 726, Cambridge, Massachusetts, 28-31 October 1986.

8. Abd-Allah, M. A., "Eigenimage Filtering of Medical Images Using Multispectral Image Sequences," Ph.D. dissertation, University of Toledo, June 1986.

9. Windham, J. P., Abd-Allah, M. A., et al., "Eigenimage Filtering in MR Imaging," JOURNAL OF COMPUTER ASSISTED TOMOGRAPHY, Vol. 12, No. 1, January/February, 1988, pp. 1-9.

10. Davis, V. L., "Computer Hardware and Software for Robotic Control: The Kennedy Space Center (KSC) Robotics Applications Development Laboratory (RADL)," 1987 Goddard Conference on Space Applications of Artificial Intelligence (AI) and Robotics, May 14, 1987.

11. Grissom, W. A.; Abd-Allah, M. A.; White, C. L., "Concept for a Large Master/Slave-Controlled Robotic Hand," PROCEEDINGS OF THE SECOND ANNUAL WORKSHOP ON SPACE OPERATIONS AUTOMATION AND ROBOTICS (SOAR), July 1988, pp. 353-359.

12. Marcus, B. A.; Churchill, P. J., "Sensing Human Hand Motions for Controlling Dexterous Robots," PROCEEDINGS OF THE SECOND ANNUAL WORKSHOP ON SPACE OPERATIONS AUTOMATION AND ROBOTICS (SOAR), July 1988, pp. 481-485.

COMPUTER SIMULATION OF RADIATION DAMAGE IN GALLIUM ARSENIDE

John J. Stith, James C. Davenport, and Randolph L. Copeland
Department of Physics
Virginia State University
Petersburg, Virginia

ABSTRACT

A version of the binary-collision simulation code MARLOWE has been used to study the spatial characteristics of radiation damage in proton and electron irradiated gallium arsenide. Comparisons made with experimental results have proved to be encouraging.

COMPUTER SIMULATION OF RADIATION DAMAGE IN GALLIUM ARSENIDE

The main objective of this research is to study radiation damage and annealing in gallium arsenide through the use of computer simulation.

Electronic devices manufactured from semiconductors are vital to the space program. These devices must be capable of surviving and operating in an environment where various types of radiation are present. In order to design the devices for maximum tolerance to the radiation encountered in the space environment, the damaging effects of the radiation on the semiconductor must be studied. Extensive laboratory testing and/or computer simulations of the effects of the specific radiation on the semiconductor are required. The present study was done with computer simulation.

Gallium arsenide has received considerable attention over the past few years due to its potential usefulness in high-power space-energy systems where high operating temperature is a limiting factor for other semiconductors. However, space radiation may be a limiting factor unless sufficient shielding is provided to keep damage levels within acceptable limits.

In order to determine design parameters for a specific space environment, a fundamental understanding of specific radiation interaction with the semiconductor is required.

On impinging upon the semiconductor, radiation produces a variety of defects. The defects which are of the most interest to researchers include interstitials, vacancies, vacancy clusters, and improper replacements for binary crystals such as gallium arsenide. There are at least three classes of electrically active defects that are produced in gallium arsenide, and they are the following: (1) those that do not anneal (including improper replacements, some distant interstitial-vacancy pairs, and some vacancy clusters), (2) those that anneal at relative low temperatures, and (3) those that anneal at high temperatures.

In space, simultaneous radiation exposure and annealing might result in very limited degradation because the duration of radiation exposure is many mean-annealing-times. A terrestrial experiment to verify this would be inconclusive since the usual duration of radiation exposure will be less than the required annealing time. A laboratory experiment which properly simulates the effect of simultaneous irradiation and annealing in space would be costly and difficult. Computer simulation provides a convenient technique for studying atomic scattering in crystals. It is particularly useful at moderate energies where crystal effects may be pronounced, but where clear distinction between random and aligned processes is difficult.

A theoretical understanding of the effects of displacements in semiconductors caused by radiation requires a detailed analysis of the dependence of the number of point defects and their spatial distribution on the energy of the primary recoil atom.

The binary-collision simulation code MARLOWE has been modified to run on NASA LaRC computer system and used to simulate radiation damage produced in a gallium arsenide crystal when it is irradiated with electrons and protons. Primary recoil atoms possessing energies corresponding to the average energy transfer between a 1-Mev electron and a gallium or arsenic atom, and primary recoil atoms possessing energies corresponding to the average energy transfer between a 100-Kev proton and

a gallium or arsenic atom were used to start the displacement cascades in the crystal. The 1-Mev electron is used in the equivalent fluence testing of devices and the 100-Kev proton has been shown through theory and experiment to be most effective in damaging the .5 and .8 micron junction gallium arsenide solar cells.[2,3]

The results from the computer simulations yielded information on the spatial distribution of the defect pairs (close pairs, near pairs and distant pairs), as well as details on possible clusters of defects, such as multiple vacancies.

Analysis of vacancy-interstitial pairs was made. The graphs in figures 1 and 2 show the distribution of the separations of the pairs for the 20 and 90 eV recoil energies, respectively. The distributions include close, near, and distant pairs. When the distributions on the two graphs are compared, it is clear that there is a greater number of interstitial-vacancy pairs for the higher-energy cascades than for the lower-energy cascades. Figures 3 and 4 are included to show the relative positions of the interstitials and the vacancies produced in the crystal. Close, near and distant pairs are displayed. In figures 5 and 6 the close pairs are not included since it is a good possibility that the vacancies and interstitials that form the close pairs will combine (self-anneal). Figures 7 and 8 only display the distant pairs which may still exist after annealing of the crystal which stimulates the near pairs to combine. When a proper pair combines, two defects are eliminated, but when an improper pair combines, two defects are reduced to one defect which is different from either of the two original defects. The distant pairs will most likely remain as stable defects within the crystal even through the annealing process. There is a sizeable difference between the number of distant pairs for the high-energy primary recoil atoms. This is in good agreement with the experimental results that demonstrated a high degree of difficulty in annealing proton radiation damage as compared with annealing electron radiation damage in gallium arsenide.

References

1. Robinson, M.T. and Torrens, I.M.; Phy. Rev. B, 1974, 9(12), 5008.

2. Stith, J.J. and Wilson, J.W.; Proc. of the Eighteenth IEEE Photovoltaic Specialists Conf., 1985, 1716.

3. Wilson, J.W., Walker, G.H., and Outlaw, R.A.; IEEE Electron Devices, 1984, Vol. 31, 421.

4. Benedek, R.; J. Appl. Phys., 1981, 52(9), 5557.

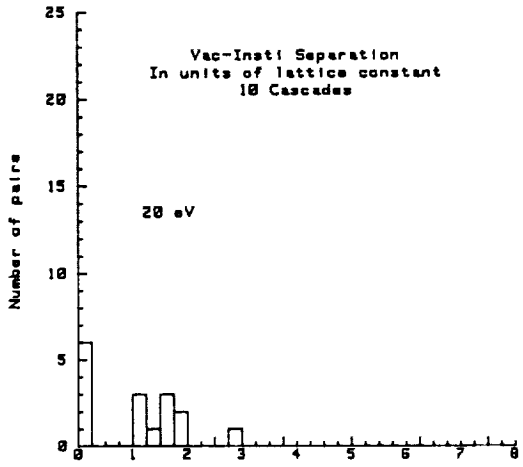

Figure 1

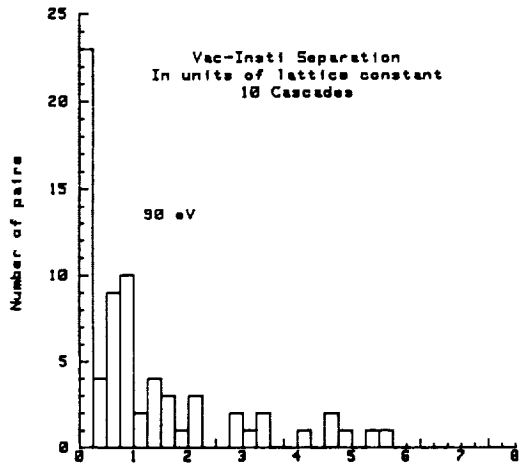

Figure 2

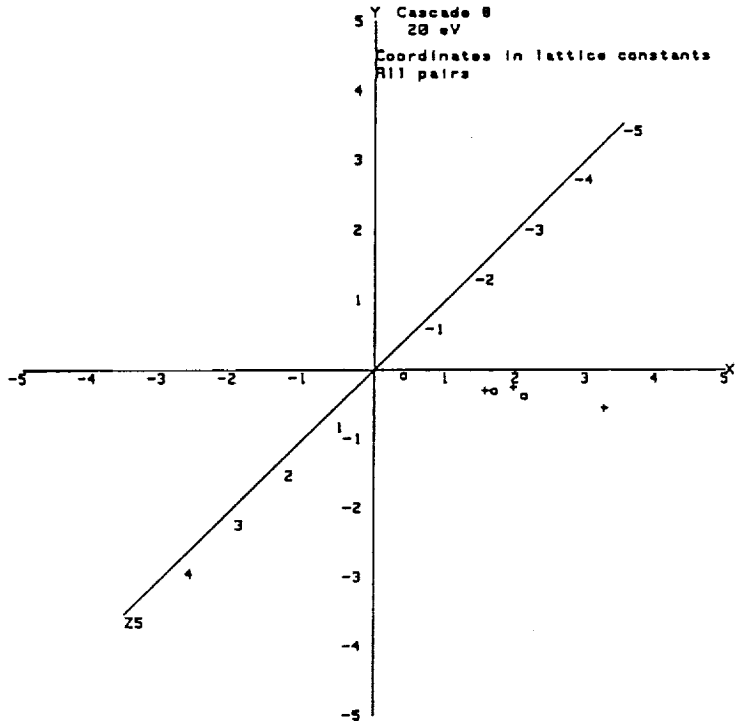

Figure 3

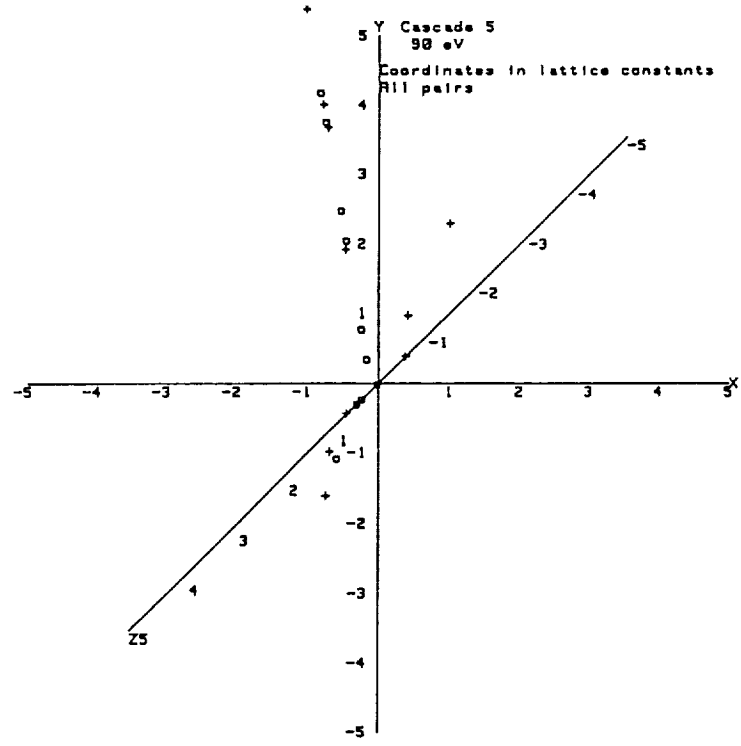

Figure 4

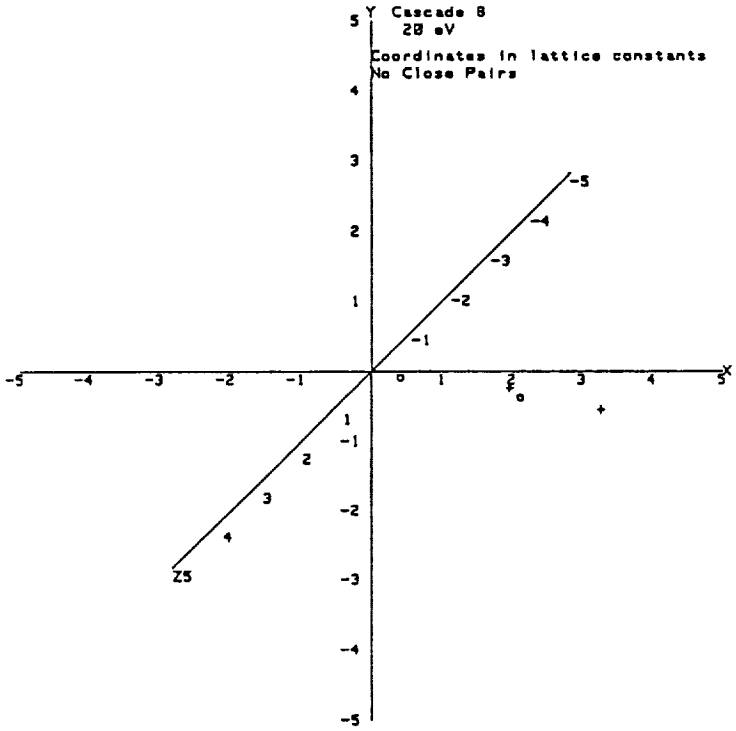

Figure 5

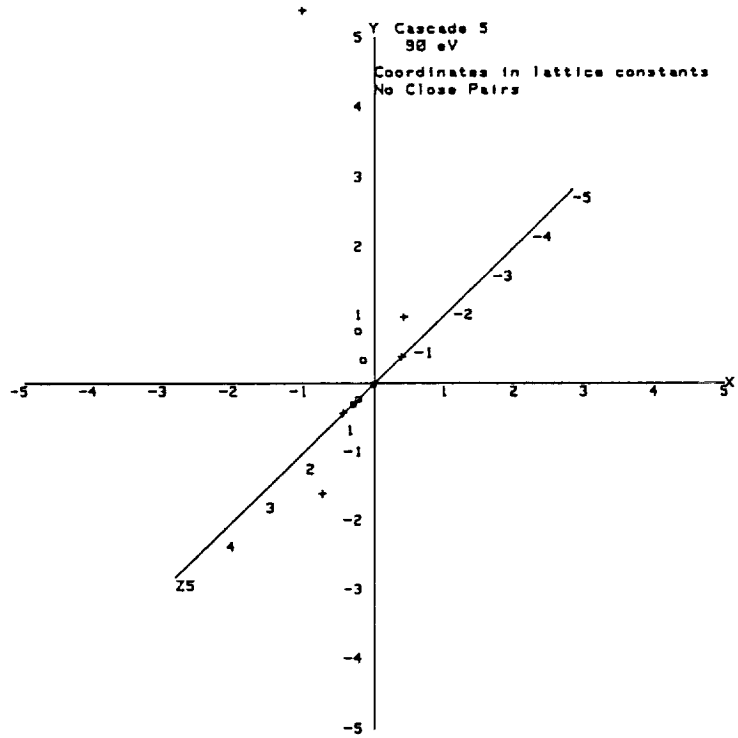

Figure 6

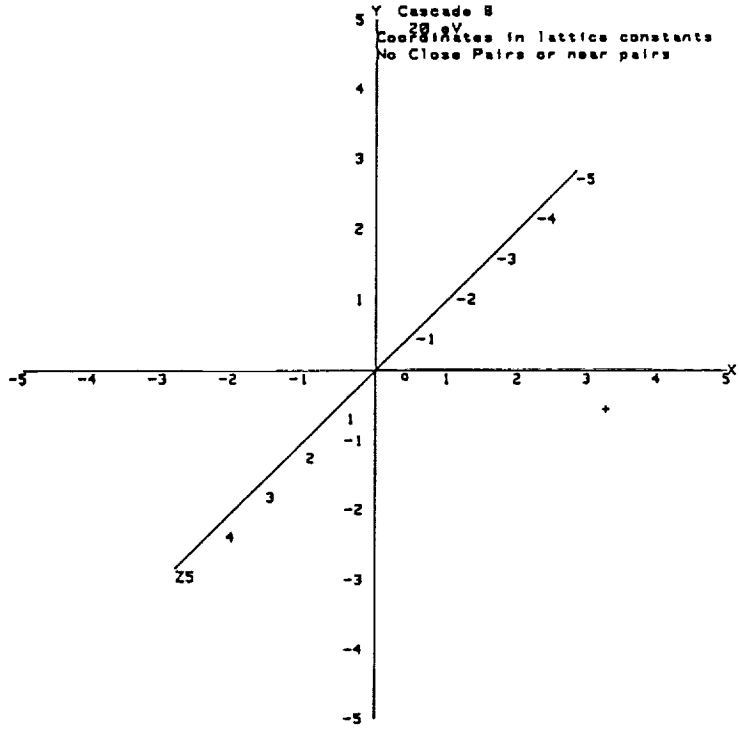

Figure 7

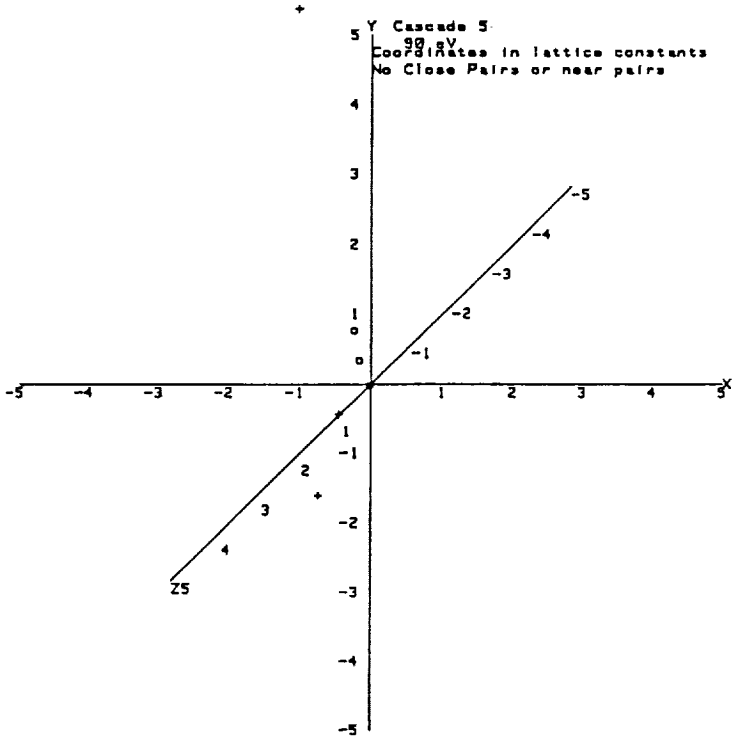

Figure 8

FORCED CONVECTION AND FLOW BOILING WITH AND WITHOUT ENHANCEMENT DEVICES FOR TOP-SIDE-HEATED HORIZONTAL CHANNELS

Ronald D. Boyd, Sr., and Jerry C. Turknett
Department of Mechanical Engineering
Prairie View A&M University
P.O. Box 397
Prairie View, TX

ABSTRACT

A three-year research program has been launched to study the effect of enhancement devices on flow boiling heat transfer in coolant channels, which are heated either from the top side or uniformly. Although the study will include other orientations and working fluids in subsequent years, the first years will involve studies of the variations in the local (axial and circumferential) and mean heat transfer coefficients in horizontal, top-heated coolant channels with smooth walls and internal heat transfer enhancement devices. Initially, the working fluid will be freon-11. The objectives of the fiscal year's work are to: (1) examine the variations in both the mean and local (axial and circumferential) heat transfer coefficients for a circular coolant channel with either smooth walls or with both a twisted tape and spiral finned walls, (2) examine the effect of channel diameter (and the length-to-diameter aspect ratio) variations for the smooth wall channel, and (3) develop an improved data reduction analysis.

The case of the top-heated, horizontal flow channel with smooth wall (1.37 cm inside diameter, and 122 cm heated length) has been completed. The data have been reduced using a preliminary analysis based on the heated hydraulic diameter. Preliminary examination of the local heat transfer coefficient variations indicates that there are significant axial and circumferential variations. However, it appears that the circumferential variation is more significant than the axial ones. In some cases, the circumferential variations were as much as a factor of ten. The axial variations rarely exceeded a factor of three. Integrated averaged heat transfer coefficients will be obtained after the improved data reduction model has been implemented.

Nomenclature

h	Local heat transfer coefficient, $W / m^2 °C$
h_∞	Mean heat transfer coefficient due to natural convection between the test section and the ambient, $W / m^2 °C$
q_c	Heat loss from the test section due to convection, W
q_R	Heat loss from the test section due to radiation, W
r	Radial coordinate for the data reduction model, m
T_f	Bulk temperature of the flowing fluid, °C
T_m	Local measured outside wall temperature of the test section, °C
Tsat	Saturation temperature (316 K at 0.19 MPa for freon-11), °C
T_∞	Ambient temperature, °C
Z, Z_i	Axial coordinate for heated portion of the test section; in Figures 3a through 3d, Zi represents Z_i , where Z_i = 20.32 (i-1), cm

Greek Letters

φ	Circumferential coordinate; see Figure 1a for the datum. In figures 3a through 3d, φ is also referred to as "**Phi.**"
π	Half of a full rotation of 180°; in Figures 3a through 3d, π is also referred to as "**Pi.**"

FORCED CONVECTION AND FLOW BOILING WITH AND WITHOUT ENHANCEMENT DEVICES FOR TOP-SIDE-HEATED HORIZONTAL CHANNELS

Introduction

Space commercialization will require efficient heat transfer systems. The future success of many efforts will be based on our understanding of the behavior of two-phase flow boiling in both the space (zero-g or reduced-g) and earth environments. This three-year program is intended to focus on the following fundamental characteristics (e.g., nonuniform heat flux distribution, Marangoni effects, and single and double enhancement devices) of experimental flow boiling heat transfer and pressure drop in the earth environment [1].

The objectives of the first year's efforts are to: (1) examine the variations in both the mean and local (axial and circumferential) heat transfer coefficients for a circular coolant channel with either smooth walls or with both a twisted tape and spiral finned walls, (2) examine the effect of channel diameter (length-to-diameter ratio) variations for the smooth wall channel, and (3) develop an improved data reduction analysis.

In this paper, we report on forced convection and flow boiling of freon-11 in a smooth-wall horizontal coolant channel (1.37 cm inside diameter and 122.0 cm heated length) heated from the top side. The inlet freon temperature was 24°C, the exit pressure was 0.19 MPa absolute, and the mass velocity was 0.28 Mg / m^2s.

Experimental Investigation

The reader is referred to references 1 and 2 for detailed descriptions of the experimental flow loop, procedures, and data acquisition. Figure 1a is a schematic of the cross section of the heated portion of the test section [which is preceded by an upstream unheated portion for flow development]. The measured wall temperatures are used along with the data reduction analysis to determine the unknown heat transfer coefficient, h. Recently, a data reduction technique based on the heated hydraulic diameter [2] (see Figure 1b) was used to reduce the experimental data. This approach will result in, at most, a qualitative indication of the local distribution of h. Work is proceeding on more viable data reduction approaches; e.g., finite difference for local h and analytical for mean h.

In applying either model, knowledge of the fluid's bulk temperature must be used. An iteration scheme is used to compute the inside wall temperature, T_w, of the flow channel. The fluid's temperature is chosen based on the magnitude of the inside wall temperature relative to the wall temperature required to cause the onset to nucleate boiling T_{ONB}. If T_w is greater than T_{ONB}, the fluid temperature is set equal to the saturation temperature. However, if the above condition is not satisfied, the fluid temperature is computed from the energy equation, using the measured inlet fluid temperature and the measured net thermal energy transfer to the fluid.

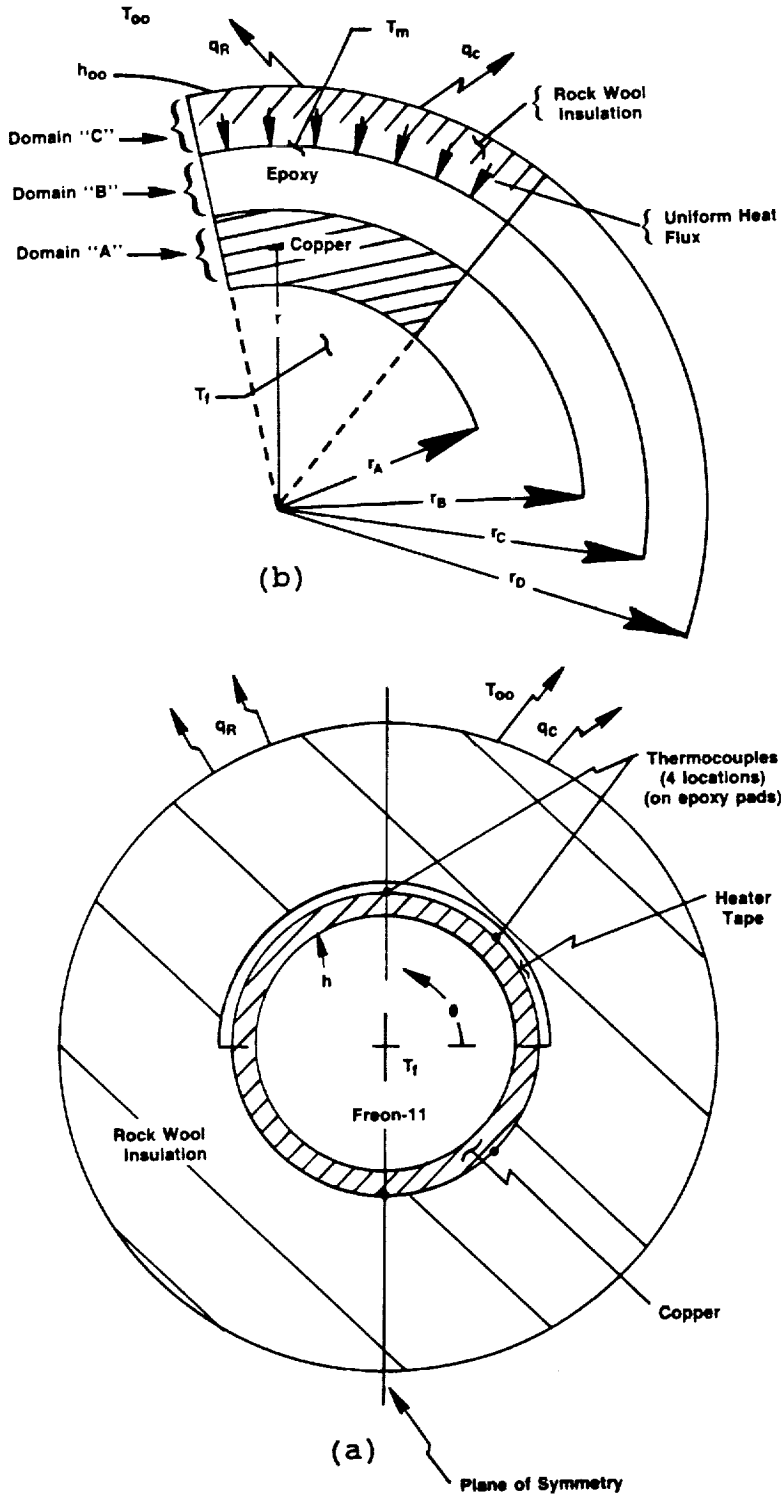

Figure 1: (a) Cross section of the heated portion of the test section.

(b) Control volume of heated hydraulic diameter model.

Results

The results are presented for the case of forced convection and flow boiling with freon-11 flowing in a horizontal channel with smooth walls.

The variation in the heat transfer coefficient is more pronounced in the circumferential direction than the axial direction. The heat transfer coefficients for the single-phase and hypocritical regions are shown in Figure 2. The fully developed nucleated boiling region does not appear in the figure but occurs somewhere in a narrow range between $\varphi = 7\pi/4$ and $\pi/4$ (see Figure 1a for the datum for φ). The heat transfer coefficient in this narrow region is expected to be greater than any of those shown.

The last two highest points on each of the curves show an increase in the heat transfer coefficient. For $\varphi = 3\pi/2$ and $7\pi/4$, the increase is due to the onset of nucleate boiling which we see results in more than a fifty percent increase in h. For these two locations we see that there is only a secondary variation in h with φ.

Both axial and circumferential variations in h are found to be significant. Comparisons of Figures 3a ($\varphi = \pi/2$), 3b ($\varphi = \pi/4$), 3c ($\varphi = 7\pi/4$) and 3d ($\varphi = 3\pi/2$) reveal the complex nature of the variations. The variation in the local heat transfer coefficient increases from the bottom ($\varphi = 3\pi/2$) to the top ($\varphi = \pi/2$) of the test section at all axial locations. As noted earlier, the variation between $7\pi/4$ and $3\pi/2$ is small even at the locations where incipient nucleate boiling occurs ($h = 1400\ W/m^2K$). It is interesting to compare the magnitude of h for the three regimes: (1) single-phase ($800\ W/m^2K$), (2) incipient nucleate boiling ($1400\ W/m^2K$) and (3) film boiling (10 to $100\ W/m^2K$).

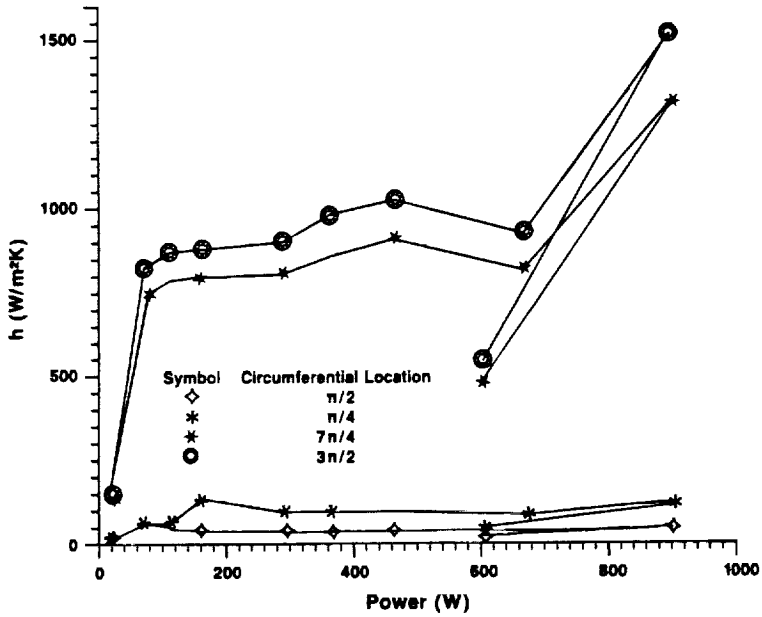

Figure 2: Heat transfer coefficient versus power generation and circumferential location at Z = Z4 = 61.96 cm (center of the test section) for top-side-heated smooth tubes for: 0.19 Mpa exit pressure, 0.281 Mg/m^2s mass velocity, 1.22 m heated length.

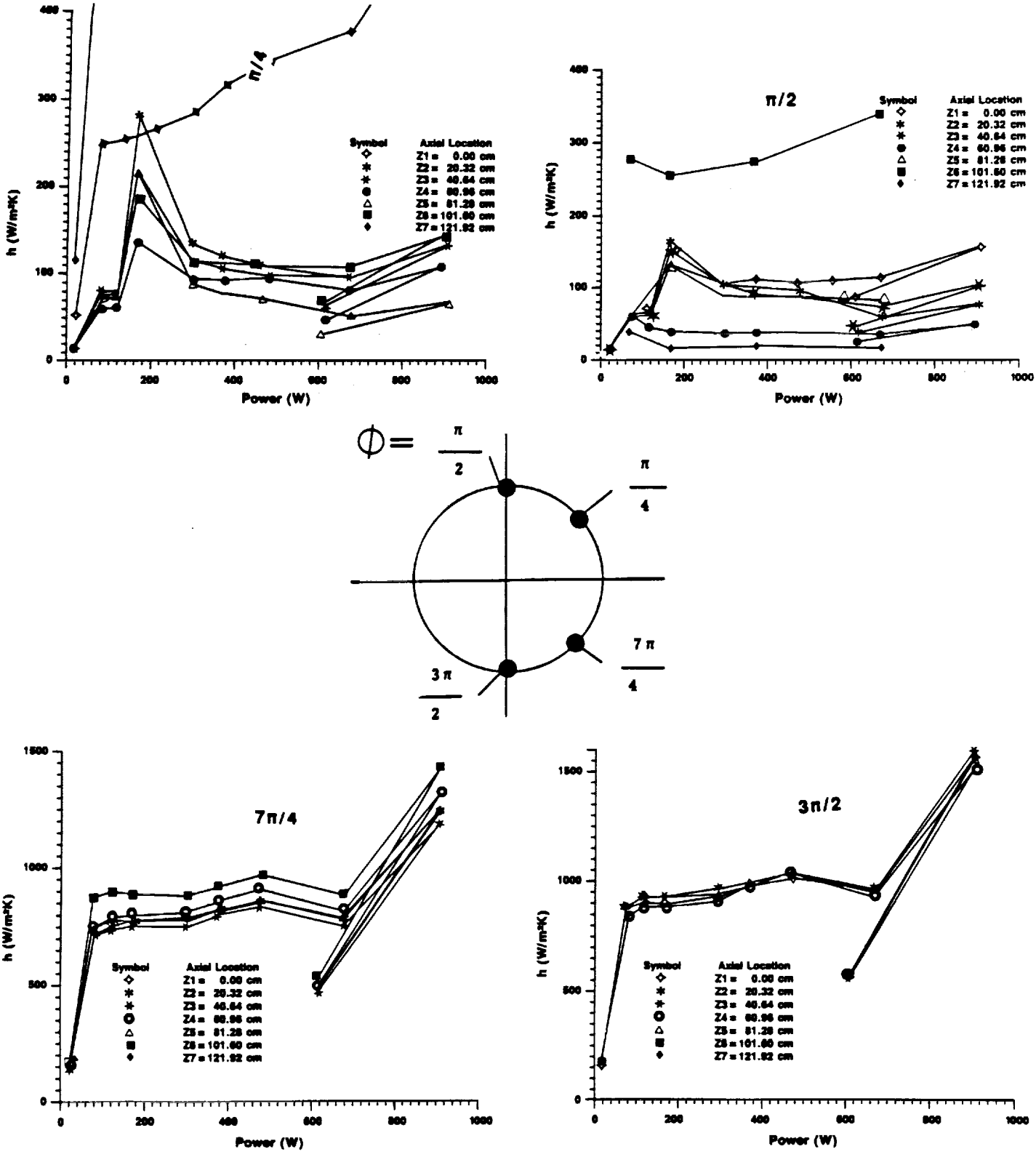

Figure 3: Heat transfer coefficient versus power and axial location at Phi = Pi/2 (top), Pi/4, 7Pi/4, and 3Pi/2 (bottom) for top-side heated smooth tubes at 0.19 MPa and 0.281 Mg/m^{2}s. Channel diameter = 1.27cm, heated length = 1.22m.

If one takes time to study the relative positions of the curves and use the reduced wall temperature, some of the character of the flow is revealed (e.g., see Figure 3a). In particular, notice from Figure 3a that: (1) h at Z_5 and Z_3 are almost identical at between 380 and 640 W, (2) h at Z_6 is much higher than all values of h at other locations, and (3) in some cases curves are crossing one another. These observations may imply a slug type of flow. For example, at Z_6 the unusually large value of the heat transfer coefficient could be due to local cooling (slug flow). Contrasting the above description, Figure 3b ($\varphi = \pi/4$) shows that between Z_2 and Z_5 the heat transfer coefficient decreases in the downstream direction. This is consistent with the previous observations made. That is, at $\varphi = \pi/4$ the film boiling regime predominates.

Conclusions

Local (axial and circumferential) measurements of the outside wall temperature have been made for horizontal freon-11 flow (0.19 MPa exit pressure and 24°C inlet temperature) through a 1.37 cm inside diameter coolant channel with smooth walls and heated from the top side. A preliminary data reduction model was used to relate the measured wall temperatures to the local heat transfer coefficient. Although the local temperature measurements are quantitative, the preliminary data reduction model results in what may be only qualitative local heat transfer measurements. Work is proceeding to evaluate and improve, if necessary, the existing data reduction model.

The preliminary heat transfer data indicate that there are significant axial and circumferential variations in the local heat transfer coefficient. However, it appears that the circumferential variation is more significant than the axial ones. The single phase heat transfer coefficient (near 900 W/m^2K) is increased by more than 50% at the onset of nucleate boiling. For the test performed, the circumferential heat transfer coefficient varied from the hypocritical to the single phase heat transfer regimes. This resulted in some cases in a factor of ten increase in the local heat transfer coefficient. The axial variations rarely exceeded a factor of three.

Acknowledgments

The authors would like to acknowledge Richard Parish, Dr. Joseph Atkinson, Dr. Y. Freeman, and Richard Kennedy for their support and assistance. The authors would also like to thank other NASA personnel, both at headquarters and JSC, for their support.

References

1. Boyd, R.D, "Flow Boiling with and without Enhancement Devices for Horizontal, Top-Heated, Coolant Channels for Cold Plate Coolant Channel Design Applications, Preliminary Report," Department of Mechanical Engineering, Prairie View A&M University, Prairie View, TX, Submitted to NASA (JSC), Contract no. 9-16899 (Task-5), December, 1986.

2. Turknett, J.C, "Forced Convection Flow Boiling with and without Enhancement Devices for Top-Side-Heated Horizontal Channels," MS Thesis, Department of Mechanical Engineering, Prairie View A&M University, Prairie View, TX (to be published).

PROGRESS IN PROTON TRANSPORT CODE DEVELOPMENT: MICROELECTRONIC APPLICATION

Duc M. Ngo, W.W. Buck, and T.N. Fogarty
Physics Department
Hampton University
Hampton, VA

and

J.W. Wilson
NASA, Langley Research Center
Hampton, VA

ABSTRACT

The process of target nucleus fragmentation by energetic protons is examined and their effects on microelectronic devices considered. A formalism for target fragment transport is presented with future applications to microelectronic effects discussed.

PROGRESS IN PROTON TRANSPORT CODE DEVELOPMENT: MICROELECTRONIC APPLICATION

Introduction

Since the early suggestion that some spacecraft anomalies may result from the passage of the galactic ions through microelectric circuits (ref. 1), it has now been well established as a fact. Although the direct ionization of protons appear as unlikely candidates, their nuclear reaction products are suspected as a source of Single Event Upset (SEU) phenomena (ref. 2-4). As a result a number of fundamental experimental and theoretical studies were undertaken to better understand the phenomena. McNulty and coworkers examined the energy deposition of proton reaction products in Si using surface barrier detectors of various thickness from 2.5 to 200 μm (ref. 5). They also developed a Monte Carlo code for theoretical evaluation of energy deposition from such products (ref. 5,6). Comparisons of McNulty's work with the well established MECC7 developed by Bertini and coworkers at Oak Ridge National Laboratory showed some differences in predicted reaction products and even greater differences in energy spectral contributions (ref. 7). An evaluation of Si reaction products was likewise made by Petersen (ref. 4), and although no direct comparison was made to McNulty's experiments, an estimate of SEU rates in the trapped proton environment was made.

Following these fundamental studies came more detailed application to devise specific questions. Bradford evolved an energy deposition formalism (ref. 8) using the cross sections of Hamm et. al. (ref. 7). The McNulty Group applied the Monte Carlo model to DRAM devices with reasonable success and discussed the implications of heavy ion SEU phenomena on proton induced SEU events through secondary reaction processes (ref. 9). The fundamental consideration is the evaluation of the energy deposited within the sensitive volume (depletion region) of the device in question due to a passing proton. The ionization of the proton itself makes only a small contribution to the critical charge. Nuclear reaction events usually produce several reaction products (usually a heavy fragment and several lighter particles although a few heavy fragments may be produced simultaneously on some occasions) and all of the resultant products can make important contributions to the energy deposited. Such nuclear event products are of course correlated in both time and space.

There are three distinct approaches to a fundamental description of the energy deposition events. McNulty and coworkers have developed a Monte Carlo code in which multiparticle events are calculated explicitly including spatial and specific event (temporal) correlation effects. Although this is the most straightforward way of treating the full detail, it is a complex computational task. A second class of methods begins with the volumetric source of collision events and calculates the SEU probability using the cord length distribution (ref. 8,10). Although in principle the correlation effects could be so incorporated, they appear to be ignored in both of the cited references. A third approach, in which LET distributions and cord length distributions are used, seems most appropriate for external sources (ref. 11,12). It would seem that this last approach applies if the LET distribution from external sources is constant over the sensitive volume but its applicability to volumetric sources is questionable. At the very least this approach ignores correlation effects.

In an earlier work we examined nuclear data bases for biological systems (ref. 13). In that work we found that the MECC7 results underestimated by nearly a factor of two the cross section for multiple charged ion products. In a more detail analysis, we found the Silberberg-Tsao fragmentation parameters to be superior to the MECC7 results (ref. 14). The primary differences appear for the lighter of the

multiple charged fragments. Further comparison with experiments of Al targets show all three Monte Carlo nuclear models (OMNI, VEGAS as well as MECC7) to underestimate production cross sections for products lighter than fluorine in proton induced reaction. Although these intranuclear cascade models are capable of representing multiparticle correlation, the inherent inaccuracies in predicting cross sections is a serious limitation. In the present paper we examine the implication of the nuclear recoil effects on electronic devices and begin the development of a formalism for application to specific device parameters.

Microelectronic Upsets

An electronic device is sensitive to the sudden introduction of charge into active elements of its circuits. The amount of such charge which is sufficient to change state in a logic circuit is called the critical charge. There is a rough relationship between the critical charge Q_c and the device feature size L (ref. 11) as shown in Fig. 1. This relationship is approximately

$$Q_c \approx 0.0156L^2 \tag{1}$$

where Q_c has units pC and L has units μm. Upsets in a device are then dependent on the charge produced compared to the critical charge.

The charge released ΔQ in a material due to the passage of an energetic ion is related to the kinetic energy lost ΔE during the passage given by

$$\Delta Q = \frac{\Delta E}{22.5} \tag{2}$$

where ΔQ has units pC and ΔE has units MeV.

The energy lost by an ion in passing through a region is related to its stopping power $(-\frac{dE}{dx} = S_z(E'))$ in the medium. The distance traveled before coming to rest is

$$R_z(E) = \int_0^E \frac{dE'}{S_z(E')}. \tag{3}$$

If an ion is known to come to rest in distance x then its energy is found through the inverse of the relation (3) as

$$E = R_z^{-1}(x) \tag{4}$$

and we note that equation (4) is used to calculate energy loss. The energy loss by an ion of charge Z and energy E in passing through a device with collection length L will have its energy reduced by

$$\Delta E = E - R_z^{-1}[R_z(E) - L_c] \tag{5}$$

and

$$L_c = W_{epi} + W_n \quad (6)$$

where W_{epi} is the epi thickness and W_n is the depletion width.

We note in passing that ΔE does not depend on the particle isotope (i.e., ion mass). The range energy relations described elsewhere (ref. 14) are utilized. As a practical matter to reduce numerical error inherent to numerical interpolation, we use

$$\Delta E = R_z^{-1}[R_z(E)] - R_z^{-1}[R_z(E) - L_c] \quad (7)$$

in place of equation (5). Note the result of equation (5) depends on the global error (fixed at 1 percent) of the code while equation (7) depends only on the local relative error (quite small). The charge introduced is given by equation (2) and (7). An example of a particular collection length of 2μm is shown in Fig. 2 for each ion type. We assume a simplified geometry in which the channel length and width and the collection length are take as equal to the feature size. We take the critical energy as the upper and lower limit of the range of energy for which

$$\Delta Q(E) \geq Q_c \quad (8)$$

which depends on the feature size L. The ion mass for each A is taken as the natural mass. The critical energies are shown in Fig. 3. Also shown in Fig. 3 are the average recoil energy from the fragmentation of ^{16}O and ^{28}Si produced by collision with a high energy proton (ref. 14).

It is doubtful that any of the fragments are produced in the 4μm and larger devices (note that we have used simplified geometries). Also, the lighter fragments of Li, He, and H are not suspected for SEU events, at least in this simple geometry. Also note that Fig. 3 is applicable to cosmic ray ions.

Nuclear Fragmentation Cross Section

Although nuclear fragmentation has been under study for nearly 50 years, the absolute cross sections still stir some controversy. The experimental problem is that the reaction products could be directly observed only in recent years and even now only in rather sophisticated experiments. Rudstam studied the systematics of nuclear fragmentation and supposed the fragment isotopes to be distributed in a bell-shaped distribution about the nuclear stability line (ref. 15). Silberberg et al. continued the Rudstam parametric approach and added many correction factors as new experimental evidence became available (ref. 12).

Concurrently, Monte Carlo simulation of the Serber model (ref. 16) coupled with final decay through compound nuclear models showed some success (ref. 7, 17). Even so, Monte Carlo simulations show little success in predicting fragments whose mass is small compared to the original target nuclear mass (ref. 13,18). Of the various models for nucleon induced fragmentation in ^{28}Si, probably that of Silberberg et al. (ref. 12) is currently most reliable. The main limitation of their model is that only inclusive cross sections are predicted and particle correlations will undoubtedly prove important in predicting SEU.

Measurements of ^{27}Al fragmentation in proton beams have been made by Kwaitkowski (ref. 18). These experiments are compared in Fig. 4 to the Monte Carlo results of OMNI, VEGAS, and MECC7.

Also shown are the results of Silberberg et al. Generally the Silberberg et al. results appear to be within a factor of 2 of the experiments and this is the only model which predicts significant contributions in the important range below $Z_f = 6$.

The spectrum of average recoil energy is calculated using the Silberberg - Tsao cross sections and compared with the spectrum according to Bertini cross sections in Fig. 5. The Bertini cross section is a serious underestimate above 8 MeV and greatly overestimates below 3 MeV. Experimental evidence indicates that even the Silberberg-Tsao values are too small above 6 MeV (ref. 18).

Nuclear Recoil Transport

The transport of the recoil fragments is described by the following

$$[\Omega \cdot \nabla - \frac{\partial}{\partial E} S_z(E)]\phi_z(x,\Omega,E) = \zeta_z(\Omega,E) \tag{9}$$

where $\phi_z(x,\Omega,E)$ is the ion flux and $\zeta_z(\Omega,E)$ is the ion source density assumed to be uniformly distributed through the media. The solution to equation (9) is to be found in the closed region bounded by the surface Γ subject to the boundary condition

$$\phi_z(\Gamma,\Omega,E) = F_z(\Omega,E) \quad \text{for } n \cdot \Omega < 1 \tag{10}$$

where n is the outward directed normal. The solution as found using the method of characteristic (ref. 19) is:

$$\phi_z(x,\Omega,E) = \frac{S_z(E_b)}{S_z(E)}\phi_z(\Gamma,\Omega,E_b) + \frac{1}{S_z(E)}\int_E^{E_b} \zeta_z(\Omega,E')dE' \tag{11}$$

where Γ is taken as the point on the boundary by projecting x along $-\Omega$ and

$$E_b = R_z^{-1}[R_z(E) + b] \tag{12}$$

where

$$b = \Omega \cdot (x - \Gamma). \tag{13}$$

Using equation (11), we may evaluate the spectrum of particles leaving the region which can be related to the spectrum of energy deposited in the media. Such a task will be completed in the near future.

References

1. D. Binder, et al., IEEE Nucl. Sci. Trans., 1975, NS-25, 2675-2680.

2. R.C. Wyatt, P.J. McNulty, P. Toumbas, P.L. Rothwell, and R.C. Filz, IEEE Nucl. Sci. Trans., 1979. NS-26, 4905 - 4910.

3. C.S. Guenzer, R.G. Allen, et al., IEEE Nucl. Trans., 1980 NS-27, 1485-1489.

4. E.L. Petersen, IEEE Nucl. Sci. Trans., 1980, NS-27, 1485-1489.

5. P.J. McNulty, G.E. Farrell, R.C. Wyatt, P.L. Rothwell, R.C. Filz, and J.N. Blanford, IEEE Nucl. Sci. Trans., 1980, NS-27, 1516-1520.

6. P.J. McNulty, G.E. Farrell, and W.P. Tucker, IEEE Nucl. Sci. Trans., 1981, NS-28, 4007-4012.

7. R.N. Hamm, M.L. Rustgi, H.A. Wright, and J.E. Turner, IEEE Nucl. Sci. Trans., 1981, NS-28, 4004-4006.

8. J.N. Bradford, IEEE Nucl. Sci. Trans., 1982, Ns-29, 2085-2089.

9. J.M. Bisgrave, J.E. Lynch, P.J. McNulty, W.G. Abdel-Kader, V. Kletnicks, W.A. Kolasinski, IEEE Nucl. Sci. Trans., 1986, NS-33, 1571-1576.

10. K.W. Fernald and S.E. Kerns, IEEE Nucl. Sci. Trans., 1988, Ns-35, 981-986.

11. E.L. Petersen, P. Shapiro, J.H. Adams, and E.A. Burke, IEEE Nucl. Sci. Trans., 1982, 2055-2063.

12. R. Silberberg, C.H. Tsao, and J. Letaw, D. Reidel Publ. Co., 1976, 49-81.

13. J.W. Wilson, S. Y. Chun, W.W. Buck, and L.W. Townsend, Health Physics, 1988, 55, 817-819.

14. J.W. Wilson, L.W. Townsend, S.Y. Chun, S.L. Lamkin, et al., 1988, NASA TP 2887.

15. C. Rudstam, Zeitschrift fur Naturforschung, 1966, 21a, 1027-1041.

16. R. Serber, Phys. Rev., 1947, 72, 1114-1115.

17. H.W. Bertini, Phys. Rev. 1969, 188, 1711-1730.

18. K. Kwaitkowski, et al., Phys. Rev. Lett., 1983, 21, 1648-1651.

19. J.W. Wilson and S.L. Lamlin, Nucl. Sci. Eng., 1975, 57, 292 - 299.

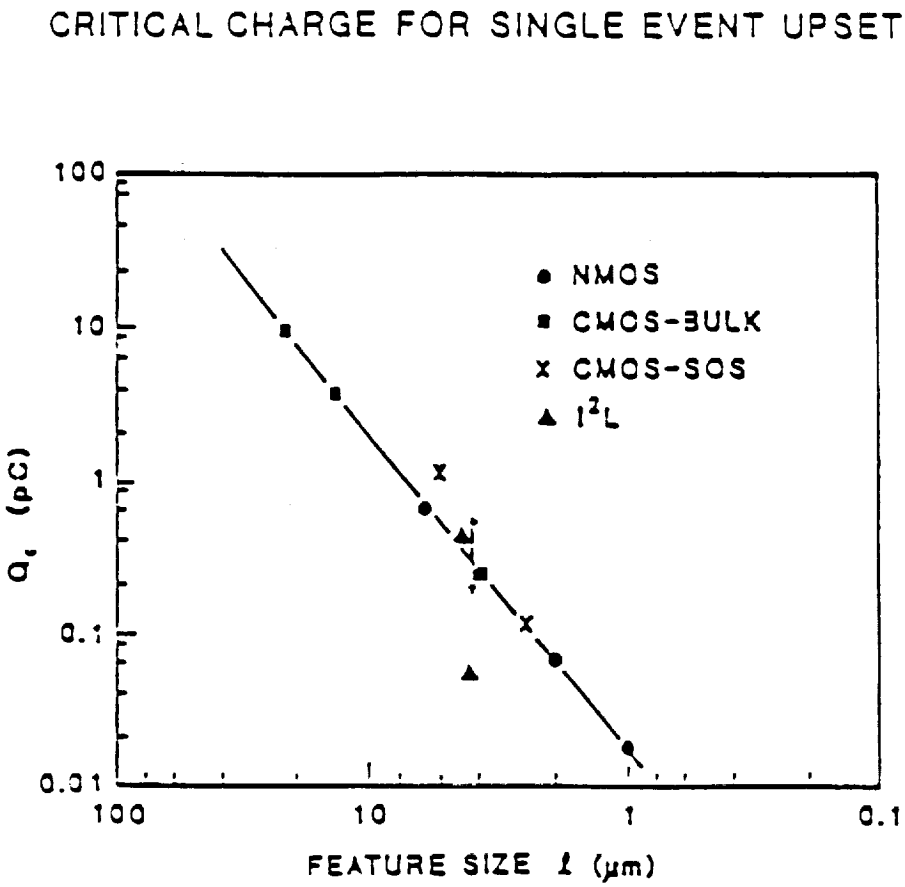

Figure 1
Critical charge Q_c as a function of feature size.

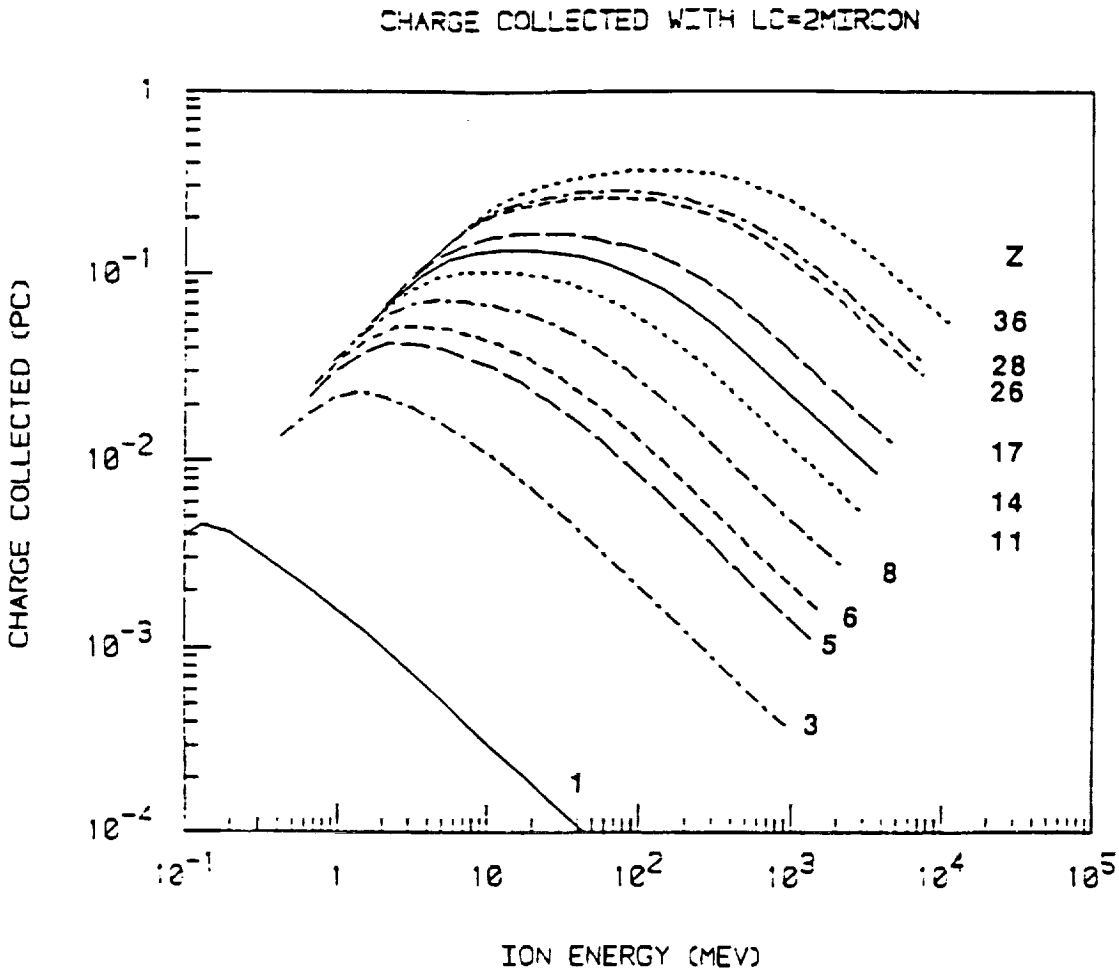

Figure 2
Charge collected as a function of ion energy.

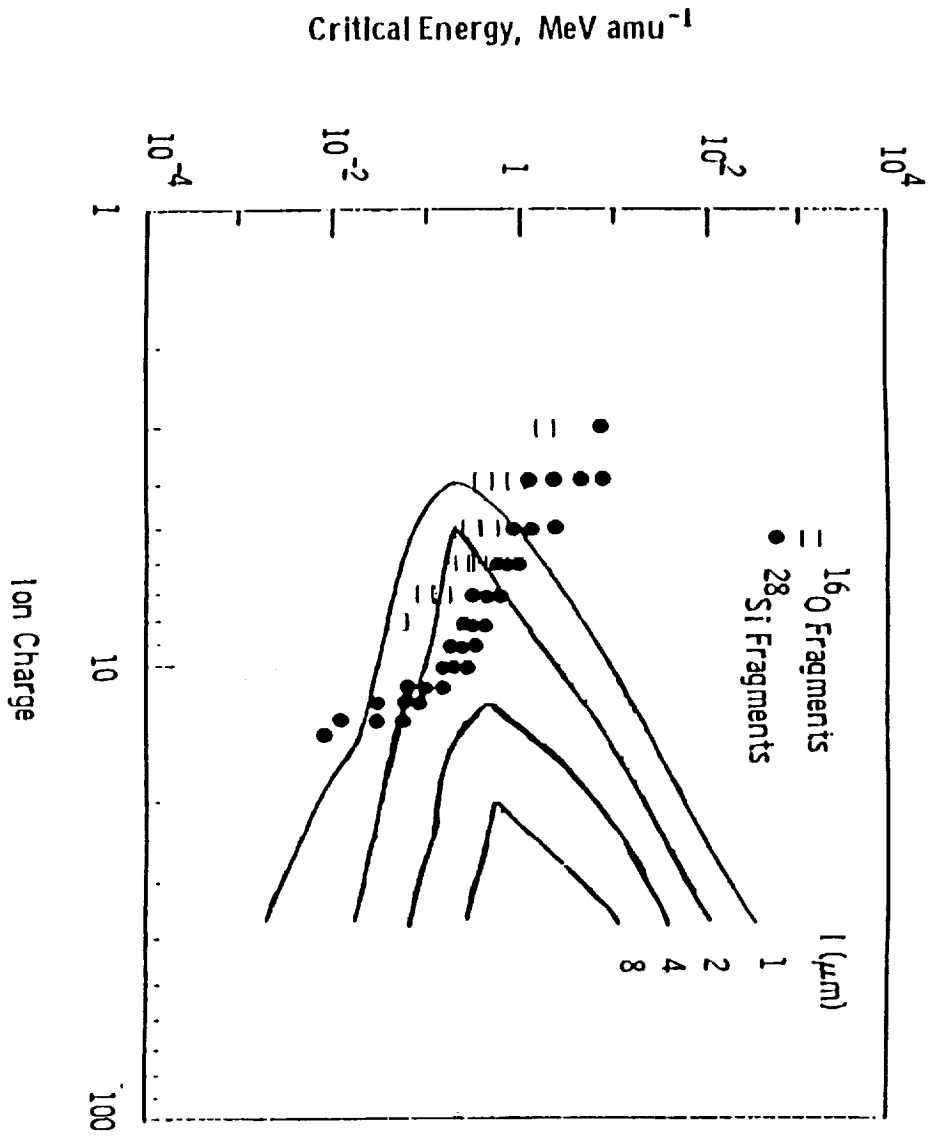

Figure 3

Critical energy as a function of ion charge for several feature sizes.

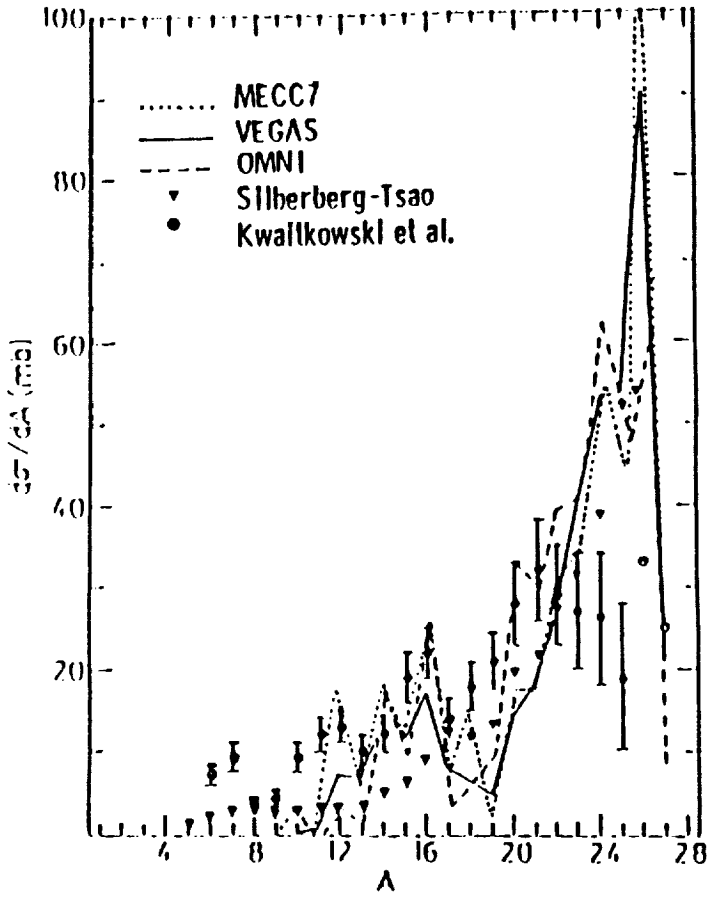

Figure 4

Fragmentation of ^{27}Al according to four models and the experiments of Kwaitkowski et al.

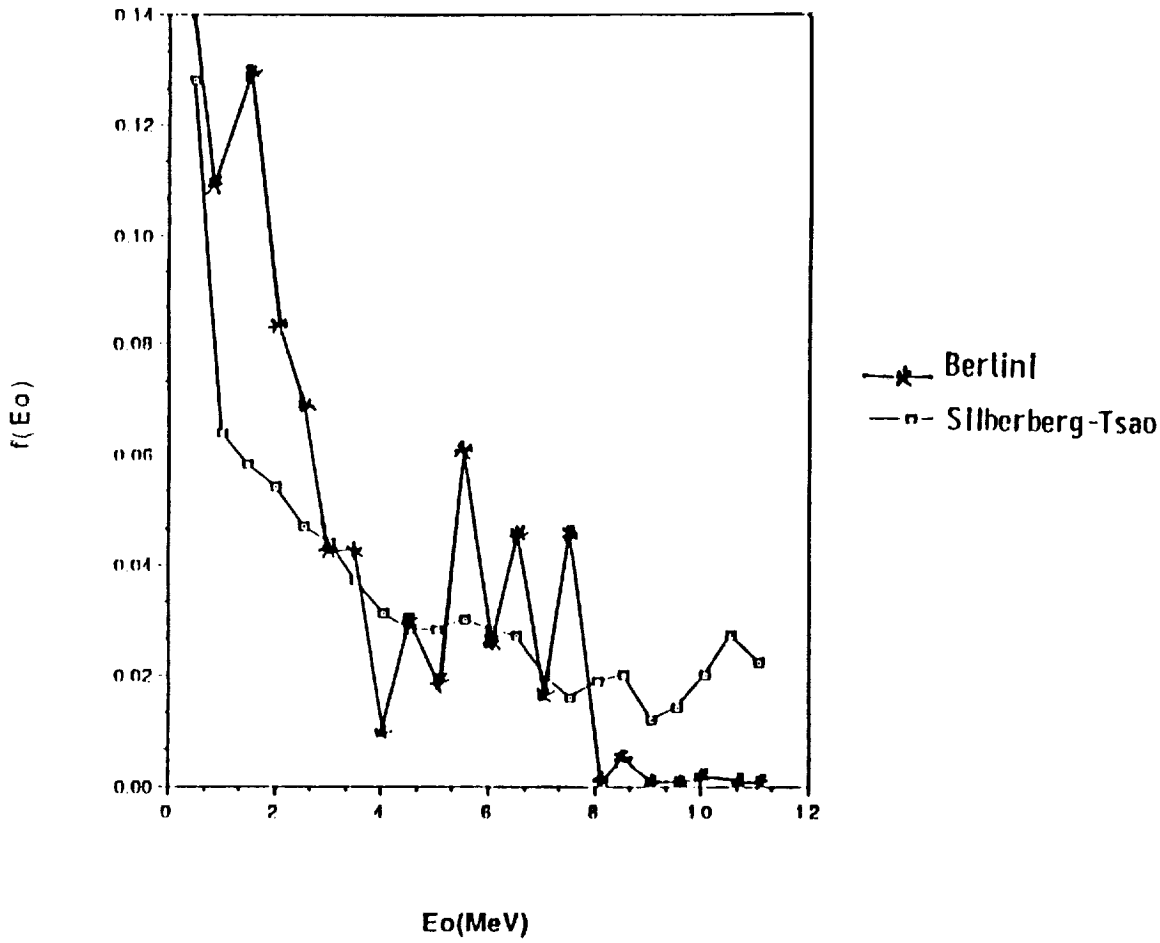

Figure 5

Spectrum of average recoil energy for the Bertini and the Silberberg-Tsao models.

A STUDY OF MICROSTRUCTURAL CHARACTERISTICS AND DIFFERENTIAL THERMAL ANALYSIS OF Ni-BASED SUPERALLOYS*

M.D. Aggarwal, R.B. Lal and S.A. Oyekenu
Department of Physics
Alabama A&M University
Normal, AL

and

Richard Parr and Stephen Gentz
Materials Laboratory, NASA/MSFC
Marshall Space Flight Center, AL

ABSTRACT

The objective of this work is to correlate the mechanical properties of the Ni-based superalloy MAR-M246(Hf) used in the space shuttle main engine, with its structural characteristics by systematic study of optical photomicrographs and differential thermal analysis. In this paper, we have developed a method of predicting the liquidus and solidus temperature of various nickel based superalloys viz., MAR-M247, Waspaloy, Udimet-4l, polycrystalline and single crystals of CMSX-2 and CMSX-3 and compared with the experimental DTA curves using Perkin-Elmer DTA 1700. The method of predicting these temperatures is based on the additive effect of the components dissolved in nickel. The results have been compared with the experimental values.

* Work supported under NASA Grant NAG8-076

A STUDY OF MICROSTRUCTURAL CHARACTERISTICS AND DIFFERENTIAL THERMAL ANALYSIS OF Ni-BASED SUPERALLOYS

Introduction

The purpose of this investigation is to study the microstructural characteristics of Ni-based superalloy MAR-M246(Hf) which is used in manufacturing the components of the space shuttle main engine. These superalloys are heat treated prior to their use. The heat treatment should be optimum to get the best performance. To find out the optimum heat treatment, the techniques of differential thermal analysis and optical photomicrographs are being utilized. Ni-based superalloys can be considered as "chemical stew" containing as many as 14 different elements.[1] Nickel serves as an ideal base for such alloys because of its high melting point, 1453°C, adequate corrosion resistance and ability to dissolve a number of other metallic elements which serve to strengthen it. The various elements go into the solid solution to provide different effects: Molybdenum, tantalum, and Tungsten go in to the alloy for strength; chromium, aluminum and tungsten add to oxidation resistance and γ' phase.

Differential thermal analysis (DTA) is a technique which continues to aid in defining the phase changes that occur in superalloys and is undoubtedly of considerable value to the metallurgist studying these complex systems. The effect of changes in major elements are easily determined. The DTA technique has proved to be a valuable technique for the superalloy metallurgist to study liquidus-solidus data, carbide precipitation reactions, γ' solvus temperatures and incipient melting temperatures.[2]

The width of the solidification range is an important casting parameter and has the controlling effect in the process of directional solidification. In a simple system, the equilibrium value of this quantity can be determined from the equilibrium diagram, but in more complicated systems like these, superalloys containing 12 to 14 elements, only approximate estimates can be obtained. In the present paper, we discuss a method of predicting the solidus and liquidus temperatures based on the additive effects of the components dissolved in nickel and the results are compared with the experimental results obtained from the DTA curves for various Ni-based superalloys such as MAR-M246(Hf), MAR-M247, Waspaloy, Udimet-41, polycrystalline and single crystals of CMSX-2 and CMSX-3.

Prediction of Solidification Range

For highly diluted systems as in Ni-based superalloys, Hayes and Chipman[3] gave a relation for the change of the melting point ΔT of the parent metal M after adding a small amount of component B:

$$\Delta T=(1-k_{0,B})\,N_{L,B}\,(T_M)^2/\Delta H_M \qquad (1)$$

where $k_{0,B}$ is the equilibrium distribution coefficient of component B in the parent metal M, ΔH_M is the heat of melting, T_M is the melting point of metal M (K), $N_{L,B}$ is the molar fraction of component B dissolved in the liquid phase of metal M, and R is the constant ($8.314\,J\,K^{-1}\,mol^{-1}$).

The equilibrium distribution coefficient $k_{0,B}$ is defined as T = constant by the relationship

$$k_{0,B} = N_{S,B} / N_{L,B} \tag{2}$$

where $N_{S,B}$ is the molar fraction of component B in the solid solution based on metal M.

For highly diluted solutions, the liquidus and solidus curves can be replaced by straight lines (Fig. 1) and the solidification range of the solution M-B, denoted by $I_B = T_{L,B} - T_{S,B}$, can be expressed by the relationship

$$I_B = (1-k_{0,B})\ \Delta T/k_{0,B} = (1-k_{0,B})^2\ T_M{}^2\ R\ N_{L,B}/k_{0,B}\ \Delta H_M . \tag{3}$$

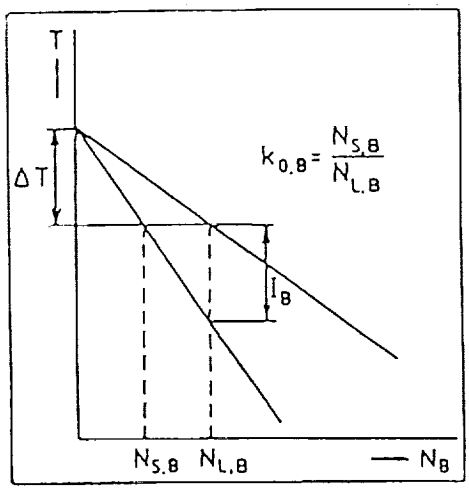

Fig. 1 Equilibrium diagram

If the metal is represented by nickel, Eq. (3) can be written in the form

$$I_B = 832.3\ (1-k_{0,B})^2\ c_B/k_{0,B}\ M_B \tag{4}$$

where c_B is the concentration of component B in weight percent, M_B is the molecular mass of component B, and I_B is in degree Celsius. If we assume the mutual independence of the effect of the components on the change of the melting point of parent metal M, the equilibrium solidification range I can be written as

$$I = \sum_B I_B . \tag{5}$$

Differential Thermal Analysis

In the differential thermal analysis (DTA) method, a reference sample and the sample under test are heated at a certain rate in a specific temperature range. The reference should exhibit no transformations within the temperature range of interest. The temperature of the sample and reference are monitored separately and the thermocouples measuring the temperature are connected in opposite polarity to measure the temperature differential ($\Delta T = T_{sample} - T_{reference}$). ΔT is amplified and then fed to Thermal Analysis Data Station (Perkin Elmer DTA 1700) which displays a plot of ΔT versus T for any sample. A schematic diagram of the DTA apparatus is shown in Fig. 2. Silver (melting point :

961 C) and nickel (melting point : 1455 C) are used to calibrate the instrument reasonably near our temperatures of interest. Sample holders/crucibles are 6 mm^3 cups made up of high density high purity alumina. Thermograms are stored in the computer's memory as well as displayed on the monitor which can be stored on floppy disks for later analysis. DTA curves of the various nickel based superalloys viz., MAR-M246(Hf), MAR-M247, Waspaloy, Udimet-41, polycrystalline and single crystals of CMSX-2 and CMSX-3 are compared with the calculated values using Eq. (5) neglecting the mutual interaction of the components.

Results and Discussion

Fig. 3 shows a typical DTA curve from which the values of solidus and liquidus can be determined. The onset for Ni-based superalloy UD-41 is 1293.8 C which represents the solidus and the minimum which represents the liquidus is at 1345.3 C. The solidification range is thus determined to be 52.5 C. Table 1 lists the values of c_B, $k_{0,B}$ and the solidification range of this alloy using Eq. (4). Table 2 lists the solidification range as obtained from DTA measurements and calculated using Eq. (5) for the other superalloys. The values for UD-41 are in better agreement than for the other superalloys. Further analysis of the data is in progress and will be reported elsewhere.

Acknowledgments

The authors wish to thank Mr. Richard J. Quigg, Vice-President of Cannon-Muskegon Corporation for providing us polycrystalline samples of CMSX-2 and CMSX-3. Thanks are due to Mr. Gregory Bell of Howmet Corporation for providing single crystal samples of CMSX-2 and CMSX-3. We also thank Mr. Sam O. Mancuso of Special Metals Corporation for providing us with samples of MAR-M247, UD-41 and Waspaloy. Thanks are also due to Dr. Bill Bhat, NASA/MSFC for useful discussion during the progress of this work.

References

1. Sims, C.T.; Stoloff, N.S. and Hagel, W.C., Eds. Superalloys (John Wiley, New York, 1987).

2. Wendlandt, W.W., Thermal Analysis (John Wiley, New York, 1986).

3. Hayes, A. and Chipman, J., Trans. AIME, 1939, 135, 85.

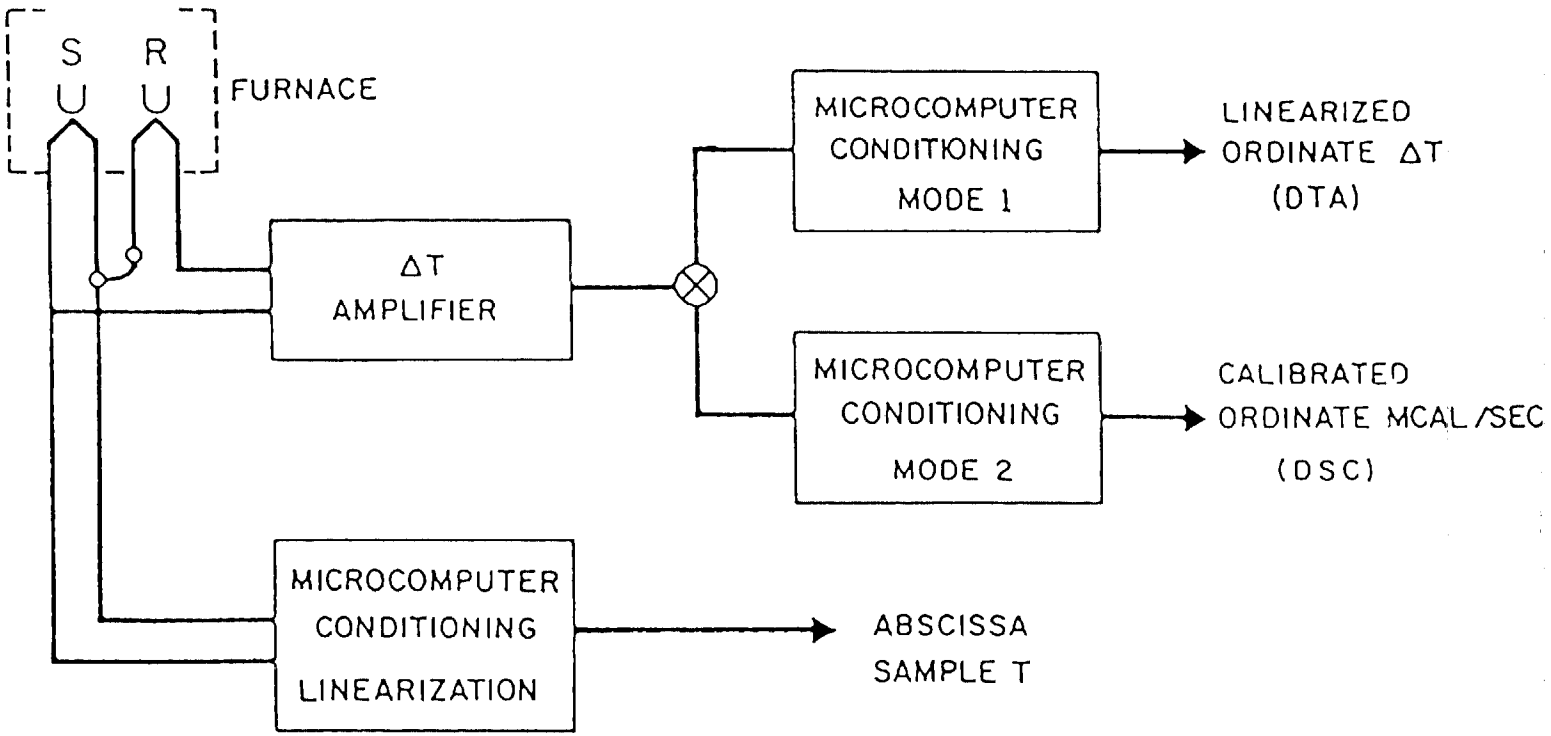
S
R
FURNACE
ΔT
AMPLIFIER
MICROCOMPUTER
CONDITIONING
MODE 1
LINEARIZED
ORDINATE ΔT
(DTA)
MICROCOMPUTER
CONDITIONING
MODE 2
CALIBRATED
ORDINATE MCAL/SEC
(DSC)
MICROCOMPUTER
CONDITIONING
LINEARIZATION
ABSCISSA
SAMPLE T

Figure 2.

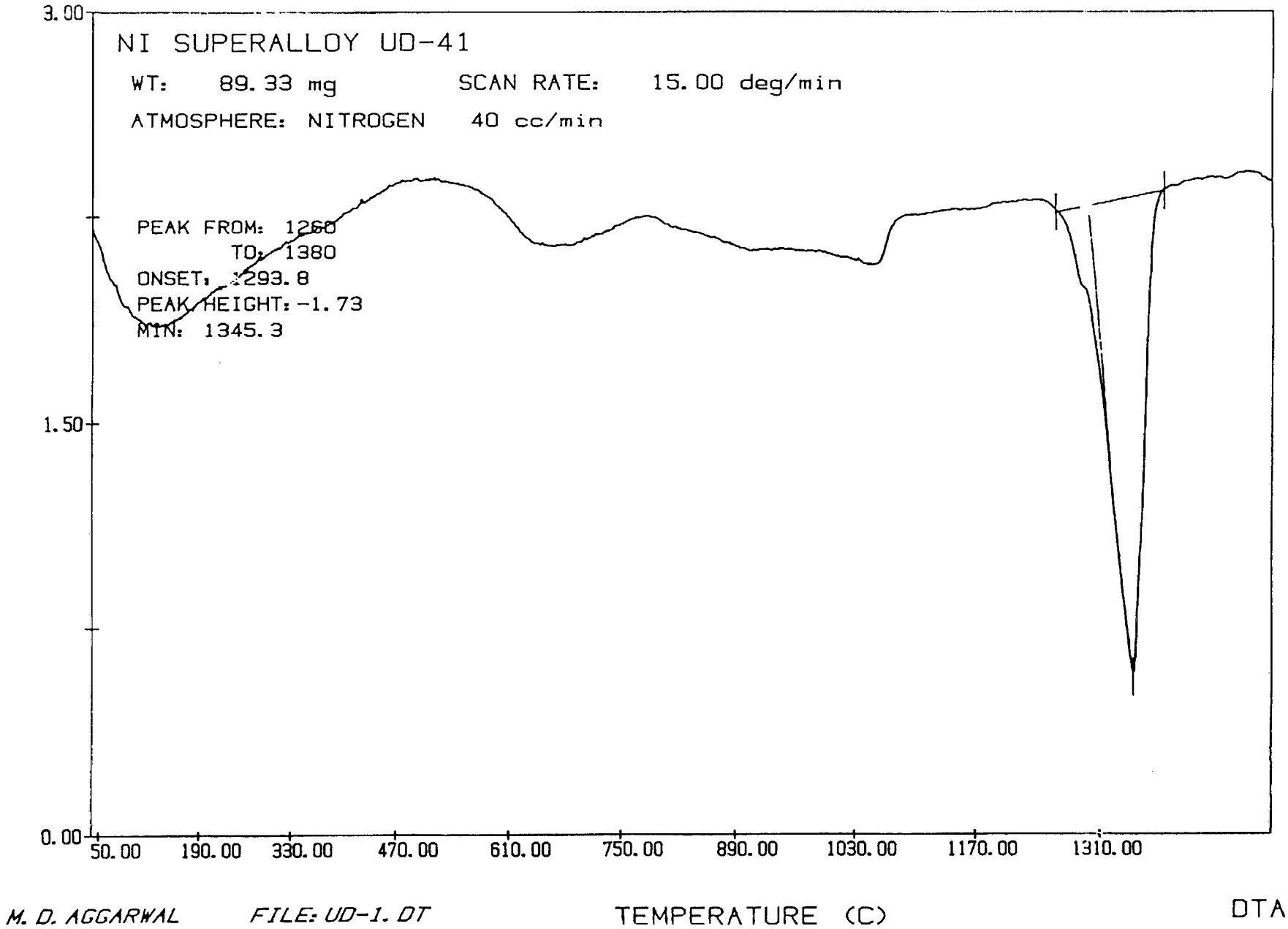
NI SUPERALLOY UD-41
WT: 89.33 mg
SCAN RATE: 15.00 deg/min
ATMOSPHERE: NITROGEN 40 cc/min
PEAK FROM: 1260
TO: 1380
ONSET: 1293.8
PEAK HEIGHT: -1.73
MIN: 1345.3
3.00
1.50
0.00
50.00
190.00
330.00
470.00
610.00
750.00
890.00
1030.00
1170.00
1310.00
M. D. AGGARWAL
FILE: UD-1.DT
TEMPERATURE (C)
DTA

Figure 3.

TABLE 1
Ni-based Superalloy UD-41

Element	C_B	$k_{0,b}$	M_b	Solidification range
C	0.08	0.22	12.01	15.33
Mn	0.10	0.72	54.94	0.16
Si	0.10	0.36	28.08	3.37
Cr	18.70	0.82	51.99	11.83
Ni	Bal	1.00	58.70	
Co	10.80	1.03	58.93	0.14
Mo	9.80	0.89	95.94	1.16
Ti	3.21	0.73	47.90	5.57
Al	1.59	0.87	26.98	0.95
Zr	0.07	0.09	91.22	6.20
P	0	0.01	30.97	8.85
Cu	0.01	0.82	63.55	0.01
Ta	0.01	0.74	180.95	0.00
			Total I	53.58

From DTA Curve

TS = 1293.8 C
TL = 1345.3 C

Diff. = 52.5 C

TABLE 2
Comparison of Experimental and Calculated Values of the Solidification Range.

Ni-based Superalloys	Solidification Range	
	Experimental (DTA)	Calculated (Eq.5)
UD-41	52.5 C	53.58 C
Waspaloy	40.3 C	52.49 C
CMSX-2 (Polycrystal.)	33.4 C	26.07 C
CMSX-3 (Polycrystal.)	39.8 C	26.315 C
CMSX-2 (single crystal)	32.9 C	25.97 C
CMSX-3 (single crystal)	36.2 C	25.95 C
MAR-M246(Hf)	44.4 C	56.31 C

N91-28116

SUBCOOLED FREON-11 FLOW BOILING IN TOP-HEATED FINNED COOLANT CHANNELS WITH AND WITHOUT A TWISTED TAPE

Alvin Smith and Ronald D. Boyd, Sr.
Department Of Mechanical Engineering
P.O. Box 397
Prairie View A&M University
Prairie View, Texas

ABSTRACT

An experimental study has been conducted in top-heated finned horizontal tubes to study the effect of enhancement devices on flow boiling heat transfer in coolant channels.The objectives of the present work are to: (1) examine the variations in both the mean and local (axial and circumferential) heat transfer coefficients for circular coolant channels with spiral finned walls and/or spiral fins with a twisted tape, and (2) improve the data reduction technique of a previous investigator. The working fluid is freon-11 with an inlet temperature of 22.2°C (approximately 21°C subcooling). The coolant channel's exit pressure and mass velocity are 0.19 M Pa (absolute) and 0.21 Mg/m^2s, respectively. Two tube configurations were examined; i.e., tubes had either 6.52 (small pitch) or 4.0 (large pitch) fins/cm of the circumferential length (26 and 16 fins, respectively). The large pitch fins were also examined with a twisted tape insert. The inside nominal diameter of the copper channels at the root of the fins was 1.0 cm.

The results show that by adding enhancement devices, boiling occurs almost simultaneously at all axial locations. The case of spiral fins with large pitch resulted in larger mean (circumferentially averaged) heat transfer coefficients, h_m, at all axial locations. Finally, when a twisted tape is added to the tube with the large-pitched fins, the power required for the onset of boiling is reduced at all axial and circumferential locations.

SUBCOOLED FREON-11 FLOW BOILING IN TOP-HEATED FINNED COOLANT CHANNELS WITH AND WITHOUT A TWISTED TAPE

Nomenclature

A_c	Cross sectional area, m^2	N	Number of fins per test section
A_s	Surface area, m^2	p	Static exit pressure, $M\,Pa$
CHF	Critical heat flux, W/m^2	q	Heat flux W/m^2
D	Tube diameter, cm	r	Radial coordiante for data reduction model, m
D_h	Heated hydraulic diameter, m	R	Tube radius, cm
G	Mass velocity, kg/m^2s	T_f	Bulk temperature of the flowing fluid, ^oC
h	Local heat transfer coefficient, $W/m^{2o}C$	T_m	Local measured outside wall temp. of the tube, ^oC
h_m	Mean heat transfer coefficient, $W/m^{2o}C$	T_s	Local inside wall temp. of the tube, ^oC
H	fin height	T_{sat}	Saturation temperature, ^oC
K	Thermal conductivity, $W/m\,K$	T_∞	Ambient temperature, ^oC
L	Heated length of test section, m	Z	Axial coordinate for heated portin of test section, cm

Greek Letters

ρ Density, kg/m^3; φ Circumferential coordinate; π Half of a full rotation or 180 ^{o}(bottom of test section)

Introduction

Subcooled flow boiling (locally boiling fluid whose mean temperature is below its saturation temperature while flowing over a surface exposed to a high heat flux) has the greatest potential of accommodating high heat fluxes [1]. In space, the active cooling of cold plates, turbine blades, fusion reactor components, chemical reactor components, electronic components, refrigeration systems components, and other systems necessary for the successful commercialization of space will require an efficient heat transfer system. Therefore, the need to understand the behavior of two-phase flow boiling in both the space (zero-g or reduced-g) and earth environments is essential to thermal designers, especially where pumping power requirements must be optimized. Since thermal designers are forced on occasion to use data from uniform heat flux applications for non-uniform heat flux applications, it is important to assess the effect of the non-uniformity on the local and mean heat transfer.

Ideal heat transfer is achieved when the sum of the component thermal resistances is reduced to a minimum. However, flow dynamics through plain tubes rarely provides the ideal conditions needed, because the stationary fluid layer at the tube wall leads to the buildup of a slow moving laminar boundary layer caused by frictional drag forces. This results in heat transfer being principally controlled by fluid conductivity and the thickness of this layer.

Research related to enhanced surfaces for heat transfer has increased in recent years [2]. The immediate benefit from recent research has led to increasing efficiency of heat exchanges and to the development of the spirally fluted tube [3]. Fins (sometimes called extended surfaces) are often used to increase heat transfer rates to fluids in cases where low heat transfer coefficients exist. If the wall temperature is sufficiently high to cause film boiling and all other resistances are small, fins will cause an increase in the heat transfer rates in a boiling situation [4]. Examples include cooling of nuclear fuel

rods, cooling of electrical equipment such as radio-power tubes, and some evaporators. Devices for the establishment of fluid swirl are often used to increase heat transfer in tube flows. The increase in pressure drop, however, is less than the increase in heat transfer in many cases. Twisted tape inserts have been studied by Hong and Bergles [5], who found that in laminar flow, heat transfer could be increased by a factor of as much as 9 whereas pressure drop increased by a factor of less than 4 over empty tube values. In turbulent flow, twisted tape inserts can improve heat transfer by a factor of 2 over empty tube values, but the pressure drop is increased by several orders of magnitude. Brown Fintube Company reported in its literature that increases in heat transfer rate of up to 300 percent have been achieved in viscous fluids with nominal increases in pressure drop with the addition of twisted tapes.

Experimental Investigation

The flow loop (Figure 1) is a closed system designed to control the working fluid (freon-11) and reservoir temperatures, pressures, heating capabilities, and overall system stability. The reader is referred to references 6-8 for detailed descriptions of the experimental flow loop, procedures, and data acquisition.

The loop was designed to study both saturated and subcooled flow boiling, although only subcooled flow boiling was considered here. By allowing both saturated and subcooled flow regimes, the heat rejection can be either isothermal or at a slightly variable axial temperature. The latter case (subcooled flow boiling) will result in enhanced heat rejection capability (above the saturated case) to the extent that the given application will allow a variable axial temperature.

Referring to Figure 1, the reader should be made aware of the possible circulation patterns of the working fluid that can be accomplished by opening and closing various valves within the loop. However, for the tests performed within this investigation, only reservoir #1 was utilized.

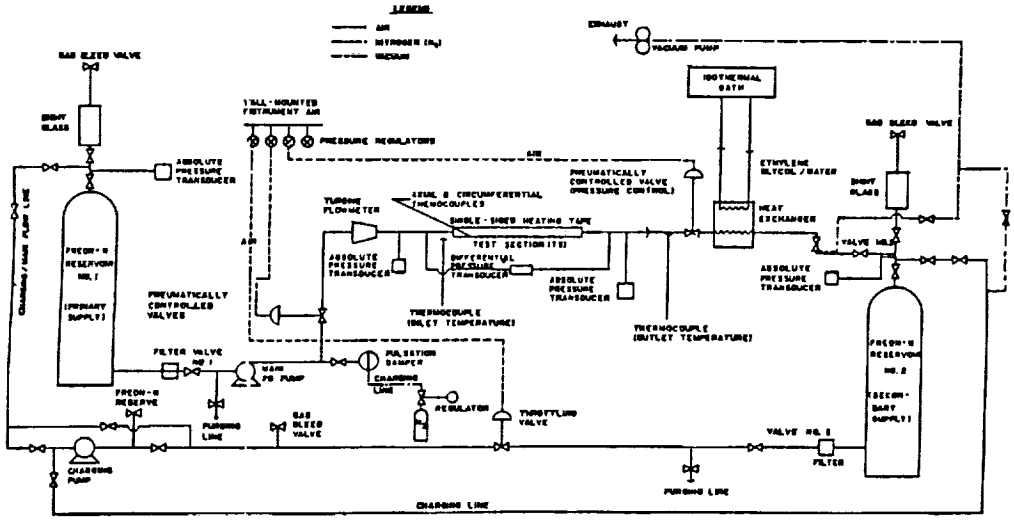

Figure 1. Freon-11 flow loop for both subcooled and saturated flow boiling experiments.

The measured outside wall temperatures of the test sections were used to calculate the unknown heat transfer coefficient, h. This was achieved through a data reduction technique developed by Turknett and Boyd [7], based on the heated hydraulic diameter, D_h. This approach will result in, at most, a qualitative indication of the local (axial and circumferential) distribution of h. A piece-wise linear profile method was used to evaluate the mean (circumferentially averaged) distribution of h_m. A finite difference technique (although not used for the present work) was developed to evaluate the local h [8].

Results

The results are presented for the case of subcooled freon-11 boiling in top-heated horizontal channels with internal fins and/or twisted tape inserts.

Figure 2 shows the circumferential variations in the heat transfer coefficient at the axial location Z_4 (center of the heated portion of the test section). It is evident that the variations in heat transfer coefficients in the circumferential location are increased by adding more enhancement devices. The spiral fin with large pitch shows no variations in the single phase region located at the bottom ($\frac{3\pi}{4}$ and π) of the tube, and minor variations at the top (0 and $\frac{\pi}{4}$) of the tube in the film boiling region. Adding a twisted tape (spiral fin large pitch tape) decreased variations in heat transfer coefficients in the film boiling region (0 and $\frac{\pi}{4}$), but increased the variations in the single phase region ($\frac{3\pi}{4}$ and π). The spiral fin small pitch shows the largest variation of h in the single phase region ($\frac{3\pi}{4}$ and π) and only a minor variation in the film boiling region (0 and $\frac{\pi}{4}$).

The axial variation of h as a function of power for the three (3) cases is presented in Figure 3. The axial locations Z_1 and Z_7 are excluded due to end losses and the effect of axial conduction. At circumferential location 0 (top of the tube), the onset of boiling appears to occur more uniformly along the length of the channels than at circumferential location $\frac{\pi}{4}$. At circumferential location $\frac{\pi}{4}$, the spiral fin large pitch (3a.2) provides higher heat transfer coefficients than any case presented. By adding a twisted tape to the large pitch tube, the power required for the onset of nucleate boiling was reduced at all axial and circumferential locations, but the average heat transfer coefficients were reduced (Figure 3b.2). The spiral fin small pitch tube at circumferential location $\frac{\pi}{4}$ (Figure 3c.2), provided a more uniform onset of boiling in the axial direction than the tubes with large pitch or large pitch with a twisted tape insert. However, at circumferential location 0, the tube with twisted tape had a more uniform onset of nucleate boiling. The average axial heat transfer coefficients at circumferential location 0 (top of the tube) were higher for the case of the tube with a small pitch than the other cases (spiral fin large pitch and spiral fin large pitch with tape), but were found considerably lower at circumferential location $\frac{\pi}{4}$ for the same cases.

Figure 4 is a plot of the mean (circumferentially averaged) heat transfer coefficient h_m, as a function of power. The averaged h (i.e., h_m) appears to be consistently higher for the case of the spiral fin large pitch (4a) than the cases with a tape (4b) and small pitch (4c). In some cases, the addition of the tape to the spiral fin large pitch reduced the average heat transfer coefficients in the axial direction. However, adding a twisted tape or reducing the pitch of the fins caused boiling to occur more uniformly over the length of the test section. Heat transfer coefficients literally remained unchanged in the spiral pitch tube (4c) in the axial direction when compared with Figure 3.

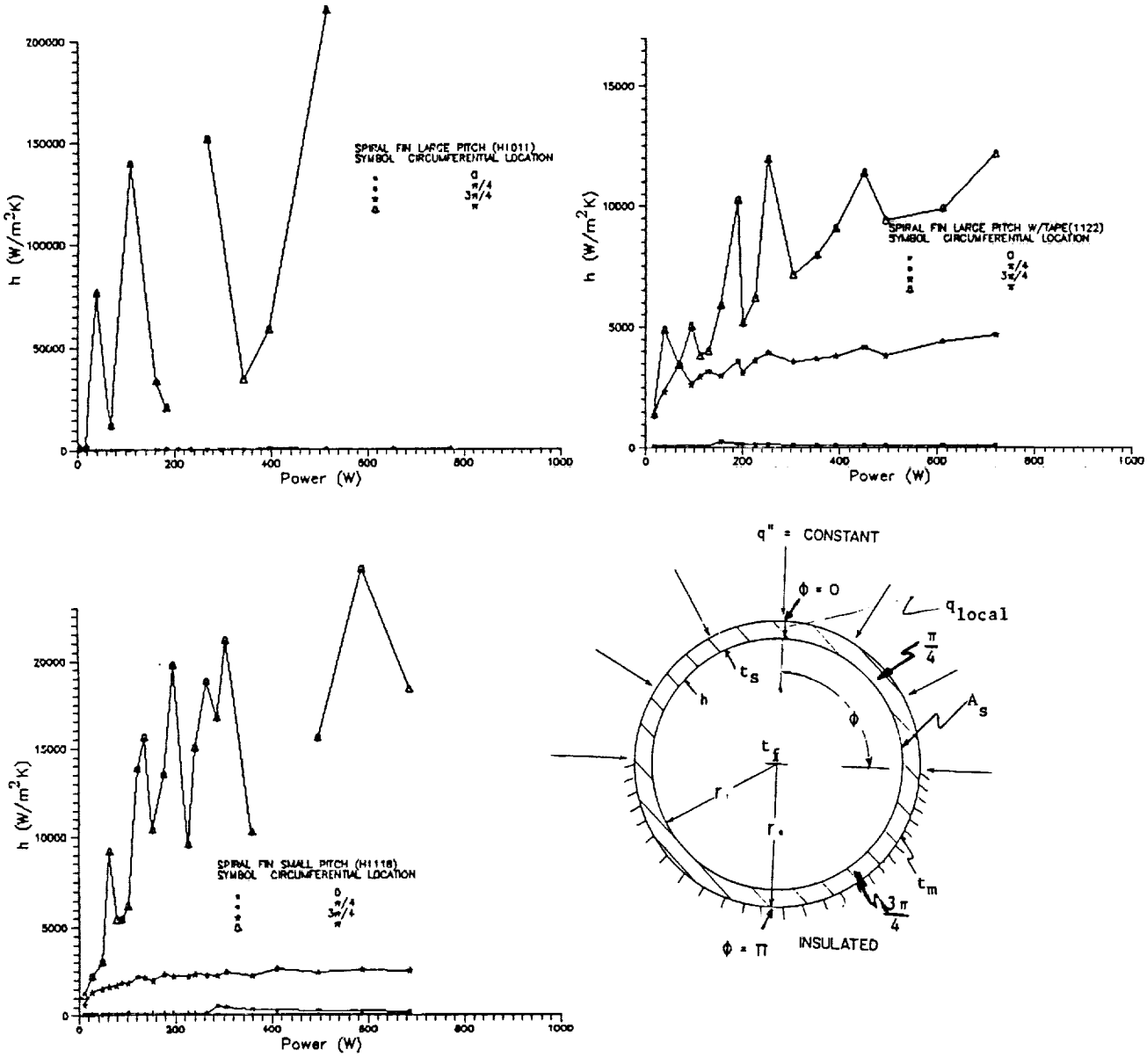

Figure 2. Heat transfer coefficient versus power at axial location $Z = Z_4$ (center of heated section of the test section) for top-heated finned tubes at 0.19 MPa and 0.210 Mg/m^2s. Channel diameter = 1.27 cm, Heated length = 1.22 m.

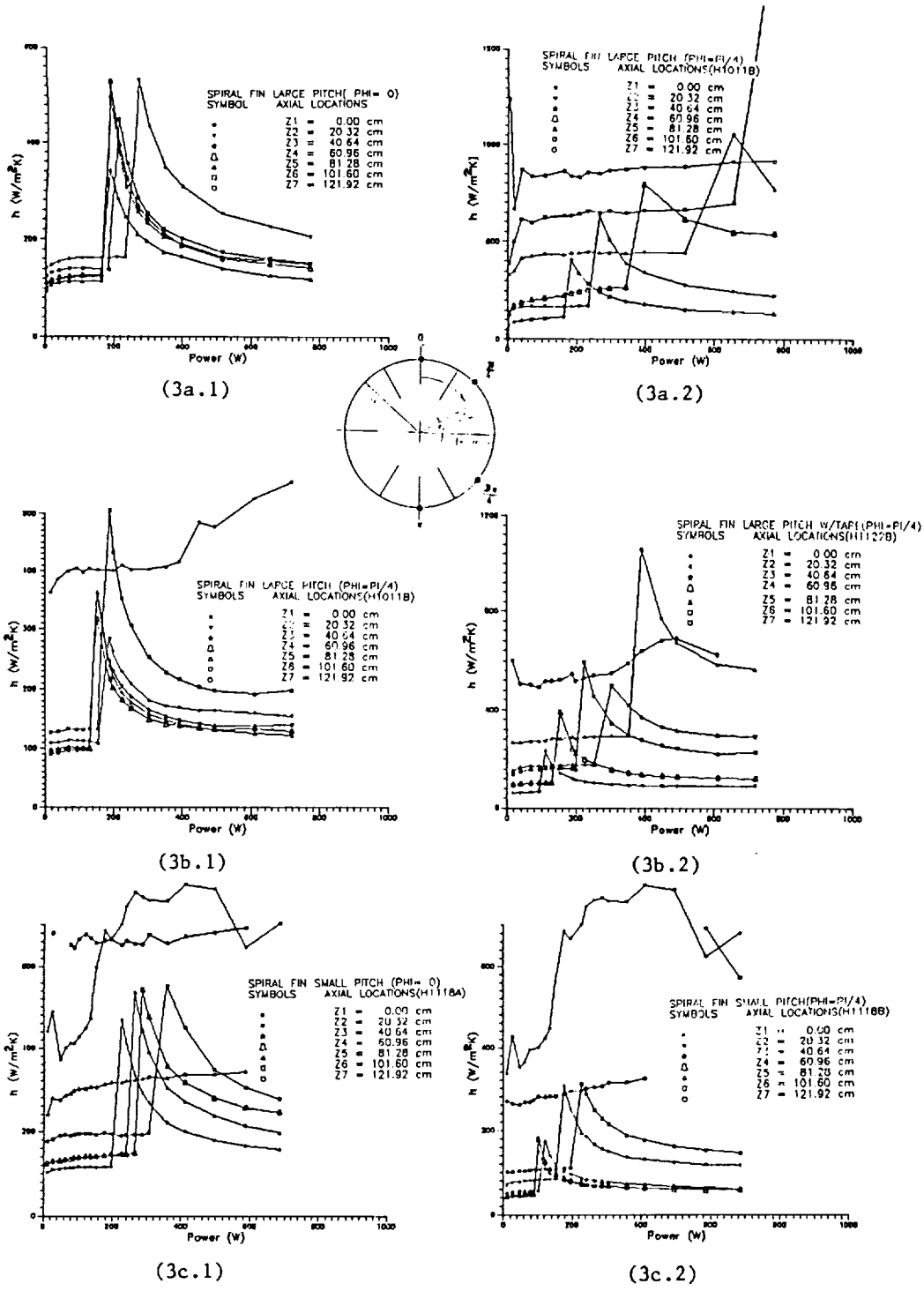

Figure 3. Axial variations of h versus power at circumferential locations 0 and $\frac{\pi}{4}$ for spiral fin large pitch (3a), spiral fin large pitch with tape (3b), and spiral fin small pitch (3c).

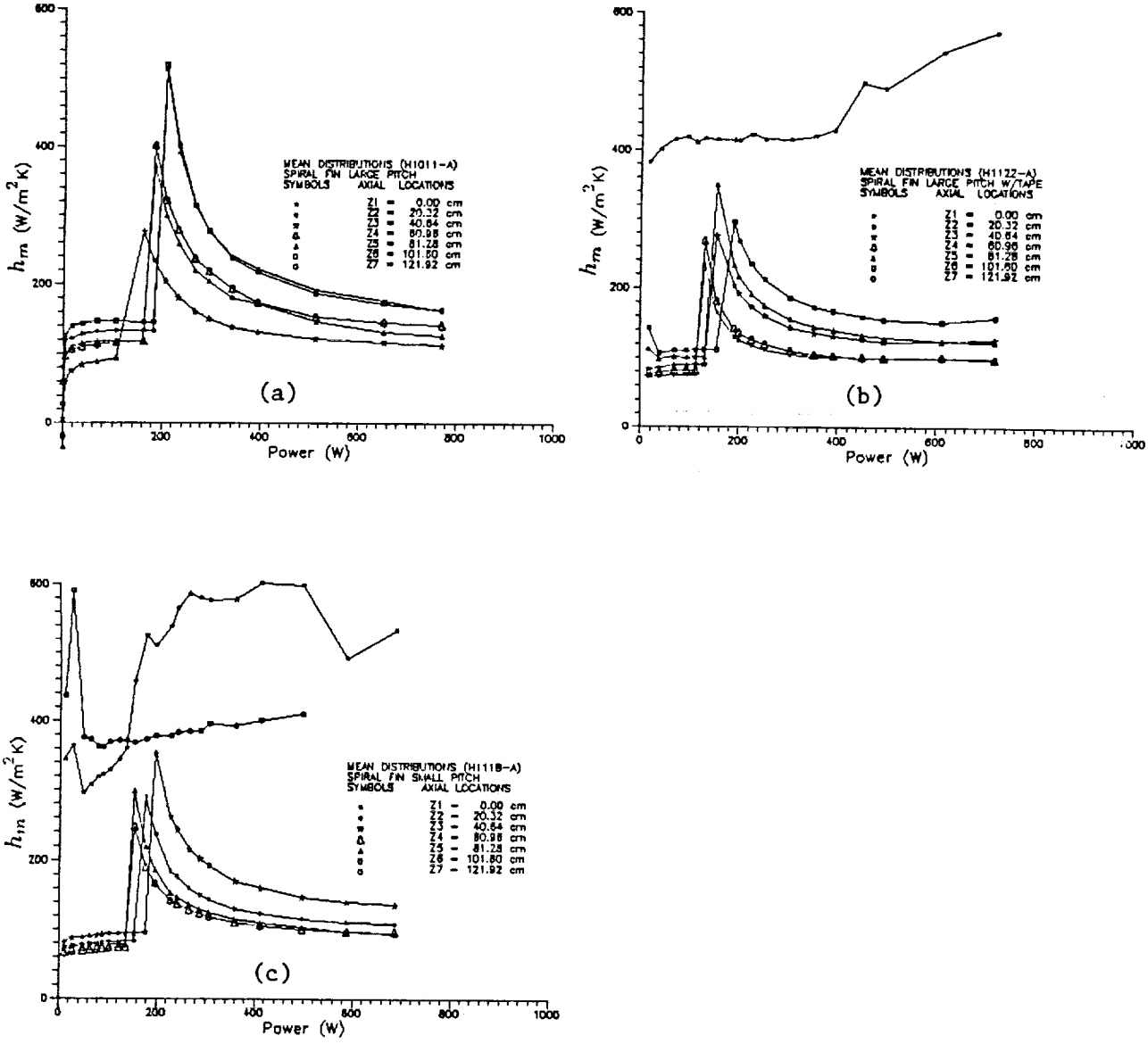

Figure 4. Mean heat transfer coefficient versus power for spiral fin large pitch (4a), spiral fin large pitch with tape (4b), and spiral fin small pitch (4c).

Acknowledgments

Support for this study was provided by Sandia National Laboratories and NASA (JSC). The authors would like to thank the personnel at these facilities for their support.

References

1. Boyd, R.D., "Subcooled Flow Boiling Experiments Using Small Diameter Uniformly-Heated Tubes," ASME, 86-HT-23, AIAA/ASME 3th Joint Thermophysics and Heat Transfer Conference, Boston, Mass., June, 1986.

2. Bergles, A.E., and Webb, R.L., "A Guide to the Literature on Convective Heat Transfer Augmentation," **Advances in Enhanced Heat Transfer - 1985**, ASME Publication, HTD-Vol. 43, 1985, pp. 81-89.

3. Panchal, C.B., et al., "A Spirally Fluted Tube Heat Exchanger as a Condenser and Evaporator," Proc. 4th Miami Intl. Symp. on Multi-Phase Transport and Particulate Phenomena, Dec. 1986.

4. Burmeister, L.C., **Convective Heat Transfer**, John Wiley & Sons, New York, 1983, pp. 615-616.

5. Hong, S.W. and Bergles, A.E., "Augmentation of Laminar Flow Heat Transfer in Tubes by Means of Twisted-Tape Inserts," Journal of Heat Transfer, Trans. ASME, Vol. 98, May, 1976, pp. 251-256.

6. Boyd, R.D., "Flow Boiling With and Without Enhancement Devices for Horizontal, Top-Heated Coolant Channels for Cold Plate Design Applications, Preliminary Report," Department of Mechanical Engineering, Prairie View A&M University, Prairie View, TX., Submitted to NASA(JSC), Contract No. 9-16899 (Task-5), December, 1986.

7. Boyd, R.D. and Turknett, J.C., "Forced Convection and Flow Boiling With and Without Enhancement Devices for Top-Side-Heated Horizontal Channels," Department of Mechanical Engineering, Prairie View A&M University, Prairie View, TX., (presented at these proceedings).

8. Smith, A., "Subcooled Freon-11 Flow Boiling Heat Transfer With and Without Enhancement Devices for Top-Heated Horizontal Tubes," MS Thesis, Department of Mechanical Engineering, Prairie View A&M University, Prairie View, TX., (to be published).

XeCl LASER PUMPED IODINE LASER USING t-C_4F_9I

In H. Hwang and Kwang S. Han
Department of Physics
Hampton University
Hampton, VA

ABSTRACT

An iodine photodissociation laser using t-C_4F_9I as the active material was pumped by an XeCl laser. An iodine laser output energy of 3 mJ with pulse duration of 25 ns was obtained when the pumping pulse energy was 80 mJ, the iodide pressure was 70 torr, and the reflectance of the output mirror was 85%. The high pumping efficiency and low threshold pump power achieved in this experiment are attributable to the high absorption cross section at the pump laser wavelength (308 nm) of the iodide used.

XeCl LASER PUMPED IODINE LASER USING t-C_4F_9I

I. Introduction

Since the atomic iodine photodissociation laser was discovered by Kasper and Pimentel in 1964 [1], numerous research efforts have been concentrated on this laser to increase the power level needed for laser fusion [2,3]. The fusion-experiment-oriented iodine laser is constructed in a master-oscillator-power-amplifier (MOPA) architecture [4].

The iodine laser is also being considered as a direct solar pumped laser for space applications such as the laser propulsion for an orbital transfer vehicle. The first solar simulator pumped iodine laser was reported in 1981 by Lee, et. al. [5]. This laser was operated in quasi-continuous-wave mode. After this report, various iodine compounds were tested and evaluated as candidates for direct solar pumped laser materials [6,7,8].

Although many space applications are best served by a continuous wave (CW) laser, a continuously pulsed laser also has good applicability in space, especially for laser propulsion. If weak pumping (such as solar radiation pumping) of laser materials exists, use of a MOPA system is essential for obtaining high peak power when the laser material has a long upper-state lifetime like an iodine atom. In previous research, the feasibility of the oscillator-amplifier scheme was proposed and tested for the solar pumped iodine laser [7.9].

In order to be incorporated in the MOPA system, the iodine laser oscillator must generate temporally smooth and short pulses. In the fusion-oriented-iodine-laser-experiment the short pulse is provided by mode-locking of the flashlamp-pumped oscillator. However, the repetition rate of the flashlamp-pumped oscillator is usually very low (<5Hz), and the mode-locking devices are generally complicated. An excimer laser pumped iodine laser oscillator was demonstrated by Fill et. al. [10]. In their experiment, a 500-mJ excimer laser was used for the pumping of the iodine laser, and a temporally smooth laser pulse with duration from 2.6 ns to 12 ns was obtained by using i-C_3F_7I as the laser material.

In this report, a XeCI laser pumped iodine laser using t-C_4F_9I is described. This laser oscillator has much a higher efficiency and a lower threshold pump power than the system using i-C_3F_7I. The laser output energy dependence on the gas-filled pressure and on the reflectance of the output mirrors are measured for both longitudinal and transverse pumping.

II. XeCI Excimer Laser

A laboratory built XeCI laser was used for the pumping of the iodine laser in this experiment. The electrical circuit of the XeCI laser is shown in Fig. 1. A pyrex tube with an I.D. of 0.1 m and a length of 0.66 m was used as the laser chamber. The two brass electrodes were rounded in order not to develop an arc discharge in the discharge volume. The width of the electrodes was 20 mm, and the length was about 0.45 m. The separation between the two electrodes was 20 mm. Seventeen pairs of arc arrays were located beside the electrodes so that the discharge volume could be preionized uniformly. The optimized gas composition was HCI: Xe: Ar: He = 0.2% : 5.9% : 19.5% : 74.4% at a total pressure of 2 atm. The addition of argon gas improved the discharge uniformity at the higher operating voltage.

When the XeCI laser was operated at the charging voltage of 25 kV, the output energy was 80 mJ per pulse. If the charging voltage was increased, the output energy also increased, but an arc discharge developed between the electrodes. Thus, operation above 25 kV was not pursued. A typical laser pulse is shown in Fig. 2. The half width (FWHM) of the XeCI laser pulse was about 25 nsec, and no significant variation of the laser pulse was found for prolonged operation.

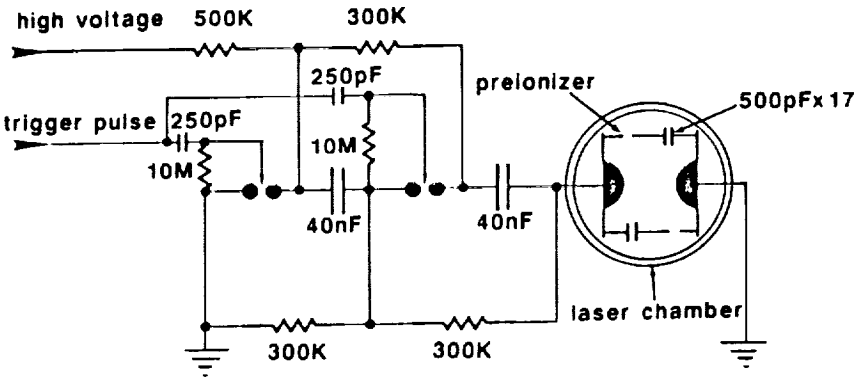

Figure 1
Electrical circuit diagram of the XeCI excimer laser.

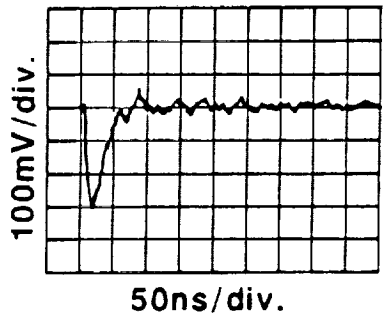

Figure 2
A typical pulse shape of the XeCI laser output.

III. Iodine Laser Experiment

The iodide used in this experiment was t-C_4F_9I (perfluoro-tertiary-butyl iodide). This material was chosen mainly due to the absorption cross section at the wavelength of XeCl laser light (308 nm). The published data show that the absorption cross section of t-C_4F_9I at 308 nm is about 3.6 x 10 -10 cm^2 [7]. Also, t-C_4F_9I has shown good chemical reversibility in a flashlamp-pumped system [6,7], and thus the iodine molecule buildup in the laser cell is minimized. The main disadvantage of this iodide is the low vapor pressure ($\approx$85 torr) at room temperature. The other chemical kinetic properties are nearly the same or better than other commonly used perfluoralkyl iodides in the flashlamp-pumped experiment [7]. The quantum yield of excited atomic iodine in the UV photodissociation is nearly unity [11].

A quartz cuvette with a square cross section of 1 cm^2 and length of 50 mm was used as the iodine laser cell. The windows of the laser cell were nearly perpendicular to the optic axis of the laser cell. Both longitudinal and transverse pumping of the iodine laser were employed.

When the iodine laser was pumped longitudinally, a dichroic mirror was used to introduce the XeCl laser light into the iodine laser cell. The dichroic mirror transmitted about 80% of the XeCl laser light and fully reflected the iodine laser light. The XeCl laser light was directed through the dichroic mirror and was focused into the center of the laser cell by a quartz spherical lens of focal length 0.2 m. When the iodine laser was pumped transversely, a quartz cylindrical lens of focal length 0.3 m was used to focus the XeCl laser light into the iodine laser cell.

The output energy dependence on the gas filled pressure at different output mirror reflectances is shown in Figs. 3 and 4. As shown in Fig. 3, there is an optimum iodide pressure for each output mirror reflectance for the longitudinal pumping. However, for the transverse pumping, the laser output energy increases monotonically with the t-C_4F_9I pressure as shown in Fig. 4 The results in Figs. 3 and 4 were taken when the laser was operated at 2-Hz repetition rate. When the pulse repetition rate was increased to 5 Hz, the laser output energy per pulse was reduced slightly ($\approx$10%) due to the reduction of the XeCl laser pumped energy.

A typical laser output is shown in Fig. 5. The half width (FWHM) of the pulse is about 25 nsec. The iodine laser onset is delayed from the XeCl pump laser and occurs at the end of the pump pulse. The pulse shape is nearly the same for both pumping geometries.

IV. Discussion

In this experiment, a XeCl laser pumped iodine laser was developed and tested by using t-C_4F_9I as the laser material. This lasant t-C_4F_9I has a larger absorption cross section at the XeCl laser line compared with other iodides used in the laser experiment, such as i-C_3F_7I. The larger absorption cross section allows the high utilization of pumping energy in short gain length and low pressure operation of the iodine laser. The low-pressure operation of the iodine laser is suitable for single longitudinal mode output because of the reduced pressure broadening of the gain profile. The single-longitudinal mode operation of the laser oscillator is necessary to obtain a temporally smooth pulse.

The iodine laser described in this report was operated up to 5 Hz, which was limited by the power supply of the XeCl laser. Further increase of the repetition rate can be made by scaling up the pump laser system. The iodine laser was operated in a sealed-off mode. There was no significant reduction of the laser output energy after a few hundred pumpings with a single fill t-C_4F_9I in the laser cell. There

was also no noticeable change in the t-C_4F_9I gas after a few hundred pumpings and no deposits on the wall of the laser cell (contrary to the report of Ref. 10 where t-C_3F_7I was used). This may be attributable to the superior chemical reversibility of the iodide used.

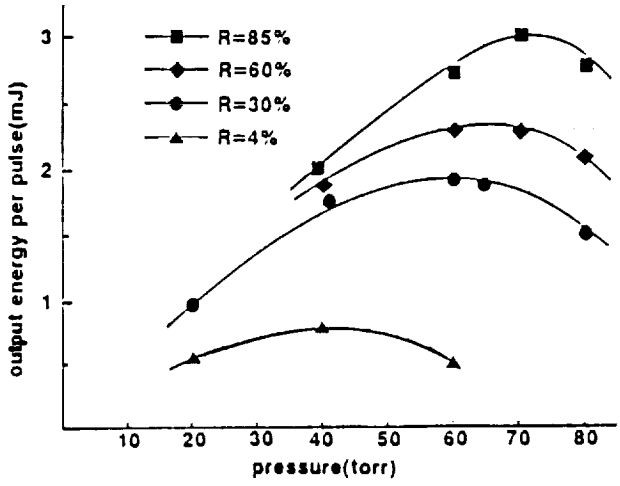

Figure 3 - Iodine output energy dependence on the gas fill pressure in the laser cell at each output mirror reflectance. The iodine laser was pumped longitudinally with the XeCI laser of pulse energy 80 mJ.

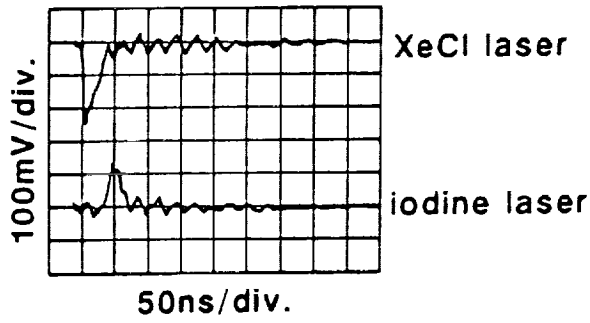

Figure 4 - Iodine laser output energy dependence on the gas fill pressure when the iodine laser was pumped transversely. The pumping energy from the XeCI laser was fixed to 80 mJ.

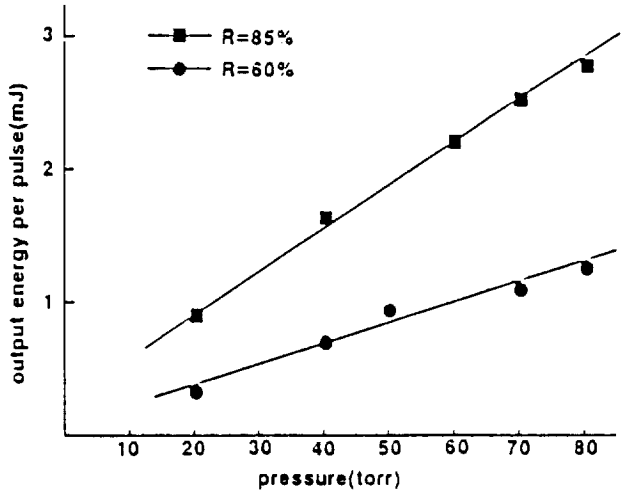

Figure 5 - A typical iodine laser pulse shape which is compared with the pumping pulse. (a) XeCl pump laser pulse. (b) Iodine laser output pulse.

V. Conclusion

An iodine laser oscillator pumped by an XeCl laser was developed using t-C_4F_9I as the laser material, and a 3 mJ laser output energy was obtained with only 80 mJ pumping energy. Compared with previous results, the pumping energy was dramatically reduced in this experiment, The pumping efficiency (i.e., the ratio of the iodine laser energy and the XeCl laser energy) was 3.75%. This experiment also demonstrated a repetitive operation of the iodine laser oscillator with a stable output. Since the threshold pumping energy (20 mJ) is low for t-C_4F_9I, a moderate size XeCl laser may suffice for the pumping of the high-repetition-rate laser oscillator required for solar pumped master-oscillator power-amplifier systems.

Acknowledgments

This work is supported by NASA grant NAG1-441.

References

1. J.V.V. Kasper and G.C. Pimentel, Appl. Phys. Lett. 5, 231 (1964).

2. G. Brederlow, E. Fill and K.J. Witte, "High-Power Iodine Laser," Springer-Verlag, New York, N.Y. (1983).

3. S.B. Kormer, Izvesteriya Akademii Nauk SSSR. Seriya Fizicheskaya 44, 2002 (1980).

4. K.J. Witte, Czech. J. Phys. B34, 790 (1984).

5. J.H. Lee and W.R. Weaver, Appl. Phys. Lett. 39, 137 (1981).

6. J.H. Lee, J.W. Wilson, T. Anderson, D.H. Hume, W.R. Weaver and B.M. Tabibi, Optics Comm. 53, 367 (9185).

7. B.M. Tabibi, M.H. Lee, J.H. Lee and W.R. Weaver, Proceedings of International Conference on Lasers' 86, pp 144-149 (1986).

8. R.J. Deyoung, IEEE. J. Quant. Electron. QE-22, 1019 (1986).

9. I.H. Hwang, J.H. Lee and M.H. Lee, Optics Comm. 58, 47 (1986).

10. E. Fill, W. Skrlac and K.J.K. Witte, Optics Comm. 37, 123 (1981).

11. A.B. Alekseev, A.M. Pravilov, I.I. Didorov and V.A. Skorohodov, Sov. J. Quantum Electron. 17, 1539 (1987).

CHARACTERIZATION OF QUANTUM WELL STRUCTURES USING A PHOTOCATHODE ELECTRON MICROSCOPE

M.G. Spencer
Department of Electrical Engineering
Howard University
Washington, D.C.

C.J. Scott
Naval Research Laboratory

Introduction

Present day integrated circuits pose a challenge to conventional electronic and mechanical test methods. Feature sizes in the submicron and nanometric regime require radical approaches in order to facilitate electrical contact to circuits and devices being tested. In addition, microwave operating frequencies require careful attention to distributed effects when considering the electrical signal paths within and external to the device under test. In this paper an alternative testing approach which combines the best of electrical and optical time domain testing will be presented, namely photocathode electron microscope quantitative voltage contrast (PEMQVC).

Comparison of Test Methods

High speed electrical characterization of microstructures using a stroboscopic quantitative voltage contrast electron beam probe has advantages over mechanical and optical methods. For comparison the photocathode electron microscope and other time domain test methods are listed in table 1.[1]. It can be seen that the PEMQVC offers superior spatial and temporal resolution at the expense of voltage accuracy. Electro-optic probing eliminates some of the spatial transition problems which can introduce considerable error in high frequency mechanical probe measurements. Alternatively, when characterizing micron scale structures, electron beam testing has the following advantages over the electro-optical method: 1) the spatial resolution of the electron beam is limited to the minimum primary gaussian electron beam current waist (typically $\geq$ 80A) as compared to the diffraction limited beam waist of monochromatic light (typically $\geq$ 1um), 2) the sampling media is not limited to materials with intrinsic birefringence such as GaAs and $LiTaO_3$ so that silicon, InP and other materials with low electroptic figures of merit can be tested, and 3) the necessity of gold coating and polishing the backside of the test sample is eliminated.

PEMQVC Components

A standard SEM is modified by: 1) replacing the conventional thermionic electron gun with a photo-excited electron gun, 2) enhancing the SE detector electrostatic environment to measure the energy spectrum of the scattered secondary electrons, and 3) providing feed-throughs for electrical signals. Schematic diagrams of a conventional SEM and the photocathode electron microscope are shown in Figure 1. The instrument can be used in a dual mode for either conventional SEM work or time domain characterization if the SEM conversion is done properly. A circuit can be examined for visual defects and then exercised at speed functionality evaluation. There are three different test modes the photocathode electron microscope can operate in: 1) static voltage contrast, 2) quantitative voltage contrast, and 3) stroboscopic voltage contrast.The first mode gives a qualitative indication of voltage levels on the sample. The second mode gives a quantitative voltage for the sample but no time domain information. The third mode gives both voltage and time quantitatively.

The photostated provides a picosecond electron source by photoemission of electrons using a frequency quadrupled Nd Yag (1.06 mm) laser source. A KDP crystal is used for the first frequency doubling stage and a BBO crystal is used for the second frequency doubling stage. BBO is an efficient second harmonic generation medium for the 532/266 nm doubling process. The emission surface is a 200A thick Au layer on a polished 40 mm Al_3O_2 substrate. The photo cathode is held at the primary electron acceleration potential (~ 1KV).

A Feuerbaum [2] or planar type detection scheme is used to quantize the SE spectral shift (Fig. 2). This type of analyzer simplifies the electrostatic field pattern analysis for detector refinement for achieving higher measured signal resolution. The retarding potential sets the lower limit of integration for the photomultiplier tube (PMT). The nonlinear photomultiplier tube (PMT) "S curve" currents are linearized using a computer controlled feedback loop to establish the required retarding potential to maintain a preset PMT output current. The retarding potential is equal to the sample potential. Temporal delay is implemented on the optical bench with a right angle prism on a sliding optical rail.

Summary

The electron beam testing apparatus will provide direct experimental verification for numerical simulations and a means of contactless probing of devices and interconnects at spatial and temporal resolutions not achievable by any other means. When the flexibility and high spatial resolution of the electron beam technique is combined with the inherent high speed capabilities of optical pulse generation, this contactless probing method may prove to be an essential tool in any integrated circuit research and development facility.

References

[1] G. Chiu, J. Halbout, and P. May, J. Vac. Sci. Technol. 6,1814 (1988)

[2] H.P. Feuerbaum, SEM/I, pp. 285-296, (1979)

	tr	Vr	x	Jitter
Superconductive	20ps	1uV/$\sqrt{hz}$	100um	5ps
Analog	25ps	7uV/$\sqrt{hz}$	100um	10ps
E-Beam Strobe	100ps	3mV/$\sqrt{hz}$	0.1um	10ps
E-Beam Photo	5ps	3mv/$\sqrt{hz}$	0.1um	5ps
E/O Sampling	5ps	5uV/$\sqrt{hz}$	3um	5ps

Table 1.
Time domain measurement comparison.

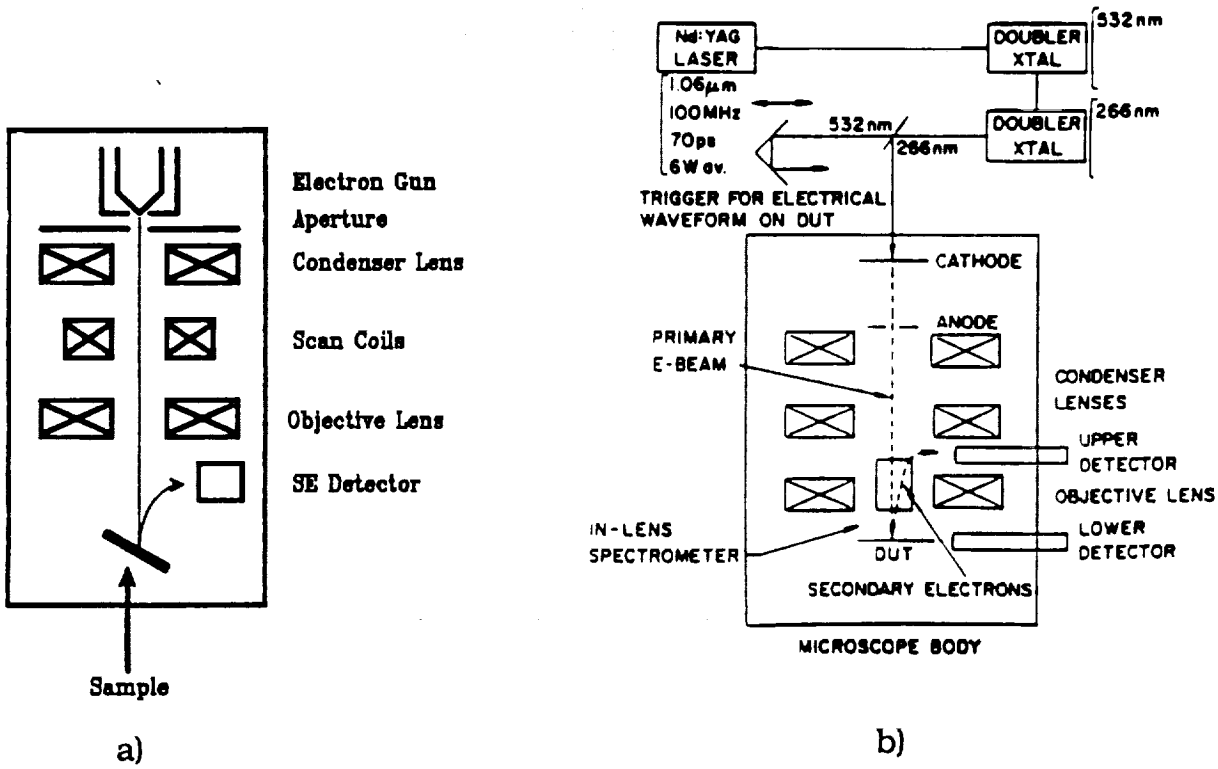

Figure 1.
Schematic diagrams of
a) a conventional SEM and
b) a photocathode electron microscope.

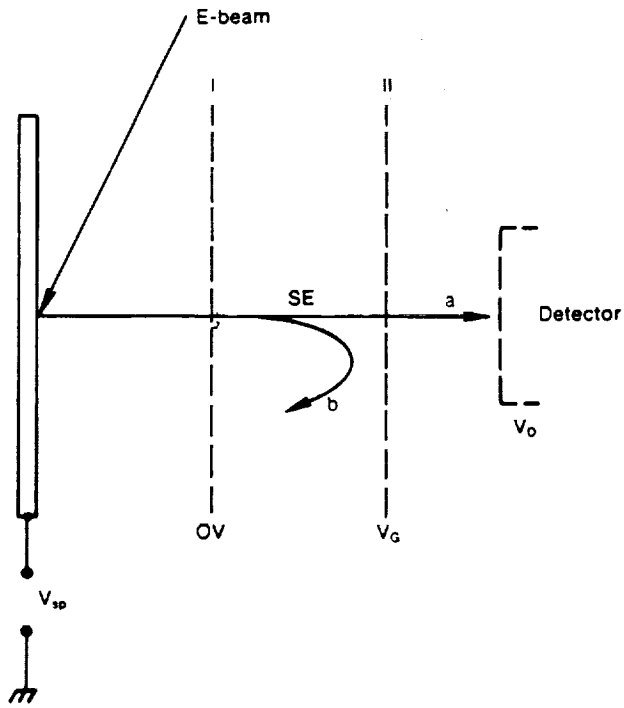

$$I_{SED} = I_{SEmax} \int_{eV_G}^{50eV} N\,(E + eV_{sp})\,dE$$

Figure 2.
A Feuerbaum type SE detector.

A DENSITOMETRIC ANALYSIS OF COMMERCIAL 35mm FILMS

Ernest C. Hammond, Jr. and Christopher Ruffin, III
Morgan State University
Baltimore, MD

and

Gerald R. Baker
Technical Monitor
Laboratory of Astronomy and Solar Physics
Goddard Space Flight Center

ABSTRACT

IIaO films have been subjected to various sensitometric tests. They have included thermal and aging effects and reciprocity failure studies. In order to compare the special IIaO film with popular brands of 35mm films and their possible use in astrophotography, the following brands: Agfa, Fuji and Kodak print and slide formats, as well as black and white and color formats, were subjected to sensitometric, as well as densitometric analysis. A scanning electron microscope was also used to analyze grain structure size, and shape a function of both speed and brand. Preliminary analysis of the grain structure using an ISI-SS40 scanning electron microscope indicates that the grain sizes for darker densities are much larger than the grain size for lighter densities. We will analyze the scanning electron microscope findings of the various grains versus densities as well as enhancement of the grains, using the IP-8500 Digital Image Processor.

A DENSITOMETRIC ANALYSIS OF COMMERCIAL 35mm FILMS

Intorduction

As the United States reestablishes its space exploration program, accurate reproduction by electronic and photographic recording techniques will remain an integral part of these studies. The use of film as a recording medium in astronomy is well documented. In hopes of establishing another method of calibration, and to determine whether or not commercial films can be used in astrophotography, films of color, black & white, print and slide formats were subjected to various tests. We wish to make it perfectly clear that this paper is analyzing films after development, and the results are not to be misinterpreted as proof of a particular film's superiority over another brand.

Experimental Procedure

The films were exposed on a densitometer which contained thirty neutral density wedges of differing values. These wedges simulate thirty different exposure times. Once the rolls were processed, by the same commercial lab, a densitometer was used to obtain the gray levels of the wedges. These levels were recorded and then plotted for each film. The lightest and darkest wedges of each sample were then placed in our ISI-ss40 scanning electron microscope. (*The terms light and dark refer to the translucence of the film.*) Photographs were made of each wedge at two different energy levels to analyze both the surface and the grains of each wedge. At 10 kv, the electrons lack the energy to fully penetrate the emulsion of the film, thereby showing the grains, peaks and valleys of the surface. When the energy is increased to 30 kv, the surface effects are lost and the grains are seen as they react to the secondary electrons. The Polaroids were then digitized using our Gould IP-8500 digital image processor. The enhanced and false color images were then studied. Grain counts and sizes were made and plotted for a visual comparison. The results of these tests follow.

Light Surfaces

For Plus X, (Fig. 1.3R) hereinafter referred to as Px5062, the boundaries of the larger conglomerates of grains and their depth or proximity to the surface is assumed by their focal clarity. This ambiguity may be overcome by placing the image in false color. Pcmake is one of the methods used to do this. Through experimentation and carefully choosing contrasting and complementary colors, the background grains, emulsion, and grain boundaries can be enhanced or diminished (Figs. 6.1 & 6.2).

While looking at the Tri-X, Tx5063 (Fig. 1.4R), one is immediately able to see that there are fewer but larger grains present on this surface. The pcmake version gave the illusion of depth for a 3-D effect and had great resolution, but still did not fully isolate the foreground. The pseudocolor image lacked resolution, but did a better job of separating the foreground and background of the emulsion (Figs. 6.5 & 6.6).

The T-Max 400, Tmy5053, had a surface unlike any of the previous samples. Fewer and smaller grains with a few conglomerates appear to be the composition of this film. The pseudocolor version

showed three fairly distinct regional densities. Other samples tended to have more uniform dispersion of the density.

Fuji Pr.III, referred to simply as Fuji, has a surface that is more like the Tmy5053 than any other. The pcmake and pseudocolor versions again show a more regional grouping of grain densities than in previous samples.

Dark Surfaces

It is immediately apparent that on the surface, the dark wedge has many more grains. This is both characteristic and to be expected. The dark wedges have far more grains, and thus allow less light to pass through. Fig. 1.3L is of Px5062, and the pcmake version gives a 3-D effect, while the pseudocolor mode decreases the background (Figs. 6.3 & 6.4).

Fig. 1.4L is of the surface of the dark Tx-5063 wedge. More spaces or holes are present than in the Px5062, but again the film has more grains than its light counterpart. However, this time the pcmake version has done a better job of separating the background from the higher level grains.

The Tmy5053 surface is interesting because it seems to have a couple of separate levels; one with loose grains suspended in space, and the other more of a surface like the lighter wedges.

The final surface to be analyzed here is that of Fuji. This surface has very few loose grains, and has a more uniform density. A change in density occurs near the edge of the sample.

Light Grains

The energy of the electrons was increased to 30 kv so that they would have the energy necessary to penetrate the emulsions of the film. There are fewer but larger grains than were previously seen. By placing the image in pcmake false color, the boundaries of the grains become more distinguishable.

Figure 5.1R is of Px5062 and set next to its dark counterpart for a contrast. The large but relatively fewer grains are clearly evident in this side by side comparison.

The number of grains present in Tx5063 (Fig. 5.2R) was still further reduced. An increase in the size of the grains is noticeable, especially in the pseudocolor version of the sample, where the boundaries of the grains are readily discernible.

The grains of Tmy5053 (Fig. 5.3L) appear to be twice as large as those of Tx5063. The pcmake version highlights the few grains closest to the surface of the emulsion.

The light Fuji (Fig. 5.4R) film grains in the equalized version were an unresolved blob. The pcmake version turns the image into a well defined image of the grains. Similarly, the pseudocolor view makes boundary and size analysis possible.

Dark Grains

The last samples to be analyzed by electron microscopy are the dark wedge grains. Px5062 (Fig. 5.1L) had a far greater number of grains that were considerably smaller. The large number of grains would make boundary identification and size distinction very difficult if not for the false coloring techniques.

The dark wedge grains of Tx5063 (Fig. 5.2L) revealed the difference that choosing different colors can make in analysis. This first pcmake version decreased the background, and defined the boundaries better than the second version which tended to only moderately decrease the background.

Tmy5053 (Fig. 5.3R) showed a considerable grouping of grains towards the bottom center of the wedge. The pseudocolor image supports the pcmake analysis.

Fuji (Fig. 5.4L) had a fairly uniform clustering of grains throughout the wedge. The pseudocolor image better defines the grain boundaries than does pcmake, which, however, had a better resolution.

Graphs of the Gray Levels

The gray levels of the films were plotted against each other by color format (Figs. 1.1 & 1.2). In analyzing the graphs of the films, Fuji, Pan-X, Plus-X, and T-Max have relatively the same optical densities. As the exposure increases, their optical densities vary significantly. Based upon this, one can assume that a fairly reasonable amount of quality control is present. The films that vary from the beginning have a significantly different ASA. The same situation is true for the color format. The curious difference is that the highest ASA film in black & white has the highest optical density, while the opposite is true in the color format. Research is being conducted to find the reason for this behavior.

The Grain Chart

The average and number of grains in a 9 cm^2 area were calculated and recorded on the chart (Fig. 2). An approximation of the shape of the grains was made. The grains were categorized by translucence. The chart should require no explanation.

Bar Graphs

The average area of the grains of the light and dark wedges were graphed together as were the number of grains in a 9 cm^2 area. A possibly significant but definitely interesting trend was found (Figs. 3 & 4). In each case of either a light or dark wedge the highest value peak has as its counterpart not the lowest, but the next to the lowest peak of the opposite wedge.

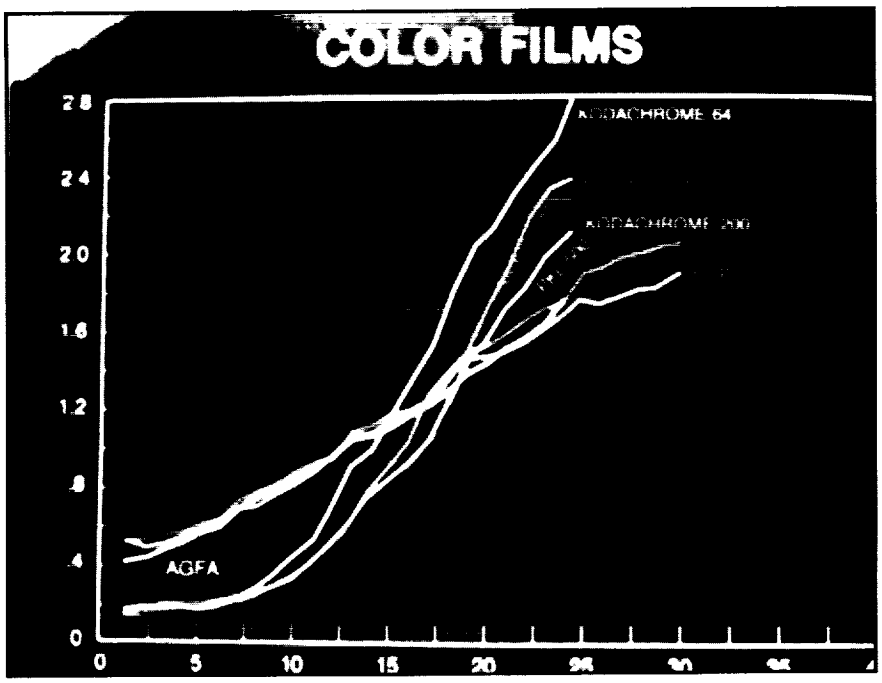

Figure 1.1

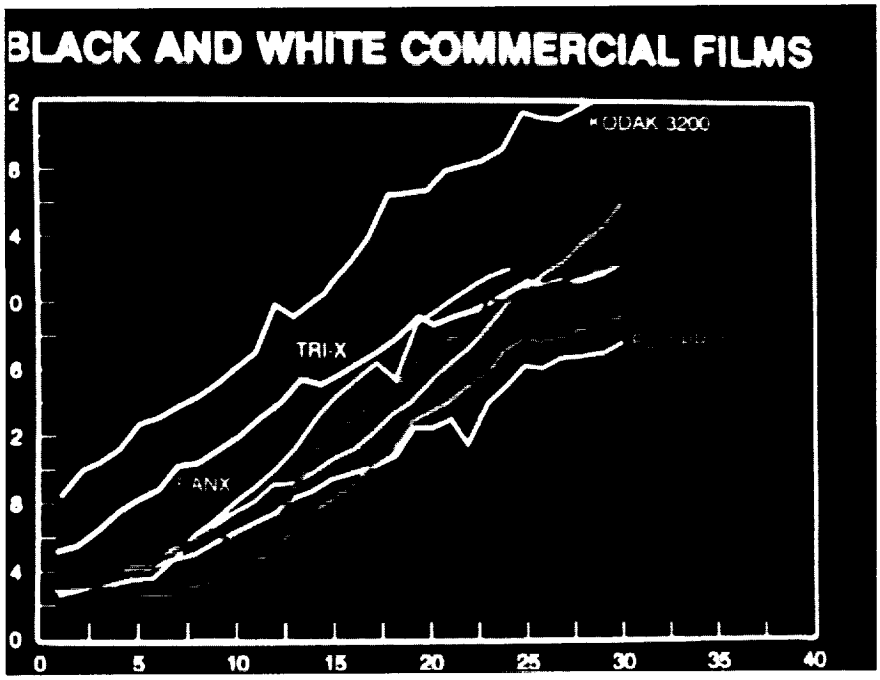

Figure 1.2

ORIGINAL PAGE
BLACK AND WHITE PHOTOGRAPH

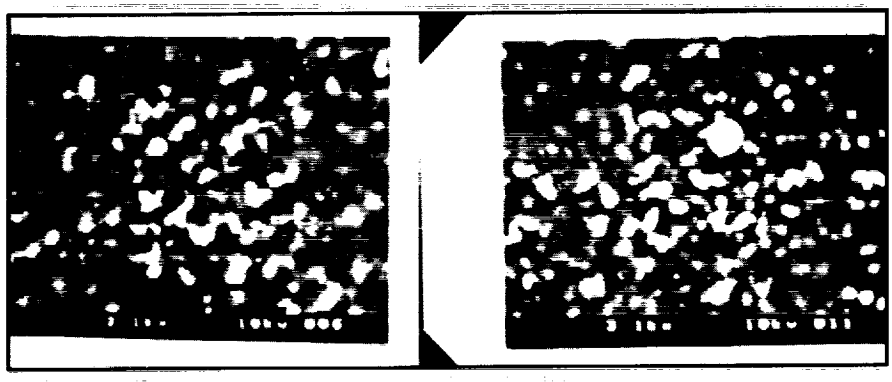

L Figure 1.3 R

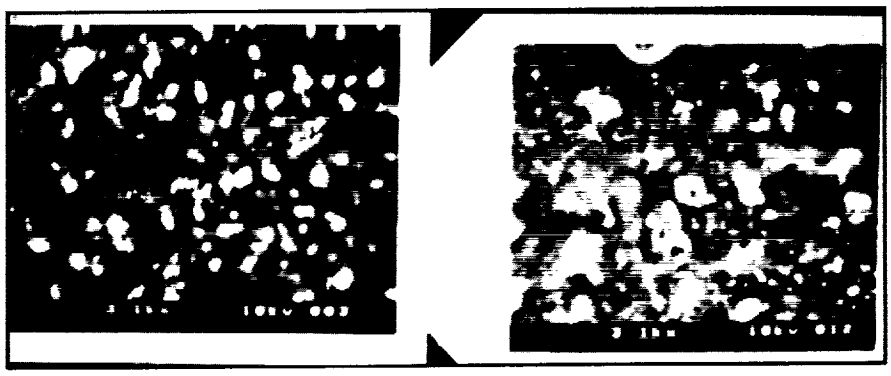

L Figure 1.4 R

Film Type	# grains/9 cm*cm	Average Area μ^2	Shape
Px 5062	80+	2,200	pebble
Tx 5063	50	9,070	elongated
Tmy 5053	50	5,050	pebble
Fuji	40	7,370	irregular

Dark Grains

Film Type	# grains/9 cm*cm	Average Area μ^2	Shape
Px 5062	12	7,980	pebble
Tx 5063	11	11,280	elongated
Tmy 5053	13	21,260	pebble
Fuji	17	12,230	irregular

Light Grains

Figure 2

Figure 3.

Figure 4.

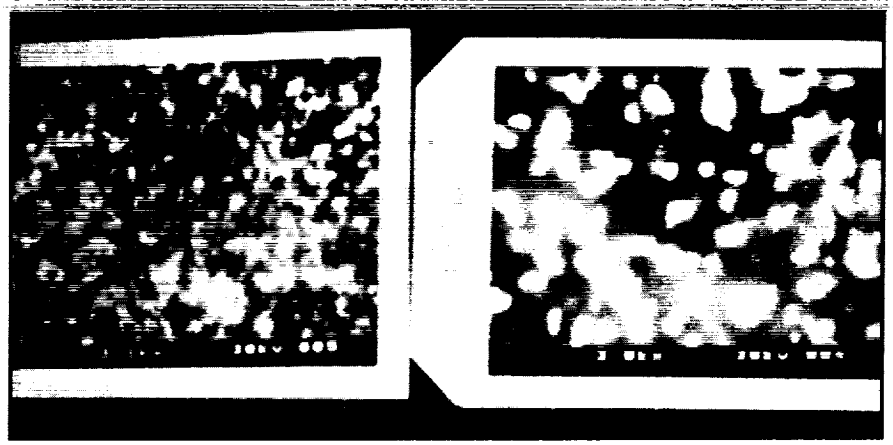

L Figure 5.1 R

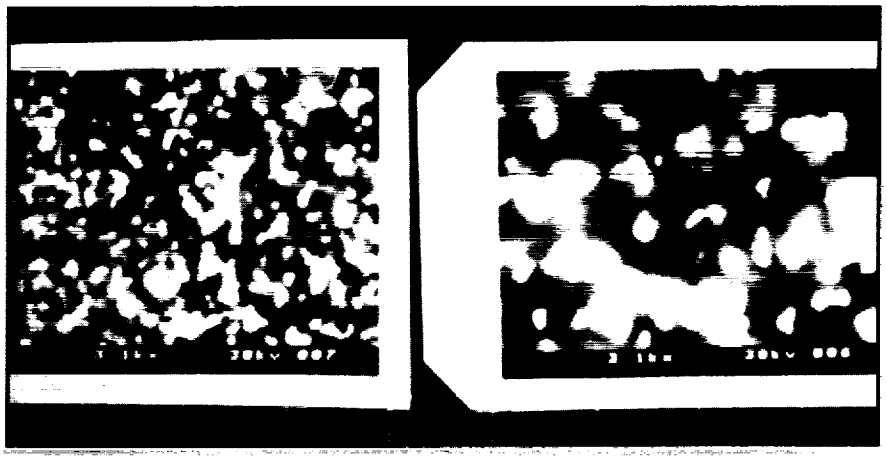

L Figure 5.2 R

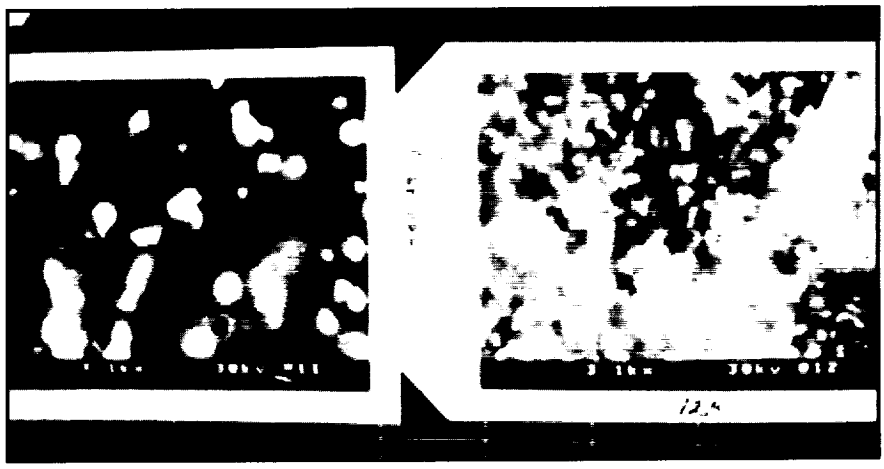

L Figure 5.3 R

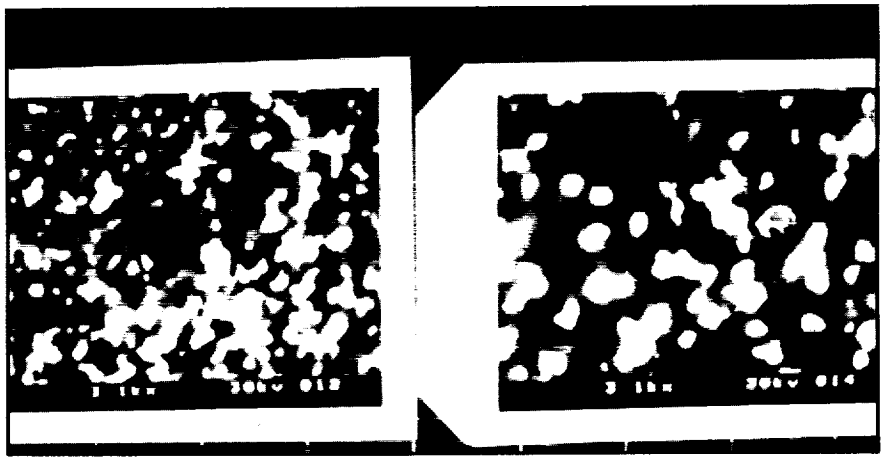

L Figure 5.4 R

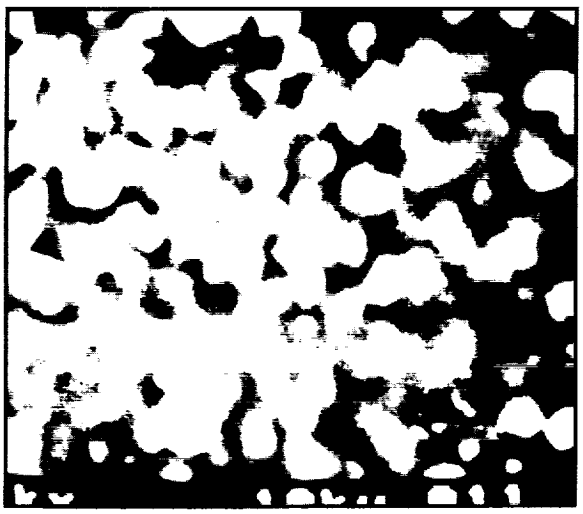

Figure 6.1

Figure 6.2

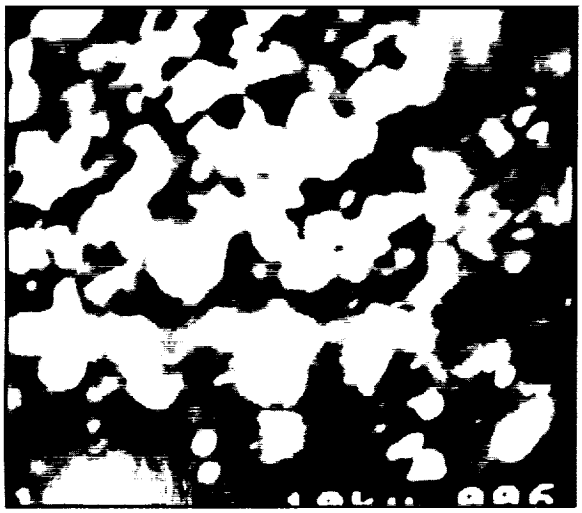

Figure 6.3

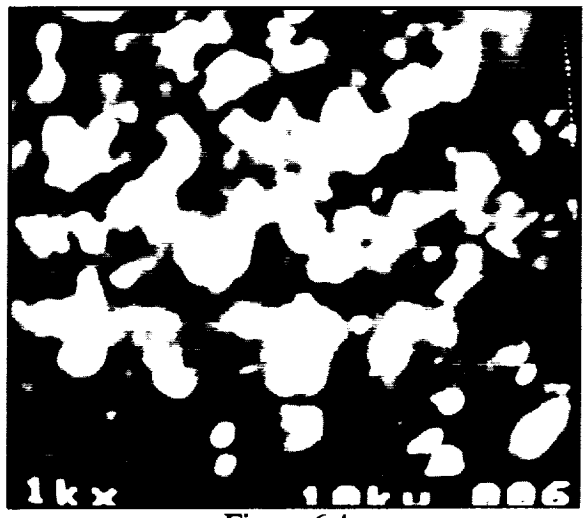

Figure 6.4

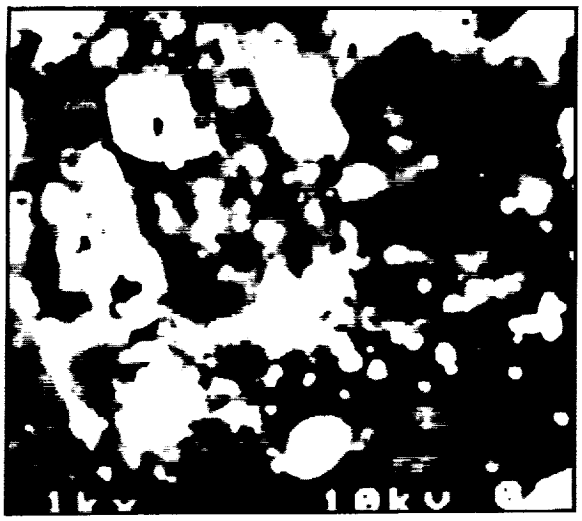

Figure 6.5

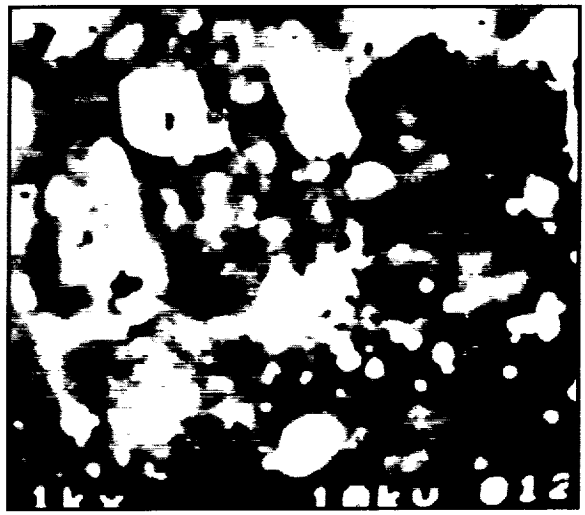

Figure 6.6

Conclusion

Because of the triple layer of emulsion, the color films were set aside until the black and white films were understood. The densitometric analysis is a viable method of calibration and comparison. Insofar as the use of commercial films in astro-photography is concerned, one has but to consult the density plot and choose a film based on the anticipated lighting.

Acknowledgments

The author is indebted to Gerry Baker and Al Stober of the Small Payloads Section of the laboratory for Solar Physics and Astronomy of the Goddard Space Flight Center, Greenbelt, Maryland for their support. I would also like to thank the following students: Dana Dunsen, Theresa Williams, and Michael Blake for their assistance with this project. A special thanks to Ernest C. Hammond, Jr., for without your discussions and support, this project would not have been completed.

N91-28120

DEVELOPMENT OF FLASHLAMP-PUMPED Q-SWITCHED Ho:Tm:Cr:YAG LASERS FOR MID-INFRARED LIDAR APPLICATION

557-36
26638
R-6

Young S. Choi, Kyong H. Kim, and Donald A. Whitney
Department of Physics
Hampton University
Hampton, Virginia

Robert V. Hess, Norman P. Barnes, Clayton H. Bair, and Philip Brockman
NASA Langley Research Center
Hampton, Virginia

ABSTRACT

A flashlamp-pumped 2.1 μm Ho:Tm:Cr:YAG laser has been studied for both normal mode and Q-switched operations under a wide variety of experimental conditions in order to optimize performance. Laser output energy, slope efficiency, threshold and pulselength were determined as a function of operating temperature, output mirror reflectivity, input electrical energy and Q-switch opening time. The measured normal-mode laser thresholds of a Ho^{3+} (0.45 atomic %) :Tm^{3+} (2.5 at. %) :Cr^{3+} (0.8 at. %) : YAG crystal ranged from 26 to 50 J between 120° and 200° Kelvin with slope efficiencies up to 0.36% with a 60% reflective output mirror. Under Q-switched operation the slope efficiency was 90% of the normal-mode result.

DEVELOPMENT OF FLASHLAMP-PUMPED Q-SWITCHED Ho:Tm:Cr:YAG LASERS FOR MID-INFRARED LIDAR APPLICATION

Introduction

Development of solid state lasers with Ho^{3+}, Tm^{3+} and(or) Er^{3+} doped crystals has been pursued by NASA for eye-safe mid-infrared LIDAR (light detection and ranging) application. As a part of the project we have been working on evaluation of Ho^{3+}:Tm^{3+}:Cr^{3+}:YAG crystals for normal-mode and Q-switched 2.1 μm laser operations in order to determine an optimum Tm^{3+} concentration under flashlamp pumping conditions.

Lasing properties of the Ho^{3+} in the mid-infrared region have been studied by many research groups since the early 1960's.[1-5] However, the technology of those lasers is still premature for lidar application. In order to overcome the inefficiency related to narrow absorption bands of the Ho^{3+}, Tm^{3+} and Er^{3+}, the erbium has been replaced by chromium. The improvement in flashlamp-pumped Ho^{3+} laser efficiency has been demonstrated recently by several research groups[6,7] by utilizing the broad absorption spectrum of Cr^{3+} which covers the flashlamp's emission spectrum. Efficient energy transfer to the Tm^{3+} and then the Ho^{3+} occurs subsequently. It is known that high Tm^{3+} concentration and low Ho^{3+} concentration are preferred to achieve a quantum efficiency approaching two and to avoid large reabsorption losses.[6] However, determination of the optimum Tm^{3+} concentration required to ensure efficient energy transfer from Cr^{3+} to Tm^{3+} and from Tm^{3+} to Ho^{3+} has not been made in the Ho:Tm:Cr:YAG crystal. This paper will present the results obtained so far with one out of the three Ho:Tm:Cr:YAG crystals with three different Tm^{3+} concentrations with similar Cr^{3+} and Ho^{3+} concentrations.

Quantum Processes in Ho^{3+}, Tm^{3+} and Cr^{3+} -Ions

The energy levels of the Cr^{3+}, Tm^{3+} and Ho^{3+}-ions and the energy transfer mechanisms among the ions in a YAG crystal are illustrated in Fig. 1. The use of Cr^{3+} for flashlamp pumping is based on its broad absorption spectrum provided by the transitions from the ground $^4A_2$ state to the upper $^4T_1$ and $^4T_2$ states. Subsequently, efficient near resonant energy transfer to the $^3H_4$ state of the Tm^{3+} occurs. Fig. 2 shows the absorption spectrum of the Ho^{3+} (0.45 atomic %) :Tm^{3+} (2.5 at. %) :Cr^{3+} (nominally 1.5 at. %) :YAG crystal. The chromium concentration of 1.5 atomic % stated by vendor turns out to be 0.8 atomic % based on absorption measurement. The two broad bands in the visible region correspond to the chromium absorption while the other sharp peaks correspond to the absorption by the holmium and thulium ions. Armagan, et al.'s work (Ref. 8) showed that the energy transfer processes are more effective in crystals with low Cr^{3+} and high Tm^{3+} concentrations.

For high Tm concentrations, the transition from the $^3H_4$ manifold to the $^3F_4$ manifold induces the cross relaxation process which provides two Tm ions in the $^3F_4$ manifold from a single Tm ion in the $^3H_4$ manifold. As a result, the quantum efficiency approaches two. Then, the near resonant energy transfer process from the $^3F_4$ manifold of Tm to the $^5I_7$ manifold of Ho provides an efficient pumping mechanism of the Ho-ions. In order to operate the 2.1 μm Ho laser efficiently at room temperature, the Ho^{3+} concentration must be low. The increase of the Ho^{3+} concentration increases the ground state population of $^5I_8$ of Ho manifold which causes high resonant reabsorption losses for the $^5I_{7(Ho)}$ - $^5I_{8(Ho)}$

laser transition. However, as the temperature goes down, the upper levels of the lower laser manifold of the Ho^{3+} become thermally unpopulated. By decreasing the temperature and the population density of the lower laser levels, the efficiency of the laser performance increases. Since the upper laser level lifetime of the Ho^{3+} is longer than 5 ms when at room temperature, efficient storage time for the Q-switched operation is possible. A high holmium ion concentration may be effective for high Q-switched laser output since the population in the $^5I_7$ manifold can be increased.

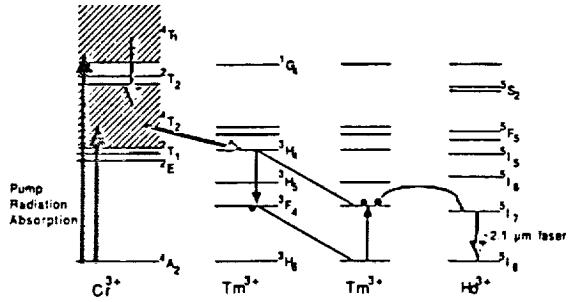

Figure 1. Energy transfer processes in a Ho:Tm:Cr:YAG crystal.

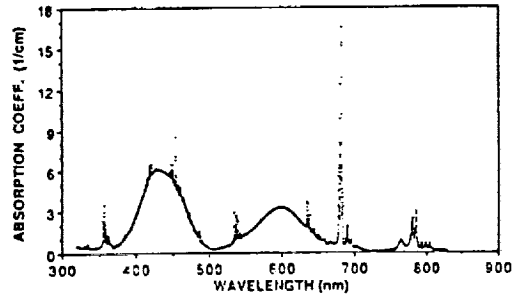

Figure 2. Absorption spectrum of the Ho:Tm:Cr:YAG crystal (0.45% Ho, 2.5% Tm, 0.8% Cr).

Experimental Methods

The experimental configuration used in this research is shown in Fig. 3. The temperature of the laser rod was varied from 120°K to room temperature by circulating cold nitrogen gas around the rod. The flashlamp was cooled by circulating deionized water. The flashlamp and laser rod were placed in a pumping cavity made of highly reflective aluminum. This cavity was 76.2 mm long and had an elliptical cross section with major and minor axes of 152.4 mm and 149.1 mm, respectively. The detailed cavity design was reported elsewhere.[9] In order to achieve thermal isolation, the entire pumping cavity was placed in a vacuum system. Good thermal isolation was necessary since the cooling capacity of liquid nitrogen vapor was limited. A 450 torr Xe flashlamp with 4 mm bore diameter and 76.2 mm arc length was used and surrounded by a uranium doped flow tube water jacket to reduce possible solarization effects. The size of the Ho: Tm: Cr: YAG laser rod used was 4 mm in diameter and 55 mm in length.

Since the Ho: TM: Cr: YAG has a long upper laser level lifetime, the pulse forming network (PFN) for the flashlamp was designed for long pulse operations. With a 146.5 μf capacitor and a 184 μH inductor critically damped pulses of 300 μs FWHM pulse length were obtained. At the input voltage of 905 volts required for a critically damped pulse, the electrical input energy was 60 J. A highly reflective mirror at 2.1 μm with a 10 m radius of curvature was attached to one end of the vacuum box as a window, and an antireflection coated quartz flat was place on the other side of the vacuum box. Flat mirrors with various reflectivities were used as output couplers. The total resonator length was 88 cm. In Q-switched operations a lithium niobate crystal ($LiNbO_3$) with dimensions of 9 mm x 9 mm x 25 mm and a ZnSe polarizer of 2.17 mm thickness were used as a Q-switch. The hold-off voltage for the Q-switch crystal was 1.62 kV. The Q-switch trigger signal could be delayed from 0 to several ms with respect to the trigger for the flashlamp.

The laser output energy and pulse shape were measured with a pyroelectric energy meter and with a liquid N_2 cooled HgCdTe detector, respectively. The bandwidth of the HgCdTe detector was 10 MHz.

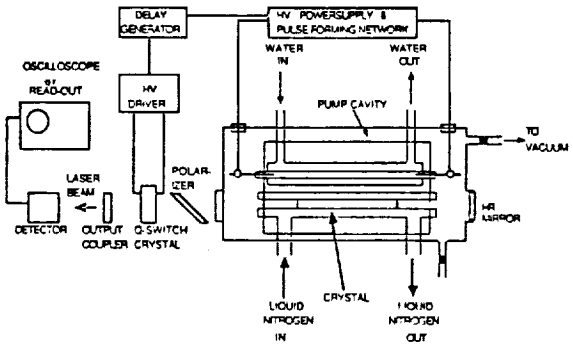

Figure 3. Schematic diagram for the experimental setup.

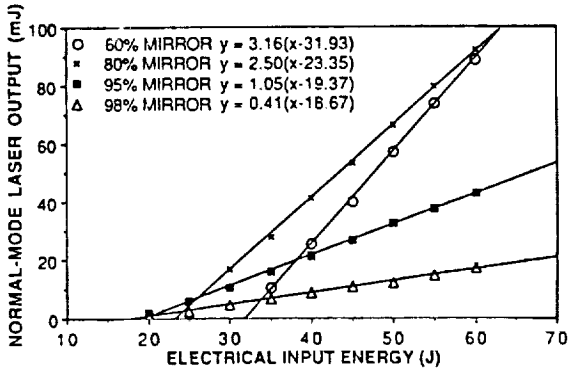

Figure 4. Normal-mode laser output energy of the Ho:Tm:Cr:YAG crystal as a function of electrical input energy at 150 K.

Results

Fig. 4 shows the normal-mode laser output energies of the Ho(0.45%) :Tm(2.5%) :Cr(0.8%) :YAG crystal measured as a function of the electrical energy stored in the capacitor for various output mirror reflectivities at the operating temperature of 150°K. As expected, the slope efficiency and threshold energy increase with the decreasing mirror reflectivity. The measured normal-mode laser output energies as a function of operating temperature at various electrical input energies with a 60% reflectivity mirror are shown in Fig. 5. The decrease of the laser output energy with the increasing temperature clearly indicates the effect due to thermal population in the lower laser level. Figs. 6 and 7 show the dependence of the laser threshold and slope efficiency, respectively, on the operating temperature at various mirror reflectivities. The highest slope efficiency, 0.36 %, was obtained with a 60% mirror at 120 K, while the lowest extrapolated threshold electrical input energy of 14.8 J was achieved at 120 K with a 90% mirror. The low slope efficiency may be attributed to several causes. The laser crystal diameter is relatively small compared to the mode diameter of about 2.8 mm. The Cr^{3+} and Tm^{3+} concentrations in the crystal are low. The laser rod is short compared to the flashlamp and produces poor optical coupling between the flashlamp and the laser rod. Low cavity reflectivity which was less than 80% at 633 nm also causes poor optical coupling.

The measured Q-switched and normal-mode laser outputs are plotted in Fig. 8 as a function of the electrical input energy stored in the capacitor at various temperatures. The output mirror used in this comparative measurement had a 60% reflectivity and the normal-mode operation was done with the Q-switch crystal and ZnSE polarizer in the resonator. The Q-switched laser output and slope efficiency are only slightly lower and the threshold is slightly higher than those of normal mode operation. The observed slope efficiencies are 0.123% for normal-mode and 0.111% for Q-switched operation at the operating temperature of 130°K. The Q-switched slope efficiency of the Ho:Tm:Cr: YAG crystal corresponds to approximately 90% of the normal-mode slope efficiency. The measured wavelength of the Ho:Tm:Cr:YAG laser with a spectrometer was about 2.095 μm.

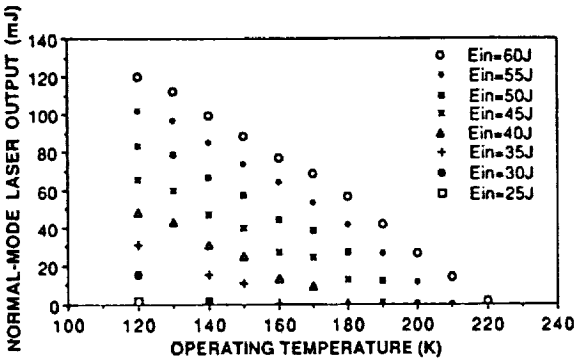

Figure 5. Normal-mode laser output energy as a function of the operating temperature with a 60% reflectivity output mirror.

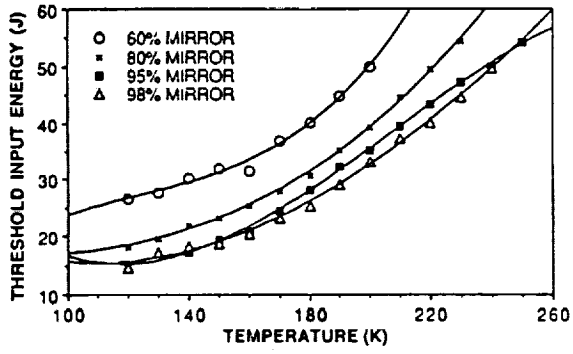

Figure 6. Threshold input electrical energy as a function of the operating temperature with various output mirror reflectivities.

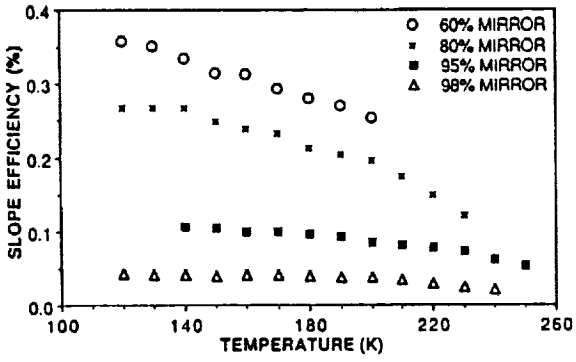

Figure 7. Slope efficiency as a function of temperature with various mirror reflectivities.

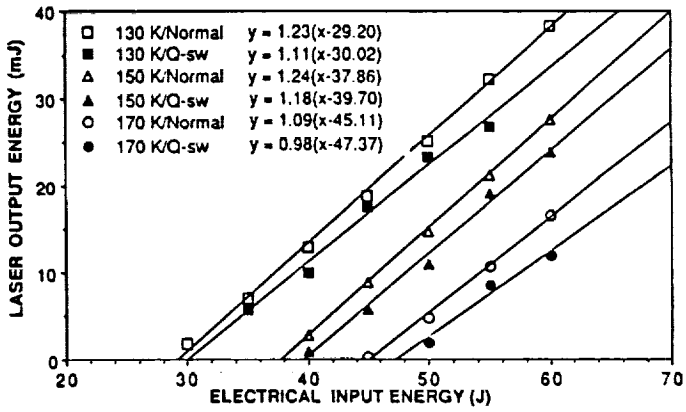

Figure 8. Normal-mode and Q-switched laser output energies as a function of the input energy with a 60% reflective mirror.

Conclusion

A Ho:Tm:Cr:YAG laser with concentrations of 0.45 at. % Ho, 2.5 at. % Tm and 0.8 at. % Cr has been studied for both normal mode and Q-switched 2.1 μm laser operation under flashlamp pumping at various operating temperatures, various output mirror reflectivities, and various input energies. Continuing work on the evaluation of the other two crystals with different Tm^{3+}-ion concentrations is in progress and will provide an optimum Tm concentration in the Ho:Tm:Cr:YAG crystal.

Acknowledgments

This work was supported by NASA under grant number NAG-1-877. We acknowledge that Mark E. Storm and Coherent Technology provided the laser crystals and Lewis G. Burney, Donald Gettemy, Edward A. Moldin, and Keith E. Murray provided the technical support during the course of this research work. We also appreciate valuable discussion with Dr. Alfred M. Buoncristiani.

References

1. Johnson, L.F., Boyd, G.D., Nassau, K., Proc. IRE, **1962**, 50, 87.

2. Chicklis, E.P., Naiman, C.S., Folweileer, R.C., Gabbe, D.R., Jenssen, H.P., Linz, A. Appl. Phys. Lett. **1971**, 19(4), 119.

3. Barnes, N.P., Gettemy, D.J., IEEE J. Quantum Electron., **1981**, QE-17(7), 1303.

4. Lotem, H., Kalisky, Y., Kagan, J., Sagie, D., IEEE J. Quantum Electron., **1988**, 24(6), 119.

5. Duczunski, E.W., Huber, G., Appl. Phys. Lett., **1986**, 48(23), 1562.

6. Mitzscherlich, P., Tunable Solid-State Lasers II (Edited by Budfor et al.), Springer-Verlag, New York, **1986**, p. 282.

7. Scherbakov, I.A., Tunable Solid-State Lasers II (Edited by Budgor et al.), Springer-Verlag, New York, **1986**, p. 293.

8. Armagan, G., Di Bartolo, ., Buoncristiani, A.M., "Spectroscopic Investigation of the Cr to Tm Energy Transfer in Yttrium Aluminum Garnet Crystals," to be published. (**1989**).

9. Gettemy, D.J., Barnes, N.P., Griggs, E., Rev. Sci. Instrum. **1980**, 51(9), 1194.

N91-28121

EFFECT OF GRINDING ON THE FATIGUE LIFE OF TITANIUM ALLOY (5 Al - 2.5 Sn) UNDER DRY AND WET CONDITIONS*

Partha Rangaswamy, Hendra Terutung, and Shaik Jeelani
Materials Research Laboratory
School of Engineering and Architecture
Tuskegee University, AL

ABSTRACT

The principal factors in the performance of aerospace materials are strength-to-weight ratio, fatigue life, fracture toughness, survivability and, of course, reliability. Machining processes and, in particular, grinding under adverse conditions have been found to cause damage to surface integrity and affect the residual stress distribution in the surface and subsurface region. These effects have a direct bearing on the fatigue life.

In this investigation the effects of grinding conditions on the fatigue life of Titanium 5 Al-2.5Sn were studied. This alloy is used in ground form in the manufacturing of some critical components in the space shuttle's main engine. It is essential that materials for such applications be properly characterized for use in severe service conditions.

Flat sub-size specimens 0.1 inch thick were ground on a surface grinding machine equipped with a variable speed motor at speeds of 2000-6000 rpm using SiC wheels of grit sizes 60 and 120. The grinding parameters used in this investigation were chosen from a separate study. The ground specimens were then fatigued at a selected stress and the resulting lives were compared with that of the virgin material. The surfaces of the specimens were examined under a scanning electron microscope, and the roughness and hardness were measured using a standard profilometer and microhardness tester, respectively.

The fatigue life of the ground specimens was found to decrease with the increase in speed for both dry and wet conditions. For both grit sizes, the fatigue life was lower than that of the virgin material for the dry condition. The fatigue life of specimens ground under wet conditions showed a significant increase at the wheel speed of 2000 rpm for both the grit sizes and thereafter decreased with increase in speed to below that of the virgin material. The results of the investigation are explained using profilometry, microhardness measurements and scanning electron microscopic examination.

* Work supported by NASA Grant NAG8-068

EFFECT OF GRINDING ON THE FATIGUE LIFE OF TITANIUM ALLOY (5 Al - 2.5 Sn) UNDER DRY AND WET CONDITIONS

Introduction

Titanium alloys are extensively used in aerospace applications because they meet the design and service requirements. It is observed that during manufacturing the consistent preservation of their inherent strength is difficult to achieve. Catastrophic failures have resulted from damage to the surface integrity by machining during manufacturing. Therefore, manufacturing procedures are required to be specified to avoid damage to the surface and the sub-surface, and, if possible, to specify processing which will enhance part performance. This makes it imperative for the design engineer to possess complete information about the surface characteristics of a component and the mechanical properties of the bulk material before the component is designed so that manufacturing procedures could be suggested to withstand service conditions such as fatigue, creep and stress corrosion cracking [1-3]. Previous investigations have shown that in the machining of metals a damaged surfaced region is produced that is different from the bulk of the material [4-7]. Changes in material surface properties can, in turn, influence mechanical properties of which fatigue life and stress corrosion resistance are usually of the most concern [8-11].

Of the various material removal processes studied to date, grinding causes the most impact on material properties [12,13]. Grinding is an abrasive machining process (more precisely termed micro-machining process) and it differs from machining in that grinding speeds are much faster, depth of cut smaller and there is very little quantitative information on the geometry of individual grits at the periphery of grinding wheels. Studies on surface alterations due to grinding have revealed that the extent of deformed layer depends on the size of the grit as well as its rake angle, grinding speed and depth of cut [14]. Studies carried out on grinding of titanium and titanium alloys (Ti-6Al-4V) have also revealed that a large scale redeposition of metal on the surface accounts for poor surface finish at high speeds using silicon carbide (SiC) and aluminum oxide(Al_2O_3) grinding wheels [15]. Also, the high temperatures developed at the wheel-work interface due to the vast range of process parameters involving rapid rates of material removal have led to lowering the level of surface integrity and producing extremely complex pattern of residual stress distribution [8,12]. These factors have a detrimental effect on the fatigue strength and the fatigue life of the components.

The objective of this research was to investigate the effects of grinding on the fatigue life of Ti-5Al-2.5Sn at room temperature under dry and wet conditions. There are no data available at the test range considered in this work to show what effect, if any, grinding has on the fatigue life of a Ti-5Al-2.5Sn alloy at various grinding speeds and for various grit sizes.

Experimental Work:

A) Specimen Preparation

The Ti-5Al-2.5Sn alloy used in this investigation is an alpha type alloy and is the most widely used commercial alloy in this group. It exhibits excellent fracture toughness and corrosive resistance and is widely used for structural and cryogenics applications. Mechanical properties and chemical composition of the material are give in Tables 1 and 2, respectively.

The sub-sized specimen and the loading grips used in this investigation to hold it were selected from the work done earlier by Jeelani et al [17]. The specimen was designed with 0.1 inch gauge section width and 1.0 inch gauge section length. The specimen thickness was 0.1 inch. These specimens were made as per the specification shown in Figure 1, on a numerically controlled machining center. These specimens were made out of a 2-inch long flat plate, 0.75 inch wide and 0.125 inch in thickness.

After the specimens were fabricated, they were annealed by heating and holding at 1400° for 60 minutes and at 1600° for 10 minutes and then cooling in air. Stress relieving was performed by soaking the specimens for 1 hour at 1000°F. However, it should be noted that Ti-5Al-2.5Sn cannot be hardened by heat treatment. It is used only in annealed condition [18].

The oxidized layer and the toolmarks and other surface irregularities were removed by wet grinding/polishing using silicon carbide emery papers of sizes ranging from 60 to 4000 grits per square inch.

B) Grinding Tests

The grinding of all the specimens was carried on a precision surface grinding machine, (BOYAR-SCHULTZ 1A618 Hydraulic Surface Grinder), equipped with a 2 hp variable speed motor (0-6000 rpm) powered by Volkmann Drives 2 HP Adjustable drive unit which converts the fixed input AC frequency to the motor to a variable frequency range, thus changing the usually fixed motor speed to variable speed.

Grinding was carried out with silicon carbide (39C60H8VK and 39C120I8VK) wheels. The wheels were of 6 inch diameter and 1/2 inch width received in dressed condition (coarse dressing). Grinding wheel speeds of 2000 - 4000 - 6000 rpm were used and a table speed of 40 rpm. All grinding tests were made in a single pass. Table 3 shows a summary of the grinding conditions used in this investigation. These conditions are based on the recommendations of the METCUT [12].

C) Fatigue Testing

For testing the virgin and the ground specimens a direct tension-compression fatigue testing machine (Fatigue Dynamics Model DS-6000 HLM) which is equipped with a hydraulic load maintainer was used. It adjusts the preload continuously to preset value without affecting the cyclical load. The cyclical load can be adjusted manually up to 6000 pound force. The test frequency of the machine ranges from 600 to 2200 cycles/minute. A load cell is provided to read tensile or compressive load on the specimen, directly. The load cell is connected to the strain indicator which is calibrated to read the load on the specimen. A stress ratio of R = 0 was used in this investigation. Throughout the test, the cycle speed was maintained constant at 200 cycles per minute. Tests were performed at room temperature.

D) Surface Examination

Small pieces approximately 0.25 X 0.25 inch were cut from all virgin and ground specimens. The pieces were cleaned in an aqueous methanol solution, and were then air dried. The ground surfaces were examined by a scanning electron microscope over a wide range of magnification.

A Bendix profilometer group 7L equipped with a Sheffield Profilometer, Model QED-6, Digital amplifier, Sheffield Profilometer type VEG Gated Pilator and type LK tracer with Ft skidmount was used to measure the roughness of the surfaces produced. A tracer stroke of 0.5 inch was used with a selected cut-off of 0.0125 inch. The roughness measurements were made on the specimens in the direction parallel to the work-tool motion. Surface roughness measurements of the parent metal specimens as well as those of the ground specimens were taken.

Microhardness measurements using Buhler Micromet II Digital Microhardness tester were made on the ground surfaces produced at all wheel peripheral speeds. At least five measurements were made on each specimen and the average taken for comparison.

Results and Discussion

Figure 2 shows the S-N diagram generated by using 30 polished specimens of Ti-5Al-2.5Sn alloy. Approximately five specimens were tested at each stress level and the fatigue life data were obtained at five stress levels. A software called Grapher especially used for producing two-dimensional graphs was used to produce the S-N curve. Point REF in the diagram, which corresponds to a stress of 100,000 psi and the fatigue life of 125,000 cycles was used as a reference for comparison of the lives of the specimens ground under various conditions used in this investigation.

Figure 3 shows the effect of the type and speed of the grinding wheel and the presence or absence of the cutting fluid on the fatigue life of the specimens. Each data point on the graph represents an average of five tests. For the specimens ground with wheels of both grit sizes (60 and 120) the fatigue life decreases with an increase in the speed. This trend is consistent with the data published in previous studies [8,19,20]. The fatigue life of the specimens ground under dry conditions was lower than that of the virgin specimens. Dry grinding is also termed abusive grinding, which has been shown to cause severe damage to the surface integrity and affect the residual distribution at the surface, lowering the fatigue strength, therefore resulting in lowered fatigue life. Published data have indicated that dry grinding generally produces tensile stress near to the surface under conditions far from low stress condition [7,21,22].

Figure 4 shows the variation in the surface roughness due to a change in the type and speed of the grinding wheel and the presence or absence of the cutting fluid. It can be seen that for all the grinding conditions used in this investigation the surface roughness is higher than that of the virgin material, and increases as the grinding speed is increased. The presence of cutting fluid in the grinding region has decreased the surface roughness, but the change does not appear to be significant. The graph shows that the surface roughness changes due to a change in the grit size of the grinding wheel, but the change is not significant enough to establish a trend.

Figure 5 shows the variation in the microhardness due to a change in the type and speed of the grinding wheel and the presence or absence of the cutting fluid. For all the grinding conditions used in this investigation it can be seen that the microhardness values show a decrease in hardness with an

increase in grinding speed. The presence of cutting fluid slightly increases the hardness values of the specimens ground under wet conditions as compared with the specimens ground dry. At the low grinding speed of 2000 fpm the hardness of the specimens ground under wet conditions is higher than that of specimens ground dry. This trend is consistent up to 4000 fpm but thereafter it is observed that with an increase in the grinding speed the specimens ground with the wheel of grit size 120 for both the dry and wet conditions show slightly higher hardness values than those of the specimens ground with the wheel of 60 grit size. Here again, the graph shows that the microhardness changes due to a change in the grit size of the grinding wheel, but again, the change is not significant enough to establish a trend.

The scanning electron micrographs of the surfaces produced under both dry and wet conditions showed that the surfaces consisted of microcracks and tears showing plowing of the metal by the abrasive action of the grit, evidence of large scale plastic deformation, redeposition and cavities. The texture showed grooves of non-uniform width and spacing for all the grinding speeds [23].

Figures 6a and 6b show scanning electron photomicrographs of the surfaces produced when ground under dry conditions with the wheel of 60 grit size at the lowest and highest grinding speed in the range tested. These photomicrographs reveal a drastic change in texture ranging from long straight grooves parallel to the wheel-work direction to short discontinuous grooves which vary in width and depth with an increase in the grinding speed. This also explains the high roughness values obtained with increase in speed. It was also observed that at a speed of 6000 rpm the ground surfaces revealed cracks and microcracks for both the grit sizes. The cracking occurs because of the generation of heat during the transfer of metal (redeposition) back onto the ground surface at high speeds and subsequent rapid cooling. These cracks and microcracks could be one of the reasons for the decrease in fatigue life of the specimens ground under dry conditions at higher speeds. The effects of rubbing, plowing and cutting, characteristic of the grinding process, were present for all three speeds [12].

Figures 7a and 7b show scanning electron photomicrographs of the surfaces produced when ground under wet conditions with the wheel of 60 grit size at the lowest and highest grinding speed in the range tested. The texture was well defined at the low grinding speed of 2000 fpm indicating that considerably lesser amounts of redeposition on the surface had taken place. Also, the micrographs revealed that the extent of severity of damage caused to the surface was considerably less than the surface ground under dry conditions. But at the speed of 6000 rpm, the surface did reveal cracks transverse to the direction of grinding similar to that of the surfaces ground under dry conditions which had resulted in a considerable decrease in fatigue life. This shows that the presence of cutting fluid, which appreciably reduced the wheel-workpiece temperature and also aided in removing the grinding chips, thereby minimizing redeposition, had virtually no effect in preventing damage to the surface in the form of cracks as a result of increase in process intensity caused by an increase in grinding speed.

Studies have shown that grinding carried out at low speeds in the presence of a lubricant results in producing residual stresses which are compressive in nature in the surface and sub-surface region [12]. For the titanium alloy used in this investigation, there are no data reported yet concerning the nature of the residual stresses in the surface and subsurface due to grinding.

The surface roughness measurements also show that the roughness increases with an increase in the grinding speed, an observation which is supported by the SEM photomicrographs as shown in Figures 6 and 7. It is to be noted as mentioned earlier that this particular alloy cannot be hardened and therefore the high temperatures reached due to heat generated at the work-wheel interface anneal the workpiece, thereby softening the workpiece at the surface and the sub-surface region. This is one of the reasons for the microhardness measurement showing a decrease with an increase in the grinding

speed. Also, visual examination of the surface of the specimens ground under dry condition at high speeds showed evidence of burnt marks.

Conclusion

From the results of the investigation of the effect of grinding conditions on the fatigue life of Titanium 5AL-2.5Sn, the following conclusions may be drawn:

1. The results of the study indicated that fatigue life of the specimens decreased considerably with an increase in the speed. The fatigue life of the specimens ground under dry conditions was lower than that of the virgin specimens for the speed range tested. The fatigue life of the specimens ground with cutting fluid was higher than that of the virgin specimens in the range of 2000 - 4000 rpm.

2. The results of surface roughness measurements over the entire speed range of the ground specimens showed an increase in roughness with an increase in the speed. The roughness values of the specimens ground under dry and wet conditions were higher than those of the virgin specimens. The roughness of the specimens ground under dry conditions was higher than that of the specimens ground under wet conditions at all speeds and for both grit sizes.

3. The microhardness measurements for both the grit sizes and for both the dry and wet conditions used in this investigation showed a decreasing trend in hardness for all the speeds.

4. The grit sizes of the grinding wheel selected for this study showed no significant effect on the fatigue life.

References

1. Ramakrishnan,K. "Surface and subsurface damage in machining of 18% nickel maraging steel, 6242-titanium alloy, and red brass". M.S. Thesis, Tuskegee Institute, 1979.

2. Koster, W.P., Field, M., Fritz, L.J., Gatto, L.R. and Kahles, J.F. "Surface integrity of machined structural components", USAF Technical Report AFML-TR-70-11, Metcut Research Associates Inc., Cincinatti, OH, 1970.

3. Koster, W.P. and Field, M. "Effect of Machining variables on the surface and structural integrity of titanium", Proceedings of North Americal Metalworking Research Confernce, McMaster University, Hamilton, Ontario, Canada, May 14-15, 1973, (Hamilton: McMaster University, 1973), Vol.2-Metal Cutting and Electrical Machining, pp.67-87.

4. Bailey, J.A. and Jeelani, S. "Surface integrity in the machining of annealed 18% nickel maraging steel", SME Trans (1974) pp 174-185.

5. Bailey, J.A. and Jeelani, S. " Determination of subsurface plastic strain in machining using an embossed grid", Wear 36 No 2 (1976) pp 199-206.

6. Bailey, J.A. and Jeelani, S. "Surface integrity in the machining of quenched and tempered AISI-4340 steel", ASME, J Engng Ind 98 No 3 (1976) p 999.

7. Bailey, J.A. and Jeelani, S. "State of subsurface region in machining solution treated and aged 18% nickel maraging steel" Wear 72 (1981) p 237.

8. Koster, W.P. "Surface integrity of machined materials", USAF Technical Report AFML-TR-74-60, Metcut Research Associates Inc., Cincinatti, OH, 1974.

9. Bellows, G. and Kohls, J.B. "Surface integrity of nontraditional material removal processes", Technical Paper MRR76-12, Society of Manufacturing Engineers, Dearbon, MI, 1976.

10. Jeelani, S. and Musial, M. "Effect of cutting speed and tool rake angle on the fatigue life of 2024-T351 aluminium alloy", In J Fatigue 6 No 3 (1984) pp 169-172.

11. Jeelani, S. and Collins, M.R. "Effect of electric discharge machining on the fatigue life of Inconel 718", In J Fatigue 10 no 2 (1988) pp 121-125.

12. Bellows, G."Low Stress Grinding", Machinability Data Center Publication No. MDC 83-103, 1983.

13. Cammett, J.T., III. "Fatigue crack initiation in surface ground Ti-6Al-4V", In Proceedings of the International Conference on Production Engineering, Tokyo 1974 (Part II), pp 132-136. Tokyo, Japan: Japan Society of Precision Engineering, 1974.

14. Turley, D.M. and Doyle, E.D. "Factors affecting workpiece deformation during grinding", Materials Science and Engineering, 21 (1975) pp 261-271.

15. Turley, D.M. "Factors affecting surface finish when grinding titanium and a titanium alloy (Ti-6Al-4V)", Wear., 104, 1985 pp 323-335.

16. Jeelani, S., Natarajan, R. and Reddy, G.R. "A subsized fatigue specimen", Int J Fatigue 8 No 3 (1986) pp 159-164.

17. D.O.D. Aerospace Structural Metals Handbook, Vol. 4, Code 3706, pp 1-13.

18. Kahles, J.F., Field, M., Eylon, D. and Froes, F.H. " Machining of Titanium alloys", Journal of Metals, 1985 pp 27-35.

19. Imamn M.A. and Gilmore, D.M. "Fatigue and microstructural properties of quenched Ti-6Al-4V", Met. Trans. (A) 14A, 1983 pp233.

20. Leverant, G.R., Langer, B.S., Yuen, A. and Hopkins, S.W. "Surface residual stresses, surface topography and the fatigue behavior of Ti-6Al-4V", Met. Trans. (A) 10A 1979 pp 251-257.

21. Takemato, T., Jimg, K.L., Tsakalakos, T., Weissmann, S. and Dramer, I.R. "The importance of surface layer on fatigue behavior on a Ti-6Al-4V alloy." Met. Trans. (A) 14A 1983 pp 127-132.

22. Rangaswamy, Partha., "Effect of grinding on the fatigue life of Ti-5Al-2.5Sn under unlubricated conditions", M.S. Thesis, Tuskegee Institute, 1989.

23. Terutung, Hendra., "Effect of grinding on the fatigue life of Ti-5Al-2.5Sn under lubricated conditions", M.S. Thesis, Tuskegee Institute, 1989.

Acknowledgments

The authors gratefully acknowledge the support of NASA- Marshall Space Flight Center through Grant NAG8-068 for this study.

TABLE 1. MECHANICAL AND PHYSICAL PROPERTIES OF TITANIUM 5AL 2.5 SN

Ultimate Tensile Stength	120 Ksi
Yield Strength (0.2 % offset)	115 Ksi
Hardness (Rockwell C)	36 Rc
Elongation in 2 in.	10 %
Reduction of Area	25 %
Impact, Charpy V	19 Ft.lb
Rupture Stress	108 Ksi
Modulus of Elasticity, tension	16 Mpsi
Modulus of Elasticity, torsion	6.5 Mpsi
Density	0.162 lb/cu in.
Melting Range	2822-3000 °F
Sp. Elec. Resis.	157 10^{-6}Ohm-cm
Specific Heat	0.125 (Btu/lb°F)
Mean Coeff. of Ther. Exp.,/ °F	5.2 X 10^{-6}

TABLE 2. CHEMICAL COMPOSITION

Element	Percent (weight)
Al	4.0 - 6.0
C	0.15
H	0.003 - 0.020
Fe	0.5
Mn	0.3
N	0.07
O	0.2
Sn	2.0 - 3.0
Ti	Balance

TABLE 3. SUMMARY OF GRINDING CONDITIONS

Wheel Type	39C60H8VK, 39C120I8VK
Wheel Speed(fpm)	2000, 4000, 6000
Table Speed(fpm)	50
Down Feed per pass(inch/pass)	0.0005 (16 passes)* 0.0004 (2 passes) 0.0002 (6 passes)**
Cross Feed(inch/pass)	0.05
Wheel Classification	Soft grade (H , I) Open Structure (8) Grain Size (60, 12)

*All Grinding done in Single Pass

**Wheel Dressed before Final Pass (Coarse dressing done to maintain sharpness)

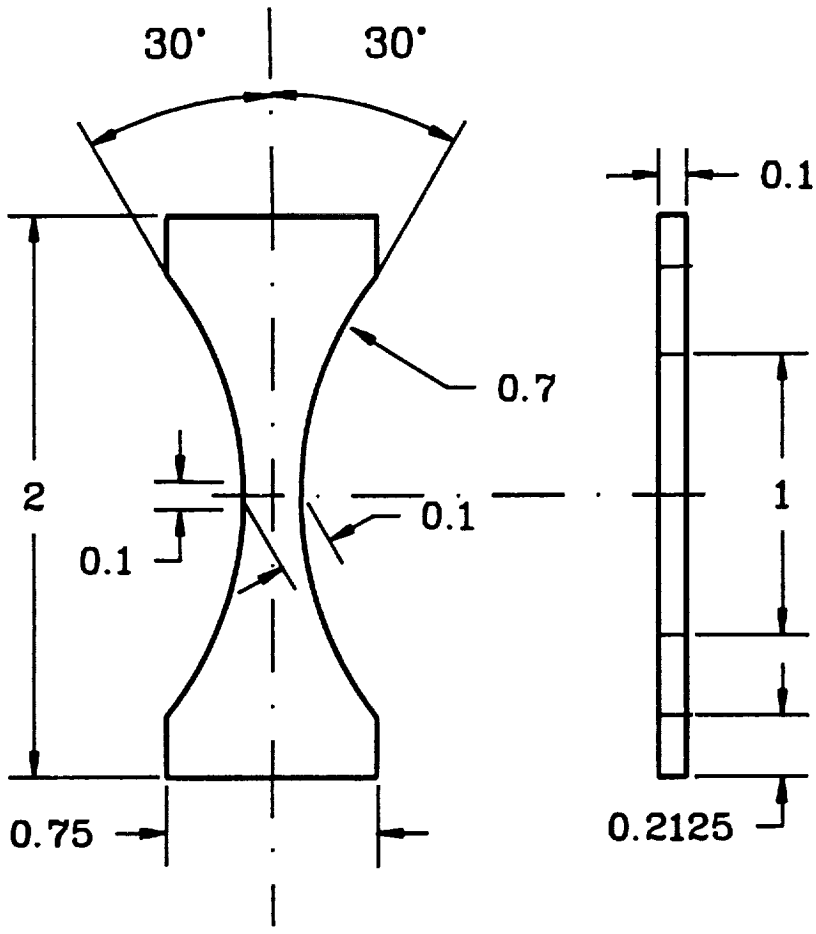

Figure 1. Fatigue specimen.

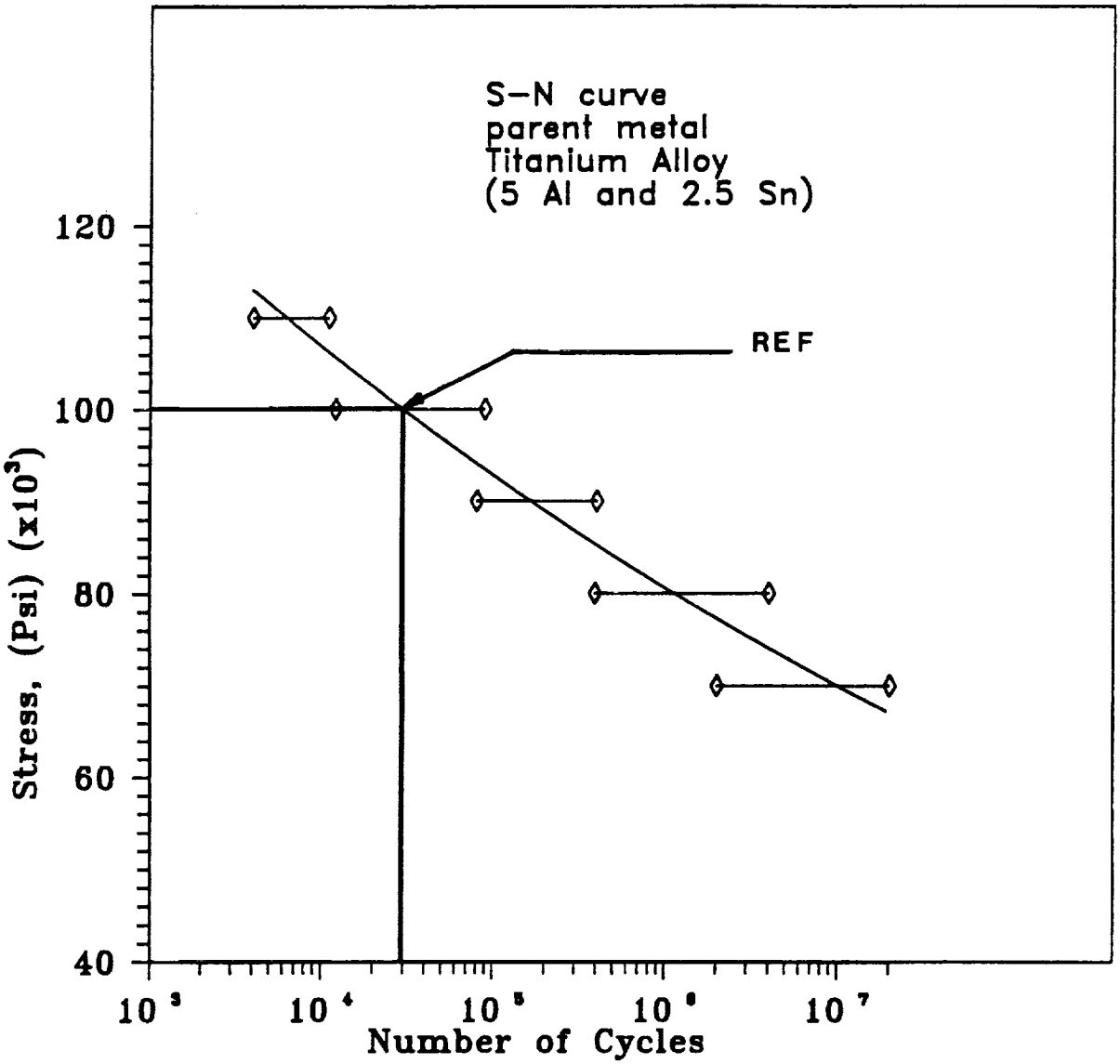

Figure 2. S/N Diagram for Titanium alloy virgin material.

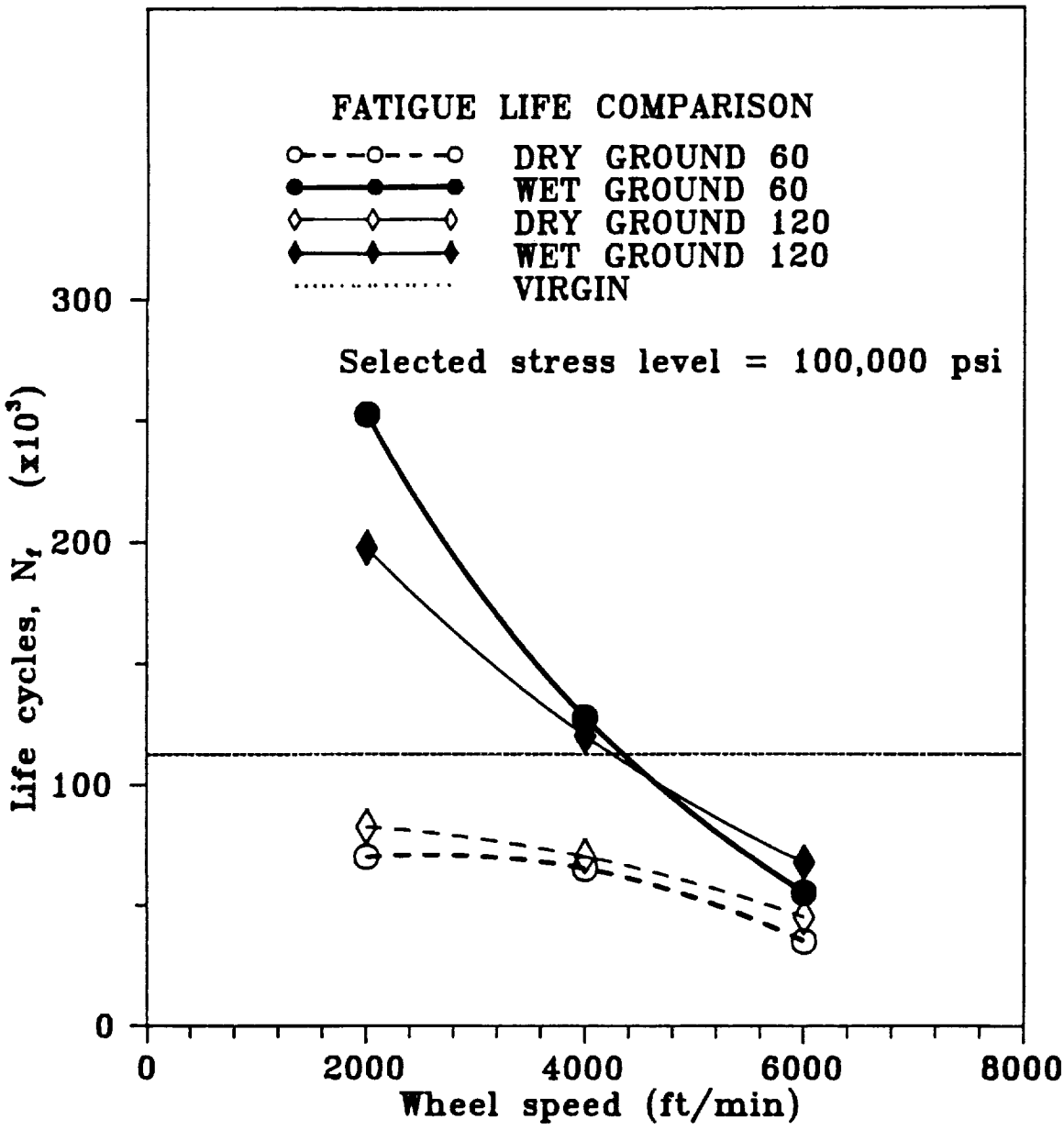

Figure 3. Fatigue life vs wheel speed: virgin material and ground specimens.

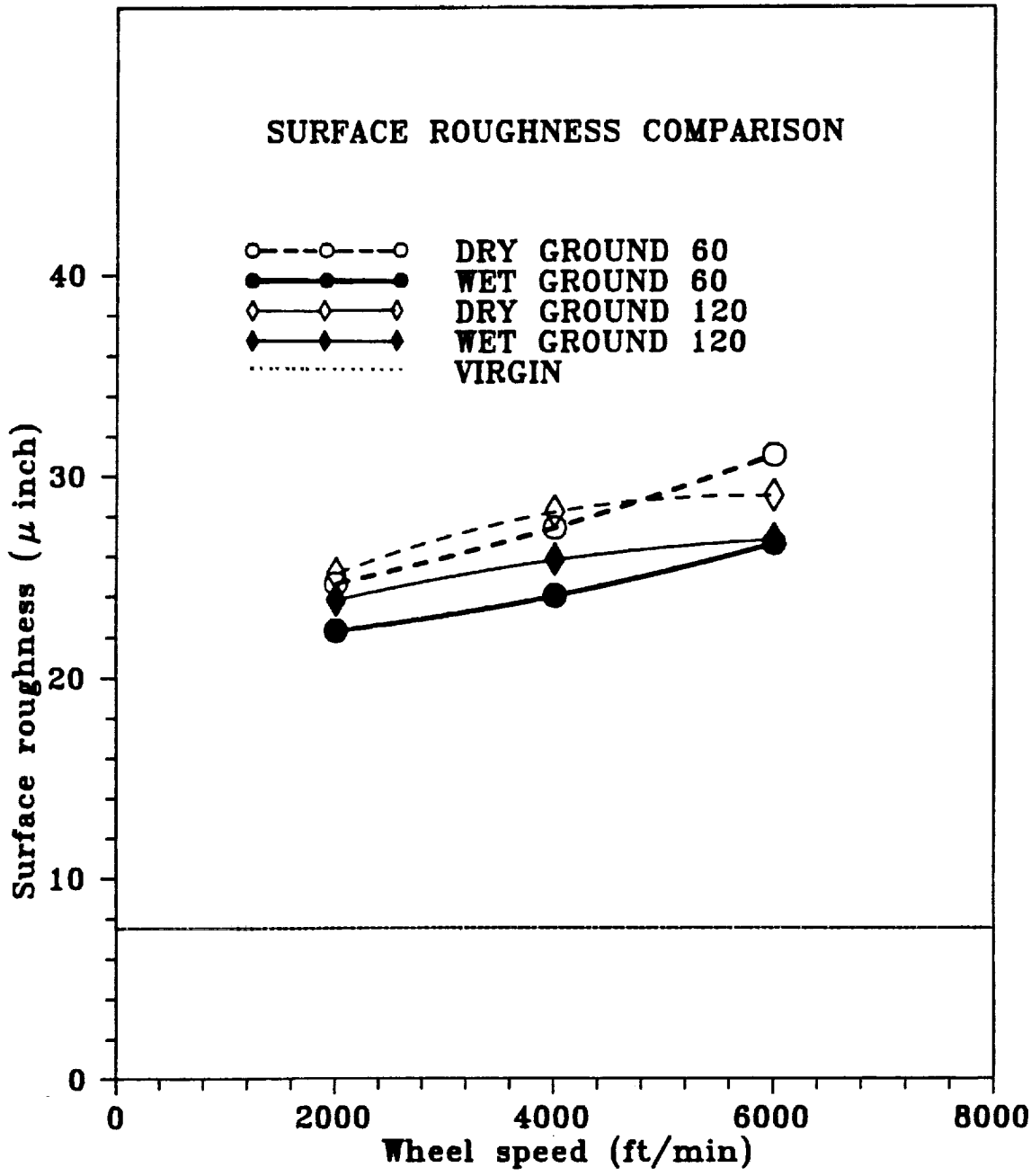

Figure 4. Surface roughness vs wheel speed: virgin material and ground specimens.

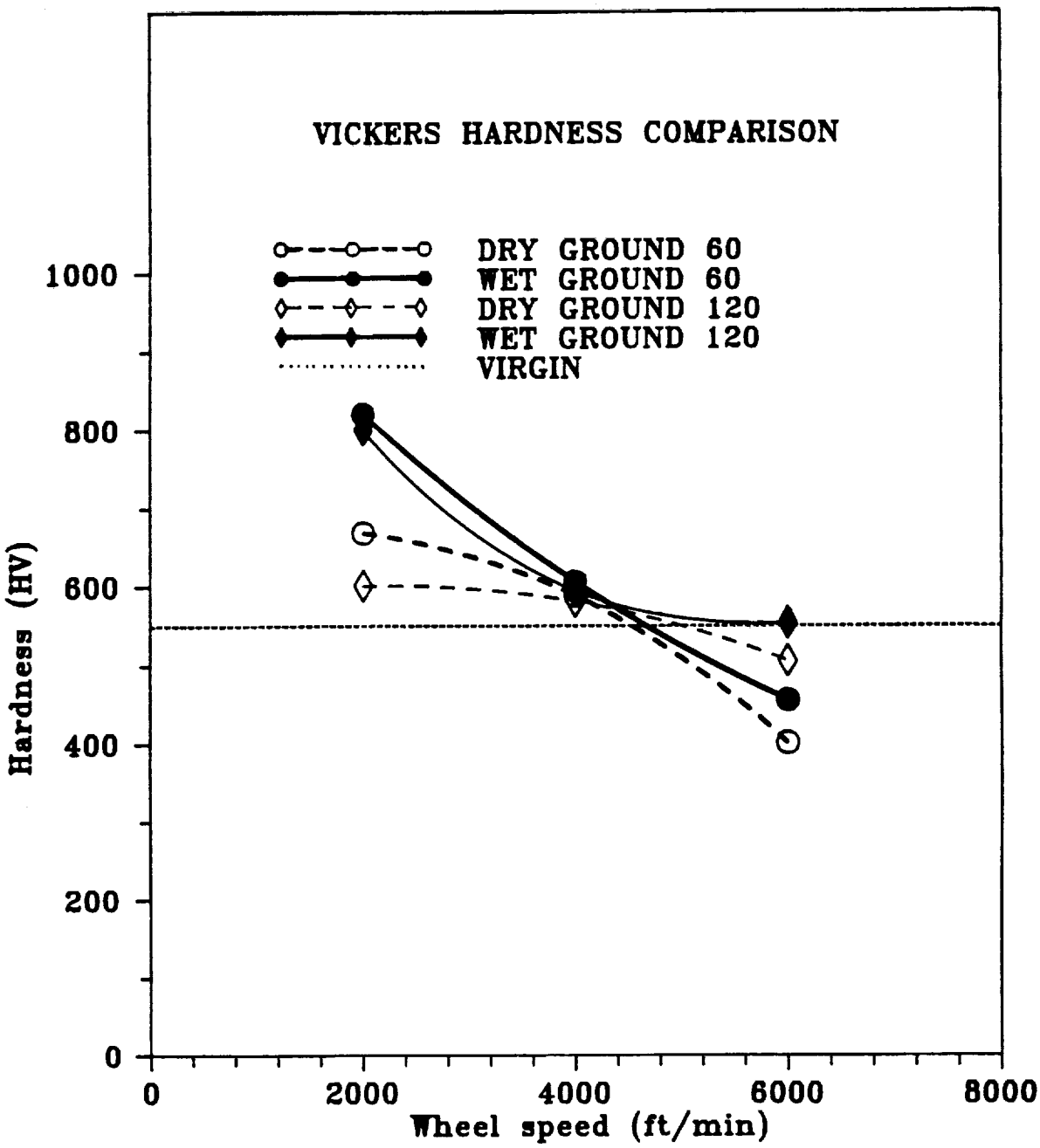

Figure 5. Vickers hardness vs wheel speed: virgin material and ground specimens.

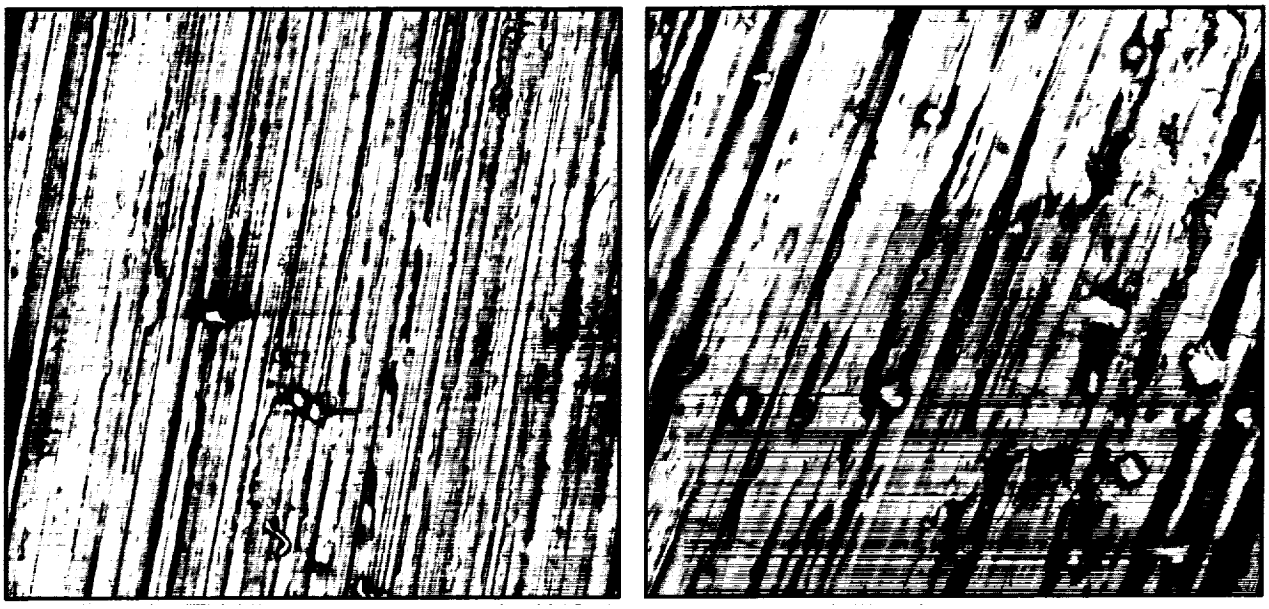

Figure 6. Scanning electron micrographs of surfaces ground under dry condition:
(a) magnification X150, grinding speed 2000 feet/minute.
(b) magnification X150, grinding speed 6000 feet/minute.

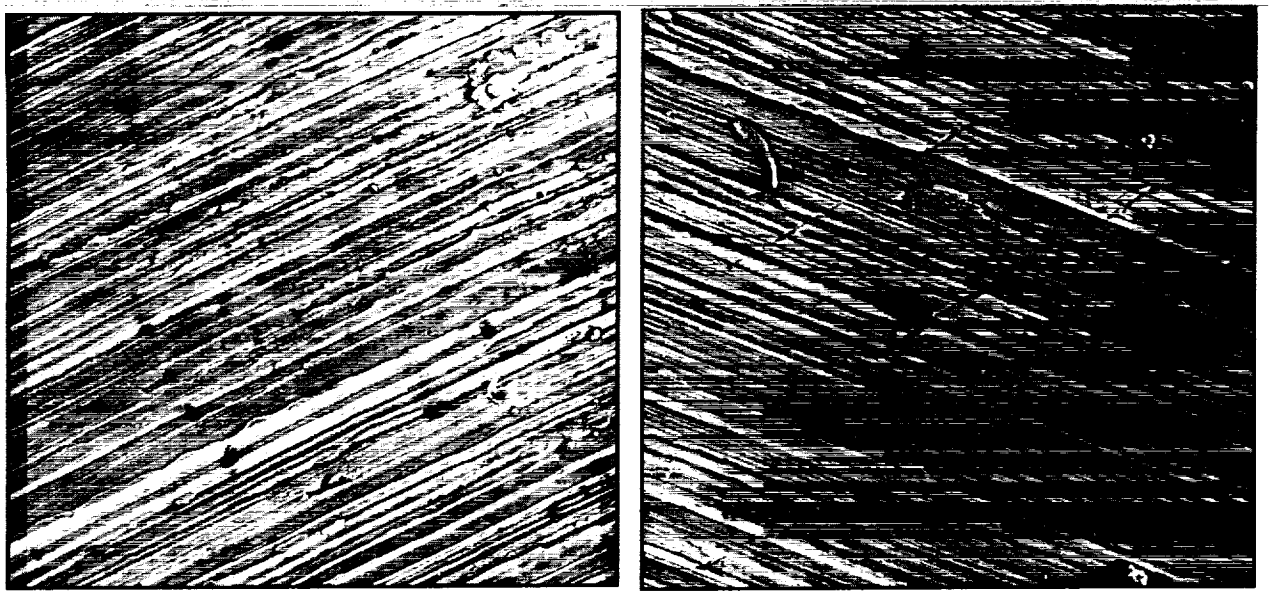

Figure 7. Scanning electron micrographs of surfaces ground under wet condition:
(a) magnification X150, grinding speed 2000 feet/minute.
(b) magnification X150, grinding speed 6000 feet/minute.

ENGINEERING MANAGEMENT OF LARGE SCALE SYSTEMS

Serita Sanders, Tepper L. Gill, and Arthur S. Paul
Department of Electrical Engineering
and
Department of Systems & Computer Science
Howard University
Washington, D.C.

Introduction

The organization of high technology and engineering problem solving, has given rise to an emerging concept. Reasoning principles for integrating traditional engineering problem solving with systems theory, management sciences, behavioral decision theory, and planning and design approaches can be incorporated into a methodological approach to solving problems with a long range perspective.

Long range planning has a great potential to improve productivity by using a systematic and organized approach. Thus, efficiency and cost effectiveness are the driving forces in promoting the organization of engineering problems.

This paper broadly covers aspects of systems engineering that provide an understanding of management of large scale systems. Due to the focus and application of research, other significant factors (e.g. human behavior, decision making, etc.) were not emphasized but were considered.

Systems Engineering Concepts

A. Definition and Objective of Systems Engineering

A system is a combination of parts or elements to form a unitary whole. Systems engineering is a management of technology. This is accomplished by the following activities: (1) Transforming an operational need into a description of systems performance parameters and a systems configuration through the use of a process of definition, synthesis, analysis, design, test, and evaluation; (2) Integrating related technical parameters and ensuring compatibility of all physical, functional, and program interfaces in a manner that optimizes the total system definition and design; and (3) Integrating reliability, maintainability, safety, survivability, human, and other such factors into the total engineering effort to meet cost, schedule, and technical performance objectives.

A uniform systems engineering process is required to manage projects because:

1. The science and technology required to design and produce a completely integrated and coherent system exceeds any one person's capability to master;

2. There is a need for a communication vehicle for specialists with dissimilar technical knowledge, skills, and interests to contribute to an integrated system design and development process; and

3. Systems engineering, to be effective, must provide the process for making many technical and management decisions progressively as the need occurs in system design and development.

B. System Life Cycle

A life cycle is used to develop a system. It begins with the initial identification of a need and extends through planning, research, design, production or construction, evaluation, consumer use, field support, and an ultimate product phase out (illustrated in figure 1).

Challenges of Large Scale Systems

A. Large product organization

Large scale systems require combined inputs of specialists representing a wide variety of engineering disciplines. These engineers must be able to communicate with one another as well as be conversant with such interface areas as purchasing, accounting, personnel management, and to some extent legal requirements. Technological and economic feasibility are no longer the main determinants for the engineer.

Large scale systems usually require fluctuating the manpower loading, and depending on the functions to be performed on the project, applying a phase-by-phase development process implementation.

Subcontracting is a major factor associated with large projects. The development of large scale systems can involve extensive contracting and subcontracting.

B. Technological growth and change

Technological growth occurs continuously and is stimulated by an attempt to respond to some unmet current need and/or to perform on-going activities in a more effective and efficient manner. In addition, these changes are being stimulated by social changes, political objectives and ecological factors.

Figure 1
A life cycle is used to integrate various support mechanisms that ultimately bring a system into existence.

THE SYSTEM LIFE CYCLE			
	CONSUMER	Identification of Need	"Wants or desires" for systems (because of obvious deficiencies/problems or made evident through basic research results).
	PRODUCER	System Planning Function	Marketing analysis; feasibility study; advanced system planning (system selection, specifications and plans, acquisition plan research/design/ production, evaluation plan, system use and logistic support plan); planning review; proposal.
		System Research Function	Basic research; applied research ("need" oriented); research methods; results of research; evolution from basic research to system design and development.
		System Design Function	Design requirements; conceptual design; preliminary system design; detailed design; design support; engineering model/prototype development; transition from design to production.
		Production and/or Construction Function	Production and/or construction requirements; industrial engineering and operations analysis (plant engineering, manufacturing engineering, methods engineering, production control); quality control; production operations.
	CONSUMER	System Evaluation Function	Evaluation requirements; categories of test and evaluation; test preparation phase (planning, resource requirements, etc); formal test and evaluation; data collection, analysis, reporting, and corrective action; retesting.
		System Use and Logistic Support Function	System distribution and operational use; elements of logistics and life cycle maintenance support; system evaluation; modifications, product phase-out; material disposal, reclamation, and or recycling.

Systems Engineering Management

Systems engineering management (SEM) provides the necessary overview functions to ensure that all required engineering disciplines and related specialties are properly integrated (Figure 2). These functions include planning, organizing and staffing, monitoring, and controlling which are used to design, develop and produce a system that will meet the stated need in an effective manner. The result is a system that has the proper mix of resource hardware, software, facilities, personnel, and data. The underlying objective is to produce a system at the right location, at the right time, with a minimum expenditure of resources.

A. Planning

Planning is a process for developing and formulating a course of action to be taken in the future. The systems engineering management plan includes the appropriate planning information for the project as an entity. All projects should include a single top level document of this type to provide successful project guidance.

B. Organizing and Staffing

The first step in organizing the project is to determine the governing activities. Grouping these identified activities in terms of a functional oriented structure of some type (e.g. unit, group, department, or division) establishes organization. Staffing the structure with appropriate personnel skills to perform the designated activities in a coordinated manner is the next step.

C. Monitoring

Figure 3 is a basic milestone chart that gives the status of the project at a glance. It includes scheduled, actual and anticipated completion dates. This allows for careful scrutiny of the project status.

D. Directing and Controlling

Directing program implementation consists of day-to-day managerial functions and the identification of responsibilities to ensure that project objective(s) are met. Project control is the sustaining of on-going management activity that will guide, monitor, and evaluate project accomplishment by the stated objective(s).

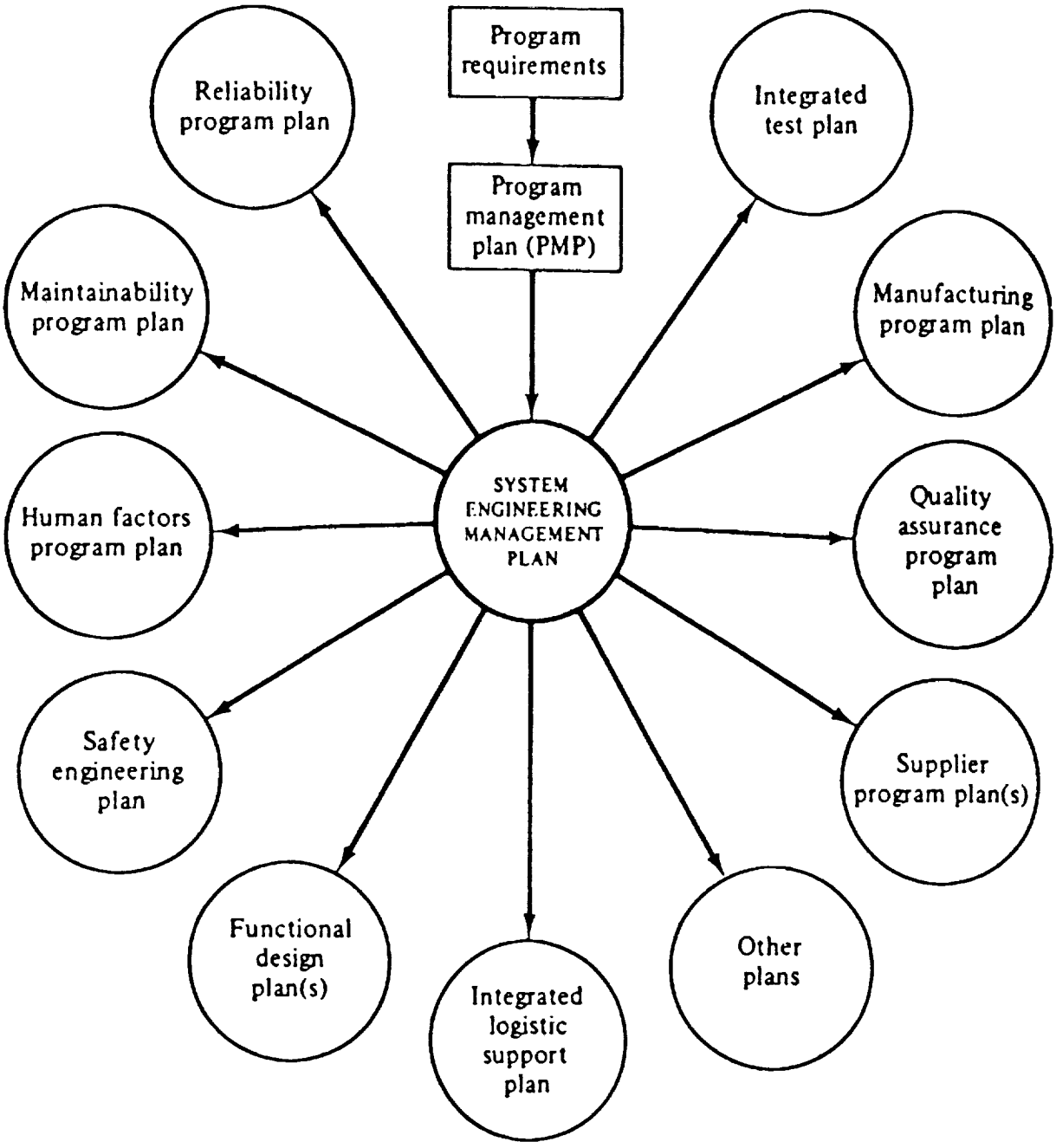

Figure 2.
Program Plan Relationships
This figure depicts the relationship between the PMP and governing activity, all of which need systems engineering management for preparation.

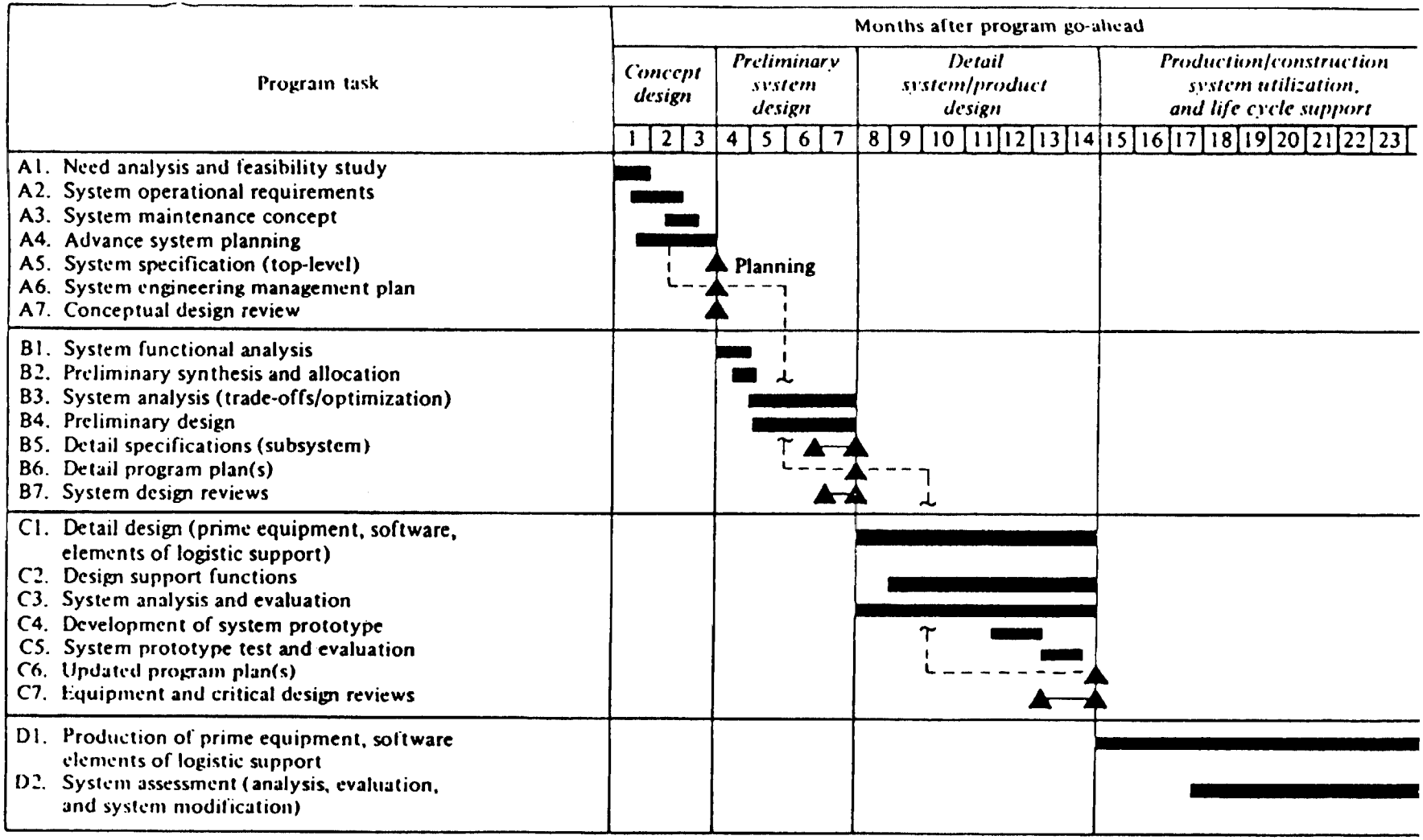

Figure 3.
Basic Milestone Chart

Summary

Considering the following questions when implementing systems engineering practices will ensure a well managed system of any magnitude.

1. Have systems engineering tasks been identified?

2. Have the responsibilities for systems engineering functions been established?

3. Has a systems management plan been developed?

4. Have detailed program plans been developed for reliability and maintainability?

5. Has a corrective action procedure been established to handle proposed system changes?

6. Have conceptual system equipment and critical design reviews been scheduled?

References

1. Blanchard, B.S. and Fabrycky, W.J. Systems Engineering and Analysis, (Englewood Cliffs, New Jersey: Prentice-Hall), 1981.

2. Churchman, C. West, The Systems Approach, (New York: Dell Publishing Co., Inc.) 1968.

3. Hall, Arthur D., A Methodology for Systems Engineering, (New York: Van Nostrand Reinhold Company), 1962.

4. Mission Operations and Data Systems Directorate System Management Policy, (Greenbelt, Maryland: NASA Goddard Space Flight Center), 1986.

5. Nadler, Gerald, "Systems Methodology and Design", (IEEE, Vol. 15, No. 6) November/ December 1985.

6. Sage, Andrew P., Methodology for Large Scale Systems, (New York: McGraw-Hill Book Company), 1977.

N91-28123

AN EVALUATION OF THE INTERFACIAL BOND PROPERTIES BETWEEN CARBON PHENOLIC AND GLASS PHENOLIC COMPOSITES*

Kelvin Jordan
Hughes Aircraft Company
Tucson, Arizona

Raymond Clinton
NASA - Marshall Space Flight Center
Huntsville, Alabama

Shaik Jeelani
Materials Research Laboratory
Tuskegee University, Tuskegee, Alabama

ABSTRACT

The effects of moisture and surface finish on the mechanical and physical properties of the interfacial bond between the carbon/phenolic (C/P) and glass/phenolic (G/P) composite materials are presented in this paper.

Four flat panel laminates were fabricated using the C/P and G/P materials. Of the four laminates, one panel was fabricated in which the C/P and G/P materials were cured simultaneously. It was identified as the cocure. The remaining laminates were processed with an initial simultaneous cure of the three C/P billets. Two surface finishes, one on each half, were applied to the top surface. Prior to the application and cure of the G/P material to the machined surface of the three C/P panels, each was subjected to the specific environmental conditioning. Types of conditioning included: (a) nominal fabrication environment, (b) a prescribed drying cycle, and (c) a total immersion in water at 160°F.

Physical property tests were performed on specimens removed from the C/P materials of each laminate for determination of the specific gravity, residual volatiles and resin content. Comparison of results with shuttle solid rocket motor (SRM) nozzle material specifications verified that the materials used in fabricating the laminates met acceptance criteria and were representative of SRM nozzle materials.

Mechanical property tests were performed at room temperature on specimens removed from the G/P, the C/P and the interface between the two materials for each laminate. The double-notched shear strength test was used to determine the ultimate interlaminar shear strength. Results indicate no appreciable difference in the C/P material of the four laminates with the exception of the cocure laminate, where a 20 percent reduction in the strength was observed. The most significant effect occurred in the bondline specimens. The failure mode was shifted from the C/P material to the interface and the ultimate strength was significantly reduced in the wet material. No appreciable variation was noted between the surface finishes in the wet laminate.

*Work supported by NASA Grant

AN EVALUATION OF THE INTERFACIAL BOND PROPERTIES BETWEEN CARBON PHENOLIC AND GLASS PHENOLIC COMPOSITES

Introduction

The Space Shuttle's solid rocket motor (SRM) nozzle is constructed from carbon/phenolic (C/P) and glass/phenolic (G/P) composite material. The C/P is used as the outer or ablative material of the nozzle ring and it is backed by a thin G/P insulator. These composite rings are adhesively bonded to a structural metal housing, forming the nozzle. Anomalies in performance of the ablative material during flight and static testing have stimulated research to examine the effects of moisture, cure cycles and surface finish on the integrity of the interfacial bond between G/P and the C/P rings.

It is well recognized and reported that the high performance composites absorb moisture from their surrounding environments, especially under warm and humid conditions [1-6]. In epoxy-based composites, absorbed moisture has been shown to affect the matrix and the interface dominated properties of the composite. Degradation is evident in the interlaminar shear strength and ultimate strength specifically, as well as other mechanical properties [1-11]. In contrast to the fairly large literature base for the epoxy-based composites, the phenolic-based composites have essentially remained unstudied with respect to the effect of moisture.

The objective of this research was to assess the integrity of the interfacial bond between the C/P and the G/P material as a function of the moisture/volatile content present in the C/P material prior to the bonding of the G/P material. Another variable, the effect of surface finish applied to the bonding surface of the C/P prior to the bonding of the G/P material, was also investigated.

Materials

Materials were obtained from the Wasatch Division of Morton Thiokol Incorporated (MTI) for use in nozzle material development research. MTI purchased the materials in the form of 48-inch width preimpregnated (prepreg) broadgoods from the Fiberite Corporation. The C/P and G/P materials are designated by Fiberite as MX-4926 and MXB-6001, respectively. The constituent materials of the MX-4926 prepreg were Polycarbon CSA, an eight-harness satin rayon-based carbon fabric, Borden's SC1008 phenolic resin system and Fiberite 1148 carbon black filler. The constituent materials of the MXB-6001 were United Merchant 184 weave S-glass fabric and Borden's SC1008 phenolic resin system.

A series of physical property tests were conducted on the prepreg materials to ensure conformity with MTI material acceptance specifications, STW5-2651F and STW5-3279A from the G/P and C/P materials, respectively [12,13]. The critical properties measured to assess the quality of the materials were the resin content, filler content, volatile content, resin flow, sodium content and cloth content.

A summary of the prepreg acceptance test results may be found elsewhere [14]. All prepreg physical properties met the acceptance criteria stated in MTI specifications. Based on the compliance of all the prepreg physical properties with the specification limits, the materials were accepted for use in the program.

Carbon-phenolic and glass-phenolic 10 inch (fill) by 12 inch (warp) plies were arranged in stacks which when cured yielded an inch thick laminate. The C/P and G/P stacks contained 84 and 40 plies respectively with the J-type 30 gage thermocouples place at the designated plies to monitor temperatures during debulking and subsequent curing.

The C/P and G/P stacks were individually debulked in a tetrahedron press to 86 percent of their cured density simulating the nominal debulk obtained during the tape wrapping of the materials during the processing of SRM nozzle components.

3. Fabrication of Glass-Phenolic and Carbon-Phenolic Test Articles:

a) Lay-up and Cure of Carbon-Phenolic Laminates:

Three C/P laminates were assembled using the six debulked stacks CP-1 thru CP-6 (figure 1) as follows: (a) Panel A consisted of stacks CP-1 and CP-2, (b) Panel B consisted of stacks CP-3 and CP-4, and (c) Panel C consisted of stacks CP-5 and CP-6. The three panels were assembled and bagged on a trilateralcure tool. The hydroclave trilateral tool was designed to simultaneously cure three flat panel laminates with cured thickness of 2.5 inches each. The laminates were cured according to the hydroclave cure cycle designed by MTI [15].

After the cure, the laminates were nondestructively examined using X-rays to ensure the quality of each. No low density indications or delaminations were observed in any of the laminates.

b) Surface Preparation:

For investigation of the interfacial properties, precise and reproducible duplications of the surface finishes are critical to the creditability and validity of the results. Surface finishes of 125 and 250 microinches were precisely duplicated to match the finishes produced at MTI. The 250 microinch surface finish (maximum upper limit) is applied by MTI to cured C/P surfaces of SRM nozzle components, prior to over-wrap of the G/P insulator.

c) Conditioning:

The panels were subjected to prescribed environmental conditioning detailed in the following sections.

Panel A. Panel A (also identified as the as-received panel) was the control. This laminate was fabricated according to nominal processing conditions and environments. In this manner, it represented the typical state of the SRM C/P material prior to the overwrap and curing of the G/P insulator.

Panel B. Many authors have noted that microcracking was induced in polymeric materials when the material was subjected to extreme thermal gradients [2,8,11,16]. This damage to the material was irreversible and resulted in degradation of the ultimate interlaminar shear strength and ultimate tensile strength. Such damage can be unintentionally created in materials during conditioning if sufficient precautions are not observed.

In the phenolic-based composites, there are additional concerns relating to potential effects on the properties by changing the state of cure when these materials are subjected to extreme thermal gradients.

A research program was initiated at Southern Research Institute (SRI) [17] to determine an effective and nondamaging drying process for C/P materials, which provided accelerated weight loss without altering the cured state or microcracking in one-half inch cube samples.

Panel B (also identified as the dry panel) was subjected to a modified SRI drying cycle which included corrections for size and shape of the laminates. The drying cycle was designed to yield drying of the bonding surface to a depth of 0.50 inches into the thickness of the laminate. The cycle was as follows:

a. Dessicate for 66 days,
b. Dry at 100 ° F and 0.1 Torr vacuum for 11 days,
c. Dry at 140 ° F and 0.1 Torr vacuum for 6 days,
d. Dry at 160 ° F and 0.1 Torr vacuum for 13 days.

Panel C (also identified as the wet panel) was subjected to controlled moisture conditioning. It was originally placed into an environmental chamber maintained at 160 °F and 95% relative humidity (RH). After 47 days in the chamber, the panel was relocated and submerged in water at 160 °F with the machined surface placed upward in a pan. This was done to accelerate the absorption process.

Percent weight gain versus time data were plotted as shown in Figure 2. The conditioning resulted in a 0.96 percent weight gain.

d) Lay-up and Cure of Glass/Phenolic to Carbon/Phenolic Laminates:

Lay-up and cure of the G/P immediately followed the conditioning of the C/P laminates. Prior to the lay-up of the G/P debulked stacks, the stacks GP-1 thru GP-3 (Figure 3) were machined to equal the dimensions of their respective C/P laminates. The lay-up and bagging sequences for cure may be found in reference [14]. The composite laminates were machined and test sections removed.

e) Lay-up and Cure of Cocure Laminate:

A COCURE laminate was fabricated using the debulked C/P stacks CP-7 and CP-8 and the debulked G/P stack GP-4. The laminate was assembled and cured according to the autoclave cure cycle presented in [18]. The cured laminate was machined and test sections removed.

Experimental Testing and Examination

a) Physical Property Tests:

A series of physical property test were conducted on the C/P and G/P materials of each cured laminate to ensure the quality of the materials after curing. The tests were performed according to the procedures contained in the MTI cured material acceptance specification STW5-2845D, which con-

sisted of residual volatile content, specific gravity and resin content [19]. The MTI specifications require that resin content tests be performed using the tested residual volatile specimens. The same test geometry was used for each of the above three tests. The specimen geometry is shown in Figure 4.

b) Optical Photomicroscopy:

Optical photomicroscopy examinations were conducted on specimens taken from the C/P, G/P and at the interfaces of each laminate. The objectives were to : (a) observe material for possible microstructural damage; (b) characterize the appearance of the microstructure of the C/P and G/P materials; and (c) characterize the appearance of the different interfaces between the C/P and G/P laminates. A typical final machined specimen is presented in Figure 5. Prior to the examination, each specimen was mounted in epoxy and then polished. Photomicrographs were taken of each specimen at several magnifications.

c) Interlaminar Shear Strength Test:

Matrix/interface dominated properties are considered to be among the most critical to solid rocket motor nozzles and the critical failure mode for phenolics was determined to be delamination [20]. Observations made in the past after static and flight tests, which support delamination as being the critical failure mode, include ply-lift in the virgin C/P material and separation of the insulating (G/P) material from the ablative (C/P) material. The critical properties for prediction of the margin of safety for delamination at the G/P and C/P interface are interlaminar shear and across-ply tension. In this program, the property selected for evaluation of surface finish and moisture effects on the interface between the C/P and G/P materials was interlaminar shear strength. A double-notched shear specimen was used for the determination of the ultimate interlaminar shear strength at room temperature (70°F) for the C/P, G/P and at the interface between these materials.

The basic cutting plans for the specimen removal may be found elsewhere [14]. Specimens were first excised as blanks, then machined to the specified dimensions shown in the schematic presented in Figure 6. The gage section was maintained at 0.375 inches (fill) by 0.300 inches (warp) by 0.050 inches (A/P), allowing four plies to be isolated in the gage section for the C/P specimens and two plies in the gage section for the G/P specimens. The number of plies isolated in the gage section was determined by dividing the A/P dimension of the gage section by the cured ply thickness of each material. For the interface specimens, approximately 2 plies of C/P and 1 ply of G/P were isolated in the gage section with the bondline centered in the gage section. The specimens were loaded in axial compression to provide pure shear at the gage section. Each specimen was loaded at a rate of 10,000 pounds per minute [21]. The load versus time plot obtained from the Instron for each specimen was transformed into a stress versus time plot by dividing load values by the shear (gage) area. The data obtained from the linear stress versus time plot were used to determine the ultimate interlaminar shear strength.

Results and Discussion

a) Physical Property Tests:

A summary of the physical property test results is presented in Table 1. Based on the compliance of all the physical property test results with the specification requirements, the C/P and G/P materials of the four laminates were accepted as representative nozzle materials.

b) Photomicroscopy:

Examination of the photomicroscopy specimens at a magnification of 1000 revealed no evidence of microstructural damage such as microcracks, voids or delaminations in any of the materials. The shape of the fibers and presence of fillers in the matrix materials were used in characterizing the appearance of the materials. The C/P fibers exhibited the typical non-uniform crenulated cross-section, while the G/P fibers exhibited uniform circular cross-sections. The matrix material of the C/P material revealed the presence of the carbon-black filler; no fillers were present in the G/P matrix material. The carbon-black filler appears in the photomicrograph as the light spots in the matrix material.

The different C/P to G/P interfaces were also characterized based upon their appearances. Three different interfaces were observed: (a) 125 microinch; (b) 250 microinch; and (c) the cocure interface. Surface finish is defined as the mean distance between peak and valley measured in microinches. Observed from the examination was that the distance from peak to valley for the 125 microinch finish was half that of the 250 microinch interface. The appearance of the cocure interface was unmachined with evidence of the carbon-black filler migration across the interface. The migration was attributed to the cocuring of both the G/P and C/P materials.

c) Interlaminar Shear Strength:

The results of the interlaminar shear strength tests are summarized and presented in Table 2 for the four laminates. Analysis of the data yielded the following results:

(a) There were no appreciable differences in the ultimate strength observed for the G/P material among the four laminates.

(b) There was no significant difference in the ultimate strength of the C/P material of the 3 laminates which received the hydroclave cure. There was, however, a 20 percent reduction in ultimate strength in the C/P material of the cocure laminate. The reduction in the C/P material of the cocure when compared with the strengths of the 3 other laminates was attributed to the differences in the pressures of the autoclave and hydroclave cure cycles. The cocure laminate was cured using the autoclave cure cycle where the maximum pressure obtained was 240 psig, while the hydroclave cured laminates experienced maximum pressure of 1050 psig.

(c) The results from the evaluation of the interfacial bond strength showed for the cocure, dry and as-received laminates, that the ultimate strength of the interface was at least as high as that of the C/P material of each laminate, because failure occurred in the C/P material at the gage section. The most significant effect occurred in the interface specimens of the wet laminate, where the failure mode was shifted from the C/P (observed for the as-received, dry and cocure interface specimens) to the interface and the ultimate strength was significantly reduced. The effect of moisture at the interface is believed to have masked any potential variations in surface finish, and to have caused the shift in failure mode.

(d) There was no appreciable difference between the 125 and 250 microinch surface finishes for the wet laminate. A test [22] was performed to determine if there was any difference in the values of the ultimate strength for the two interfaces of the wet laminate. It was found that the individual specimen results for the 125 surface finish were within the bounds of the 95 percent confidence interval of the 250 surface finish results. The results obtained from the test showed that there was no significant difference in the ultimate strengths of the two populations.

The test results (mean value) for the C/P material of the as-received laminate were compared against the mean values of the existing MX-4926 C/P material databases [20,23] to assess the reliability of the results obtained in the program. The mean value for the ultimate strength obtained from the existing databases with curing and test parameters identical to those of this program, clearly indicates that the results are in agreement with those of previous programs.

(d) SEM Examination:

The double-notched shear specimens were visually examined after testing to determine the mode of failure. Of the specimens tested, only two distinguished modes were observed. These were across laminar and interlaminar failure.

Examination of the fracture surfaces by the conventional technique of optical microscopy rendered accurate observations impractical and therefore the scanning electron microscopy was required. Scanning electron microscopy (SEM) examination was performed using a Cambridge 250 mk2 scanning electron microscope. The fractured surfaces were etched with gold prior to their examination.

Interlaminar failure (presented in Figure 7) was characterized by a fracture surface exhibiting one or more of the following features: (a) large areas of exposed denuded fibers, (b) thin cracks between the fibers and matrix, and (c) clear imprints in the matrix where fibers were removed. This type of failure was characteristic of the interface specimens of the wet laminate and the glass phenolic material of all laminates.

Across-laminar failure (presented in Figure 8) was characterized by a fracture surface exhibiting similar features on interlaminar failure with the addition of some extensive fiber breakage across individual plies of material. This type of failure was common to all carbon phenolic material and the bondline specimens of the dry, as-received and the cocure laminates. From analysis of fracture surfaces of failed DNS C/P specimens by SRI, it was found that the predominate mode of failure was interlaminar although the presence of across-laminar failure was observed [21].

Conclusions

The following conclusions were based upon the test results presented in the previous section.

(1) Moisture substantially degrades the integrity of the interfacial bond between C/P and G/P materials.

(2) The apparent effect of autoclave curing of the C/P material reduces the ultimate interlaminar shear strength of the C/P material by nearly 20% as compared to the hydroclave curing of the C/P material.

(3) The variation in applied surface finishes had no appreciable effect on the ultimate interlaminar shear strength of the interface in the wet laminate. The variation in the applied surface finishes on the remaining three laminates was not conclusively determined due to the failure having occurred in the C/P material of the gage section for the interface specimens.

References

1. Curtis, P.T., "Residual Strains and the Effects in Fiber Reinforced Laminates", Technical Report 80045, (April 1980)

2. Desai, R., Whitesinde, J.B., "Effects of Moisture in Epoxy Resins and Composites", Advanced Composite Materials Environmental Effects, ASTM STP 658, J.R. Vinson, ed., ASTM, pp. 2-20, (1978)

3. Hertz, J., "Moisture Effects on the High Temperature Strength of Fiber-Reinforced Composites", Convair Aerospace Division of General Dynamics, National SAMPE Technology Conference, (October 1972)

4. Powell, J.H., and Zigrang, D.J., "Moisture Absorption and Desorption Characteristics of Three Graphite-Epoxy Systems", SAMPE Journal, 13:4, (1977)

5. Shen, C.H., and Springer, G.S., "Moisture Absorption and Desorption of Composite Materials", Journal of Composite Materials, 10: 1-20, (1976)

6. Springer, G.S., "Moisture Absorption in Fiber-Resin Composites", Developments in Reinforced Plastics Chapter 3: 60, (1982)

7. Browning, C.E.,"The Mechanics of Elevated Temperature Property Losses in High Performance Structural Epoxy Resin Matrix Materials After Exposure to High Humidity Environments", Polymer Engineering and Science, 18:31, (1978)

8. Mazor, A., Broutman, L.J., and Erkstein, B.H., "Effects of Long Term Water Exposure on Properties of Carbon and Graphite Fiber Reinforced Epoxies", Journal of Material Science, 15:751-754, (1980)

9. Morgan, R.J., O'Neal, J.E., and Fanter, D.L., "The Effects of Moisture on the Physical and Mechanical Integrity of Epoxies", Polymer Engineering and Science, 18:31, (1978)

10. Scola, D.A., "A Study to Determine the Mechanisms of S-Glass/Epoxy Resin Composite Degradation Due to Moisture and Solvent Environments", Society of Plastics Industry 30th Annual Technology Conference, Reinforced Plastics Composites Institute, (February 1975)

11. Young, H.L. and Greener, W.L., "High Temperature Strength Degradation of Composites During Aging in Ambient Atmosphere", Hercules Incorporated, (May 1972)

12. Morton Thiokol Incorporated, "Glass Cloth Phenolic Preimpregnated Specification", STW5-2651F, (May 1987)

13. Morton Thiokol Incorporated, "Glass Cloth Phenolic Preimpregnated Specification", STW5-3279A, (May 1987)

14. Morton Thiokol Incorporated, "Aft Inlet Ring Manufacturing Plan", C.P.I. Number HP30L, (October 1984)

15. McKague, L., "Environmental Synergism and Simulation in Resin Matrix Composites", Advanced Composite Materials-Environmental Effects, ASTM-STP 658, J.R. Vinson, ed., p. 193, (1978)

16. Stokes, E., "Moisture Diffusion in Carbon Phenolic Composites", Southern Research Institute, JANNAF Conference, (October 1987)

17. Morton Thiokol Incorporated, "Aft Exit Cone, Second Wrap Manufacturing Plan", C.P.I. Number HP43W, (November 1986)

18. Morton Thiokol Incorporated, "SRM Nozzle Tag End Testing Specification", STW5-2845D, (September 1988)

19. Canfield, A.R., Mathis, J.R., Starett, H.S., and Koenig, J.R., "Materials Property Definition and Generation for Carbon-Carbon and Carbon-Phenolic Materials", AIAA/ASME/ ASEE/SAE 23rd Joint Propulsion Conference, (June 29 - July 2, 1987)

20. Stokes, E., "Personal Communication", Southern Research Institute, (August 1988)

21. Freeman, D. Pisani, and Purves, R. "Statistics", W.W. Norton and Company Publishers, New York, (1978)

22. Neighbors, B., "MX-4926 and FM-5055 Carbon-Phenolics", SORI EAS-86-340-5694-3-I-F, (April 1986)

Acknowledgments

The authors gratefully acknowledge the support from NASA - Marshall Space Flight Center through grant NGT - 50130 for this study.

TABLE 1: SUMMARY OF THE PHYSICAL PROPERTY TEST RESULTS

Panel	Status	Material	Residual Volatiles	Resin Content	Specific gravity
As - received	*	C/P	2.9	30.9	1.5
	**	C/P	2.6	30.8	1.5
	**	G/P	1.1	22.2	2.1
Dry	*	C/P	2.9	31.1	1.5
	**	C/P	2.7	30.7	1.5
	**	G/P	1.1	22.1	2.1
Wet	*	C/P	2.9	31.1	1.5
	**	C/P	2.8	29.5	1.5
	**	G/P	1.1	22.6	2.1
Cocure	**	C/P	2.8	32.4	1.5
		G/P	1.2	23.6	2.1

* - Proceeding C - P cure and prior to conditioning

** - Proceeding the G - P cure

TABLE 2: SUMMARY OF INTERLAMINAR SHEAR TEST RESULTS

Panel	Glass - phenolic (Psi)	Carbon - phenolic (Psi)	(125 S.F.) Interface	(250 S. F.) Interface
Cocure	3650	2988	3374 CP *	
	(5.71)	(2.93)	(3.71)	
As - received	3650	3672	3838 CP	3840 CP
	(2.58)	(3.49)	(3.49)	(2.38)
Dry	4226	3790	3734 CP	3726 CP
	(5.89)	(4.96)	(3.38)	(6.79)
Wet	3832	4008	1843 BL	2038 BL
	(3.01)	(12.22)	(4.44)	(7.00)

( ) - coefficient of variation

* - Surface finish not applicable

CP - Failed in carbon - phenolic

BL - Bondline failure

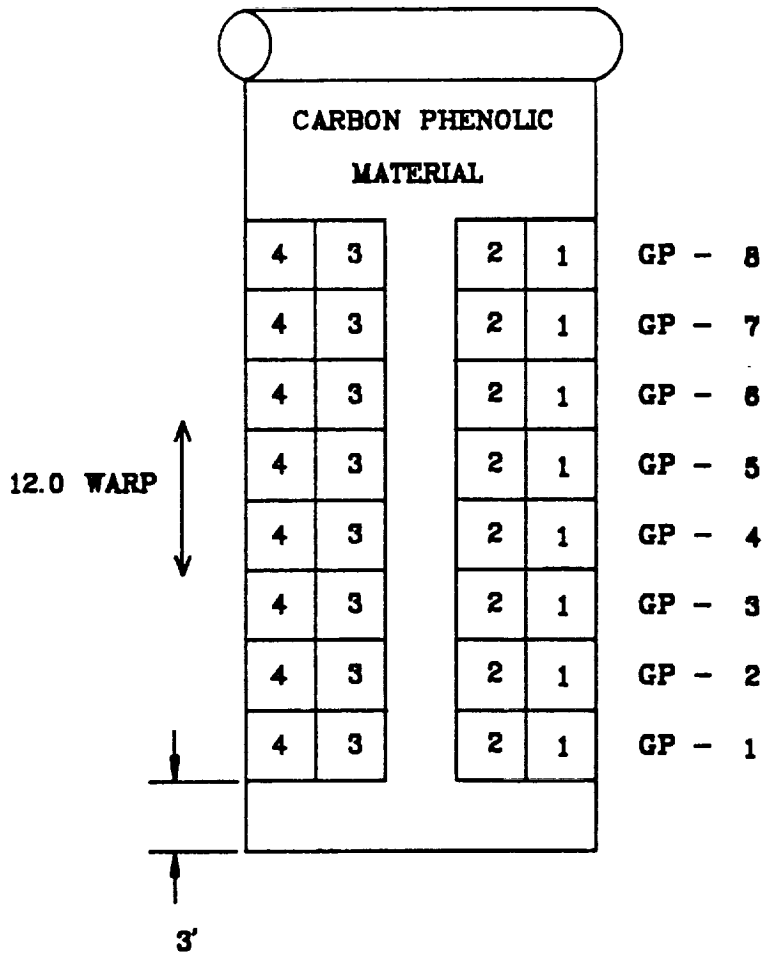

NOTES:

1. CUT 3 FOOT SWATCHES AT THE BEGINNING AND AFTER EVERY 168 PLIES UNTIL 504 PLIES ARE CUT.

2. CUT 504 [10 IN BY 12 IN (WARP)] PLIES OF C/P MATERIAL. MAKE 6 STACKS (84 PLIES PER STACK), BY STACKING THE FIRST 4 PLIES, SMOOTH SIDE UP, IN STACK CP - 1, THE NEXT 4 IN STACK CP - 2, ETC. UNTIL EACH STACK CONTAINS 84 PLIES.

Figure 1. Cutting and stacking plan for carbon phenolic material (Roll 1B).

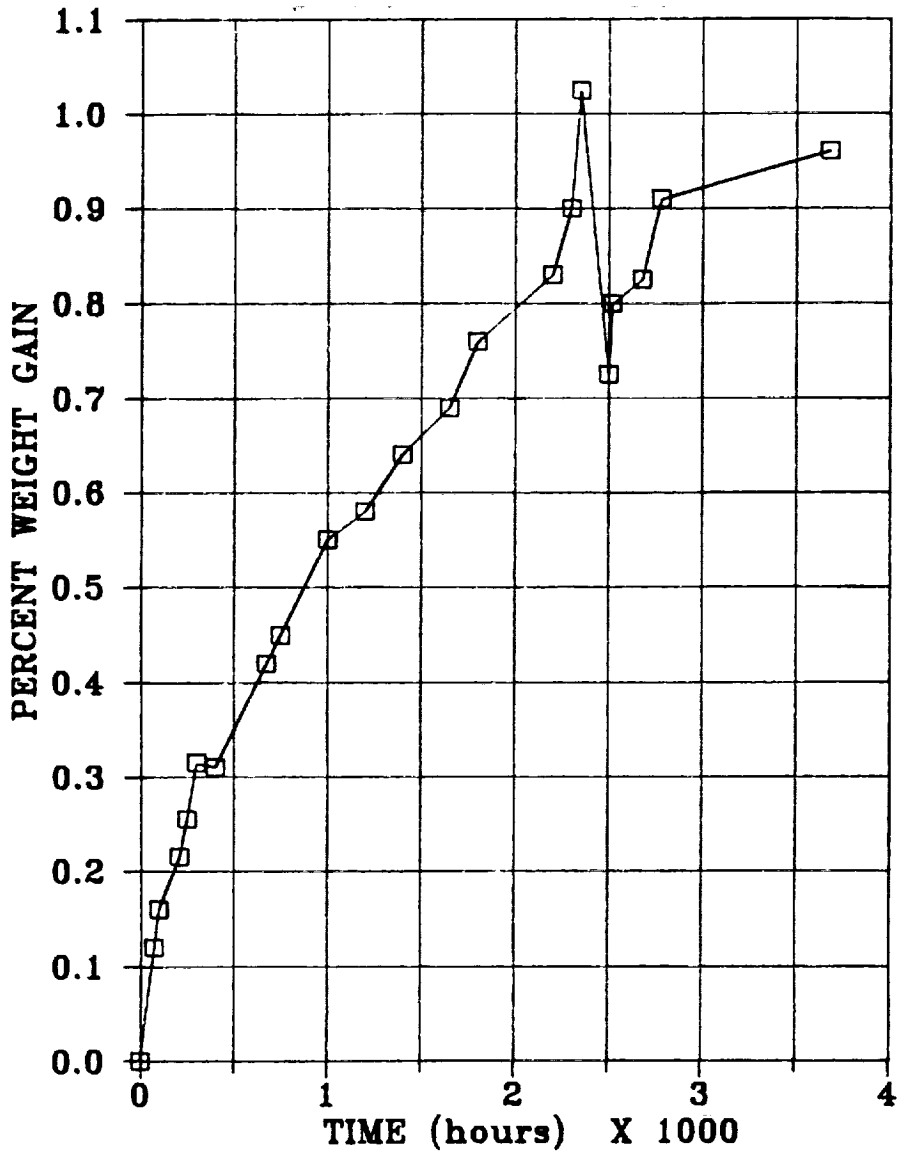

Figure 2. Percent weight gain for wet panel.

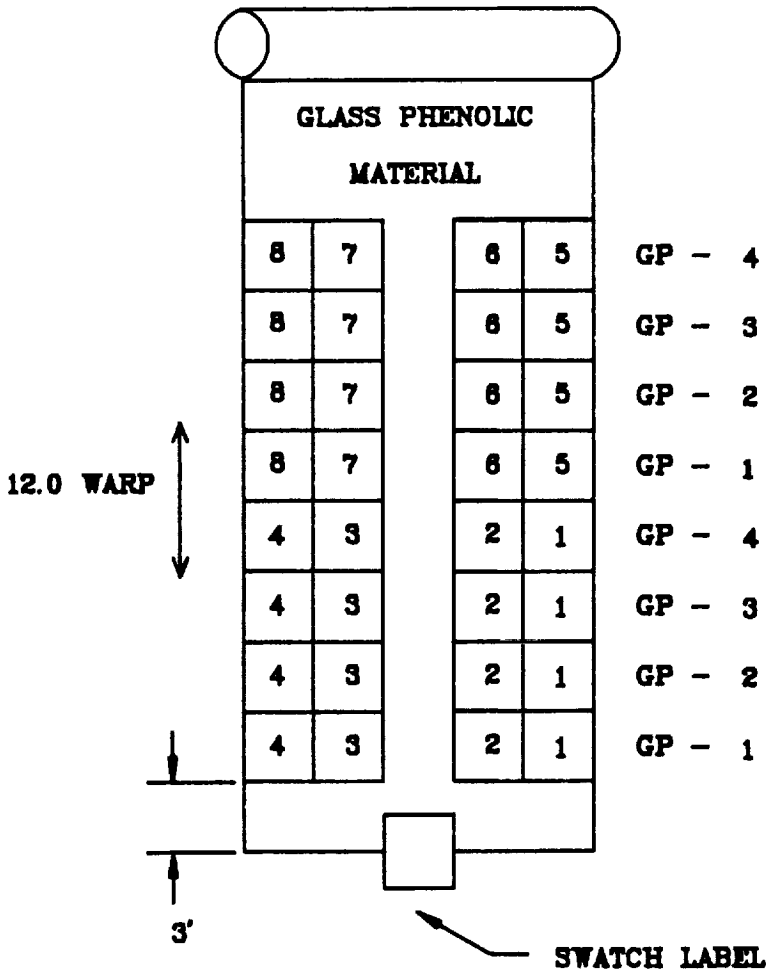

NOTES:

1. CUT 160 10 IN BY 12 IN (WARP) PLIES.
2. MAKE 4 STACKS BY STACKING THE FIRST 4 PLIES IN STACK GP - 1, THE NEXT 4 IN GP - 2, ETC., UNTIL EACH STACK CONTAINS 40 PLIES.

Figure 3. Cutting and stacking plan for glass phenolic material (Roll 1).

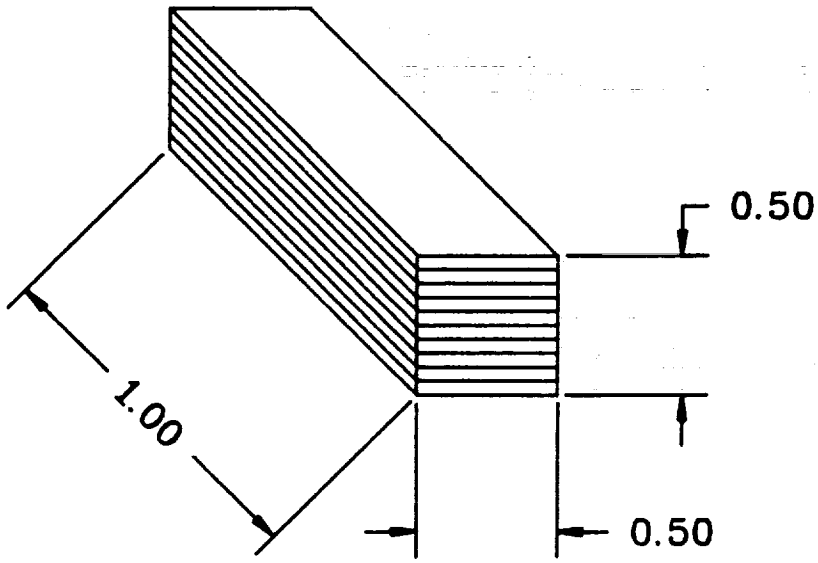

Figure 4. Specimen geometry of specific gravity, residual volatile, and resin content tests.

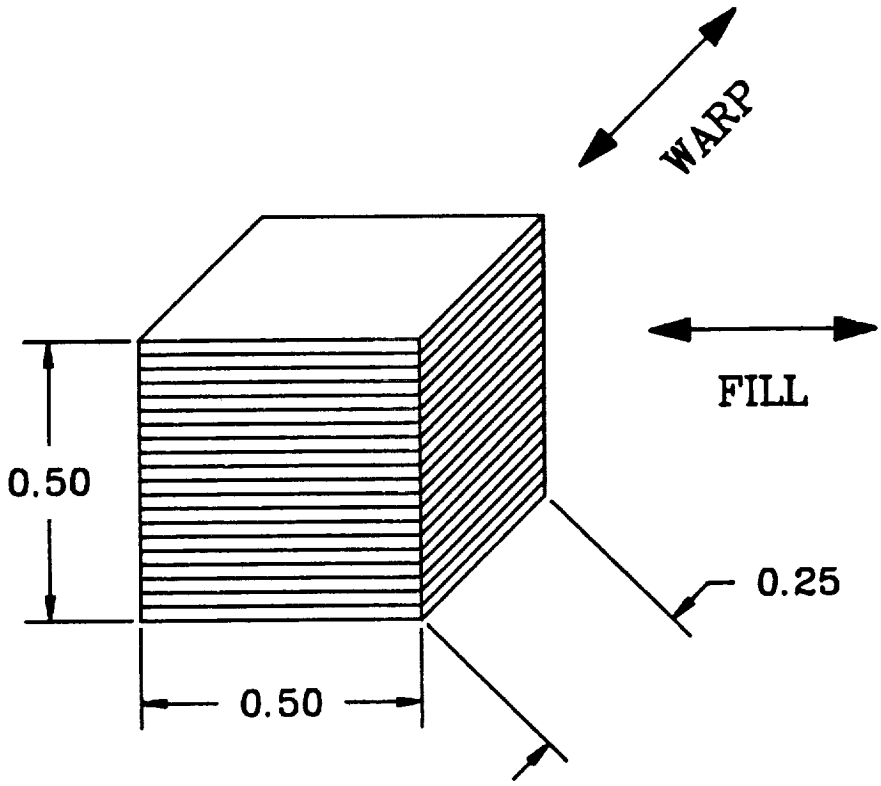

Figure 5. Specimen geometry for photomicroscopy evaluation.

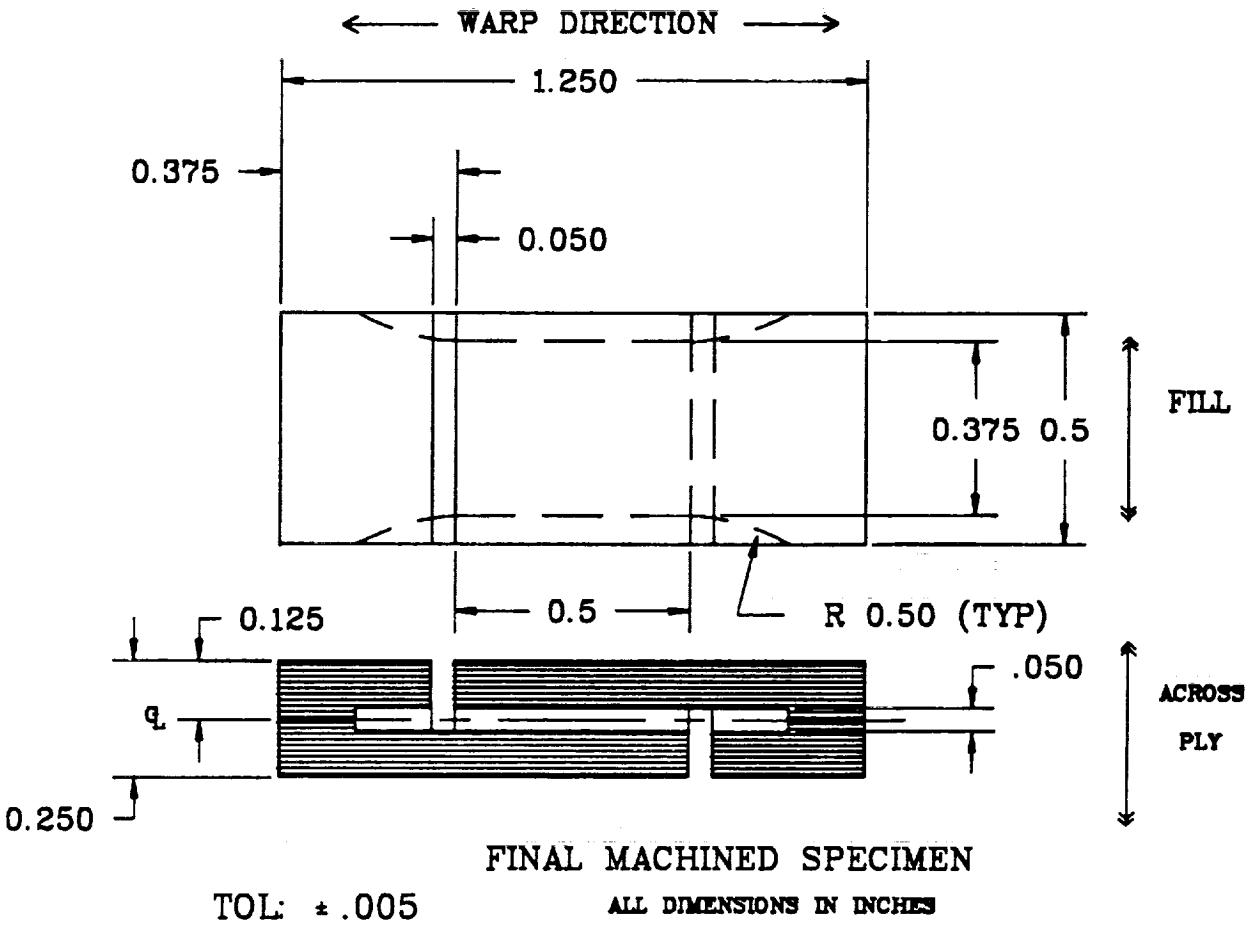

Figure 6. Specimen geometry for DNS test.

Figure 7a. SEM photomicrograph at 15X of fracture surface depicting interlaminar failure.

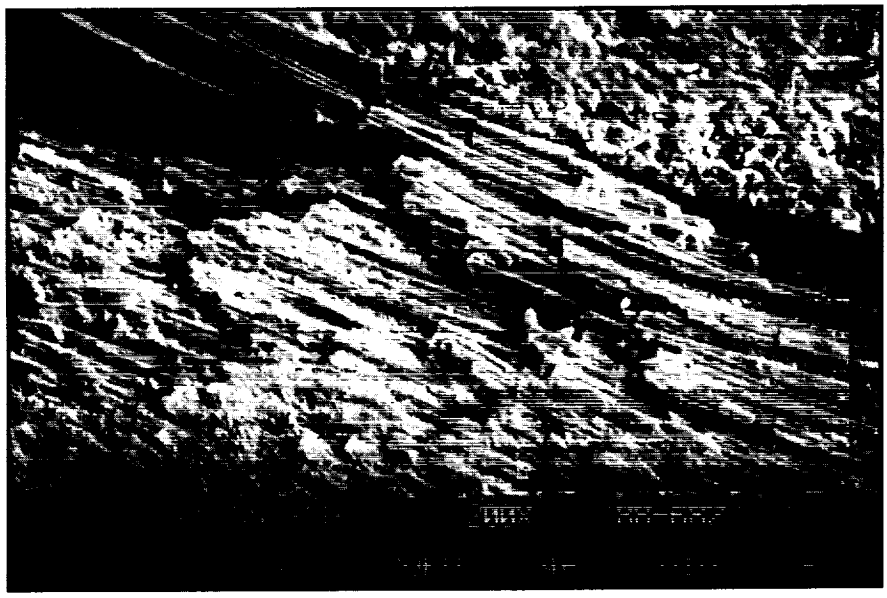

Figure 7b. SEM photomicrograph at 200X of fracture surface depicting interlaminar failure.

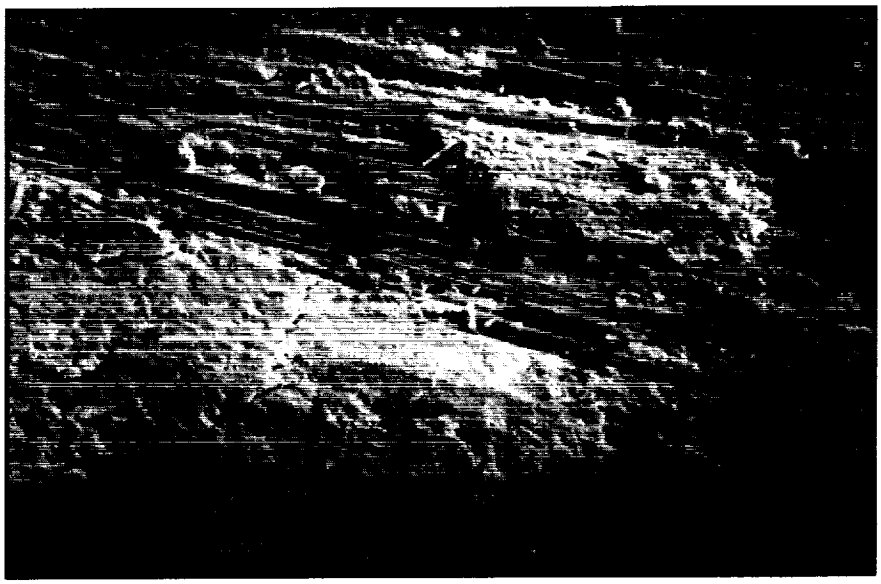

Figure 7c. SEM photomicrograph at 200X of fracture surface depicting interlaminar failure.

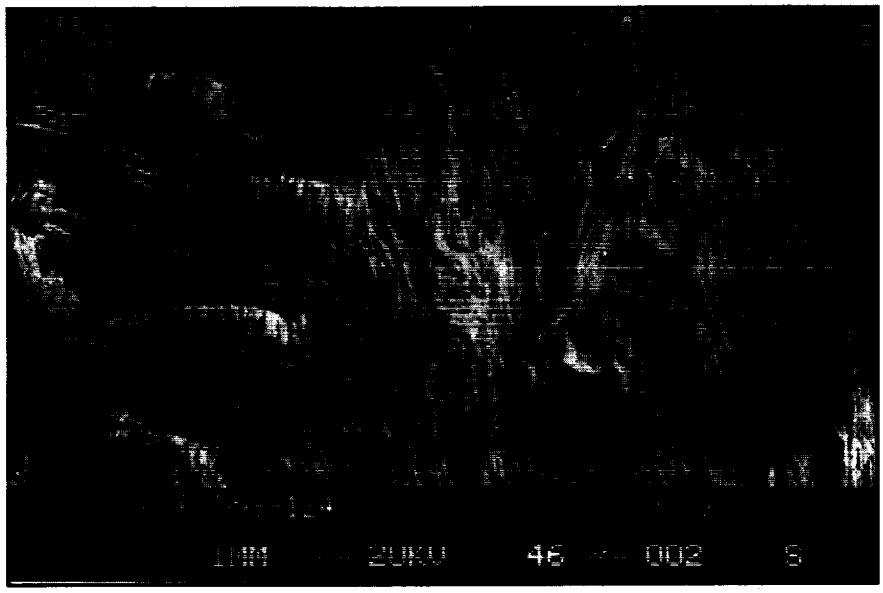

Figure 8a. SEM photomicrograph at 15X of fracture surface depicting across-laminar failure.

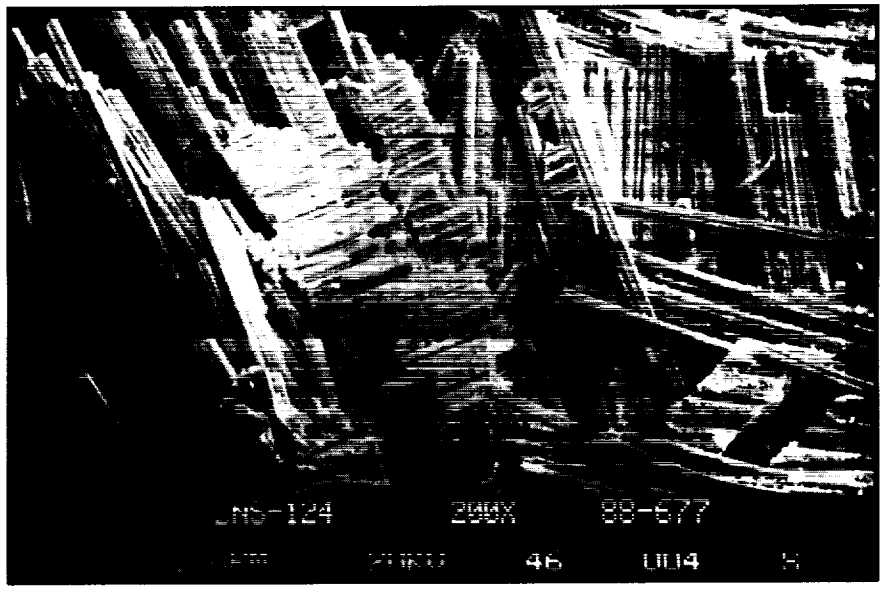

Figure 8b. SEM photomicrograph at 200X of fracture surface depicting across-laminar failure.

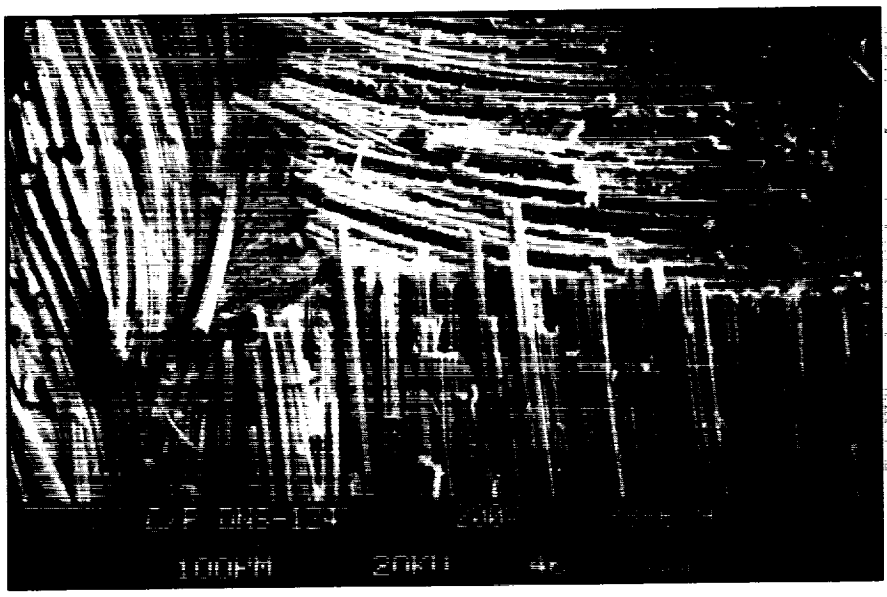

Figure 8c. SEM photomicrograph at 200X of fracture surface depicting across-laminar failure.

LOW ENERGY SPUTTERING OF COBALT BY CESIUM IONS*

A. Handoo and P. Ray
School of Engineering and Architecture
Tuskegee University
Tuskegee, AL

ABSTRACT

An experimental facility to investigate low energy (<500 eV) sputtering of metal surfaces with ions produced by an ion gun is described. Results are reported on the sputtering yield of cobalt by cesium ions in the 100 to 500 eV energy range at a pressure of 1×10^{-6} Torr. The target was electroplated on a copper substrate. The sputtered atoms were collected on a cobalt foil surrounding the target. ^{57}Co was used as a tracer to determine the sputtering yield.

*Work supported by NASA Grant NAG8-020

LOW ENERGY SPUTTERING OF COBALT BY CESIUM IONS

1. Introduction

Electron bombardment ion engines are required to have operational lifetimes of up to 15,000 hours at 2 A beam current for successful completion of many proposed space missions [1]. From the mission profile life tests, it was observed that the major life-limiting mechanism is the formation of flakes of sputtered material which might be of sufficient size to cause electrical shorts or arcing in the discharge chamber [2]. The internal surfaces of the discharge chamber where the erosion is most severe are subjected to bombardment by ions having energies less than 100 eV, assuming that up to triply charged ions exist in the plasma potential of 32 V within the discharge chamber where the ions are generated. However, the data on yields from low energy sputtering are sparse and there are uncertainties due to difficulty in detecting the extremely low sputtering yields [3-5]. In view of the scarcity of sputtering yield data at low energies, a systematic experimental study is being undertaken using a radioactive tracer technique. In the present study cesium ions having well-defined ion energies impinge on a cobalt target mixed with a small amount of cobalt-57. Cobalt is chosen as the target material for initial studies because its tracer, cobalt-57, has a relatively long half-life of 270 days and decays predominantly by emitting low-energy (122 KeV) gamma rays. Since the total sputtering yield at low incident ion energies is expected to be very small even after a prolonged exposure, the radioactive tracer technique appears to be quite useful. The sputtering yield data reported are taken at a pressure of 1×10^{-6} Torr with energy of the cesium ions varying from 100 to 500 eV.

2. Experimental Design and Procedure

The vacuum chamber is 10 cm in diameter, 22.5 cm long and has six ports. The ion gun enters from the left through a 150 mm CF port. The target assembly is introduced from the right port by a linear motion feedthrough which is connected to the vacuum chamber through a 150 mm CF adapting nipple. The ionization gauge is mounted on another 70 mm CF port. A viewport is attached through a 115 mm port on the top and there is also a provision to introduce a SIMS probe through an auxiliary 70 mm CF port which is at a 45° angle.

a) Vacuum system:

Before any successful sputtering can be undertaken, the surface should be made as free of adsorbed layers of gases as possible. This can be achieved by baking and maintaining a very high vacuum in the system. A turbomolecular pump of 170 ls^{-1} pumping speed is used to maintain the vacuum. All the flanges used in the chamber are metal gaskets sealed to have minimal outgassing and diffusion rates. A hot cathode ionization gauge with its digital readout controller is used to monitor the pressure level inside the vacuum chamber.

b) Ion Gun:

It is desirable that the ion beam impinges on the target in a small area with a high current density. However, space charge in the ion beam represents the fundamental limit on the ion current density. Hence, the lower the kinetic energy of the beam, the lower is the maximum current density that can be

generated. The ion gun used in the present setup is procured from Kimball Physics Inc. and is capable of producing low-energy ion beam at well defined energies for both Cesium and noble gases. This will enable us to cross check the sputtering yield data using a variety of ions.

c) Target and collector assembly:

The target and collector assembly is shown in Fig. 1. At the end of the linear motion feedthrough is the holding rod with a tapped hole at the end. The target is cobalt (99.9% and 0.1% ^{57}Co) electroplated on the tip of a 4.8 mm diameter copper specimen. The edge of the copper specimen on which the cobalt is electroplated is at an angle of 45°, so the surface of the target is elliptical in shape with an area of 25.8 mm^2. The surface density of cobalt is approximately 50 μg / cm^2, which resulted in an activity of the target of 110 μCi. The other end of the specimen, which is threaded, is attached to the holding rod. The copper specimen is completely surrounded by a 19 mm diameter hollow cylinder, the inside of which is lined with a 0.05 mm thick cobalt foil. The distance between the target and the ion gun was optimized for maximum sputtering yield after conducting several initial runs under similar experimental conditions. The operating distance was found to be about 19 mm (Fig. 2).

The vacuum chamber is pumped down to a pressure of 1 x 10^{-6} Torr. The ions are extracted and accelerated to the desired energy by setting corresponding grid voltages. The beam current is then measured with a Faraday cup which is pneumatically operated to intercept the beam. The ion beam impinges on the target at a 45° angle. The target is exposed to the ion beam for a period ranging from 5 to 20 minutes depending on the beam energy level. The experiments were run for beam energies of 100, 200, 300, 400 and 500 eV for both focused and unfocused ion beams. The focused ion beam diameter is about 1 mm whereas the unfocused beam diameter is about 3 mm. The ion beam current ranged from 0.45 microampere at 100 eV to 1.15 microampere at 500 eV. After bombarding the target with cesium ions, the cobalt foil is removed from the vacuum chamber and taken to a multichannel analyzer for counting the gamma rays emitted by the disintegrating ^{57}Co atoms deposited on the foil. The analyzer is set so that only photoelectric peak is counted. A standard ^{57}Co source of 0.115 μCi is used to determine the efficiency of the counter. The amount of radioactive atoms in the sputtered material is then a measure of the total sputtering yield.

3. Sputtering Yield Measurement

Let N be the number of total atoms counted under the photoelectric peak in time t_c. Then the total number of radioactive atoms N_R on the cobalt foil is given by

$$N_R = N / (tc\, \lambda \eta)$$

where λ is the disintegration constant of ^{57}Co and η the efficiency of the counter. The percentage of radioactive atoms on the target, γ, decreases with time and is determined by

$$\gamma = \gamma_o\ e^{-\lambda T}$$

where γ_o is the percentage of radioactive atoms on the target at the time of electroplating, and T is the elapsed time between electroplating the sample and the day the data were taken. Assuming that all the sputtered atoms are deposited on cobalt foil, the sputtering yield S is given by

$$S = (N_R\, q) / (\gamma\, I\, t_e)$$

where q is the charge of an ion, I the ion beam current and t_e the beam exposure time of the target.

4. Results and Discussion

The sputtering yields of cobalt by cesium ions at 100, 200, 300, 400, and 500 eV are presented in Fig. 3 for both focused and unfocused ion beams. For comparison, the sputtering yield of cobalt by mercury ions reported by Wehner is also presented, although the experiments were performed under different conditions [3]. The sputtering yield values obtained by Wehner are 2 to 5 times higher than those obtained from our experiments with focused beams.

The discrepancy in the sputtering yield values can be traced to the vacuum chamber pressure and the ion current densities at which these data were taken. Wehner's experiments were performed with the target immersed in a low-pressure mercury plasma discharge at about 1×10^{-6} Torr and 5 mA/cm^2 ion current density. The highest current density obtained in our experiments was 0.15 mA/cm^2. At 0.15 mA/cm^2 a surface atom of the target receives about 30 impacts per minute form the incident ions whereas the residual gas molecules at 1×10^{-6} Torr will impinge about 10 times on the surface atoms during the same period [6]. Thus, the surface of the target will have an appreciable amount of adsorbed gases which inhibit the sputtering process significantly.

The effect of ion current density on the sputtering yield can be clearly seen in Table 1, where the ratios of the sputtering yields for the focused and the unfocused beams at various ion energies are listed. At all ion energies the sputtering yields of unfocused beams are lower by factors of 10 to 14. The focused and the unfocused ion beam densities differ by about the same values. It is obvious that a very high vacuum is required to minimize the effect of the residual gas on the sputtering yields at low ion current densities. In view of this, our vacuum system is being upgraded to a pressure of 10^{-8} Torr. Currently, we are in the process of obtaining data for sputtering yield of cobalt bombarded by low energy argon ions.

The amounts of material sputtered at ion energies down to 50 eV are within the detection limits using the 110 μCi target. A higher activity target would enable us to measure sputtering yields below 100 eV.

Table 1.
Ratio of the Sputtering Yields for the Focused and the Unfocused Ion Beams.

ION ENERGY (eV)	RATIO
100	10.4
200	10.0
300	13.7
400	11.9
500	11.1

References

1. Austin, R.E., "Solar Electric Propulsion Systems (SEPS), Tomorrow's Propulsion System Today", Paper no. AIAA-79-2045, Oct. 1979.

2. Bechtel, R.T.; Trump, G.E.; James, E.J., "Results of the Mission Profile Life Test", Paper No. AIAA-82-1905, Nov. 1982, 22.

3. Wehner, G.K., Phys. Rev., 1956, 102, 690.

4. Laegreid, N.; Wehner, G.K., J. Appl. Phys., 1961, 32, 365.

5. Rosenberg, D.; Wehner, G.K., J. Appl. Phys., 1962, 33, 1842.

6. Chopra, K.L., Thin Film Phenomena (McGraw-Hill, New York, 1969).

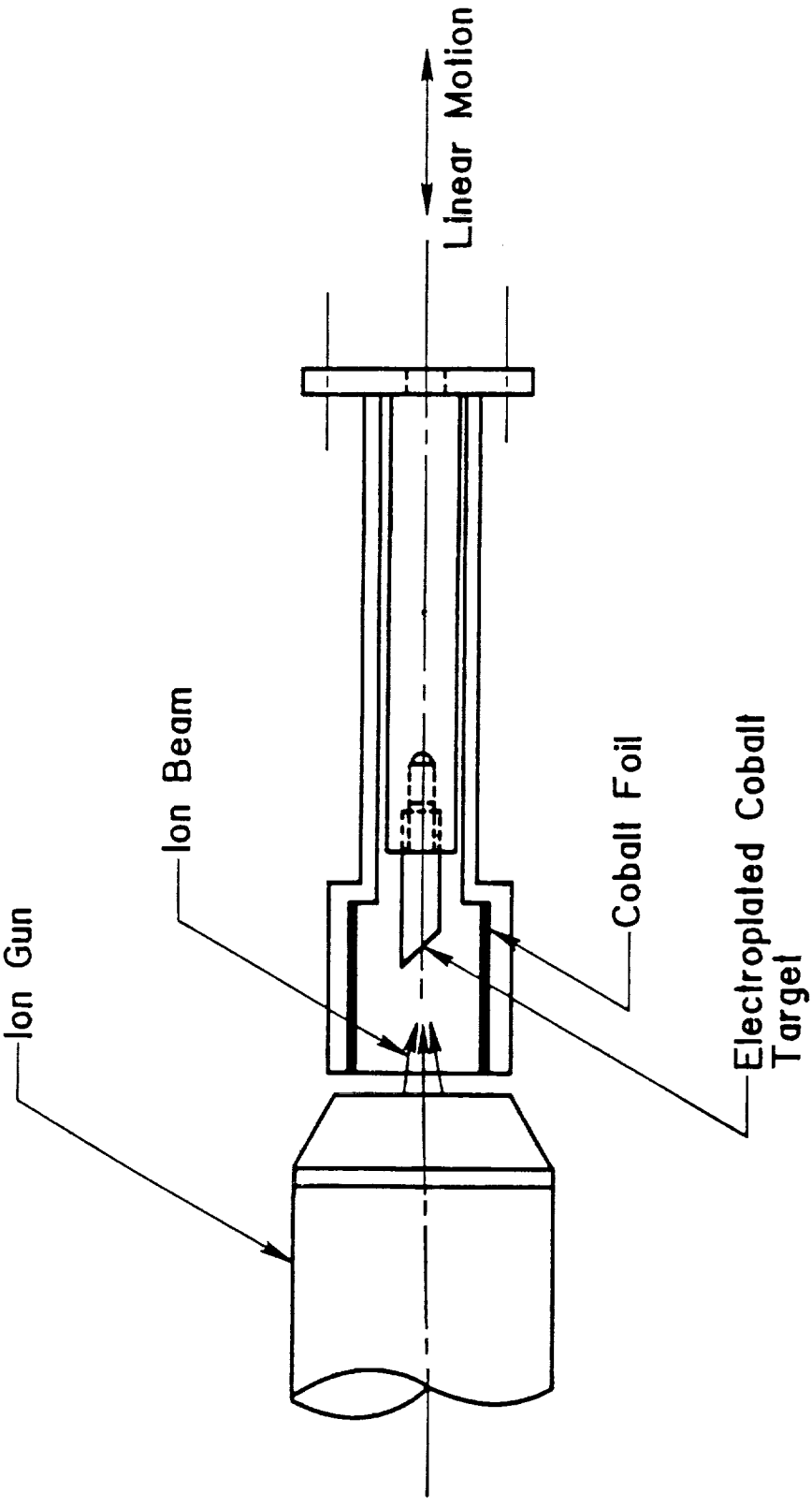

Figure 1. Schematic diagram of the experimental setup.

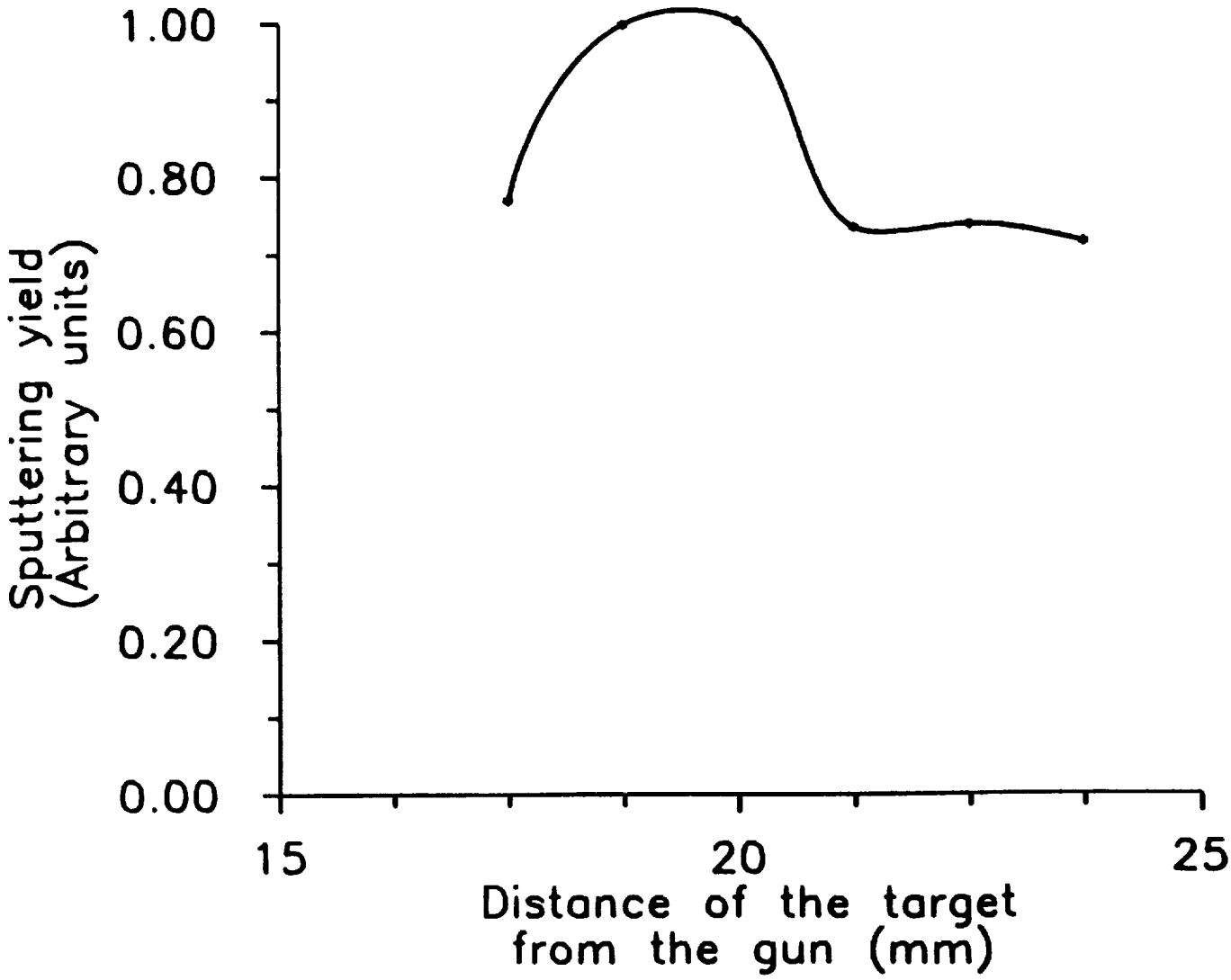

Figure 2. Variation of sputtering yield with distance.

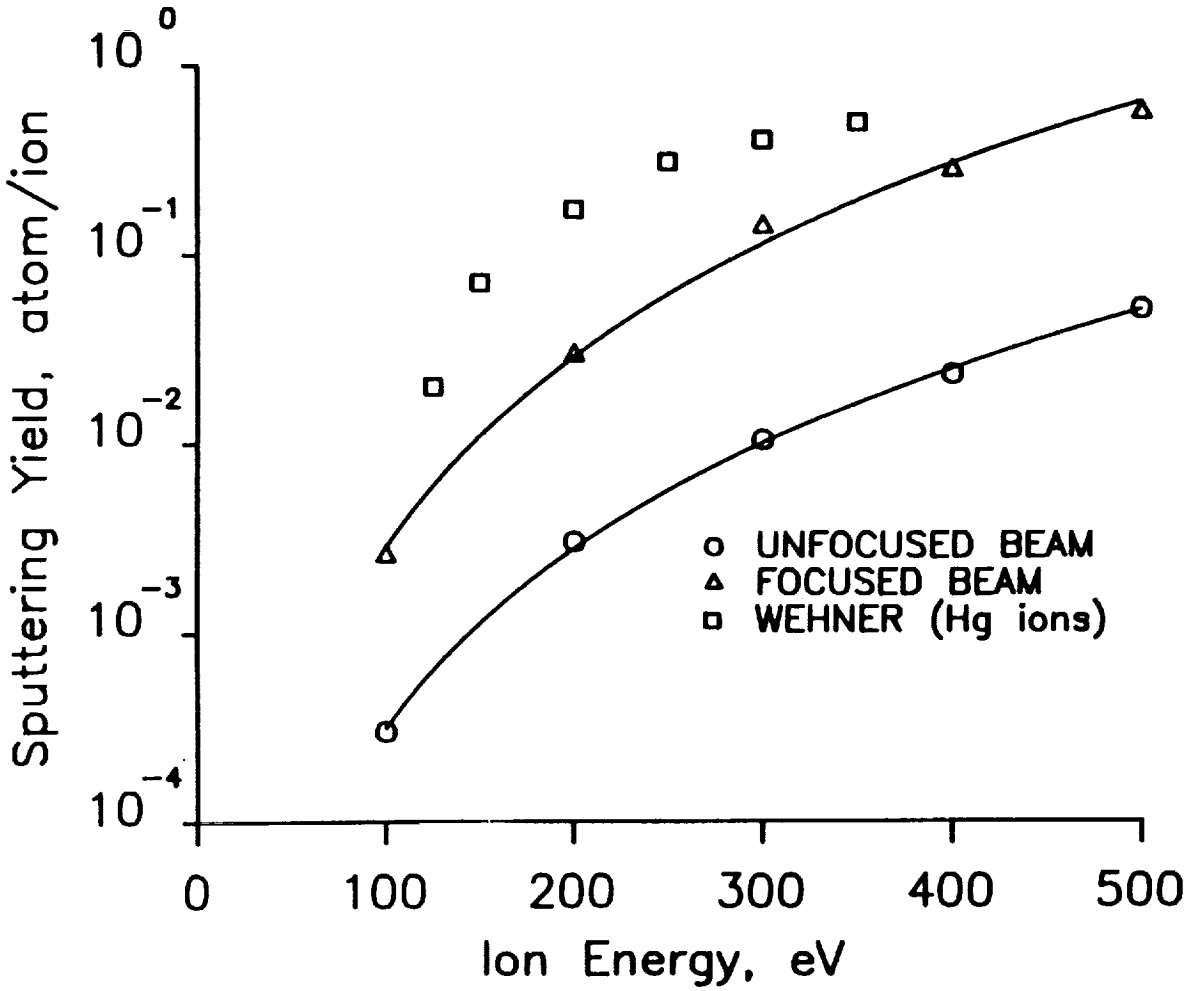

Figure 3. Sputtering yield of cobalt by cesium ions at various ion energies.

PARAMETERS OF TENSILE STRENGTH, ELONGATION, AND TENACITY OF 70mm IIaO SPECTROSCOPIC FILM

Ernest C. Hammond, Jr. and Kevin A. Peters
Morgan State University

and

Gerald R. Baker
Technical Monitor
Laboratory of Astronomy and Solar Physics
Goddard Space Flight Center

ABSTRACT

70mm IIaO spectroscopic film was tested to determine its tensile strength, elongation, and breaking strength, using an Instron (strength & compression) 4201 Test Instrument. These data provides information leading to the upper and lower limits of the above parameters for 70mm IIaO spectroscopic film. This film will be developed by a commercial developing machine after the Ultraviolet Telescope Space Shuttle Mission returns to the earth in the early 1990's; thus it is necessary to understand these force parameters.

Several test strips of approximately 200 mm in length were used. The results indicate that when a stress load of 100 kg was applied, the film elongated approximately 1.06 mm and the breaking strength was 19.45 kilograms.

PARAMETERS OF TENSILE STRENGTH, ELONGATION, AND TENACITY OF 70mm IIaO SPECTROSCOPIC FILM

Introduction

IIaO spectroscopic film is a special ultraviolet sensitive film which will be used on the ultraviolet imaging telescope to be launched by the space shuttle in the early 1990's. Quality control of this film is an important ingredient in understanding the various parameters that the film will undergo in space and the extraterrestrial environment.

NASA uses a large commercial developing machine to develop its 70mm IIaO spectroscopic film. During the process, the film is exposed to various forces that could cause possible stress or strain on the film. The purpose of this research is to study the parameters of elongation (strain), tenacity strength (breaking point), and tensile strength (load strength) of 70mm IIaO spectroscopic film.

Materials and Methods

Five samples of developed and five samples of undeveloped 70mm IIaO spectroscopic film were cut to a gage length of 5 inches for testing purposes. An Instron 4200 strength and compression instrument was used to test the properties of elongation and tenacity of the film. Each sample was exposed to a maximum load range of 500 kg for stretching purposes. The film was put in a 2-inch grip on the instrument and streched to its breaking point. Elongation curves for each sample were made using a graphic recorder connected to the Instron instrument for further analysis.

Results

From the analysis of the elongation curves, the undeveloped film shows greater strength than do the developed film samples. The undeveloped film appears to begin stretching at a load range of 50 kg and continues stretching until it reaches a breaking point at approximately 86 kg. The undeveloped film appears to elongate a total of 2 inches during the experiment. The developed film appears to stretch at approximately 30 kg and continues stretching until it reaches a breaking point of approximately 75 kg. The developed film appears to elongate a total of 1.5 inches during the experiment.

Discussion

The adhesive properties of the undeveloped film appear to give the film added strength as compared with the developed samples. These results are demonstrated by the differences in the breaking points of the undeveloped film versus the developed film samples. The tension associated with the developing machine is needed in order to complete this study. This information will be obtained when the machine is set up again at Goddard's Laboratory of Solar Physics. Most of the concern for stretcthing of film is with the science of astrometry where very crude and sensitive measurements are needed relative to distances and positions of stars. If film stretches in the machine by any significant amount, it could distort images and sensitive measurements that are made by researchers in astrometry.

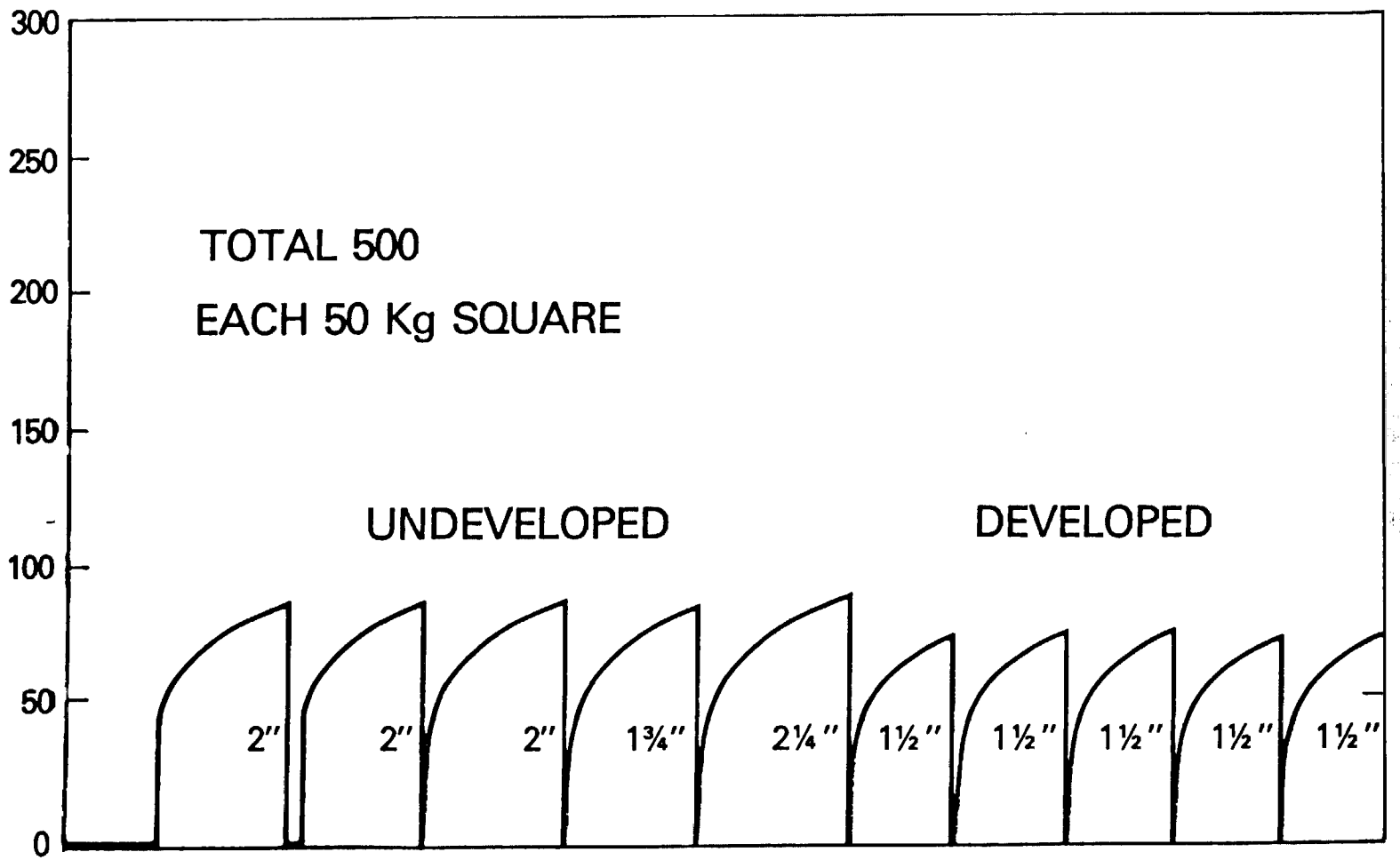
300
250
200
150
100
50
0
TOTAL 500
EACH 50 Kg SQUARE
UNDEVELOPED
DEVELOPED
2"
2"
2"
1¾"
2¼"
1½"
1½"
1½"
1½"
1½"

Figure 1.

SURFACE ROUGHNESS OF FLAT AND CURVED OPTICAL SURFACES

M. C. George, B. R. Reddy, H. Jagannath,
M. Perera, and P. Venkateswarlu
Department of Physics
Alabama A&M University
Normal, Alabama

ABSTRACT

A profilometer has been fabricated based on optical heterodyne detection technique. The vertical height sensitivity of the technique has been improved to much better than 10Å rms. The surface roughness of several coated and uncoated samples has been measured. A typical surface profile and surface characterization plots are also shown.

SURFACE ROUGHNESS OF FLAT AND CURVED OPTICAL SURFACES

Introduction

Surface roughness measurement has several applications. Even a few Å roughness will cause scattered light in optical systems. Smooth surfaces are required in a wide variety of instruments. For example, the outputs of the high power lasers are limited by the surface roughness of mirrors and windows. Similarly, the information storage capacity of magnetic media is limited by the roughness of the surface. Roughness reduces the resolving power of optics and distorts images. The performance of certain thin film components in electronic industries is affected by the roughness on the film surface. X-ray astronomical telescopes require smooth curved surfaces. To improve the surface quality, super sensitive detection methods are required. Wide ranging measurement techniques are developed based on interferometry, electron microscopy, X-rays, ellipsometry, light scattering, and using mechanical stylus, etc. Though there are several techniques[1,2] available for measurement and evaluation of the surfaces, no single technique is fully adequate. Also, the technique used should be nondestructive and highly sensitive. So, we fabricated an optical heterodyne profilometer[3] and its current sensitivity is much better than 10Å rms. It is a noncontact and nondestructive technique. The instrument can be operated even by unskilled personnel for routine measurements.

Principle

The principle[4] behind the technique is simple and elegant. Briefly, in this experiment, a laser beam is split into two parts and focused at two different points on the surface under investigation, and then the phase variation of the reflected beams is measured, which directly relates to the height difference between the two points. A brief description of its theoretical background is given elsewhere[4].

Experimental

A block diagram of the experimental setup is shown in Fig. 1. The experiment uses a 1mW Zeeman split (Δw = 1.5 MHz) He Ne laser (HP 5501A) whose frequencies are collinear but orthogonally polarized. The laser output is passed through a spatial filter/telescope combination to reduce the spatial noise and the beam size to ~0.5 mm. The laser beam is split into two parts of unequal intensities, but both parts contain the two Zeeman components. One part is detected by a receiver (HP 10780B) whose output is hereafter called reference signal and the other part is directed vertically upwards to the surface mounted on an airbearing rotary table (Dover Instruments). Before falling on the sample, the beam passes through a wollaston prism and on exit the two frequencies are spatially separated and then focused at two different points on the surface of the sample. The beam path is arranged such that one of them falls at the axis of rotation of the table and the other is separated from it by only a fraction of a millimeter. The reflected beams are recombined by the wollaston prism and then directed to another identical receiver (HP 10780B) whose output is hereafter called measurement signal. Whenever two different frequency signals fall on a detector its output is an average dc current proportional to the

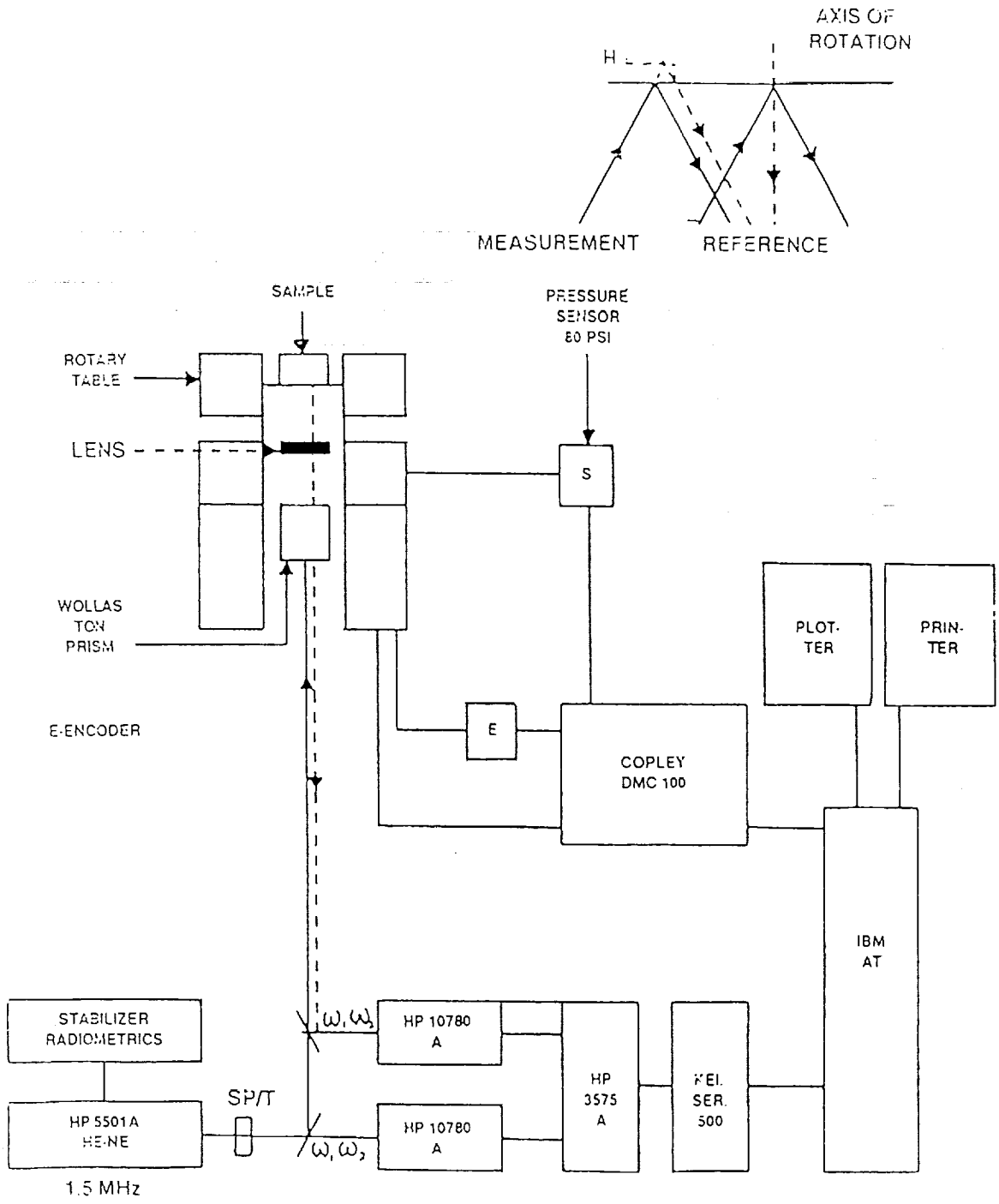

Figure 1. Block Diagram of the Experimental Set Up.

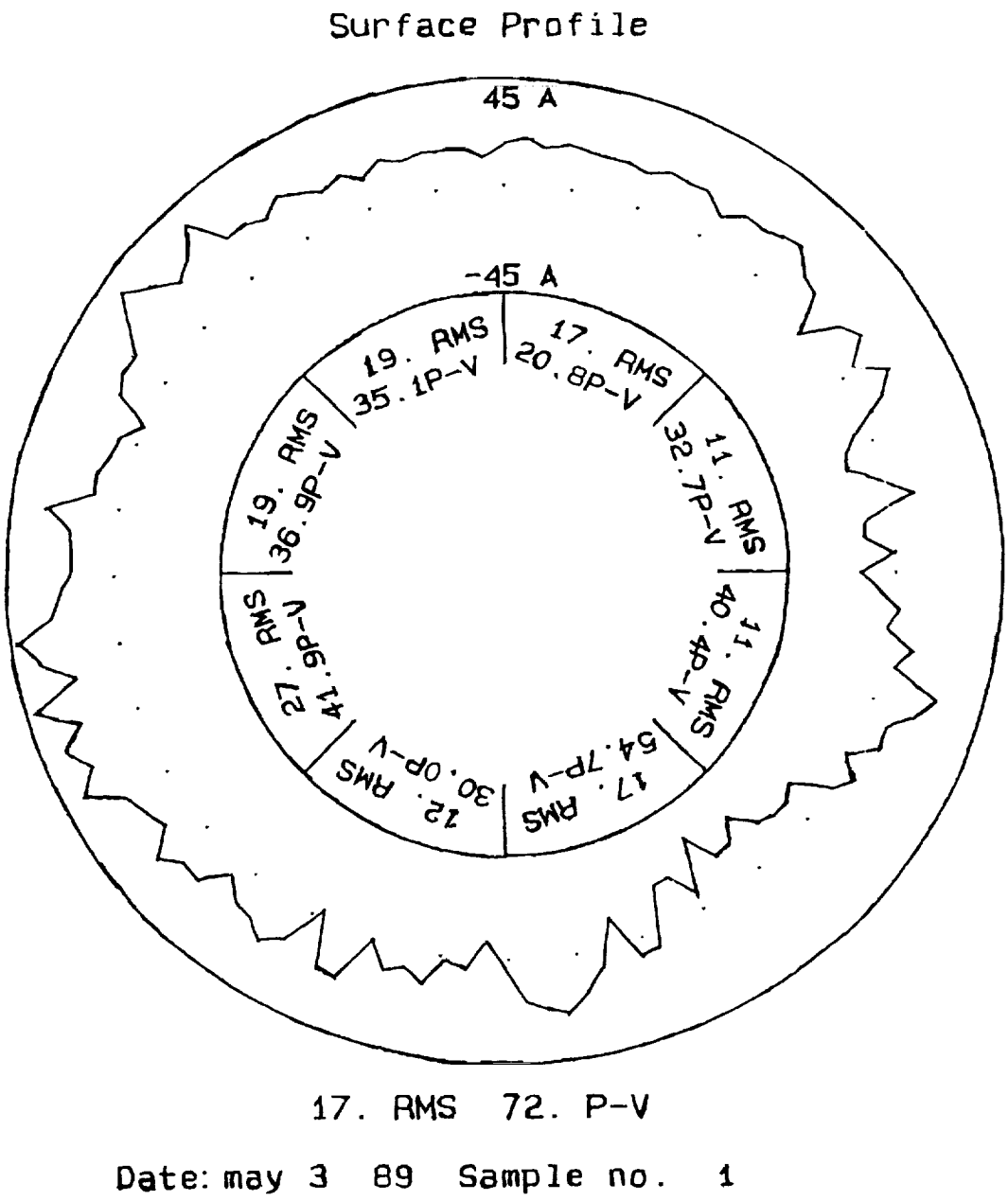

Figure 2. Surface Profile of a GaAs Wafer.

intensity plus an rf signal at the beat frequency (Δw). The dc part is elemented by a preamplifier built into the reciever (HP 10780B). The outputs of the two receivers are rf signals at 1.5 MHz (Δw), but the phase of the measurement signal varies due to roughness. The two rf outputs are given to the two inputs of a phasemeter (HP 3575A) whose output is an analog signal and its amplitude is proportional to the phase difference between the two inputs (10 mV/degree). The analog output of the phasemeter is interfaced with an IBM-AT computer using a 14 bit-A/D converter (Keithley series 500). A dc motor is attached to the table and its motion is controlled by a DMC 100 controller (Copley controls), and a two channel incremental encoder (Teledyne Gurley) provides feedback from the motor to the controller. There is one general program in BASIC that triggers DMC 100 for table rotation and initiates Keithley module for online data acquisition. The sample/table is rotated at the rate of one revolution per two minutes and data are acquired at the rate of 128 samples per revolution or an integral multiple of it. During table motion one of the spots is stationary and the other encounters different points in a circular path and so the measured signals are plotted in circular format.

Results and Discussion

The measured phase difference $\Delta\phi$ and the surface height variation or roughness ΔH ($\Delta H \approx \frac{\Delta Z}{2}$) are related by $\Delta\phi \approx \frac{2\pi}{\lambda}\Delta z$ where Δz is the extra pathlength traveled by one of the beams due to roughness. A typical surface profile of a GaAs wafer is shown in Fig. 2. The rms values of the roughness and peak-to-valley (P-V) values are calculated for eight different segments and the entire profile and are printed in the same figure. A number of functions are used to characterize the surfaces like autocovariance, spectral density, height and slope distribution functions. Autocovariance function refers to the distribution of correlation lengths, which are separations between similar topographic features. The spectral density function describes the angular distribution of the scattered light. Classical scattering theories were based on the assumption that the autocovariance and height distribution functions are gaussian which may not be true for every surface. All these functions have been calculated using the formulas given in reference 4 and are plotted in Fig. 3. Obviously, the autocovariance function deviates from gaussian distribution.

Sensitivity

Sensitivity of the technique is determined from the relation $\Delta\phi \approx \frac{4\pi}{\lambda}\Delta H$. Roughness ($\Delta H$) ≈ 1Å will cause a phase change of $\sim 0.1^\circ$ which is the resolution of the phasemeter. A severe limitation to the sensitivity is set by improper alignment of the optical beams. Some of the important criteria to be fulfilled are (1) one of the spots has to fall at the axis of rotation, (2) the surface normal has to be parallel to the axis of rotation and (3) the contact area between the table top and the sample are to be free from dust. When all these criteria are fulfilled the sensitivity of the instrument will be improved to the theoretical limit ~ 1Å, because the noise from other sources is insignificant.

This work was supported by NASA-Grant No. NAG8-029.

References

1. Bennett, J. M., Appl. Opt. 1976, 15, 2705.

2. Lindsey, K.; Penfold, A. B., Opt. Engg. 1976, 15, 220.

3. George, M. C.; Jagannath, H.; Reddy, B. R.; Perera, G. M.; Venkateswarlu, P., Opt. Fab. and Test. (OSA) 1988, Tech. Dig. Ser., 13, 61.

4. Sommargren, G. E., Appl. Opt. 1981, 20, 610.

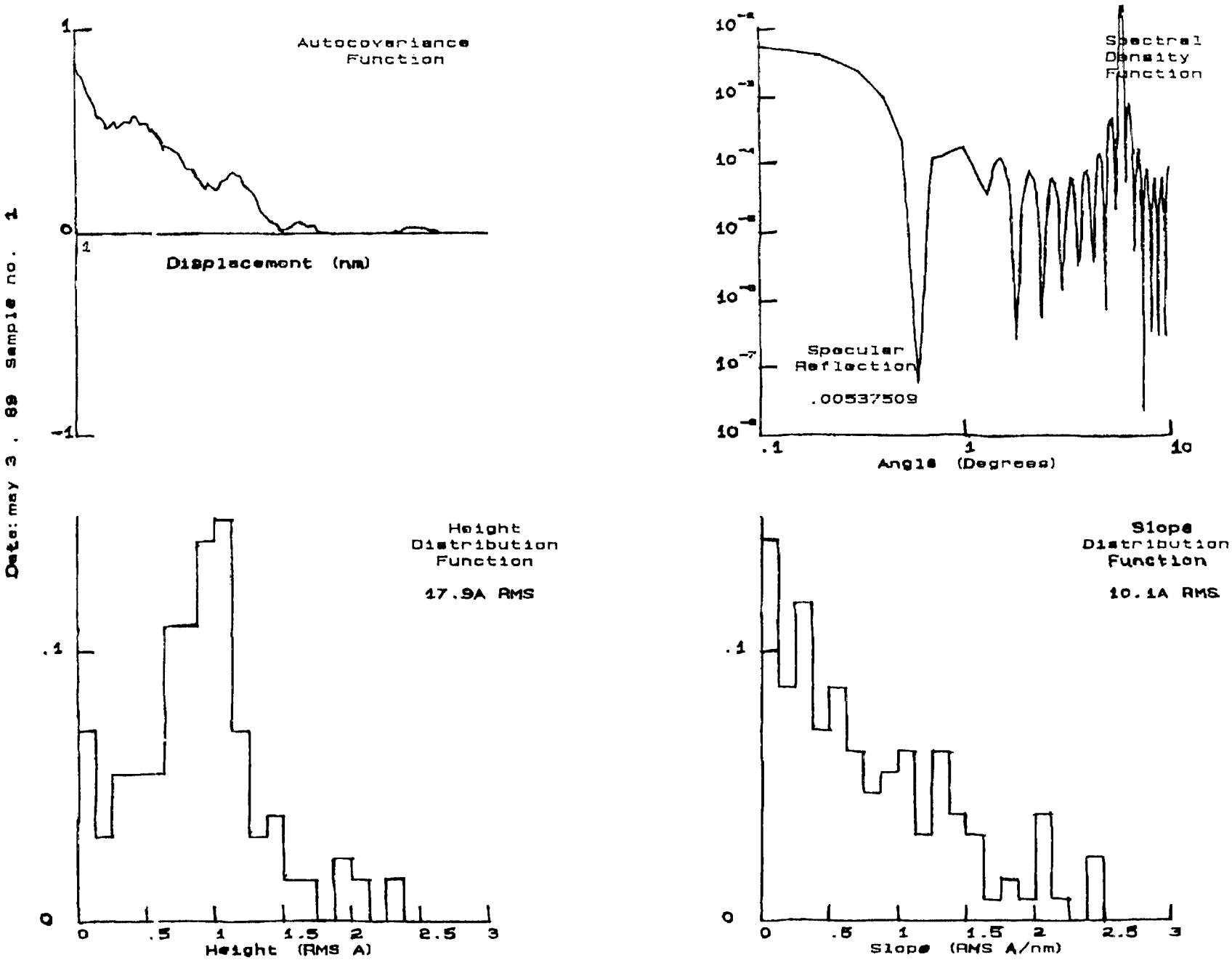

Figure 3. Surface Characterzation Plots.

SUGGESTED CRITERIA FOR EVALUATING SYSTEMS ENGINEERING METHODOLOGIES

Audrey Gates, Arthur Paul, and Tepper Gill,
Department of Systems and Computer Science
and
Department of Electrical Engineering
Howard University
Washington, D.C.

ABSTRACT

Systems engineering is the application of mathematical and scientific principles to practical ends in the life-cycle of a system. A methodology for systems engineering is a carefully developed, relatively complex procedure or process for applying these mathematical and scientific principles. There are many systems engineering methodologies [or possibly many versions of a few methodologies] currently in use in government and industry. These methodologies are usually tailored to meet the needs of a particular organization. It has been observed, however, that many technical and non-technical problems arise when inadequate systems engineering methodologies are applied by organizations to their systems development projects. This paper discusses various criteria for evaluating systems engineering methodologies. Such criteria are developed to assist methodology-users in identifying and selecting methodologies that best fit the needs of the organization.

SUGGESTED CRITERIA FOR EVALUATING SYSTEMS ENGINEERING METHODOLOGIES

Introduction

This paper is one of several results of a Dynamic Systems Engineering Methodology Research Study being conducted at Howard University under a grant from NASA. The study is sponsored by the Networks Division of the Mission Operations and Data Systems Directorate (MO&DSD) at Goddard Space Flight Center. The objective of the study is to examine systems engineering methodologies in light of changing environments and changing needs. The results of this investigation are to be used to identify and validate new methodologies with potential applications to NASA's systems life-cycle processes.

The study is divided into two phases. Phase One is a study of NASA's projects, its organization, resources, and environment to identify factors that affect the successful application of systems engineering methodologies. Phase Two involves evaluating existing methodologies, tools, and techniques with potential application to NASA's systems project.

The criteria for evaluating systems engineering methodologies were developed based on the findings in Phase One. These criteria are to be used as a guide and weighing scale for evaluating existing systems engineering methodologies in Phase Two of the project, and in making recommendations to NASA.

Purpose of a Systems Engineering Methodology

Systems engineering as described by Blanchard is a process employed in the evolution of system's development from the time when a need is identified through production and/or construction to the ultimate deployment of that system[1, p. 11]. The series of steps involved in this process is a systems engineering methodology. A methodology is primarily used to improve the effectiveness of the overall system. It provides a means to increase reliability, decrease downtime, maintain cost effectiveness, and avoid redundant and wasted efforts. Furthermore, it provides a means of checking, cross checking, and quality control.

A systems engineering methodology is almost vital for large-scale projects because the success of such projects depends upon a strong systems approach to integrate diverse elements into a harmonious whole[2, p. 2]. It is also vital to proper project management. The steps of a systems engineering methodology are generally presented in the context of a system life-cycle. A life-cycle is a logical evolutionary flow of what has to be done for the duration of the project.

Participants in the Systems Engineering Process

There are two basic participants involved in the systems engineering process—the problem originator and problem solver. The problem originator is the individual who has a problem that needs to be solved. Typically, the problem originator is referred to as the client, decision-maker, manager, sponsor, or problem owner[3]. The problem solver is responsible for providing the problem originator with a solution to his problem. This role is likely to be filled by a person called a consultant, analyst, or designer. The problem solver is also the methodology-user for (s)he is the one who uses the set of procedures, which may or may not be formally defined, to create an environment whereby a solution can be brought about[3]. Therefore, it is essential that the user identifies what tasks must be carried out to obtain the desired results. These tasks and the persons responsible for completing each task must be clearly defined in the organization's methodology.

Suggested Criteria for Evaluating Systems Engineering Methodologies

The criteria that were developed to evaluate a systems engineering methodology fall within five major categories: Structure, Flexibility, Accountability, Documentation, and Special Considerations of User (in this case NASA). Structure addresses the composition of the system life cycle process and its ability to accommodate simple to large-scale systems. Flexibility refers to the methodology's ability to adapt to change. The third area of interest is accountability. Accountability addresses the ability of the systems engineering methodology to ensure that proper procedures are being applied as intended and that appropriate procedures are being kept. Documentation refers to how well the methodology is written; the level of detail, clarity and ease with which it can be followed. Lastly, because all methodologies are tailored to meet an organization's particular needs, it is necessary to examine the factors that are of critical concern to that organization (in this case NASA). The criteria that were developed for each category are as follows:

1. Structure

   - Does the methodology address activities that are likely to involve engineering work such as design, construction, installation, and operation?
   - Is it structured to handle large-scale or complex systems (interacting components to achieve defined objectives)?
   - Is it structured to handle at least one component that is extensively hardware?
   - Is the methodology partitioned into clearly defined and logical phases, processes, activities, or tasks that can be used as a basis for resource allocation and events such as the start or completion of phases that can be used as milestones or decision points?

2. Flexibility

- Does the methodology accommodate systems of varying size, nature (such as utility/public sector, military, consumer products), and complexity?
- Does the methodology address ways of handling new information, feedback, or unforeseen circumstances (such as new requirements)?
- Does the methodology allow for acquisition through a variety of approaches (procurement, development, etc.)?
- Does the methodology allow maximum flexibility with time-allocation (scheduling) of resources?
- Does the methodology address ways of identifying and selecting the best human and material resources to assign or allocate to its various phases?

3. Accountability

- Does the methodology specify the documentation that is appropriate at different points during its application?
- Does the methodology provide for communication and information exchange to ensure that all participants are aware of significant project decisions and have the most up-to-date information on the project status and activities?
- Does the methodology specify an auditing or tracking procedure to ensure that it has been applied as intended?
- Does the methodology suggest a management structure to ensure that it is applied as intended?
- Does the methodology identify its intended users, class of systems, and scope of its intended applications?
- Does the methodology provide ways of addressing critical considerations such as national security, risk (environmental, evolving technologies), human safety, etc.?

4. Documentation

- Is the methodology written clearly, precisely, completely, and at a level of detail that is appropriate for its intended users? Is it a good road map?

5. Special Considerations of NASA

- Is the methodology fairly independent of organizational structure?
- Does the methodology allow for the retention of key personnel throughout the life-cycle?
- Does the methodology provide for the incorporation of requirements identified during the system analysis, design, or subsequent phases?
- Does the methodology provide tools and techniques for predicting or projecting future requirements, through the planning horizon?
- Does the methodology suggest strategies and techniques for designing and developing systems in the absence of specific requirements?
- Does the methodology provide tools and techniques (including graphics and prototyping) for communicating among individuals and various organizations or organizational units working on major systems projects?
- Does the methodology provide tools and techniques for redesigning and making major modifications to extend the useful life of a system in operation?
-

Summary

As mentioned, these criteria will be used in Phase Two of the project to evaluate other agencies' and authors' systems engineering methodologies with potential applications to NASA. They will serve as a guide and weighing mechanism for justifying our recommendation to NASA/Goddard.

References

1. Blanchard, Benjamin S. *Engineering Organization and Management.* Prentice-Hall, Inc., New Jersey. 1976.
2. Davidson, Frank Paul. *Macro-Engineering and the Future: Management Perspective.* Westview Press. 1982.
3. Keys, Paul. "A Methodology for Methodology Choice." Department of Management Systems and Sciences, University of Hull, U.K. 1987 pp. 65-76.

OMIT TO END

1989 NASA-HBCU SPACE SCIENCE AND ENGINEERING RESEARCH FORUM

List of Participants

*Mr. Hossin Abdeldayem
Department of Physics
P.O. Box 1268
Alabama A&M University
Normal, AL 35762
205-851-5306

Dr. A. A. Adeyiga
Department of Engineering
Hampton University
Hampton, VA 23668
804-727-5589

Dr. M. D. Aggarwal
Department of Physics
Alabama A&M University
Normal, AL 35762
205-851-5306

Dr. Selina Ahmed
Dept. of Home Economics
Texas Southern University
3100 Cleburne
Houston, TX 77004
713-527-7636

*Mr. Warsame Ali
Dept. of Electrical Engineering
Prarie View A&M University
Prarie View, TX 77446

Dr. Ates Akyurtlu
Department of Engineering
Hampton University
Hampton, VA 23668
804-727-5599

Mr. Keith Allen
Department of Physics
Alabama A&M University
Normal, AL 35762
205-851-5306

Dr. Lew Allen
Director
Jet Propulsion Laboratory
4800 Oak Grove Drive
Pasadena, CA 91109
818-354-3407

*Mr. Charles Alleyne
Howard University
8750 Georgia Avenue, #1416B
Silver Springs, MD 20910

Dr. Sidney Alterescu
National Aeronautics and Space Administration
Code 702
Goddard Space Flight Center
Greenbelt, MD 20785
301-286-6705

*Mr. Ololo Anthony
Alabama A&M University
Normal, AL 35762
205-851-5306

Mr. Ray J. Arnold
Director
Communications and Information Systems Division
NASA Headquarters
600 Independence Avenue, NW
Washington, DC 20546
202-453-1510

Dr. Joseph D. Atkinson, Jr.
Chief, Equal Opportunity Programs Office
Johnson Space Flight Center
NASA Road 1
Houston, TX 77058
713-483-4831

*Mr. Samuel Awonigi
Florida State University
Tallahassee, FL 32307

*Student

Dr. Annas Aytch
Department of Mathematics
Alabama A&M University
Normal, AL 35762
205-851-5316

*Ms. Virginia Bailey
Jackson State University
Jackson, MS 39217

Mr. George Baker
Xavier University of Louisiana
New Orleans, LA 70125
504-486-7411

*Ms. Linda Balew
Fisk University
1000 17th Avenue N.
Nashville, TN 37208

Dr. A. K. Batra
Department of Physics
Alabama A&M University
Normal, AL 35762
205-851-5306

Dr. Ed Bernstein
School of Engineering and Technology
Alabama A&M University
Normal, AL 35762
205-851-5581

Dr. James W. Bilbro
National Aeronautics and Space Administration
Marshall Space Flight Center
Marshall Space Flight Center, AL 35812
205-544-3467

Dr. P. C. Biswas
G.W. Carver Experiment Station
Tuskegee University
Tuskegee, AL 36088
205-727-8124

*Ms. Jean A. Blake
Alabama A&M University
Normal, AL 35762

Dr. R. R. Bommareddi
Department of Physics
Alabama A&M University
Normal, AL 35762
205-851-5306

Dr. C. K. Bonsi
G.W. Carver Experiment Station
Tuskegee University
Tuskegee, AL 36088
205-727-8124

*Mr. Raymond Bosk
Alabama A&M University
Normal, AL 35762
205-851-5306

Dr. Kofi Bota
Department of Mathematical and Computer Sciences
Clark-Atlanta University
223 James P. Brawley Dr.
Atlanta, GA 30314-4391
404-681-0257

Dr. Ronald D. Boyd, Sr.
Department of Mechanical Engineering
P.O. Box 397
Prairie View A&M University
Prairie View, TX 77446
409-857-3311

Dr. Sylvia T. Bozeman
Department of Mathematics
P.O. Box 953
Spelman College
Atlanta, GA 30314
404-681-3643 ext. 504

*Mr. Vincent Brackett
Department of Engineering
Hampton University
Hampton, VA 23668
804-727-5593

Dr. Eugene Brams
Agricultural Research Center
College of Applied Sciences
P.O. Box U
Prairie View A&M University
Prairie View, TX 77446-2886
409-857-4012

*Ms. Alfreda Branch
Hampton University
Hampton, VA 23668

Mr. William V. Brewer
Department of Technology
Jackson State University
P.O. Box 18480
Jackson, MS 39217-0880
601-968-2121

*Mr. Chandra Britt
Spelman College
350 Spelman Lane
Atlanta, GA 30314
404-681-3643

Gen. Elmer T. Brooks
Acting Deputy Associate Administrator
for Management
NASA Headquarters
400 Maryland Ave., SW
Washington, DC 20546
202-453-2870

Dr. Taft Broome
Howard University
Washington, DC 20059
202-636-7737

*Mr. Christopher L. Brown
Morgan State University
Cold Spring Ln. & Hillen Rd.
Baltimore, MD 21239
301-444-3333

Dr. Rather Brown
Director
Minority Access to Research Careers
Alabama A&M University
Normal, AL 35762
205-851-5329

*Mr. William G. Bryant
Alabama A&M University
Normal, AL 35762

Dr. Warren W. Buck
Department of Physics
Hampton University
Hampton, VA 23668
804-727-5277

*Mr. Ian Bullock
Manufacturing Engineering Department
Central State University
Wilberforce, OH 45384
513-376-6435

*Ms. Audrey Burden
Alabama A&M University
Normal, AL 35762

Dr. A. Burger
Physics Department
Fisk University
P.O. Box 15
Nashville, TN 37208
615-329-8555

Dr. Michael R. Busby
The Center of Excellence in Information Systems
Tennessee State University
330 10th Avenue North, Suite 265
Nashville, TN 37203-3401
615-320-3432

*Mr. Michael Bush
Chemical Engineering Department
Tuskegee University
Tuskegee, AL 36088
205-727-8355

Dr. Beatriz Cardelino
D.E. Milligan Science Research Institute
Atlanta University Center
440 Westview Dr.
Atlanta, GA 30310
404-523-5150

*Mr. Dewayne F. Carr
3660 Linvingston Rd.
Jackson, MS 39217

Dr. P. Chandra Sekhar
Department of Physics
Alabama A&M University
Normal, AL 35762
205-851-5306

Dr. Ki Joon Chang
Department of Chemistry
Alabama A&M University
P.O. Box 176
Normal, AL 35762
205-851-5350

Dr. Charles R. Chappell
Associate Director for Science
NASA/MSFC/DS01
Marshall Space Flight Center, AL 35812
205-544-3033

Ms. Jo Ann Charleston
National Aeronautics and Space Administration
Lewis Research Center
21000 Brookpark Road
Cleveland, OH 44135
216-433-2957

Dr. Joseph Chi, Chairman
Department of Mechanical Engineering
University of the District of Columbia
4200 Connecticut Ave., NW
Washington, DC 20008
202-282-7550

*Ms. Karleen A. Chin
Morgan State University
Cold Spring Ln. & Hillen Rd.
Baltimore, MD 21239

*Mr. Young Soo Choi
Hampton University
Hampton, VA 23668

Dr. Raj Chowdhary
Department of Physics and Astronomy
Howard University
Washington, DC 20059
202-636-6592

Dr. Michael D. Christensen
Deputy Assistant Director, HQ Operations
NASA Headquarters
400 Maryland Avenue, SW
Washington, DC 20546
202-453-1800

Ms. Marian Christmon
Fisk University
1000 17th Avenue N.
Nashville, TN 37208
615-329-8555

Mr. Clyde Christopher
Computer Science
Jackson State University
1400 J.R. Lynch Street
Jackson, MS 39217
601-968-2105

*Mr. Y. C. Chu
12029 Veirs Mill Rd. - #202
Whaton, MD 20906

Mr. Kunar P. Chunduru
Department of Physics
Alabama A&M University
Normal, AL 35762
205-851-5306

Mr. Johnnie Clark
NASA/MSFC
Marshall Space Flight Center, AL 35812
205-544-2799

Dr. Louis P. Clark
Senior Staff Engineer
NASA HQ - Code QR
600 Independence Avenue
Washington, DC 20546
202-453-2647

Ms. Sheila Cloud
NASA/Marshall Space Flight Center
Marshall Space Flight Center, AL 35812
205-544-0024

Dr. Dale L. Compton
Deputy Director
Ames Research Center
Mail Stop 200-2
Moffett Field, CA 94035
415-965-5000

*Mr. Randolph Copeland
Department of Physics and Astronomy
Howard University
Washington, DC 20059
202-636-6592

*Mr. Randy Copeland
Virginia State University
Petersburg, VA 23803

*Ms. Pauline V. Cornish
Texas Southern University
3100 Cleburne
Houston, TX 77004

*Mr. Trevor Correia
Department of Physics and Astronomy
Howard University
Washington, DC 20059
202-636-6592

Ms. Ernestine Cothran
University Affairs Officer
NASA/MSFC
Marshall Space Flight Center, AL 35812
205-544-0649

*Ms. Amanda Cox
Texas Southern University
3100 Cleburne
Houston, TX 77004

Dr. Andre D. Cropper
School of Technology
Norfolk State University
2401 Corprew Av.
Norfolk, VA 23504
804-623-8670

*Mr. Michael Curley
4110 Triana Blvd.
Huntsville, AL 35805

Ms. Janice Daniels
Chemistry Department
Alabama A&M University
Normal, AL 35762
205-851-5350

*Mr. Robert C. Daniels
Texas Southern University
3100 Cleburne
Houston, TX 77004
713-527-7003

Dr. James C. Davenport
Virginia State University
Petersburg, VA 23803
804-524-5913

*Ms. Dominique C. David
Fisk University
1000 17th Avenue N.
Nashville, TN 37208

Dr. Bruce E. Davis
Center for Spatial Data Research and Applications
Jackson State University
1400 J. R. Lynch St.
P.O. Box 18739
Jackson, MS 39217
601-968-2121

*Mr. David Davis
Howard University
3707 Clairton Dr.
Mitch, MD 20716

*Ms. Francine Davis
Virginia State University
P.O. Box 42
Petersburg, VA 23803

*Mr. Michael R. Davis
Virginia State University
P.O. Box 358
Petersburg, VA 23803
804-524-5913

*Mr. Derrick Dean
Chemistry Department
Tuskegee University
Tuskegee, AL 36088
205-727-8833

Mr. J. Albert Diggs
Director, Equal Opportunity Program Office
NASA Kennedy Space Center
Kennedy Space Center, FL 32899
407-867-3382

Ms. Barbara L. Diggs
NASA Kennedy Space Center
Kennedy Space Center, FL 32899
407-867-3382

*Mr. C. T. Diggs
NASA Kennedy Space Center
Kennedy Space Center, FL 32899
407-867-3382

*Mr. D. Demond Diggs
NASA Kennedy Space Center
Kennedy Space Center, FL 32899
407-867-3382

Mr. Mostafa Dukhanian
Department of Physics
Alabama A&M University
Normal, AL 35762
205-851-5306

Dr. Julian Earls
Chief, Health, Safety and Security Division
MS 21-8
21000 Brookpark Road
Cleveland, OH 44135
216-433-3014

Mr. J. L. Early
Florida A&M University
Tallahassee, FL 32307

Dr. Norris Allen Edney, Director
Division of Arts and Sciences
Alcorn State University
P.O. Box 960
Lorman, MS 39096
601-877-2251

*Mr. Greg Elliott
P.O. Box 18739
Jackson State University
Jackson, MS 39217

*Mr. Kuah Kah Eng
Tennessee State University
944 21st Avenue N. - Apt. 604
Nashville, TN 37208

*Mr. Daniel Ephraim
Mathematics/Computer Science
Clark-Atlanta University
P.O. Box 102
240 James P. Brawley Dr.
Atlanta, GA 30314

Mr. Kyle Fairchild
Manager for Technology and Enterprise
NASA-Johnson Space Center
Houston, TX 77058
713-483-3111

Dr. Etta Falconer
Spelman College
350 Spelman Lane
Atlanta, GA 30314
404-681-3643

Dr. Usamah Farrukh
Department of Engineering
Hampton University
Hampton, VA 23668
804-727-5593

Ms. Nancy Faulkner
Manufacturing Engineering Department
Central State University
Wilberforce, OH 45384
513-376-6435

Dr. Leonard Fisher, Jr.
Lawrence Livermore National Laboratory
L-Code 610
P.O. Box 5500
Livermore, CA 94551-0610
415-423-0192

Dr. Tom Fogarty
Hampton University
P.O. Box 4593
Hampton, VA 23668
804-727-5000

Mr. Robert L. Ford
Southern University
Baton Rouge, LA 70807
504-771-2011

Mr. Paul Forte, Jr.
Administrative Coordinator
JPL Initiative on HBCUs
4800 Oak Grove Drive
Pasadena, CA 91109-8099

Dr. Donald O. Frazier
Space Science Lab NASA/MSFC
Marshall Space Flight Center, AL 35812
205-544-7825

Dr. Yvonne B. Freeman
Manager, Minority University Programs
Equal Opportunity Programs/HQ
Code U
400 Maryland Avenue, SW
Washington, DC 20546
202-453-2171

Dr. John Fuller
Electrical Engineering Department
Prairie View A&M University
Prairie View, TX 77446
409-857-3923

Dr. Richard A. Galle
Mail Code HA40
Stennis Space Center, MS 39529
601-688-1931

*Ms. Audrey Gates
Department of Systems and Computer Science
Howard University
Washington, DC 20059
202-636-6585

Dr. M. C. George
Department of Physics
Alabama A&M University
Normal, AL 35762
205-851-5305

Dr. Stephen J. Gewirtz
Morgan State University
Cold Spring Ln. & Hillen Rd.
Baltimore, MD 21239
301-444-3405

*Mr. A. Ghosh
Mechanical Engineering Department
Tuskegee University
Tuskegee, AL 36088
205-727-8918

Mr. Ray L. Gilbert
B 100 Code U
NASA Headquarters
Washington, DC 20546
202-453–2107

Dr. Tepper L. Gill
Department of Systems and Computer Science
Howard University
Washington, DC 20059
202-636-6585

Mr. Isaac Gillam
Senior Vice President
OAO Corporation
110 South Arroyo Blvd.
Pasadena, CA 91105
818-354-8049

*Ms. Ruth Gilliam
Morgan State University
Cold Spring Ln. & Hillen Rd.
Baltimore, MD 21239
301-444-3405

*Mr. Victor A. Glasgow
Howard University
Washington, DC 20059

Ms. Sherryl Goffer
Director, University Relations
Alabama A&M University
Normal, AL 35762
205-851-5230

*Mr. Marquer Griffin
Jackson State University
1400 J. R. Lynch St.
Jackson, MS 39217
601-968-2144

Dr. William A. Grissom
Manufacturing Engineering Department
Central State University
Wilberforce, OH 45384
513-376-6435

Dr. Naidu Gudivada
Department of Computer Science
Jackson State University
Jackson, MS 39217
601-968-2105

Dr. M. Gunasekaran
Dept. of Biology
Fisk University
Nashville, TN 37203
615-329-8555

*Ms. Lori Ann Guy
Spelman College
P.O. Box 929
350 Spelman Lane
Atlanta, GA 30314

*Mr. Bobby Hall
Jackson State University
433 Cally #A8
Jackson, MS 39217

Ms. Gloria G. Hall
EO Officer
Ames Research Center
Equal Opportunity Programs Office
Mail Stop 241-7
Moffet Field, CA 94035
415-694-5626

Dr. John Hall
Milligan Science Research Institute
Atlanta University Center
440 Westview Dr., SW
Atlanta, GA 30310
404-523-5150

Ms. Oceola S. Hall
Director, Discrimination Complaints Division
NASA HQ - Code UC
Office of Equal Opportunity Programs
400 Maryland Avenue, SW
Washington, DC 20546
202-453-2180

Dr. Joshua B. Halpern
Chemistry Department
Howard University
Washington, DC 20059
202-636-6895

Prof. Ernest C. Hammond, Jr.
Dept. of Physics
Morgan State University
Cold Spring Ln. & Hillen Rd.
Baltimore, MD 21239
301-444-3405

Dr. Kwang S. Han
Department of Physics
Hampton University
Hampton, VA 23668
804-727-5277

*Mr. A. Handoo
Mechanical Engineering Department
Tuskegee University
Tuskegee, AL 36088
205-727-8918

Mr. A. Haquiz
Mechanical Engineering Department
Tuskegee University
Tuskegee, AL 36088
205-727-8918

Ms. Amanda Harris
NASA/MSFC
Marshall Space Flight Center, Al 35812
205-544-7381

Dr. Leonard A. Harris
Chief Engineer for Aeronautics
and Space Technology
NASA HQ - Office of Aeronautics
and Space Technology
Code R
600 Independence Avenue, SW
Washington, DC 20546
202-453-2727

Dr. William H. Harris
President
Texas Southern University
Houston, TX 77004
713-527-7036

Dr. Linda Hayden
University of the District of Columbia
Washington, DC 20008
202-282-7550

*Mr. Anthony Helm
Virginia State University
P.O. Box 42
Petersburg, VA 23803
804-520-6152

Mr. Arthur Henderson
NASA/MSFC
Marshall Space Flight Center, AL 35812
205-544-2577

Dr. D. Henderson
Physics Department
Fisk University
P.O. Box 15
Nashville, TN 37208
615-329-8555

Dr. George W. Henderson
Virginia State University
Box 42
Petersburg, VA 23803
804-520-6152

The Honorable Steve Hettinger
Mayor of Huntsville
Office of the Mayor
P.O. Box 308
Huntsville, AL 35804
205-532-7304

Dr. Walter A. Hill
G.W. Carver Experiment Station
Tuskegee University
Tuskegee, AL 36088
205-727-8315

Dr. Noel W. Hinners
Associate Deputy Administrator
National Aeronautics and Space Administration
400 Maryland Avenue, NW
Washington, DC 20546
202-453-1024

*Mr. Richard A. Hogg
Florida A&M University
Tallahassee, FL 32307

Mr. Carl Holden, Jr.
NASA/MSFC
Marshall Space Flight Center, AL 35758
205-544-3837

Mr. Quintanny Holifield
Biology Department
Alabama A&M University
Normal, AL 35762
205-851-5329

Dr. Lawrence R. Holland
Department of Physics
Alabama A&M University
Normal, AL 35762
205-851-5306

Mr. Paul F. Holloway
Deputy Director
Langley Research Center
Mail Stop 103A
Hampton, VA 23665
804-864-1000

*Mr. Byungsik Hong
Dept. of Physics
Hampton University
Hampton, VA 23668

Mr. J. D. Horne
Director, Executive Staff
Marshall Space Flight Center
DX01
Marshall Space Flight Center, AL 35812
205-544-1913

Dr. In Heon Hwang
Hampton University
Hampton, VA 23668
804-727-5320

*Mr. Mahdi Ibrahim
Department of Physics
Alabama A&M University
Normal, AL 35762
205-851-5306

*Mr. John S. Idasetima
Dept. of Physics
Alabama A&M University
Normal, AL 35762
205-851-5306

Dr. Daryush Ila
Department of Physics
Alabama A&M University
Normal, AL 35762
205-851-5306

*Mr. Weldon Jackson
Morehouse College
830 Westview Dr.
Atlanta, GA 30314

Dr. Shaik Jeelani
Chemistry Department
Tuskegee University
Tuskegee, AL 36088
205-727-8833

Dr. Mae C. Jemison
NASA Astronaut
NASA Johnson Space Center
Houston, TX 77058
713-483-2629

*Mr. Hemanta Jena
Department of Physics
Alabama A&M University
Normal, AL 35762
205-851-5306

Dr. Harriett G. Jenkins
Assistant Administrator for
Equal Opportunity Programs
NASA Headquarters
Office of Equal Opportunity Programs
400 Maryland Avenue, SW
Washington, DC 20546
202-453-2167

Dr. Joseph R. Jenkins
School of Engineering and Technology
Alabama A&M University
Normal, AL 35762
205-851-5581

*Mr. David Johns
Manufacturing Engineering Department
Central State University
Wilberforce, OH 45384
513-376-6435

Ms. Jewel Joiner
Coordinator, Sponsored Programs
Alabama A&M University
Normal, AL 35762
205-851-5677

Dr. Bessie Jones
Dean, School of Arts and Sciences
Alabama A&M University
Normal, AL 35762
205-851-5300

Dr. Jeanette Jones
Dept. of Biology
Alabama A&M University
Normal, AL 35762
205-851-5329

Mr. Kevin Jordan
School of Engineering and Architecture
Tuskegee University
Tuskegee, AL 36088
205-727-8970

*Mr. B. Joseph
Department of Biology
Alabama A&M University
Normal, AL 35762
205-851-5329

Dr. Purushottam Kale
Department of Biology
Alabama A&M University
Normal, AL 35762
205-851-5329

Dr. Ranjini Kale
Department of Biology
Alabama A&M University
P.O. Box 610
Normal, AL 35762
205-851-5329

*Mr. Mohammad Kalin
E.E.T. Department
Alabama A&M University
Normal, AL 35762
205-851-5581

Mr. Sher S. Kannar
Miles College
P.O. Box 3800
Birmingham, AL 35208
205-923-2771

Mr. Richard J. Keegan, Jr.
Executive Assistant to the
Associate Deputy Administrator
National Aeronautics and Space Administration
400 Maryland Avenue, NW
Washington, DC 20546
202-453-1024

Dr. Kyong H. Kim
Physics Department
Hampton University
Hampton, VA 23668
804-727-5320

Dr. Carl H. Kirksey
Department of Mathematics/Computer Science
Bowie State University
Bowie, MD 20715-9465
301-464-3000

*Ms. Yvonne Knight
Chemistry Department
Tuskegee University
Tuskegee, AL 36088
205-727-8833

Dr. R. B. Lal
Department of Physics
Alabama A&M University
P.O. Box 71
Normal, AL 35762
205-851-5306

*Mr. Carlos Lara
Alabama A&M University
Normal, AL 35762

Mr. Robert F. Lawrence
Chief, Office of Equal Opportunity Programs
NASA Lewis Research Center
21000 Brookpark Road
MS 500-311
Cleveland, OH 44135
216-433-2323

Dr. Robert Leflore
ARCC
Jackson State University
P.O. Box 18769
Jackson, MS 39217
601-968-2332

Dr. Martin H. Leipold
Manager of HBCU Programs
Jet Propulsion Laboratory
4800 Oak Grove Drive
Pasadena, CA 91109
818-354-3931

*Ms. Janice Lewis
Alabama A&M University
Normal, AL 35762

Dr. Feiyue Li
Howard University
Washington, DC 20059
202-636-6100

Dr. G. S. Liaw
Civil Engineering Department
Alabama A&M University
Normal, AL 35762
205-851-5581

Dr. Phil Loretan
GWC Agricultural Expt. Station
Farm Mechanization Bldg., Room 100
Tuskegee University
Tuskegee, AL 36088
205-727-8315

Dr. Steven Lukefahr
Food Science and Animal Industries
Alabama A&M University
P.O. Box 264
Normal, AL 35762
205-851-5445

Mr. W. I. Bill Lupton
Jackson State University
1400 J. R. Lynch St.
Jackson, MS 39217
601-968-2121

*Mr. Gratian Macharaga
Department of Physics
Alabama A&M University
Normal, AL 35762
205-851-5306

Dr. Anthony B. Maddox
MassPep, Inc.
P.O. Box 1081
Waltham, MA 02254
617-647-0042

Ms. Renee Smith-Maddox
MassPep, Inc.
P.O. Box 1081
Waltham, MA 02254
617-647-0042

Dr. Abayomi J. Ajayi-Majebi
Manufacturing Engineering Department
Central State University
Wilberforce, OH 45384
513-376-6435

Mr. Sal Majied
Manager, Advanced Information Systems
The BDM Corporation
7915 Jones Branch Drive
McLean, VA 22102
703-848-5000

Dr. Carl Harris Marbury
President
Alabama A&M University
Normal, AL 35762
205-851-5230

Dr. Benjamin Martin
Spelman College
350 Spelman Lane
Atlanta, GA 30314
404-681-3643

*Mr. Mark Martin
Department of Mechanical Engineering
Prairie View A&M University
Prairie View, TX 77446
409-857-4023

*Mr. Edwin Martinez
GWC Agricultural Experimental Station
Tuskegee University
Tuskegee, AL 36088
205-727-8124

Dr. Samuel E. Massenberg
Head, University Affairs Office
NASA Langley Research Center
MS 105A
Hampton, VA 23665
804-865-2188

*Mr. Khin Maung Maung
Department of Physics
Hampton University
Hampton, VA 23668
804-727-5277

C-7

Mr. M.Mayo

Mr. P. Mbuthia
Biology Department
Alabama A&M University
Normal, AL 35762
205-851-5329

Dr. Caldwell McCoy, Jr.
Deputy Director
Communications and Information Systems Division
NASA Headquarters
600 Independence Avenue, SW
Washington, DC 20546
202-453-1495

Dr. Frank B. McDonald
Associate Director/Chief Scientist
Goddard Space Flight Center
Code 100 - Bldg. 8/Room 650
Greenbelt, MD 20785
301-286-8936

Ms. Sherri McGee
NASA Headquarters
University Programs Branch
Educational Affairs Division
Code XEU
Washington, DC 20546
202-453-8344

Ms. Cherryl McGhee
Manufacturing Engineering Department
Central State University
Wilberforce, OH 45384
513-376-6435

Dr. Saundra Y. McGuire
Department of Chemistry
Cornell University
P.O. Box 354
Ithaca, NY 14850
607-255-6121

Dr. Stephen S. McGuire
Cornell University
5151 Upson Hall
Ithaca, NY 14853
607-255-7425

Dr. Negash Medhin
Department of Mathematics
Clark-Atlanta University
Atlanta, GA 30314
404-681-0251

Mr. Dillard Menchan
Equal Opportunity Programs Manager
NASA/Goddard Space Flight Center
Equal Opportunity Programs Office
Greenbelt Road
Greenbelt, MD 20771
202-824-2698

*Mr. Alan Miahnari
Department of Physics
Alabama A&M University
Normal, AL 35762
205-851-5306

*Ms. Monique Michaux
Texas Southern University
3100 Cleburne Avenue
Houston, TX 77004
713-527-7003

Dr. Ronald E. Mickens
Clark-Atlanta University
P.O. Box 306
Atlanta, GA 30314
404-653-8662

*Ms. Marjorie Miller
Fisk University
1000 17th Avenue N.
Nashville, TN 37208
615-329-8555

Mr. Mehdi Moghbel
Department of Physics
Alabama A&M University
Normal, AL 35762
205-851-5306

Mr. Peter M. Molton
Battelle K2-12
Pacific Northwest Laboratories
P.O. Box 999
Richland, WA 99352

Dr. DeLester Monk, Jr.
Howard University
2300 6th Street, NW
Washington, DC 20059
202-636-6100

Dr. Francis J. Montegani
Chief, Office of University Affairs
NASA Lewis Research Center
MS 3-7
21000 Brookpark Road
Cleveland, OH 44135
216-433-2956

Dr. Oscar Montgomery
Director, Office of Government Relations
Alabama A&M University
Normal, AL 35762
205-851-5675

Dr. S. Morgan
Physics Department
Fisk University
P.O. Box 15
Nashville, TN 37208
615-329-8555

Dr. Carole Morning
Project PRESERVE
Xavier University of New Orleans
7325 Palmetto Street
New Orleans, LA 70125
504-486-7411

Dr. Carlton Morris
GWC Agricultural Expt. Station
Tuskegee University
Tuskegee, AL 36088
205-727-8315

Mr. Desmond Mortley
204 Farm Mech. Building
Tuskegee University
Tuskegee, AL 36088
205-727-8315

Dr. S. R. Murty
Alabama A&M University
P.O. Box 47
Normal, AL 35762
205-851-5581

*Mr. Duc M. Ngo
Department of Physics
Hampton University
Hampton, VA 23668
804-727-5277

*Mr. Quoc A. Nguyen
Howard University
Washington, DC 20059

Ms. Anne Nissen
Gallaudet University
Experimental Programs Off Campus
Kendall Green
800 Florida University, NE
Washington, DC 20002
202-651-5000

Dr. James Nixon
City College of New York
140th Street & Convent Avenue
New York, NY 10031

Mr. Gregory Odom
Physics Department
Florida A&M University
Tallahassee, FL 32307
904-599-3470

Dr. Cyriacus Ogbuhei
GWC Agricultural Experimental Station
Tuskegee University
Tuskegee, AL 36088
205-727-8315

Dr. Hideo Okabe
Chemistry Department
Howard University
Washington, DC 20059
202-636-6100

Dr. Frederick Oliver
Morgan State University
Cold Spring Ln. & Hillen Rd.
Baltimore, MD 21239
301-444-3333

*Mr. Ronald C. Oliver
5415 Oakwood Rd.
Huntsville, AL 35896

*Mr. Sawandi Olugbala
1130 Cleary St.
Jackson, MS 39217

*Mr. Chi Onuoha
Plant and Soil Science
Alabama A&M University
Normal, AL 35762
205-851-5785

*Mr. Albert Osei
3887 Oakwood Avenue
Huntsville, AL 35816

*Mr. Samuel A. Oyekenu
Department of Physics
Alabama A&M University
Normal, AL 35762
205-851-5306

Dr. Sunil K. Pancholy
Research Director
Florida A&M University
Tallahassee, FL 32307
904-599-3225

*Mr. Osborne C. Parchment
Morgan State University
P.O. Box 2178
Wheaton, MD 20902
301-444-3405

Mr. Keith S. Parker
UCLA
1103 Ueberroth Building
405 Hilgard Avenue
Los Angeles, CA 90024

Dr. Larry D. Parks
National Aeronautics and Space Administration
Science and Technology Department
Code HA41
Stennis Space Center, MS 39529
601-688-2211

Dr. Arthur S. Paul
Department of Systems and Computer Science
Howard University
Washington, DC 20059
202-636-6595

Ms. Hazelyn Patterson
NASA/MSFC
Marshall Space Flight Center, AL 35812
205-544-2583

*Mr. Ronald B. Paulus
1705 Laverne Dr.
Huntsville, AL 35816

*Mr. Stephen D. Pearson
Dept. of Physics
Alabama A&M University
Normal, AL 35762
205-851-5306

Mr. Benjamin Penn
Space Science Lab
NASA/MSFC
Marshall Space Flight Center, AL 35812
205-544-7809

*Ms. Samara Perdue
Queen Street Dorm - Rm. 254
Hampton University
Hampton, VA 23668
804-727-5589

*Mr. Gerard M. Perera
Department of Physics
Alabama A&M University
Normal, AL 35762
205-851-5306

*Mr. Cortes L. Perry
P.O. Box 4325
Huntsville, AL 35815

Mr. Wayne D. Perry
Prairie View A&M University
P.O. Box 2415
Prairie View, TX 77446
409-857-4510

Mr. Burnett W. Peters, Jr.
Equal Opportunity Programs Manager
Langley Research Center
Hampton, VA 23665
804-865-3487

*Mr. Kevin Peters
Morgan State University
Cold Spring Ln. & Hillen Rd.
Baltimore, MD 21239
301-444-3405

*Ms. Maggie Linton-Petza
Morgan State University
Cold Spring Ln. & Hillen Rd.
Baltimore, MD 21239
301-444-3405

Dr. Delbert Philpott
Ames Research Center
Mail Stop 239-14
Moffett Field, CA 94035
415-965-5000

Dr. Ralph P. Prince
NASA MD-RES
J. F. Kennedy Research Center, FL 32899
305-853-5153

Dr. O. P. Puri
Clark-Atlanta University
240 J. P. Brawley Dr., SW
Atlanta, GA 30314
404-681-3080

*Ms. Brenda J. Queen
Morgan State University
Cold Spring Ln. & Hillen Rd.
Baltimore, MD 21239
301-444-3405

Dr. Joseph L. Randall
NASA/MSFC
EB 31
Marshall Space Flight Center, AL 35812
205-544-3282

*Mr. Partha Rangaswamy
School of Engineering and Architecture
Tuskegee University
P.O. Box 959
Tuskegee, AL 36088
205-727-8355

Dr. Sistla M. Rao
Department of Physics
Alabama A&M University
Normal, AL 35762
205-851-5306

Mr. S. C. Subba Rao
Lincoln University
Lincoln University, PA 19352
215-932-8300

Dr. Pradosh K. Ray
Mechanical Engineering Department
Tuskegee University
Tuskegee, AL 36088
205-727-8918

Mr. William Raymond
Lawrence Livermore National Laboratory
Livermore, CA 94551-0610
415-423-0192

Dr. Anugu S. Reddy
Selma University
1501 Lapsley St.
Selma, AL 36701
205-872-2533

Dr. Bandi Jagannadha Reddy
Bowie State University
Bowie, MD 20715
301-464-3000

Dr. Phillip Redrick
Director, Institutional Advancement
Alabama A&M University
Normal, AL 35762
205-851-5755

Dr. Robert Reiss
Department of Mechanical Engineering
Howard University
Washington, DC 20059
202-636-6608

Dr. Howard Renfro
Special Assistant to the Director
NASA/Johnson Space Center
Houston, TX 77586
713-483-3111

*Ms. Margaret Reynolds
Jackson State University
Jackson, MS 39217
601-968-2121

Mr. James Rice
Equal Opportunity Officer
NASA/MSFC - CE01
Marshall Space Flight Center, AL 35812
205-544-4927

*Mr. Muhammad Rizvi
Alcorn State University
Lorman, MS 39096
601-877-2251

Ms. Audrey Robinson
NASA/MSFC
Marshall Space Flight Center, AL 35812
205-544-2732

Mr. Gilbert Rochon
Remote Sensing UGIS Lab
Dillard University
New Orleans, LA 70122
504-283-8822

Dr. Decatur B. Rogers, Dean
School of Engineering and Technology
Tennessee State University
3500 John Merritt Blvd.
Nashville, TN 37209-1561
615-320-3550

*Ms. Zelma Rozier
Jackson State University
Jackson, MS 39217
601-968-2121

Mr. Jesse R. Rubalcaba
Manager,Jet Propulsion Laboratory
Affirmative Action Program Office
4800 Oak Grove Dr. - MS 114-121
Pasadena, CA 91109
818-354-6400

Dr. Rudolph C. Ruff
NASA/MFSC
JA 63
Marshall Space Flight Center, AL 35812
205-544-1990

*Mr. Christopher M. Ruffin
Morgan State University
Cold Spring Ln. & Hillen Rd.
Baltimore, MD 21239
301-444-3405

Mr. David Rupert
DOE/Oak Ridge National Laboratory
P.O. Box 2008
Oak Ridge, TN 40402
615-574-0762

Mr. Joseph L. Russell
Alcorn State University
Lorman, MS 39096
601-877-2251

Dr. Elias G. Abu-Saba
Department of Architecture and Engineering
North Carolina A&T State University
McNair Building, Room 455
Greensboro, NC 27411
919-334-7940

Dr. M. Sambandham
Mathematics Department
Morehouse College
Atlanta, GA 30314
404-681-2800

*Ms. Serita Sanders
Dept. of Electrical Engineering
Howard University
Washington, DC 20059
202-636-6585

Ms. Yvonne D. Sanders
Department of Physics
Alabama A&M University
Normal, AL 35762
205-851-5311

Mr. Walter J. Sapp
Dept. of Biology
Tuskegee University
Tuskegee, AL 36088
205-727-8822

*Mr. Craig Scott
School of Engineering
Material Science Center
Howard University
Washington, DC 20059
202-636-6618

Dr. Jennie Sethna
Director, Dual Degree Engineering and
Computer Science Program
Wilberforce University
226 Walker Center,
Wilberforce, OH 45384
513-376-2911

Mr. Rony Shahidair
Tennessee State University
3500 John Merritt Blvd.
Nashville, TN 37209
615-320-3432

Dr. Prasanta Sharma
Natural Science Division
Miles College
P.O. Box 3800
Birmingham, AL 35208
205-923-2771

Dr. Earl D. Shaw
AT&T Bell Laboratories
Room 1E330
600 Mountain Avenue
Murray Hill, NJ 07974
201-582-5403

Ms. Angela Shields
NASA/MSFC
Marshall Space Flight Center, AL 35812
205-544-2793

Dr. John Shoosmith
NASA Langley Research Center
Hampton University
Hampton, VA 23668
804-864-1000

Mr. Roya Siddiqi
Tennessee State University
Nashville, TN 37209
615-320-3432

Dr. E. Silberman
Physics Department
Fisk University
P.O. Box 15
Nashville, TN 37208
615-329-8620

*Mr. Alvin Smith
Department of Mechanical Engineering
Prairie View A&M University
Prairie View, TX 77446
409-857-4023

Mr. Jim Smith
Consultant, NASA Headquarters
1000 Rivermist Ct.
Brinklow, MI 20862

*Ms. Laverne Smith
Texas Southern University
3100 Cleburne Avenue
Houston, TX 77004
713-527-7004

*Ms. Sharonda D. Smith
Tennessee State University
Hale Hall
P.O. Box 309
Nashville, TN 37209
615-320-3432

*Mr. Woodrow Smith
Alabama A&M University
Normal, AL 35762

Dr. Michael Spencer
School of Engineering
Material Science Center
Howard University
Washington, DC 20059
202-636-6618

Mr. John Springer
Fisk University
Nashville, TN 37208
615-329-8621

Dr. T. Springer
Physics Department
Fisk University
P.O. Box 15
Nashville, TN 37208
615-329-8621

Dr. Shobha Sriharan
Division of Natural Sciences
Selma University
1501 Lapsley Street
Selma, AL 36701
205-872-2533

Dr. T. P. Sriharan
Division of Natural Sciences
Selma University
1501 Lapsley Street
Selma, AL 36701
205-872-2533

Dr. Sandanand Srivastava
Bowie State University
Bowie, MD 20715
301-464-3000

Dr. Mary Stanley
Department of English and Foreign Language
Alabama A&M University
Normal, AL 35762
205-851-5381

Dr. Arthur W. Stelson
Atlanta University Center
440 Westview Dr., SW
Atlanta, GA 30310
404-523-5153

Mr. Carrington H. Stewart, P.E.
NASA Johnson Space Center
Houston, TX 77058
713-483-3111

Dr. Robert E. Stickel, Jr.
D. E. Milligan Science Research Institute
Atlanta University Center, Inc.
440 Westview Dr., SW
Atlanta, GA 30310
404-523-5148

*Mr. Narvaez Stinson
Department of Physics
Alabama A&M University
Normal, AL 35762
205-851-5305

Dr. John J. Stith
Dept. of Physics
Virginia State University
P.O. Box 42
Petersburg, VA 23803
804-520-6152

Ms. Sheree D. Stovall
NASA Headquarters (Code DU)
400 Maryland Ave., SW
Washington, DC 20546
202-953-2180

Dr. Carey E. Stronach
Virginia State University
P.O. Box 358
Petersburg, VA 23803
804-520-6153

Mr. Avaine Strong
Denmark Tech.
Denmark, SC

Dr. Ellis E. Sykes
Albany State College
504 College Drive
Albany, GA 31705
912-430-4604

Dr. Bagher M. Tabibi
Department of Physics
Hampton University
Hampton, VA 23668
804-727-5277

Dr. Mahasin Tadros
Department of Biology
Alabama A&M University
P.O. Box 13
Normal, AL 35762
205-851-5329

Dr. Shawky Tadros
Department of Chemistry
Alabama A&M University
Normal, AL 35762
205-851-5350

*Mr. Mathias Teke
Tennessee State University
330 10th Avenue North
Nashville, TN 37203-3401
615-320-3432

Dr. Hendra Terutung
School of Engineering and Architecture
Tuskegee University
Tuskegee, AL 36088
205-727-8355

Dr. Sidney Tetenbaum
Department of Electrical Engineering
Tennessee State University
3500 John A. Merritt Blvd.
Nashville, TN 37209-1561
615-646-1952

Dr. James M. Thompson
Chemistry Department
Alabama A&M University
Normal, AL 35762
205-851-5350

Mr. James R. Thompson
Director, NASA/MSFC
Marshall Space Flight Center, AL 35812
205-544-1910

Dr. Arthur N. Thorpe
Howard University
Washington, DC 20059
202-636-6244

Mr. E. R. Tossie
Florida A&M University
Tallahassee, FL 32307

Dr. Tung Tsang
Department of Physics and Astronomy
Howard University
Washington, DC 20059
202-636-6244

*Mr. Roy Tucker
Physics Department
Florida A&M University
P.O. Box 981
Tallahassee, FL 32307
904-599-3470

*Mr. Jerry C. Turknett, Jr.
888 Hunting Horn Way
Evans, GA 30809

*Ms. Patricia N. Ubaike
Alabama A&M University
Normal, AL 35762

Mr. Nader Vahdat
Chemical Engineering Department
Tuskegee University
Tuskegee, AL 36088
205-727-8978

Ms. Jacqueline Van Sertima
347 Felton Avenue
Highland Park, NJ 08904
201-932-4023

Dr. Ivan Van Sertima
347 Felton Avenue
Highland Park, NJ 08904
201-932-4023

Mr. Bill Vardaman
Center for Space and Advanced Technology
500 Boulevard, South
Huntsville, AL 35801

Dr. Demetrius D. Venable
Department of Physics
Hampton University
Hampton, VA 23668
804-727-5277

Dr. P. Venkateswarlu
Department of Physics
Alabama A&M University
Normal, AL 35762
205-851-5305

Dr. M. Lucius Walker, Jr.
Office of the Dean
School of Engineering
Howard University
2300-6th Street, NW
Washington, DC 20059
202-636-6555

Dr. Reginald L. Walker
Department of Computer Science
Hampton University
Hampton, VA 23668
804-727-5552

Mr. Robert Walker
NASA/MSFC
Marshall Space Flight Center, AL 35812
205-544-4927

Mr. Scotty Walker
Biology Department
Alabama A&M University
Normal, AL 35762
205-851-5329

Dr. Jae-Ching Wang
Department of Physics
Alabama A&M University
Normal, AL 35762
205-851-5305

*Ms. Jacqueline Ware
Morgan State University
Cold Spring Ln. & Hillen Rd.
Baltimore, MD 21239
301-444-3405

Mr. Lewin S. Warren
Deputy Assistant Director
NASA Headquarters,Equal Opportunity Programs
400 Maryland Avenue, SW
Washington, DC 20546
202-453-2171

Prof. Nazir A. Warsi
Department of Mathematical and Computer Sciences
Clark-Atlanta University
223 James P. Brawley Dr.
Atlanta, GA 30314-4391
404-523-5150

Ms. Jamesina Watson
Staff Assistant
Space Life Sciences Training Program
Florida A&M University
Tallahassee, FL 32307
904-599-3636

Dr. Walter C. Watson
Department of Physics
Alabama A&M University
Normal, AL 35762
205-851-5305

Dr. Charles A. Weatherford
Physics Department
Florida A&M University
P.O. Box 981
Tallahassee, FL 32307
904-599-3470

Mr. Charles Weaver
Assistant Operator
Florida A&M University
Tallahassee, FL 32307
904-599-3636

Mr. Paul J. Weitz
Deputy Director
NASA Johnson Space Center
Houston, TX 77586
713-483-3111

Mr. W. Ida Westbrook
Chemistry Department
Alabama A&M University
Normal, AL 35762
205-851-5350

*Mr. Stacey White
Jackson State University
Jackson, MS 39217

Dr. Donald A. Whitney
Physics Department
Hampton University
Hampton, VA 23668
804-727-5277

Dr. Alton Williams
Department of Physics
Alabama A&M University
Normal, AL 35762
205-851-5305

Dr. Carol S. Williams
Department of Biology
Tuskegee University
Tuskegee, AL 36088
205-727-8822

Dr. Willie Williams
Physics Department
Lincoln University
Lincoln University, PA 19352
215-932-8107

*Ms. Danette Willis
Electrical Engineering Department
Prairie View A&M University
Prairie View, TX 77445
409-857-3923

Dr. Leonard Wilmer
Chairman,Division of Natural Sciences
Southern University-Shreveport
3050 Martin Luther King, Jr. Dr.
Shreveport, LA 71107
318-674-3300

Dr. Bobby Wilson
Texas Southern University
3100 Cleburne
Houston, TX 77004
713-527-7004

*Ms. Melanie Wilson
Texas Southern University
3100 Cleburne Avenue
Houston, TX 77004
713-527-7004

Dr. Ray F. Wilson
Texas Southern University
3100 Cleburne St.
Houston, TX 77004
713-527-7004

*Mr. Brian Wingard
Manufacturing Engineering Department
Central State University
Wilberforce, OH 45384
513-376-6435

*Mr. D'Anthony Woods
Virginia State University
P.O. Box 358
Petersburg, VA 23803
804-520-6153

Dr. Mildred Wyatt
NASA/Goddard Space Flight Center
Equal Opportunity Programs Office
Greenbelt Road
Greenbelt, MD 20771
301-286-7913

Dr. Varona L. Wynn
Mathematics/Computer Science
Clark- Atlanta University
P.O. Box 155
240 James P. Brawley Dr.
Atlanta, GA 30314
404-523-5150

*Mr. Li Yang
Department of Physics
Alabama A&M University
Normal, AL 35762
205-851-5305

Dr. Gil Yanow
Jet Propulsion Laboratory
4800 Oak Grove Drive
Pasadena, CA 91109
818-354-7546

Dr. Art Zygielbaum
Jet Propulsion Laboratory
4800 Oak Grove Drive
Pasadena, CA 91109
818-354-7546

*Student

AUTHORS INDEX